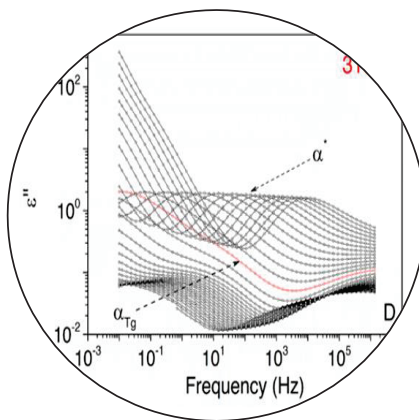
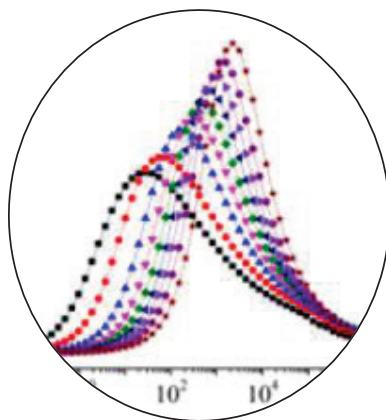




UNIVERSITAT
POLITÈCNICA
DE VALÈNCIA

DESIGN AND CHARACTERIZATION
OF POLYMERIC MATERIALS FOR
THEIR APPLICATION AS
ELECTROLYTES IN FUEL CELLS



Author:
Borja Pascual José

Supervisor:
Prof. Amparo Ribes Greus

València, June 2023



UNIVERSITAT
POLITÈCNICA
DE VALÈNCIA

Design and Characterization of Polymeric Materials for their Application as Electrolytes in Fuel Cells

June 2023

Author: Borja Pascual José

Supervisor: Prof. Amparo Ribes Greus

Acknowledgements

*The time you enjoy wasting is not
wasted time.*

Bertrand Russell

I would like to thank Prof. Amparo Ribes Greus for accepting me in her research group and allowing me to complete my PhD. We all know how cumbersome Dielectric Thermal Analysis can be. She has been a valuable source of knowledge and I could have not completed this process without her guidance.

Moreover, I would like to thank Dr. Roberto Teruel Juanes for his support and all the countless hours dedicated to our scientific discussions.

Finally, I would like to thank my family for their unconditional support during this period of my life. I will be eternally grateful.

València, 21st April 2023

Borja Pascual José.

Summary

Hydrogen or bioalcohol fuel cells are a promising technology for clean and efficient energy generation in the current attempt to reverse the severe effects caused by climate change. However, in order to achieve its general use, this technology must be optimized. Specifically, the proton exchange membrane is a crucial component to improve your overall performance. This line of research, among others, is included in most of the current national and European strategic lines with the aim of implementing these sustainable energy production systems in the near future. In this doctoral thesis, a robust and reliable procedure is presented that allows the design of proton exchange membranes through the characterization and analysis of various polymeric materials with the intention of predicting their behaviour under operating conditions. In this sense, four different types of microstructures are analysed.

In Chapter 4, two series of membranes based on sulfonated block copolymers of styrene-ethylene-butylene-styrene (SEBS) are discussed. The microstructure has been adjusted for its suitability in fuel cell applications. Subsequently, a sulfonation, UV photocrosslinking, and hybridization process are applied to the samples.

In Chapter 5, a series of polyvinyl alcohol (PVA) membranes suitably modified for their suitability as proton exchange membranes in direct methanol fuel cells (DMFC) are discussed. The analysis focuses on whether crosslinking and sulfonation using SSA improve stability and increase proton conduction in the PVA structure as initially expected. In addition, the effect of the addition of graphene oxide (GO) on the dielectric spectra, and proton conductivity is evaluated.

In Chapter 6 two series of membranes based on copolymers of poly (epichlorohydrin) (PECH) and poly (epichlorohydrin-co-ethylene oxide) (PECH-co-EO) are analysed. Both membranes are modified with 3,4,5-tris[4-(n-dodecan-1-yloxy)benzyloxy]benzoate units. The analysis focuses on the ability of these membranes to form channels, promoted by thermal orientation, which improves the charge transfer mechanisms and the proton conductivity.

In Chapter 7, the analysis of a membrane synthesized from a covalent adaptive network (CAN) is performed. The most important characteristic of this type of polymer is the presence of reversible bonds in the structure that allows them to display physical properties such as self-healing, weldability, and recyclability. These properties could improve the life cycle of proton exchange membranes. The analysis carried out includes an evaluation of the two most important temperatures from the viscoelastic point of view, that is, the glass transition (T_g) and the freezing transition temperature of the topology (T_v), and their impact on the proton conductivity.

As a result of this study, a methodology is developed to analyse various polymeric membranes with different microstructures by means of Dielectric Thermal Analysis (DETA). Consequently, the study of the dielectric properties, in terms of the complex permittivity (ϵ^*), together with the analysis of the complex conductivity (σ^*), allows us to obtain information on the molecular dynamics that efficiently favour the charge transfer mechanisms. The proton conductivity (σ_{prot}) will be estimated from the dielectric data, which will allow the evaluation of the tested polymeric membranes for their application as proton exchange

membranes. Consequently, the functioning of proton exchange membranes can be optimized, and their massive implementation is promoted.

Resumen

Las pilas de combustible de hidrógeno o bioalcohol son una tecnología prometedora para la generación de energía limpia y eficiente en el intento actual de revertir los severos efectos causados por el cambio climático. No obstante, para lograr generalizar su uso, esta tecnología debe optimizarse. Concretamente, la membrana de intercambio de protones es un componente crucial para mejorar su rendimiento general. Esta línea de investigación, entre otras, está incluida en la mayoría de las actuales líneas estratégicas nacionales y europeas con el objetivo de implantar estos sistemas de producción de energía sostenibles en un futuro próximo. En la presente tesis doctoral se presenta un procedimiento robusto y fiable que permite el diseño de membranas de intercambio de protones mediante la caracterización y análisis de varios materiales poliméricos con la intención de predecir su comportamiento en condiciones operativas. En ese sentido, se analizan cuatro tipos diferentes de microestructuras.

En el Capítulo 4 se analizan dos series de membranas basadas en copolímeros en bloque sulfonados de estireno-etileno-butileno-estireno (SEBS). La microestructura se ha ajustado para su idoneidad en aplicaciones de pilas de combustible. Posteriormente, se aplica a las muestras un proceso de sulfonación, fotorreticulación UV e hibridación.

En el Capítulo 5 se analiza una serie de membranas de poli(alcohol vinílico) (PVA) convenientemente modificadas para su idoneidad como membranas de intercambio de protones en celdas de combustible de metanol directo (DMFC). El análisis se centra en si la reticulación y la sulfonación mediante el uso de SSA mejoran la estabilidad y aumentan la conducción de protones en la estructura de PVA tal y como se esperaba inicialmente. Además, se evalúa el efecto de la adición de óxido de grafeno (GO) en los espectros dieléctricos y la conductividad protónica.

En el Capítulo 6 se analizan dos series de membranas a base de copolímero de poli(epiclorhidrina) (PECH) y poli(epiclorhidrina-co-óxido de etileno) (PECH-co-EO). Ambas membranas están modificadas con unidades de 3,4,5-tris[4-(n-dodecan-1-iloxi)benciloxi]benzoato. El análisis se centra en la capacidad de estas membranas para formar canales, promovidos por la orientación térmica, lo que mejora los mecanismos de transferencia de carga y la conductividad de los protones.

En el Capítulo 7 se realiza el análisis de una membrana sintetizada a partir de una red adaptable covalente (CAN). La característica más importante de este tipo de polímeros es la presencia de enlaces reversibles en la estructura que les permite mostrar propiedades físicas como la autoreparación, la soldabilidad y la reciclabilidad. Estas propiedades podrían mejorar el ciclo de vida de las membranas de intercambio protónico. El análisis realizado incluye una evaluación de las dos temperaturas más importantes desde el punto de vista viscoelástico, es decir, la transición vítrea (T_g) y la temperatura de transición de congelación de la topología (T_v), y su impacto en la conductividad protónica.

Como resultado de este estudio, se desarrolla una metodología para analizar diversas membranas poliméricas con diferentes microestructuras mediante Análisis Térmico Dieléctrico (DETA). En consecuencia, el estudio de las propiedades dieléctricas, en términos de la permitividad compleja (ϵ^*), junto con el análisis de la conductividad compleja (σ^*), permite obtener información sobre la dinámica molecular que favorece eficientemente los mecanismos de transferen-

cia de carga. La conductividad protónica (σ_{prot}) se estimará a partir de los datos dieléctricos, lo que permitirá evaluar las membranas poliméricas ensayadas para su aplicación como membranas de intercambio protónico. En consecuencia, se puede optimizar el funcionamiento de las membranas de intercambio de protones, y se promueve su implementación masiva.

Resum

Les piles de combustible d'hidrogen o bioalcohol són una tecnologia prometedora per a la generació d'energia neta i eficient en l'intent actual de revertir els severos efectes causats pel canvi climàtic. No obstant això, per a aconseguir generalitzar el seu ús, aquesta tecnologia ha d'optimitzar-se. Concretament, la membrana d'intercanvi de protons és un component crucial per a millorar el seu rendiment general. Aquesta línia d'investigació, entre d'altres, està inclosa en la majoria de les actuals línies estratègiques nacionals i europees amb l'objectiu d'implantar aquests sistemes de producció d'energia sostenibles en un futur pròxim. En la present tesi doctoral es presenta un procediment robust i fiable que permet el disseny de membranes d'intercanvi de protons mitjançant la caracterització i anàlisi de diversos materials polimèrics amb la intenció de predir el seu comportament en condicions operatives. En aquest sentit, s'analitzen quatre tipus diferents de microestructures.

En el Capítol 4 s'analitzen dues sèries de membranes basades en copolímers en bloc sulfonats d'estiré-etilè-butilè-estiré (SEBS). La microestructura s'ha ajustat per a la seua idoneïtat en aplicacions de piles de combustible. Posteriorment, s'aplica a les mostres un procés de sulfonació, fotorreticulació UV i hibridació.

En el Capítol 5 s'analitza una sèrie de membranes de poli(alcohol vinílic) (PVA) convenientment modificades per a la seua idoneïtat com a membranes d'intercanvi de protons en una pila de combustible de metanol directe (DMFC). L'anàlisi se centra en si la reticulació i la sulfonació mitjançant l'ús de SSA milloren l'estabilitat i augmenten la conducció de protons en l'estructura de PVA tal com s'esperava inicialment. A més, s'avalua l'efecte de l'addició d'òxid de grafé (GO) en els espectres dielèctrics i la conductivitat protònica.

En el Capítol 6 s'analitzen dues sèries de membranes a base de copolímer de poli (epiclorhidrina) (PECH) i poli (epiclorhidrina-co-òxid d'etilé) (PECH-co-EO). Totes dues membranes estan modificades amb unitats de 3,4,5-tris[4-(n-dodecan-1-iloxi)benciloxi] benzoato. L'anàlisi es centra en la capacitat d'aquestes membranes per a formar canals, promoguts per l'orientació tèrmica, la qual cosa millora els mecanismes de transferència de càrrega i la conductivitat dels protons.

En el Capítol 7 es realitza l'anàlisi d'una membrana sintetitzada a partir d'una xarxa adaptable covalent (CA). La característica més important d'aquesta mena de polímers és la presència d'enllaços reversibles en l'estructura que els permet mostrar propietats físiques com l'autoreparació, la soldabilitat i la reciclabilitat. Aquestes propietats podrien millorar el cicle de vida de les membranes d'intercanvi protònic. L'anàlisi realitzada inclou una avaluació de les dues temperatures més importants des del punt de vista viscoelàstic, és a dir, la transició vítria (T_g) i la temperatura de transició de congelació de la topologia (T_v), i el seu impacte en la conductivitat protònica.

Com a resultat d'aquest estudi, es desenvolupa una metodologia per a analitzar diverses membranes polimèriques amb diferents microestructures mitjançant Anàlisi Tèrmic Dielèctric (DETA). En conseqüència, l'estudi de les propietats dielèctriques, en termes de la permitivitat complexa (ε^*), juntament amb l'anàlisi de la conductivitat complexa (σ^*), permet obtindre informació sobre la dinàmica molecular que afavoreix eficientment els mecanismes de transferència de càrrega. La conductivitat protònica (σ_{prot}) s'estimarà a partir de les dades dielèctriques,

la qual cosa permetrà avaluar les membranes polimèriques assajades per a la seua aplicació com a membranes d'intercanvi protònic. En conseqüència, es pot optimitzar el funcionament de les membranes d'intercanvi de protons, i es promou la seua implementació massiva.

Abbreviations

Symbols

$C(\omega)$	Capacitance
$D(t)$	Dielectric induction
$E(t)$	Alternating electric field
F	Helmholtz's Function
G	Gibbs Free Energy
$G(\omega)$	Conductance
H	Enthalpy
I	Intensity
K_{eq}	Equilibrium constant
M^*	Complex electric modulus
M'	Real part of the complex electric modulus
M''	Imaginary part of the complex electric modulus
P	Polarization

P_w	Power
Q	Heat
S	Entropy
$\tan \delta$	Tangent of δ
T_g	Glass transition temperature
T_v	Vogel temperature
U	Internal Energy
V	Voltage
W	Work
$\Delta\varepsilon$	Relaxation strength
ε^*	Complex permittivity
ε'	Real part of the complex permittivity
ε''	Imaginary part of the complex permittivity
$\mu_{activation}$	Activation polarization
μ_{conc}	Concentration polarization
μ_{ohm}	Ohmic polarization
$\rho^*(\omega)$	Resistivity
σ^*	Complex conductivity
σ'	Real part of the complex conductivity
σ''	Imaginary part of the complex conductivity
σ_{prot}	Proton Conductivity
τ	Relaxation time
ω	Frequency

Acronyms

AFC	Alkaline Fuel Cell
CAN	Covalent Adaptable Network
CCS	Carbon dioxide Capture and Storage
COP21	United Nations Conference against Climate Change 2015
COP27	United Nations Conference against Climate Change 2022
DEFC	Direct Ethanol Fuel Cell
DETA	Dielectric Thermal Analysis
DMFC	Direct Methanol Fuel Cell
DSC	Differential Scanning Calorimetry
EIS	Electrochemical Impedance Spectroscopy
EU	European Union
FC	Fuel Cell
FCH-JU	Fuel Cells and Hydrogen Joint Undertaking
FTIR	Fourier Transform Infrared
G20	The Group of Twenty
GHG	Greenhouse Gases
GO	Graphene Oxide
IEA	International Energy Agency
IPHE	International Association for Hydrogen and Fuel Cells in Economy
IRENA	International Renewable Energy Agency
MCFC	Molten Carbonate Fuel Cell
MEA	Membrane Electrode Assembly
MMT	Montmorillonite
PAEK	Poly arylene ether ketone
PAFC	Phosphoric Acid Fuel Cell

PANI	Polyaniline
PBI	Polybenzimidazole
PEMFC	Proton-Exchange Membrane Fuel Cell
PES	Polyethersulfone
PPSU	Poly phenylsulfone
PPy	Polypyrrole
PS	Polystyrene
PTE-HPC	Spanish Technological Platform for Hydrogen and Fuel Cells
PTFE	Polytetrafluoroethylene
PVA	Poly(Vynil Alcohol)
PVA/GO	Poly(Vynil Alcohol)/Graphene Oxide
PVA/SSA/GO	Poly(Vynil Alcohol)/Sulfosuccinic Acid/Graphene Oxide
PVC	Polyvinyl Chloride
PVP	Polyvinylpyrrolidone
SEBS	Styrene-Ethylene-Butylene-Styrene
SGO	Sulphonated Graphene Oxide
SMR	Steam Methane Reforming
SOFC	Solid Oxide Fuel Cell
SPAEK	Sulphonated Poly Arylene Ether Ketone
SPEEK	Sulphonated poly ether ether ketone
SPES	Sulphonated polyethersulphone
SSA	Sulfosuccinic Acid
sSEBS	Sulphonated Styrene-Ethylene-Butylene-Styrene
SSIP	Sharm-el-Sheikh Implementation Plan
TEM	Transmission Electron Microscopy
TGA	Thermogravimetric Analysis
TRL	Technology Readiness Levels

TTS	Time Temperature Superposition principle
UN	United Nations
VFTH	Vogel-Fulcher-Tamman-Hesse
WLF	Williams-Landel-Ferry

Contents

Summary	v
Contents	xxv
I Introduction	1
1 Motivation & aim	3
1.1 Overview	3
1.2 Aim of the thesis	11
1.3 Outline of the thesis	12
1.4 References	14
2 Fundamentals	19
2.1 Overview of Fuel Cell Technology	19
2.2 Basic Components in Proton-Exchange Membranes Fuel Cells (PEMFC). .	47
2.3 Proton-Exchange Membranes (PEM)	57
2.4 References	78
3 Characterization Techniques	93

3.1	Dielectric Thermal Analysis (DETA)	94
3.2	Fourier Transformed Infrared Spectroscopy (FTIR)	121
3.3	Thermogravimetric Analysis (TGA)	129
3.4	Differential Scanning Calorimetry (DSC)	140
3.5	Membrane characterization in Single cell test	143
3.6	References	147
II Results & Discussion		153
4 Membranes based on block copolymers		155
4.1	Introduction	156
4.2	Materials	163
4.3	Results	166
4.4	Discussion	245
4.5	Summary	277
4.6	References	279
5 Membranes based on nanocomposite & crosslinked polymers		289
5.1	Introduction	290
5.2	Materials	297
5.3	Results	300
5.4	Discussion	318
5.5	Summary	327
5.6	References	328
6 Membranes based on liquid crystals		337
6.1	Introduction	338
6.2	Materials	344
6.3	Results	346
6.4	Discussion	401
6.5	Summary	419
6.6	References	421

7	Membranes based on covalent adaptable networks	427
7.1	Introduction	428
7.2	Materials	437
7.3	Results	439
7.4	Discussion	452
7.5	Summary	464
7.6	References	466
III	Conclusions & Future work	473
8	Conclusions and future work	475
8.1	Conclusions	477
8.2	Future work	479
IV	Annexes	483
9	Dissemination of research results	485
9.1	Scientific publications indexed in JCR journals	486
9.2	Scientific Congresses	487

List of Figures

1.1	Colour code of hydrogen based on the processes used to generate it. Source: [18]	8
2.1	(A) General schematic of a fuel cell. (B) Schematic of a hydrogen PEMFC. Source: [1].	20
2.2	Applications of proton-exchange membrane fuel cells in the transport industry. Schematic of a fuel cell bus. Source: [4]	21
2.3	An example of a polarization curve.	34
2.4	An example of Tafel plot.	36
2.5	Schematic of a concentration gradient.	37
2.6	Schematic of concentration polarization processes.	38
2.7	Voltage drop in a fuel cell.	40
2.8	Polarization processes.	42
2.9	Voltage, current density and FC power.	43
2.10	Effect of temperature on the potential.	44
2.11	Cell voltage as a function of flow.	46
2.12	Exploded view of PEMFCs. Source: [4]	47
2.13	Schematic diagram of a Proton Exchange Membrane Fuel Cell (PEMFC).	48
2.14	Schematic diagram of a direct methanol fuel cell (DMFC).	52

2.15	Schematic representation of transport and crossover in DMFC.	53
2.16	Schematic representation of different transport mechanisms in DMFC . . .	56
2.17	Schematic of the different transport mechanisms. Source: [35].	58
2.18	Nafion® chemical structure.	59
2.19	Gierke's cluster network model where d is the cluster diameter and D is inter-cluster distance. Source: [39].	59
2.20	Schematic of several membrane preparation methods.	73
2.21	Complexity in the design of PEM. Operating parameters influencing the performance. Source: [4].	76
2.22	Example of a MEA deformation during swelling. Source: [116].	76
3.1	Isochronal curves for several recycled polylactides at a frequency of (Top) 10^3 Hz and (Bottom) 10^{-1} Hz. Source: [3].	94
3.2	Isothermal curves of the imaginary part (ϵ'') of the complex permittivity (ϵ^*) for several recycled polylactides. The lines are displayed in steps of 10 K from 323 to 393 K in increasing order. Source: [3].	95
3.3	Novocontrol Alpha Analyser.	97
3.4	Decomposition of the dielectric spectrum into its individual relaxation pro- cesses through the Havriliak-Negami model.	98
3.5	Molecular motions and Length scales in polymeric systems. Source:[7]. . .	98
3.6	Example of an Arrhenius plot in the low- and high-temperature region for a series of recycled polylactides. Source: [3].	107
3.7	Example of an Eyring plot for a group of recycled polylactides. Source: [3].	116
3.8	Schematic of commonly observed mechanisms in an Arrhenius plot. Source: [5].	117
3.9	Generic behaviour of temperature dependence of permittivity components recorded for an amorphous polymer with considerable ionic conductivity. Source: [5].	118
3.10	An example of the electric vector of a light wave. The alternating polarity of the electric vector is reflected in the + and - signs. Source:[27].	122
3.11	Example of an FTIR spectrum. Source:[27].	122
3.12	The electromagnetic spectrum. Source:[27].	124

3.13	FTIR spectra for the pure (M0%) and blended (M1-2%, M1-10%, M2-2%, and M2-10%) membranes.	128
3.14	Scheme of the thermogravimetric process.	129
3.15	Thermogravimetric curve (TG) and its corresponding differential curve (DTG) for a series of polysulfones membranes.	131
3.16	Example of a generalized equivalent circuit element for a single cell fuel. Source: [44].	144
3.17	The defining relation and impedance for ideal bulk electrical elements. Source: [44].	145
3.18	Example of a Bode plot Source: [40].	146
3.19	Example of a Nyquist plot. Source: [40].	147
4.1	Schematic illustration of microstructures of diblock A-b-B on increasing the volume fraction of the B block. Source: [3].	157
4.2	Chemical structure of the photocrosslinked and post-sulfonated SEBS-DVB membranes. Source: [17].	162
4.3	Synthetic route of the hybrid sulfonated SEBS membranes. Source: [41].	163
4.4	3D plot of the real (ϵ') and imaginary part (ϵ'') parts of the complex permittivity (ϵ^*) of the SEBS membrane.	168
4.5	3D plot of $\tan \delta$ and of the imaginary part (M'') of the complex electric modulus (M^*) of the SEBS membrane.	169
4.6	(Top) Eyring plot and (Bottom) Arrhenius plot of the SEBS membrane.	170
4.7	Isothermal curves of the module of the complex conductivity ($ \sigma $) for the SEBS membrane.	171
4.8	Phase angle (ϕ) and modulus of the serial impedance ($ Z_s $) of the SEBS membrane.	172
4.9	3D plot of the real (ϵ') and imaginary part (ϵ'') parts of the complex permittivity (ϵ^*) of the SEBS-DVB membrane.	174
4.10	3D plot of $\tan \delta$ and of the imaginary part (M'') of the complex electric modulus (M^*) of the SEBS-DVB membrane.	175
4.11	(Top) Eyring plot and (Bottom) Arrhenius plot of the SEBS-DVB membrane.	176

4.12 Isothermal curves of the module of the complex conductivity ($ \sigma $) for the SEBS-DVB membrane.	177
4.13 Phase angle (ϕ) and modulus of the serial impedance ($ Z_s $) of the SEBS-DVB membrane.	178
4.14 3D plot of the real (ϵ') and imaginary part (ϵ'') parts of the complex permittivity (ϵ^*) of the SEBS-DVB-15I membrane.	180
4.15 3D plot of $\tan \delta$ and of the imaginary part (M'') of the complex electric modulus (M^*) of the SEBS-DVB-15I membrane.	181
4.16 (Top) Eyring plot and (Bottom) Arrhenius plot of the SEBS-DVB-15I membrane.	182
4.17 Isothermal curves of the module of the complex conductivity ($ \sigma $) for the SEBS-DVB-15I membrane.	183
4.18 Phase angle (ϕ) and modulus of the serial impedance ($ Z_s $) of the SEBS-DVB-15I membrane.	184
4.19 3D plot of the real (ϵ') and imaginary part (ϵ'') parts of the complex permittivity (ϵ^*) of the SEBS-DVB-15I-S1 membrane.	186
4.20 3D plot of $\tan \delta$ and of the imaginary part (M'') of the complex electric modulus (M^*) of the SEBS-DVB-15I-S1 membrane.	187
4.21 (Top) Eyring plot and (Bottom) Arrhenius plot of the SEBS-DVB-15I-S1 membrane.	188
4.22 Isothermal curves of the module of the complex conductivity ($ \sigma $) for the SEBS-DVB-15I-S1 membrane.	189
4.23 Phase angle (ϕ) and modulus of the serial impedance ($ Z_s $) of the SEBS-DVB-15I-S1 membrane.	190
4.24 3D plot of the real (ϵ') and imaginary part (ϵ'') parts of the complex permittivity (ϵ^*) of the SEBS-DVB-15I-S1 membrane.	192
4.25 3D plot of $\tan \delta$ and of the imaginary part (M'') of the complex electric modulus (M^*) of the SEBS-DVB-15I-S1 membrane.	193
4.26 (Top) Eyring plot and (Bottom) Arrhenius plot of the SEBS-DVB-15I-S1 membrane.	194

4.27	Isothermal curves of the module of the complex conductivity ($ \sigma $) for the SEBS-DVB-15I-S1 membrane.	195
4.28	Phase angle (ϕ) and modulus of the serial impedance ($ Z_s $) of the SEBS-DVB-15I-S1 membrane.	196
4.29	3D plot of the real (ϵ') and imaginary part (ϵ'') parts of the complex permittivity (ϵ^*) of the SEBS-DVB-30I membrane.	198
4.30	3D plot of $\tan \delta$ and of the imaginary part (M'') of the complex electric modulus (M^*) of the SEBS-DVB-30I membrane.	199
4.31	(Top) Eyring plot and (Bottom) Arrhenius plot of the SEBS-DVB-30I membrane.	200
4.32	Isothermal curves of the module of the complex conductivity ($ \sigma $) for the SEBS-DVB-30I membrane.	201
4.33	Phase angle (ϕ) and modulus of the serial impedance ($ Z_s $) of the SEBS-DVB-30I membrane.	202
4.34	3D plot of the real (ϵ') and imaginary part (ϵ'') parts of the complex permittivity (ϵ^*) of the SEBS-DVB-30I-S1 membrane.	204
4.35	3D plot of $\tan \delta$ and of the imaginary part (M'') of the complex electric modulus (M^*) of the SEBS-DVB-30I-S1 membrane.	205
4.36	(Top) Eyring plot and (Bottom) Arrhenius plot of the SEBS-DVB-30I-S1 membrane.	206
4.37	Isothermal curves of the module of the complex conductivity ($ \sigma $) for the SEBS-DVB-30I-S1 membrane.	207
4.38	Phase angle (ϕ) and modulus of the serial impedance ($ Z_s $) of the SEBS-DVB-30I-S1 membrane.	208
4.39	3D plot of the real (ϵ') and imaginary part (ϵ'') parts of the complex permittivity (ϵ^*) of the SEBS-DVB-30I-S2 membrane.	210
4.40	3D plot of $\tan \delta$ and of the imaginary part (M'') of the complex electric modulus (M^*) of the SEBS-DVB-30I-S2 membrane.	211
4.41	(Top) Eyring plot and (Bottom) Arrhenius plot of the SEBS-DVB-30I-S2 membrane.	212

4.42	Isothermal curves of the module of the complex conductivity ($ \sigma $) for the SEBS-DVB-30I-S2 membrane.	213
4.43	Phase angle (ϕ) and modulus of the serial impedance ($ Z_s $) of the SEBS-DVB-30I-S2 membrane.	214
4.44	3D plot of the real (ϵ') and imaginary part (ϵ'') parts of the complex permittivity (ϵ^*) of the sSEBS membrane.	216
4.45	3D plot of $\tan \delta$ and of the imaginary part (M'') of the complex electric modulus (M^*) of the sSEBS membrane.	217
4.46	(Top) Eyring plot and (Bottom) Arrhenius plot of the sSEBS membrane.	218
4.47	Isothermal curves of the module of the complex conductivity ($ \sigma $) for the sSEBS membrane.	219
4.48	Phase angle (ϕ) and modulus of the serial impedance ($ Z_s $) of the sSEBS membrane.	220
4.49	3D plot of the real (ϵ') and imaginary part (ϵ'') parts of the complex permittivity (ϵ^*) of the sSEBS-Zr5 membrane.	222
4.50	3D plot of $\tan \delta$ and of the imaginary part (M'') of the complex electric modulus (M^*) of the sSEBS-Zr5 membrane.	223
4.51	(Top) Eyring plot and (Bottom) Arrhenius plot of the sSEBS-Zr5 membrane.	224
4.52	Isothermal curves of the module of the complex conductivity ($ \sigma $) for the sSEBS-Zr5 membrane.	225
4.53	Phase angle (ϕ) and modulus of the serial impedance ($ Z_s $) of the sSEBS-Zr5 membrane.	226
4.54	3D plot of the real (ϵ') and imaginary part (ϵ'') parts of the complex permittivity (ϵ^*) of the sSEBS-Zr10 membrane.	228
4.55	3D plot of $\tan \delta$ and of the imaginary part (M'') of the complex electric modulus (M^*) of the sSEBS-Zr10 membrane.	229
4.56	(Top) Eyring plot and (Bottom) Arrhenius plot of the sSEBS-Zr10 membrane.	230
4.57	Isothermal curves of the module of the complex conductivity ($ \sigma $) for the sSEBS-Zr10 membrane.	231
4.58	Phase angle (ϕ) and modulus of the serial impedance ($ Z_s $) of the sSEBS-Zr10 membrane.	232

4.59	3D plot of the real (ϵ') and imaginary part (ϵ'') parts of the complex permittivity (ϵ^*) of the sSEBS-Zr20 membrane.	234
4.60	3D plot of $\tan \delta$ and of the imaginary part (M'') of the complex electric modulus (M^*) of the sSEBS-Zr20 membrane.	235
4.61	(Top) Eyring plot and (Bottom) Arrhenius plot of the sSEBS-Zr20 membrane.	236
4.62	Isothermal curves of the module of the complex conductivity ($ \sigma $) for the sSEBS-Zr20 membrane.	237
4.63	Phase angle (ϕ) and modulus of the serial impedance ($ Z_s $) of the sSEBS-Zr20 membrane.	238
4.64	3D plot of the real (ϵ') and imaginary part (ϵ'') parts of the complex permittivity (ϵ^*) of the sSEBS-ZrZr40 membrane.	240
4.65	3D plot of $\tan \delta$ and of the imaginary part (M'') of the complex electric modulus (M^*) of the sSEBS-Zr40 membrane.	241
4.66	(Top) Eyring plot and (Bottom) Arrhenius plot of the sSEBS-Zr40 membrane.	242
4.67	Isothermal curves of the module of the complex conductivity ($ \sigma $) for the sSEBS-Zr40 membrane.	243
4.68	Phase angle (ϕ) and modulus of the serial impedance ($ Z_s $) of the sSEBS-Zr40 membrane.	244
4.69	Arrhenius map containing the β relaxation for all the photocrosslinked membranes.	246
4.70	Arrhenius map containing the α_{EB} relaxation for all the photocrosslinked membranes.	247
4.71	Arrhenius map containing the α_{PS} relaxation for all the photocrosslinked membranes.	248
4.72	Isochronal curves of ϵ'' for the β relaxation of the photocrosslinked membranes.	249
4.73	Isochronal curves of ϵ'' for the α_{EB} relaxation of the photocrosslinked membranes.	252
4.74	Isochronal curves of ϵ'' for the α_{PS} relaxation of the photocrosslinked membranes.	254
4.75	Numerically determined proton conductivity (dry) at 333 K for the photocrosslinked membranes.	257

4.76	Experimentally determined protonic conductivity at 333 K and 100% relative humidity for the photocrosslinked membranes.	258
4.77	FTIR spectra of SEBS and sulfonated SEBS (sSEBS).	259
4.78	FTIR spectra the hybrid sulfonated SEBS.	260
4.79	DSC thermogram of the 1 st heating.	261
4.80	DSC thermogram of the cooling.	262
4.81	DSC thermogram of the 2 nd heating.	263
4.82	Thermogravimetric curves of sSEBS and all hybrid sSEBS (sSEBS-Zr5, sSEBS-Zr10, sSEBS-Zr20, and sSEBS-Zr40) membranes.	264
4.83	Arrhenius map containing the β relaxation for the sulfonated SEBS (sSEBS) and all hybrid sSEBS (sSEBS-Zr5, sSEBS-Zr10, sSEBS-Zr20 and sSEBS-Zr40) membranes.	265
4.84	Arrhenius map containing the α_{EB} relaxation for the sulfonated SEBS (sSEBS) and all hybrid sSEBS (sSEBS-Zr5, sSEBS-Zr10, sSEBS-Zr20 and sSEBS-Zr40) membranes.	266
4.85	Arrhenius map containing the α_{PS} relaxation for the sulfonated SEBS (sSEBS) and all hybrid sSEBS (sSEBS-Zr5, sSEBS-Zr10, sSEBS-Zr20 and sSEBS-Zr40) membranes.	267
4.86	Isochronal curves of ϵ'' of the β relaxation relaxation for the sulfonated SEBS (sSEBS) and all hybrid SEBS (sSEBS-Zr5, sSEBS-Zr10, sSEBS-Zr20 and sSEBS-Zr40) at 1 kHz.	268
4.87	Isochronal curves of ϵ'' of the α_{EB} relaxation relaxation for the sulfonated SEBS (sSEBS) and all hybrid SEBS (sSEBS-Zr5, sSEBS-Zr10, sSEBS-Zr20 and sSEBS-Zr40) at 1 kHz.	269
4.88	Isochronal curves of ϵ'' of the α_{PS} relaxation relaxation for the sulfonated SEBS (sSEBS) and all hybrid SEBS (sSEBS-Zr5, sSEBS-Zr10, sSEBS-Zr20 and sSEBS-Zr40) at 1 kHz.	272
4.89	Through-plane protonic conductivity (dry) at 333 K for the hybrid sSEBS membranes. Source: [41].	274

4.90	Arrhenius plot of the DC conductivity (σ_{DC}) for the neat (SEBS), sulfonated (sSEBS) and hybrid (sSEBS-Zr5, sSEBS-Zr10, sSEBS-Zr20, and sSEBS-Zr40) membranes.	275
5.1	Chemical Structure of PVA: (a) fully hydrolyzed and (b) partially hydrolyzed. Source: [10].	291
5.2	Chemical structure of graphene oxide (GO) proposed by Lerf and Klinowski. Source: [20,21].	294
5.3	Chemical structure of the sulfonated graphene oxide (SGO) obtained by modification with aryl radicals. Source: [23].	296
5.4	3D plot of the real (ϵ') and imaginary part (ϵ'') parts of the complex permittivity (ϵ^*) of the M-0 membrane.	301
5.5	3D plot of $\tan \delta$ and of the imaginary part (M'') of the complex electric modulus (M^*) of the M-0 membrane.	302
5.6	(Top) Eyring plot and (Bottom) Arrhenius plot of the M-0 membrane. . .	303
5.7	Isothermal curves of the module of the complex conductivity ($ \sigma $) for the M-0 membrane.	304
5.8	Phase angle (ϕ) and modulus of the serial impedance ($ Z_s $) of the M-0 membrane.	305
5.9	3D plot of the real (ϵ') and imaginary part (ϵ'') parts of the complex permittivity (ϵ^*) of the M-05 membrane.	307
5.10	3D plot of $\tan \delta$ and of the imaginary part (M'') of the complex electric modulus (M^*) of the M-05 membrane.	308
5.11	(Top) Eyring plot and (Bottom) Arrhenius plot of the M-05 membrane. . .	309
5.12	Isothermal curves of the module of the complex conductivity ($ \sigma $) for the M-05 membrane.	310
5.13	Phase angle (ϕ) and modulus of the serial impedance ($ Z_s $) of the M-05 membrane.	311
5.14	3D plot of the real (ϵ') and imaginary part (ϵ'') parts of the complex permittivity (ϵ^*) of the M-1 membrane.	313
5.15	3D plot of $\tan \delta$ and of the imaginary part (M'') of the complex electric modulus (M^*) of the M-1 membrane.	314

5.16	(Top) Eyring plot and (Bottom) Arrhenius plot of the M-05 membrane.	315
5.17	Isothermal curves of the modulus of the complex conductivity ($ \sigma $) for the M-1 membrane.	316
5.18	Phase angle (ϕ) and modulus of the serial impedance ($ Z_s $) of the M-1 membrane.	317
5.19	Arrhenius plot of all the membranes.	318
5.20	Eyring plot of all the membranes.	319
5.21	Fourier transform infrared spectra of the membranes.	320
5.22	Superposed calorimetric (298 - 473 K) and derivative thermogravimetric (298 - 873 K) thermograms.	321
5.23	Logarithm of σ_{DC} as a function of the membrane composition and temperature, obtained from the membranes in their original (dry) state.	323
5.24	Numerical proton conductivity (σ_{Prot}) as a function of the membrane composition and temperature, obtained from the membranes in their original (dry) state.	324
5.25	Comparison of the σ_{prot} in the dry and wet states as a function of the membrane composition.	325
5.26	Scheme of the proposed contribution of the Grotthuss and vehicular proton transport.	326
6.1	Molecular structure of P(ECH-co-EO).	341
6.2	Molecular structure of the PECH40 and PECH80.	343
6.3	3D plot of the real (ϵ') and imaginary part (ϵ'') parts of the complex permittivity (ϵ^*) of the PECH40 membrane.	348
6.4	3D plot of $\tan \delta$ and of the imaginary part (M'') of the complex electric modulus (M^*) of the PECH40 membrane.	349
6.5	(Top) Eyring plot and (Bottom) Arrhenius plot of the PECH40 membrane.	350
6.6	Isothermal curves of the modulus of the complex conductivity ($ \sigma $) for the PECH40 membrane.	351
6.7	Phase angle (ϕ) and modulus of the serial impedance ($ Z_s $) of the PECH40 membrane.	352

6.8	3D plot of the real (ϵ') and imaginary part (ϵ'') parts of the complex permittivity (ϵ^*) of the PECH40-O membrane.	354
6.9	3D plot of $\tan \delta$ and of the imaginary part (M'') of the complex electric modulus (M^*) of the PECH40-O membrane.	355
6.10	(Top) Eyring plot and (Bottom) Arrhenius plot of the PECH40-O membrane.	356
6.11	Isothermal curves of the modulus of the complex conductivity ($ \sigma $) for the PECH40-O membrane.	357
6.12	Phase angle (ϕ) and modulus of the serial impedance ($ Z_s $) of the PECH40-O membrane.	358
6.13	3D plot of the real (ϵ') and imaginary part (ϵ'') parts of the complex permittivity (ϵ^*) of the PECH80 membrane.	360
6.14	3D plot of $\tan \delta$ and of the imaginary part (M'') of the complex electric modulus (M^*) of the PECH80 membrane.	361
6.15	(Top) Eyring plot and (Bottom) Arrhenius plot of the PECH80 membrane.	362
6.16	Isothermal curves of the modulus of the complex conductivity ($ \sigma $) for the PECH80 membrane.	363
6.17	Phase angle (ϕ) and modulus of the serial impedance ($ Z_s $) of the PECH80 membrane.	364
6.18	3D plot of the real (ϵ') and imaginary part (ϵ'') parts of the complex permittivity (ϵ^*) of the PECH80-O membrane.	366
6.19	3D plot of $\tan \delta$ and of the imaginary part (M'') of the complex electric modulus (M^*) of the PECH80-O membrane.	367
6.20	(Top) Eyring plot and (Bottom) Arrhenius plot of the PECH80-O membrane.	368
6.21	Isothermal curves of the modulus of the complex conductivity ($ \sigma $) for the PECH80-O membrane.	369
6.22	Phase angle (ϕ) and modulus of the serial impedance ($ Z_s $) of the PECH80-O membrane.	370
6.23	3D plot of the real (ϵ') and imaginary part (ϵ'') parts of the complex permittivity (ϵ^*) of the CP0 membrane.	372
6.24	3D plot of $\tan \delta$ and of the imaginary part (M'') of the complex electric modulus (M^*) of the CP0 membrane.	373

6.25 (Top) Eyring plot and (Bottom) Arrhenius plot of the CP0 membrane.	374
6.26 Isothermal curves of the modulus of the complex conductivity ($ \sigma $) for the CP0 membrane.	375
6.27 Phase angle (ϕ) and modulus of the serial impedance ($ Z_s $) of the CP0 membrane.	376
6.28 3D plot of the real (ϵ') and imaginary part (ϵ'') parts of the complex permittivity (ϵ^*) of the CP20 membrane.	378
6.29 3D plot of $\tan \delta$ and of the imaginary part (M'') of the complex electric modulus (M^*) of the CP20 membrane.	379
6.30 (Top) Eyring plot and (Bottom) Arrhenius plot of the CP20 membrane.	380
6.31 Isothermal curves of the modulus of the complex conductivity ($ \sigma $) for the CP20 membrane.	381
6.32 Phase angle (ϕ) and modulus of the serial impedance ($ Z_s $) of the CP20 membrane.	382
6.33 3D plot of the real (ϵ') and imaginary part (ϵ'') parts of the complex permittivity (ϵ^*) of the CP20-O membrane.	384
6.34 3D plot of $\tan \delta$ and of the imaginary part (M'') of the complex electric modulus (M^*) of the CP20-O membrane.	385
6.35 (Top) Eyring plot and (Bottom) Arrhenius plot of the CP20-O membrane.	386
6.36 Isothermal curves of the modulus of the complex conductivity ($ \sigma $) for the CP20-O membrane.	387
6.37 Phase angle (ϕ) and modulus of the serial impedance ($ Z_s $) of the CP20-O membrane.	388
6.38 3D plot of the real (ϵ') and imaginary part (ϵ'') parts of the complex permittivity (ϵ^*) of the CP40 membrane.	390
6.39 3D plot of $\tan \delta$ and of the imaginary part (M'') of the complex electric modulus (M^*) of the CP40 membrane.	391
6.40 (Top) Eyring plot and (Bottom) Arrhenius plot of the CP40 membrane.	392
6.41 Isothermal curves of the modulus of the complex conductivity ($ \sigma $) for the CP40 membrane.	393

6.42	Phase angle (ϕ) and modulus of the serial impedance ($ Z_s $) of the CP40 membrane.	394
6.43	3D plot of the real (ϵ') and imaginary part (ϵ'') parts of the complex permittivity (ϵ^*) of the CP40-0 membrane.	396
6.44	3D plot of $\tan \delta$ and of the imaginary part (M'') of the complex electric modulus (M^*) of the CP40-0 membrane.	397
6.45	(Top) Eyring plot and (Bottom) Arrhenius plot of the CP40-0 membrane.	398
6.46	Isothermal curves of the modulus of the complex conductivity ($ \sigma $) for the CP40-0 membrane.	399
6.47	Phase angle (ϕ) and modulus of the serial impedance ($ Z_s $) of the CP40-0 membrane.	400
6.48	Isothermal plots curves of the imaginary (ϵ'') part of the complex (ϵ^*) permittivity for the unoriented and oriented PECH membranes from 213 to 363 K.	402
6.49	Arrhenius map for the oriented and unoriented copolymers.	403
6.50	Eyring map for the oriented and unoriented copolymers.	404
6.51	Numerical $\sigma_{\sigma_{prot}}$ for the oriented and unoriented copolymers.	407
6.52	Isothermal plots curves of the imaginary (ϵ'') part of the complex (ϵ^*) permittivity for the unoriented and oriented copolymer membranes from 213 to 383 K.	410
6.53	Arrhenius map for the unoriented (full symbols) and oriented (hollow symbols) modified copolymers.	412
6.54	Eyring plot for the pure, unoriented (full symbols) and oriented (hollow symbols) modified copolymers.	413
6.55	DC conductivity for the neat (CP0), modified unoriented (CP20, CP40), and oriented (CP20-O, CP40-O) copolymers.	416
6.56	Proton conductivity for the neat (CP0) and modified oriented (CP20, CP40) and oriented (CP20-O, CP40-O) membranes at three different temperatures.	417
7.1	Covalent Adaptable Networks (CANs) understood the intermediate stage where the best of both worlds, thermosets and thermoplastics, is achieved. Source: [2].	428

7.2	(a) Dissociative CANs where bond breakage precedes bond formation; (b) Associative CANs, also known as vitrimers, where bond formation precedes bond breakage. Source: [3].	430
7.3	Synthesis route of the HDI-S3 network.	437
7.4	3D plot of the real (ϵ') and imaginary part (ϵ'') parts of the complex permittivity (ϵ^*) of the HDI-S3-1% membrane.	441
7.5	3D plot of $\tan \delta$ and of the imaginary part (M'') of the complex electric modulus (M^*) of the HDI-S3-1% membrane.	442
7.6	(Top) Eyring plot and (Bottom) Arrhenius plot of the HDI-S3-1% membrane.	443
7.7	Isothermal curves of the modulus of the complex conductivity ($ \sigma $) for the HDI-S3-1% membrane.	444
7.8	Phase angle (ϕ) and modulus of the serial impedance ($ Z_s $) of the HDI-S3-1% membrane.	445
7.9	3D plot of the real (ϵ') and imaginary part (ϵ'') parts of the complex permittivity (ϵ^*) of the HDI-S3-4% membrane.	447
7.10	3D plot of $\tan \delta$ and of the imaginary part (M'') of the complex electric modulus (M^*) of the HDI-S3-4% membrane.	448
7.11	(Top) Eyring plot and (Bottom) Arrhenius plot of the HDI-S3-4% membrane.	449
7.12	Isothermal curves of the modulus of the complex conductivity ($ \sigma $) for the HDI-S3-4% membrane.	450
7.13	Phase angle (ϕ) and modulus of the serial impedance ($ Z_s $) of the HDI-S3-4% membrane.	451
7.14	FTIR spectrum of the HDI-S3 sample.	452
7.15	Thermogravimetric curves for the HDI-S3-DBTDL-4% sample.	454
7.16	Isochronal curves of the imaginary (ϵ'') part of the complex permittivity (ϵ^*) for the HDI-S3-1% and HDI-S3-4%.	455
7.17	Isothermal curves for the HDI-S3-DBTDL 1% and HDI-S3-DBTDL 4% samples between 255.65K and 373K.	456
7.18	Arrhenius plot for the low-temperature zone. Solid lines represent fitted lines.	457
7.19	Arrhenius plot for the high-temperature zone. Solid lines represent fitted lines.	458

7.20	Isothermal curves for the HDI-S3-DBTDL-4% sample in the temperature range between 255 and 343 K. The red line signals the onset temperature for the bond exchange reaction.	460
7.21	Arrhenius plot comparing the α_{Tg} dielectric relaxation for the HDI-S3-DBTDL-1% and HDI-S3-DBTDL-4%.	460
7.22	DSC thermograms of the 1 st heating, cooling, and 2 nd heating for the HDI-S3-DBTDL-4% sample.	461
7.23	Proton conductivity (σ_{prot}) of the HDI-S3-DBTDL-4%.	464

Part I

Introduction

Chapter 1

Motivation & aim

1.1 Overview

The United Nations (UN) define climate change as long-term shifts in temperature and weather patterns that may be natural. However, since the 1800s, human activities have been the main driver of climate change, primarily due to burning fossil fuels like coal, oil and gas [1].

To mitigate the effects on the Earth, the United Nations Framework Convention on Climate Change (UNFCCC) holds annually the Conference of the Parties (COP). The 12th of December 2015 a legally binding agreement, known as the Paris Agreement, was signed by 196 parties at the COP21 meeting in Paris. The main objective of the document was the long-term reduction of the Earth's temperature by at least 2 degrees Celsius, compared to pre-industrial levels. Accordingly, the signing countries had to increase their efforts in the fight for

the eradication of greenhouse gases (GHG) to achieve the long-awaited climate neutrality in the middle of this century [1].

This agreement is a basic pillar in the global fight against climate change, and for the future of the human species itself, since it lays the foundations of the ambitious common effort that all countries must make to lessen the effects of the current climate change on the planet. Unfortunately, not all the signing parties have demonstrated a solid adherence to the agreed principles. However, more and more countries, regions, cities, and companies are aware of the consequences of climate change, and are establishing actions in favour of climate neutrality. Policies in favour of zero carbon emission solutions are beginning to be competitive in different sectors, and even the economic and energy sectors are beginning to value them as a real investment alternative to the more common ones offered by fossil fuels. According to the United Nations, by 2030, zero-emission solutions will be competitive in sectors that represent more than 70% of global GHG emissions [1].

Recently, the COP27 has been held in Sharm el-Sheikh (Egypt). The final document, known as the Sharm el-Sheikh Implementation Plan (SSIP), reaches the following conclusions regarding the energy transition [2]:

- Emphasizes the urgent need for immediate, deep, rapid, and sustained reductions in global greenhouse gas emissions by parties across all applicable sectors, including through an increase in low-emission and renewable energy, just energy transition partnerships, and other cooperative actions.
- Recognizes that the unprecedented global energy crisis underlines the urgency to rapidly transform energy systems to be more secure, reliable, resilient, and including by accelerating clean and just transitions to renewable energy during this critical decade of action.
- Stresses the importance of enhancing a clean energy mix, including low-emission and renewable energy, at all levels as part of diversifying energy

mixes and systems, in line with national circumstances and recognizing the need for support towards just transitions.

Furthermore, the gathered parties reaffirmed the goal of reducing the global temperature to 1.5 degrees Celsius, with regard to pre-industrial levels. Likewise, the package of approved measures also includes financial and technological support for developing countries that comply with regulations against climate change. Moreover, the Sharm el-Sheikh Implementation Plan, stresses that the annual cost of transforming the current global economy to a low-emissions economy will be approximately \$4.6 trillion. This figure underlines the importance of the changes that are being undertaken since in order to adapt to an economy based on renewable energy, countries must carry out a complete transformation of their social, productive, and economic sectors. Consequently, the Sharm el-Sheikh Implementation Plan also highlights the need to involve the main actors in the economic sphere, that is, central & commercial banks, institutional investors and other financial actors, for this transformative process to work, because otherwise, the energy transition towards climate neutrality is just impossible [1,2].

On a continental scale, the European Union firmly supports the decarbonisation of the economy of the member countries. The current armed conflict between Russia and Ukraine, and the current and future consequences on the European energy market, further reinforces the idea that it is necessary to diversify and decarbonise the EU's energy sector. With the REPowerEU Plan, the European Commission clearly expressed its ambition to become independent from Russian fossil fuels by increasing green energy production, diversifying energy supplies, and reducing energy demand. It is in this context that the relevance of hydrogen as an energy vector becomes truly important in order to achieve decarbonization and diversification of the energy sector. Likewise, this process will help to improve the competitiveness of European industries, while meeting the climate objectives contemplated by the United Nations [3].

EU leadership in the field of renewable energy has been developed over the last few years through policies and legislation - *The European Green Deal (2019)*, *An EU Strategy for Energy System Integration (2020)*, *A hydrogen strategy for a climate-neutral Europe (2020)*, *Sustainable and Smart Mobility Strategy (2020)*, *European Climate Law (2021)*, *New Industrial Strategy (2021)*, *Fit for 55 targeting on the way to climate neutrality (2022)*, *EU Strategy on Standardisation (2022)*, *Guidelines on State aid for climate, environmental protection, and energy (2022)*, *REPowerEU (2022)* - to initiate the emergence of a hydrogen value chain serving a multitude of industrial sectors and other uses, which according to some forecasts could employ up to a million people in the coming years. Additionally, the EU has established a roadmap in which one of the fronts contemplated is to develop international standards with other global players. This task will be carried out by the main international institutions such as the International Association for Hydrogen and Fuel Cells in the Economy (IPHE), the International Energy Agency (IEA) and the International Renewable Energy Agency (IRENA), together with the Group of Twenty (G20) [4-6].

Today, the Fuel Cells and Hydrogen Joint Undertaking (FCH-JU) is the most important European instrument to support research and technological development in hydrogen energy. It is a public-private partnership made up of three members (the European Commission, Hydrogen Europe Research, and Hydrogen Europe) comprising respectively public authorities, research communities, and industrial partners. Aligning the efforts of public and private stakeholders was identified as a necessary condition for the deployment of a hydrogen economy in the EU [7,8].

In Spain, this organization is represented by the Spanish Technological Platform for Hydrogen and Fuel Cells. In addition to this support, investments in fundamental and applied research must continue to be an ongoing aspect of public policy. Well-designed European and national funding, to support programs covering the entire TRL chain, is needed to prepare the next generation of systems and technologies in the medium to long term, as well as to contin-

uously reduce the cost of technologies and improve the competitiveness of the European industry [4-8].

Fuel cells are one of the most promising technologies to provide independence from fossil fuels. A fuel cell is a device that directly transforms chemical energy into an electrical form. There are several types depending on the operating temperature. This doctoral thesis is focused on low-temperature fuel cells, specifically proton-exchange membrane fuel cells (PEMFC). This class of fuel cells consists of anode and cathode electrodes, a catalyst layer, a gas diffusion layer, bipolar plates, and a proton exchange membrane [9-11].

Fuels used by low-temperature PEMFCs are hydrogen, methanol and other alcohols like ethanol. PEMFCs can guarantee the production of electricity with a considerable reduction in GHG emissions. Besides, it has a much higher efficiency since it is a direct conversion from chemical to electrical energy, contrarily to what occurs in thermal engines where the chemical to electrical energy is converted in several stages (heat \implies mechanical \implies electrical energy). The power requirements vary between applications, but in general, the power output for cars and buses ranges from 20 to 250 kW, whereas portable power for consumer electronics ranges from 5 to 50 W [12-16].

More advantages of PEMFCs are the lack of noise during operation, quick start-up, and applicability in several fields such as vehicles or consumer electronics. However, PEMFCs also displays certain drawbacks, as for instance, the unavailability of hydrogen or methanol due to the lack of infrastructure for its production. Indeed, the main issue with methanol, and other alcohols like ethanol, is their generation provided that 1st generation biomass feedstock, mainly food crops, are used as raw materials. This poses a serious problem because it could raise the price of the food crops, and thus, create a potential famine in less developed countries. Therefore, research is focused on finding new methodologies that use 2nd generation biomass, i.e, agricultural, biomass and/or timber waste as the raw material for methanol production [16,17].

The generation process of hydrogen is expensive, and it can be very pollutant since 96% of the worldwide production of hydrogen use fossil fuels in the process. These processes are mainly steam methane reforming (SMR) of natural gas and coal gasification. The resultant hydrogen is known as grey hydrogen or brown hydrogen, respectively. Note that 6% of the annual consumption of natural gas is due to grey hydrogen production. In order to obtain a more environmentally friendly generation process a stage of carbon dioxide capture and storage (CCS) is added to either the SMR or coal gasification processes. This is known as blue hydrogen. However, despite diminishing GHG emissions, the CCS stage cannot capture all CO_2 emissions, and thus GHG are still being emitted to the atmosphere. On the other hand, when renewable energy sources are used during the complete production process of hydrogen, then it is known as green hydrogen [18,19]. In Figure 1.1 the most relevant hydrogen production processes are shown.

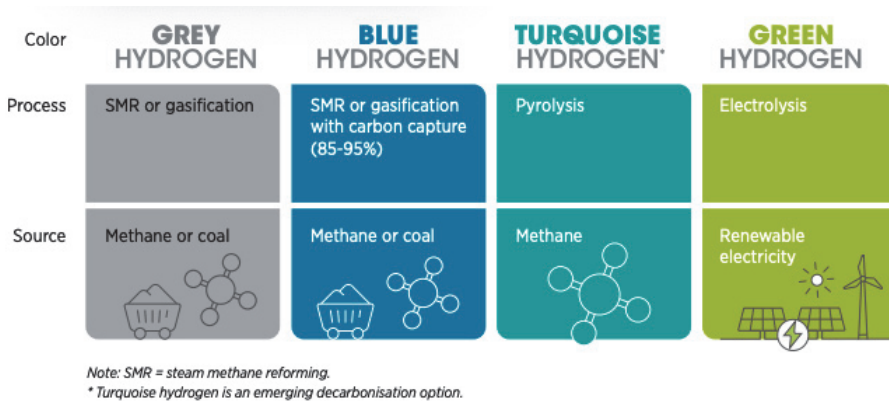


Figure 1.1: Colour code of hydrogen based on the processes used to generate it. Source: [18].

Performance-wise, one of the most crucial components is the proton-exchange membrane (PEM). Its correct functioning provides a barrier that avoids the mixing of the reactives while allowing the protons to be transported through the membrane. Accordingly, the optimal membrane must guarantee the following

characteristics: high proton conductivity, low electric conductivity, high chemical, mechanical, oxidative, and hydrolytic stability in operating conditions, low fuel permeability, and a fair price. Nowadays, the standard membrane in the industry is Nafion® from Dupont [20-22].

Nafion® is a random copolymer consisting of perfluoro ether side chains, in which sulfonic acid groups are randomly distributed along the polymer backbone. Its almost prevailing use in PEMFC at an industrial level is due to a special molecular structure that favours proton conductivity. Hydrophobic perfluorinated polyethylene and highly hydrophilic sulfonic acid-terminated perfluorovinyl ether side groups can form nanoscale domains with ion migration. The network of clusters in the Nafion membrane is created by connecting sulfonated ion clusters of 4 nm and narrow channels of 1 nm. The ionic groups are formed by the aggregation of highly hydrophilic sulfonic acid groups, which causes water and proton to pass through [22-23].

The optimal working conditions required by PEM, such as the temperature range below 80°C and a high degree of hydration level, may become a drawback. A combination of low humidity together with high temperature would be detrimental for the overall performance since it would result in a decrease in proton conductivity. Subsequently, the management of temperature and humidity in PEMFC, and generally in low-temperature cells, is crucial to obtain good performance. Consequently, a lot of effort has been made in manufacturing new membranes based on Nafion®. Significant advances regarding fluorinated and partially fluorinated membranes in terms of chemical and mechanical stability, and proton conductivity have been made. Several synthesis methodologies have been proposed to develop membranes for PEMFCs. Among them, the most employed are graft polymerization, crosslinking, sol-gel, and direct polymerization of monomers [24-34].

Nevertheless, problems such as fuel crossover, excessive swelling and water loss at high temperatures, are still present, since it is not easy to modify the microstructure to reach a high performance in all these aspects. This is the reason

why researchers are working on the development of new non-fluorinated membranes, which could meet the majority of the following characteristics [20]:

- (1) Low hydration conditions in operating regime.
- (2) Good performance at elevated temperatures.
- (3) Ability to increase the efficiency of the catalyst, and therefore, improve its effectiveness.
- (4) Decrease the susceptibility to impurities of the anodic catalyst.
- (5) Reduce the need for high thermal regulation.
- (6) Reduce the cost compared to Nafion®.

Despite Nafion®-based polymer membranes are expected to dominate the market for the next 5 - 10 years [27,29], over the past decades, many fluorinated, partially-fluorinated and non-fluorinated membranes have been analysed with the objective to replace Nafion® as the standard proton-exchange membrane in PEMFCs, as it will be discussed in Chapter 2.

Less expensive non-perfluorinated PEMs capable of operating under low relative humidity conditions (below 40%) are expected to gain more prominence. Some examples of polymers with high proton conductivity, thermal stability at high temperatures and humidities that can be considered suitable for their applicability as proton-exchange membranes (PEMs) are the following: sulfonated poly(ether ether ketone)s (SPEEK), sulfonated poly(ether sulfone) (SPES), sulfonated polyimides (SPI) and sulfonated polyphenylenes (SPP) [27,29]. Many hydrocarbon-based PEMs usually suffer from relatively low conductivity at low relative humidity, compared with Nafion®. Indeed, the continuous improvements in PEMs are expected to contribute 10-20% to the improvement of power density in PEMFCs [29]. Although advances have been registered, consensus on a definitive polymeric membrane has not been reached yet, since none of

them have demonstrated a real improvement with respect to Nafion® in terms of overall cell performance, durability and cost.

1.2 Aim of the thesis

The main objective of this doctoral thesis is to develop a methodology that allows the analysis of various polymeric membranes with different microstructures through Dielectric Thermal Spectroscopy (DETA). Consequently, the work performed is the development of a robust and reliable procedure, that improve the design of proton exchange membranes, by means of characterizing polymeric materials to predict their behaviour in operating conditions. In this context, the operation of proton exchange membranes is optimized, as a means to improve the efficiency of PEMFCs, and to promote their implementation on a mass usage.

To achieve this goal, the following partial research objectives have been carried out:

- **To characterize the physicochemical properties of the synthesized membranes prepared from polymeric materials in different experimental conditions.** The membranes would be characterized through Fourier Transformed Infrared Spectroscopy (FTIR), Differential Scanning Calorimetry (DSC), and Thermogravimetric Analysis (TGA).
- **To establish relationships between morphology, molecular mobility, and ionic conductivity of the polymeric membranes.** The membranes would be characterized through Brodband Dielectric Spectroscopy. The study of the dielectric properties in terms of the complex permittivity (ϵ^*), in combination with the analysis of the complex conductivity (σ^*), will provide insight into the molecular dynamics which efficiently favours the charge transfer mechanisms.

- **To model the behaviour of the polymeric membranes in operating conditions.** The proton conductivity (σ_{prot}) would be estimated from the dielectric data, and the suitability of the tested polymeric membranes as promising candidates for proton-exchange membranes would be assessed.

1.3 Outline of the thesis

This thesis consists of four parts with its corresponding chapters, which are divided as follows.

Part I. Introduction

- *Chapter 1.* It presents a brief introduction on the importance of doing research on the improvement of fuel cells. The aim, as well as the outline, of the thesis are also included in this chapter.
- *Chapter 2.* It introduces proton-exchange membrane fuel cells (PEMFCs) technology. Accordingly, an overview of the main components is done, with special focus on the state-of-the-art of proton-exchange membranes.
- *Chapter 3.* It includes the fundamentals on Dielectric Analysis together with the detailed description of the methodology used in this thesis for the characterization of polymeric membranes in operating conditions. Moreover, a description of the fundamentals of the other characterization techniques used in this thesis is included, i.e., Fourier Transformed Infrared Spectroscopy (FTIR), Thermogravimetric analysis (TGA), and Differential Scanning Calorimetry (DSC).

Part II. Results & Discussion

- *Chapter 4.* It contains the analysis of two series of membranes based on sulfonated styrene-ethylene-butylene-styrene (SEBS) block copolymer. The microstructure has been fine-tuned for their suitability for fuel cell applications, and subsequently, a process of sulfonation, UV photocrosslinking and hybridization are applied to the samples. The analysis performed will provide insights on how the restrictions on the segmental mobility at low and high scale caused by both photocrosslinking, and subsequent sulfonation, affect the ionic diffusivities. Moreover, the importance of the infiltration time in the dielectric spectra and the proton conductivity is assessed on the hybrid membranes
- *Chapter 5.* It contains the analysis of a series of poly(vinyl alcohol) (PVA) membranes conveniently modified for their suitability as proton-exchange membranes in direct methanol fuel cells (DMFCs). The analysis is focused on whether the crosslinking and sulfonation by the use of SSA enhances the stability and increase the proton-conducting sites in the PVA structure as initially expected. Furthermore, the effect of the addition of graphene oxide (GO) in the dielectric spectra and proton conductivity is assessed.
- *Chapter 6.* It contains the analysis of two series of membranes based on poly(epichlorohydrin) (PECH) and poly(epichlorohydrin-co-ethylene oxide)(PECH-co-EO) copolymer. Both membranes are modified with dendron 3,4,5-tris[4-(n-dodecan-1-yloxy)benzyloxy] benzoate units. The analysis focus on the ability of these membranes to form channels promoted by the thermal orientation, which enhances the charge transfer mechanisms, and the proton conductivity.
- *Chapter 7.* It contains the analysis of a membrane synthesized from a covalent adaptable network (CAN). The most important feature of CANs is the presence of reversible bonds in the structure which allows them displaying physical properties such as self-healing, weldability, and recyclability.

These properties could enhance the life cycle of the proton-exchange membranes. The analysis performed includes an assessment of the two most important temperatures from a viscoelastic point of view, i.e., the glass transition (T_g) and the freezing topology temperature (T_v), and its impact on proton conductivity.

Part III. Conclusions & Future work

- *Chapter 8.* It discusses the general conclusions obtained from the present study. Moreover, it discusses on the future work that will be initiated from the obtained conclusions in this thesis.

Part IV. Annexes

- *Chapter 9.* It includes a list of all the scientific articles published in scientific journals indexed in JCR.
- *Chapter 10.* It contains all the contributions to scientific congresses.

1.4 References

- [1] United Nations Framework Convention on Climate Change (UNFCCC), <https://unfccc.int/process-and-meetings/the-paris-agreement/the-paris-agreement>, (2022).
- [2] United Nations Framework Convention on Climate Change (UNFCCC), Sharm el-Sheikh Implementation Plan - COP27, Sharm El-Sheikh Clim. Chang. Conf. (2022) 1-10.
- [3] Hydrogen Research EU, Hydrogen europe research is committed to re-power the EU, (2022).

- [4] F. Cuevas, J. Zhang, M. Latroche, The Vision of France, Germany, and the European Union on Future Hydrogen Energy Research and Innovation, *Engineering* 7 (2021) 715-718.
- [5] Fuel Cells and Hydrogen Observatory, Chapter 3 2021 EU and National Policies Report, (2021) 1-36.
- [6] Fuel Cells and Hydrogen Observatory, Chapter 1 Technology and Market, *Clean Hydrog. JU.* (2022).
- [8] Fuel cells and Hydrogen Observatory, Chapter 2. 2022 Hydrogen Supply Capacity and Demand, Chapter 2 (2022) 125.
- [9] Fuel cells and Hydrogen Observatory, Chapter 4 2022 Standards, (2022).
- [10] A. Boudghene Stambouli, E. Traversa, Fuel cells, an alternative to standard sources of energy, *Renew. Sustain. Energy Rev.* 6 (2002) 295-304.
- [11] S. Edition, W. Virginia, Fuel cell handbook, *Choice Rev. Online* 26 (1989) 26-6292.
- [12] P.C. Okonkwo, C. Otor, A review of gas diffusion layer properties and water management in proton exchange membrane fuel cell system, *Int. J. Energy Res.* 45 (2021) 3780-3800.
- [13] H. Basma, Y. Zhou, F. Rodríguez, Fuel-Cell Hydrogen Long-Haul Trucks in Europe: a Total Cost of Ownership Analysis, (2022).
- [14] B.G. Pollet, S.S. Kocha, I. Staffell, Current status of automotive fuel cells for sustainable transport, *Curr. Opin. Electrochem.* 16 (2019) 90-95.
- [15] M.K. Singla, P. Nijhawan, A.S. Oberoi, Hydrogen fuel and fuel cell technology for cleaner future: a review, *Environ. Sci. Pollut. Res.* 28 (2021) 15607-15626.
- [16] B.C. Ong, S.K. Kamarudin, S. Basri, Direct liquid fuel cells: A review, *Int. J. Hydrogen Energy* 42 (2017) 10142-10157.

- [17] T.J. Deka, A.I. Osman, D.C. Baruah, D.W. Rooney, Methanol fuel production, utilization, and techno-economy: a review, *Environ. Chem. Lett.* 20 (2022) 3525-3554.
- [18] World Economic Forum, <https://www.weforum.org/agenda/2021/07/clean-energy-green-hydrogen>, (2021)
- [19] R.W. Howarth, M.Z. Jacobson, How green is blue hydrogen?, *Energy Sci. Eng.* 9 (2021) 1676-1687.
- [20] A. Alaswad, A. Omran, J.R. Sodre, T. Wilberforce, G. Pignatelli, M. Dassisti, A. Baroutaji, A.G. Olabi, Technical and commercial challenges of proton-exchange membrane (PEM) fuel cells, *Energies* 14 (2021) 1-21.
- [21] P.C. Okonkwo, I. Ben Belgacem, W. Emori, P.C. Uzoma, Nafion degradation mechanisms in proton exchange membrane fuel cell (PEMFC) system: A review, *Int. J. Hydrogen Energy* 46 (2021) 27956-27973.
- [22] M. Tawalbeh, S. Alarab, A. Al-Othman, R.M.N. Javed, The Operating Parameters, Structural Composition, and Fuel Sustainability Aspects of PEM Fuel Cells: A Mini Review, *Fuels* 3 (2022) 449-474.
- [23] M. Pan, C. Pan, C. Li, J. Zhao, A review of membranes in proton exchange membrane fuel cells: Transport phenomena, performance and durability, *Renew. Sustain. Energy Rev.* 141 (2021) 110771.
- [24] R. Vinodh, R. Atchudan, K. Hee-Je, Y. Moonsuk, Recent Advancements in Polysulfone Based Membranes for fuel cell (PEMFCs, DMFCs and AMFCs) applications: A critical review, *Polymers* 14 (2022) 300.
- [25] L.Y. Zhu, Y.C. Li, J. Liu, J. He, L.Y. Wang, J. Du Lei, Recent developments in high-performance Nafion membranes for hydrogen fuel cells applications, *Pet. Sci.* 19 (2022) 1371-1381.

- [26] Y. Zhang, Y. Tao, J. Shao, Application of porous materials for the flow field in polymer electrolyte membrane fuel cells, *J. Power Sources* 492 (2021) 229664.
- [27] M. Adamski, N. Peressin, S. Holdcroft, On the evolution of sulfonated polyphenylenes as proton exchange membranes for fuel cells, *Mater. Adv.* 2 (2021) 4966-5005.
- [28] Z. Feng, J. Huang, S. Jin, G. Wang, Y. Chen, Artificial intelligence-based multi-objective optimisation for proton exchange membrane fuel cell: A literature review, *J. Power Sources* 520 (2022) 230808.
- [29] K. Jiao, J. Xuan, Q. Du, Z. Bao, B. Xie, B. Wang, Y. Zhao, L. Fan, H. Wang, Z. Hou, S. Huo, N.P. Brandon, Y. Yin, M.D. Guiver, Designing the next generation of proton-exchange membrane fuel cells, *Nature* 595 (2021) 361-369.
- [30] R.M. Nauman Javed, A. Al-Othman, M. Tawalbeh, A.G. Olabi, Recent developments in graphene and graphene oxide materials for polymer electrolyte membrane fuel cells applications, *Renew. Sustain. Energy Rev.* 168 (2022) 112836.
- [31] Q. Liu, F. Lan, J. Chen, C. Zeng, J. Wang, A review of proton exchange membrane fuel cell water management: Membrane electrode assembly, *J. Power Sources* 517 (2022) 230723.
- [32] Y. Ke, W. Yuan, F. Zhou, W. Guo, J. Li, Z. Zhuang, X. Su, B. Lu, Y. Zhao, Y. Tang, Y. Chen, J. Song, A critical review on surface-pattern engineering of nafion membrane for fuel cell applications, *Renew. Sustain. Energy Rev.* 145 (2021) 110860.
- [33] R. Haider, Y. Wen, Z.F. Ma, D.P. Wilkinson, L. Zhang, X. Yuan, S. Song, J. Zhang, High temperature proton exchange membrane fuel cells: Progress in advanced materials and key technologies, *Chem. Soc. Rev.* 50 (2021) 1138-1187.

- [34] A.R. Motz, M.-C. Kuo, J.L. Horan, R. Yadav, S. Seifert, T.P. Pandey, S. Galioto, Y. Yang, N. V Dale, S.J. Hamrock, Heteropoly acid functionalized fluoroelastomer with outstanding chemical durability and performance for vehicular fuel cells, *Energy Environ. Sci.* 11 (2018) 1499-1509.

Chapter 2

Fundamentals

Chapter 2 presents an overview of fuel cell technology. It also includes a survey of proton-exchange membrane fuel cells (PEM-FCs) technology. Moreover, given the importance of the proton-exchange membrane, a state-of-the-art review is performed.

2.1 Overview of Fuel Cell Technology

A fuel cell (FC) is an environmentally friendly device which allows the direct conversion of chemical energy into an electrical form with high efficiency. Unlike more conventional power generation methods, FCs are not submitted to thermodynamic limitations like, for instance, combustion engines or gas turbines, and subsequently, they are more efficient. Moreover, FCs produce power with minimum, or even none, GHG emissions since the combustion process is avoided [1].

A general schematic of a FC is shown in Figure 2.1A. Accordingly, the FC is being continuously fed through the anode (fuel) and the cathode (air, O_2 , CO_2 , etc.). Then, a series of electrochemical reactions occur and an electric current

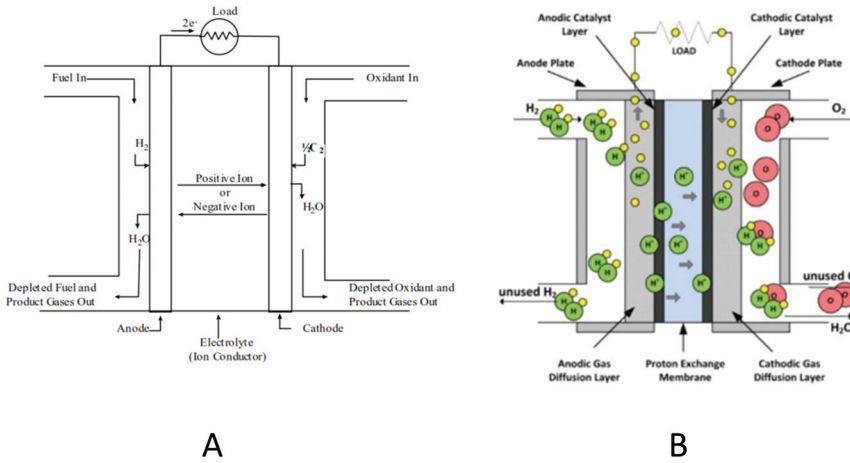


Figure 2.1: (A) General schematic of a fuel cell. (B) Schematic of a hydrogen PEMFC. Source: [1].

is produced through the electrolyte, while driving a complementary electric current that performs work on the load [1-3].

Although similarities can be found with batteries, they differ in many ways. For instance, a battery would end its life cycle when the chemical reactants are consumed. Contrarily, this cannot occur in a fuel cell provided that both, fuel and oxidant, are being supplied continuously. Potential fields of application vary from consumer electronics, aeronautics, residential or industrial power generation, marine vessels, or vehicle industry [1,4], as shown in Figure 2.2.

Classification of fuel cells

There are several types of fuel cells which are utilised depending on the operation temperature and the application field. Accordingly, factors such as the fuel or the electrolyte differ among them. Examples of high-temperature FCs are solid oxide acid fuel cells (SOFC) or molten carbonate fuel cells (MCFC), which

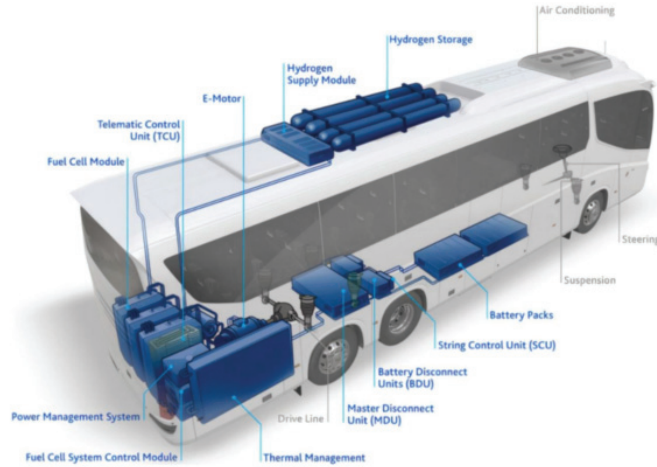


Figure 2.2: Applications of fuel cells in the transport industry. Schematic of a fuel cell bus. Source: [4]

are usually used in power generation. On the other hand, proton-exchange membrane fuel cells (PEMFC) - either with hydrogen, methanol or ethanol as fuel - are an example of low-temperature fuel cells [1-4]. Table 2.1 gathers the most relevant features of each type. A brief description is included as follows [1]:

- **Proton-Exchange Membrane Fuel Cell (PEMFC).** It uses an ion exchange membrane as an electrolyte. Given the characteristics of the polymeric electrolytes the operating temperature is generally between 60 to 85°C for FCs operating in the low-temperature range, and up to 200°C for FCs operating in the high-temperature range. Furthermore, due to problems with water balance, a H-rich gas with minimal or no carbon monoxide is used. Higher catalyst loading is needed, generally Pt, for both the anode and cathode. Since the anode is easily poisoned, extensive fuel processing is compulsory.
- **Alkaline Fuel Cell (AFC).** It uses potassium hydroxide as the electrolyte, and its concentration varies depending on the working temperature. For instance, a concentration of 85 wt.% if the FC is operating at

high temperatures ($\approx 250^\circ\text{C}$) whereas a concentration of 35 to 50 wt.% is utilised at low operating temperatures ($< 120^\circ\text{C}$). A wide range of electro-catalysts can be employed such as Ni, Ag or metal oxides. Regarding the fuel, generally hydrogen is preferred. Nonetheless, the high sensitivity of the electrolyte to carbon dioxide forces to utilise highly pure hydrogen as fuel. It displays an excellent performance on hydrogen and oxygen compared to other FCs thanks to its flexibility in the range of electro-catalyst.

- **Phosphoric Acid Fuel Cell (PAFC).** It uses phosphoric acid as the electrolyte. At low temperatures the phosphoric acid has a poor ionic conductivity, and it suffers of carbon monoxide poisoning of the catalyst (Pt) in the anode. Consequently, provided the high relative stability of phosphoric acid, the operating temperature is generally between 150 to 220°C . Moreover, the use of concentrated acid diminishes water management requirements. Accordingly, PAFCs have proved system efficiencies around 42%. However, some of its drawbacks are the need for extensive fuel processing, and the use of expensive materials in the stack given the corrosive nature of phosphoric acid.
- **Molten Carbonate Fuel Cell (MCFC).** It uses alkali carbonates as polyelectrolytes, and thus, the operating temperatures ranges from 600 to 700°C because the alkali carbonates form a highly conductive molten salt, with carbonate ions providing ionic conduction. The catalyst used in MCFC are generally nickel and nickel oxide. Accordingly, no expensive catalyst are employed. Furthermore, carbon monoxide (CO), as well as certain hydrocarbons, can be used as fuels in MCFCs, and CO_2 in the cathode. However, the high temperatures pose problems with the materials used in the fabrication of the stack's components.
- **Solid Oxide Fuel Cell (SOFC).** It uses a solid nonporous metal oxide as electrolyte, and the operating temperature is generally between 800 - 1000°C , where the ionic conduction by oxygen ions occurs. However, the use of newly developed thin-electrolyte cells allow for an operating tem-

perature range of 650 - 850°C. It uses nickel as catalyst. Furthermore, despite SOFCs display low corrosion problems, and the kinetics are relatively fast, the high temperatures place several constraints on the materials for its fabrication. This issue can affect the power density of the stack, and its life cycle.

Table 2.1: Types of fuel cells and its characteristics features.

Characteristics	PEMFC	AFC	PAFC	MCFC	SOFC
Operation Temperature	80°C	65-220°C	205°C	650°C	800-1000°C
Charge Carrier	H ⁺	OH ⁻	H ⁺	CO ₃ ²⁻	O ²⁻
Catalyst	Pt	Pt	Pt	Ni	Ni
Cell materials	Carbon	Carbon	Graphite	Iron Steel	Ceramics
Water management	Evaporation	Evaporation	Evaporation	Gas	Gas
Electrolyte	Cationic PEM	KOH	H ₃ PO ₄	CO ₃ ²⁻	Ceramics

2.1.1 Thermodynamics and Electrochemistry in Fuel cells

Fuel Cells Thermodynamics

Combining the First and Second Law of thermodynamics it is possible to define the four thermodynamic potentials, or the four fundamental equations of thermodynamics for a multicomponent system, as shown in Eq. 2.1 for a chemical reaction [5-8].

$$\begin{array}{ll}
\text{Internal energy} & dU = TdS - pdV + \sum_{i=1} \mu_i \cdot dN_i \\
\text{Helmholtz's Function} & dF = -SdT - pdV + \sum_{i=1} \mu_i \cdot dN_i \\
\text{Enthalpy} & dH = TdS + Vdp + \sum_{i=1} \mu_i \cdot dN_i \\
\text{Gibbs Free Energy} & dG = -SdT + Vdp + \sum_{i=1} \mu_i \cdot dN_i
\end{array} \tag{2.1}$$

Where N_i represents the number of moles of a compound in a mixture, and μ_i are the chemical potentials of each compound that contribute the different total energies.

These thermodynamic potentials (U, H, F, and G) are very useful to calculate the maximum useful work, when any of its variables, for example, internal energy represents the work in a process that is adiabatic and reversible of a closed system, while enthalpy represent the work in an adiabatic and reversible process of a flow system.

Gibbs free energy (ΔG) is a particularly interesting potential for processes or reactions that occur at constant temperature and pressure, since under these conditions it coincides with the variation of the chemical potential of the species present, and allows establishing an equilibrium criterion. Thus, if a system is in equilibrium, then $\Delta G = 0$. On the contrary $\Delta G \neq 0$ when the system moves away from the equilibrium position.

The value of ΔG also provides a criterion of spontaneity, given that if the process is spontaneous then $\Delta G < 0$. On the other hand, if it is not, then $\Delta G > 0$. Therefore, as shown in 2.2:

$$\begin{array}{ll}
\Delta G = 0 & \text{Equilibrium process} \\
\Delta G > 0 & \text{Spontaneous process} \\
\Delta G < 0 & \text{Non-spontaneous process}
\end{array} \tag{2.2}$$

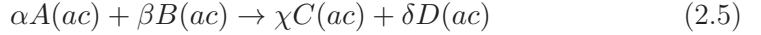
The Gibbs free energy can be related to the equilibrium constant, and therefore, to the compositions of the compounds. From the complete expression of the Gibbs energy for multicomponent systems shown in Eq. 2.3:

$$dG = -SdT + Vdp + \sum_{i=1} \mu_i \cdot dN_i \quad (2.3)$$

If temperature and pressure remain constant as in a chemical reaction, it is possible to obtain Eq. 2.4:

$$\Delta G = \Delta G^0 + R \cdot T \cdot \ln \prod \hat{a}_i^{v_i} \quad (2.4)$$

for a reaction of the type shown in Eq. 2.5:



where $\prod \hat{a}_i^{v_i}$ is the product of the activities of each compound raised to its stoichiometric coefficient v_i , products are in the numerator and reactants are in the denominator. The activity \hat{a}_i in each compound represents an effective concentration. In slightly concentrated solutions, the activity can be associated with the concentration, and in gas mixtures with the partial pressure of each component (Eq. 2.6).

$$\Delta G = \Delta G^0 + R \cdot T \cdot \ln \frac{[C]^\chi \cdot [D]^\delta}{[A]^\alpha \cdot [B]^\beta} \quad (2.6)$$

and for the equilibrium condition ($\Delta G = 0$) the expression allows it to be related to the equilibrium constant K_{eq} at every temperature (Eq. 2.7),

$$K_{eq} = \frac{[C]_{eq}^\chi \cdot [D]_{eq}^\delta}{[A]_{eq}^\alpha \cdot [B]_{eq}^\beta} \quad (2.7)$$

The Gibbs free energy can also be defined from the values of enthalpy and entropy, according to Eq. 2.8:

$$\Delta G = \Delta H - T \cdot \Delta S \quad (2.8)$$

And the values of ΔH and ΔS can be calculated from the specific heats, if it is assumed that both quantities do not depend on the pressure, as shown in Eq. 2.9:

$$\begin{cases} \Delta H = \Delta H^0 + \Delta a(T - 298) + \frac{1}{2}\Delta b(T^2 - 298^2) + \frac{1}{3}\Delta c(T^3 - 298^3) \\ \Delta S = \Delta S^0 + \Delta a \ln\left(\frac{T}{298}\right) + \frac{1}{2}\Delta b(T - 298) + \frac{1}{2}\Delta c(T^2 - 298^2) \end{cases} \quad (2.9)$$

This allows estimating the value of ΔG , given that the reference values ΔH^0 and ΔS^0 are tabulated, as are the specific heat constants a , b , and c .

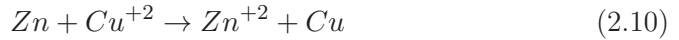
Since a FC allows extracting the energy contained in a fuel, and transforming it directly into electricity. The maximum useful work that can be transformed into electricity is determined by the variation of the Gibbs free energy that occurs during the hydrogen combustion reaction, that is, by the global reaction of formation of water from hydrogen and oxygen, assuming the reaction occurs at constant temperature and pressure. Consequently, the amount of energy that can be obtained from hydrogen fuel is $\Delta G = -237.34 \text{ kJ} \cdot \text{mol}^{-1}$, given that $\Delta G = \Delta H - T\Delta S$ is applied to the chemical reaction for the formation of water ($\Delta G_{\text{Products}} - \Delta G_{\text{Reactants}}$).

Fuel Cells Electrochemistry

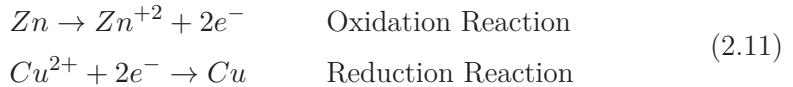
As previously mentioned, the reactions that occur in a FC are electrochemical reactions, of electron transfer, in which a compound gives up electrons (the reducer) to another that accepts them (the oxidizer), producing a change in the reduction indices of both. What determines which of the two compounds

behaves as an oxidizer or as a reducer is the value of their affinity to capture electrons (electronegativity).

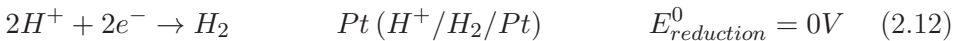
An example of an electrochemical reaction is shown in Eq. 2.10, in which the zinc has been oxidized (has acted as a reducer) by the copper that has been reduced (has acted as an oxidant). The electrons have passed Zn to Cu^{+2} , neutralizing the latter the positive charge it had. The result of this reaction is the generation of a potential (E), voltage (V) or electromotive force (emf.)



Although for an oxidation reaction to take place, there must be a simultaneous reduction reaction, it is possible to express the above reaction as a sum of coupled half-reactions, as shown in Eq. 2.11:



All reactions such as the above, which involve electron transfer, have an associated electrical potential E. As another coupled reaction would be necessary for there to be electron capture, a standard reduction reaction is used as a reference. This reaction is the reduction of H^{+} to H_2 on a platinum catalyst, which is assigned the potential 0 V (Eq. 2.12).



Under the same conditions, the reduction of a compound always gives the same potential. Considering temperature of 298 K, pressure of 1 atmosphere and concentrations of 1 M for all compounds. This potential measured under these conditions is known as the standard reversible potential ($E_{oxidation}^0, E_{reduction}^0$). In a fuel cell, oxidation occurs at the anode and reduction occurs at the cathode

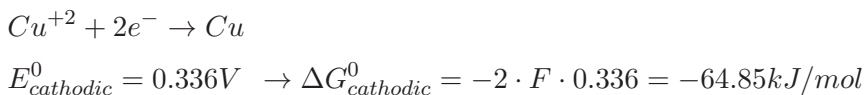
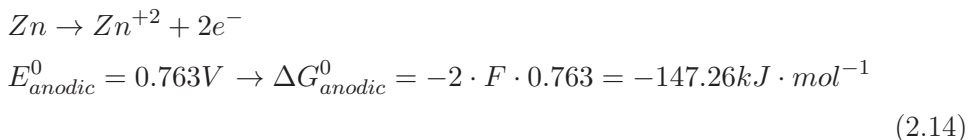
(E_{anodic}^0 , $E_{cathodic}^0$). In general, they are expressed as reduction reactions, and the corresponding oxidation reactions would have the same potential, but with the opposite sign ($-E$).

The potential (or voltage) and the Gibbs free energy are related by Eq. 2.13:

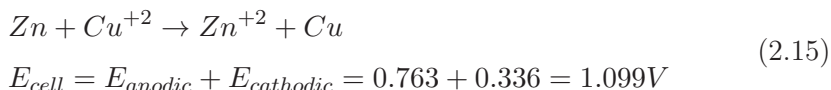
$$\Delta G = -n \cdot F \cdot E \quad (2.13)$$

where n is the number of electrons involved in the overall transfer reaction, E is the potential of the battery (in Voltios, V), and F is Faraday's constant.

For the example above, you would get the following values displayed in Eq. 2.14:



The sum of which gives the reversible or ideal cell potential, as shown in Eq. 2.15:



With a global free energy of $\Delta G^0 = \Delta G_{anodic}^0 + \Delta G_{cathodic}^0 = -2 \cdot F \cdot 1.099 = -212.11kJ$.

Since the value of ΔG is negative, the reaction will take place spontaneously. For a reaction to take place spontaneously its value of potential E will have to be positive ($E > 0$).

Thus, if the reduction potentials of the compounds involved are known, it is possible to predict the direction of the electrochemical reaction: if any species has a value less than $E_{reduction}^0$ the first will act as a reducer of this one which will be oxidized, and vice versa.

Nernst's Law

Provided that the reduction and oxidation potentials depend on the conditions in which the electrochemical reactions take place, so variables such as temperature, pressure, concentration of the species. Until now, only standard conditions have been considered (E^0).

To evaluate this dependency, Eq. 2.16 is taken into account:

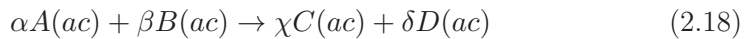
$$\Delta G = \Delta G^0 + R \cdot T \cdot \ln \prod \hat{a}_i^{v_i} \quad (2.16)$$

From the relationship between the Gibbs free energy and the reaction potentials, Eq. 2.17, known as Nernst's law, can be obtained.

$$E = E^0 - \frac{R \cdot T}{F \cdot n} \cdot \ln \prod \hat{a}_i^{v_i} \quad (2.17)$$

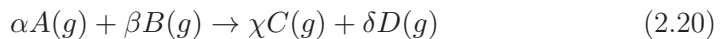
Eq. 2.17 can take the following forms (Eq. 2.19 - Eq. 2.20):

For a reaction in solution



$$E = E^0 - \frac{R \cdot T}{F \cdot n} \cdot \ln \frac{[C]^\chi \cdot [D]^\delta}{[A]^\alpha \cdot [B]^\beta} \quad (2.19)$$

or for the same reaction in the gas phase

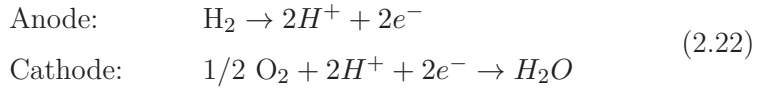


$$E = E^0 - \frac{R \cdot T}{F \cdot n} \cdot \ln \frac{P_C^\chi \cdot P_D^\delta}{P_A^\alpha \cdot P_B^\beta} \quad (2.21)$$

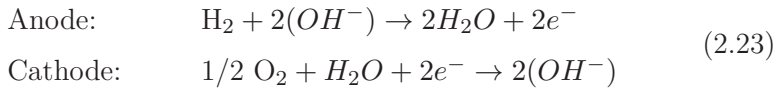
In a FC operating in steady state and with an ideal behaviour, the input concentrations of A, B and the output concentrations of C, D remain constant over time, so that the operation of the cell would be maintained throughout moment away from equilibrium.

The anode and cathode reactions corresponding to each type of fuel cell are shown below:

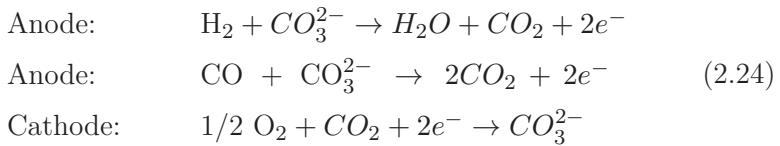
- PEMFC & PAFC in Eq. 2.22:



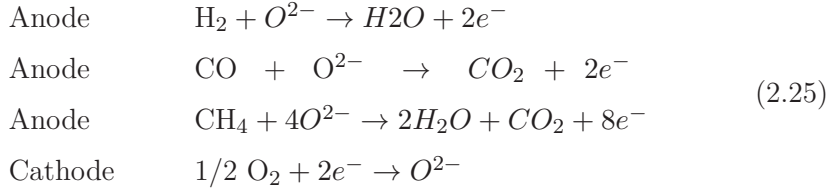
- AFC in Eq. 2.23:



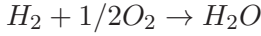
- MCFC in Eq. 2.24:



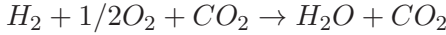
- SOFC in Eq. 2.25:



The ideal behaviour of the system when it is not in the standard conditions (E^0) is determined by the Nernst equation. The corresponding equations for the different types of chemical reactions occurring in FCs are gathered in Eq. 2.26.



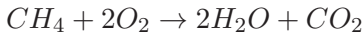
$$E = E^0 + \frac{R \cdot T}{2 \cdot F} \cdot \ln \frac{P_{\text{H}_2}}{P_{\text{H}_2\text{O}}} + \frac{R \cdot T}{2 \cdot F} \cdot \ln P_{\text{O}_2}^{1/2}$$



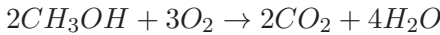
$$E = E^0 + \frac{R \cdot T}{2 \cdot F} \cdot \ln \frac{P_{\text{H}_2}}{P_{\text{H}_2\text{O}} \cdot P_{\text{CO}_2}} + \frac{R \cdot T}{2 \cdot F} \cdot \ln (P_{\text{O}_2}^{1/2} \cdot P_{\text{CO}_2})$$



$$E = E^0 + \frac{R \cdot T}{2 \cdot F} \cdot \ln \frac{P_{\text{CO}}}{P_{\text{CO}_2}} + \frac{R \cdot T}{2 \cdot F} \cdot \ln P_{\text{O}_2}^{1/2} \tag{2.26}$$



$$E = E^0 + \frac{R \cdot T}{8 \cdot F} \cdot \ln \frac{P_{\text{CH}_4}}{P_{\text{H}_2\text{O}}^{1/2} \cdot P_{\text{CO}_2}} + \frac{R \cdot T}{8 \cdot F} \cdot \ln P_{\text{O}_2}^{1/2}$$



$$E = E^0 + \frac{R \cdot T}{12 \cdot F} \cdot \ln \frac{P_{\text{CH}_3\text{OH}}}{P_{\text{H}_2\text{O}}^4 \cdot P_{\text{CO}_2}^2} + \frac{R \cdot T}{12 \cdot F} \cdot \ln P_{\text{O}_2}^{1/3}$$

The reversible cell potential under standard conditions for the oxidation of H_2 (E^0), when the generated water is liquid, is $E^0 = 1.229V$, while $E^0 = 1.18V$ if the water is generated in the vapour phase.

The potential therefore depends on the partial pressure of each compound, so that variations in the inlet conditions at the anode and cathode will produce an effect on the ideal emf.

Energy balance in the fuel cell

The energy balance can be raised from the expression found for the 1st law or balance of energy in open systems, as shown in Eq. 2.27:

$$\frac{d(mu)_{VC}}{dt}|_{VC} + \sum_s h_s \cdot \dot{m}_s - \sum_e h_e \cdot \dot{m}_e = \dot{Q} - \dot{W} \quad (2.27)$$

and for FCs it is shown in Eq. 2.28:

$$\sum_s \Delta h_s - \sum_e \Delta h_e = Q - W_{electric} \quad (2.28)$$

The maximum energy that could be obtained from a system is given by the enthalpy difference of the products and reactants, as displayed in Eq. 2.29

$$\Delta H = \sum_s \Delta h_s - \sum_e \Delta h_e \quad (2.29)$$

Of this energy, only a certain percentage will be transformed into electrical work, while the rest will be lost in the form of heat (Q) with the possibility of it being reused. Returning to the definition of the Gibbs free energy:

$$\Delta G = \Delta H - T \cdot \Delta S \quad (2.30)$$

ΔG , displayed in Eq. 2.31, represents the useful usable energy that will be transformed into electrical energy from the total, shown in 2.32.

$$\Delta G = -n \cdot F \cdot E \quad (2.31)$$

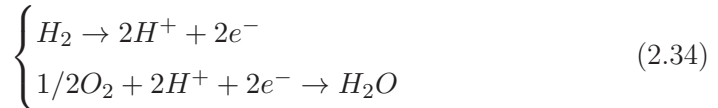
$$\begin{aligned} \Delta H &= \Delta G + T\Delta S \\ \mu &= \frac{\Delta G}{\Delta H} \end{aligned} \quad (2.32)$$

Meanwhile the rest will be lost in the form of heat or entropy generated by irreversibilities, as shown in 2.33.

$$\Delta S = \int \frac{dQ}{T} + \Delta S_{generated} \quad (2.33)$$

Electrical power of a fuel cell

To evaluate the electrical power that a fuel cell can generate, one must consider both the voltage provided by the electrochemical reactions (V) as the number of electrons that are transported per unit of time (intensity, I). This last term depends on the speed with which the reagents are supplied to the anode and cathode. In particular, for the case of an electrochemical hydrogen oxidation reaction:



The contribution of electrons (and therefore the intensity) depends on the flow of hydrogen at the anode. For each molecule of hydrogen, two electrons are transferred, or what is the same, each mole of hydrogen generates two equivalents of electrons.

The real behaviour of fuel cells

In general, the companies are in charge of preparing computer models that allow predicting the behaviour of the FCs in operation. On the other hand, real tests are carried out under different conditions that allow obtaining semi-empirical thermodynamic correlations.

Overpotentials, polarization

The power obtained depends on both the voltage and the intensity of the cell ($P = I \cdot U$). Considering that the voltage depends on the nature of the oxidation-reduction reactions, it can be said that it is interesting to work with sufficiently high current densities to obtain good results. However, as the current density increases, so do the efficiency losses, which translates into a decrease in potential with respect to the ideal equilibrium potential (E^0).

Thus, a typical potential (E) - intensity (I) polarization curve is found in the following figure 2.3.

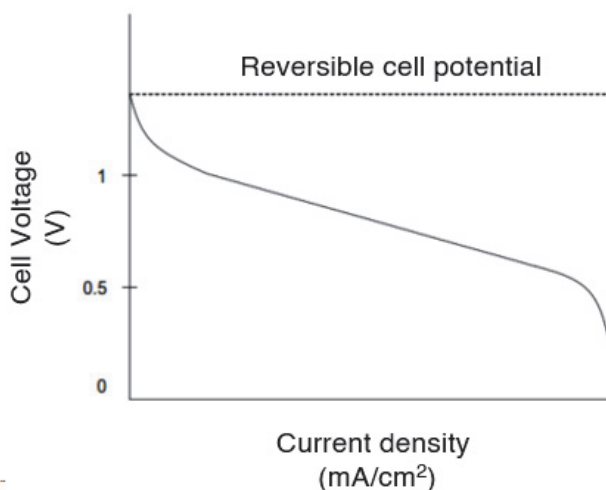


Figure 2.3: An example of a polarization curve.

These irreversible losses (called polarization, overpotential or overvoltage losses) can have three causes: polarization by activation (μ_{act}), ohmic polarization (μ_{ohm}) and concentration polarization (μ_{conc}), which results into a reduction above the ideal potential E ($V = E - losses$).

Activation polarization

This type of loss occurs when the electrochemical reaction is controlled by the kinetics of the electrodes, and results in an activation energy that the system must overcome for the corresponding reactions to take place.

For electrochemical reactions with relatively high values of activation overpotential ($\mu_{act} \geq 50 - 100mV$), this can be expressed according to the Tafel equation:

$$\mu_{act} = \frac{RT}{\alpha nF} \ln \frac{i}{i_0} \quad (2.35)$$

where α is the electron transfer coefficient, and i_0 is the exchange current density.

The representation of μ vs $\ln(i)$ of Eq. 2.35 allows us to calculate i_0 extrapolating the curve at the point where $\mu = 0V$. Hence, i_0 results in a measure of the maximum current intensity capable of being obtained considering the polarization negligible. It is also possible to calculate the slope transfer coefficient as shown in Eq. 2.36.

$$m = \frac{RT}{\alpha nF} \quad (2.36)$$

Therefore, the Tafel curves are determined as in Eq. 2.37:

$$\mu_{act} = a + b \log i \quad (2.37)$$

with $a = -2.3 \frac{RT}{\alpha n F} \log i_0$, and $b = 2.3 \frac{RT}{\alpha n F}$. Note that $i = I/Area$, is the current density, or intensity per unit area.

The term b is the Tafel slope and its values are in the range of 100 mV/decade (log current density) at room temperature (a drop in current density of 10 units causes a drop of 100 mV). An example of a Tafel chart is displayed in Figure 2.4.

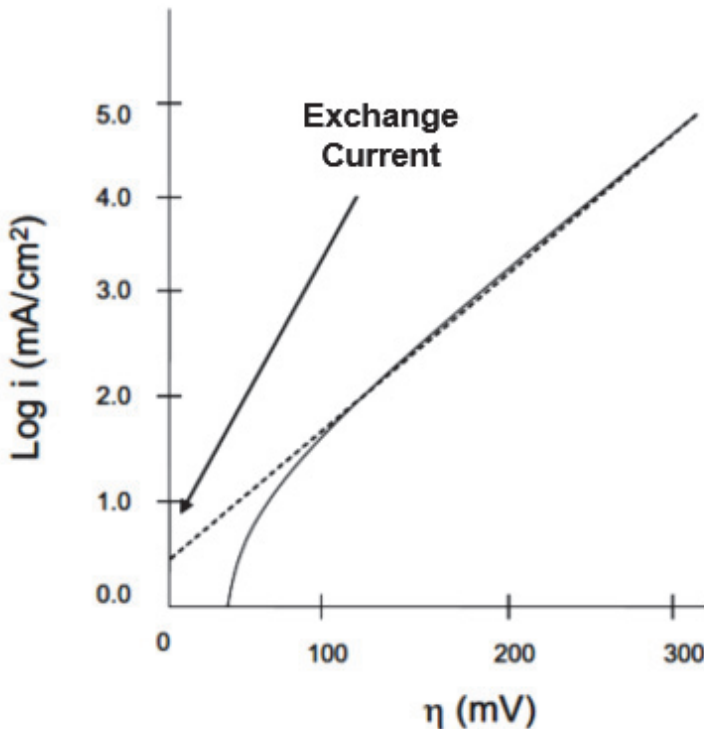


Figure 2.4: An example of Tafel plot.

Ohmic Polarization

Ohmic polarization is related to the resistance of ions to move through the electrolyte and of electrons through the electrodes. These losses can be reduced by decreasing the distance between the electrodes or by increasing the ionic

conductivity of the electrolyte. Ohmic polarization is controlled by Ohm's law, as shown in Eq. 2.38.

$$\mu_{ohm} = i \cdot R \quad (2.38)$$

where i is the current density through the cell, and R is the total resistance, including ionic, electronic, and contact resistance.

Concentration polarization

When a reagent is consumed, there is a loss of potential because it is impossible to maintain its concentration in the electrodes. This causes a concentration gradient and a boundary layer, as shown in the Figure 2.5.

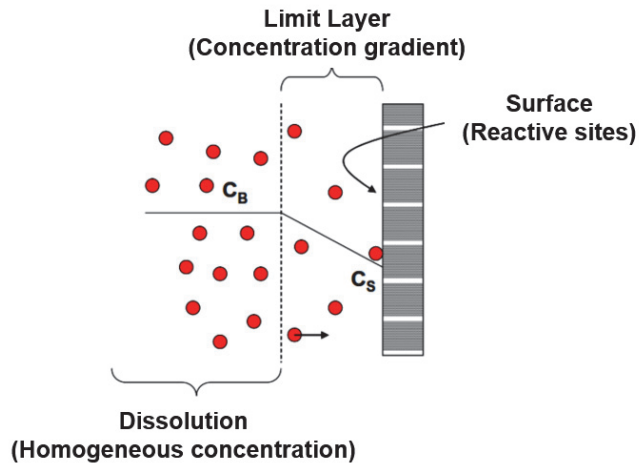


Figure 2.5: Schematic of a concentration gradient.

Several processes can contribute to concentration polarization:

- Slow diffusion from the gas phase to the electrode pores.
- Dissolution processes of reactants or products from or to the electrolyte.

- Diffusion of reactants or products through the electrolyte from or towards the active centres of reaction.

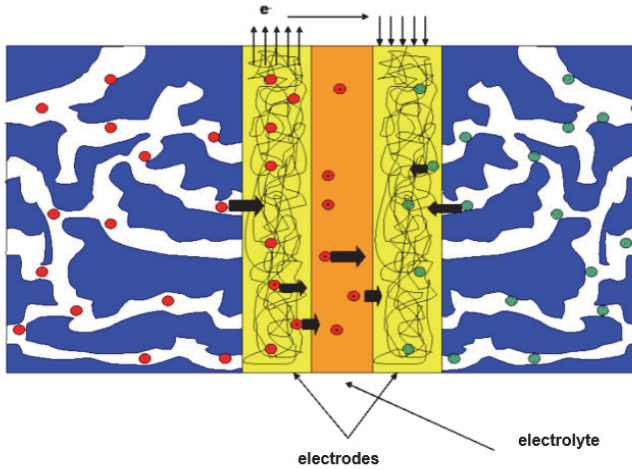


Figure 2.6: Schematic of concentration polarization processes.

For normal operating current densities, the transport of reactants or products to or from the active sites of electrochemical reaction results in the greatest contribution to concentration polarization, which gives rise to Eq. 2.39:

$$\mu_{conc} = \frac{RT}{nF} \ln\left(1 - \frac{i}{i_L}\right) \quad (2.39)$$

where i_L is the limiting current density, and represents the maximum diffusion rate of the components. Again, if data is available from μ and current density (i) it is possible to obtain the limit current.

The diffusion rate can be described in many systems by Fick's law:

$$i = \frac{nFD(C_B - C_S)}{\delta} \quad (2.40)$$

where D is the diffusion coefficient of the components, C_B is the concentration in the solution of, C_S is the concentration at the surface, and d is the diffusion laminar thickness.

The current limit current (i_L) is the measure of the maximum speed at which a reagent can be delivered to the electrode, and occurs when $C_S = 0$:

$$i_L = \frac{nFD C_B}{\delta} \quad (2.41)$$

This allows us to obtain the following relationship between concentrations and intensities:

$$\frac{C_S}{C_B} = 1 - \frac{i}{i_L} \quad (2.42)$$

The Nernst equation when there is equilibrium between all the components, that is, when there is no flow of electric current, is as follows:

$$E_{i=0} = E^0 + \frac{R \cdot T}{n \cdot F} \cdot \ln C_B \quad (2.43)$$

When there is a certain current density, then the concentration at the surface (C_S) is less than in the solution:

$$E = E^0 + \frac{R \cdot T}{n \cdot F} \cdot \ln C_S \quad (2.44)$$

potential difference (ΔE), that is, concentration polarization results:

$$\Delta E = \mu_{conc} = \frac{R \cdot T}{n \cdot F} \cdot \ln \frac{C_S}{C_B} \quad (2.45)$$

which leads to the following expression of the overpotential shown in Eq. 2.46:

$$\mu_{conc} = \frac{R \cdot T}{n \cdot F} \cdot \ln\left(1 - \frac{i}{i_L}\right) \quad (2.46)$$

In the development of all these equations, negligible activation polarization has been considered, since for concentration polarization to be significant, it is necessary to work at high current densities, for which concentration polarization is negligible.

The decrease in total potential is therefore the sum of various contributions, as exemplified in the Figure 2.7.

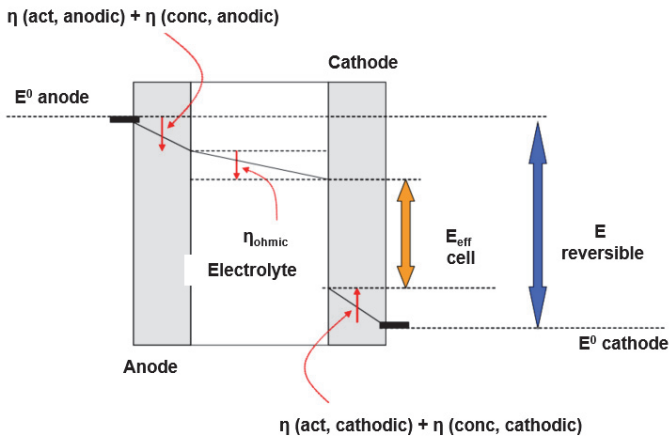


Figure 2.7: Voltage drop in a fuel cell.

In Eq. 2.47, it is shown that there is an overpotential associated with the anode and another with the cathode, with the contributions of the polarization by activation and by concentration:

$$\begin{aligned} \mu_{anode} &= \mu_{act,a} + \mu_{conc,a} \\ \mu_{cathode} &= \mu_{act,c} + \mu_{conc,c} \end{aligned} \quad (2.47)$$

Therefore, the potential at each of the electrodes is given by Eq. 2.48:

$$\begin{aligned}
 V_{anode} &= E_{anode} + |\mu_{anode}| \\
 V_{cathode} &= E_{cathode} - |\mu_{cathode}|
 \end{aligned}
 \tag{2.48}$$

Therefore, the final result is a reduction in the cathodic potential (the highest) and an increase in the anodic potential (the lowest), which leads to a reduction in the potential obtained.

Considering the ohmic losses, the final voltage obtained is shown in Eq. 2.49:

$$\begin{aligned}
 V_{cell} &= V_{cathode} - V_{anode} - i \cdot R \\
 V_{cell} &= E_{cathode} - |\mu_{cathode}| - (E_{anode} + |\mu_{anode}|) - i \cdot R \\
 V_{cell} &= \Delta E_{cell} - |\mu_{cathode}| - |\mu_{anode}| - i \cdot R
 \end{aligned}
 \tag{2.49}$$

which means a net decrease with respect to the ideal cell potential:

$$V_{cell} = \Delta E_{cell} - losses \tag{2.50}$$

Although the three phenomena can take place simultaneously, there are some operating regimes in which one of them predominates over the others. (See Figure 2.8). Activation polarization is dominant at low current densities, since the overcoming of the electronic barrier is prior to the flow of ions. This polarization increases slightly when the current density increases. The ohmic bias increases linearly with current, increasing over the entire operating range as the resistance remains constant. This type of polarization is dominant in a medium range of current densities. Finally, concentration polarization losses occur over the entire operating range, but are prominent at high currents, when the diffusion rate of gases becomes too low to deliver reactants to active sites.

The operation of fuel cells will depend on the operating variables (temperature, pressure, gas composition, current density...) and other factors such as impuri-

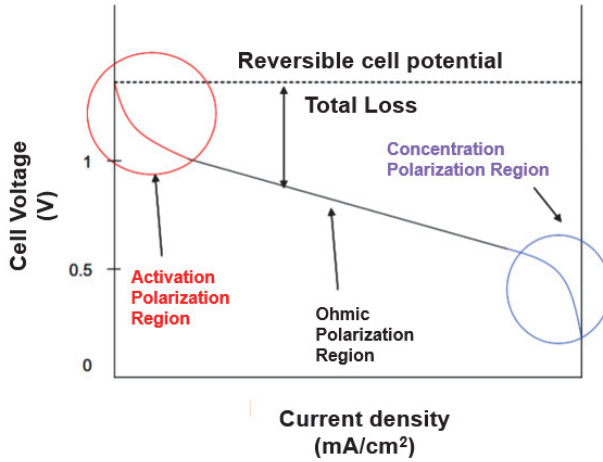


Figure 2.8: Polarization processes.

ties or lifetime. In general, the objective in the design of FCs is that the values of ΔE_{cell} and V_{cell} , are as similar as possible, minimizing polarization losses. This can be achieved by modifying the design of the cell (better electrodes, more efficient electrocatalysts, more conductive electrolytes...) but also by modifying the working conditions (increasing the working partial pressures, varying the temperature, reducing impurities in the input currents...). However, it must be taken into account that the modifications can trigger the cost of operation, and create problems in the materials.

Functioning of a fuel cell. Variables.

Changes in the work variables can produce an improvement in the operation of the stack, with greater efficiencies and / or lower costs, but they can increase the cost of auxiliary operations. On the other hand, the operating conditions are usually determined by system requirements, such as the weight of the battery, the power provided, the voltage and other needs of current densities.

High current density values will provide smaller cell sizes and therefore lower costs, but lower efficiencies will be obtained. It may be more interesting to

obtain high current densities, or low currents and high voltage values. Figure 2.9 shows an example of how voltage, current density and power obtained cannot be optimized at the same operating point.

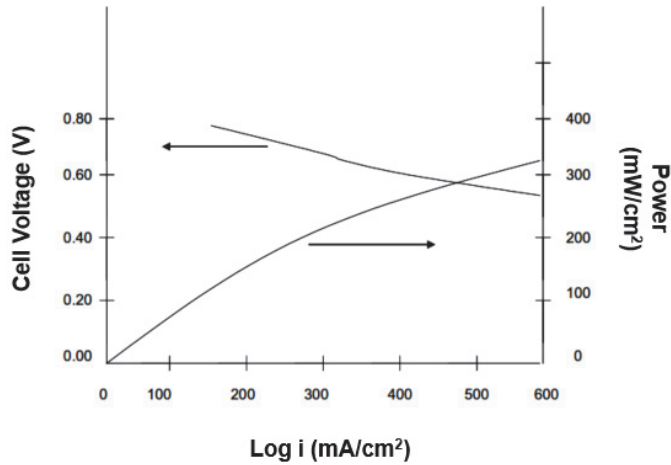


Figure 2.9: Voltage, current density and FC power

Effect of pressure and temperature

According to the fundamental equations of the thermodynamics the effect of both variables can be studied from the derivatives of the potential E with respect to the temperature and pressure:

$$\left\{ \begin{array}{l} \left(\frac{\partial E}{\partial T} \right)_P = \frac{\Delta S}{nF} \\ \left(\frac{\partial E}{\partial P} \right)_T = \frac{-\Delta V}{nF} \end{array} \right. \quad (2.51)$$

As the change in entropy of the reaction H_2/O_2 is negative, then the reversible potential of the reaction is decreased by increasing the temperature. On the other hand, since the volume change is negative, then the reversible potential will increase as the pressure increases ($0.84 \text{ mV}/^\circ\text{C}$).

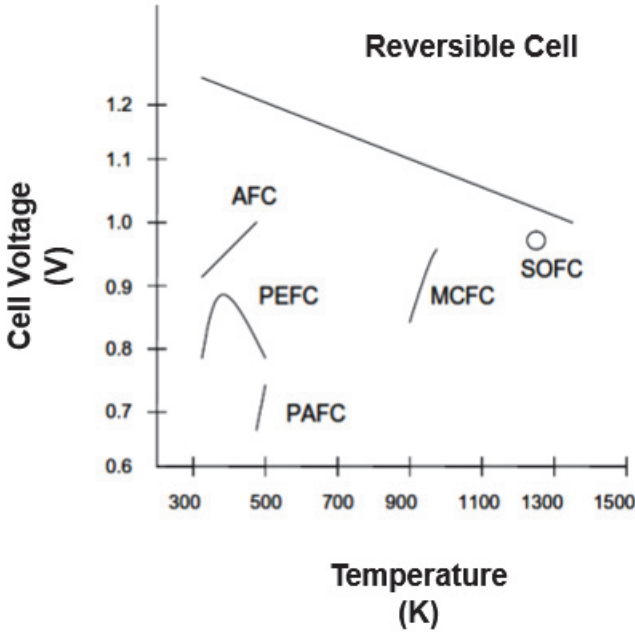


Figure 2.10: Effect of temperature on the potential.

However, the relationships between potential and temperature and pressure depend not only on equilibrium thermodynamic conditions, but also on other kinetic and chemical factors, etc. equally dependent on temperature and pressure. Figure 2.10 reflects the actual behaviour of the potential as a function of temperature and it can be seen that each type of fuel cell shows a different behaviour.

Indeed, it can be observed that the reversible behaviour, and the real behaviour of the different types of FCs is different for each of them. In general, an increase in temperature generates an increase in real efficiency, which is mainly due to changes in polarization depending on temperature. From the kinetic point of view, increasing the temperature increases the reaction rate, mass transfer and decreases cell resistance by increasing ionic conductivity. CO tolerance increases

with increasing temperature as well. On the other hand, there are problems derived from corrosion, degradation of the electrodes or recrystallization, and even loss of electrolyte due to evaporation, if the temperature is too high, which must be considered in the final design.

On the other hand, an increase in pressure represents an improvement in the operation of the cell, by increasing the partial pressure of the reactants, the solubility of the gas and the mass transfer. Efficiencies are also improved. However, an extra investment will have to be made to compress the gases, and there may be problems of resistance of materials that will have to be evaluated in the total balance of costs.

Effect of the composition of the reactive gas

The composition of the reactive gas has a major effect on the operation of the cell and on the overall efficiency. From the Nernst equations it follows that an increase in the partial pressure of the fuel and the oxidant will cause a higher cell potential. You can define the fuel utilization (U_f) as the fraction of fuel u oxidizing introduced in the FC that electrochemically reacts.

In the case of FCs working at low temperatures, U_f it is very easy to determine when H_2 is the reactant, since it is the only gas present in the stream:

$$U_f = \frac{H_{2,in} - H_{2,out}}{H_{2,in}} = \frac{H_{2,consumed}}{H_{2,in}} \quad (2.52)$$

where $H_{2,in}$ and $H_{2,out}$ are the FC entry and exit flows of H_2 , respectively.

The effect of the composition of the reactive gases is more interesting in the case of FCs working at high temperatures, as for instance MCFCs. In them, you can use both, O_2 and CO_2 , although O_2 is generally used.

Generally the O_2 is the reactant in excess while the CO_2 is the limiting reagent, so it is used for oxidant flow rates calculations. These FCs allow the use of CO

as well, although the reaction is much slower than the oxidation of the H_2 . The definition of U_f is as follows for a MCFC:

$$U_f = \frac{H_{2,consumed}}{H_{2,in} + CO_{in}} \quad (2.53)$$

In summary, the effect of the input composition on the potential calculated according to Nernst's law for a MCFC can be observed in Eq. 2.54:

$$E = E^0 + \frac{RT}{2F} \ln \frac{X_{H_2} X_{O_2} X_{CO_2,cathode} P^{1/2}}{X_{H_2O,anode} X_{CO_2,anode}} \quad (2.54)$$

where X_i are the mole fractions of gases, and P is the absolute pressure. The dependence of the reversible cell potential on utilization can be seen in Figure 2.11.

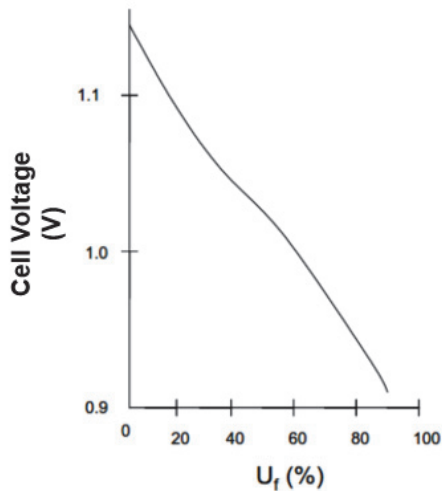


Figure 2.11: Cell voltage as a function of flow.

2.2 Basic Components in Proton-Exchange Membranes Fuel Cells (PEMFC).

The structure of PEMFCs, shown in Figure 2.12, consists of the following elements: anode and cathode electrodes, proton-exchange membrane (PEM), catalyst layer (CL), gas diffusion layer (GDL), and bipolar plates (BPs). In general, the operating sequence is the following: the reactant gases flow into the anode and cathode through the delivery manifolds. At the interface between the electrode and the membrane is where the reduction and oxidation reactions occur. Concerning the gas diffusion layer, its functions are twofold: first, to ensure that the gas moves towards the catalyst layer; and second, to ensure the flow of electrons to and from the catalyst [1,4,9-13].

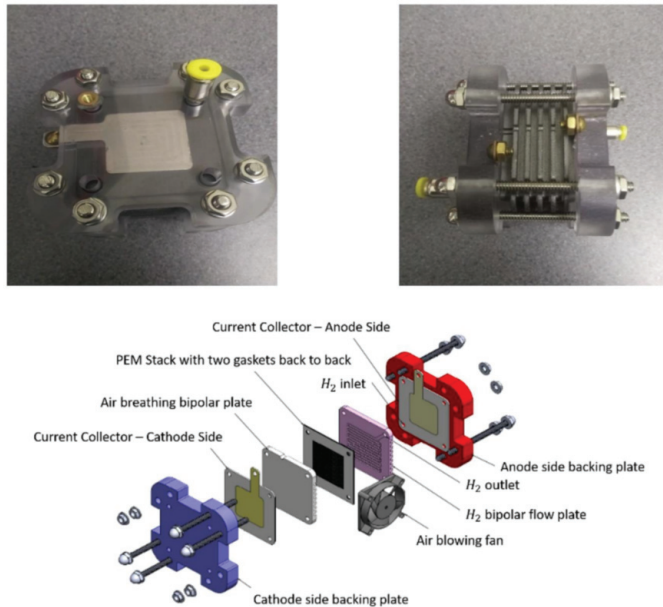


Figure 2.12: Exploded view of PEMFCs. Source: [4]

Proton-exchange membrane fuel cells (PEMFCs) are FCs that typically utilize as reactants hydrogen, that is filled in the anode, and oxygen, that would be

supplied in the cathode. The membrane is normally made of Nafion®, and it acts as an electrolyte. A general schematic is included in Figure 2.13.

Regarding the operating temperature, it shows great versatility and it can operate in both, the low-temperature (333 - 353 K) and the high-temperature (403 - 473 K) range. Accordingly, in low-temperature PEMFCs when the applied hydrogen is obtained through hydrocarbon reforming, catalyst poisoning can occur unless the presence of carbon monoxide is erased. On the contrary, in high-temperature PEMFCs this issues is negligible. Some advantages of PEMFCs are its high power density, lightness, and compactness which allow them to be easily assembled in stacks [4].

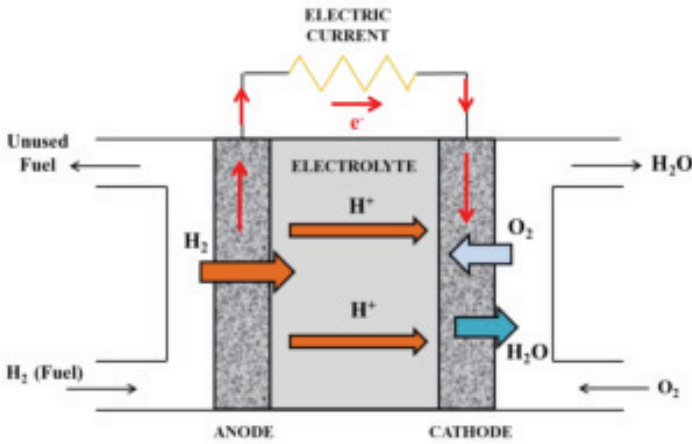
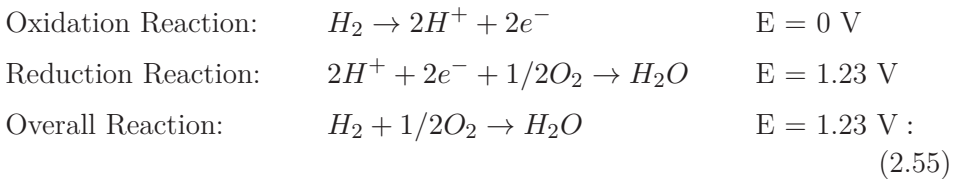


Figure 2.13: Schematic diagram of a Proton Exchange Membrane Fuel Cell (PEMFC).

The overall reaction leading to the generation of electrical energy and water is displayed in Eq. 2.55.



A brief description of the major components is provided as follows:

- **Membrane:** It is located between the catalyst layers of the anode and cathode. Its principal functions involve the following: (i) to separate both electrodes; (ii) to carry along protons from anode to cathode; and (iii) to block the transfer of electrons. Subsequently, the chosen material must display features such as high ionic conductivity, low electric conductivity, good thermal, mechanical and chemical stability. Proton conduction in membranes is caused by three transfer mechanisms: surface diffusion, Grotthuss hopping, and vehicular diffusion [7,14]. The Grotthuss hopping mechanism occurs when the protons jump from one hydrolysed site to another. Contrarily, the vehicular diffusion mechanism occurs when a hydrated proton is diffused with the aid of electroosmotic drag. These mechanisms need high hydration levels. Accordingly, the level of hydration influences the proton conductivity of the membranes. Another important factor influencing proton conductivity is the membrane's thickness [15-19]. Thus, a drop in thickness results in more water adsorption which facilitates proton conductivity. The surface diffusion mechanism occurs when the protons hop between sulfonic sites, and it requires a low hydration level [3].
- **Anode and cathode electrodes:** The electrochemical reaction is paramount to obtain a good performance. In order to achieve good rates, the hydrogen oxidation reaction and the oxygen reduction reaction are meticulously designed. An increment in the surface area of the catalyst is sought after to improve the whole cell performance. A typical electrode assemble in a PEMFC is made of a catalyst layer, gas diffusion layer, and a microporous layer. Generally, Pt or Pt-based alloys are used as catalyst. However, it is not abundant, thus expensive, and it is easily poisoned by carbon monoxide. Therefore, researchers are focused on finding other alternatives [3].

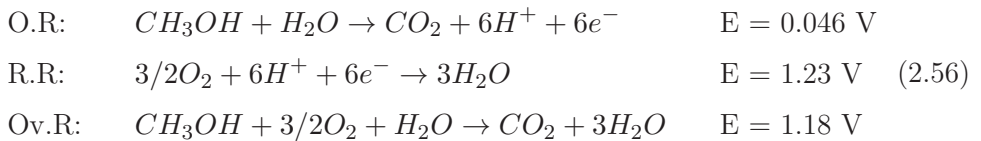
- **Bipolar plates:** The function of the bipolar plates (BPs) is to act as separator between two-unit cells and provide mechanical strength to the stack, and therefore, are also an important component in PEMFCs. Furthermore, BPs play the role of the transportation of reactants, products, electrons and heat released among the unit cells. A good BP must display high thermal and electrical conductivity, good resistance to corrosion and mechanical properties since it represents 60% - 80% of the total weight. Accordingly, the most common material utilised for the preparation of BPs is graphite. Nevertheless, its brittle nature together with its unsettled production has made other candidates, like metal and alloys, more desirable. During the design stage, factors such as a correct design of the flow field, the choice of suitable materials, and the fabrication process have a significant impact on the final cost. Indeed, it represents 40% - 50% of the total cost [3].
- **Other major components:** A *current collector plate* is located in a PEMFC attached to the BPs, and its main function is to collect all the electric current that is generated in the PEMFC. In order to increase its efficiency, the chosen material must be light, exhibit a high electric conductivity, and display high mechanical and electromechanical stability. Subsequently, titanium, aluminum, copper and stainless steel are preferred. Another paramount component is the *sealing material*. It is located amidst the membrane and the BPs, and its function is related to limit leakages. The selected material should display good gas impermeability together with high thermal, electrochemical, and chemical stability. Generally, PTFE, PTFE-based, and silicon elastomers are the materials of choice. The *end plates* are located at both ends of the PEMFCs, i.e., at the anode and cathode ends. In an attempt to decrease total cost and to increase lightness, aluminum and polymer-based materials are selected for the fabrication process stage [3].

Overall, low-temperature FCs fuelled by hydrogen are a promising alternative to the use of conventional fossil fuels in many applications, but in particular, in the car industry. It is noteworthy to mention that hydrogen is a good energy vector, has a high energy density and its oxidation reaction has the formation of water as its only product. Nevertheless, as it has been mentioned in Chapter 1, hydrogen production is only free of GHG emissions when renewable energies are used. Another inconvenient of hydrogen PEMFCs is that due to its high flammability, its use in some applications pose some problems. Accordingly, in the case of on board storage, a lot of restrictions must be accomplished for the sake of safety. Consequently, another type of PEMFCs that make use of methanol as fuel are considered.

Direct Methanol Fuel Cells (DMFCs)

Methanol is liquid in the temperature range from 176 to 337 K at atmospheric pressure. This property is of great interest for transport and storage purposes, which makes DMFCs a great choice for small portable devices, specially in the field of consumer electronics. In Chapter 1 the problematic with its production has been already discussed. However, as long as 2nd generation biomass is used, the production process should not contribute to increment GHG emissions [20].

DMFCs are based on the oxidation of methanol in the anode of a PEMFC according to the reaction displayed in Eq. 2.56. Moreover, an schematic is included in Figure 2.14.



Their working principle is similar to hydrogen PEMFCs. Indeed, instead of a gas the use of a liquid mixture avoids the use of reforming operations. The biggest problem caused by DMFCs is the crossover phenomenon. It consists of

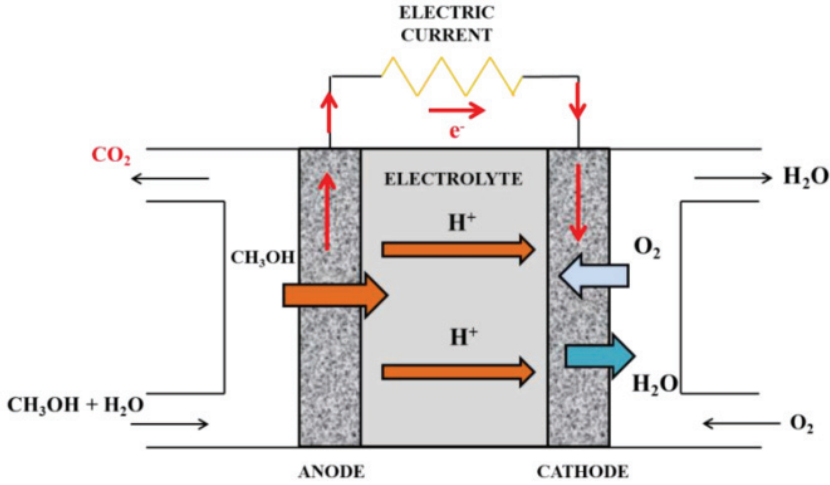


Figure 2.14: Schematic diagram of a direct methanol fuel cell (DMFC).

the flow of unreacted alcohol through the electrolyte, and its reaction with the oxygen in the cathode, which results in a normal combustion reaction. This represents a significant 30% loss of efficiency in DMFCs.

In recent years, DMFC patent numbers have increased substantially. Most commercial systems are integrated into an active system, i.e., which is a system which provides humidity and temperature control. Nonetheless, given its higher price and larger energy consumption, most of the work performed on DMFCs is focused on passive systems [20].

Transport phenomena through the electrolyte. Fuel Crossover

In DMFCs, and in FCs in general, transport phenomena is paramount to obtain a good performance. The transport of protons through a polymeric membrane is determined by its proton conductivity (σ_{Prot}), and it is usually stated in $S \cdot cm^{-1}$. The experiments carried out to determine σ_{Prot} , usually utilize frequency analysers in proton saturated conditions [21,22].

The fuel crossover is the most important limitation that DMFCs suffer. In membranes undergoing crossover the methanol molecules flow from the anode to the cathode and react with the oxygen in a conventional combustion reaction as shown in Figure 2.15. Studies to reduce crossover must consider the transport mechanisms of the different compounds namely, methanol, water and protons [20-22].

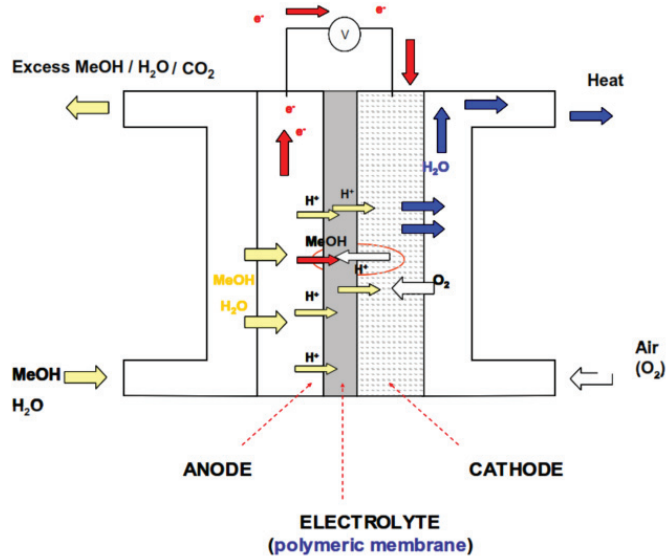


Figure 2.15: Schematic representation of transport and crossover in DMFC.

In general, transport of small molecules across a dense polymer follows a solution diffusion mechanism [20]. Solutes are absorbed in the membrane, diffuse across the membrane and desorb out of the membrane. The transport rate is determined by a permeability coefficient (P) which includes the solubility (S) and the diffusion coefficients (D), as described in Eq. 2.57.

$$P = S \cdot D \quad (2.57)$$

For transport phenomena in PEM some other parameters must be considered, such as the ion transport or the ionic structure of the polymer. Moreover, the driving force is not only the concentration difference but also the electric potential difference [6].

Ideally, the transport of protons (desired) and methanol (undesired) can be described separately [6]. Accordingly, the proton conductivity can be related to the diffusion coefficient σ_1 as shown in Eq. 2.58.

$$\sigma_1 = \frac{D_1 C_1 F^2}{R T} \quad (2.58)$$

This is based on the Nernst-Planck equation, and relates the proton conductivity (σ_{Prot}) to the diffusion coefficient (D_1), the concentration (C_1) and charge of protons, the Faradays constant (F), and the absolute temperature (T).

On the other hand, for methanol transport, and under certain circumstances, the steady-state flux can be described by the Fick's law (Eq. 2.59).

$$j_2 = \frac{P_2 C_2}{L} = \frac{D_2 K_2 C_2}{L} \quad (2.59)$$

where K_2 is the partition coefficient, i.e. ratio of methanol concentration inside the membrane to that in the adjacent solution, $D_2 K_2$ is the methanol permeability (P_2), and j_2 is the methanol flux.

From these equations, it is possible to define the selectivity for protons to methanol as described in Eq. 2.60.

$$\alpha_{1/2} = \frac{\sigma_1}{P_2} = \frac{D_1 C_1 F^2}{D_2 C_2 R T} \quad (2.60)$$

Conductivity and permeability are proportional to their respective diffusion coefficients, and can be separately measured in the development of PEM studies. For enhanced α are desired. DMFC performance, high values of $\alpha_{1/2}$ are desired.

The factors that affect the membrane selectivity are interdependent and also depend on other parameters. D_2 is a function of water and methanol concentration and also of the free volume of the polymer. K_2 depends on C_1 and also on the water/methanol uptake and the solute-polymer interaction parameter. Finally, D_1 also depends on C_1 and on the water content and on the structure of the membrane.

These interrelationships makes the design of new membranes having enhanced selectivity ($\alpha_{1/2}$) a complex task. Furthermore, experiments with different membranes have shown that protons and methanol have similar molecular transport mechanisms in membranes containing sulfonic acid groups [6].

The transport of protons, water and methanol in PEM is very complicated, and occur simultaneously and over a wide length of scales. Furthermore, the influence of the voltage must also be considered. It is widely assumed that there are two main mechanisms for proton transport in PEM, namely, proton hopping and the vehicular or electroosmotic drag mechanisms. The hopping mechanism occurs when protons (H^+) hop from one hydrolysed site ($SO_3^- H_3O^+$) to another by the formation and destruction of hydrogen bonds [6].

The transport of water also occurs by two suggested mechanisms: electroosmotic drag and concentration gradient (as self-associated clusters), while the diffusion of methanol in water can be accounted for in a number of ways: as self-associated clusters $(CH_3OH)_\alpha$, as complex hydrogen-bonded to water $(CH_3OH)_m(H_2O)_n$ and also as a complex bound to protons $H^+(CH_3OH)_b$, which is similar to electroosmotic drag [6]. The interconnection between the transport mechanisms is summarised in Figure 2.16.

The final transport mechanism must also include multicomponent diffusion, the interactions between the solutes and the polymer, and the electrostatic potential gradient for methanol and water. Therefore, all the transport equations should incorporate the Nernst-Planck and Stefan-Maxwell framework (considering electrostatic and multicomponent effects).

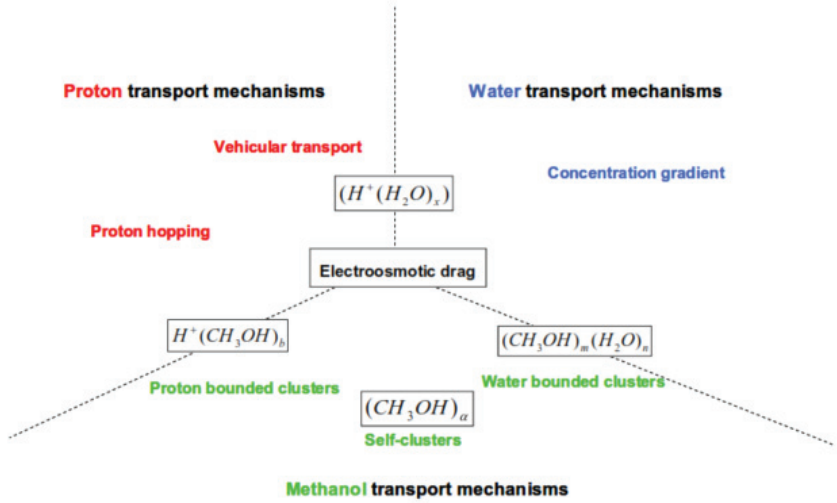


Figure 2.16: Schematic representation of different transport mechanisms in DMFC.

PEM must be designed to retain a certain degree of hydration in the membrane since water is involved in proton transport. It is important to achieve a balance of the classes of water in the electrolyte. Two main types of water can be found in the membranes: free water and bound or structural water. The first can be readily removed from the membrane and is responsible for the vehicular transport, while the latter remains in the structure of the polymer. The amount of water in the membrane will depend on the water present initially in the membrane, the water produced at the cathode, the water evaporated, and the water dragged by the exhausted air at the cathode. The degree of humidity in the membrane can be also controlled by humidification of the fuel used (hydrogen, methanol, ethanol...), and by the temperature. The water balance in the cell should also consider the electro-osmotic drag of water from the anode to the cathode caused by the electrical potential drop through the membrane. The electro-osmotic drag coefficient (K) can be calculated as the ratio of the water molecules and the protons transferred through the membrane [6].

2.3 Proton-Exchange Membranes (PEM)

One of the most important components in a PEMFC is the proton-exchange membrane (PEM). Due to the complexity in the chemical environment inside the PEMFC, the ideal PEM would meet the following requirements [23-38]:

- High proton conductivity.
- High electronic resistance.
- Chemical stability in both, anode and cathode, environments.
- Good mechanical strength.
- Minimal fuel crossover.
- High durability.
- Ease of fabrication.
- Cost-effective.

Given the importance that the complex mass and energy transfer processes have on the overall performance, to reach a high proton conductivity is critical.

As it has been mentioned above, proton transport in hydrated membranes is explained mainly through three mechanisms, vehicular and Grotthuss, and surface as shown in Figure 2.17.

Protons can also be transported through a structural diffusion process where protons are transferred across a chain of hydrogen bonds followed by reorientation of the water dipoles. This structural diffusion is referred to as the Grotthuss mechanism. Lastly, proton transport can occur via a molecular diffusion process, known as the vehicular mechanism, where a hydrated proton aggregate moves through the aqueous channel as a single entity. The mechanism by which

protons hop between the sulfonic acid groups that line the pore wall mediated by intermediate water molecules is known as the surface mechanism.

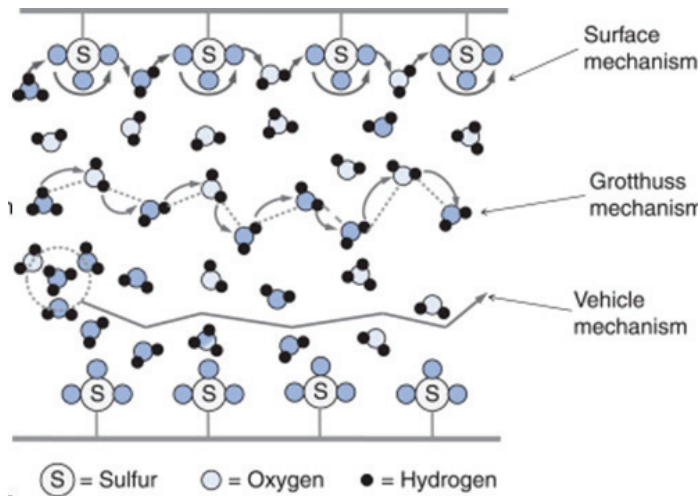


Figure 2.17: Schematic of the different transport mechanisms. Source: [35].

Nafion® is the benchmark membrane used in commercial FCs. Introduced by DuPont in the 1960s, is made by sulfonated polytetrafluoroethylene as shown in Figure 2.18. It displays a series of features like high proton conductivity, water permeability, high chemical and electronic resistance, that has converted it into a standard for FC manufacturers. However, it also has its drawbacks. Indeed, in PEMFCs, the limiting factor is the relative humidity that must be high in order to optimize the proton conductivity, and therefore, the operating temperature must be limited, generally, at temperatures below 80°C.

Gierke proposed a cluster network model where the structure is described as an inverted micelle [39]. The ion exchange sites are separated from the fluorocarbon backbone forming clusters with a diameter of approximately 4 nm are interconnected by short narrow channels with a diameter of about 1 nm. Figure 2.19 shows the cluster network model proposed by Gierke.

Perfluorinated membranes pose a series of issues that need to be addressed, as for instance:

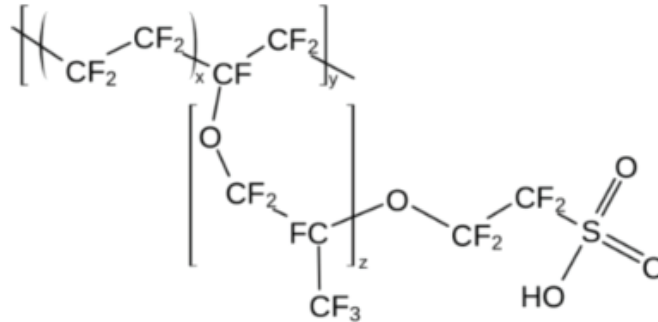


Figure 2.18: Nafion® chemical structure.

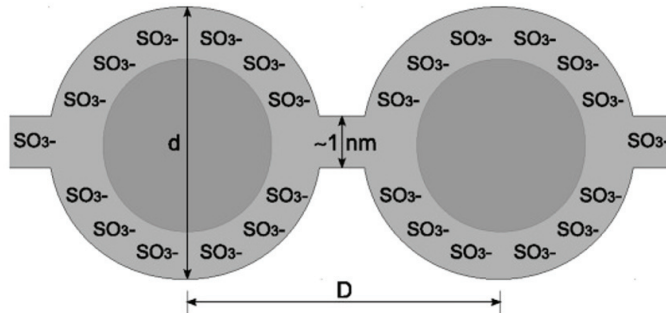


Figure 2.19: Gierke's cluster network model where d is the cluster diameter and D is inter-cluster distance. Source: [39].

- Useless in the high-temperature regime.
- Cost of materials is high.
- Required relative humidity cannot be reached unless a humidification equipment is used.
- Hazardous waste.
- Water uptake promotes swelling and shrinking.
- Chemical degradation.

To overcome them, alternatives to Nafion® must be sought in order to fabricate cost-effective membranes that provide high levels of proton conductivity, together with good mechanical, thermal, and chemical stability; a reduced fuel crossover is also a sought-after feature to maximize overall performance. Consequently, these alternatives to Nafion® are grouped in three categories: partially fluorinated, non-fluorinated and composite membranes [25].

Partially fluorinated membranes were initially designed to solve the hydration issues posed by Nafion® membranes. These membranes are mainly Nafion® membranes modified with organic or inorganic additives like ZrO_2 , TiO_2 , $TiSiO_4$, and Silica to increase water retention. Accordingly, physicochemical properties such as the elastic modulus, the tensile strength, and hydrophobicity are enhanced without negatively impacting on proton conduction. Nonetheless, their commercial application is not yet massive since the trifluorostyrene monomer availability is scarce, which increments costs. To reduce them, hydrocarbon polymer are currently being studied by researchers given its high proton conductivity [25].

Non-fluorinated membranes are an attempt to completely replace fluorinated materials from the fabrication of PEM, by using widely available polymers with the consequent cost reduction. Some of examples of these polymers that are used for PEM applications are polystyrene (PS), Poly (arylene ether ketone) (PAEK), Acid-doped polybenzimidazole (PBI), or Poly (vinyl chloride) (PVC). Despite non-fluorinated membranes are promising, tests show that these membranes still do not match fluorinated and partially-fluorinated membranes in terms of proton conductivity, thermal and chemical properties. Note that this class of membranes is not exclusively formed by polymers, ceramic materials have also been tested, and good proton transport, high water uptake and high hydrogen permeability were obtained [25].

Composite membranes are the least expensive ones in comparison with the previous types. It exhibits good properties for its application in PEM, such as high levels of water uptake, has a high-temperature range, and it can be recycled.

Nevertheless, it also has certain drawbacks, as for instance, low thermal and proton conductivity, and it lacks chemical stability. There is still a lot of work left to find composite membranes that outperform Nafion® membranes not only under certain conditions. However, composite membranes could be suitable in light applications where a high performance is not required [25].

This section presents a state of the art of the novel membranes developed during the past decades for such purpose. Given the different characteristics needed for PEMFCs fuelled by hydrogen and methanol, the review would focus on each type of PEMFC individually.

2.3.1 PEMs for hydrogen FCs

In recent years, the importance and need to replace Nafion® to avoid its drawbacks and allow the massive use of this technology has been demonstrated. Accordingly, the following studies have been highlighted.

Inorganic Fillers

Fillers are introduced in polymer membranes to enhance physicochemical properties like thermal stability, mechanical strength and water uptake, so that the membranes can be operated at low relative humidities and/or high temperatures [30]. The incorporation of a filler augments the path of the hydrogen molecules, i.e. tortuosity increases, and thus, it contributes to prevent the crossover phenomenon. Furthermore, fillers might be functionalised as well, which can help to promote proton conductivity without increasing other detrimental effects for the overall performance of FCs [30].

- *Nafion®/Metal Oxides membranes:* In Di Noto et al. Nafion® was mixed with different metal oxides (TiO₂, ZrO₂, HfO₂, TaO, and WO₃) to analyse its effect on proton conductivity. Results show the applicability of these membranes for high-temperature PEMFC provided that they were found to be thermally stable below 443 K. The sulphonic side group was found

to interact with different water domains (bulk and solvating ions), and this interaction depended on the metal oxide considered. Lastly, proton hopping was found to be the proton transfer mechanism [40]. In Adjemian et al. also studied composite membranes with several metal oxide fillers (TiO_2 , SiO_2 , Al_2O_3 , and ZrO_2) varying the temperature range from 353 to 403 K. At higher temperatures and low relative humidity membranes containing TiO_2 or SiO_2 performed better in comparison with pristine Nafion® [41]. In Pineda-Delgado et al. Nafion®/ HfO_2 prepared composite membranes. Water uptake was highly improved, 61% vs 29% at 373 K. Consequently, a better proton conductivity was obtained, 112 vs 82 $mS \cdot cm^{-1}$. A maximum power density of 0.336 $W \cdot cm^{-2}$ compared to 0.188 $W \cdot cm^{-2}$ was achieved at 373 K [42].

- *Nafion®/Silica membranes:* In Oh et al. prepared sulphonated silica Nafion® composite membranes with different filler concentrations (0.5, 1, and 1.5%). The filler was synthesized through a sol-gel calcination process. The optimum filler concentration was found to be 1%. Transmission electron microscopy (TEM) micrographs revealed that the performance gains were obtained thanks to a more efficient proton transport due to well-defined phases in the membrane structure [43]. In Xu et al. silica Nafion composite membranes were fabricated by swelling the Nafion® membrane with silica, as opposed to the solution casting technique, in order to find a better filler dispersion. An advantage of using this technique is that the ordered nanophase-separation structure of Nafion is not altered, and thus, a higher water uptake with low swelling was achieved. The lower internal resistance of the composite membrane explains the better performance in comparison with Nafion® [44].

Other polymers were used to prepare electrolytes as polybenzimidazole (PBI), sulphonated polyethersulphone (SPES), and sulphonated poly arylene ether ketone (SPAEEK).

- *PBI/Metal Oxides membranes*: In Ozdemir et al. composite membranes with PBI as the polymeric matrix and several metal oxides (SiO_2 , TiO_2 , ZrP) as fillers were synthesized for high-temperature PEMFCs. Unlike TiO_2/PBI , the proton conductivity of SiO_2/PBI and ZrP/PBI membranes was higher than pristine PBI. In the case of TiO_2/PBI , a bad distribution of the filler is the cause for the performance worsening. SiO_2/PBI and ZrP/PBI exhibited the highest values of conductivity at 453 K [45]. In Lee et al. PBI with sulfophenylated titanium oxide nanoparticles membranes were synthesized for its application in high-temperature FCs. The addition of the filler helped improving both, proton conductivity and acid retention. Moreover, at 423 K, the peak power output ($621 \text{ mW} \cdot \text{cm}^{-2}$) was higher than the one obtained with pristine PBI ($471 \text{ mW} \cdot \text{cm}^{-2}$) [46].
- *SPES/Metal Oxides membranes*: In Elakkiya et al. sulphonated TiO_2 coated in polyaniline within a SPES polymer matrix composite membranes were evaluated. Incorporating the filler enhanced water uptake and proton conductivity [47].
- *SPAEEK/Metal Oxides membranes*: In Lee et al. studied sulphonated silicon dioxide (SiO_2) within sulphonated poly arylene ether ketone (SPAEEK). The addition of the filler promoted a better performance at 60°C and at 70 and 100% RH. Moreover, the membrane with the functionalised filler provided better results than the non-functionalised one because the sulphonic groups retained more water, which promoted proton conductivity [48].

Carbon Nanomaterial Fillers

Carbon nanomaterials, in particular graphene oxide (GO), have gained popularity due to the great amount of functional groups containing oxygen, which attract water molecules, and thus allow it to retain higher levels of water which enhances proton transport [49].

- *Nafion®/GO membranes*: In Maiti et al. a composite Nafion membrane comprising of graphene oxide and an ionic liquid (dihydrogen phosphate functionalised imidazolium) was synthesised for its application in high-temperature PEMFCs. The thermal analysis revealed that the ionic liquid is stable up to 503 K. Composite membranes exhibited better proton conductivity than Nafion® 117 in the temperature range from 343 to 383 K. Moreover, in single cell tests the composite membrane showed higher current densities in dry conditions [50]. In Ibrahim et al. analysed the performance of GO composite membranes fabricated via solution casting with different thicknesses at intermediate operating temperatures. Mechanical properties and water uptake were improved when compared to pristine Nafion®. The in-situ fuel cell testing revealed the importance of the membrane thickness. Indeed, the 30 μm composite membrane tested at 373 and 393 K exceeded the performance of the 50 μm Nafion membrane at 353 K. The reason is twofold: the thickness reduction and that more water molecules were retained thanks to the presence of the GO [51].
- *PBI/GO membranes*: In Uregen et al. investigated the performance of a graphene oxide/polybenzimidazole membrane for its application in high-temperature FCs. Proton conduction was enhanced by the presence of GO when compared to pristine PBI. Fuel cell testing was performed at 438 K and with dry hydrogen and air. Results showed that the composite membrane exhibited a better maximum power density than pristine PBI. A 500 h durability test showed that the performance loss of the composite membrane was lower, and mainly due to acid leaching and hydrogen crossover [52]. In Abouzari-Lotf et al. synthesised a PBI membrane functionalised with 2,6-Pyridine with phosphonated graphene oxide for its application in high-temperature fuel cells. Proton conductivity was remarkably improved by the addition of the phosphonated graphene oxide measured at 413 K [53].

- *SPAES/GO membranes*: In Lee et al. fabricated a membrane that consisted in SPAES composite with GO grafted onto sulfonated poly(arylene thioether sulfone) as the filler. Results show that mechanical properties and oxidative resistance were enhanced. Moreover, it showed an improved proton conductivity when compared to pristine SPAES [54].
- *PES-PVP membranes*: In Dai et al. novel composite membranes consisting of carbon dots of different sizes and with varying levels of hydrophilicity within a matrix of polyvinylpyrrolidone (PVP) and polyethersulfone (PES) were fabricated. Single cell tests were run at 423 K, and the composite membrane displayed a higher peak power density when compared to pristine PES-PVP [55].

To conclude, the high versatility of fillers allow their incorporation into polymeric matrices being able to improve several characteristics like low relative humidity, increasing mechanical strength, preventing acid leaching, increasing proton conductivity, or allowing PEMs to be operated in the high-temperature regime [30]. Furthermore, functionalisation can be applied which helps to enhance these features. The different studies show promising results performance-wise, however only Nafion® meet the industry requirements in terms of durability and lifetime. Therefore, more research is needed to find new membranes that can substitute Nafion®.

2.3.2 PEMs for direct alcohol FCs

Concerning DMFCs/DEFCs, Nafion® is utilised as well due to its chemical stability and high ionic conductivity. Nonetheless, its major drawback is its high degree of methanol permeability which originates an overall loss of performance due to fuel crossover. This is caused by the following factors: (i) an active transport of protons and water; (ii) diffusion through the water-filled pores within the Nafion-structure; (iii) diffusion through Nafion® itself. Consequently, DMFCs are providing less performance than PEMFCs fueled by hydrogen, which is a major concern for its widespread use.

Regarding the Nafion®-based, fillers are added in order to offer chemical stability and mechanical reinforcement to the Nafion® membrane. Among them there are three classes: organic, inorganic, and carbon nano-material filler-based.

Nafion-based composite membranes with organic fillers.

Polytetrafluoroethylene (PTFE) is the most used organic filler used as reinforcement of Nafion membrane due to its chemical stability, corrosion resistance and mechanical strength. Several studies have analysed the performance of Nafion/PTFE in DMFCs [30]. In addition, Chen et al synthesized a Nafion/PTFE membrane and included zirconium phosphate (ZrP) in the structure. Results show that the methanol crossover was reduced, however, a poor proton conductivity was obtained in the case of the Nafion/PTFE/Zr membrane. Overall, the performance of Nafion/PTFE membranes was superior, and display values similar to Nafion® 112 but higher than Nafion® 117 and 115 [56].

Another requirement for new membranes is to reduce costs. Accordingly, other alternatives such as polybenzimidazole (PBI), polyvinyl alcohol (PVA), polyaniline (PANI), polypyrrole (PPy), sulphonated poly arylene ether ketone (SPAEEK), and sulphonated poly ether ether ketone (SPEEK) are studied.

- *Nafion®/PBI membranes:* The fabrication method of the membranes was shown to be very important. Indeed, [58] tested the results of two membranes with different techniques, spin coating & dipping (T1), screen printing (T2). Results for the T1-membranes showed that the methanol crossover was reduced, however, high impedances were found. Contrarily, T2-membranes exhibited the a reduced methanol crossover but without the increment in the impedance. The overall performance was found to increase only at high concentrations of methanol (3.2M) [57,58].
- *Nafion®/PVA membranes:* The performance of pristine Nafion® & Nafion®/PVA membranes was found to be the same at low thickness. Nonetheless, At high thickness values Nafion®/PVA membranes exhibited a better be-

haviour at high temperatures. At any fixed condition (thickness, temperature, and methanol concentration) the OCV of Nafion®/PVA membranes was higher than pristine Nafion®. This means that Nafion®/PVA effectively reduce methanol crossover [58-63].

- *Nafion®/PPy membranes:* Results show that the electrostatic interaction between the sulphonate groups of Nafion and PPy decreased the pore volume of Nafion membrane which led to low methanol permeability. However, this interaction increased membrane and cell resistance, and therefore, it was not so beneficial for the proton conductivity, that diminish. This effect was more intense at high current densities [64-68].
- *Nafion®/PANI membranes:* DMFCs tests results showed that Nafion®/PANI membranes exhibited a reduced methanol permeability and an augmented ionic conductivity when compared against the pristine Nafion® membrane. In general, Nafion®/PANI membranes provide better results than Nafion®/PPy membranes. However, it must be noted that the best performance is always found at high concentration values of methanol [69-71].
- *Nafion®/SPAEK membranes:* The reason to choose SPAEK is due to its high proton conductivity and methanol resistance. Several concentrations were tested (1 to 4M) but the best results were found for 2M. The minimum power density is found for 4M, and therefore, this loss of performance is due to methanol crossover [72,73].
- *Nafion®/SPEEK membranes:* The reason to choose SPEEK is due to its good mechanical properties, proton conductivity and good processing capacity. Results showed that the Nafion®/SPEEK membrane presented low levels of methanol permeability, higher open circuit voltages, and better single-cell performance in comparison with Nafion® 115 [74,75].

Nafion-based composite membranes with inorganic fillers.

The addition of inorganic particles into Nafion® is done to improve its thermal stability and proton conductivity. Fillers such as silica, metal oxides, montmorillonite, and zeolites are considered due to their chemical and thermal properties.

- *Silica*: Silica is chosen because it possesses high surface area and high chemical stability. Moreover, the addition of silica compounds into polymer membrane is thought of reducing methanol crossover. Results show that there is a decrease in methanol permeability. However, there is also a decrease in proton conductivity as a result of the hydrophobic side chains of TEOS that reduced the water content of the Nafion®/Si membrane. DMFC tests showed a good performance at high methanol concentration [76-81].
- *Metal Oxides*: Nafion® membranes, where metal oxides such as SiO₂, TiO₂, WO₃ were incorporated, have been studied for DMFCs. In general, these composite membranes provide better performance when compared to Nafion®. In particular, Nafion®/TiO₂ membranes were found to improve water uptake and reduce methanol absorbance. Nafion®/SiO₂ exhibited less methanol permeability compared to the Nafion® membrane. Nafion®/SiO₂-TiO₂ have been studied as well. Results showed that proton conductivity improve by a 25% the result provided by Nafion® 117 at 75°C; water uptake similar to Nafion®; and the power densities were higher than the Nafion® equivalent. However, using metal oxides have its drawbacks. Firstly, to achieve a homogeneous dispersion in the membrane is difficult, therefore, the performance might not be uniform throughout the bulk of the membrane. Secondly, metal oxides accelerate the degradation of the membrane, and thus, it can pose durability issues [82-85].
- *Montmorillonite (MMT)*: Nafion®/MMT membranes improve the thermal and mechanical properties in comparison to the Nafion® membrane. It is noteworthy that the proton conductivity does not increase, in fact, it

slightly decreases. However, the loss of performance is minimized by the fact that the methanol crossover decreases [86-90].

- *Zeolites:* Are microporous crystalline materials containing silicon, aluminium and oxygen in their framework. They are based on an infinitely extending 3D network of AlO_4 and SiO_4 tetrahedra linked by sharing atoms. The zeolite composite membranes depend on the zeolite pore size and surface tension (i.e. hydrophobicity and hydrophilicity). The filler favour proton migration through the membrane whereas its homogeneous distribution helped to reduce methanol permeability [91-93].

Nafion-based composite membranes with carbon nanomaterial fillers.

Graphene Oxide (GO) is utilised as filler in Nafion® membranes due to it facilitates proton transport and, thanks to its high surface area, it exhibits good water uptake. Furthermore, it is an electrically insulating and hydrophilic material due to the presence of epoxide, hydroxide, carbonyl and carboxyl groups. Moreover, it shows other interesting properties such as mechanical strength, and gas impermeability [94].

Although Nafion/GO membranes were found to enhance thermal backbone and side chains stability due to the interactions between GO sheets, methanol permeability was shown to decrease in the presence of sulphonated graphene oxide (SGO), since the methanol migration throughout the membrane is blocked. Furthermore, Nafion/SGO is used to avoid aggregation of GO in the polymer matrix. In DMFC test, the SGO/Nafion composite membrane exhibited higher current, and power densities than commercial Nafion® 115. In addition, proton conductivity augmented with increasing amounts of SGO, as the SGO was distributed throughout the matrix and created more interconnected transfer channels. A lower catalyst activation loss was displayed, which promoted fast reaction kinetics and lower methanol crossover [95]. In [96] DMFCs test varying methanol solution from 5 to 15 M were performed. Significant performance improvement was found at high concentration methanol solutions.

These membranes can be considered as promising candidates for DMFCs, however all of them achieve good results at high concentrations of methanol, and no durability tests have been performed.

Non-perfluorinated polymer composite membranes

Non-fluorinated membranes are promising candidates for DMFCs, and a cheaper alternative to replace fluorinated membranes that have a high methanol crossover. Aromatic polymers are considered adequate to operate as polymer electrolytes due to the following characteristics: Availability, variety of chemical composition, and stability in the cell environment. Among them, poly ether ether ketone, polyvinyl alcohol, poly (arylene ether sulfone), and their derivatives are being extensively studied by researchers.

Poly(ether ether ketone) (PEEK) is a semicrystalline polymer with high thermal and chemical stability. The sulphonation process (SPEEK) produces polymers with sulphonic acids in the aromatic backbone. It shows good properties for DMFCs. Low methanol crossover, good ion conductivity, thermal stability, and mechanical strength. Researchers investigate other formulations: SPEEK-based membranes with phenoxy resin, poly phenylsulfone (PPSU), solid heteropolyacids, polyaniline, SiO₂, and zirconium phosphate (ZrP), zeolite, polypyrrole (PPy) [97-101]. In addition, MMT or PBI is also utilised with SPEEK. Indeed, in [101] a SPEEK/MMT membrane is tested in a DMFC single cell, and compared to pristine SPEEK and Nafion® membranes. Several percentages of MMT were studied, and it was found that the best performer was the membrane containing 1wt.% MMT. However, despite the maximum power density was increased, the thermal stability was remarkably lessen. On the other hand, in [102] a SPEEK/PBI membrane was studied. At 60°C, the values of maximum power density were better than the ones exhibited by Nafion® 117. Furthermore, thermal stability was not compromised up to 60°C. Nevertheless, a further increment of the temperature results in stability issues with the consequential drop in performance.

A drawback of sulphonating polymers is that high sulfonation levels induce excessive swelling, and even soluble in methanol/water solutions following a mechanical failure of the membrane. Thus, sulfonated membranes should include organic or inorganic fillers. For instance, graphene oxide (GO) is selected to increment proton conductivity. Subsequently, SPEEK/GO membranes have been studied, and results show that the ion exchange capacity (IEC) decreases, as well as the water uptake, when compared with Nafion®. Although it displays better performance than SPEEK membranes, the overall proton conductivity remains low. Therefore, it was concluded that provided that the low levels of proton conduction is due to the lack of proton conductive groups in GO, these membranes are not suitable for DMFCs [103]. Also, in [103] SPEEK/SGO membranes were studied. It was found that incrementing the levels of SGO, the membranes show even higher IEC and proton conduction compared to Nafion® 112, which make them suitable for DMFC applications. However, SPEEK/GO membranes are not exempt of issues. Consequently, incrementing the content of SGO causes in an increment in methanol permeability. Therefore, the fuel utility decreases, the lifetime of the cathode catalyst decreases, and as a consequence, a low performance is obtained.

In order to reduce undesired swelling and methanol crossover of sulphonated membranes is to crosslink membranes [104,105]. The behaviour of Sulphonated poly (arylene ether sulfone) (SPAES) copolymers with propenyl groups then crosslinked using benzoyl peroxide varying the crosslinking has been evaluated by several researchers [106,107]. Results show that Proton conductivity of SPAES membrane increased, and it is similar to that of Nafion® 117. Moreover, methanol permeability was lower than that of Nafion® 117. The reason is that less pronounced hydrophobic/hydrophilic separation of sulfonated polyaryls compared to Nafion® correspond to narrower, less connected hydrophilic channels and larger separations of the less acidic sulfonic acid functional groups, which affected the permeability of methanol [107].

Polyvinyl Alcohol (PVA) is widely available polymer that acts as a good barrier to methanol. Nonetheless, it lacks of any negative charge ions, and thus, it lacks of proton conductivity. Crosslinking with sulfosuccinic acid (SSA) is usually done in order to improve the mechanical properties, and at the same time, it increments proton conducting sites thanks to the inclusion of sulfonic groups in the polymer matrix.

Nevertheless, the crosslinked PVA composites membranes performance in a fuel cell device does not reach the same behaviour than a commercial membrane of Nafion®. Furthermore, it suffers of high water solubility, for that reason the use of crosslinking agent in combination with fillers may be considered. Fillers such as SiO₂, polyrataxane, and MMT have been evaluated [113-115]. For instance, PVA/MMT membranes have shown high levels of ionic conductivity, reduced methanol crossover in comparison with Nafion® 117. Although, the maximum power density was found at high methanol concentrations (2M). Several more studies have shown how PVA polymer membranes lead to reduce methanol crossover.

To conclude, materials like PTFE, PVA, SiO₂ or MMT will not help to the increment of the proton conductivity since they are not proton-conductive materials but given that they produce an increment in the tortuosity of the membrane, a reduction of the methanol crossover phenomenon is achieved. Accordingly, either optimising the filler content or functionalising the filler are the two most common approaches to increment the proton conductivity. Finally, the highest performance is achieved by membranes with fillers, provided that the reduced methanol permeability compensate for the low proton conductivity achieved by these composite membranes.

2.3.3 Preparation Techniques of Proton-Exchange Membranes.

Membrane preparation methods have been studied extensively over decades. Its study is of paramount importance given the enormous impact that can have on the properties of the membrane. Examples of the most common methodologies are shown in Figure 2.20. The selection of the preparation method, and the parameters employed is based on the type of polymer [11].

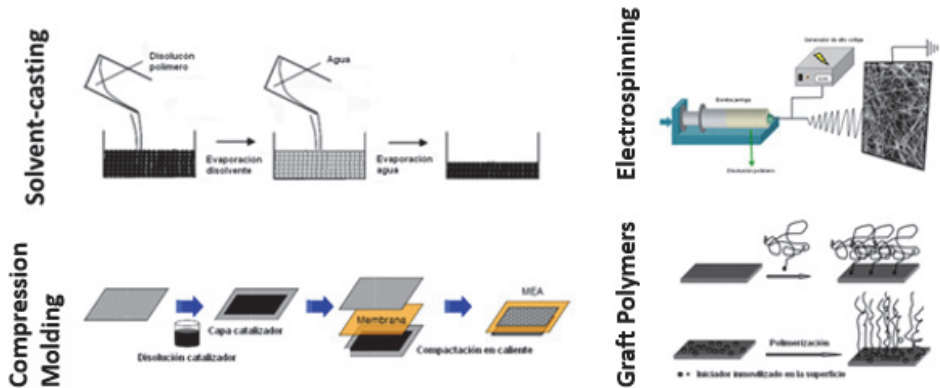


Figure 2.20: Schematic of several membrane preparation methods.

A brief description of the most common processes is included as follows [11]:

- **Solution casting** is a well-known method to prepare membrane samples on a laboratory scale. Many different variations exist of this method. Generally, a viscous polymer solution is first prepared in a solvent. The prepared solution is then cast in the form of a film on a flat substrate using a casting knife. This methodology can be used as well in order to prepare membranes with multiple layers. In that case, after the evaporation of the solvent is complete a new layer is done by pouring a different polymer solution, and the same process is repeated until reaching the desired number of layers. Important factors to control during the process are the type of solvent, the composition of the casting solution, the duration

of the solvent, the temperature, and the crystallization, vitrification, and gelation behaviour.

- **Electrospinning** is a flexible method used to produce nanofibres. It demands utilization of a high-potential electrostatic field between a grounded collector and a droplet of polymer solution. The surface-tension forces of the droplet are overcome as the electrostatic potential increases. Then, a charged liquid polymer jet leaving the spinneret is formed. Decreasing surface tension results in a conic droplet known as the Taylor cone before leaving the spinneret tip and forming into a charged jet. An electric field is in charge of controlling the route of the charged liquid jet. Subsequently, a fibre is formed from the liquid jet and the solidified spun fibre is gathered into a stationary or rotating-conductive collector. Control over the fibre aspect ratio and morphology is one of the greatest advantages of this technique. Furthermore, the pore size, porosity and hydrophobicity can be modified by varying parameters such as the applied potential and flow rate of the solution. Composite membranes can be fabricated by means of this technique as well.
- **Dip coating** is a widespread technique used for developing coatings. It is used both at an industrial- and laboratory-scale because of its low cost. Polymeric and metallic materials can be dip coated by dipping them into a solution. Then the sample is removed from the solution. The process of dip coating is also referred to as a layer-by-layer assembly process, and in recent years it has been used as well to create membranes for DMFC and PEMFC application. It allows for the obtention of ultra-thin layers ($\geq 1\text{-}2\ \mu\text{m}$), and it allows for the application of multiple layers. Properties can be optimised by variation of parameters such as the hydrophilicity/hydrophobicity of the starting layer, choice of solvent for coating solution, coating-solution concentration, solution temperature, and dipping speed/rate.
- **Hot pressing** is a well-known technique utilised for the preparation of membrane electrode assembly (MEA) for fuel cells. Accordingly, the mem-

brane is placed between the GDLs coated with electrocatalyst ink, and hot pressed together. Moreover, to form a multi-layer membrane system a process alike is followed. In hot pressing, mechanical bonds are formed between the adjacent layers thanks to the high temperature, and pressure applied. Therefore, factors like the temperature, pressure, and compatibility of all polymer/non-polymer layers must be carefully considered.

2.3.4 Challenges in PEM design

The complexity in the design of PEMs strives from the obtention of the optimal operating parameters. In Figure 2.21, the complex network of the relationships that ultimately determine the power and efficiency, and thus the overall performance, of the FCs is displayed. Its complexity strives in the fact that these relationships are not linear. For instance, a high voltage results in an increment in power and efficiency. Nevertheless, the FC is defined to deliver a specific load, which indeed, determines the actual current parameters. Such configuration would increment the losses, and consequently, it would diminish the performance.

Factors such as the partial pressure of the reactants, stack temperature, and membrane humidity have a great influence. Indeed, the operating conditions inside a FC are changeable. The high variability of the temperature and humidity conditions result in a dynamic environment with multiple factors such as continual start-up and shutdown cycles, fuel shortage, impure gas feed, operation under low-RH conditions, gas crossover due to intrinsic porosity of PEM, and electrocatalyst loss, that promote membrane degradation [1-4].

The conductivity in polymeric membranes, either protonic or cationic, is essentially lower than in metals by orders of magnitude. Therefore, to maximise conductivity it is paramount to decrease the ionic resistance through the reduction of the path traversed by ions when moving from the anode to the cathode, i.e., reducing the membrane thickness. Nevertheless, utilising a thin membrane causes other issues such as reduced mechanical strength, electrical shorting, di-

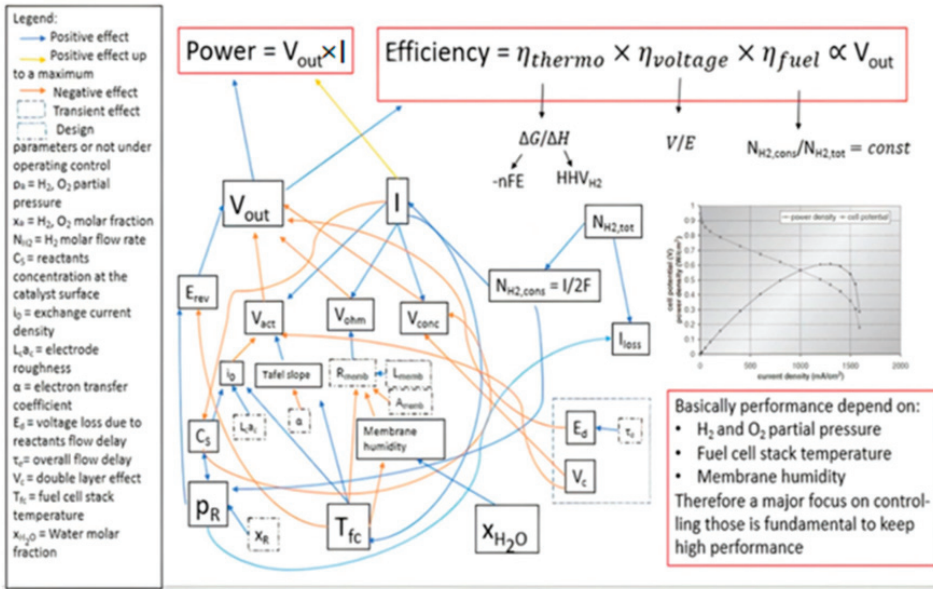


Figure 2.21: Complexity in the design of PEM. Operating parameters influencing the performance. Source: [4].

electric breakdown or fuel crossover. Therefore, finding the optimum thickness is of paramount importance to maximize the overall efficiency of the FC [4].

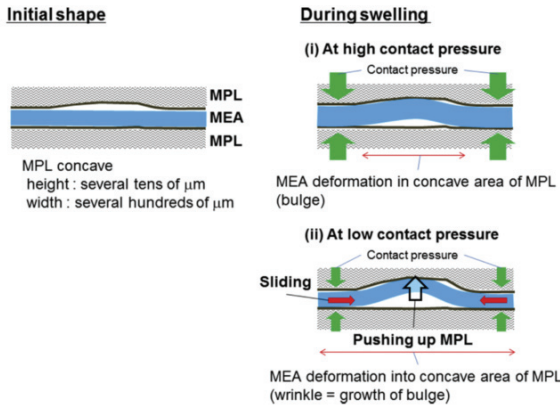


Figure 2.22: Example of a MEA deformation during swelling. Source: [116].

Mechanical properties of PEM are crucial to achieve durability and good performance, as illustrated in Figure 2.22. Accordingly, pressure and concentration gradients exist producing convection and diffusion of gasses. This lead to occurrence of direct reactions inside of the membrane that lead to thinning, pinhole formation, degradation and, eventually, failure of the membrane. Moreover, swelling, and contraction are continuously testing the mechanical resistance of the PEM. Finally, hydrogen crossover is also a common issue which should be tackled in order to increment the overall performance of the FC [116].

2.3.5 Membranes studied in the present PhD thesis

The materials studied and characterized in the present PhD thesis are described as follows:

- **Membranes based on block copolymers:** Two series of membranes based on sulfonated styrene-ethylene-butylene-styrene (SEBS) are studied. The microstructure has been fine-tuned for their suitability for fuel cell applications, and subsequently, a process of sulfonation, UV photocrosslinking and hybridization are applied to the samples.
- **Membranes based on nanocomposite & crosslinked polymers:** A series of poly(vinyl alcohol) (PVA) membranes, conveniently modified by addition of sulfosuccinic acid (SSA) and graphene oxide (GO) in different percentages, are studied for their suitability as PEM in DMFCs.
- **Membranes based on liquid crystals:** Two series of membranes based on poly (epichlorohydrin) (PECH) and poly (epichlorohydrin-co-ethylene oxide) (PECH-co-EO) copolymer modified with dendron 3,4,5-tris[4-(n-dodecan1-yloxy) benzyloxy] benzoate units. These membranes are submitted to a thermal orientation process.
- **Membranes based on covalent adaptable network:** A poly(thiourethane) network based on hexamethylene diisocyanate (HDI), trimethylolpropane tris(3-mercaptopropionate) (S3), and dibutyltin dilau-

rate (DBTDL) as catalyst is studied. Different catalyst percentages are utilised.

2.4 References

- [1] I. EG&G Technical Services, Fuel Cell Handbook, US Department of Energy, 2004.
- [2] V. Hacker, S. Mitsushima, Fuel Cells and Hydrogen, Elsevier, 2018.
- [3] G. Kaur, PEM Fuel Cells, Elsevier, 2016.
- [4] A. Alaswad, A. Omran, J.R. Sodre, T. Wilberforce, G. Pignatelli, M. Dassisti, A. Baroutaji, A.G. Olabi, Technical and commercial challenges of proton-exchange membrane (PEM) fuel cells, *Energies*, 14 (2021) 1-21.
- [5] D.P. Wilkinson, J. Zhang, R. Hui, J. Fergus, X. Li, Proton exchange membrane fuel cells: materials properties and performance, CRC press, 2009.
- [6] S.N. Lvov, Introduction to Electrochemical Science and Engineering, CRC Press, 2021.
- [7] J. Larminie, A. Dicks, M.S. McDonald, Fuel cell systems explained, J. Wiley Chichester, UK, 2003.
- [8] R. O'hayre, S.-W. Cha, W. Colella, F.B. Prinz, Fuel cell fundamentals, John Wiley & Sons, 2016.
- [9] Y. Wang, H. Yuan, A. Martinez, P. Hong, H. Xu, F.R. Bockmiller, Polymer electrolyte membrane fuel cell and hydrogen station networks for automobiles: Status, technology, and perspectives, *Adv. Appl. Energy* 2 (2021) 100011.

- [10] K. Xiong, W. Wu, S. Wang, L. Zhang, Modeling, design, materials and fabrication of bipolar plates for proton exchange membrane fuel cell: A review, *Appl. Energy* 301 (2021) 117443.
- [11] A. Albarbar, M. Alrweq, Proton exchange membrane fuel cells: Design, modelling and performance assessment techniques, *Prot. Exch. Membr. Fuel Cells Des. Model. Perform. Assess. Tech.* (2017) 1-163.
- [12] Z. Dimitrovar, W.B. Nader, PEM fuel cell as an auxiliary power unit for range extended hybrid electric vehicles, *Energy* 239 (2022) 121933.
- [13] Z. Qi, *Proton Exchange Membrane Fuel Cells*, 2013.
- [14] N.C. Osti, T.N. Etampawala, U.M. Shrestha, D. Aryal, M. Tyagi, S.O. Diallo, E. Mamontov, C.J. Cornelius, D. Perahia, Water dynamics in rigid ionomer networks, *J. Chem. Phys.* 145 (2016) 224901.
- [15] C. Wallmark, P. Alvfors, Design of stationary PEFC system configurations to meet heat and power demands, *J. Power Sources* 106 (2002) 83-92.
- [16] R. Devanathan, Recent developments in proton exchange membranes for fuel cells, *Energy Environ. Sci.* 1 (2008) 101-119.
- [17] D. Huang, X. Li, C. Luo, P. Wei, Y. Sui, J. Wen, C. Cong, X. Zhang, X. Meng, Q. Zhou, Consecutive and reliable proton transfer channels construction based on the compatible interface between nanofiber and SPEEK, *J. Memb. Sci.* 662 (2022) 121001.
- [18] S. Kim, I. Hong, Effects of humidity and temperature on a proton exchange membrane fuel cell (PEMFC) stack, *J. Ind. Eng. Chem.* 14 (2008) 357-364.
- [19] Q. Li, Q. Liu, J. Zhao, Y. Hua, J. Sun, J. Duan, W. Jin, High efficient water/ethanol separation by a mixed matrix membrane incorporating MOF filler with high water adsorption capacity, *J. Memb. Sci.* 544 (2017) 68-78.

- [20] A.L. Dicks, D.A.J. Rand, Direct Liquid Fuel Cells, 2018.
- [21] M. Ahmed, I. Dincer, A review on methanol crossover in direct methanol fuel cells: challenges and achievements, *Int. J. Energy Res.* 35 (2011) 1213-1228.
- [22] N.W. Deluca, Y.A. Elabd, Polymer electrolyte membranes for the direct methanol fuel cell: a review, *J. Polym. Sci. Part B Polym. Phys.* 44 (2006) 2201-2225.
- [23] K. Jiao, J. Xuan, Q. Du, Z. Bao, B. Xie, B. Wang, Y. Zhao, L. Fan, H. Wang, Z. Hou, S. Huo, N.P. Brandon, Y. Yin, M.D. Guiver, Designing the next generation of proton-exchange membrane fuel cells, *Nature* 595 (2021) 361-369.
- [24] Alhussein Albarbar, Mohmad Alrweq, Proton Exchange Membrane Fuel Cells, Elsevier, 2018.
- [25] E. Ogungbemi, O. Ijaodola, F.N. Khatib, T. Wilberforce, Z. El Hassan, J. Thompson, M. Ramadan, A.G. Olabi, Fuel cell membranes Pros and cons, *Energy* 172 (2019) 155172.
- [26] S. Sharma, Membranes for Low Temperature Fuel Cells, 2019.
- [27] F.T. Chikumba, M. Tamer, L. Akyalçn, S. Kaytakoglu, The development of sulfonated polyether ether ketone (sPEEK) and titanium silicon oxide (TiSiO₄) composite membranes for DMFC applications, *Int. J. Hydrogen Energy* (2023).
- [28] N.A. Agudelo, J. Palacio, B.L. Lopez, Effect of the preparation method on the morphology and proton conductivity of membranes based on sulfonated ABA triblock copolymers, *J. Mater. Sci.* 54 (2019) 41354153.
- [29] C. Simari, M. Prejano, E. Lufrano, E. Sicilia, I. Nicotera, Exploring the structure-performance relationship of sulfonated polysulfone proton ex-

- change membrane by a combined computational and experimental approach, *Polymers (Basel)* 13 (2021).
- [30] G.G. Gagliardi, A. Ibrahim, D. Borello, A. El-Kharouf, Composite polymers development and application for polymer electrolyte membrane technologies - a review, *Molecules* 25 (2020).
- [31] M. Mariani, A. Basso Peressut, S. Latorrata, R. Balzarotti, M. Sansotera, G. Dotelli, The role of fluorinated polymers in the water management of proton exchange membrane fuel cells: A review, *Energies* 14 (2021) 1-17.
- [32] J. Gao, X. Dong, Q. Tian, Y. He, Carbon nanotubes reinforced proton exchange membranes in fuel cells: An overview, *Int. J. Hydrogen Energy* 48 (2023) 32163231.
- [33] N. Esmaeili, E.M.A. Gray, C.J. Webb, Non-Fluorinated Polymer Composite Proton Exchange Membranes for Fuel Cell Applications A Review, *ChemPhysChem.* 20 (2019) 20162053.
- [34] M. Mohammadi, S. Mehdipour-Ataei, Durable sulfonated partially fluorinated polysulfones as membrane for PEM fuel cell, *Renew. Energy* 158 (2020) 421430.
- [35] H. Nguyen, F. Lombeck, C. Schwarz, P.A. Heizmann, M. Adamski, H.F. Lee, B. Britton, S. Holdcroft, S. Vierrath, M. Breitwieser, Hydrocarbon-based Pemion™ proton exchange membrane fuel cells with state-of-the-art performance, *Sustain. Energy Fuels* 5 (2021) 36873699.
- [36] . Ru, Y. Gu, Y. Duan, C. Zhao, H. Na, Enhancement in proton conductivity and methanol resistance of Nafion membrane induced by blending sulfonated poly(arylene ether ketones) for direct methanol fuel cells, *J. Memb. Sci.* 573 (2019) 439447.
- [37] S.N.S. Sayed Daud, M.N.A. Mohd Norddin, J. Jaafar, R. Sudirman, Fabrication, Properties, and Performance of Polymer Nanocomposite Ion Ex-

- change Membranes for Fuel Cell Applications: A Review, *J. Appl. Membr. Sci. Technol.* 26 (2022) 1149.
- [38] Vinothkannan, A.R. Kim, D.J. Yoo, Potential carbon nanomaterials as additives for state-of-the-art Nafion electrolyte in proton-exchange membrane fuel cells: A concise review, *RSC Adv.* 11 (2021) 1835118370.
- [39] Andrada, H. E., Franzoni, M. B., Carreras, A. C., Chavez, F. V., Dynamics and spatial distribution of water in Nafion 117 membrane investigated by NMR spin-spin relaxation, *international journal of hydrogen energy* 43 (2018) 8936-8943.
- [40] Di Noto, V., Lavina, S., Negro, E., Vittadello, M., Conti, F., Piga, M., Pace, G., Hybrid inorganic-organic proton conducting membranes based on Naon and 5 wt% of $MxOy$ ($M = Ti, Zr, Hf, Ta$ and W). Part II: Relaxation phenomena and conductivity mechanism, *J. Power Sources* 187 (2009) 57-66.
- [41] Adjemian, K.T., Dominey, R., Krishnan, L., Ota, H., Majsztrik, P., Zhang, T., Mann, J., Kirby, B., Gatto, L., Velo-Simpson, M., et al., Function and Characterization of Metal Oxide Nafion Composite Membranes for Elevated-Temperature H_2/O_2 PEM Fuel Cells, *Chem. Mater.* 18 (2006) 2238-2248.
- [42] Pineda-Delgado, J.L., Gutierrez, C.K., Rivas, S., Arjona, N., Arriaga, L.G., Chávez-Ramírez, A., Synthesis and evaluation of H_fO_2 as a prospective filler in inorganicorganic hybrid membranes based on Nafion for PEM fuel cells, *Nanotechnology* 30 (2019) 105707.
- [43] Oh, K., Kwon, O., Son, B., Lee, D.H., Shanmugam, S., Nafion-sulfonated silica composite membrane for proton exchange membrane fuel cells under operating low humidity condition, *J. Membr. Sci.* 583 (2019) 103-109.
- [44] Xu, G., Wu, Z., Wei, Z., Zhang, W., Wu, J., Li, Y., Li, J., Qu, K., Cai, W., Non-destructive fabrication of Nafion/silica composite membrane via

- swelling-filling modification strategy for high temperature and low humidity PEM fuel cell, *Renew. Energy* 153 (2020) 935-939.
- [45] Özdemir, Y., Üregen, N., Devrim, Y., Polybenzimidazole based nanocomposite membranes with enhanced proton conductivity for high temperature PEM fuel cells, *Int. J. Hydrog. Energy* 42 (2017) 2648-2657.
- [46] Lee, S., Seo, K., Ghorpade, R.V., Nam, K.H., Han, H., High temperature anhydrous proton exchange membranes based on chemically-functionalized titanium/polybenzimidazole composites for fuel cells, *Mater. Lett.* 263 (2020) 127167.
- [47] Elakkiya, S., Arthanareeswaran, G., Ismail, A.F., Das, D.B., Suganya, R., Polyaniline coated sulfonated TiO₂ nanoparticles for effective application in proton conductive polymer membrane fuel cell, *Eur. Polym. J.* 112 (2019) 696-703.
- [48] Lee, K.H., Chu, J.Y., Kim, A.R., Yoo, D.J., Effect of functionalized SiO₂ toward proton conductivity of composite membranes for PEMFC application, *Energy Res.* 43 (2019) 5333-5345.
- [49] He, D., Tang, H., Kou, Z., Pan, M., Sun, X., Zhang, J., Mu, S., Engineered Graphene Materials: Synthesis and Applications for Polymer Electrolyte Membrane Fuel Cells, *Adv. Mater.* 29 (2017) 1-8.
- [50] Maiti, J., Kakati, N., Woo, S.P., Yoon, Y.S., Nafion based hybrid composite membrane containing GO and dihydrogen phosphate functionalized ionic liquid for high temperature polymer electrolyte membrane fuel cell, *Compos. Sci. Technol.* 155 (2018) 189-196.
- [51] Ibrahim, A., Hossain, O., Chaggar, J., Steinberger-Wilckens, R., El-kharouf, A, GO-Nafion composite membrane development for enabling intermediate temperature operation of polymer electrolyte fuel cell, *Int. J. Hydrog. Energy* 45 (2019) 5526-5534.

- [52] Üregen, N., Pehlivanoglu, K., Özdemir, Y., Devrim, Y., Development of polybenzimidazole/graphene oxide composite membranes for high temperature PEM fuel cells, *Int. J. Hydrog. Energy* 42 (2017) 2636-2647.
- [53] Abouzari Lotf, E., Zakeri, M., Nasef, M.M., Miyake, M., Mozarmnia, P., Bazilah, N.A., Emelin, N.F., Ahmad, A., Highly durable polybenzimidazole composite membranes with phosphonated graphene oxide for high temperature polymer electrolyte membrane fuel cells, *J. Power Sources* 412 (2019) 238-245.
- [54] Lee, H., Han, J., Kim, K., Kim, J., Kim, E., Shin, H., Lee, J.C., Highly sulfonated polymer-grafted graphene oxide composite membranes for proton exchange membrane fuel cells, *J. Ind. Eng. Chem.* 74 (2019) 223-232.
- [55] Dai, Y., Wang, J., Tao, P., He, R., Various hydrophilic carbon dots doped high temperature proton exchange composite membranes based on polyvinylpyrrolidone and polyethersulfone, *J. Colloid Interface Sci.* 553 (2019) 503-511.
- [56] Chen, L.C., Yu, T.L., Lin, H.L., Yeh, S.H., Nafio/PTFE and zirconium phosphate modified Nafion/PTFE composite membranes for direct methanol fuel cells, *J. Membr. Sci.* 307 (2008) 10-20.
- [57] Hobson, L.J., Nakano, Y., Ozu, H., Hayase, S., Targeting improved DMFC performance, *J. Power Sources* 104 (2002) 79-84.
- [58] Molla, S., Compan, V., Polyvinyl alcohol nanofiber reinforced Nafion membranes for fuel cell applications, *J. Membr. Sci.* 372 (2011) 191-200.
- [59] Wong, C.Y., Wong, W.Y., Loh, K.S., Daud, W.R.W., Lim, K.L., Khalid, M., Walvekar, R., Development of Poly(Vinyl Alcohol)-Based Polymers as Proton Exchange Membranes and Challenges in Fuel Cell Application: A Review, *Polym. Rev.* 2020, 60, 171-202.

- [60] Shao, Z.G., Wang, X., Hsing, I.M., Composite Nafion/polyvinyl alcohol membranes for the direct methanol fuel cell, *J. Membr. Sci.* 210 (2002) 147-153.
- [61] Molla, S., Compan, V., Performance of composite Nafion/PVA membranes for direct methanol fuel cells, *J. Power Sources* 196 (2011) 2699-2708.
- [62] Shao, Z.G., Hsing, I.M., Nafion Membrane Coated with Sulfonated Poly(vinyl alcohol)-Nafion Film for Direct Methanol Fuel Cells, *Electrochem. Solid State Lett.*, 5 (2002) 185.
- [63] Lin, H.L., Wang, S.H., Chiu, C.K., Yu, T.L., Chen, L.C., Huang, C.C., Cheng, T.H., Lin, J.M., Preparation of Nafion/poly(vinyl alcohol) electrospun fiber composite membranes for direct methanol fuel cells, *J. Membr. Sci.* 365 (2010) 114-122.
- [64] Ausejo, J.G., Cabedo, L., Gamez-Perez, J., Molla, S., Gimenez, E., Compan, V., Modication of Nafion Membranes with Polyaniline to Reduce Methanol Permeability, *J. Electrochem. Soc.* 162 (2015) 325-333.
- [65] Ben Jadi, S., El Guerraf, A., Bazzaoui, E.A., Wang, R., Martins, J.I., Bazzaoui, M., Synthesis characterization and transport properties of Nafion-polypyrrole membrane for direct methanol fuel cell (DMFC) application, *J. Solid State Electrochem.* 23 (2019) 2423-2433.
- [66] Penner, R.M., Martin, C.R., Electronically Conductive Composite Polymer Membranes. *J. Electrochem. Soc.* 133 (1986) 310.
- [67] Sata, T., Funakoshi, T., Akai, K., Preparation and Transport Properties of Composite Membranes Composed of Cation Exchange Membranes and Polypyrrole, *Macromolecules* 29 (1996) 4029-4035.
- [68] Zhu, J., Sattler, R.R., Garsuch, A., Yopez, O., Pickup, P.G., Optimisation of polypyrrole/Nafion composite membranes for direct methanol fuel cells, *Electrochim. Acta* 51 (2006) 4052-4060.

- [69] Wang, C.H., Chenc, C.C., Hsud, H.C., Dud, H.Y., Chend, C.P., Hwangd, J.Y., Chend, L.C., Shihb, H.C., Stejskal, J., Chena, K.H, Low methanol-permeable polyaniline/Nafion composite membrane for direct methanol fuel cells, *J. Power Sources* 190 (2009) 279-284.
- [70] Escudero-Cid, R., Montiel, M., Sotomayor, L., Loureiro, B., Fatas, E., Ocon, P., Evaluation of polyaniline-Nafion composite membranes for direct methanol fuel cells durability tests, *Int. J. Hydrog. Energy* 40 (2015) 8182-8192.
- [71] Huang, Q.M., Zhanga, Q.L., Huang, H.L., Li, W.S., Huang, Y.J., Luoc, J.L., Methanol permeability and proton conductivity of Nafion membranes modified electrochemically with polyaniline, *J. Power Sources* 184 (2008) 338-343.
- [72] Wang, B., Hong, L., Li, Y., Zhao, L., Wei, Y., Zhao, C., Na, H., Considerations of the Effects of Naphthalene Moieties on the Design of Proton-Conductive Poly(arylene ether ketone) Membranes for Direct Methanol Fuel Cells, *ACS Appl. Mater. Interfaces* 8 (2016) 24079-24088.
- [73] Kim, T., Choi, J., Kim, S., Blend membranes of Naon/sulfonated poly(aryl ether ketone) for direct methanol fuel cell, *J. Membr. Sci.* 300 (2007) 28-35.
- [74] Bauer, B., Jones, D.J., Roziere, J., Tchicaya, L., Alberti, G., Casciola, M., Massinelli, L., Peraio, A., Besse, S., Ramunni, E., Electrochemical characterisation of sulfonated polyetherketone membranes, *J. New Mat. Elect. Syst.* 3 (2000) 93-98.
- [75] Fu, T.Z., Wang, J., Ni, J., Cui, Z.M., Zhong, S.L., Zhao, C.J., Na, H., Xing, W, Sulfonated poly(ether ether ketone)/aminopropyltriethoxysilane /phosphotungstic acid hybrid membranes with non-covalent bond: Characterization, thermal stability, and proton conductivity, *Solid State Ion* 179 (2008) 2265-2273.

-
- [76] Ye, G., Hayden, C.A., Goward, G.R., Proton Dynamics of Nafion and Nafion/SiO₂ Composites by Solid State NMR and Pulse Field Gradient NMR, *Macromolecules* 40 (2007) 1529-1537.
- [77] Peighambardoust, S.J., Rowshanzamir, S., Amjadi, M., Review of the proton exchange membranes for fuel cell applications, *Int. J. Hydrog. Energy* 35 (2010) 9349-9384.
- [78] Mishra, A.K., Bose, S., Kuila, T., Kim, N.H., Lee, J.H., Silicate-based polymer-nanocomposite membranes for polymer electrolyte membrane fuel cells, *Prog. Polym. Sci.* 37 (2012) 842-869.
- [79] Junoh, H., Jaafar, J., Nordin, N.A.H.M., Ismail, A.F., Othman, M.H.D., Rahman, M.A., Aziz, F., Yusof, N., Salleh, W.N.W, Porous Proton Exchange Membrane Based Zeolitic Imidazolate Framework-8 (ZIF-8), *J. Membr. Sci. Res.* 5 (2019) 65-75.
- [80] Lufrano, F., Baglio, V., Di Blasi, O., Staiti, P., Antonucci, V., Arico, A.S., Design of efficient methanol impermeable membranes for fuel cell applications, *Phys. Chem. Chem. Phys.* E 14 (2012) 2718.
- [81] Ren, S., Sun, G., Li, C., Liang, Z., Wu, Z., Jin, W., Qin, X., Yang, X., Organic silica/Nafion composite membrane for direct methanol fuel cells, *J. Membr. Sci.* 282 (2006) 450-455.
- [82] Shao, Z.G., Xu, H., Li, M., Hsing, I.M., Hybrid Nafioninorganic oxides membrane doped with heteropolyacids for high temperature operation of proton exchange membrane fuel cell, *Solid State Ion* 177 (2006) 779-785.
- [83] Hammami, R., Ahamed, Z., Charradi, K., Beji, Z., Assaker, I.B., Naceur, J.B., Auvity, B., Squadrito, G., Chtourou, R., Elaboration and characterization of hybrid polymer electrolytes NafionTiO₂ for PEMFCs, *Int. J. Hydrog. Energy* 38 (2003) 11583-11590.

- [84] Kim, J.H., Kim, S.K., Namb, K., Kim, D.W., Composite proton conducting membranes based on Nafion and sulfonated SiO₂ nanoparticles, *J. Membr. Sci.* 415 (2012) 696-701.
- [85] Ercelik, M., Ozden, A., Devrim, Y., Colpan, C.O., Investigation of Nafion based composite membranes on the performance of DMFCs, *Int. J. Hydrog. Energy* 42 (2017) 2658-2668.
- [86] Paul, D.R., Robeson, L.M., Polymer nanotechnology: Nanocomposites, *Polym. Nanotechnol.* 49 (2008) 3187-3204.
- [87] Wu, X., Wu, N., Shi, C., Zheng, Z., Qi, H., Wang, Y., Proton conductive montmorillonite-Nafion composite membranes for direct ethanol fuel cells, *Appl. Surf. Sci.* 388 (2016) 239-244.
- [88] Song, M., Park, S., Kim, Y., Kim, K., Min, S., Rhee, H., Characterization of polymer-layered silicate nanocomposite membranes for direct methanol fuel cells, *Electrochim. Acta* 50 (2004) 639-643.
- [89] Rhee, C., Kim, H., Chang, H., Lee, J., Nafion/Sulfonated Montmorillonite Composite: A New Concept Electrolyte Membrane for Direct Methanol Fuel Cells, *Chem. Mater.* 17 (2005) 1691-1697.
- [90] Lin, Y., Yen, C., Hung, C., Hsiao, Y., Ma, C., A novel composite membranes based on sulfonated montmorillonite modified Nafion for DMFCs, *J. Power Sources* 168 (2007) 162-166.
- [91] Keselj, D., Lazic, D., Skudric, B., Penavin-Skudric, J., Perusic, M., The possibility of hydrothermal synthesis of nay zeolite using different mineral acids, *Int. J. Latest Res. Sci. Technol.* 4 (2015) 37-41.
- [92] Tricoli, V., Nannetti, F., ZeoliteNafion composites as ion conducting membrane materials, *Electrochim. Acta* 48 (2003) 2625-2633.

-
- [93] Makertihartha, I.G.B.N., Zunita, M., Rizki, Z., Dharmawijaya, P.T., Recent advances on zeolite modification for direct alcohol fuel cells (DAFCs), *AIP Conf. Proc.* 2017 1818.
- [94] Pumera, M., Electrochemistry of graphene, graphene oxide and other graphenoids: Review, *Electrochem. Commun.* 36 (2013) 14-18.
- [95] Chien, H., Tsai, L., Huang, C., Kang, C., Lin, J., Chang, F., Sulfonated graphene oxide/Nafion composite membranes for high-performance direct methanol fuel cells, *Int. J. Hydrog. Energy* 38 (2013) 13792-13801.
- [96] Yan, X.H., Wu, R., Xu, J.B., Luo, Z., Zhao, T.S., A monolayer graphene-Nafion sandwich membrane for direct methanol fuel cells, *J. Power Sources* 311 (2016) 188-194.
- [97] Di Vona, M.L., DEpifanio, A., Marani, D., Trombetta, M., Traversa, E., Licoccia, S., SPEEK/PPSU-based organicinorganic membranes: Proton conducting electrolytes in anhydrous and wet environments, *J. Membr. Sci.* 279 (2006) 186-191.
- [98] Zaidi, S.M.J., Mikhailenko, S.D., Robertson, G.P., Guiver, M.D., Kaliaguine, S., Proton conducting composite membranes from polyether ether ketone and heteropolyacids for fuel cell applications, *J. Membr. Sci.* 173 (2000) 17-34.
- [99] Nagarale, R.K., Gohil, G.S., Shahi, V.K., Sulfonated poly(ether ether ketone)/polyaniline composite proton-exchange membrane, *J. Membr. Sci.* 280 (2006) 389-396.
- [100] Zhang, H., Fan, X., Zhang, J., Zhou, Z., Modification research of sulfonated PEEK membranes used in DMFC, *Solid State Ion* 179 (2008) 1409-1412.
- [101] Sengul, E., Erdener, H., Akay, R.G., Yucel, H., Bac, H.N., Eroglu, I., Effects of sulfonated polyether-ether ketone (SPEEK) and composite mem-

branes on the proton exchange membrane fuel cell (PEMFC) performance, *Int. J. Hydrog. Energy* 34 (2009) 4645-4652.

- [101] Gosalawit, R., Chirachanchai, S., Shishatskiy, S., Nunes, S.P., Sulfonated montmorillonite/sulfonated poly(ether ether ketone) (SMMT/SPEEK) nanocomposite membrane for direct methanol fuel cells (DMFCs). *J. Membr. Sci.* 323 (2008) 337-346.
- [102] Pasupathi, S., Ji, S., Bladergroen, B.J., Linkov, V., High DMFC performance output using modified acidbase polymer blend, *Int. J. Hydrog. Energy* 33 (2008) 3132-3136.
- [103] Jiang, Z., Zhao, X., Manthiram, A., Sulfonated poly(ether ether ketone) membranes with sulfonated graphene oxide fillers for direct methanol fuel cells, *Int. J. Hydrog. Energy*, 38 (2013) 5875-5884.
- [104] Mikhailenko, S.D., Robertson, G.P., Guiver, M.D., Kaliaguine, S., Properties of PEMs based on cross-linked sulfonated poly(ether ether ketone), *J. Membr. Sci.* 285 (2006) 306316.
- [105] Zhong, S., Cui, X., Cai, H., Fu, T., Zhao, C., Na, H., Crosslinked sulfonated poly(ether ether ketone) proton exchange membranes for direct methanol fuel cell applications, *J. Power Sources* 164 (2007) 65-72.
- [106] Feng, S., Shang, Y., Xie, X., Wang, Y., Xu, J., Synthesis and characterization of crosslinked sulfonated poly(arylene ether sulfone) membranes for DMFC applications, *J. Membr. Sci.* 335 (2009) 13-20.
- [107] Kreuer, K.D., On the development of proton conducting polymer membranes for hydrogen and methanol fuel cells, *J. Membr. Sci.* 185 (2001) 29-39.
- [108] Ballester, Soraya Carmen Sánchez, Synthesis and characterization of new polymer electrolytes to use in fuel cells fed with bio-alcohols, 2017, Universitat Politècnica de València.

- [109] González-Guisasola, C., Ribes-Greus, A., Dielectric relaxations and conductivity of cross-linked PVA/SSA/GO composite membranes for fuel cells, *Polymer Testing* 67 (2018) 55-67.
- [110] Sánchez-Ballester, S. C., Soria, V., Rydzek, G., Ariga, K., Ribes-Greus, A., Synthesis and characterization of bisulfonated poly (vinyl alcohol)/graphene oxide composite membranes with improved proton exchange capabilities, *Polymer Testing* 91 (2020) 106752.
- [111] Martínez-Felipe, A., Moliner-Estopiñán, C., Imrie, C. T., Ribes-Greus, A., Characterization of crosslinked poly (vinyl alcohol)based membranes with different hydrolysis degrees for their use as electrolytes in direct methanol fuel cells, *Journal of applied polymer science* 124 (2012) 1000-1011.
- [112] Torres-Giner, S., Echegoyen, Y., Teruel-Juanes, R., Badia, J. D., Ribes-Greus, A., Lagaron, J. M., Electrospun poly (ethylene-co-vinyl alcohol) / graphene nanoplatelets composites of interest in intelligent food packaging applications, *Nanomaterials* 8 (2018) 745.
- [113] Panero, S., Fiorenza, P., Navarra, M.A., Romanowska, J., Scrosati, B., Silica-Added Composite Poly(vinyl alcohol) Membranes for Fuel Cell Application, *J. Electrochem. Soc.* 152 (2005) 2400.
- [114] Son, J.H., Kang, Y.S., Won, J., Poly(vinyl alcohol)-based polymer electrolyte membranes containing polyrotaxane, *J. Membr. Sci.* 281 (2006) 345-350.
- [115] Yang, C., Lee, Y., Yang, J., Direct methanol fuel cell (DMFC) based on PVA/MMT composite polymer membranes, *J. Power Sources* 188 (2009) 30-37.
- [116] T. Uchiyama, H. Kumei, T. Yoshida, K. Ishihara, Static friction force between catalyst layer and micro porous layer and its effect on deformations of membrane electrode assemblies under swelling, *J. Power Sources* 272 (2014) 522-530.

Chapter 3

Characterization Techniques

Chapter 3 introduces the methodology, mainly based on the Dielectric Thermal Analysis (DETA) of the polymeric membranes, used to evaluate its proton conductivity and how the molecular motions either promote or prevent it. Therefore, its performance on a PEMFC can be estimated, and a decision on its appropriateness for its use as proton-exchange membrane can be reached. Furthermore, it presents the fundamentals of the other characterization techniques utilised in this thesis, i.e., Fourier Transformed Infrared Spectroscopy (FTIR), Thermogravimetric analysis (TGA), Differential Scanning Calorimetry (DSC), and Electrochemical Impedance Spectroscopy (EIS).

3.1 Dielectric Thermal Analysis (DETA)

Dielectric thermal analysis (DETA), also referred as broadband dielectric spectroscopy (BDS), alludes to a group of techniques that is sensible to the changes in different physical properties, as for instance polarization (P), permittivity (ϵ^*), and conductivity (σ^*), of a polar material with respect to temperature and/or frequency [1,2].

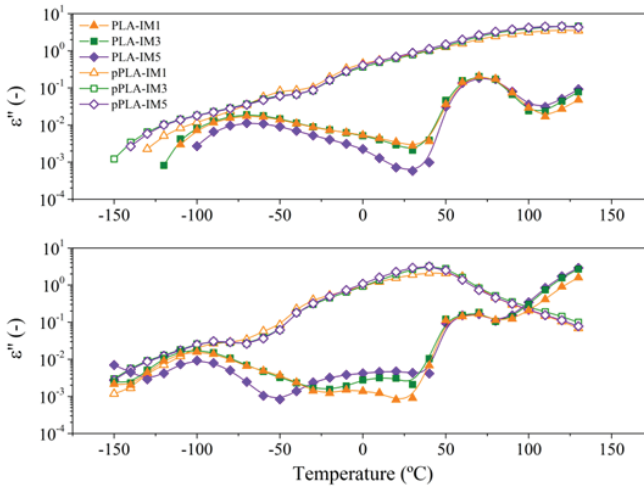


Figure 3.1: Isochronal curves for several recycled polylactides at a frequency of (Top) 10^3 Hz and (Bottom) 10^{-1} Hz. Source: [3].

The basis of the analysis, based on alternating-current (AC) dielectric methods, are the reorientation of dipoles and the translational diffusion of charged particles in an oscillating electric field. Generally, as shown in Figures 3.1 - 3.2, it involves measurements of the complex permittivity (ϵ^*) in the frequency or time domain, and at constant or varying temperature. Although DETA analysis are usually performed over a wide range of frequencies and temperatures, pressure can also be a variable to consider because the relaxation strength, relaxation time and its distribution are all remarkably affected by it. Some applications, where considering pressure variations in the analysis could be of special

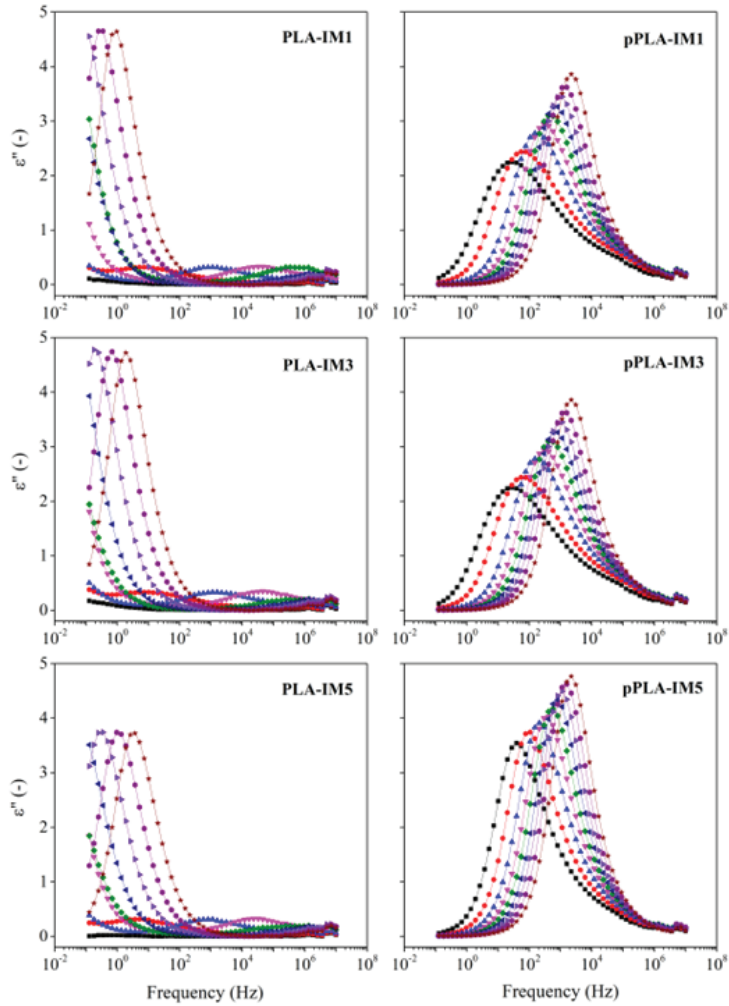


Figure 3.2: Isothermal curves of the imaginary part (ϵ'') of the complex permittivity (ϵ^*) for several recycled polylactides. The lines are displayed in steps of 10 K from 323 to 393 K in increasing order. Source: [3].

interest, are in polymers that contain overlapped relaxations or to study polymer crystallization [2,4].

In comparison with other common thermal analytical techniques where small changes in enthalpy, volume, or heat capacity are measured, in polymers, changes in the polarizability and dielectric constant are large. Accordingly, these changes are easy to detect during phase transitions, such as the glass transition, melting or crystallization, and secondary transitions [1,2,5].

A link between molecular spectroscopy and bulk properties of the material under investigation, for instance the viscosity, can be made by means of the monitoring of cooperative relaxations. Indeed, DETA analysis is the most sensitive technique to investigate local motions along the chains of polar polymers, given that the electric field affects the polar bonds. Moreover, DETA can also be used to study nonpolar polymers (e. g., polyethylene) if opportune structural modifications are performed, such as partial oxidation and labelling (e.g., by chlorination or attachment of polar pendant groups), as well as the dissolution of suitable polar probe molecules [5,6].

Furthermore, another main advantage of DETA with respect to other thermal techniques, as for instance dynamic mechanical analysis (DMA), is its broad frequency range (1 μ Hz - 100 GHz) that relies on a series of instruments for complete coverage [2,5]. In Figure 3.3 the Novocontrol Broadband Dielectric Impedance Spectrometer connected to a Novocontrol Alpha-A Frequency Response Analyser is shown, where all the dielectric measurements of this thesis work have been performed.

The dielectric spectrum can be decomposed into its individual relaxation processes as shown in Figure 3.4. The information provided by each function is related to its amplitude, i.e. relaxation strength ($\Delta\epsilon$), and the characteristic times, i.e. relaxation times (τ).

DETA is known as a useful and powerful thermal analysis approach for investigating condensed- and soft-matter dynamics.



Figure 3.3: Novocontrol Alpha Analyser.

It has been widely used in the dielectric characterization of ion conducting solids, biological systems, emulsions, colloids, mesophases (liquid crystals, etc.) and particularly polymers and related composites, in order to fabricate suitable materials for advanced engineering applications [2].

In Figure 3.5 the different length scales in polymeric systems are shown. At very small length scales, motions can only be caused by fluctuations within a monomeric unit or rotational fluctuations of a short side chain of a few dozen of carbon atoms. These processes are much slower than what occurs at larger length scales, or similarly longer times, where segmental motions associated with glass-liquid or glass-rubber transition occur. This temperature region is characterised by a significant increment in molecular motions of the polymeric matrix. Provided that these motions are related to dipole orientation, a dielectric relaxation process is found. Moreover, an increased mobility of elec-

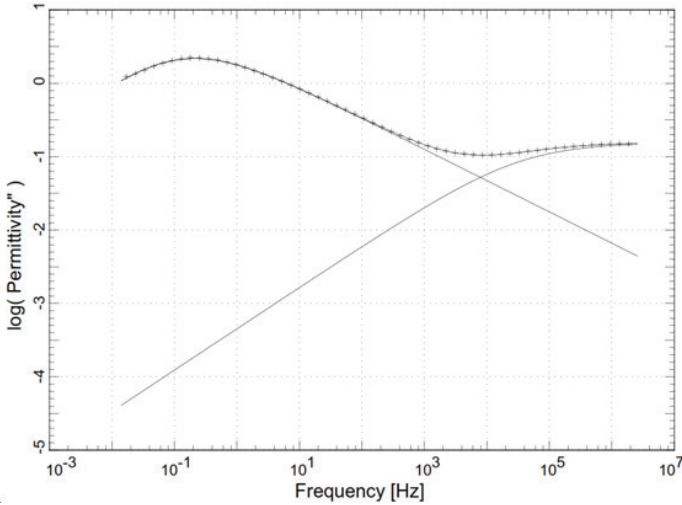


Figure 3.4: Decomposition of the dielectric spectrum into its individual relaxation processes through the Havriliak-Negami model.

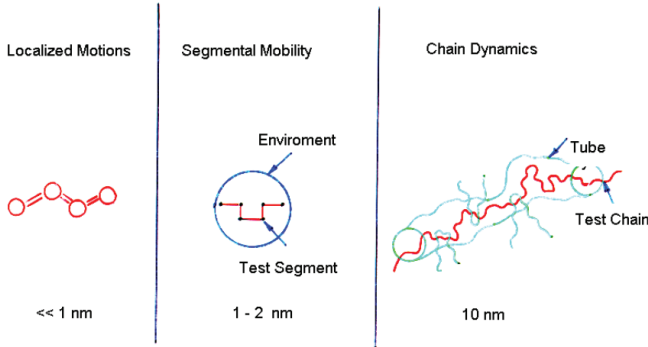


Figure 3.5: Molecular motions and Length scales in polymeric systems. Source:[7].

tric charges produces dielectric signals related with the ionic conductivity and charge-trapping/liberation processes which are more complex [2,7]. At high temperatures, interfacial polarization origins from the trapping of ions at interfaces within polymer composites. The analysis of the interfacial polarization can be a sensitive tool to study microstructural properties indirectly. The contribution of DETA to material science is remarkable in the following areas [5,7]:

1. Establishment of relationship between a polymer's configuration, dynamic properties and applications.
2. Information on surface and bulk properties in confining environments.
3. Online monitoring of chemical reactions (Polymerization, curing), physical processes (e.g., Aging), and structure formation.
4. Evaluation of charge transport and ion mobility in semiconductors, organic crystals, polymer composites and polymer electrolytes.
5. Analysis of nonlinear electrical and optical effects.
6. Dielectric characterization of polymers for engineering applications.

3.1.1 Frequency-dependent response of dielectrics: Key aspects

A dielectric is placed in a parallel-plate capacitor under an alternating voltage of angular frequency (ω) is the most common sample configuration [5]. Its dielectric properties can be described by its capacitance (C) and conductance (G), as defined in Eqs. 3.1 - 3.2.

$$C(\omega) = \varepsilon_0 \varepsilon'(\omega) \frac{S}{d} \quad (3.1)$$

$$G(\omega) = \varepsilon_0 \omega \varepsilon''(\omega) \frac{S}{d} \quad (3.2)$$

where S is the sample's cross-sectional area, d describes the thickness, and ε_0 is the permittivity of vacuum.

Eqs. 3.1 - 3.2 show the frequency dependence of the real (ε') and imaginary (ε'') parts of the complex dielectric permittivity displayed in Eq. 3.3, where $i^2 = -1$.

$$\varepsilon^* = \varepsilon' - i\varepsilon'' \quad (3.3)$$

The physical meaning of both variables is as follows [8,9]:

- The real (ϵ') part of the permittivity presents the ability of the dielectric medium to store energy. Accordingly, it consists of a sum of contributions from the vacuum, which must be real since there can be no loss associated with it, and of the real part of the susceptibility of the material medium itself.
- The imaginary (ϵ'') part of the permittivity describes the energy losses due entirely to the material medium.

Model functions

The analysis of the dielectric relaxation processes is performed through model functions. The first theoretical approach suggested for both the frequency and time domain was proposed by Debye. The Debye function for the frequency dependence of $\epsilon^*(\omega)$ is shown in Eq. 3.4 [2].

$$\epsilon^*(\omega) = \epsilon_\infty + \frac{\Delta\epsilon}{1 + i\omega\tau_D} \quad (3.4)$$

where $\Delta\epsilon = \epsilon_s - \epsilon_\infty$ is the strength of the dielectric relaxation.

The Debye model function assumes that the dielectric response is created by a single-relaxation time. However, experimental measurements depart from that assumption [9]. Instead, it is assumed that there is a distribution of relaxation times with different activation energies. Different forms for the function describing the distribution of relaxation times exist, and it depends on the model chosen to perform the analysis.

The molecular relaxation processes should be analysed using generalized relaxation functions, as already shown in Figure 3.4. Thus, the relaxation process can be characterized by at least four independent parameters [2].

A summary of the most important models for the relaxation function is included as follows [10].

- **Debye model:** ε_0 y ε_∞ represents the static and instantaneous dielectric constant respectively. Their difference constitutes the relaxation amplitude, and it is a measure of the orientation polarization.

$$\varepsilon^* = \varepsilon_\infty + \frac{\varepsilon_0 - \varepsilon_\infty}{1 + i\omega\tau} \quad (3.5)$$

$$\varepsilon' = \varepsilon_\infty + \frac{\varepsilon_0 - \varepsilon_\infty}{1 + \omega^2\tau^2} \quad (3.6)$$

$$\varepsilon'' = (\varepsilon_\infty - \varepsilon_0) + \frac{\omega\tau}{1 + \omega^2\tau^2} \quad (3.7)$$

- **Cole-Cole model:** Symmetrical ε' and ε'' are obtained, which are broader than those derived from the Debye equation. The ε'' curves also have lower amplitudes than those obtained by the Debye model.

$$\varepsilon^* = \varepsilon_\infty + \frac{\varepsilon_0 - \varepsilon_\infty}{1 + (i\omega\tau)^{1-\alpha}} \quad (3.8)$$

- **Fuoss-Kirkwood model:** Fitting experimental data of ε'' and temperature to this equation at a given frequency, the ε''_{max} and T_0 values can be directly obtained. By using the Arrhenius equation, $\tau = \tau_0 \exp\left(\frac{E_a}{RT}\right)$, it is possible to determine the apparent activation energy of the relaxation and then the m parameter at each frequency.

$$\varepsilon'' = \frac{E''_{max}}{\cosh m \frac{E_a}{R} \left(\frac{1}{T} - \frac{1}{T_0}\right)} \quad (3.9)$$

- **Davidson-Cole model:** Unlike the Cole-Cole and Fuoss-Kirkwood models that are very useful for symmetric relaxations, this model allows to

determine an asymmetric broadening of the dielectric relaxation. Indeed, the β parameter describes is introduced to describe this asymmetric broadening for frequencies $\omega > 1/\tau$. Note that for $\beta = 1$ the Debye function is recovered.

$$\varepsilon^* = \varepsilon_\infty + \frac{\varepsilon_0 - \varepsilon_\infty}{1 + (i\omega\tau)^\beta} \quad 0 < \beta < 1 \quad (3.10)$$

- **Havriliak-Negami model:** Modifies the Cole-Cole equation by introducing another empirical parameter, β . Indeed, for $\beta = 1$ the Cole-Cole model is obtained, and for $\alpha = 0$ the Davidson-Cole. The flexibility of the HN five-parameter equation makes it one of the most widely used methods of representing dielectric relaxation data. The formal expression is shown in Eq. 3.11. The real (ε') and imaginary (ε'') parts of the dielectric complex permittivity are derived in Eq. 3.12.

$$\varepsilon^* = \varepsilon_\infty + \frac{\varepsilon_0 - \varepsilon_\infty}{\left[1 + (i\omega\tau)^{1-\alpha}\right]^\beta} \quad (3.11)$$

$$\varepsilon' = \varepsilon_\infty + \frac{(\varepsilon_0 - \varepsilon_\infty) \cos \beta \phi}{1 + 2(\omega\tau)^{1-\alpha} \sin\left(\frac{\pi}{2}\right) \alpha + (\omega\tau)^{2(1-\alpha)}} \quad (3.12)$$

$$\varepsilon'' = \frac{(\varepsilon_0 - \varepsilon_\infty) \sin \beta \phi}{1 + 2(\omega\tau)^{1-\alpha} \sin\left(\frac{\pi}{2}\right) \alpha + (\omega\tau)^{2(1-\alpha)}} \quad (3.12)$$

$$\phi = \tan^{-1} \frac{(\omega\tau)^{1-\alpha} \cos\left(\frac{\pi}{2}\right) \alpha}{1 + (\omega\tau)^{1-\alpha} \sin\left(\frac{\pi}{2}\right) \alpha}$$

- **Jonscher model:** Jonscher proposed Eq. 3.13 for the loss permittivity in the context of the universal dielectric response (UDR) theory. Note

that when $\omega_1 = \omega_2$ and $m + n = 1$, Eq. 3.13 becomes the Fuoss-Kirkwood equation.

$$\varepsilon'' = \frac{a}{\left(\frac{\omega}{\omega_1}\right)^{-m} + \left(\frac{\omega}{\omega_2}\right)^{1-n}} \quad (3.13)$$

$$0 < m < 1 \quad \text{and} \quad 0 < n < 1$$

- **Hill model:** Hill proposed Eq. 3.14 to represent the dielectric loss. The necessity for the three parameters m , n and s is a consequence of the shape of the loss curves which are characterized by two power laws and an intermediate curved region.

$$\frac{\varepsilon''}{\varepsilon_0 - \varepsilon_\infty} = \frac{\omega^m}{(\omega_p^{2s} + \omega^{2s})^{(1-n+m)/2s}} \quad (3.14)$$

- **KWW model:** Williams and Watts proposed to use a stretched exponential for the decay function $\Phi(t)$, in a similar way to Kohlrausch many years ago. Thus, the normalized dielectric permittivity can be written as in Eq. 3.15. Note that L denotes the Laplace transformation.

$$\frac{\varepsilon^* - \varepsilon_\infty}{\varepsilon_0 - \varepsilon_\infty} = 1 - i\omega L[\Phi(t)] \quad (3.15)$$

- **Biparabolic model:** Huet proposed a representation of the dynamic viscoelastic properties of some bituminous asphalts by means of a biparabolic model that include one parameter more than the HN equation. Accordingly, the corresponding model for the permittivity is given by Eq. 3.16.

$$\varepsilon^* = \varepsilon_0 - \frac{\varepsilon_0 - \varepsilon_\infty}{1 + \delta'(i\omega\tau_0')^{-k} + (i\omega\tau_0')^{-h}} \quad (3.16)$$

where,

$$\delta' = \delta \left(\frac{\varepsilon_0}{\varepsilon_\infty} \right)^{(k/h)-1}$$

$$\tau_0' = \tau_0 \left(\frac{\varepsilon_0}{\varepsilon_\infty} \right)^{1/h}$$

Currently, the Havriliak and Negami (HN) model is the most used to fit dielectric data, indeed is the method included in the Novocontrol fitting software WinFit®, containing non-Debye relaxation processes. Accordingly, the dielectric relaxation is characterized through the dielectric strength ($\Delta\varepsilon$), a parameter related to the relaxation time of the dielectric process (τ_{HN}), and two shape parameters (α_{HN} and β_{HN}) ascribed to the width and the asymmetry of the loss peak, respectively.

3.1.2 Common representation of dielectric data

The general representation of dielectric data is through permittivity ($\varepsilon^*(\omega)$) plots as shown in Figures 3.1 - 3.2. Ideally, when analysing dielectric losses ($\varepsilon''(\omega)$) a bell-shaped curve with a full width at half-height and a maximum occurring at $\log(\omega_{max}) = 0$ should be encountered. Nonetheless, the loss peak for most polymeric materials are broad and asymmetric. Moreover, other parameters such as the electric modulus $M^*(\omega)$, conductivity $\sigma^*(\omega)$, and resistivity $\rho^*(\omega) = 1/\sigma^*(\omega)$ can be useful to interpret the results, given their dependence on and weighting with frequency [2,5].

The loss tangent ($\tan(\delta)$), or dissipation factor, is commonly used in the characterization of polymers for several engineering applications. Accordingly, δ is the phase lag between the alternating electric field ($E(t) = E_0 e^{i\omega t}$) and the dielectric induction ($D(t) = D_0 e^{i(\omega t - \delta)}$), and thus, it can be understood as a measure of the system's polarization inertia with regard to the electric stimu-

lus. An advantage of utilizing $\tan \delta$ is its independence on the geometry of the sample, which can in turn, be of great value when the geometry is unknown. In general, for low-loss polymers $\tan(\delta)$ values range from $\cong 10^{-4}$. On the contrary, values $\cong 1$ are generally found for high-loss materials. It can be used as well as a measure of the sensitivity of the dielectric equipment [2,5].

$$M^*(\omega) = \frac{1}{\varepsilon^*(\omega)} = M'(\omega) + iM'' = M_\infty + \frac{M_0 - M_\infty}{1 + i\omega\tau_m} \quad (3.17)$$

In Eq. 3.17 the complex electric modulus ($M^*(\omega)$) is shown. Popularized by McCrum [11], it was defined as the reciprocal of the complex permittivity in analogy with the mechanical shear and tensile moduli being the complex reciprocals of the shear and tensile compliances, respectively. Its capability to deal with conducting materials has been reported. The $M^*(\omega)$ effectively suppresses large contributions of nonlocal relaxations at low frequencies, i.e., it emphasizes the bulk properties at the expense of electrode polarization. Therefore, M'' plots are a great choice to analyse the dielectric properties of conducting polymers. It is noteworthy to mention that for large values of the dielectric strength ($\Delta\varepsilon$) the M'' spectrum appears at a much higher frequency than, for instance, the $\tan \delta$ spectrum, which, compared to the ε'' spectrum, it appears at an elevated frequency. This shift is reversed in isochronal presentations of the dielectric results [5].

Isothermal plots are usually preferred to display the dielectric data, i.e., as a function of frequency at a constant temperature. Such spectra can be easily analysed to determine relaxation characteristics and electrical properties of the polymer at the temperature of the scan. Furthermore, the chosen variable can also be exhibited as a function of temperature at a constant frequency, i.e. isochronal plots.

3.1.3 Temperature dependence of the relaxation times

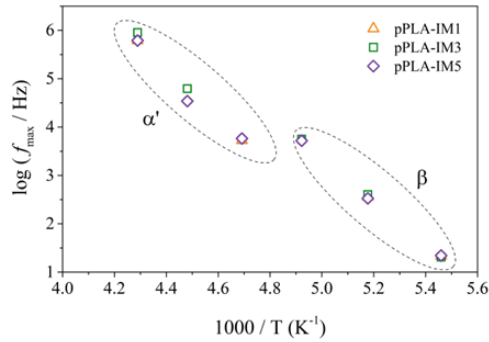
One of the most important parameters obtained from the model function is the relaxation time (τ). Its importance is related with its physical meaning that can be linked with the transition probabilities between consecutive minimum energy configurations of the dipoles [12].

Consequently, each characteristic relaxation time, as for instance the ones shown in Figure 3.6, is associated with the rotational motion of each dipole. Therefore, at higher temperatures will only appear those rotations more effectively hindered by their environment, that will display high values of τ . Hence, relaxation times are temperature-dependent, and the functional form of this dependence (linear vs non-linear) provides paramount information on the molecular motion that is associated to the dielectric process [2,5,8].

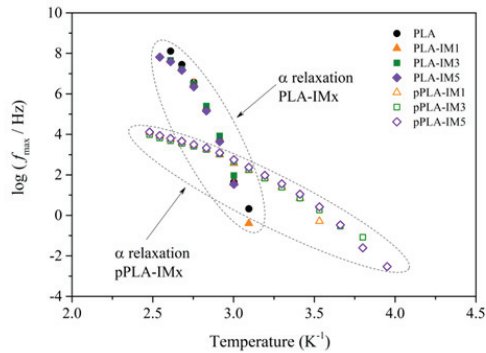
According to the Debye model, where dipoles are considered floating in a viscous fluid, at a certain temperature the obtained relaxation time will be equal for each unit, and it would be related to the viscosity of the environment. The dielectric relaxations that the ideal rotational friction model of Debye [13] or the potential barrier model of Fröhlich [14], displays a linear relationship with respect to temperature, and therefore, $\tau(T)$ can be represented through an Arrhenius-like equation, as shown in Figure 3.6a.

On the other hand, when the dielectric process originates from complex molecular motions, or ionic motion, the functional form of the temperature dependence is non-linear, as shown in Figure 3.6b. Subsequently, $\tau(T)$ can be represented through a Williams-Landel-Ferry (WLF) or a Vogel-Tammann-Fulcher-Hesse (VTFH) equation [2,5].

To understand the WLF equation it is necessary to consider the time-temperature superposition principle (TTS). Accordingly, TTS allows results for the viscoelastic response of a material to be shifted in the time domain as long as a corresponding shift is made in the temperature domain. The WLF equation is a direct consequence of the TTS principle, and it describes for a wide range of



(a) Example of an Arrhenius plot at low temperatures for a series of recycled poly lactides.



(b) Example of an Arrhenius plot at high temperatures for a series of recycled poly lactides.

Figure 3.6: Example of an Arrhenius plot in the low- and high-temperature region for a series of recycled poly lactides. Source: [3].

materials, the effect of the free volume on the relaxation behaviour of polymers in the temperature range between the glass transition temperature (T_g) and $T_g + 100^\circ\text{C}$ [2,5].

The VFTH equation is widely used to analyse segmental relaxations and similarly complex signals. In amorphous polymers, for the dielectric relaxations originated from the motion of long-chain segments, the slope of the Arrhenius plot, and the corresponding activation energy attains a maximum near T_g

[15,16]. Another important parameter is the Vogel temperature (T_v) which is understood as an indication of a phase-transition-like ideal glass transition that would occur below T_g [17]. The universality of the VTFH equation near T_g makes clear that T_v is a significant parameter for the dynamics of the glass transition.

Activation energy. The Arrhenius equation

The movement of the molecular segments that are responsible of a relaxation implies a transition through a potential energy barrier between two states with free energy F_1 y F_2 . The energy that has to be absorbed by the sample in order to overcome this barrier is called activation energy, E_a .

This activation energy can be calculated from the Arrhenius equation, which relates the dependence between the relaxation time and the temperature as shown in Eq. 3.18.

$$\tau = \tau_0 \exp\left(\frac{E_a}{RT}\right) \quad (3.18)$$

Taking natural logarithms and considering that $\tau = 1/\omega$, Eq. 3.19 is obtained.

$$\ln \omega = \ln \omega_0 - \frac{E_a}{R} \frac{1}{T} \quad (3.19)$$

If $\ln \omega$ is plotted as a function of $1/T$, the slope of the straight line corresponds to the activation energy E_a , as shown in Eq. 3.20.

$$E_a = R \frac{d \ln(aT)}{d(1/T)} \quad (3.20)$$

Experimentally, it has been demonstrated that the secondary relaxations (those which occur in the glassy state, and that are generally related to the movements

of small sections of the main chain or of lateral groups bonded to the main chain) can be well described by the Arrhenius relation.

Glass transition: Williams-Landel-Ferry and Vogel-Fulcher-Tamman-Hesse models

The relaxation associated to the glass transition in which a large scale micro-brownian movement of conformational reorganizations is assumed, produces a decrease of several decades in the modulus value. The equation that establishes the dependence of the relaxation times with the temperature is given by the Williams-Landel-Ferry equation or its equivalent, the so called Vogel-Fulcher equation.

Williams-Landel-Ferry Model

Both in the liquid and amorphous states of the polymers (at temperatures lower or around the T_g), the free volume theories are applied, from which the Williams-Landel-Ferry equation is derived.

The most used definition for the free volume is that proposed by Doolittle in Eq. 3.21.

$$v_f = v - v_0 \quad (3.21)$$

where,

- v_f is the free volume (consisting on the spaces resulting from the packing defect in the chain configuration)
- v is the total volume of the polymer at temperature T .
- v_0 is the occupied volume, that includes not only the molecules volume calculated as the Van der Waals ratio, but also the volume associated to

their vibrational movements and that was considered by Doolittle as the extrapolation of v at $T = 0$ K.

In the relaxation phenomena, it is suggested that the molecular mobility at a given temperature depends on the free volume available at this temperature. The speed of these movements increases with the free volume and therefore with the temperature.

For a great number of amorphous polymers in the glass transition surroundings, when plotting the shifting factor versus the difference $(T - T_g)$, where T_g is the dilatometric glass transition, exponential curves fitting to the following equation are obtained:

$$\log a_T = \frac{-c_1(T - T_g)}{c_2 + (T - T_g)} \quad (3.22)$$

where, c_1 y c_2 are the values of two constants at the arbitrary reference temperature T_0 . These constants can be experimentally determined for each material.

This equation can only be used in the T_g y $T_g + 373K$ range.

The theoretical demonstration of the W-L-F equation comes from the semiempirical equation proposed by Doolittle for the liquids viscosity shown in Eq. 3.23.

$$\ln \mu = \ln A + B \left(\frac{v - v_f}{v_f} \right) \quad (3.23)$$

where A, B are two parameters.

The molecular interpretation of this equation implies that the viscosity is related to the chains mobility, and this latter is in turn related to the free volume.

By assuming that above the T_g the free volume increases linearly with the temperature, and defining the fractional free volume as $f = v_f/v$, then Eq. 3.24

$$f = f_g + \xi_f(T - T_g) \quad (3.24)$$

By substituting into the Doolittle equation:

$$\ln \mu = \ln A + B \left(\frac{1}{f_g + \xi_g(T - T_g)} - 1 \right) \quad T > T_g \quad (3.25)$$

$$\ln \mu_{T_g} = \ln A + B \left(\frac{1}{f_g} - 1 \right) \quad T = T_g \quad (3.26)$$

from where:

$$\ln \frac{\mu}{\mu_{T_g}} = B \left(\frac{1}{f_g + \xi_g(T - T_g)} - \frac{1}{f_g} \right) \quad (3.27)$$

and since $\ln a_T = \ln \frac{\tau(T)}{\tau(T_g)} \approx \ln \frac{\mu}{\mu_{T_g}}$, then:

$$\ln a_T = \frac{B}{f_g} \frac{f_g - f_g + \xi_g(T - T_g)}{f_g + \xi_g(T - T_g)} = \frac{B}{f_g} \left[\frac{T - T_g}{\frac{f_g}{\xi_g} + (T - T_g)} \right] \quad (3.28)$$

By defining $c_1 = \frac{-B}{f_g}$, $c_2 = \frac{f_g}{\xi_g}$, the start equation is obtained.

The calculus of the apparent energy of a relaxation, $E_a = R \frac{d \ln(a_T)}{d(1/T)}$, can be performed on the basis of the W-L-F equation, by substituting $\ln a_T$ by:

$$\log a_T = \frac{-c_1(T - T_g)}{c_2 + (T - T_g)} \quad (3.29)$$

thus obtaining Eq. 3.30.

$$E_a = 2.303R \frac{c_1 c_2 T^2}{(c_2 + T - T_g)^2} \quad (3.30)$$

The activation energy is temperature depending, rapidly increasing when the temperature decreases.

Vogel-Fulcher-Tamman-Hesse (VFTH) Model

Fulcher and Tamman-Hesse introduced the following equation for the viscosity:

$$\log \mu = A' + \frac{B'}{(T - T_\infty)} \quad (3.31)$$

The $\ln a_T$ value can be calculated as shown in Eq. 3.32:

$$\begin{aligned} \ln a_T &= \ln \frac{\tau(T)}{\tau(T_g)} \approx \ln \frac{\mu}{\mu_{T_g}} \\ \log a_T &= \log \mu(T) - \log \mu(T_g) = A' + \frac{B'}{T - T_\infty} - A' + \frac{B'}{T - T_\infty} \\ &= \frac{B'}{T - T_\infty} - \frac{B'}{T_g - T_\infty} \end{aligned} \quad (3.32)$$

Since the second term is a non-depending temperature value: $A = \frac{-B}{T_g - T_\infty}$ and equalling $B = B'$, Vogel and Fulcher propose Eq. 3.33.

$$\log a_T = A + \frac{B}{(T - T_\infty)} \quad (3.33)$$

T_∞ is known as the Vogel temperature, and is to the temperature corresponding to a null free volume, for which no relaxation process can take place. By identifying the c_1 y c_2 parameters of W-L-F with the values shown in Eq. 3.34.

$$c_1 = \frac{B'}{(T_g - T_\infty)} \quad (3.34)$$

$$c_2 = T_g - T_\infty$$

Eq. 3.35 is obtained:

$$\begin{aligned} \log a_T &= \frac{-B}{T - T_\infty} - \frac{B}{T_g - T_\infty} = \frac{B'(T_g - T_\infty) - (T - T_\infty)}{(T_g - T_\infty) - (T - T_\infty)} \\ &= \frac{-B'(T - T_g)}{(T_g - T_\infty)(T - T_\infty)} = \frac{c_1(T - T_g)}{(T - T_\infty)} \\ &= \frac{c_1(T - T_g)}{(T - T_g) + (T_g - T_\infty)} \end{aligned} \quad (3.35)$$

From Eq. 3.35, Eq. 3.36 can be deduced, by substituting the corresponding c_1 y c_2 , thus obtaining a dependence of the activation energy with the temperature near the glass transition:

$$E_a = 2.303R \frac{c_1 c_2 T^2}{(c_2 + T - T_g)^2} = 2.303RB \left(\frac{T}{T - T_\infty} \right)^2 \quad (3.36)$$

Assessment of the macromolecular cooperativity

As in the case of low molecular weight solids and liquids, there are some secondary relaxations in polymers which have little or no activation entropy, and relatively small activation energies. The relationship between frequency and temperature can be expressed in terms of an Arrhenius equation [18-22]:

$$f = Ae^{-E_a/RT} \quad (3.37)$$

An alternative equation is derived from the theory of absolute reaction rates:

$$f = \frac{kT}{2\pi h} e^{-\Delta H^*/RT} e^{\Delta S^*/R} \quad (3.38)$$

Although these equations are slightly different in form, it is usually difficult to decide which provides a better fit for experimental data. The activation enthalpy (ΔH^*) from Eq. 3.38 is given by Eq. 3.39.

$$\Delta H^* = -R \frac{d \ln(f/T)}{d(1/T)} \quad (3.39)$$

The activation energy (E_a) from the Arrhenius equation is shown in Eq. 3.40.

$$E_a = -R \frac{d \ln f}{d(1/T)} \quad (3.40)$$

It is easily shown that

$$E_a = \Delta H^* + RT \quad (3.41)$$

The relationship between the activation energy, and the temperature T' at which $f = 1$ Hz is shown in Eq. 3.42.

$$E_a = RT' \left[1 + \ln \left(\frac{kT'}{2\pi h} \right) \right] + T' \Delta S^* \quad (f = 1 \text{ Hz}) \quad (3.42)$$

For relaxations having a zero activation entropy, this reduces to Eq. 3.43, not quite linear relationship.

$$E_a = RT' \left[1 + \ln \left(\frac{kT'}{2\pi h} \right) \right] = RT' \left(\ln T' + 22.922 \right) \quad (3.43)$$

$$(f = 1 \text{ Hz}, \Delta S^* = 0)$$

Thus the difference between the observed activation energy, and that calculated from Eq. 3.43 is $T' \Delta S^*$.

Consequently, subvitreous relaxation phenomena in polymers are often of that type. They are believed to be simple and noncooperative. In this case, the motions involved are localized and independent from each other. The interpretation of the Starkweather treatment of glass transitions is different. Glass transitions always exhibit a high apparent activation energy. This is interpreted in terms of cooperative and hierarchical constrained dynamics of the glass transition. The corresponding apparent activation entropy is shown to be so high that it cannot be given any physical meaning, and, therefore, the high value of the ΔS^* factor only results from the inability of the Arrhenius and Eyring models to reasonably describe the relaxation associated with the glass transition [18-22].

In Figure 3.7 the macromolecular cooperativity assessment of a series of recycled polylactides is performed to exemplify the applicability of the Eyring-Starkweather model. Accordingly, the black line represents the zero-entropy ($\Delta S^* = 0$) line. The experimental apparent activation energies (E_a) were plotted versus the temperature corresponding to the peak of the dielectric loss factor obtained at a frequency of 1 Hz.

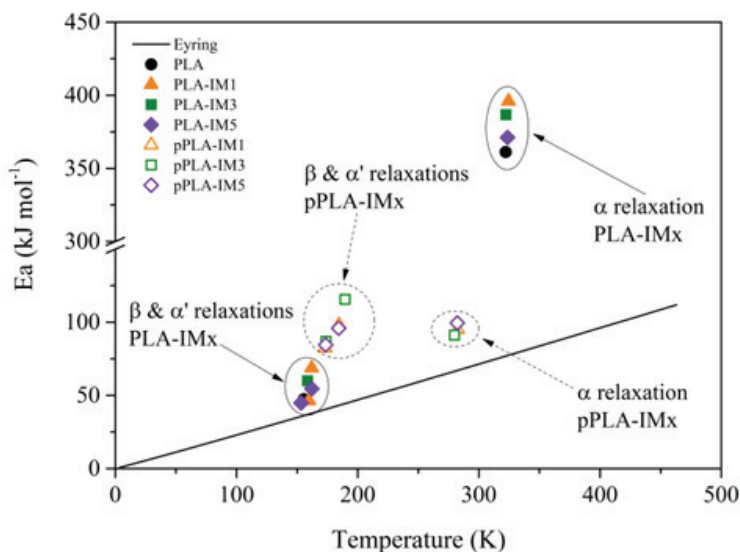


Figure 3.7: Example of an Eyring plot for a group of recycled poly(lactides). Source: [3].

Concerning Figure 3.7, the PLA-IM x presents two types of relaxation processes (β and α') occurring in the low-energy region. Subsequently, both relaxations can be considered of non-cooperative (or intramolecular) origin since the entropys role can be disregarded for this type of molecular relaxation.

Contrarily, values far from the zero-entropy line are classified as of intermolecular (or cooperative) origin because their departure from the zero-entropy values indicates that the contribution of the entropy is significant, and thus it cannot be disregarded. Therefore, at higher temperatures, only the PLA-IM x display a high-energy relaxation assigned to intermolecular movement related to the glass transition, i.e. the dielectric α relaxations. However, this is not the case of the relaxation spectrum of the plasticized poly(lactides), as all the relaxation only displays a linear behaviour deviation, which indicates very closer intramolecular movements.

3.1.4 Molecular origin of the dielectric response in polymers

The polarization phenomena in dielectrics by means of an external field might be occur by several mechanisms (Figures 3.8 - 3.9) originating from microscopic or macroscopic charge displacement. Concerning polymers, the net dipole moment per unit volume (i.e., the polarization) corresponds to the vector summation over all molecular dipole types in the repeating unit, the polymer chain, and over all chains in the system [5].

Accordingly, the deformation of the electronic shell with respect to the atomic nucleus due to the electric stimulus, i.e. electronic polarization, creates the atomic polarization, i.e., an induced dipole moment in atoms. Both processes are considered instantaneous provided that both of them exhibit high resonant frequencies. Subsequently, the rotational mobility of the permanent group dipole moments generate the largest contribution to the observed polarization phenomena. Therefore, isomeric transitions, rotations of side groups, and segmental motions are the cause for the registered changes in the localized charge density [5].

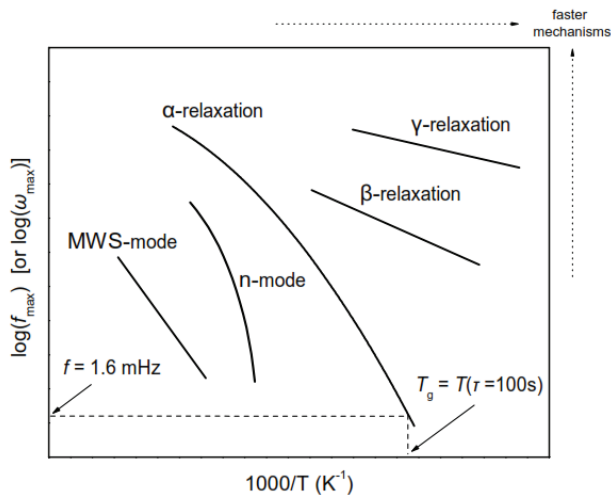


Figure 3.8: Schematic of commonly observed mechanisms in an Arrhenius plot. Source: [5].

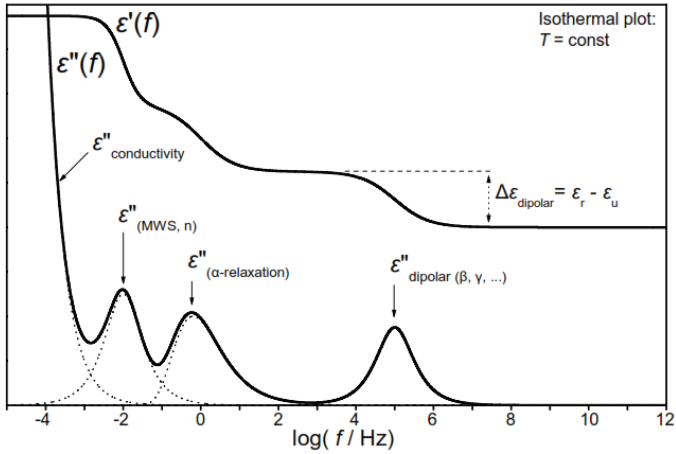


Figure 3.9: Generic behaviour of temperature dependence of permittivity components recorded for an amorphous polymer with considerable ionic conductivity. Source: [5].

According to the notation developed by Stockmayer [23] the different physical configurations for the orientation of molecular dipole vectors with respect to the backbone are summarised as follows:

- *Type A* refers to polymers that contain fixed dipoles attached parallel to the main chain, as for instance cis-1,4-polyisoprene and polyethers.
- *Type B* refers to polymers that contain dipole moments rigidly attached perpendicular to the main chain, like poly(vinyl acetate) and most synthetic polymers.
- *Type C* refers to polymers containing a flexible polar side chain, such as poly(n-alkyl methacrylate)s.

Nonetheless, note that polymers where only one type of dipole moment is present constitute an exceptional case, as seen in Figure 3.9. Figure 3.8 contains a schematic of the commonly dielectric relaxations (secondary, segmental, and n-mode) observed in amorphous polymers. Furthermore, dielectric relaxations associated to the migration of charges are also incorporated. A brief description of each of them is included as follows [5]:

- *Secondary relaxations processes:* The typical relaxations representing secondary transitions in amorphous polymers are the δ , γ , and β in order of increasing temperature. The molecular origin of these dielectric processes is generally associated with uncorrelated motions of molecular units involving a limited number of carbon atoms. For instance, the β -relaxation mechanism is a thermally activated process characterized by an Arrhenius temperature dependence of the relaxation times. Accordingly, the barrier height (E_β) describes the potential barrier between two possible equilibrium states, i.e. two different orientations of the polar group relatively to the main chain. These values usually vary between 20-60 $\text{kJ} \cdot \text{mol}^{-1}$, and are determined by the chemical composition and the stereochemical configuration of the chains.
- *Segmental relaxation process:* The onset of the micro-Brownian motion of chain segments originates the dynamic glass transition (α) process. Hence, as the structure shifts from a rigid supramolecular glass structure to a different one in the viscoelastic fluid state. Consequently, this process involves a certain degree of cooperativity, meaning that a certain segment moves in conjunction with its environment, i.e. an α relaxation involves both intramolecular and intermolecular interactions.
- *Normal mode relaxation process:* These relaxations are originated by the long-range motions of the end-to-end dipole moment vector along a polymer chain [24]. It is characteristic of type A polymers, and its peak frequency depends on the molecular weight. It shows a nonlinear temperature dependence, and therefore, it is described by a VFTH model.
- *Dielectric processes related to long-range charge migration:* DC conductivity is due to the migration of extrinsic (e.g., ionic impurities) and intrinsic (e.g., proton transfer along hydrogen bonds) charges [24]. Elements such as the chemical composition of the system, preparation conditions, sample treatment, ongoing chemical reactions, and physical processes determine the magnitude of the observed conductivity. In dielectric measurements,

the extrinsic conductivity is sufficiently suppressed, which is necessary to study intrinsic relaxation phenomena in the material, which if not it would be masked by the strong conductivity effects. The macroscopic motion of space charges is also directed to the electrodes, which may act as a total or partial barrier (blocking or non Ohmic contacts), creating a large electric dipole (electrode polarization). *Interfacial polarization*, also referred as Maxwell-Wagner-Sillars (MWS) polarization, is a characteristic bulk phenomenon in polymer systems with a heterogeneous structure. This kind of polarization is due to the build up of charged layers at the interface, resulting from unequal conduction currents within the constituent phases. When analysing the dielectric spectra, MWS signal must be expected above the glass transition temperature in isochronal measurements, and in the very low frequency region in isothermal measurements [25-26].

3.2 Fourier Transformed Infrared Spectroscopy (FTIR)

Infrared spectra (IS) is utilised to comprehend which molecules are present in a certain sample. Furthermore, IS can be useful in the quantification of each group's concentration. Despite the great variety of IS spectrometers in the market, the most conventional one is the Fourier Transformed Infrared Spectroscopy (FTIR). Section 3.2 is devoted to introduce its fundamentals. Moreover, an example of its application to the context of this thesis is included.

3.2.1 Light and its properties

Light can be described as electromagnetic radiation because it is composed of electric and magnetic waves which are referred to as the electric and magnetic vector, respectively. Indeed, both waves undulate in planes mutually perpendicular to each other, and move through space in a third direction perpendicular to the planes of undulation. Regarding the absorbance of light, the electric vector must be considered. Moreover, as shown in Figure 3.10, its amplitude changes over time and exhibits the form of a sine wave. The wave motion goes through cycles that begins at zero amplitude and ends when it has crossed the zero amplitude a third time [27].

The wavelength (λ) is defined as the distance forward travelled by a wave during a cycle, and it has units of distance per cycle. Note that light waves have different wavelengths, for instance, the mid-infrared radiation has wavelengths of about 10 microns, whereas for the ultraviolet radiation is in the range from 400 to 1 nm. In Figure 3.10 the arrows describe the wavelength.

The wavenumber (W) is defined as the number of cycles that a wave undergoes per unit length, and thus, are measured in units of cycles per centimetre (cm^{-1}). Accordingly, most infrared spectra are plotted from 4000 to 400 cm^{-1} on the x-axis, as seen in Figure 3.11.

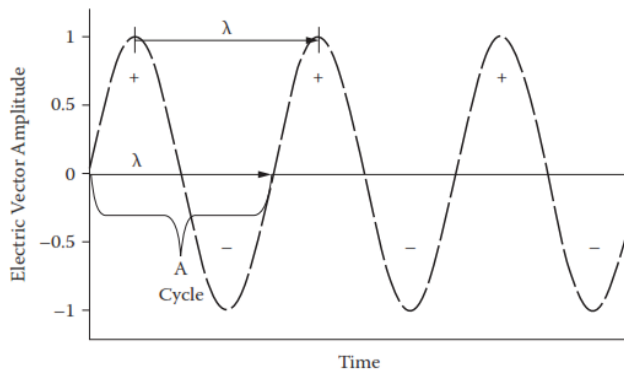


Figure 3.10: An example of the electric vector of a light wave. The alternating polarity of the electric vector is reflected in the + and - signs. Source:[27].

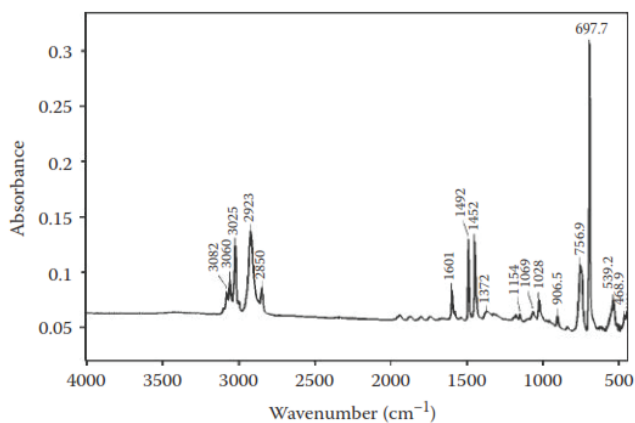


Figure 3.11: Example of an FTIR spectrum. Source:[27].

The wavelength and wavenumbers are reciprocals of each other as shown in Eq. 3.44:

$$W = \frac{1}{\lambda} \quad (3.44)$$

Where W refers to the Wavenumber, and λ is ascribed to the Wavelength.

An interesting feature of the wavenumber is it is proportional to the energy of a light wave as indicated in Eq. 3.45:

$$E = h c W \quad (3.45)$$

Where E refers to the light energy in Joules; c is ascribed to the velocity of light ($\approx 3 \times 10^{10} \text{ cm} \cdot \text{s}^{-1}$); h represent the Planck's constant ($6.63 \cdot 10^{-34} \text{ J} \cdot \text{s}$); and W relates to the wavenumber (cm^{-1}).

Given that the wavelength is proportional to the energy, accordingly high wavenumber light has more energy than low wavenumber light.

Frequency (ν) is defined as a measure of the number of cycles a wave undergoes per unit time, and it is measured in cycles per second (s^{-1}) or Hertz (Hz). The frequency range varies depending on the type of light wave. For instance, mid-infrared frequencies are on the order of 10^{14} , while ultraviolet frequencies are in the range from 10^{15} to 10^{17} .

The different properties of light waves are related to each other as described in Eq. 3.46.

$$c = \nu \lambda \quad (3.46)$$

Where c is ascribed to the velocity of light ($\approx 3 \cdot 10^{10} \text{ cm} \cdot \text{s}^{-1}$); ν relates to the frequency (s^{-1}), and λ refers to the wavelength in cm.

In Eq. 3.46 it is shown that for any light wave the frequency can be estimated if the wavelength is known, and vice versa. Thus, substituting Eq. 3.44 into Eq. 3.46 and rearranging to obtain Eq. 3.47 that allows to determine the wavenumber of a given light wave if frequency is known, and vice versa.

$$c = \frac{\nu}{W} \quad (3.47)$$

Where c refers to the velocity of light ($\approx 3 \cdot 10^{10} \text{ cm} \cdot \text{s}^{-1}$), ν is ascribed to the frequency in Hertz (s^{-1}), and W relates to the wavenumber (cm^{-1}).

The electromagnetic (EM) spectrum, shown in Figure 3.12, is defined as the the range of wavelengths or frequencies over which electromagnetic radiation extends [27]. Accordingly, lower in energy than the mid-infrared is the far-infrared that is located between 400 and 4 cm^{-1} . Molecules with heavy atoms in them vibrate in this region. Even at lower energy, microwaves are present, which register molecular rotations.

>14,000 cm^{-1} Visible & UV	14,000 to 4000 cm^{-1} Near IR	4000 to 400 cm^{-1} Mid-Infrared	400 to 4 cm^{-1} Far Infrared	< 4 cm^{-1} Microwaves
Electronic Transitions	Molecular Vibrations	Molecular Vibrations	Molecular Vibrations	Molecular Rotations

Higher Wavenumber	Lower Wavenumber
Higher Frequency	Lower Frequency
Higher Energy	Lower Energy
Shorter Wavelength	Longer Wavelength

Figure 3.12: The electromagnetic spectrum. Source:[27].

Higher in energy than the mid-infrared, from 14000 to 4000 cm^{-1} , near infrared is located. Despite molecules vibrate in this region the spectral features are fewer, broader, and more difficult to interpret than in the mid-infrared. This region is particularly interesting to measure sample properties in difficult environments like for instance a chemical reactor. The visible light and ultraviolet radiation are higher in energy than the near infrared region, with wavenumbers larger than 14000 cm^{-1} . Molecules vibrating in this region, transition from a lower electronic energy level to a higher one. FTIRs can be equipped to work in the visible and UV.

As shown in Figure 3.12, as you move from left to right across the EM spectrum a decrease in energy, wavenumber, and frequency is found. Nevertheless, an increment in wavelength is registered. Likewise, moving from right to left across Figure 3.12 results in a decrease in wavelength but an increment in energy, frequency, and wavenumber.

3.2.2 The infrared spectrum. Definition

An infrared spectrum is defined as a graph where infrared light intensity versus a property of light is plotted. Eq. 3.48 shows how to determine the absorbance spectrum [27].

$$A = \log \left(\frac{I_0}{I} \right) \quad (3.48)$$

Where A refers to the absorbance, I_0 is ascribed to the intensity in the background spectrum, and I describes the intensity in the sample spectrum.

Beer's law, displayed in Eq. 3.49, relates absorbance to the concentration of molecules in a certain sample, provided that the height, or the area, of a peak in the absorbance spectrum is proportional to the concentration.

$$A = \epsilon l c \quad (3.49)$$

Where A describes the absorbance, ϵ refers to the absorptivity, l is related to the path length, and c is ascribed to the concentration.

Alternatively, another variable can be used to plot the infrared spectrum. It is called the percent transmittance (%T), and it measures the percentage of light transmitted by a sample. It is calculated as follows (Eq. 3.50):

$$\%T = 100 \times \left(\frac{I}{I_0} \right) \quad (3.50)$$

Where %T described the percent Transmittance, I_0 is ascribed to the intensity in the background spectrum, and I is related to the intensity in the sample spectrum.

As shown by Equation 3.49, absorbance is proportional to concentration in a linear manner. On the other hand, the size of the peaks in %T spectra are not linearly proportional to concentration, and thus, this spectrum should not be used for quantitative analysis or spectral subtraction. Instead, absorbance should be used. Nevertheless, %T spectra is suitable for qualitative analysis.

3.2.3 *The infrared spectrum. Utility and application*

The utility of measuring infrared spectra is threefold. First, to perform an unknown analysis, i.e. to identify which molecules are present in the sample. Provided the high amount of FTIR spectra already published by researchers, the peak position of known molecules can be used to identify this same molecules in other samples. Second, a spectral comparison can be performed to determine how closely related two samples are. Third, FTIR spectra is used to determine the concentration of molecules in a certain sample. In order to perform this experiment, one must first prepare samples of known concentration to use it as reference. Then a calibration line is done to relate absorbance to concentration through Eq.3.49. After validation, the model can be used to determine the concentration of molecules in unknown samples. The main advantages and disadvantages of infrared spectroscopy when used as a chemical analysis technique are summarised as follows:

- **Advantages**
 - Almost universal.
 - Spectra are information rich.
 - Relatively fast and easy.

- Relatively inexpensive.
- Sensitivity.
- **Disadvantages**
 - Can't detect some molecules.
 - Mixtures.
 - Water.

FTIR is applied as a step in the characterization of the membrane. As an example the spectrum of a series of polysulfone (PSf) membranes that are blended with two different hyperbranched polyethyleneimine modified with benzoyl chloride (mG20) and phenyl isocyanate (UG20) in different percentages are shown. FTIR spectra helped in the assessment of the presence of urea and amide groups in the sample structures, respectively.

Accordingly, the FTIR spectra are displayed in Figure 3.13. Concerning the labelling, M0% refers to the pure PSf membrane. The membranes modified with mG20 are labelled as M1-2% and M1-10% depending on the percentage of mG20 added. Finally, the membranes modified with UG20 are labelled as M2-2% and M2-10% depending on the percentage of UG20 added.

The spectra displayed in Figure 3.13 contains several contributions arising from the polysulfone including stretching vibrations of the C=C double bonds from the aromatic rings ($1620 - 1430 \text{ cm}^{-1}$); the symmetric deformation of the C-H bonds ($1385 - 1350 \text{ cm}^{-1}$) [28-30]; the vibration of the C-O-C bond arising from the aryl groups [28-31]; the asymmetric ($1350 - 1280 \text{ cm}^{-1}$) and symmetric ($1180 - 1145 \text{ cm}^{-1}$) stretching of the O=S=O group [28,30-32]; in the region $1000 - 830 \text{ cm}^{-1}$ the stretching of the aromatic C-H group [28,29,31], and the peaks for the hydrogen deformation for the para-substituted phenyl groups and the C-H rocking vibrations [28,30].

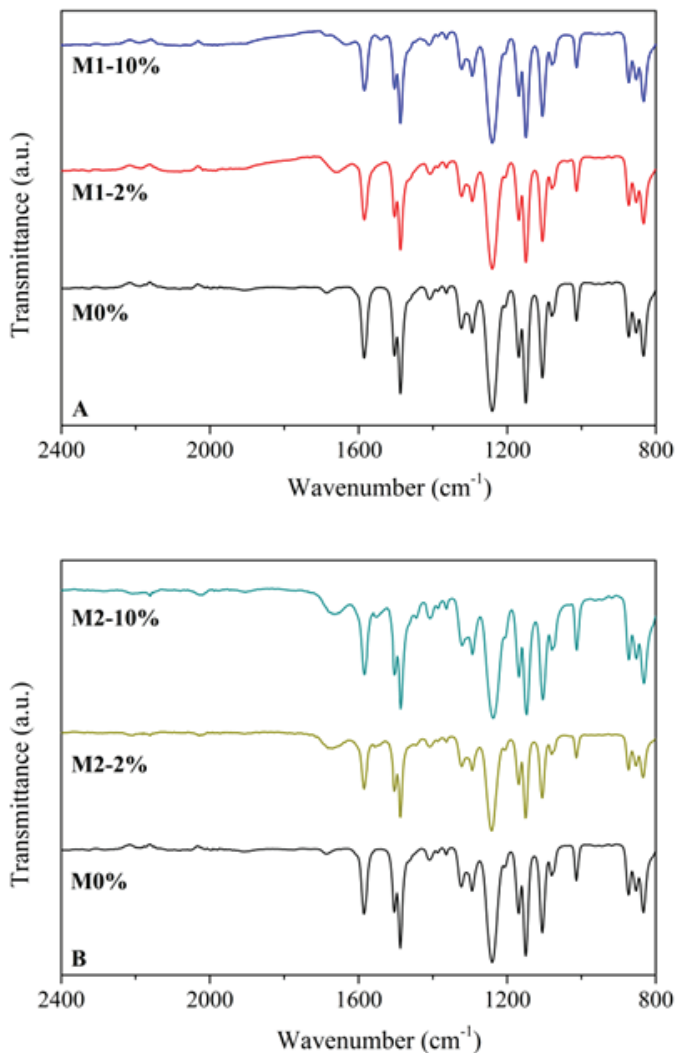


Figure 3.13: FTIR spectra for the pure (M0%) and blended (M1-2%, M1-10%, M2-2%, and M2-10%) polysulfone membranes.

The broadband highlighted in Figure 3.13B is attributed to the C=O stretching in urea, and it is the only characteristic band from UG20 present in the FTIR spectra [33]. Note that the intensity of the peak increases with the concentra-

tion, and thus, the peak is more visible in M2-10%. Regarding the mG20, a characteristic peak is found in the region from 1630 cm^{-1} to 1650 cm^{-1} that corresponds to the C=O stretching in amides. Note that this peak is more visible in M1-2% than in M1-10% since it is overlapped with other characteristic peaks from PSf.

3.3 Thermogravimetric Analysis (TGA)

Thermogravimetric analysis is defined by the International Confederation for Thermal Analysis and Calorimetry (I.C.T.A.C.) as a technique in which the mass of the sample is measured as a function of temperature, while the sample is subjected to a controlled temperature programme.

The analysis can be carried out either in a dynamic mode, by means of a heating programme at constant rate, or under isothermal conditions, as a function of time. In both cases, the mass loss or the mass loss rate (that are directly related to the removal of volatile compounds or to a chemical process), are determined at every temperature or time.

The basic components of this technique are both the mass control, and the thorough temperature control, as shown in Figure 3.14.

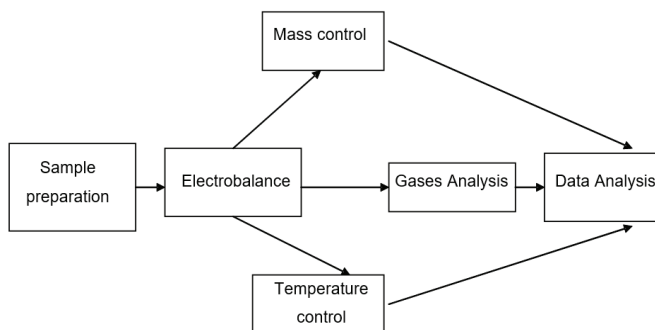


Figure 3.14: Scheme of the thermogravimetric process.

Results of Thermogravimetric Analysis are displayed in a thermogravimetric curve, also called thermogram. This consists of a sigmoidal curve with one or more stages, depending on the chemical nature of the components and the sample composition.

A weight loss at low or moderate temperature (up to 423 K) corresponds to the loss of volatile components like water, organic solvents with low molecular weight, or absorbed gases.

For temperatures in the range of 423 - 523 K, the loss of low molecular weight components can be detected, such as additives, crystallization water, plasticizers or even the first decomposition products at low temperatures.

At temperatures higher than 498 - 523 K, the thermal degradation is usually initiated. Its evolution is related to the atmosphere used during the measurement. When the thermogravimetric analysis is carried out under oxygen or air atmospheres, it is called thermo-oxidative degradation.

At temperatures about 773 K, hydrocarbonated compounds which thermal degradation do not lead to the formation of volatile fragments, are charred. These remain as residues together with non-degradable fillers or inorganic additives. If the measurements is performed under oxidant atmosphere, the char residue leads to the formation of gaseous carbon dioxide, and the inorganic residues remain as ashes of metallic oxides or of salts that cannot be oxidized.

Thermogravimetric results can also be displayed as a differential curve or DTG curve that is obtained from the first derivative of the thermogravimetric curve. In the DTG curve, the drops with the maximum slope of the thermogravimetric curve will correspond to the maxima of the differential curve, as shown in Figure 3.15.

Typical TG and DTG curves are shown in the above figure. These curves clearly show that the decomposition process of the material under study occurs from 673 K to 773 K.

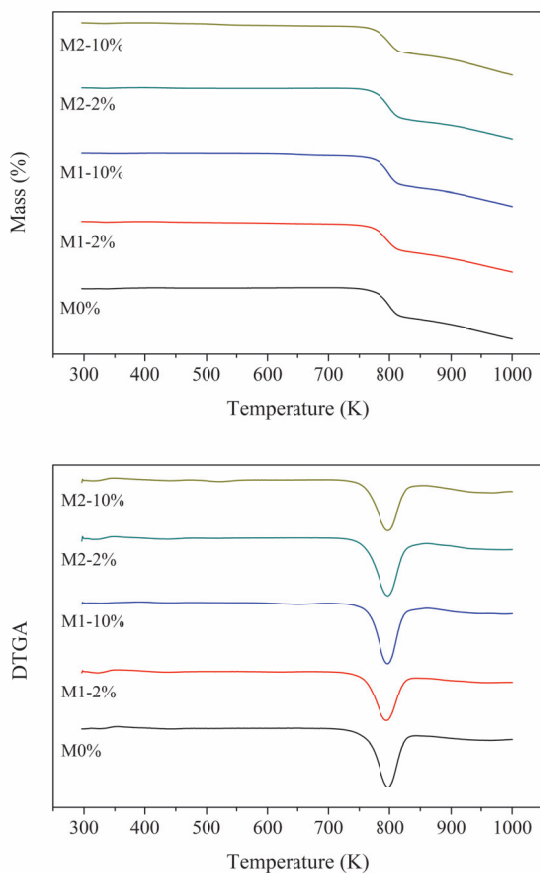


Figure 3.15: Thermogravimetric curve (TG) and its corresponding differential curve (DTG) for a series of polysulfones membranes.

This analysis technique allows the study of the thermal decomposition of polymers, the decomposition rate, the reaction order and the activation energy, but also allows the determination of additives and fillers present in complex formulations. When Thermogravimetric Analysis is coupled to another complementary analytical technique (Infrared Spectroscopy, Mass Spectrometry, etc.), information about the nature of the mass loss is provided. Such information will be

useful either for the elucidation of the mechanism of the degradation process, or for obtaining fundamental information about the material itself.

Kinetic Analysis of the Thermal Degradation Process

The kinetic study of a chemical reaction consists of different aspects. One of them is related to the study of the phenomenological kinetic laws that govern the reaction rate as a function of the concentrations of reactants and products, the temperature, etc. The second aspect is referred to establish the mechanisms of each of the chemical reactions of the thermodegradation process. It can be determined whether the chemical degradation directly leads to the depolymerization or the chains scission in the macromolecules, or whether there is a series of stages that lead to the products formation, by means of a group of intermediate species [5].

The equation for the thermal decomposition rate describes the chemical changes that occur in the system, by means of a mathematical function that depends basically on the reactant concentration and the temperature. In other words, the conversion rate or reacted fraction in relation to the time t , is established by means of two different contributions: one that depends on the reactant concentration, and another one that depends exclusively on the absolute temperature T , and that is known as rate constant (k).

$$\text{Thermal decomposition rate} = f_{(\text{reactant concentration})} \cdot k_{\text{temperature}} \quad (3.51)$$

The almost universal model accepted to fit the dependence of the reaction rate with the temperature in a degradation process is the Arrhenius equation, shown in Eq. 3.52.

$$k(T) = A \cdot \exp\left(\frac{-E}{RT}\right) \quad (3.52)$$

where R is the universal gas constant, T describes the absolute temperature, E is the activation energy, and A is the pre-exponential factor that is assumed to be independent of temperature.

The reactant concentration present at every moment in the thermodegradation process can be expressed, as suggested by Hirata, in terms of the polymer mass at every time (ω). In this case, the function that depends on the concentration will be exactly ω , and the kinetic equation will be as described in Eq. 3.53.

$$\frac{d\omega}{dt} = -\omega \cdot k(T) \quad (3.53)$$

and considering that $k(T)$ is given by the Arrhenius equation, the rate equation can be rearranged as in Eq. 3.54.

$$\frac{d\omega}{dt} = -\omega \cdot A \cdot \exp\left(\frac{-E}{RT}\right) \quad (3.54)$$

The kinetic equation can also be determined by defining the reactant concentration by means of the conversion. The degree of conversion (α) can be defined as the polymer mass lost at a time t , divided by the polymer mass that would be lost at infinite time or total mass loss:

$$\alpha = \frac{\omega_0 - \omega}{\omega_0 - \omega_\infty} \quad (3.55)$$

where ω , ω_0 , and ω_∞ are the actual, the initial, and the final mass of the sample, respectively.

Therefore, the rate equation will be given by Eq. 3.56.

$$\frac{d\alpha}{dt} = f(\alpha) \cdot k(T) \quad (3.56)$$

where $f(\alpha)$ depends on the mechanism of the degradation rate.

The combination of Eq. 3.52 and Eq. 3.54 leads to the general rate equation shown in Eq. 3.57.

$$\frac{d\alpha}{dt} = f(\alpha) \cdot A \cdot \exp\left(\frac{-E}{RT}\right) \quad (3.57)$$

Methods for the Determination of the Activation Energy

The easiest model used to designate the kinetic function $f(\alpha)$ for polymers is shown in Eq. 3.58.

$$f(\alpha) = (1 - \alpha)^n \quad (3.58)$$

where n represents the reaction order. For many reactions, it can be supposed that $n = 1$.

If the function $f(\alpha)$ is replaced by the above equation into Eq. 3.57, it gives:

$$\frac{d\alpha}{dt} = (1 - \alpha)^n \cdot A \cdot \exp\left(\frac{-E}{RT}\right) \quad (3.59)$$

In order to calculate the activation energy, Eq. 3.54 and Eq. 3.59 will be considered. These equations can be solved in their differential form or they can be integrated, thus, leading to two different methods of calculation:

The differential method

T. Hirata and K.E. Werner [34] proposed that calculating logarithms in Eq. 3.54 and separating the variables, Eq. 3.60 can be obtained.

$$\ln\left(-\frac{d\omega}{dt}\right) - \ln\omega = \ln A - \left(\frac{E}{RT}\right) \quad (3.60)$$

where ω is the polymer mass for each temperature or time.

E.S. Freeman and B. Carroll [35] proposed a different equation from Eq. 3.59, who suggested solving the differential equation as follows:

$$\Delta \left[\frac{\ln\left(\frac{d\alpha}{dt}\right)}{\Delta [\ln(1 - \alpha)]} \right] = n - \frac{E}{R} \cdot \frac{\Delta(1/T)}{\Delta [\ln(1 - \alpha)]} \quad (3.61)$$

where α is the mass loss fraction, or the fraction that has reacted, and R is the universal gas constant.

Friedman [36] suggested Eq. 3.62 to calculate the kinetic parameters:

$$\ln \left(\frac{d\alpha}{dt} \right) = n \cdot \ln(1 - \alpha) + \ln A - \frac{E}{RT} \quad (3.62)$$

The values of $\ln(d/dt)$ can be easily obtained from the differential thermogravimetric curve, whereas the values of $\ln(1 - \alpha)$ can be obtained from the thermogravimetric curve. The plot of $\ln(d\alpha/dt)$ against the reciprocal of temperature ($1/T$) should be given a straight line for each chemical process. From the slope of this straight line, the activation energy E can be calculated.

W. L. Chang [37] developed another model on the basis of Eq. 3.62:

$$\ln \left[\frac{\frac{d\alpha}{dt}}{(1 - \alpha)^n} \right] = \ln A - \frac{E}{RT} \quad (3.63)$$

The integral method.

When the sample is continuously heated at constant rate β the variation of temperature with respect to time is given by: $\beta = dT/dt$. Therefore, the reaction rate may be written as follows:

$$\frac{d\alpha}{dt} = \frac{d\alpha}{dT} \cdot \frac{dT}{dt} = \beta \cdot \frac{d\alpha}{dT} \quad (3.64)$$

The variation in the degree of conversion can then be analysed as a function of temperature. The combination of Eq. 3.59 and Eq. 3.64 leads to:

$$\begin{aligned}\frac{d\alpha}{dt} &= (1 - \alpha)^n \frac{A}{\beta} \exp\left(\frac{-E}{RT}\right) \\ \rightarrow \frac{d\alpha}{(1 - \alpha)^n} &= \frac{A}{\beta} \exp\left(\frac{-E}{RT}\right) dT\end{aligned}\tag{3.65}$$

The initial condition $\alpha = 0$ for $T = T_0$ leads to Eq. 3.66:

$$\int_0^\alpha \frac{d\alpha}{(1 - \alpha)^n} = \frac{A}{\beta} \int_{T_0}^T \exp\left(\frac{-E}{RT}\right) dT\tag{3.66}$$

All the suggested equations following the integral method are based on Eq. 3.66.

L. Reich and D.W. Levi [38] proposed that the relation between the conversion and the temperature when $n = 1$ can be represented by Eq. 3.67:

$$\ln[\ln[-(1 - \alpha)]] \cong \frac{-E}{RT} + \ln \frac{A\Delta T}{\beta}\tag{3.67}$$

where ΔT is the temperature interval used for the determination of α . Thus, the plot of $\ln[\ln[-(1 - \alpha)]]$ against the reciprocal of temperature should give a straight line, from which the activation energy E can be calculated.

Broido [39] developed the following model:

$$\ln \left[\ln \left(\frac{1}{x} \right) \right] \cong \frac{-E}{RT} + \text{const}\tag{3.68}$$

where x is the residual fraction, defined as:

$$x = 1 - \frac{\omega_0 - \omega}{\omega_0 - \omega_\infty} = \frac{\omega - \omega_\infty}{\omega_0 - \omega_\infty} \quad (3.69)$$

where ω is the sample weight at time t , ω_0 is the initial sample weight, and ω_∞ is the final sample weight or residue.

Integral Method

The Kissinger method was modified by J.H. Flynn and L.A. Wall [40] as follows.

$$\frac{-d \log \beta}{d \left(\frac{1}{T_m} \right)} = 0.457 \frac{E}{R} \quad (3.70)$$

According to the international ASTM E 698-79(1984) norm [Standard Test Method for Arrhenius Kinetic Constants for Thermally Unstable Materials], the activation energy is calculated as:

$$E = -\frac{2.3R}{D} \frac{-d \log \beta}{d \left(\frac{1}{T_m} \right)} \quad (3.71)$$

where D is a corrective parameter, which values are summarized in tables of the ASTM norm.

The methods based on the temperature at maximum reaction rate T_m are widely used, with satisfactory results, in differential scanning calorimetry, in order to determine the reaction kinetics. However, these methods cannot often be applied to study the thermal decomposition process. As it was proved by W. L. Chang [37], these methods cannot often be used if the thermodegradation process occurs in several stages, and it is not possible to exactly determine the temperature of the maximum. Thus, other models were developed, in which the dependence of the temperature with the degree of conversion is considered. Among them, the integral model proposed by Flynn-Wall-Ozawa can be mentioned. In general, the integral methods are based on an approximate integration of the integral function of conversion $g(\alpha)$, given by the Eq. 3.72.

$$g(\alpha) = \int_0^{\alpha_p} \frac{d\alpha}{f(\alpha)} = \frac{A}{\beta} \int_0^{T_p} \exp\left(\frac{-E}{RT}\right) dT \quad (3.72)$$

J.H. Flynn and L.A. Wall [40] and Ozawa [41] introduced a new variable x , defined as shown in Eq. 3.73.

$$x = \frac{E}{RT} \quad (3.73)$$

Moreover, from Eq. 3.73 the temperature and its derivative can be obtained as follows:

$$T = \frac{E}{Rx} \quad (3.74)$$

$$dT = \frac{-E}{Rx^2} dx$$

Changing the integration limits as described in Eq. 3.75,

$$\begin{cases} T \rightarrow 0 \implies x \rightarrow \infty \\ T \rightarrow T \implies x \rightarrow \frac{E}{RT} \end{cases} \quad (3.75)$$

it gives the integral shown in Eq. 3.76.

$$g(\alpha) = \frac{A}{\beta} \int_{\infty}^x \left(\frac{-E}{R}\right) \frac{1}{x^2} \exp(-x) dT \quad (3.76)$$

$$g(\alpha) = \frac{AE}{\beta R} p(x)$$

where $p(x) = \int_{\infty}^0 \frac{1}{x^2} \exp(-x) dx$

The above integral can be solved using the Doyle approximation, based on the Schlömilch expansion:

$$p(x) = \frac{\exp(-x)}{(1+x)x} \quad (3.77)$$

$$p(x) = \left(1 - \frac{1}{x+2} + \frac{2}{(x+2)(x+3)} - \frac{3}{(x+2)(x+3)(x+4)} + \dots \right)$$

Doyle suggests only the two first terms of each series to be considered:

$$p(x) = \frac{\exp(-x)}{x(x+2)} \quad (3.78)$$

Doyle also verified that taking logarithms for $x > 20$, $p(x)$ could be given by Eq. 3.79.

$$\log p(x) \approx -2.315 - 0.457x \quad (3.79)$$

On the basis of the Doyle approximation, Flynn, Wall and Ozawa proposed the following solution for Eq. 3.76.

$$g(\alpha) = \frac{AE}{\beta R} \frac{e^{-x}}{x(x+2)} \quad (3.80)$$

and taking logarithms Eq. 3.81 is obtained.

$$\log(\beta) = \log \frac{AE}{Rg(\alpha)} - 2.315 - \frac{0.457E}{RT} \quad (3.81)$$

This method allows the determination of the activation energy, without knowing the reaction mechanism. The activation energy for different conversions

can be calculated from the slope of the plots of $\log(\beta)$ versus the reciprocal temperature.

TGA can provide valuable kinetic information to evaluate the temperatures associated with important processes that can have an enormous impact in the operative conditions of the material for any engineering application. Furthermore, it also offers sensitive information to understand the mechanisms of thermal processes through a mathematical relationship between time, temperature, and conversion [5].

Nonetheless, measurements can be influenced by a series of factors, such as atmosphere effects, secondary reactions, and/or electrical considerations. Accordingly, modern thermobalances are designed to reduce or compensate for all these effects. Subsequently, unless very sensitive experiments involving small changes in mass are considered, generally corrections are not required [5].

3.4 Differential Scanning Calorimetry (DSC)

The ASTM standard E473 defines differential scanning calorimetry (DSC) as a technique in which heat flow rate difference into a substance and a reference is measured as a function of temperature while the substance and reference are subject to a controlled temperature program [5].

Accordingly, indirect techniques must be used to measure the heat since there is no heat flow meter that could directly measure the heat flowing into or out of the sample. Differential scanning calorimetry is one of these techniques, and thus, it uses the temperature difference developed between the sample, and a reference for calculation of the heat flow. An exotherm indicates heat flowing out of the sample, while an endotherm indicates heat flowing in. Accordingly, there are two types of DSC instruments exist: heat flux and power compensation [5].

Its major applications are summarised as follows:

- Easy and fast determination of the glass transition temperature.
- Determine the heat capacity jump at the glass transition.
- Calculate the melting and crystallization temperatures.
- Determination of the heat of fusion, heat of reactions, very fast purity determination, fast heat capacity measurements.
- Characterization of thermosets.
- Measurements of liquid crystal transitions.
- Determination of the kinetics of polymer crystallization.

The major applications of the DSC technique are in the polymer and pharmaceutical fields, food industry and biotechnology [5,42].

Thermodynamics in DSC

Thermodynamics studies two forms of energy transfer: heat and work. Heat is one form of transfer of energy related to the difference in temperatures of two systems. Heat is transferred spontaneously from hot to cold systems. It is an extensive thermodynamic quantity, meaning that its value is proportional to the mass of the system. The SI unit of the heat is the joule (J). The earlier unit of calorie is not in use any more [5].

The goal of thermodynamics is to establish basic functions of state, the most important of which for differential scanning calorimetry are internal energy (U), enthalpy (H), pressure (p), volume (V), entropy (S), and heat capacity at constant pressure (C_p).

In thermodynamics, the description of reversible processes is the one that is most widely used. This is called *equilibrium thermodynamics*, because it deals with equilibrium systems. *Nonequilibrium thermodynamics*, which deals with

irreversible processes, and thus has time as an additional variable to the basic parameters of state.

As mentioned above, equilibrium thermodynamics deals with reversible processes, and is based on the following four laws thermodynamics, which are empiric laws rather than theoretically deduced laws:

- The zeroth law of thermodynamics introduces the concept of temperature.
- The first law of thermodynamics, also known as the principle of energy conservation, states that the change of internal energy of a thermodynamic system equals the difference of the heat added to the system and all the work done by the system. The internal energy of a thermodynamic system is a function of state; its value depends only on the state of the system, not on the path, that is, how the system arrived at this state. Therefore, in a cyclic process $\Delta U = 0$. Thus, energy cannot be created or destroyed. The first law can be expressed as $\Delta U = Q - W$, where ΔU is the change in internal energy, Q is the heat, and W is the work.
- There are several formulations of the *second law of thermodynamics*. The so-called Clausius statement says that in spontaneous processes heat cannot flow from a lower-temperature body to a higher-temperature body. The Thomson (Lord Kelvin) statement says that heat cannot be completely converted into work.
- The *third law of thermodynamics* (Nernst law) states that the entropy of perfectly crystalline materials at 0 K is zero.

So, the zeroth law says that, there is a game (heat-to-work conversion game), and that you've got to play the game. The first law says you can't win; at best, you can only break even. But according to the second law, you can break even only at 0 K. And the third law says, you can never reach 0K [5,42]. The most important functions of state used in DSC are described in the following subsections.

Temperature is the most important quantity in differential scanning calorimetry. With DSC, in essence temperature is the only measured quantity. Everything else is calculated from the changes of temperature, from the difference between the sample and reference temperatures. We can define temperature as a primary thermodynamic parameter of a system, as a number chosen arbitrarily which represent the state of a system and it is related to the average kinetic energy of atoms and molecules of the system [5].

Temperature can be defined for *equilibrium systems* only, in which the velocity of the particles are described by the *Boltzmann distribution*. The temperature controls the flow of heat between two thermodynamic systems.

There are two laws of thermodynamics that help define temperature as a parameter of the system. The *zeroth law of thermodynamics* states that if a system A and B are separately in thermal equilibrium with system C, then they are in thermal equilibrium with each other as well. Since all these systems are in thermal equilibrium with each other, some thermodynamic parameter must exist that has the same value in all of them. This parameter is called *temperature*.

The second law of thermodynamics helps define temperature mathematically as

$$T \equiv \left(\frac{\partial U}{\partial S} \right)_V \quad (3.82)$$

in other words, temperature is the rate of increase of internal energy of the system with increasing entropy.

3.5 Membrane characterization in Single cell test

Impedance analysis is a very popular, nondestructive measurement technique that provides detailed diagnostic information about a wide range of electrochemical phenomena including charge transfer reaction at the interface elec-

trode/electrolyte, reaction mechanisms, state of charge of batteries, electrode material properties, and state of health of fuel cells, and so on [43].

The technique involves applying a low-level alternative current (AC) waveform to the electrochemical system (half cell, single cell, stack, etc.) under investigation and measuring the response of the cell to this stimulus (the AC voltage across the cell and the AC current through the cell) [43].

EIS is now applied to characterize electrode processes and complex interfaces. The analysis of the system response yields information about the reactivity and structure of the interface, also about the electrochemical reactions and mass transport limitations taking place there [43].

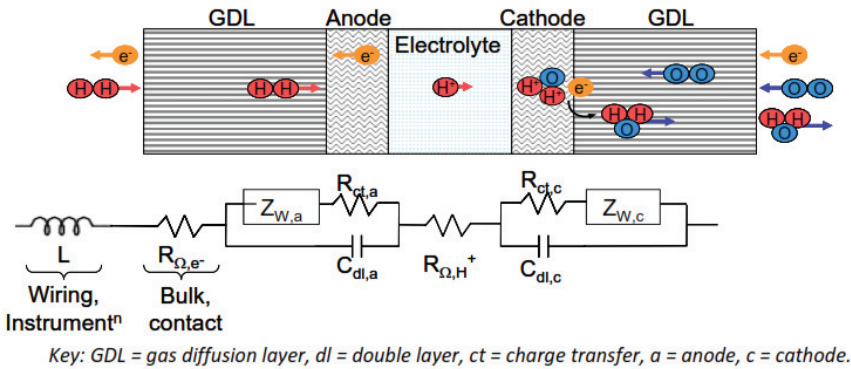


Figure 3.16: Example of a generalized equivalent circuit element for a single cell fuel. Source: [44].

Equivalent circuit modelling of EIS data is used to extract physically meaningful properties of the electrochemical system by modelling the impedance data in terms of an electrical circuit, as shown in Figure 3.16 .

In the equivalent circuit resistors represent conductive pathways for ion and electron transfer. As such, they represent the bulk resistance of a material to charge transport such as the resistance of the electrolyte to ion transport or the resistance of a conductor to electron transport. Resistors are also used to represent the resistance to the charge-transfer process at the electrode surface.

Capacitors and inductors are associated with space-charge polarization regions, such as the electrochemical double layer, and adsorption/desorption processes at an electrode, respectively [44].

The defining relation and impedance for ideal bulk electrical elements are shown below [44].


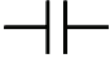

		Defining Relation	Impedance
Resistor		$V = I \times R$	$Z_R = R$
Capacitor		$I = C \frac{dV}{dt}$	$Z_C = \frac{1}{j\omega C} = -\frac{j}{\omega C}$
Inductor		$V = L \frac{dI}{dt}$	$Z_L = j\omega L$

Figure 3.17: The defining relation and impedance for ideal bulk electrical elements. Source: [44].

The impedance of elements in series is additive, as shown in Eq. 3.83.

$$Z_{Total} = Z_1 + Z_2 \quad (3.83)$$

The impedance of elements in parallel is described in Eq. 3.84 as the sum of the inverse of impedances [44].

$$\frac{1}{Z_{Total}} = \frac{1}{Z_1} + \frac{1}{Z_2} \quad (3.84)$$

The most common representations of electrochemical impedance spectra are the Bode plot (Figure 3.18), where the logarithm of impedance magnitude $|Z|$ and the phase-shift (α) are plotted versus the logarithm of the frequency (f), and the Nyquist plot (Figure 3.19), where the imaginary part of the impedance is plotted versus the real part of the impedance (Z).

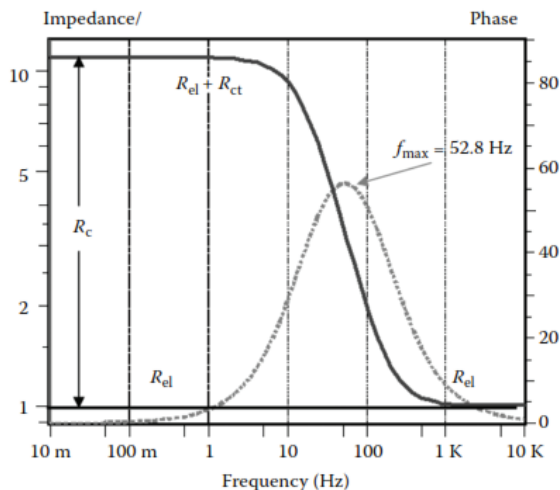


Figure 3.18: Example of a Bode plot Source: [40].

Regarding its utility, the Bode plot is used when the impedance magnitude covers a large range of sizes. From the shape of the Nyquist plot one can distinguish between different diffusion processes and evaluate the deviation of the double-layer capacity from ideal behaviour [40].

The main advantages of utilizing EIS are shown as follows [44]:

- Real FCs operating conditions can be simulated, i.e., open circuit voltage or under load (DC voltage or current).
- A high precision measurement that is non-intrusive.
- Multiple parameters can be determined from a single experiment.
- Allow to characterize bulk and interfacial properties of the system, i.e., membrane resistance and electrocatalysts.

In the present thesis work, the performance tests (H_2 / O_2) of the membrane-electrode-assembly (MEA) have been carried out on a Scribner 850e multi range fuel cell test system. Proton conductivity through the membranes was analysed

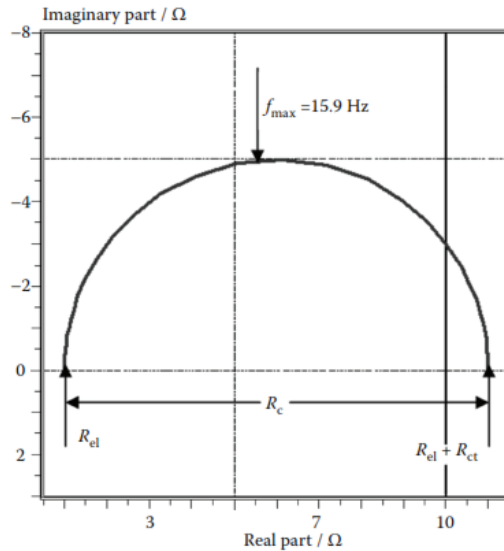


Figure 3.19: Example of a Nyquist plot. Source:[40].

by means of EIS, using an Autolab PGStat30 potentiostat equipped with an FRA module. All tests were performed at atmospheric pressure, cell temperatures of 333 K and 343 K, and 100% relative humidity.

3.6 References

- [1] U.W. Gedde, M.S. Hedenqvist, M. Hakkarainen, F. Nilsson, O. Das, Applied polymer science, Springer, 2021.
- [2] F. Kremer, A. Schönhals, Broadband Dielectric Spectroscopy, 1st ed., Springer-Verlag Berlin Heidelberg, 2003.
- [3] B. Pascual-Jose, J.D. Badia, A. Mugica, F. Addiego, A.J. Müller, A. Ribes-Greus, Analysis of plasticization and reprocessing effects on the segmental cooperativity of polylactide by dielectric thermal spectroscopy, Polymer (Guildf) 223 (2021) 123701.

- [4] G. Floudas, M. Paluch, A. Grzybowski, K. Ngai, *Molecular dynamics of glass-forming systems: effects of pressure*, Springer Science & Business Media, 2010.
- [5] J.D. Menczel, R.B. Prime, *Thermal analysis of polymers: fundamentals and applications*, John Wiley & Sons, 2009.
- [6] O. van den Berg, W.G.F. Sengers, W.F. Jager, S.J. Picken, M. Wübbenhorst, Dielectric and fluorescent probes to investigate glass transition, melt, and crystallization in polyolefins, *Macromolecules* 37 (2004) 2460-2470.
- [7] A. Schönhal, *Dielectric Spectroscopy on the Dynamics of Amorphous Polymeric Systems*, (1998) 117.
- [8] J.R. Macdonald, E. Barsoukov, *Impedance spectroscopy: theory, experiment, and applications*, John Wiley & Sons, 2018.
- [9] A. K. Jonscher, *Dielectric Relaxation in Solids*, Chelsea Dielectrics Press, 1983.
- [10] R. Riande, E., Diaz-Calleja, *Electrical Properties of Polymers*, CRC Press, 2004.
- [11] N.G. McCrum, B.E. Read, O. Williams, *Anelastic and Dielectric Effects in Polymeric Solids*, Dover Publisher, 1991.
- [12] P. Hedvig, *Dielectric spectroscopy of polymers*, Wiley, 1977.
- [13] P. Debye, Molecular forces and their electrical interpretation, *Phys. Zeitschrift.* 22 (1921) 302-308.
- [14] H. Fröhlich, *Theory of dielectrics: dielectric constant and dielectric loss*, Oxford University Press, 1958.

-
- [15] M. Wübbenhorst, J. Van Turnhout, Analysis of complex dielectric spectra. I. One-dimensional derivative techniques and three-dimensional modelling, *J. Non. Cryst. Solids.* 305 (2002) 40-49.
- [16] J. van Turnhout, M. Wübbenhorst, Analysis of complex dielectric spectra. II: Evaluation of the activation energy landscape by differential sampling, *J. Non. Cryst. Solids.* 305 (2002) 50-58.
- [17] P. Lunkenheimer, S. Kastner, M. Köhler, A. Loidl, Temperature development of glassy α -relaxation dynamics determined by broadband dielectric spectroscopy, *Phys. Rev. E.* 81 (2010) 51504.
- [18] H.W. Starkweather Jr, Simple and Complex Relaxations, *Macromolecules* 14 (1981) 1277-1281.
- [19] H.W. Starkweather Jr, P. Avakian, Conductivity and the Electric Modulus in Polymers, *J. Polym. Sci. Part B Polym. Phys.* 30 (1992) 637-641.
- [20] H.W. Starkweather, Frequency-temperature relationships for relaxations in polymers, *Thermochim. Acta.* 226 (1993) 1-5.
- [21] H.W. Starkweather, Aspects of simple, non-cooperative relaxations, *Polymer (Guildf)* 32 (1991) 2443-2448.
- [22] H.W. Starkweather, Noncooperative Relaxations, *Macromolecules* 21 (1988) 1798-1802.
- [23] W.H. Stockmayer, Dielectric dispersion in solutions of flexible polymers, *Pure Appl. Chem.* 15 (1967) 539-554.
- [24] K. Adachi, Dielectric relaxation in polymer solutions, *Dielectr. Spectrosc. Polym. Mater. Appl.* (1997) 261-282.
- [25] Emmert S., Wolf M., Gulich R., Krohns, S., Kastner S., Lunkenheimer P.; Loidl, A. Electrode Polarization Effects in Broadband Dielectric Spectroscopy, *Eur. Phys. J. B,* 83 (2011) 157-165.

- [26] Klein R. J., Zhang S., Dou S., Jones B. H., Colby R. H., Runt J., Modeling Electrode Polarization in Dielectric Spectroscopy: Ion Mobility and Mobile Ion Concentration of Single-Ion Polymer Electrolytes, *J. Chem. Phys.* 124 (2006) 14.
- [27] B.C. Smith, *Fundamentals of Fourier transform infrared spectroscopy*, CRC press, 2011.
- [28] M. Farrokhsara, F. Dorosti, New high permeable polysulfone/ionic liquid membrane for gas separation, *Chinese J. Chem. Eng.* 28 (2020) 2301-2311.
- [29] F. Denisa, A. Ficaï, G. Voicu, B.S. Vasile, C. Guran, E. Andronescu, Polysulfone based membranes with desired pores characteristics, *Mater. Plast.* 47 (2010) 24-27.
- [30] B. Tylkowski, F. Carosio, J. Castañeda, J. Alongi, R. Garcia-Valls, G. Malucelli, M. Giamberini, Permeation behavior of polysulfone membranes modified by fully organic layer-by-layer assemblies, *Ind. Eng. Chem. Res.* 52 (2013) 16406-16413.
- [31] S. Bouchareb, R. Doufnoune, F. Riahi, H. Cherif-Silini, L. Belbahri, High performance of polysulfone/graphene oxide-silver nanocomposites with excellent antibacterial capability for medical applications, *Mater. Today Commun.* 27 (2021) 102297.
- [32] A. Bhattacharya, M. Saxena, S. Sharma, Recycling of Polysulfone: Study Properties of Membranes, *Int. J. Membr. Sci. Technol.* 2 (2015) 3946.
- [33] A. Zare, L. Perna, A. Nogalska, V. Ambrogi, P. Cerruti, B. Tylkowski, R. Garcia-Valls, M. Giamberini, Polymer Blends for Improved CO₂ Capture Membranes, *Polymers (Basel)* 11 (2019) 1662-1677.
- [34] T. Hirata, K.E. Werner, Thermal analysis of cellulose treated with boric acid or ammonium phosphate in varied oxygen atmospheres, *J. Appl. Polym. Sci.* 33 (1987) 1533-1556.

-
- [35] E.S. Freeman, B. Carroll, The application of thermoanalytical techniques to reaction kinetics: the thermogravimetric evaluation of the kinetics of the decomposition of calcium oxalate monohydrate, *J. Phys. Chem.* 62 (1958) 394-397.
- [36] H.L. Friedman, Kinetics of thermal degradation of charforming plastics from thermogravimetry. Application to a phenolic plastic, in: *J. Polym. Sci. Part C Polym. Symp.*, Wiley Online Library, 1964: pp. 183-195.
- [37] W.L. Chang, Decomposition behavior of polyurethanes via mathematical simulation, *J. Appl. Polym. Sci.* 53 (1994) 1759-1769.
- [38] L. Reich, D.W. Levi, Thermal stability indices for polymeric materials based on energy considerations, *Die Makromol. Chemie Macromol. Chem. Phys.* 66 (1963) 102-113.
- [39] A. Broido, A simple, sensitive graphical method of treating thermogravimetric analysis data, *J. Polym. Sci. Part A2 Polym. Phys.* 7 (1969) 1761-1773.
- [40] J.H. Flynn, L.A. Wall, A quick, direct method for the determination of activation energy from thermogravimetric data, *J. Polym. Sci. Part B Polym. Lett.* 4 (1966) 323-328.
- [41] T. Ozawa, A new method of analyzing thermogravimetric data, *Bull. Chem. Soc. Jpn.* 38 (1965) 1881-1886.
- [42] B. Wunderlich, *Thermal analysis*, Elsevier, 2012.
- [43] H. Wang, X.-Z. Yuan, H. Li, *PEM fuel cell diagnostic tools*, CRC press, 2011.
- [44] Scribner Associates, *Electrochemical impedance spectroscopy (EIS): a powerful and cost-effective tool for fuel cell diagnostics*, 1990.

Part II

Results & Discussion

Chapter 4

Membranes based on block copolymers

In this chapter a block copolymer is studied. The microstructure has been fine-tuned for their suitability for fuel cell applications. Accordingly, a process of sulfonation, UV photocrosslinking and hybridization are applied to the samples. The purpose of Chapter 4 is twofold. Firstly, to understand the restrictions on the segmental mobility at low and high scale caused by both photocrosslinking, and subsequent sulfonation, which is basic to provide an approach to ionic diffusivities. Secondly, to understand how the infiltration time (hybridization process) affects the thermal and mechanical properties, together with the dielectric spectra, and the proton conductivity.

4.1 Introduction

Block copolymers (BCPs) are usually described as a linear sequence of monomeric units where at least one feature, either constitutional or configurational, is dissimilar from the neighbouring portions [1]. BCPs formed by two monomers A and B might display several architectures, as for instance diblock (AB), triblock (ABA), pentablock (ABABA), multiblock or segmented copolymers $(AB)_n$, and star diblocks $(AB)_nX$. When a third monomer (C) is included, linear ABC, ACB, and BAC triblocks, and also three-armed stars configurations can be formed [2].

An intriguing class of macromolecules is constituted by BCPs that are formed by two or more chemically different homopolymers that are covalently linked. This class of BCPs are popular in numerous applications and are used as, for instance, thermoplastic elastomers, adhesives and stimuli-responsive materials. Furthermore, as shown in Figure 4.1, BCPs are known to self-assemble into various periodic nanoscale structures (such as spheres, cylinders and lamellae) since the different polymer segments show an inherent thermodynamic immiscibility [3].

The origin of this behaviour has been extensively studied, and is due to an unfavourable mixing enthalpy combined with a sufficiently small de-mixing entropic penalty. This allows to generate highly ordered, three-dimensional, structural hierarchies with characteristic feature sizes. Thus, as self-organizing materials through a bottom-up approach is formed. Consequently, the multiple applications of BCPs result from the microphase separation control over the nanometre length scale and morphology, not only from the control of functionality as well as the traditional advantages of polymeric materials [4].

A main feature of BCPs is phase separation, which is originated by the existing repulsion between chemically and thermodynamically incompatible blocks. Accordingly, at the macroscopic scale there is structural arrangement of BCP that is known as self-assembly phenomenon [5]. It is responsible for the creation of

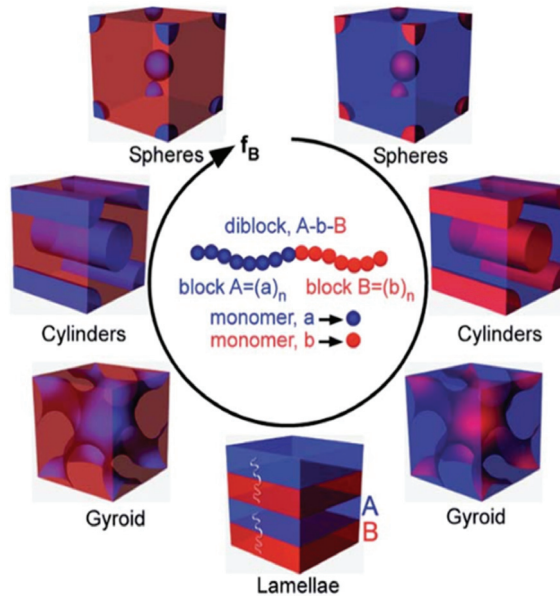


Figure 4.1: Schematic illustration of microstructures of diblock A-b-B on increasing the volume fraction of the B block. Source: [3].

new boundaries between blocks and can result in various assembly structures, as already shown in Figure 4.1. To analyse microphase separation between the blocks in BCPs, the significant parameters are the following:

- *The relative volume fraction (f) of each block.* It is used to characterize the microscopic composition of the BCP.
- *The Flory-Huggins parameter (χ).* It is used to characterize the interaction between the blocks and it is inversely proportional to the temperature change [6,7].
- *The total degree of polymerization (N).*

Among them, the parameter playing a paramount role in the separation state of BCP is χ_N , which is ascribed to the phase separation strength [8]. Subsequently,

increasing the temperature, or decreasing χ_N , results in a gradual decrease of the incompatibility between the blocks [9].

However, often these nonclassical blocks are joined by complex interactions, of inter- and intramolecular origin, that confront the general assumption that the Flory-Huggins χ parameter approach can capture segment-segment interactions in an effective manner. This problem is worsen when charged species are present. Moreover, large effective χ parameters may be exhibited by these chemically diverse block polymers, and thus, require very low molecular weights to access the order-disorder transition. This raises several questions, that end up with the introduction of new theories like the thermal up-and-down effect and mean-field theory. Accordingly, researchers have found that the improved self-consistent field theory (SCFT) can calculate the BCP phase behaviour more accurately [10,11].

The importance of block copolymers is built on two already recognised features: access to exquisite control over self-assembly, and advanced, non-scalar application of the resulting nanostructures. BCPs are outstanding self-assembling materials because of the following motives [12]:

- *Precise control over length scale:* Domain dimensions that can be varied to a great extent. For instance, BCPs microstructures have domain dimensions around 5 to 50 nm simply by varying parameters such as molecular weight, monomer structure, and temperature. This range can be extended beyond 100 nm if dilution with other polymers or solvents is utilised.
- *Control over morphology:* Different equilibrium symmetries, i.e. lamellae (L), hexagonal cylinders (C), bicontinuous gyroid (G), and body-centered cubic arrays of spherical micelles (S^{bcc}), are exhibited by pure diblock copolymers. Accordingly, composition dictates the morphology in the bulk state. Nonetheless, the equilibrium structure can also be adjusted by changes in the temperature, and diluents. In the case of triblocks (ABC) a larger variety of phases can be achieved.

- *Control over domain functionality and properties:* There is a complete freedom in the selection of the polymer for each block due to the recent advances in the fabrication techniques. Indeed, BCPs with tailored made properties can be fabricated for advanced applications.
- *Quantitative prediction of equilibrium structures:* Accurate calculations of free energies and composition profiles for the various ordered states are provided by the self-consistent mean-field (SCMF) theory. Its success is based on the relative weakness of the thermodynamic interactions ($\chi \ll 1$) combined with the large number of interchain contacts ($\approx N$.)
- *Retention of the traditional advantages of polymeric materials:* BCPs possess the same good features that polymers have, such as cost effectiveness, flexibility, toughness, low density, optical clarity, permeability, control, etc.

Modern research concerning BCPs focuses on the following topics: the application of advanced methods from a theoretical and computational perspective; the development of new synthesis routes and microstructures; and its ability to self-assemble. The former is controlled by the length scale, the morphology, domain functionality as well as the properties, in combination with the possibility to quantitatively predict the equilibrium structures while still maintaining the known benefits of polymers [12].

For instance, an example of a novel application of BCPs, Lessard et al developed a block vitrimer in an effort to achieve higher-order, nanoscale control over associative cross-link exchange and flow. Results suggested that control over chain topology in block vitrimers can be used to tune viscoelastic properties, and in that way enhanced creep resistance was achieved. Furthermore, block vitrimers are different from their statistical counterparts in the way that the resistance to macroscopic deformation arises from a microphase-separated structure. Thus, it displays the possibility to control the topology over the viscoelastic flow [13].

Regarding PEMFCs and DMFCs, many studies have been devoted to developing new membrane materials presenting a suitable dimensional stability, high ionic conductivity and low cost for a significant volume production, among them, block copolymer ionomers based on styrenic thermoplastic elastomers containing sulfonic acid groups. The introduction of ionic groups into the polystyrene blocks causes significant changes in many physical properties, not only the emergence of ionic conductivity but also changes in hydrophilicity, mechanical strength and glass transition temperature which are not detected in their non-ionic counterparts.

The interest in polystyrene multiblock copolymers as polymer electrolytes for fuel cell applications is mainly due to their ability to form ion conducting channels as a consequence of their phase-separated morphology. Additionally, its sulfonation might offer more useful features such a low methanol permeability or a higher mechanical stability. SEBS (styrene-ethylene-butylene-styrene) triblock copolymer is a commercial and economical material widely studied, which is obtained by hydrogenation of the thermoplastic elastomer of styrene and butadiene, eliminating the unsaturation of the butylene chain. In Chapter 4, styrene-ethylene-butylene-styrene (SEBS) has been the block copolymer of choice since it is a tough and elastic thermoplastic elastomer. In addition, its facility to be processed together with its high thermal stability and good levels of weathering and UV resistance make it a good candidate for its application as a polymer electrolyte for fuel cells [14].

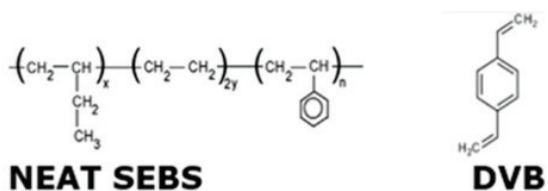
Contrarily, self-assembled BCPs can lead to well-defined nanostructures where the morphology and domain size are tunable on the nanoscopic length scale. Sulfonated BCPs are interesting materials to be used as PEM provided the high potential for highly ordered morphologies due to the combination of ionic and non-ionic domains, and therefore, transport properties can be fine-tuned [15]. The sulfonation process is done in order to increment the proton conductivity of the resultant membranes. Indeed, high degrees of sulfonation induce microphase separation into hydrophobic and hydrophilic domains, which creates

ionic channels that enhance proton transport. However, the drawback is that high concentrations of sulfonic groups produce swelling, which in turn reduces the mechanical strength of the membrane leading to a downgrade in the overall performance [14,16]

Photocrosslinking and post-sulfonation of membranes based on mixtures of SEBS and divinylbenzene (DVB), which chemical structure is shown in Figure 4.2, were successfully used to overcome these stability limitations. It was found that both the degree of photoirradiation and post-sulfonation modified the sizes and geometries of the separated nanostructure, and subsequently, the mobility of the molecular chains, which affected the proton conductivity and the behaviour of these membranes as electrolytes in the PEMFC.

One of the DMFC's most critical points is the methanol crossover through the polymer electrolyte. The transport of methanol from anode to cathode through the membrane severely reduces the cell efficiency and makes DMFCs less competitive. New composite materials consisting of a polymeric matrix and inorganic fillers are being studied to overcome these issues. Indeed, fillers such as silica, zirconium phosphate, titanium dioxide, montmorillonite, or single-walled carbon nanotubes are being used to obtain efficiencies closer to the pristine membranes with higher chemical, thermal and mechanical stability [18-40].

Hybridization, as shown in Figure 4.3, is proposed as a solution to increase thermal and mechanical stability so that the degradation of the membrane is reduced and an improved performance is obtained. Hybrid membranes consists of a polymeric matrix together with an inorganic filler. In the present work, $SiO_2 - P_2O_5 - ZrO_2$ is chosen for several main reasons. Firstly, because of its nanoporosity that enables water absorption at high temperatures, with the subsequent increase in water retention; secondly, because it has M-OH groups (with M being P, Si or Zr) that on the one hand strengthen hydrophilicity and, on the other hand, help proton transport acting as hopping sites. Moreover, the mechanical stability may be strengthened by the silicate network that, in combination with the Zr-O bonds present in the resultant oxocluster, also assists



SULFONATED AND PHOTO-IRRADIATED SEBS

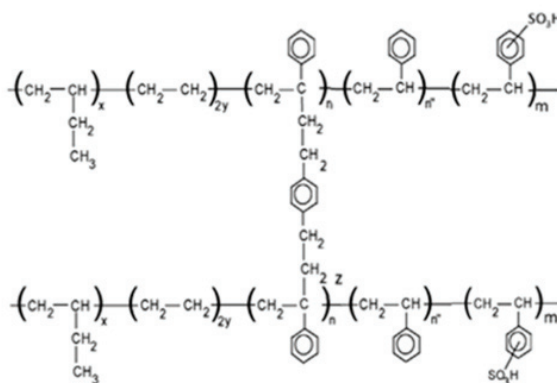


Figure 4.2: Chemical structure of the photocrosslinked and post-sulfonated SEBS-DVB membranes. Source: [17].

in improving the chemical stability and the overall durability. The membranes have been prepared by direct infiltration of the inorganic precursor into the polymeric matrix [22].

The results presented in Chapter 4 allow for the establishment of the operating relationships, and for the understanding on how parameters such as the concentration of the inorganic precursor or the synthesis route are beneficial in order to design PEM applicable for low temperature fuel cells

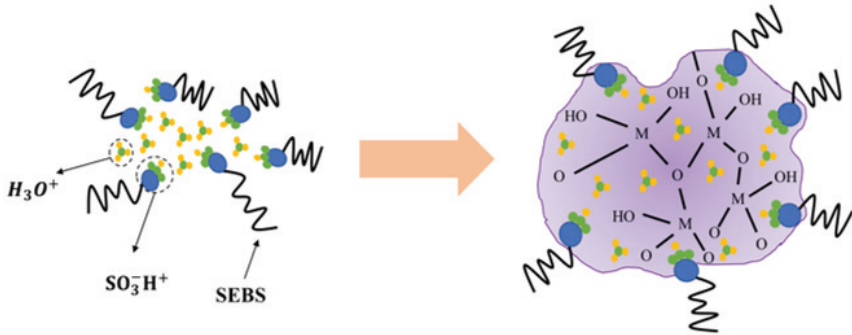


Figure 4.3: Synthetic route of the hybrid sulfonated SEBS membranes. Source: [41].

4.2 Materials

4.2.1 Photocrosslinked and post-sulfonated SEBS-DVB membranes

The starting material styrene-ethylene-butylene-styrene (SEBS) block copolymer used in this study was Calprene CH-6120 (Repsol) with 32wt.% by weight of styrene units. Other chemicals products were divinylbenzene (DVB, Sigma-Aldrich) as photocrosslinkable monomer; Irgacure 651 (IRG 651-2,2-dimethoxy-1,2-diphenylethan-1-one) (Ciba) as a photoinitiator; trimethylsilyl chlorosulfonate (99%, Sigma - Aldrich) as a sulfonation reagent; Chloroform (CHCl_3 , Scharlau); 1,2-dichloroethane (DCE, Scharlau) as solvents; all of them were employed as received without any further treatment of purification. The membranes were prepared using doctor Blade from chloroform solutions by mixing SEBS with 25% by weight of photocrosslinkable divinylbenzene (DVB) and 2% of photoinitiator based on the weight of DVB. After drying, the membranes were UV irradiated (Hamamatsu L8868) for 15 and 30 minutes. The sulfonation was performed using trimethylsilyl chlorosulfonate solutions in DCE (0.3 M 2 hours and 0.5 M 3 hours). The processes of membrane preparation, photocrosslinking and post-sulfonation were described in more detail elsewhere. In Table 4.1 shows the membrane nomenclature used according to the different experimental conditions utilised during the synthesis process.

Table 4.1: Nomenclature, composition, and UV irradiation time of the photocrosslinked and post-sulfonated SEBS-DVB membranes.

Label	Sulfonation	UV (min)
SEBS	-	-
SEBS-25DVB	-	-
SEBS-25DVB-15I	-	-
SEBS-25DVB-15I-S1	0.3 M for 2 h	15
SEBS-25DVB-15I-S2	0.5 M for 3 h	-
SEBS-25DVB-30I	-	-
SEBS-25DVB-30I-S1	0.3 M for 2 h	30
SEBS-25DVB-30I-S2	0.5 M for 3 h	-

4.2.2 Hybrid sulfonated SEBS membranes

The hybrid polymer membranes prepared from SEBS (Dynasol, Calprene CH-6120) containing 32 wt% of styrene units. The membranes were cast from chloroform solutions employing Doctor Blade technique (BYK Instruments). Regarding the sulfonation, the process was performed by immersing the membranes in a trimethylsilyl chlorosulfonate (TMSCl, Sigma-Aldrich) solution in 1,2-dichloroethane (DCE, Scharlau) with a molar concentration of 0.3 for 2 hours. Concerning the infiltration process, sulfonated SEBS membranes were swelled in H_2SO_4 1N at 353K for 2 hours and then immersed in the $40SiO_2 - 40P_2O_5 - 20ZrO_2$ sol solution at 353K for 5, 10, 20, and 40 minutes, respectively. Then they were thermally treated to perform the inorganic polycondensation reaction at 323K for 1 hour and 393K for 2 hours. Finally, the membranes were cleaned with ethanol at 353K for 2 hours for the last process step. Afterward,

the membranes were dried for another hour at the same temperature. More detailed preparation of these hybrid membranes was described elsewhere [36].

The labelling of the hybrid sulfonated membranes is done as follows. The neat and sulfonated SEBS membranes are labelled as SEBS and sSEBS, respectively. Concerning the hybrid membranes, provided that the infiltration time is the main parameter controlling their morphology, the samples are labelled as sSEBS-Zr5, sSEBS-Zr10, sSEBS-Zr20 and sSEBS-Zr40 for an infiltration time of 5, 10, 20 and 40 minutes, respectively.

4.2.3 Experimental methodology

Fourier Transformed Infrared Spectroscopy (FTIR)

The chemical structure was assessed through Fourier Transform Infrared Spectroscopy (FTIR). Analyses were carried out in a Thermo Nicolet 5700 infrared spectrometer with an attenuated total reflectance accessory (ATR). The spectra were collected from 4000 to 400 cm^{-1} at a resolution of 4 cm^{-1} along 64 scans. The spectra of three different locations of the sample were averaged. Backgrounds were collected, and results were processed through the Omnic® Software.

Differential Scanning Calorimetry (DSC)

Aluminium capsules were filled with the samples, between 2 and 4 mg, and sealed. Then, they were subjected to a heating/cooling program with a rate of 5 $K \cdot min^{-1}$ over the 263K to 473K temperature range under an inert atmosphere with a flow rate of 50 $mL \cdot min^{-1}$ of nitrogen.

Thermogravimetric Analysis (TGA)

The thermogravimetric analysis (TGA) was carried out with a Mettler Toledo TGA/STDA 851e setup. Samples with a mass between 2 and 5 mg were placed into 70 μL alumina capsules. An empty capsule was used as a blank to take the reference baseline. The analyses were performed with a heating rate of 30 $\text{K} \cdot \text{min}^{-1}$ over the 303K to 1073K temperature range using an oxidative atmosphere with a flux of 50 $\text{mL} \cdot \text{min}^{-1}$ of oxygen.

Dielectric Thermal Analysis (DETA)

The impedance measurements were conducted using a Novocontrol Broadband Dielectric Impedance Spectrometer (BDIS), connected to a Novocontrol Alfa-A Frequency Response Analyzer. The measurements were run in the frequency range of 10^{-1} to 10^{-7} Hz, at the temperature range 123K to 473K. The measurement were obtained under isothermal conditions by increasing in steps by 10K. The sample electrode assembly (SEA) consisted of two stainless steel electrodes filled with the sample. Consequently, the resulting SEA was directly placed in the cell.

4.3 Results

4.3.1 Analysis of the dielectric spectra of SEBS membrane

The dielectric spectra was plotted in terms or the real (ϵ') and imaginary (ϵ'') parts of the complex dielectric permittivity (ϵ^*), $\tan \delta$, and the imaginary part of the electric modulus (M'') in Figures 4.4 - 4.5.

In Figure 4.6A the macromolecular origin of the dielectric relaxations is assessed through the Eyring model as derived by Starkweather. As observed, the apparent activation energy (E_a) value of the β dielectric process lies close to the zero-entropy line, and therefore, initially the macromolecular origin of

this dielectric process cannot be assigned to cooperative motions. Instead, non-cooperative molecular motions must be involved. Contrarily, the α_{EB} and α_{PS} dielectric processes exhibit E_a values that lie far away from the zero-entropy line, and therefore, their molecular origin can be assigned to cooperative motions.

In Figure 4.6B shows different relaxation zones: a weak relaxation zone at low temperature labelled as β relaxation that may be related to the reorientation of small angles in relation to the longitudinal axis of the polymer in corresponding poly(ethylene-butylene) (PEB) block [21].

At higher temperatures, two additional relaxations are observed, which may be associated to both components of the block copolymer: ethylene-butylene and styrene. These relaxations are called: α_{EB} and α_{PS} , respectively in an increasing order of temperature.

In accordance with previous works [20,21], α_{EB} y α_{PS} relaxations can be attributed to the glass transition because the temperature peaks of each relaxation are in agreement with the DSC measurements to the poly(ethylene-butylene) (PEB) and poly(styrene) (PS) blocks, respectively [17].

In Figure 4.7 the isothermal curves of the module of the complex conductivity ($|\sigma|$) for the complete temperature range are displayed.

To determine the proton conductivity, the phase angle and the absolute value of the serial impedance (Z_s) are needed. Thus, both parameters are shown in Figure 4.8.

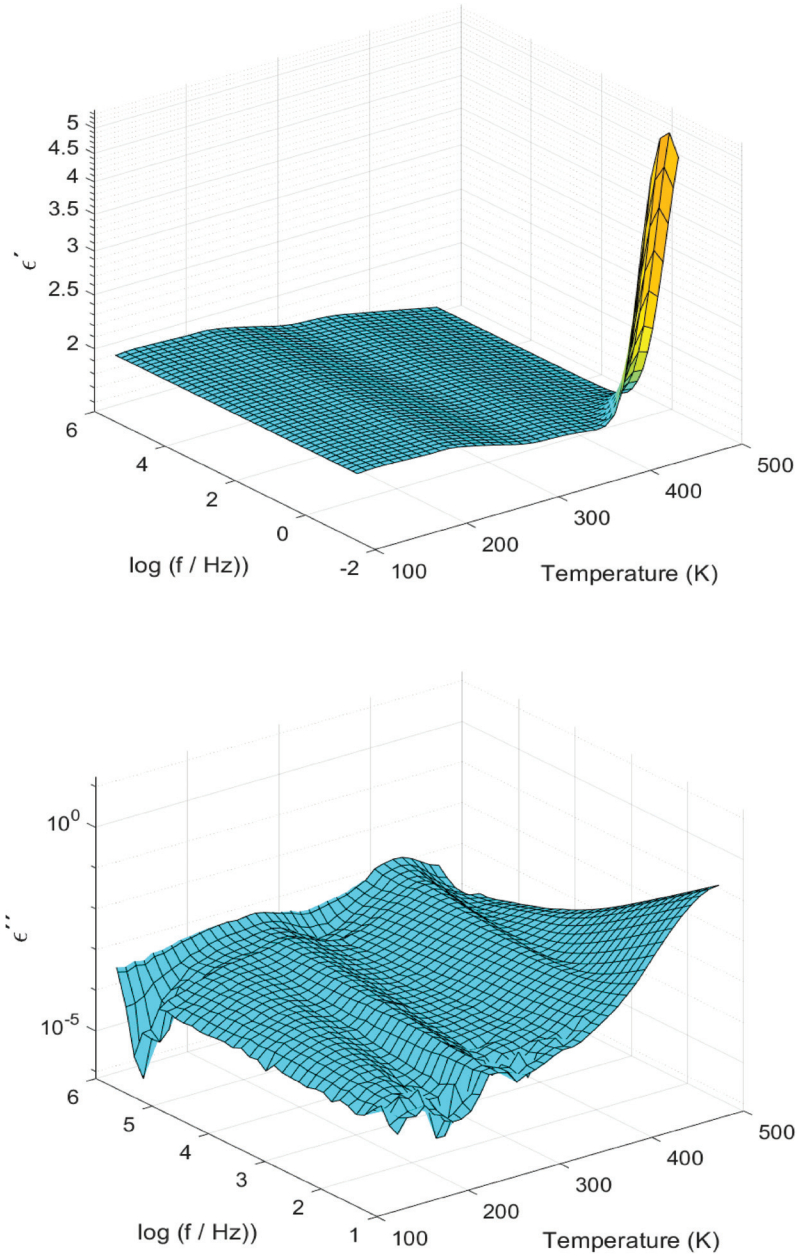


Figure 4.4: 3D plot of the real (ϵ') and imaginary part (ϵ'') parts of the complex permittivity (ϵ^*) of the SEBS membrane.

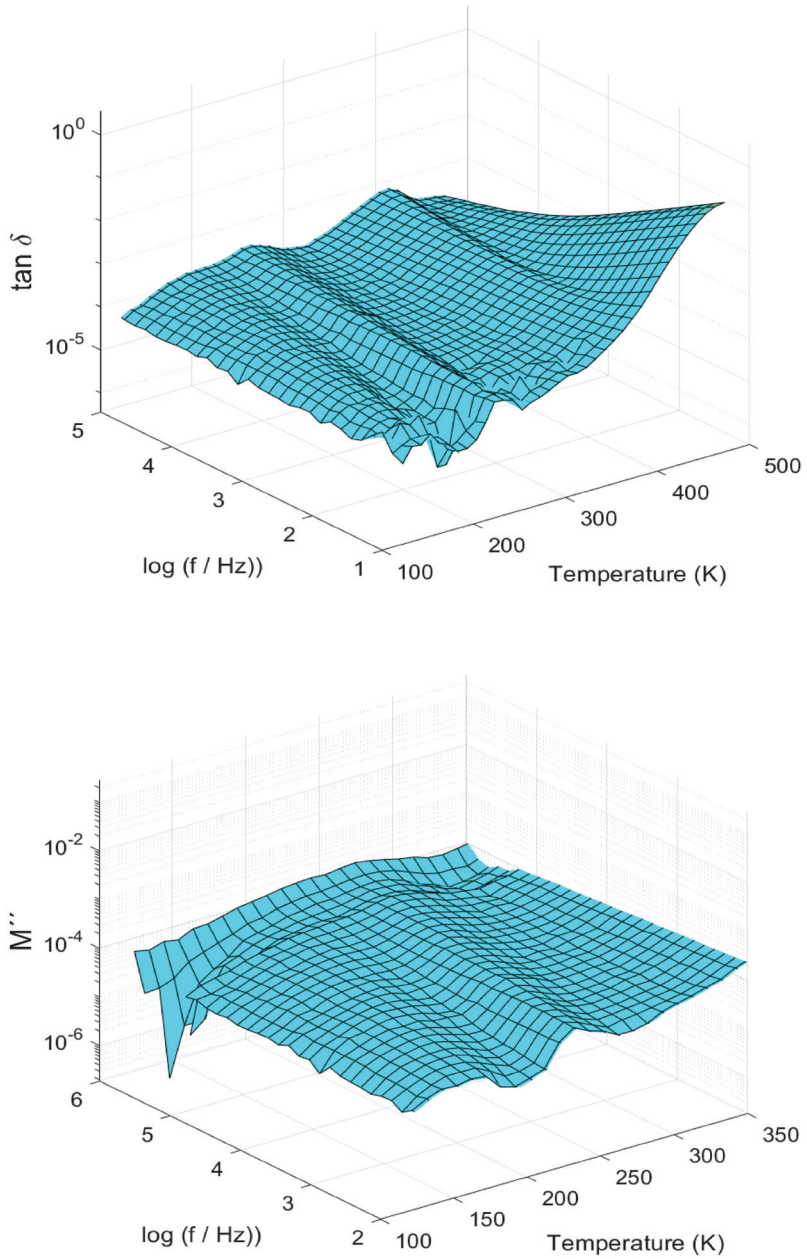


Figure 4.5: 3D plot of $\tan \delta$ and of the imaginary part (M'') of the complex electric modulus (M^*) of the SEBS membrane.

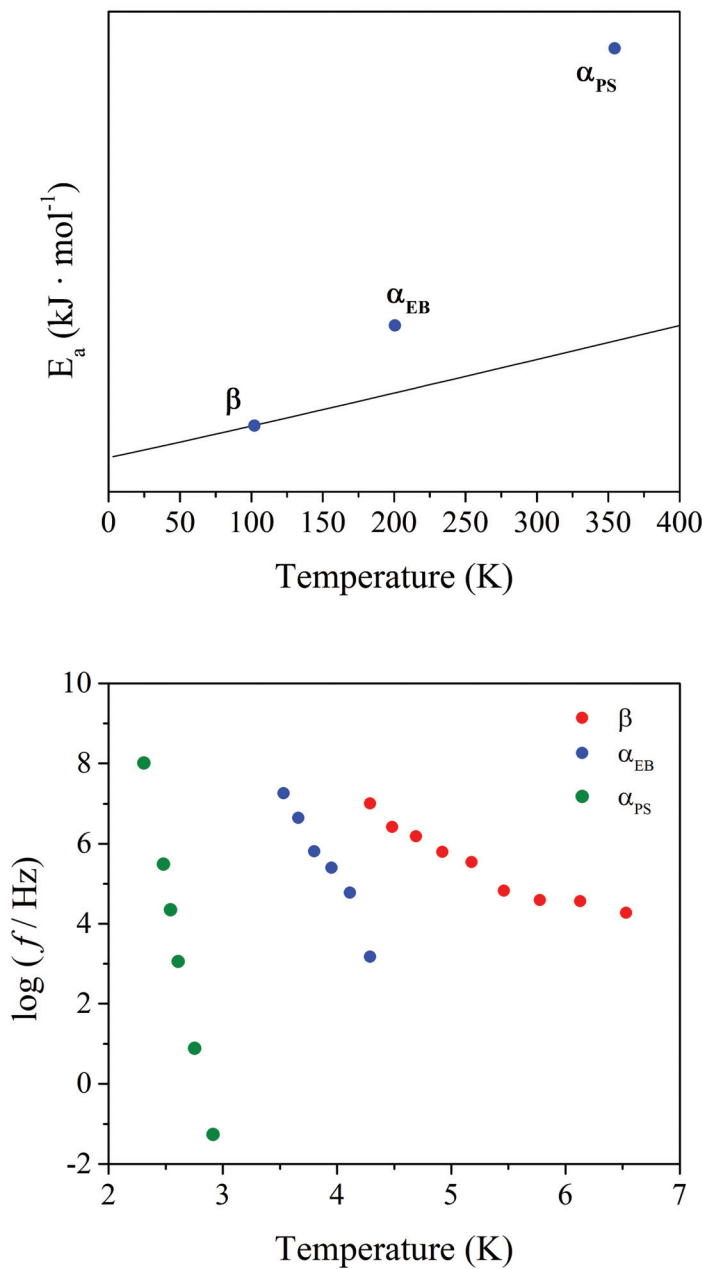


Figure 4.6: (Top) Eyring plot and (Bottom) Arrhenius plot of the SEBS membrane.

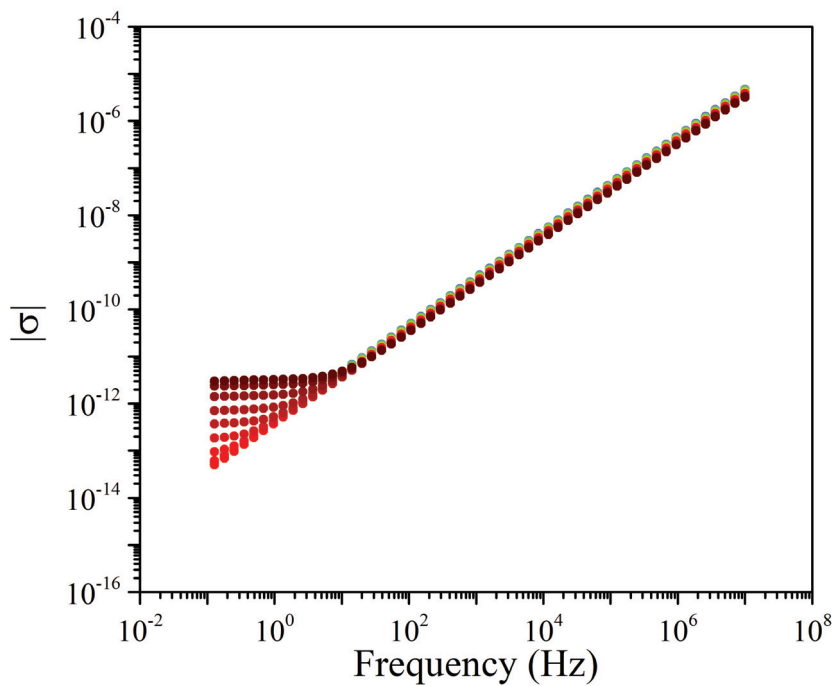


Figure 4.7: Isothermal curves of the module of the complex conductivity ($|\sigma|$) for the SEBS membrane.

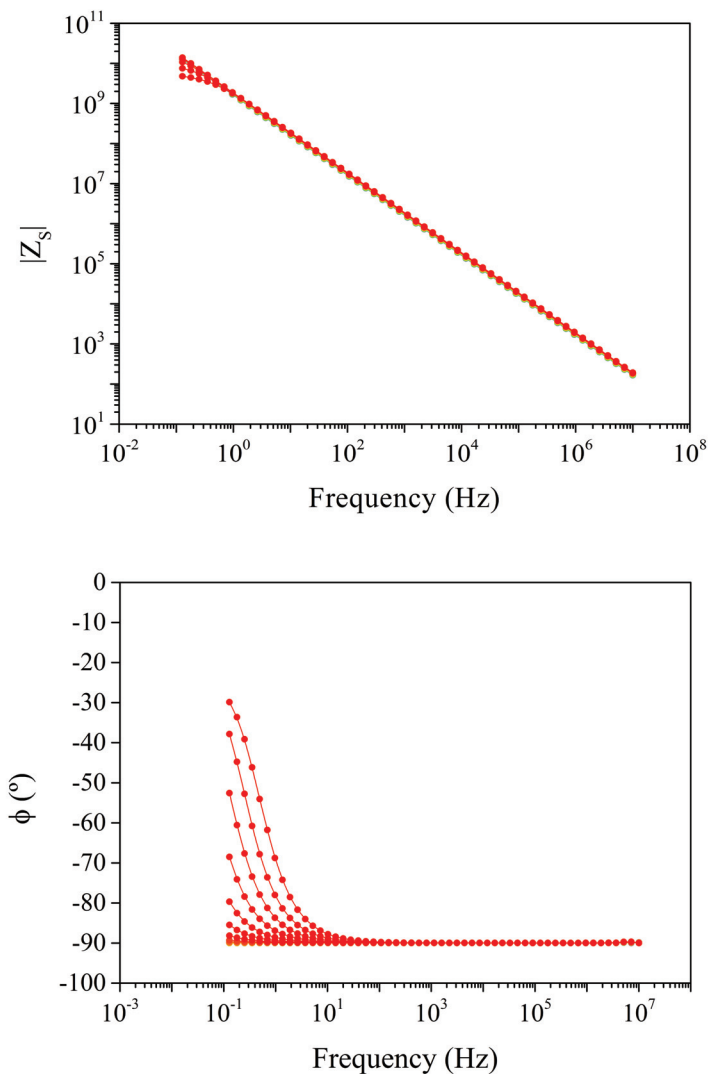


Figure 4.8: Phase angle (ϕ) and modulus of the serial impedance ($|Z_s|$) of the SEBS membrane.

4.3.2 Analysis of the dielectric spectra of SEBS-DVB membrane

The dielectric spectra was plotted in terms of the real (ϵ') and imaginary (ϵ'') parts of the complex dielectric permittivity (ϵ^*), $\tan \delta$, and the imaginary part of the electric modulus (M'') in Figures 4.9 - 4.10.

In Figure 4.11A the macromolecular origin of the dielectric relaxations is assessed through the Eyring model as derived by Starkweather.

In Figure 4.11B displays the Arrhenius plot, where the same relaxation zones (β , α_{EB} , and α_{PS}) exhibited in Figure 4.6.

In Figure 4.12 the isothermal curves of the module of the complex conductivity ($|\sigma|$) for the complete temperature range are displayed.

To determine the proton conductivity, the phase angle and the absolute value of the serial impedance (Z_s) are needed. Thus, both parameters are shown in Figure 4.13.

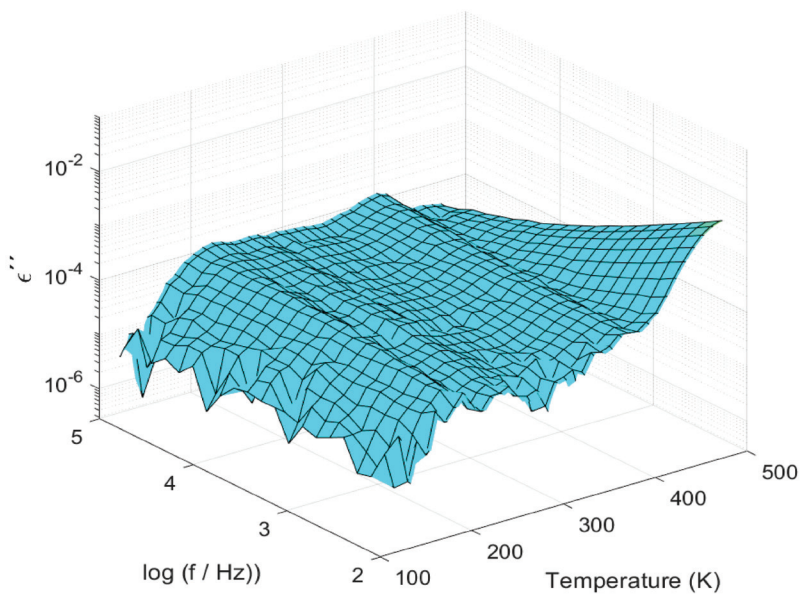
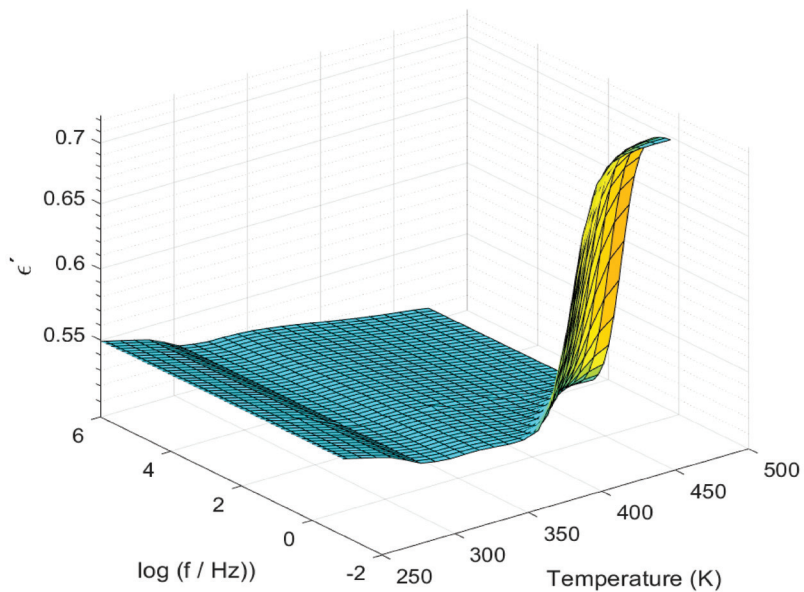


Figure 4.9: 3D plot of the real (ϵ') and imaginary part (ϵ'') parts of the complex permittivity (ϵ^*) of the SEBS-DVB membrane.

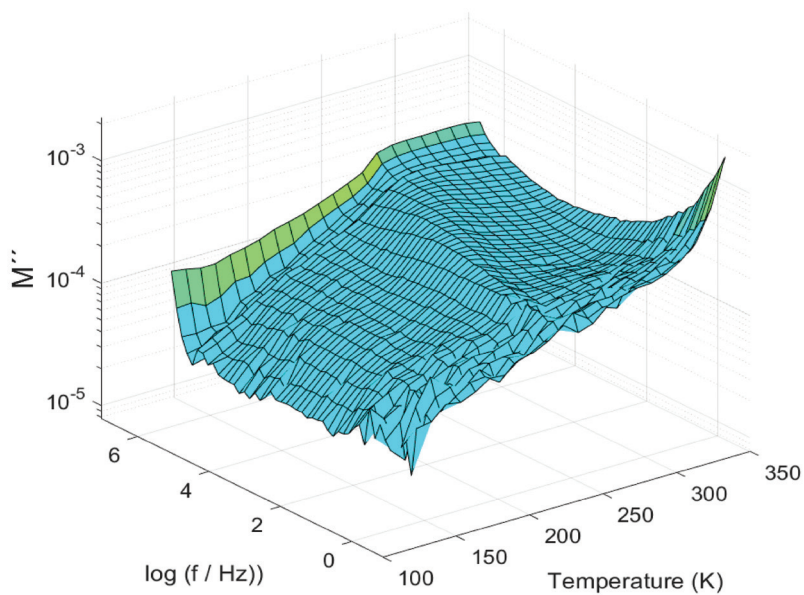
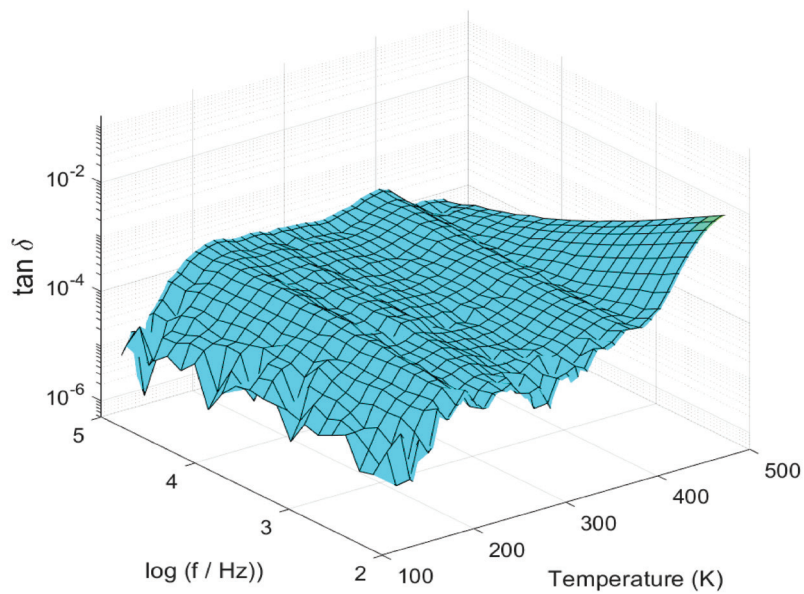


Figure 4.10: 3D plot of $\tan \delta$ and of the imaginary part (M'') of the complex electric modulus (M^*) of the SEBS-DVB membrane.

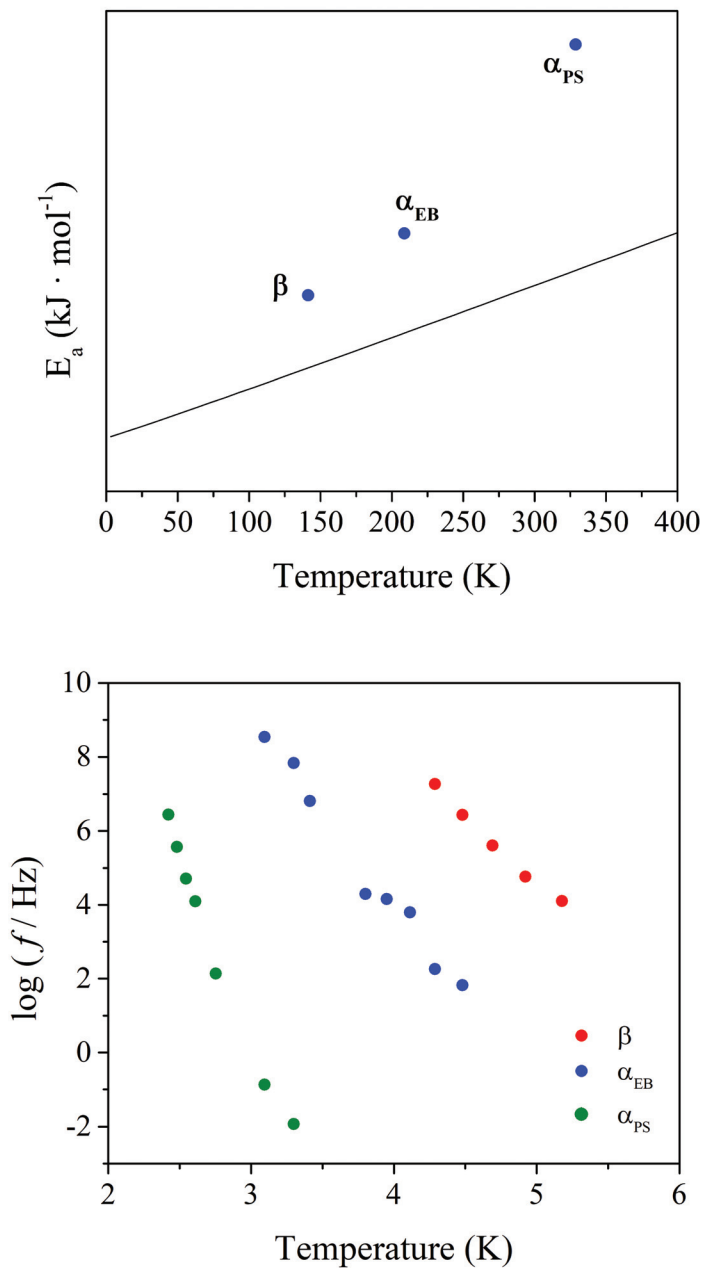


Figure 4.11: (Top) Eyring plot and (Bottom) Arrhenius plot of the SEBS-DVB membrane.

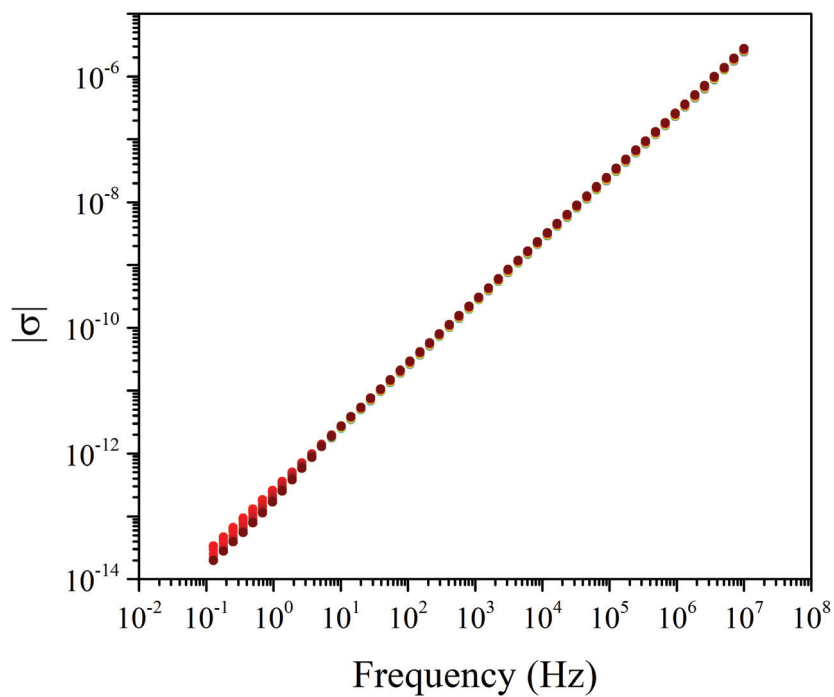


Figure 4.12: Isothermal curves of the module of the complex conductivity ($|\sigma|$) for the SEBS-DVB membrane.

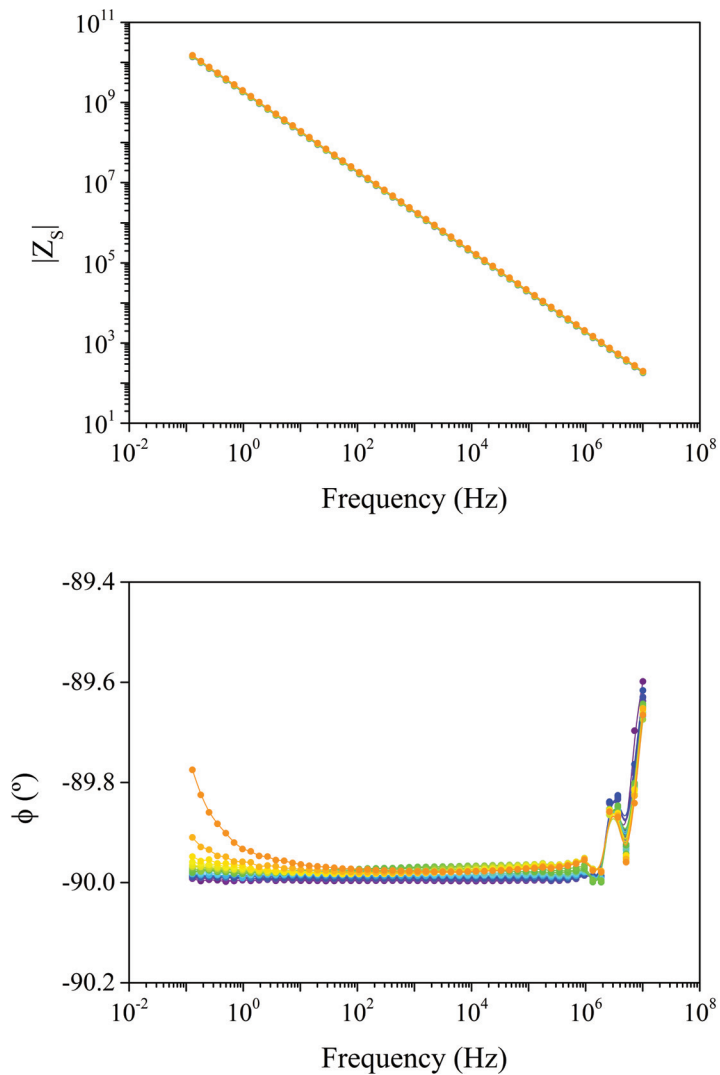


Figure 4.13: Phase angle (ϕ) and modulus of the serial impedance ($|Z_s|$) of the SEBS-DVB membrane.

4.3.3 Analysis of the dielectric spectra of SEBS-DVB-15I membrane

The dielectric spectra was plotted in terms of the real (ϵ') and imaginary (ϵ'') parts of the complex dielectric permittivity (ϵ^*), $\tan \delta$, and the imaginary part of the electric modulus (M'') in Figures 4.14 - 4.15.

In Figure 4.16A the macromolecular origin of the dielectric relaxations is assessed through the Eyring model as derived by Starkweather.

In Figure 4.16B displays the Arrhenius plot, where the same relaxation zones (β , α_{EB} , and α_{PS}) exhibited in Figure 4.6.

In Figure 4.17 the isothermal curves of the module of the complex conductivity ($|\sigma|$) for the complete temperature range are displayed.

To determine the proton conductivity, the phase angle and the absolute value of the serial impedance (Z_s) are needed. Thus, both parameters are shown in Figure 4.18.

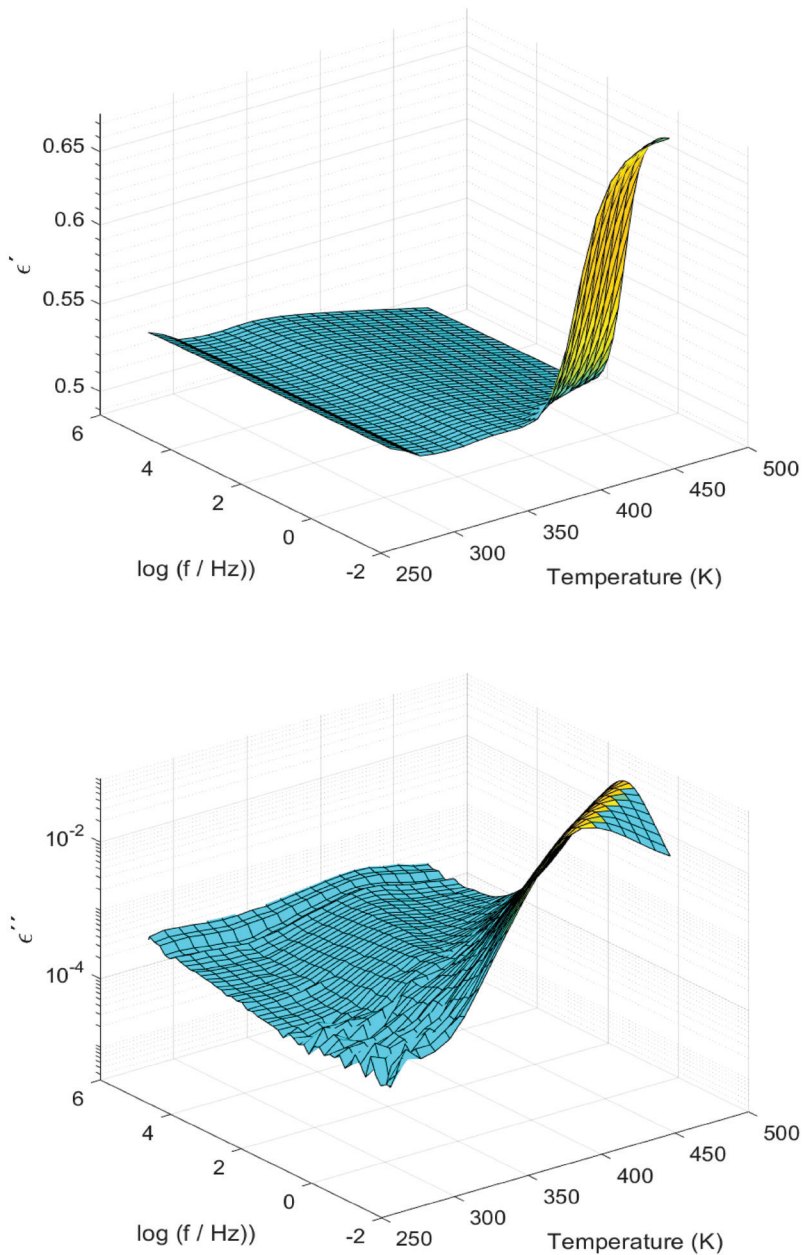


Figure 4.14: 3D plot of the real (ϵ') and imaginary part (ϵ'') parts of the complex permittivity (ϵ^*) of the SEBS-DVB-15I membrane.

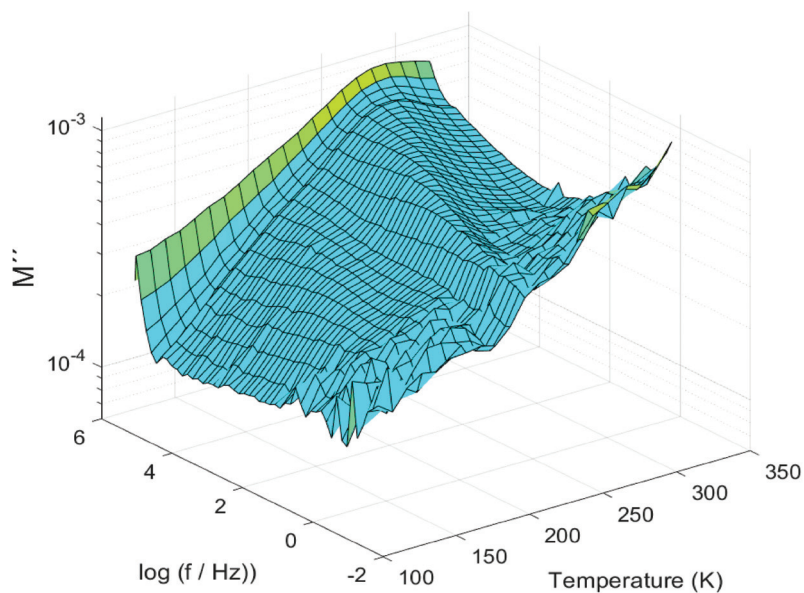
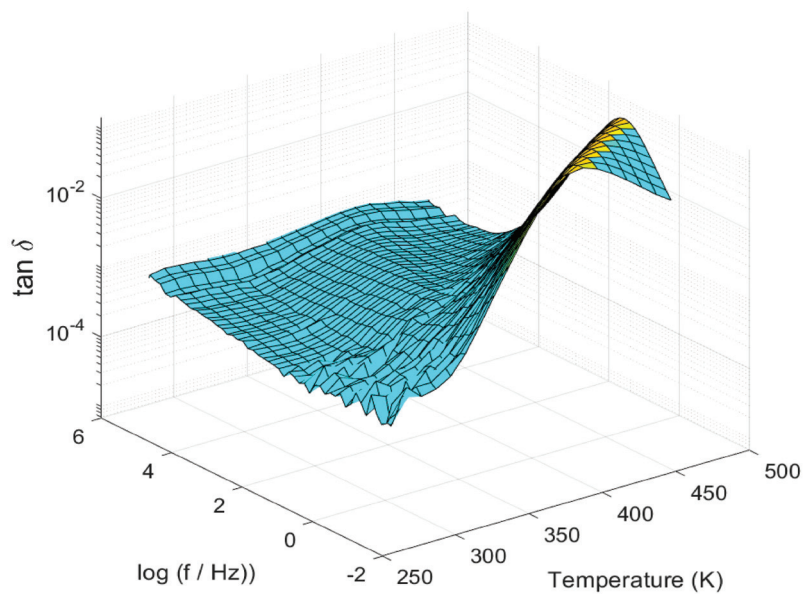


Figure 4.15: 3D plot of $\tan \delta$ and of the imaginary part (M'') of the complex electric modulus (M^*) of the SEBS-DVB-15I membrane.

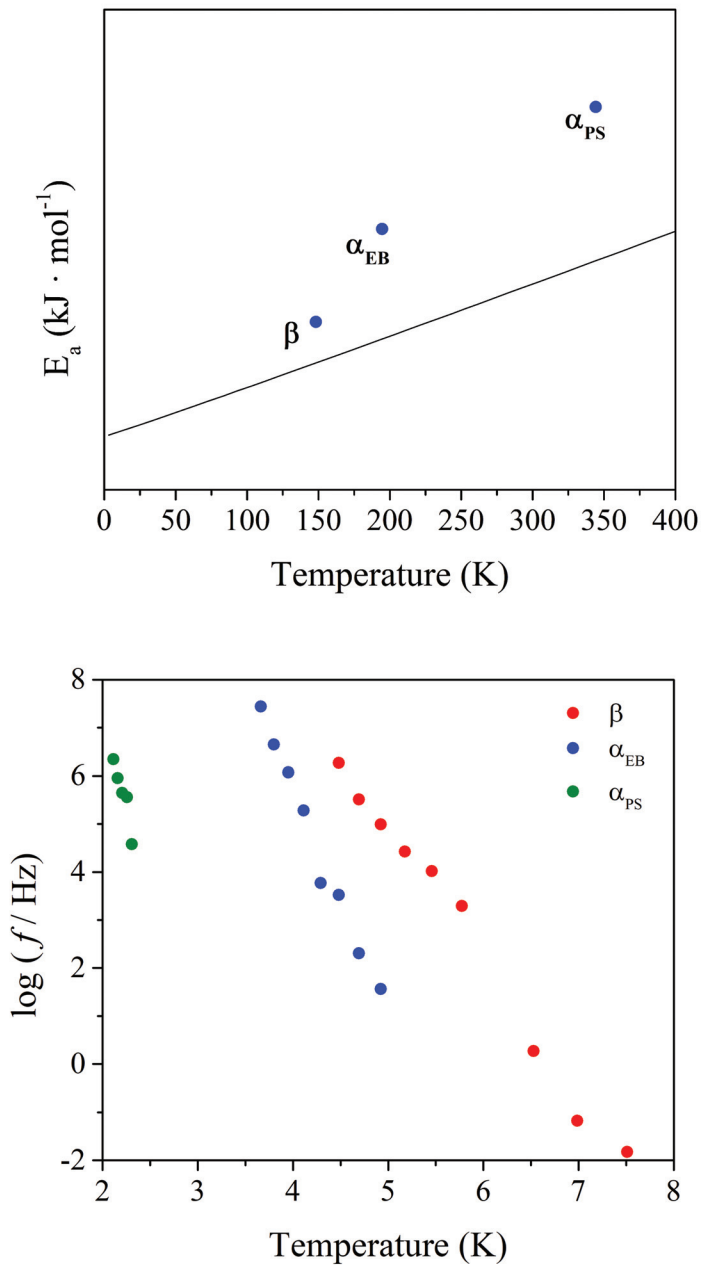


Figure 4.16: (Top) Eyring plot and (Bottom) Arrhenius plot of the SEBS-DVB-15I membrane.

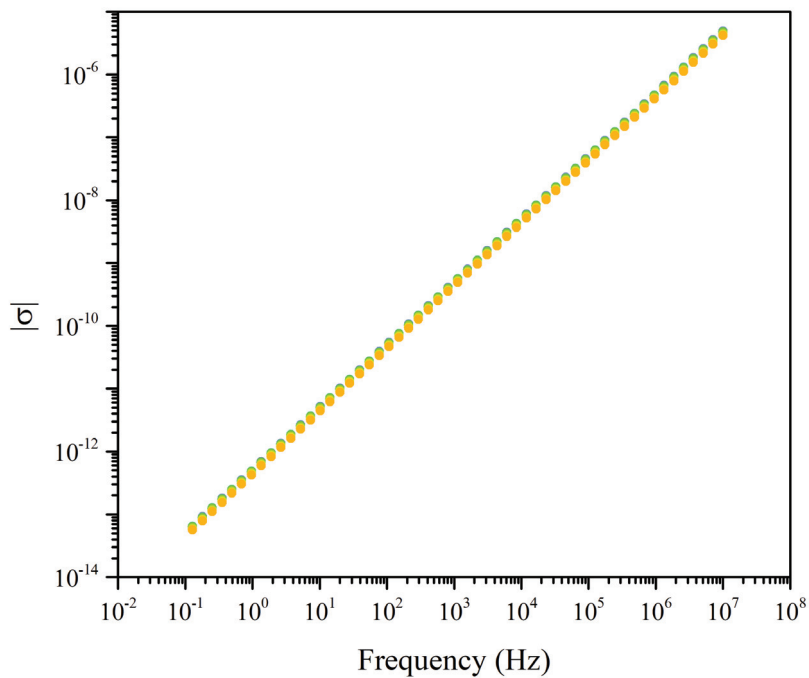


Figure 4.17: Isothermal curves of the module of the complex conductivity ($|\sigma|$) for the SEBS-DVB-15I membrane.

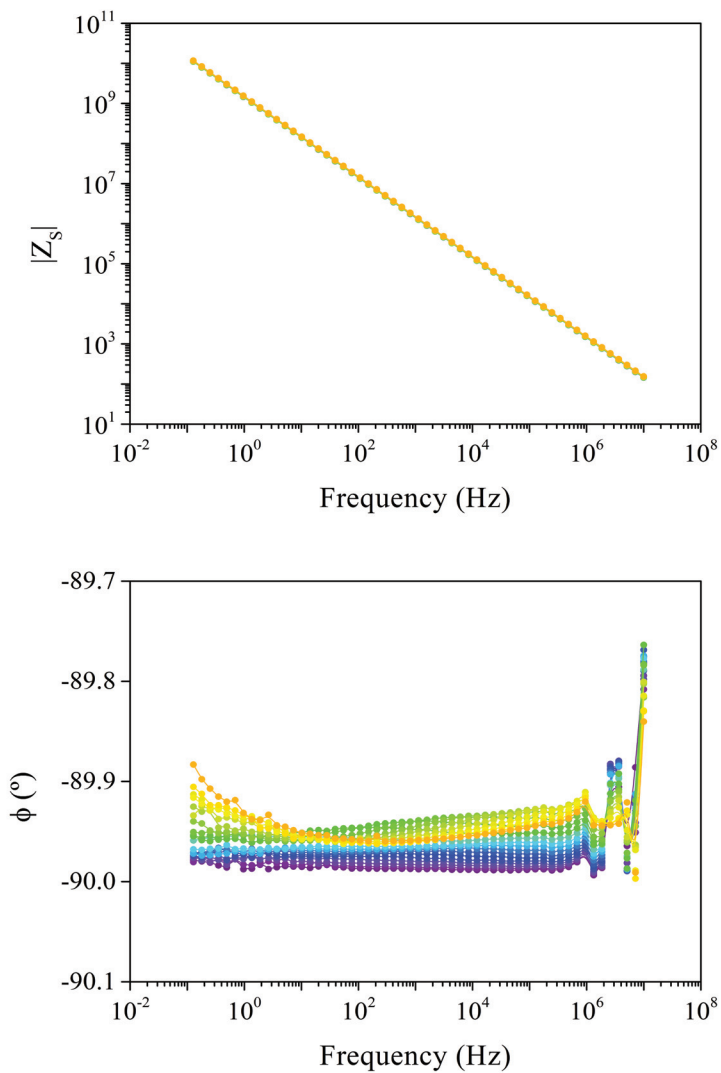


Figure 4.18: Phase angle (ϕ) and modulus of the serial impedance ($|Z_s|$) of the SEBS-DVB-15I membrane.

4.3.4 Analysis of the dielectric spectra of SEBS-DVB-15I-S1 membrane

The dielectric spectra was plotted in terms or the real (ϵ') and imaginary (ϵ'') parts of the complex dielectric permittivity (ϵ^*), $\tan \delta$, and the imaginary part of the electric modulus (M'') in Figures 4.19 - 4.20.

In Figure 4.21A the macromolecular origin of the dielectric relaxations is assessed through the Eyring model as derived by Starkweather. Unlike Figure 4.16A, the E_a value obtained for the β relaxation is higher than the one for the α_{EB} relaxation. As confirmed by the Arrhenius plot, both relaxations appear in a narrow temperature range, and therefore, a certain degree of cooperativity is registered.

In Figure 4.21B displays the Arrhenius plot, where the same relaxation zones (β , α_{EB} , and α_{PS}) exhibited in Figure 4.6.

In Figure 4.22 the isothermal curves of the module of the complex conductivity ($|\sigma|$) for the complete temperature range are displayed.

To determine the proton conductivity, the phase angle and the absolute value of the serial impedance (Z_s) are needed. Thus, both parameters are shown in Figure 4.23.

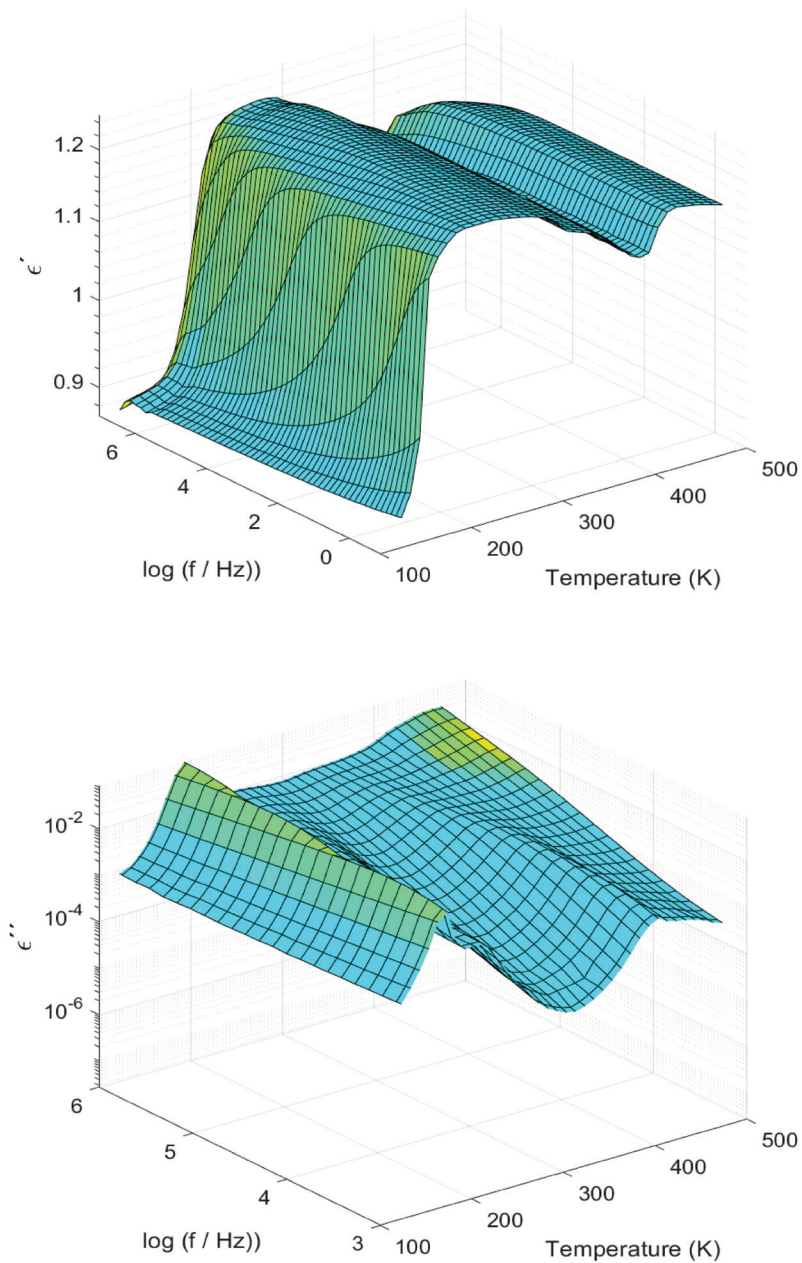


Figure 4.19: 3D plot of the real (ϵ') and imaginary part (ϵ'') parts of the complex permittivity (ϵ^*) of the SEBS-DVB-15I-S1 membrane.

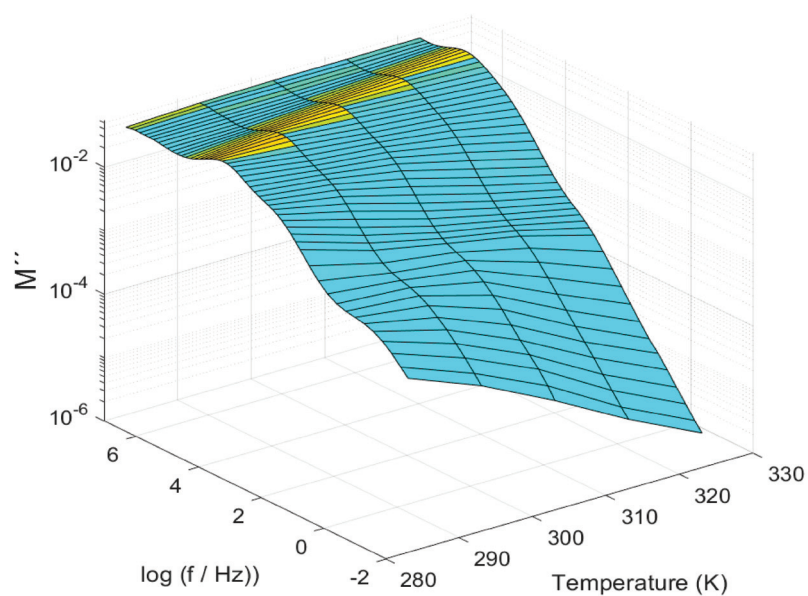
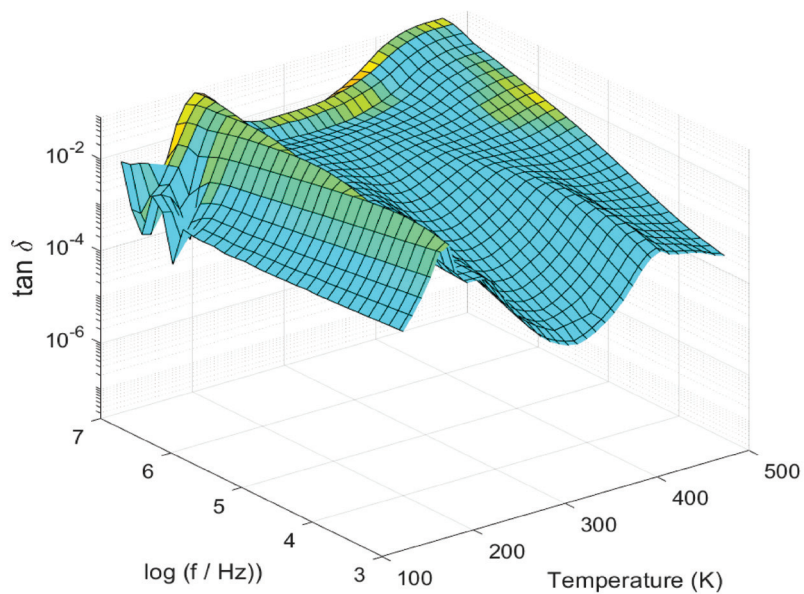


Figure 4.20: 3D plot of $\tan \delta$ and of the imaginary part (M'') of the complex electric modulus (M^*) of the SEBS-DVB-15I-S1 membrane.

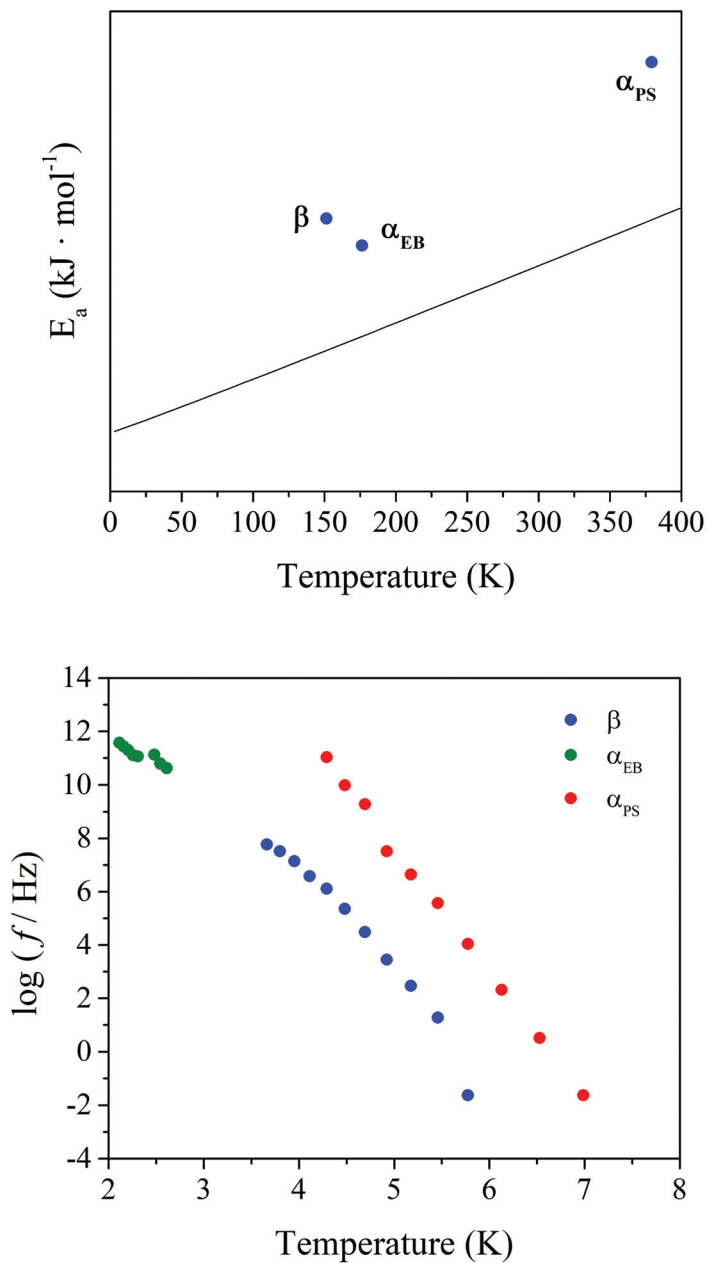


Figure 4.21: (Top) Eyring plot and (Bottom) Arrhenius plot of the SEBS-DVB-15I-S1 membrane.

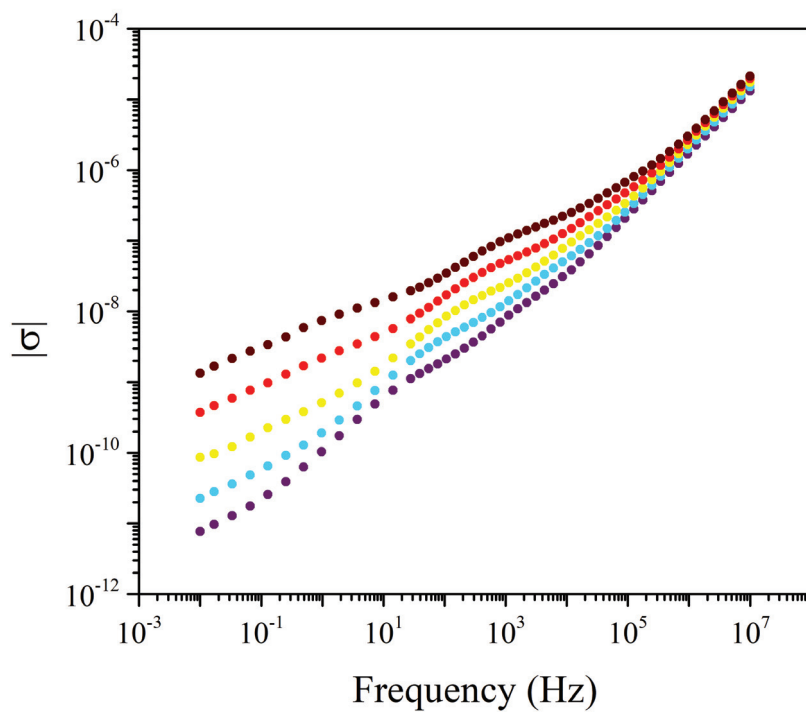


Figure 4.22: Isothermal curves of the module of the complex conductivity ($|\sigma|$) for the SEBS-DVB-15I-S1 membrane.

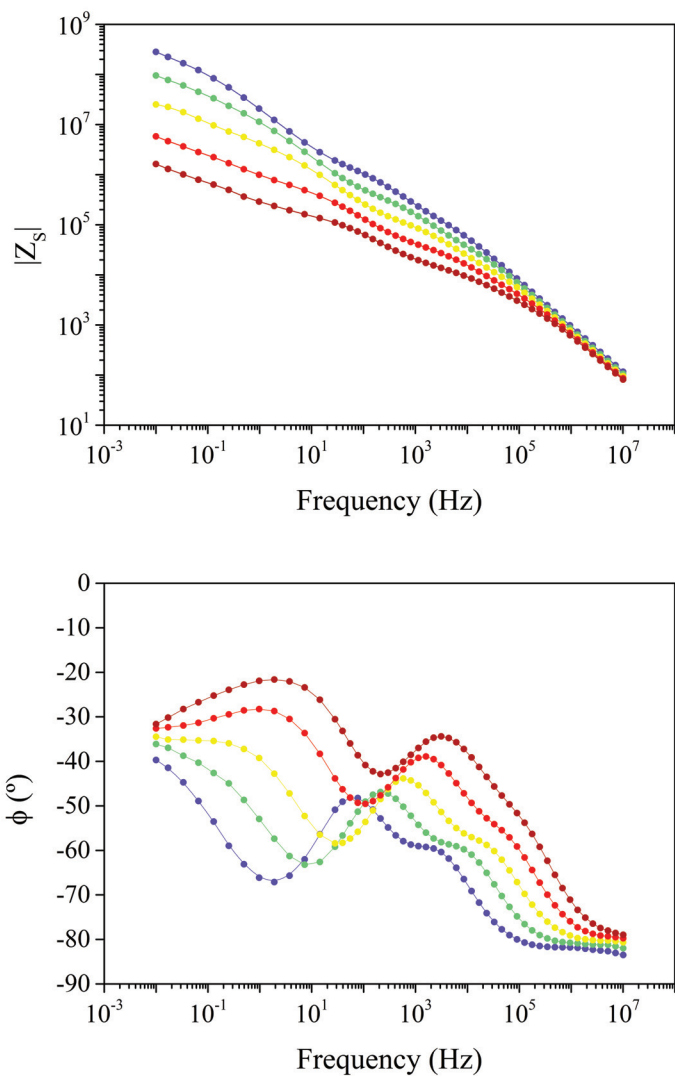


Figure 4.23: Phase angle (ϕ) and modulus of the serial impedance ($|Z_s|$) of the SEBS-DVB-15I-S1 membrane.

4.3.5 Analysis of the dielectric spectra of SEBS-DVB-15I-S2 membrane

The dielectric spectra was plotted in terms or the real (ϵ') and imaginary (ϵ'') parts of the complex dielectric permittivity (ϵ^*), $\tan \delta$, and the imaginary part of the electric modulus (M'') in Figures 4.24 - 4.25.

In Figure 4.26A the macromolecular origin of the dielectric relaxations is assessed through the Eyring model as derived by Starkweather. Unlike Figure 4.16A, the E_a value obtained for the β relaxation is higher than the one for the α_{EB} relaxation. As confirmed by the Arrhenius plot, both relaxations appear in a narrow temperature range, and therefore, a certain degree of cooperativity is registered.

In Figure 4.26B displays the Arrhenius plot, where the same relaxation zones (β , α_{EB} , and α_{PS}) exhibited in Figure 4.6.

In Figure 4.27 the isothermal curves of the module of the complex conductivity ($|\sigma|$) for the complete temperature range are displayed.

To determine the proton conductivity, the phase angle and the absolute value of the serial impedance (Z_s) are needed. Thus, both parameters are shown in Figure 4.28.

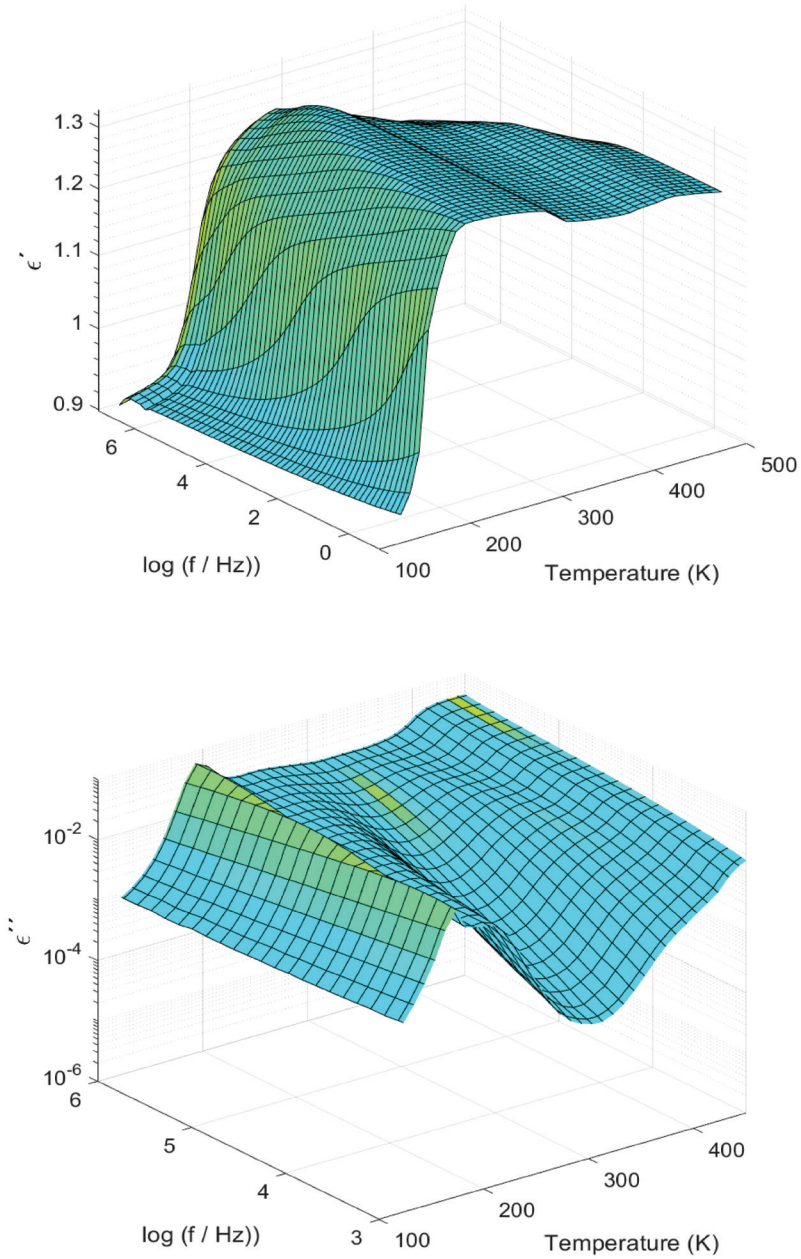


Figure 4.24: 3D plot of the real (ϵ') and imaginary part (ϵ'') parts of the complex permittivity (ϵ^*) of the SEBS-DVB-15I-S1 membrane.

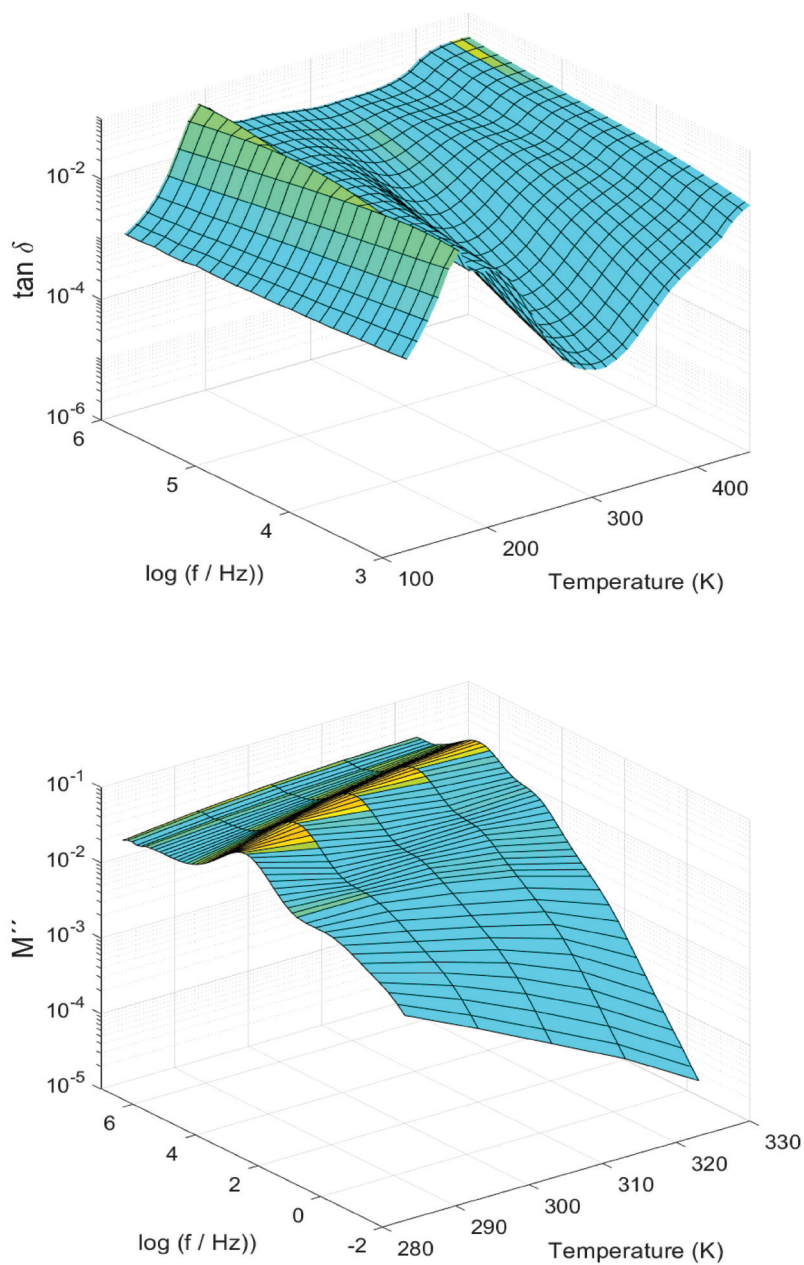


Figure 4.25: 3D plot of $\tan \delta$ and of the imaginary part (M'') of the complex electric modulus (M^*) of the SEBS-DVB-15I-S1 membrane.

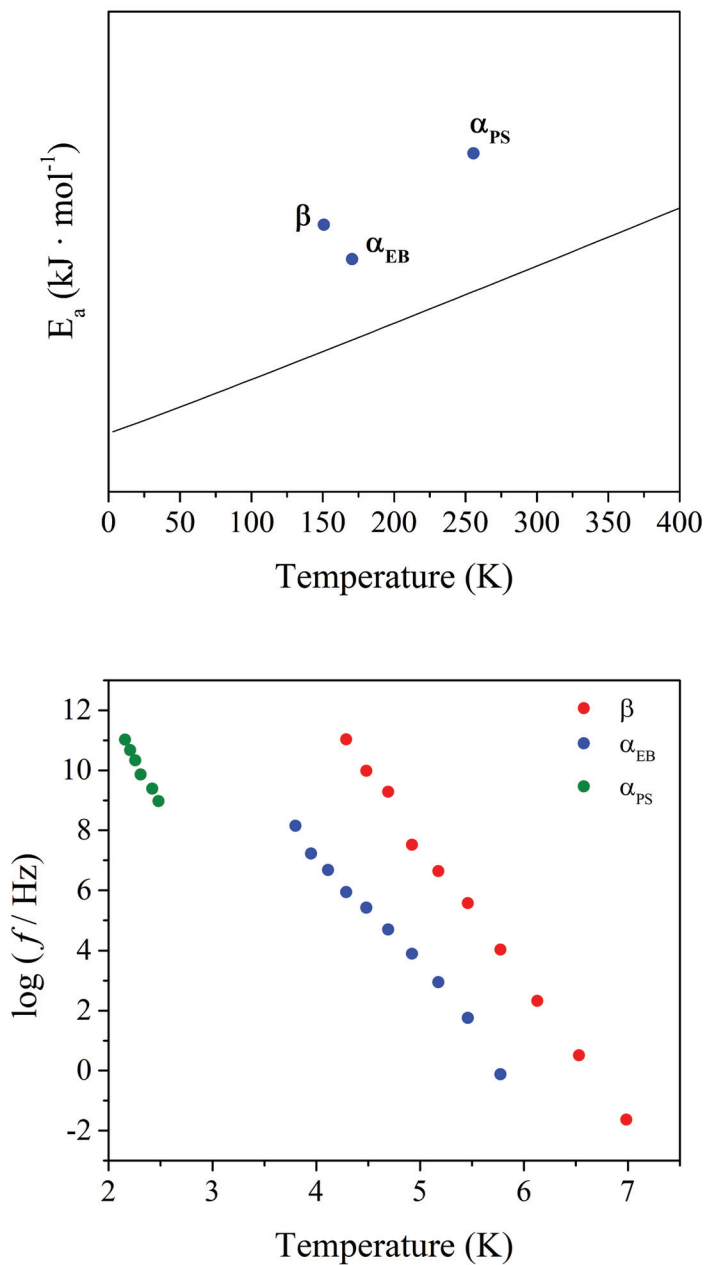


Figure 4.26: (Top) Eyring plot and (Bottom) Arrhenius plot of the SEBS-DVB-15I-S1 membrane.

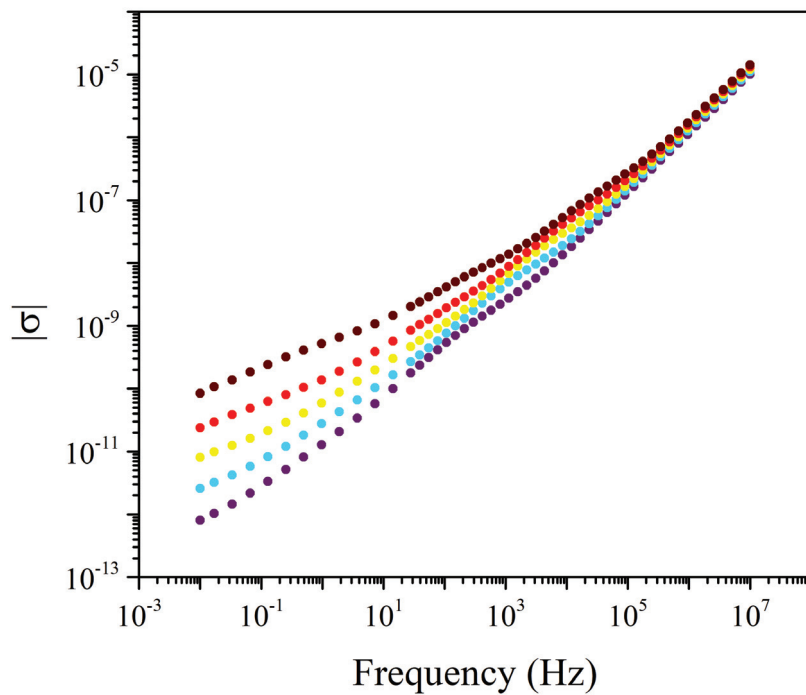


Figure 4.27: Isothermal curves of the module of the complex conductivity ($|\sigma|$) for the SEBS-DVB-15I-S1 membrane.

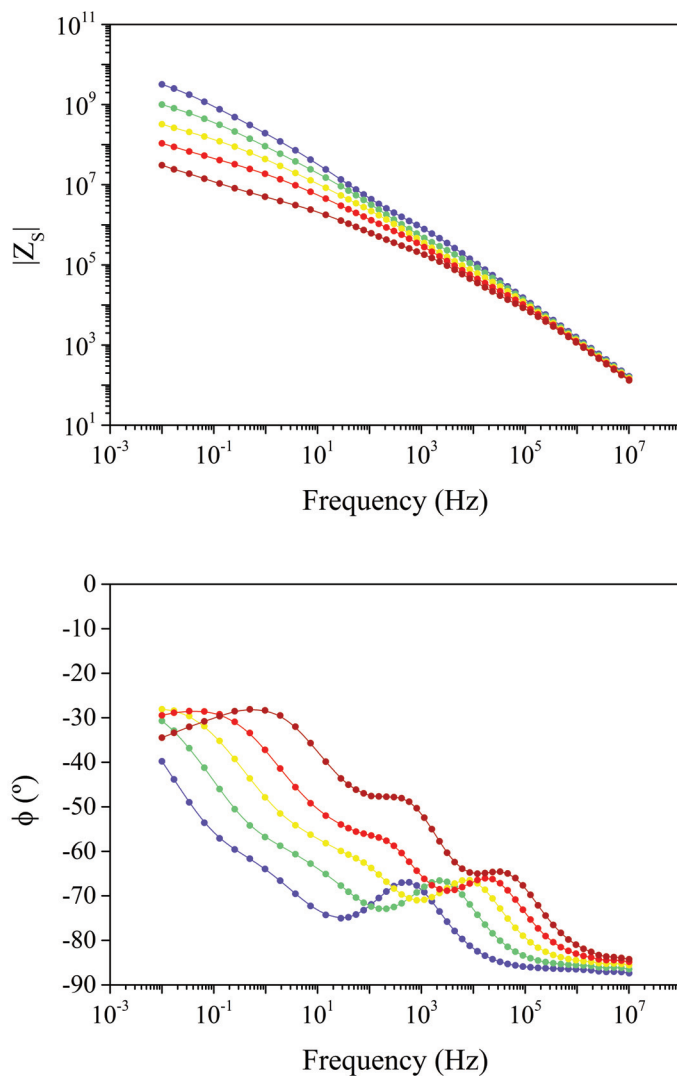


Figure 4.28: Phase angle (ϕ) and modulus of the serial impedance ($|Z_s|$) of the SEBS-DVB-15I-S1 membrane.

4.3.6 Analysis of the dielectric spectra of SEBS-DVB-30I membrane

The dielectric spectra was plotted in terms of the real (ϵ') and imaginary (ϵ'') parts of the complex dielectric permittivity (ϵ^*), $\tan \delta$, and the imaginary part of the electric modulus (M'') in Figures 4.29 - 4.30.

In Figure 4.31A the macromolecular origin of the dielectric relaxations is assessed through the Eyring model as derived by Starkweather.

In Figure 4.31B displays the Arrhenius plot, where the same relaxation zones (β , α_{EB} , and α_{PS}) exhibited in Figure 4.6.

In Figure 4.32 the isothermal curves of the module of the complex conductivity ($|\sigma|$) for the complete temperature range are displayed.

To determine the proton conductivity, the phase angle and the absolute value of the serial impedance (Z_s) are needed. Thus, both parameters are shown in Figure 4.33.

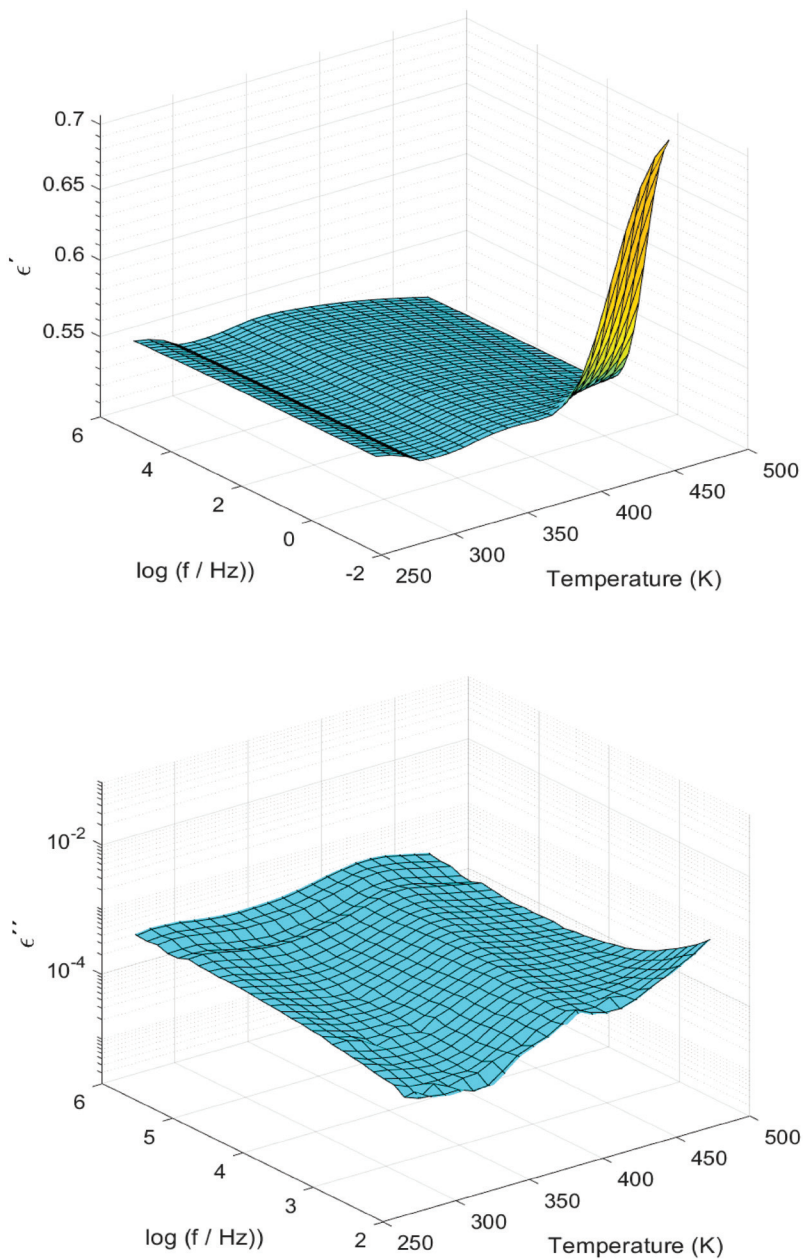


Figure 4.29: 3D plot of the real (ϵ') and imaginary part (ϵ'') parts of the complex permittivity (ϵ^*) of the SEBS-DVB-30I membrane.

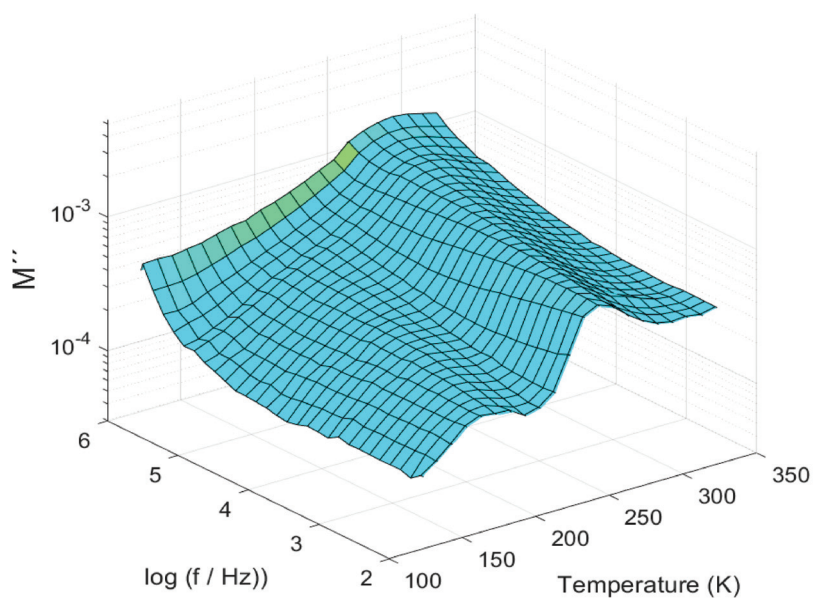
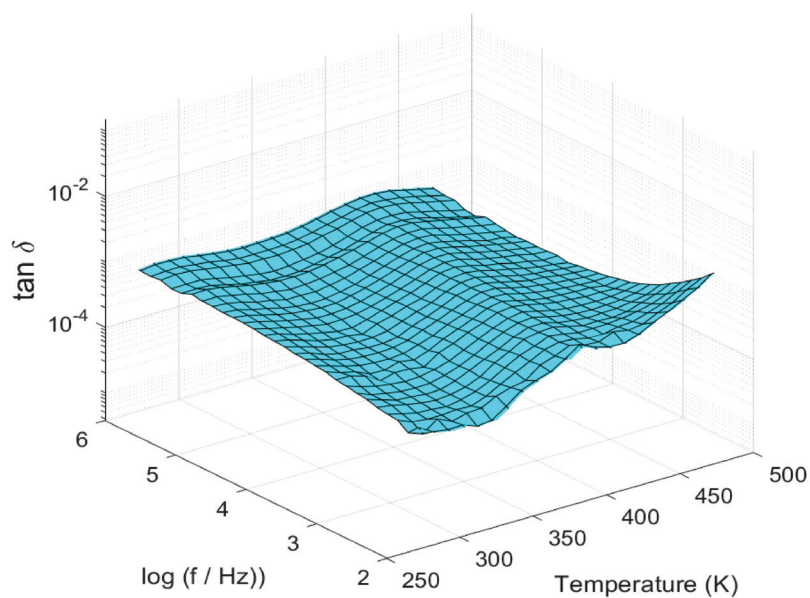


Figure 4.30: 3D plot of $\tan \delta$ and of the imaginary part (M'') of the complex electric modulus (M^*) of the SEBS-DVB-30I membrane.

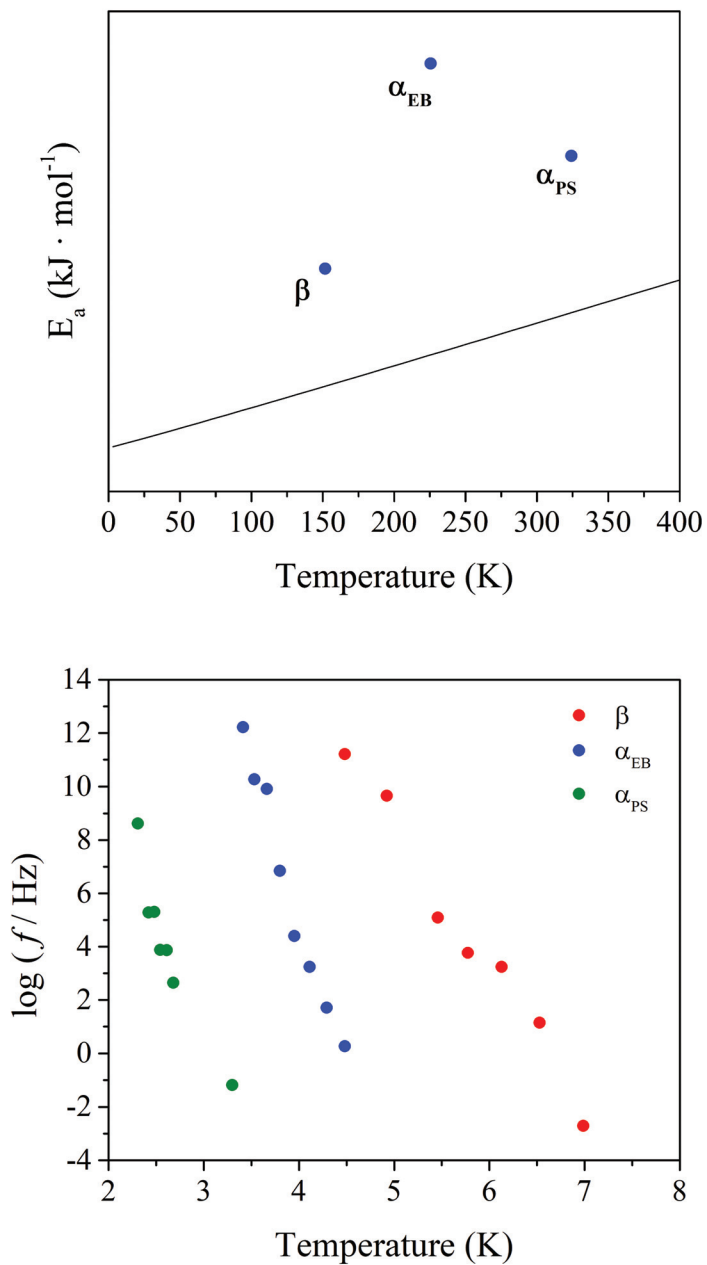


Figure 4.31: (Top) Eyring plot and (Bottom) Arrhenius plot of the SEBS-DVB-30I membrane.

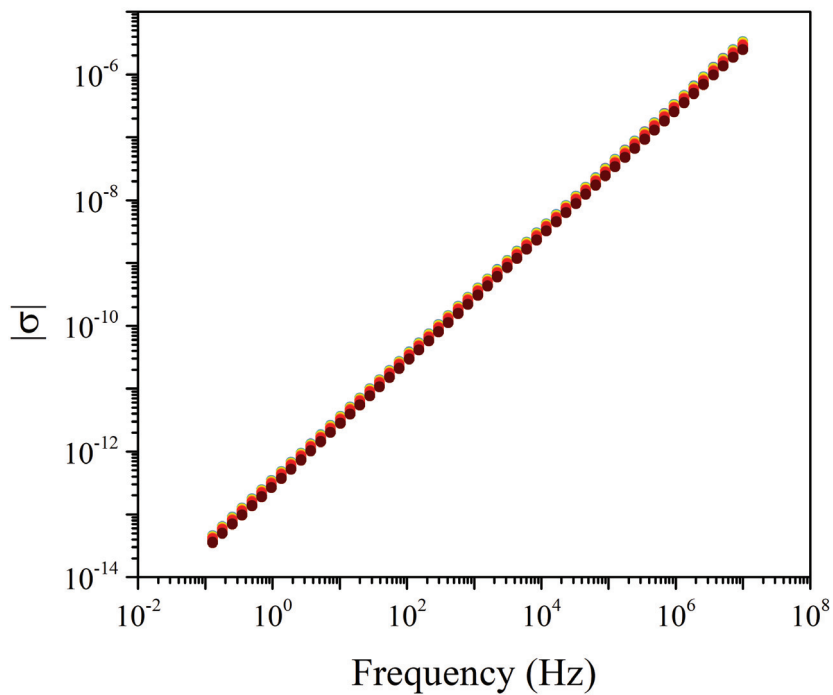


Figure 4.32: Isothermal curves of the module of the complex conductivity ($|\sigma|$) for the SEBS-DVB-30I membrane.

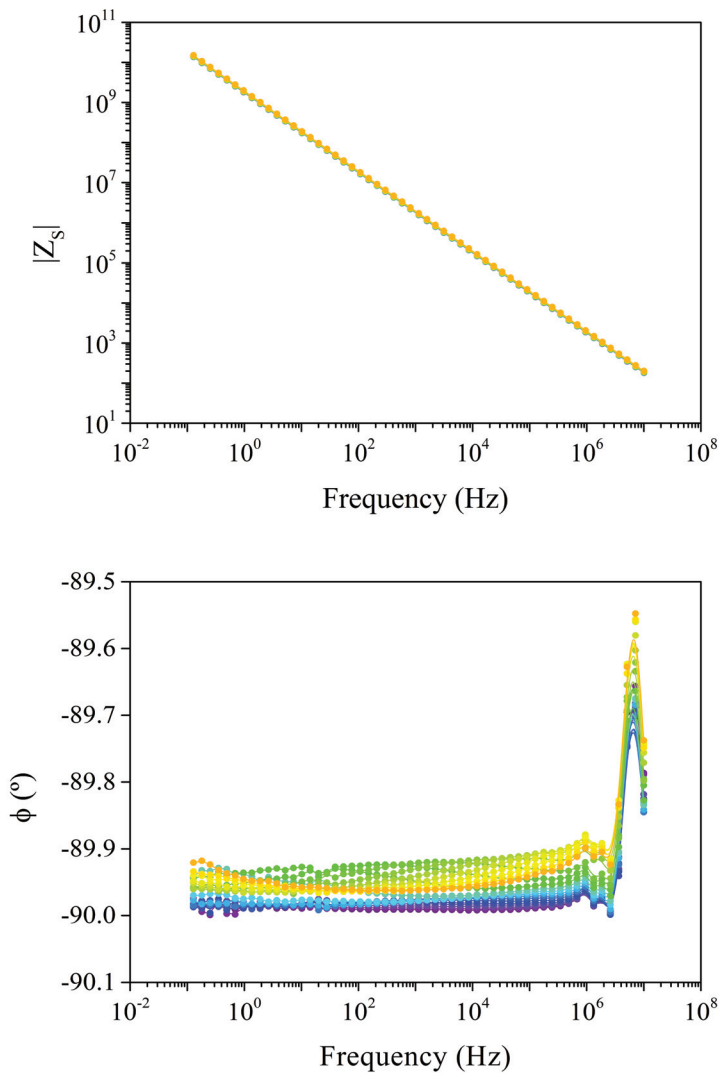


Figure 4.33: Phase angle (ϕ) and modulus of the serial impedance ($|Z_s|$) of the SEBS-DVB-30I membrane.

4.3.7 Analysis of the dielectric spectra of SEBS-DVB-30I-S1 membrane

The dielectric spectra was plotted in terms of the real (ϵ') and imaginary (ϵ'') parts of the complex dielectric permittivity (ϵ^*), $\tan \delta$, and the imaginary part of the electric modulus (M'') in Figures 4.34 - 4.35.

In Figure 4.36A the macromolecular origin of the dielectric relaxations is assessed through the Eyring model as derived by Starkweather. Likewise Figure 4.21A, and Figure 4.26A the E_a value obtained for the β relaxation is higher than the one for the α_{EB} relaxation. As confirmed by the Arrhenius plot, both relaxations appear in a narrow temperature range, and therefore, a certain degree of cooperativity is registered.

In Figure 4.36B displays the Arrhenius plot, where the same relaxation zones (β , α_{EB} , and α_{PS}) exhibited in Figure 4.6.

In Figure 4.37 the isothermal curves of the module of the complex conductivity ($|\sigma|$) for the complete temperature range are displayed.

To determine the proton conductivity, the phase angle and the absolute value of the serial impedance (Z_s) are needed. Thus, both parameters are shown in Figure 4.38.

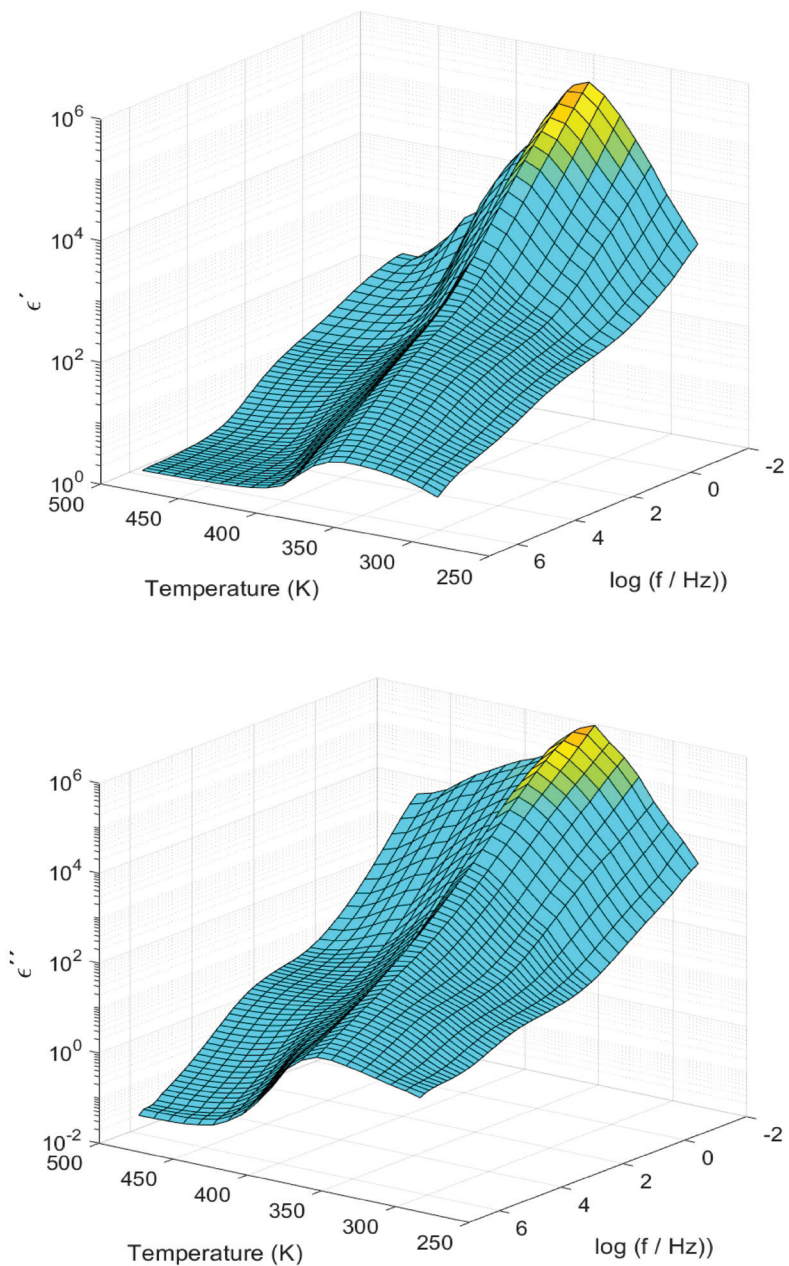


Figure 4.34: 3D plot of the real (ϵ') and imaginary part (ϵ'') parts of the complex permittivity (ϵ^*) of the SEBS-DVB-30I-S1 membrane.

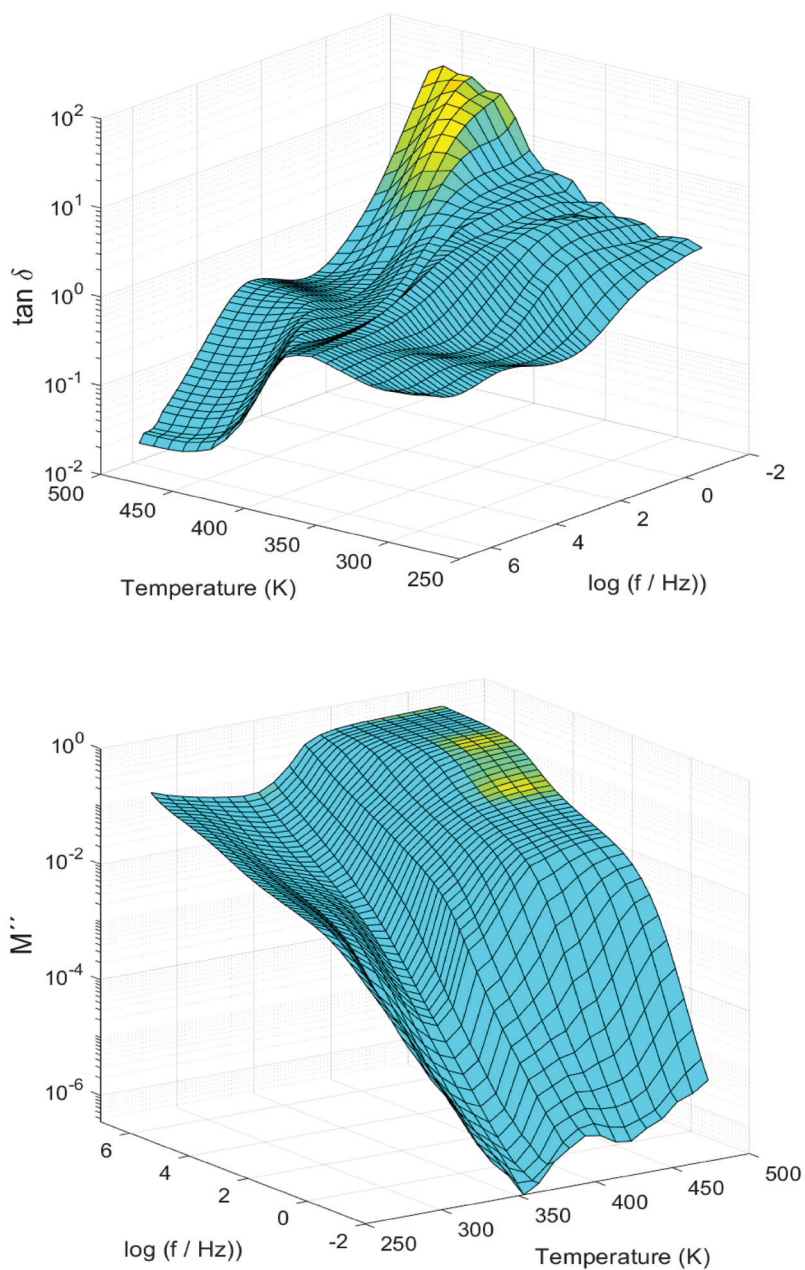


Figure 4.35: 3D plot of $\tan \delta$ and of the imaginary part (M'') of the complex electric modulus (M^*) of the SEBS-DVB-30I-S1 membrane.

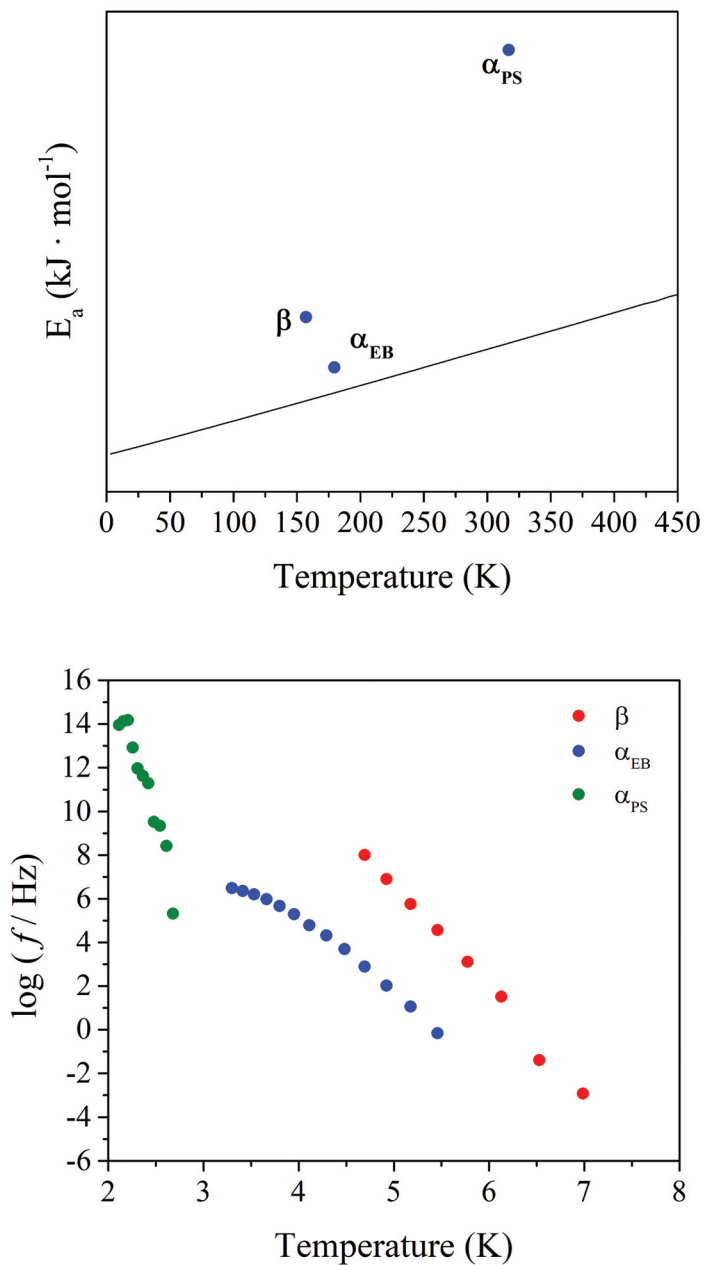


Figure 4.36: (Top) Eyring plot and (Bottom) Arrhenius plot of the SEBS-DVB-30I-S1 membrane.

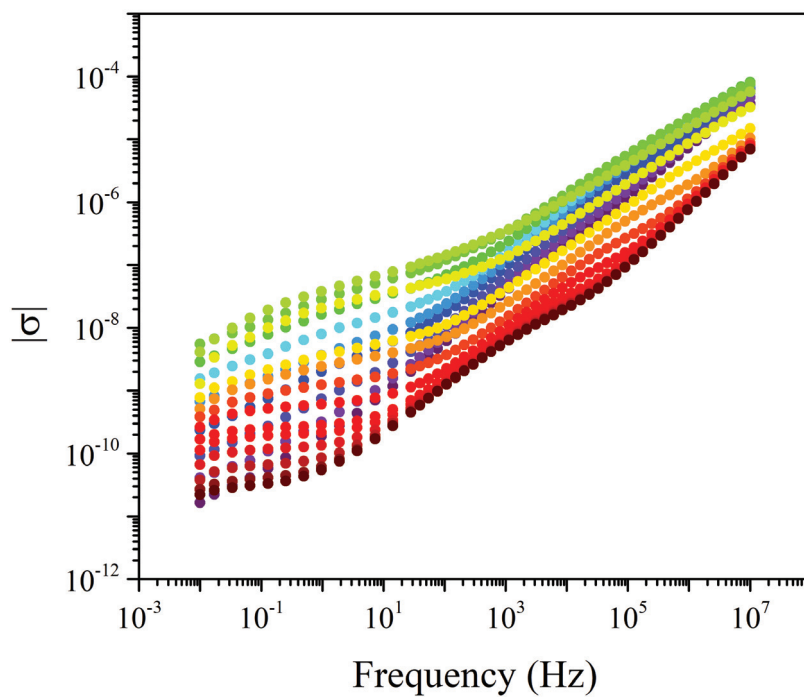


Figure 4.37: Isothermal curves of the module of the complex conductivity ($|\sigma|$) for the SEBS-DVB-30I-S1 membrane.

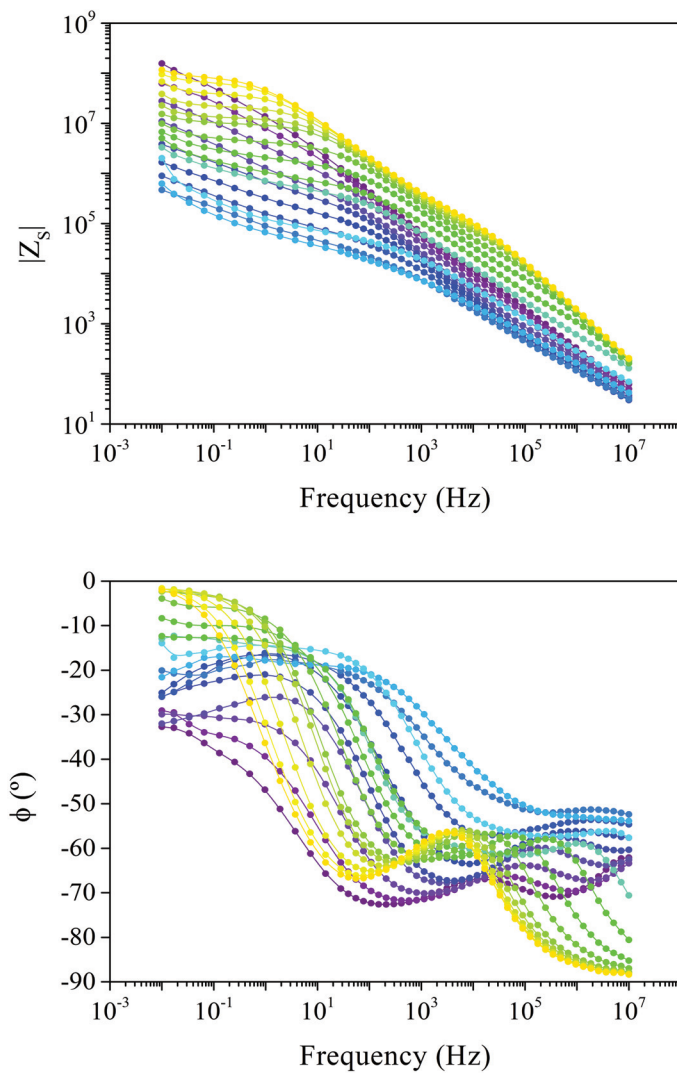


Figure 4.38: Phase angle (ϕ) and modulus of the serial impedance ($|Z_s|$) of the SEBS-DVB-30I-S1 membrane.

4.3.8 Analysis of the dielectric spectra of SEBS-DVB-30I-S2 membrane

The dielectric spectra was plotted in terms or the real (ϵ') and imaginary (ϵ'') parts of the complex dielectric permittivity (ϵ^*), $\tan \delta$, and the imaginary part of the electric modulus (M'') in Figures 4.39 - 4.40.

In Figure 4.41A the macromolecular origin of the dielectric relaxations is assessed through the Eyring model as derived by Starkweather.

In Figure 4.41B displays the Arrhenius plot, where the same relaxation zones (β , α_{EB} , and α_{PS}) exhibited in Figure 4.6.

In Figure 4.42 the isothermal curves of the module of the complex conductivity ($|\sigma|$) for the complete temperature range are displayed.

To determine the proton conductivity, the phase angle and the absolute value of the serial impedance (Z_s) are needed. Thus, both parameters are shown in Figure 4.43.

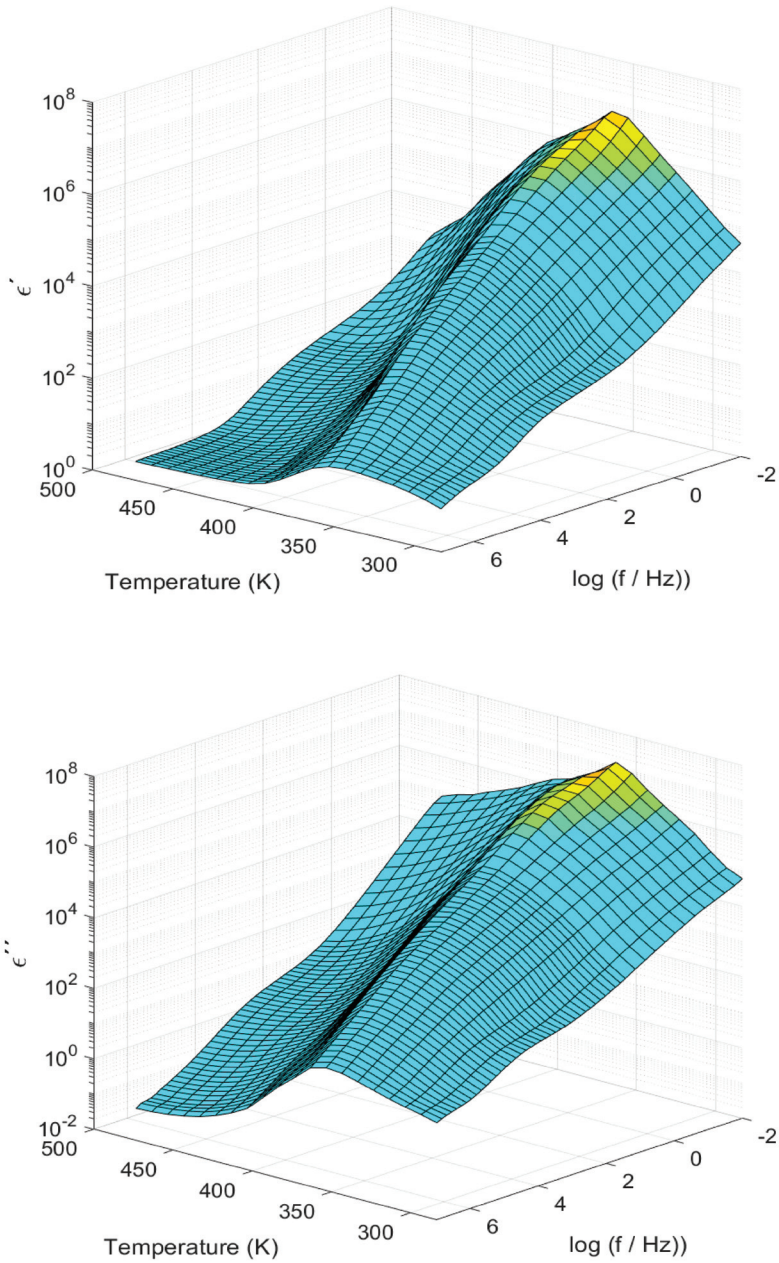


Figure 4.39: 3D plot of the real (ϵ') and imaginary part (ϵ'') parts of the complex permittivity (ϵ^*) of the SEBS-DVB-30I-S2 membrane.

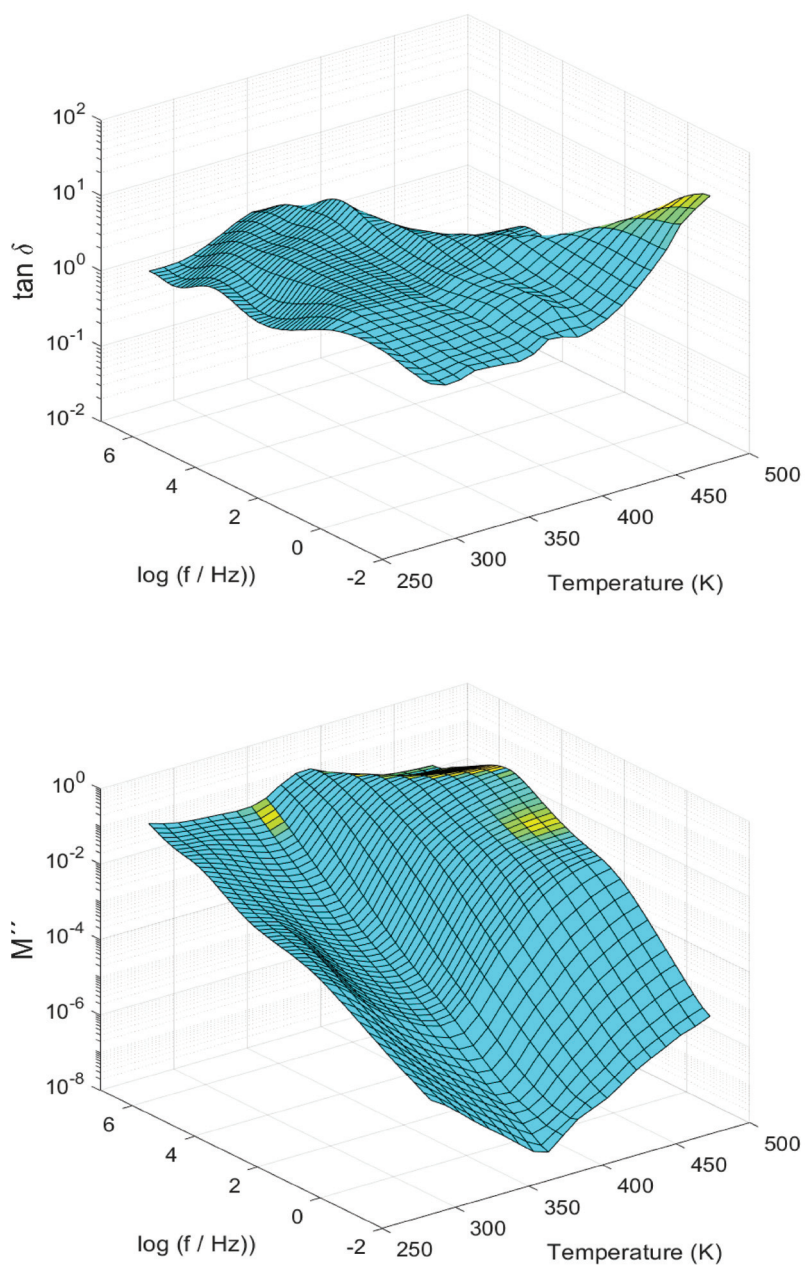


Figure 4.40: 3D plot of $\tan \delta$ and of the imaginary part (M'') of the complex electric modulus (M^*) of the SEBS-DVB-30I-S2 membrane.

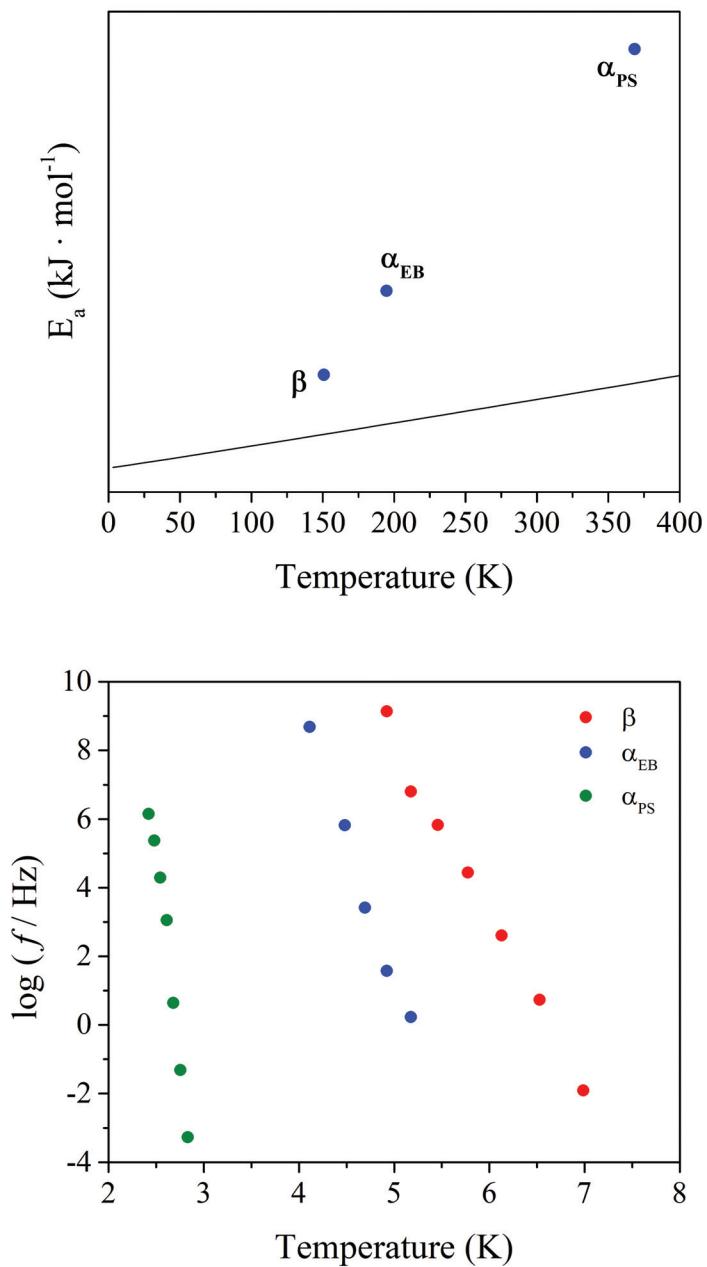


Figure 4.41: (Top) Eyring plot and (Bottom) Arrhenius plot of the SEBS-DVB-30I-S2 membrane.

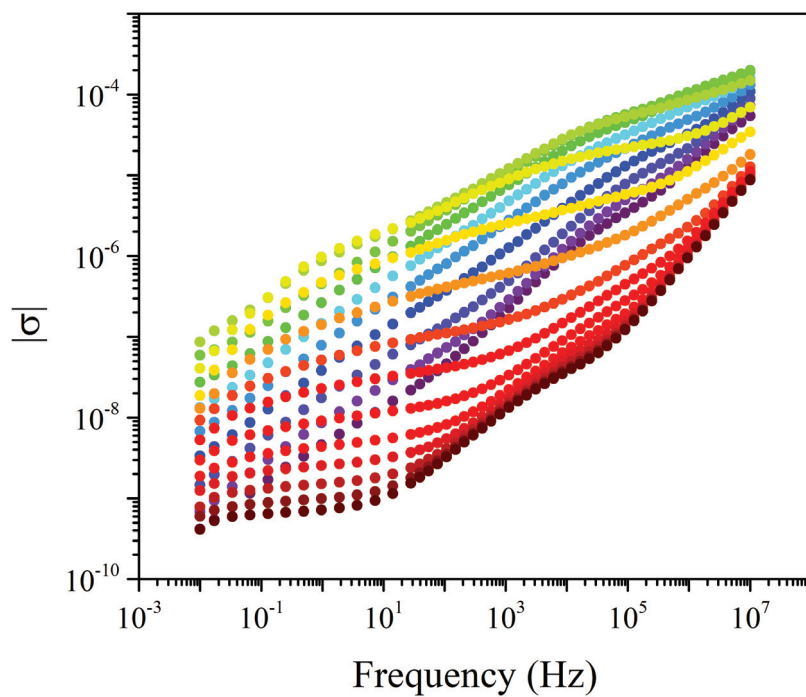


Figure 4.42: Isothermal curves of the module of the complex conductivity ($|\sigma|$) for the SEBS-DVB-30I-S2 membrane.

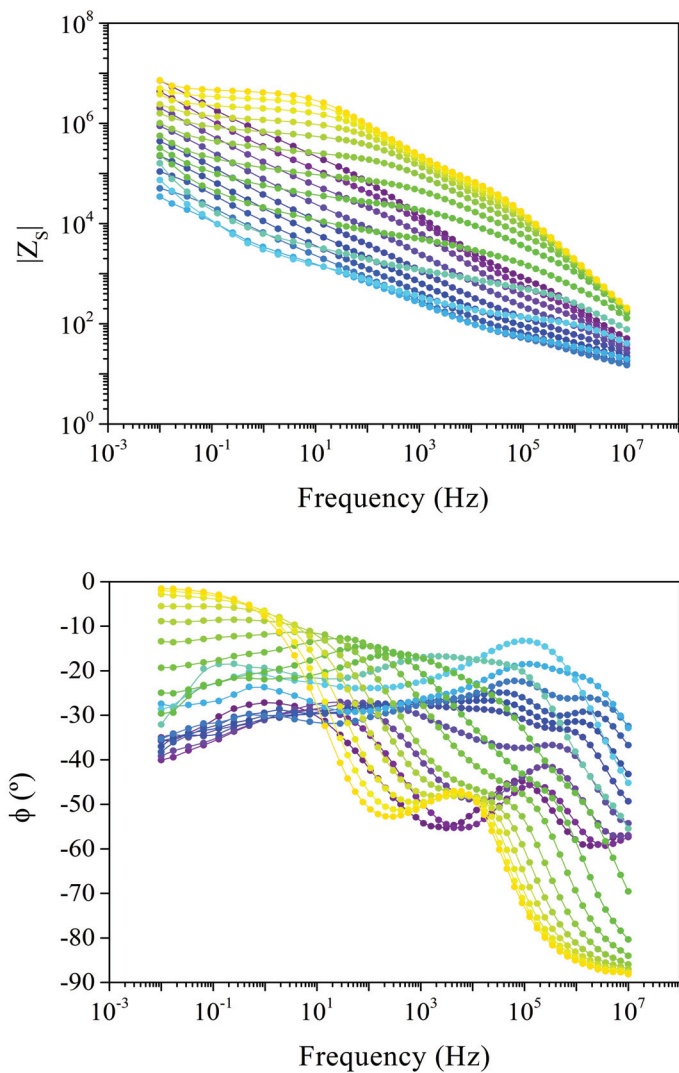


Figure 4.43: Phase angle (ϕ) and modulus of the serial impedance ($|Z_s|$) of the SEBS-DVB-30I-S2 membrane.

4.3.9 Analysis of the dielectric spectra of sSEBS membrane

The dielectric spectra was plotted in terms of the real (ϵ') and imaginary (ϵ'') parts of the complex dielectric permittivity (ϵ^*), $\tan \delta$, and the imaginary part of the electric modulus (M'') in Figures 4.44 - 4.45.

In Figure 4.46A the macromolecular origin of the dielectric relaxations is assessed through the Eyring model as derived by Starkweather. As it has been found in several of the photocrosslinked membranes, the E_a obtained for the β relaxation is higher than the one for the α_{EB} relaxation. As confirmed by the Arrhenius plot, both relaxations appear in a narrow temperature range, and therefore, a certain degree of cooperativity is registered.

In Figure 4.46B displays the Arrhenius plot, where the same relaxation zones (β , α_{EB} , and α_{PS}) exhibited in Figure 4.6.

In Figure 4.47 the isothermal curves of the module of the complex conductivity ($|\sigma|$) for the complete temperature range are displayed.

To determine the proton conductivity, the phase angle and the absolute value of the serial impedance (Z_s) are needed. Thus, both parameters are shown in Figure 4.48.

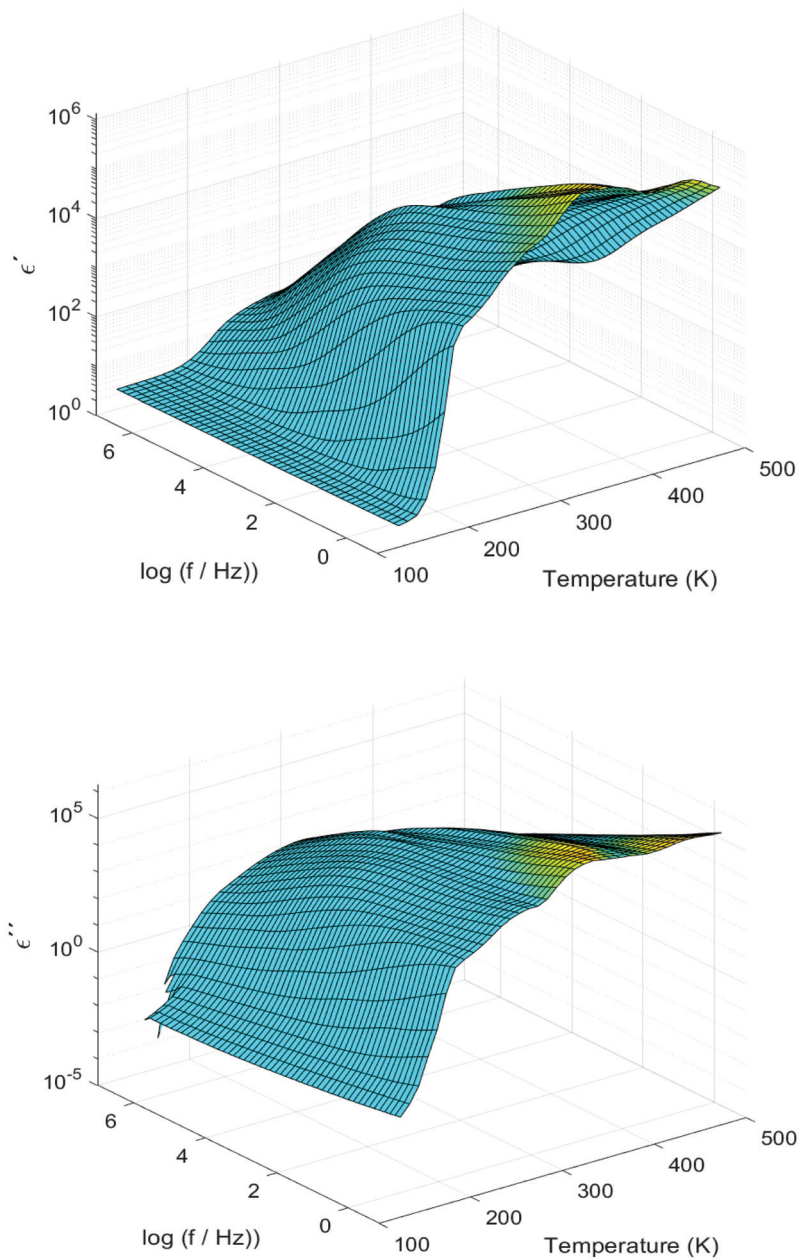


Figure 4.44: 3D plot of the real (ϵ') and imaginary part (ϵ'') parts of the complex permittivity (ϵ^*) of the sSEBS membrane.

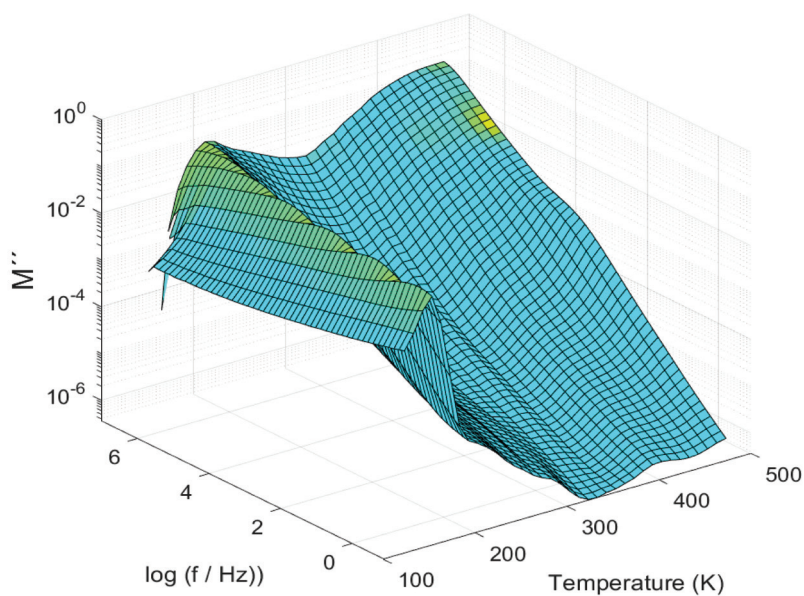
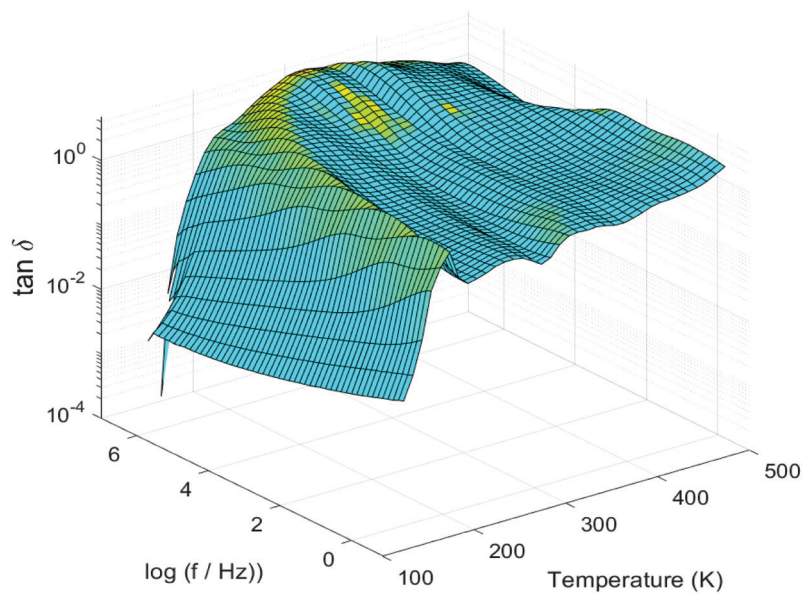


Figure 4.45: 3D plot of $\tan \delta$ and of the imaginary part (M'') of the complex electric modulus (M^*) of the sSEBS membrane.

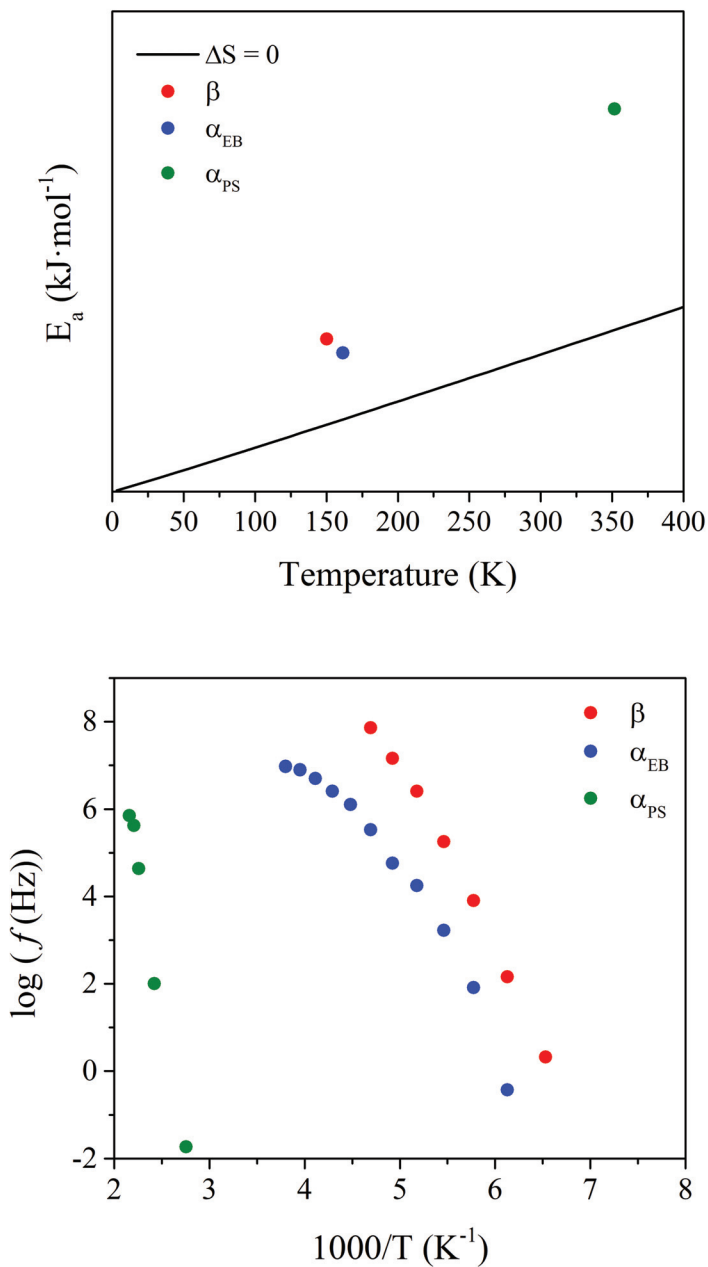


Figure 4.46: (Top) Eyring plot and (Bottom) Arrhenius plot of the sSEBS membrane.

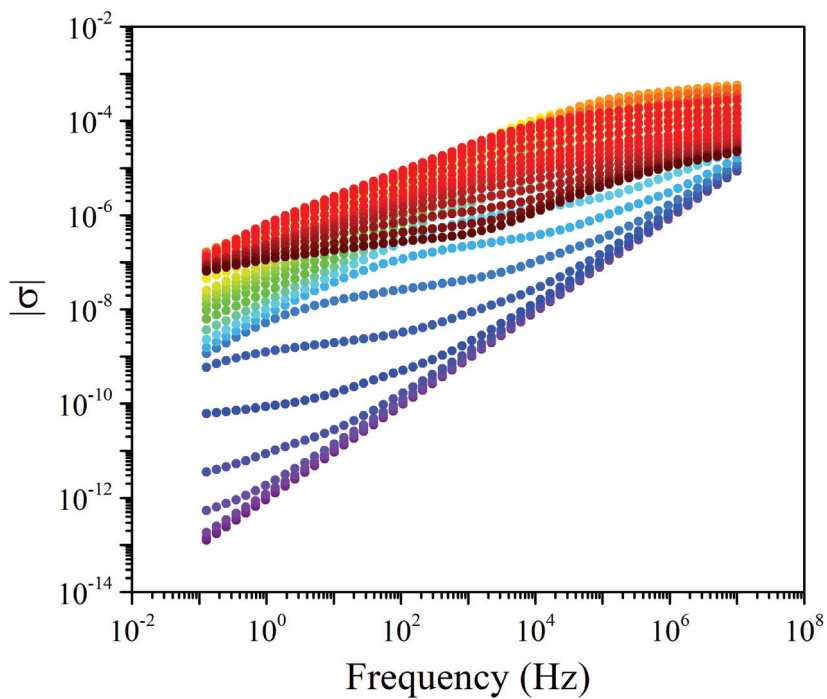


Figure 4.47: Isothermal curves of the module of the complex conductivity ($|\sigma|$) for the sSEBS membrane.

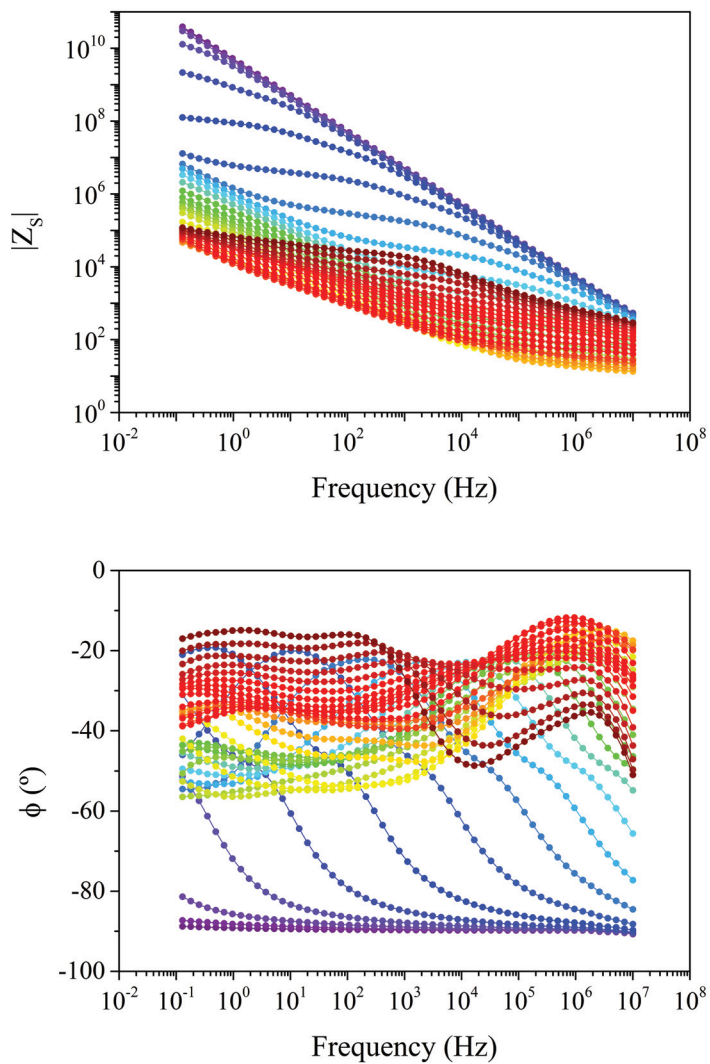


Figure 4.48: Phase angle (ϕ) and modulus of the serial impedance ($|Z_s|$) of the sSEBS membrane.

4.3.10 Analysis of the dielectric spectra of sSEBS-Zr5 membrane

The dielectric spectra was plotted in terms of the real (ϵ') and imaginary (ϵ'') parts of the complex dielectric permittivity (ϵ^*), $\tan \delta$, and the imaginary part of the electric modulus (M'') in Figures 4.49 - 4.50.

In Figure 4.51A the macromolecular origin of the dielectric relaxations is assessed through the Eyring model as derived by Starkweather. Like sSEBS, the high values of E_a obtained for the β relaxation reflects a certain degree of cooperativity due to the narrow temperature range where the β and α_{EB} occur. Moreover, unlike the sSEBS and several of the photocrosslinked membranes, the E_a obtained for the α_{PS} relaxation is lower than the one found for both, the β and α_{EB} relaxations. As confirmed by the Arrhenius plot, this result is induced by the plasticisation process that the α_{PS} relaxation undergoes.

In Figure 4.51B displays the Arrhenius plot, where the same relaxation zones (β , α_{EB} , and α_{PS}) exhibited in Figure 4.6 are found.

In Figure 4.52 the isothermal curves of the module of the complex conductivity ($|\sigma|$) for the complete temperature range are displayed.

To determine the proton conductivity, the phase angle and the absolute value of the serial impedance (Z_s) are needed. Thus, both parameters are shown in Figure 4.53.

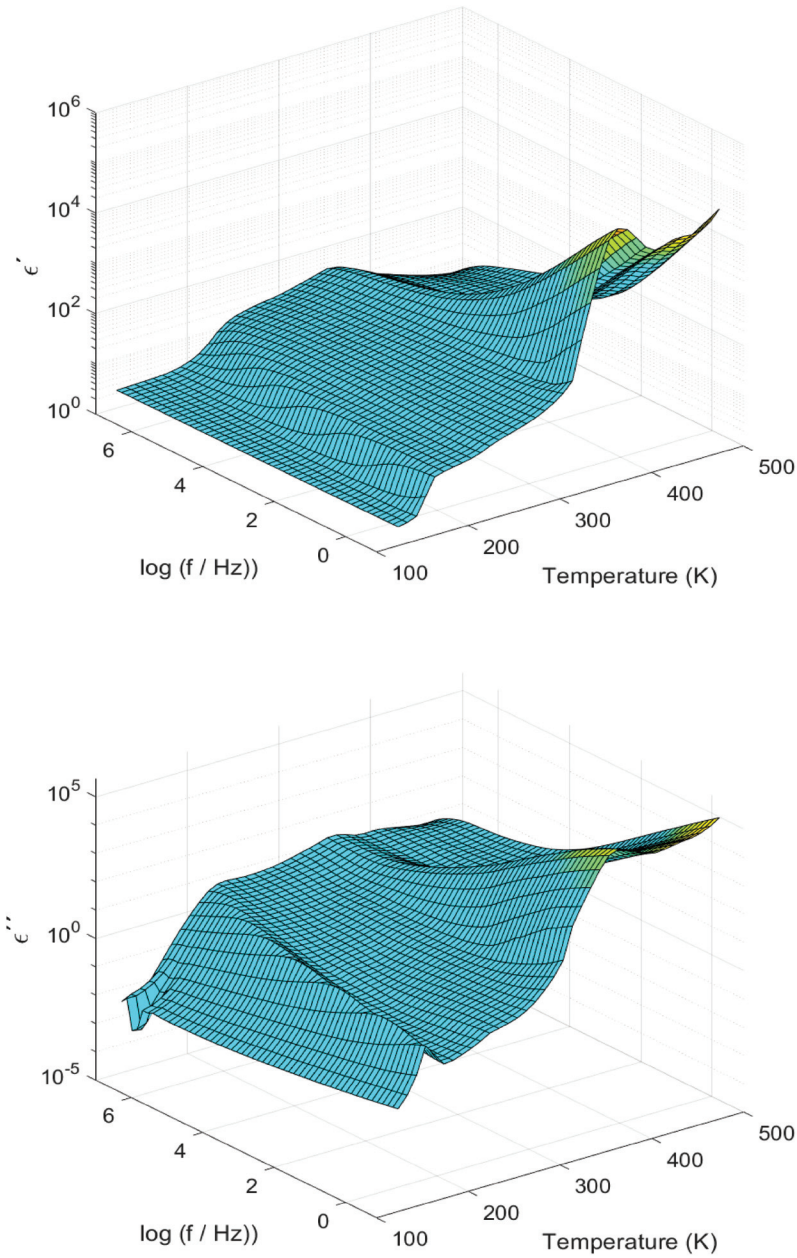


Figure 4.49: 3D plot of the real (ϵ') and imaginary part (ϵ'') parts of the complex permittivity (ϵ^*) of the sSEBS-Zr5 membrane.

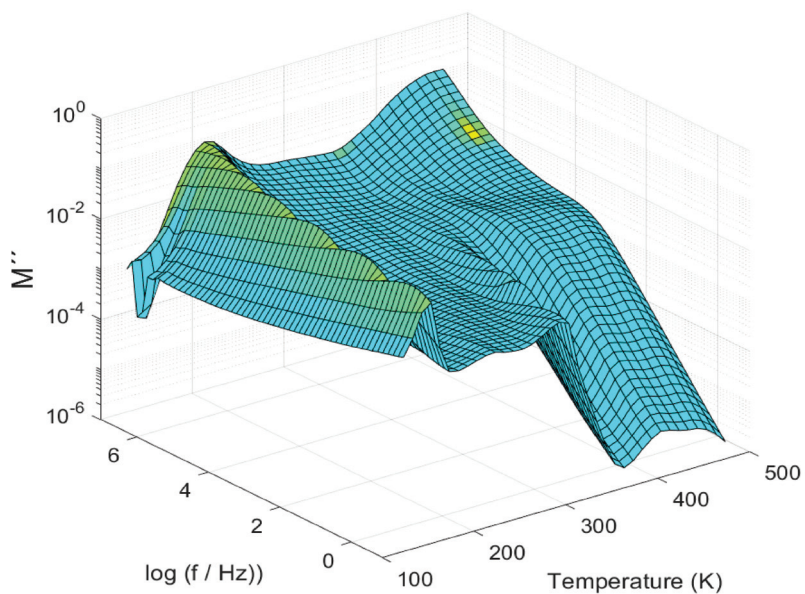
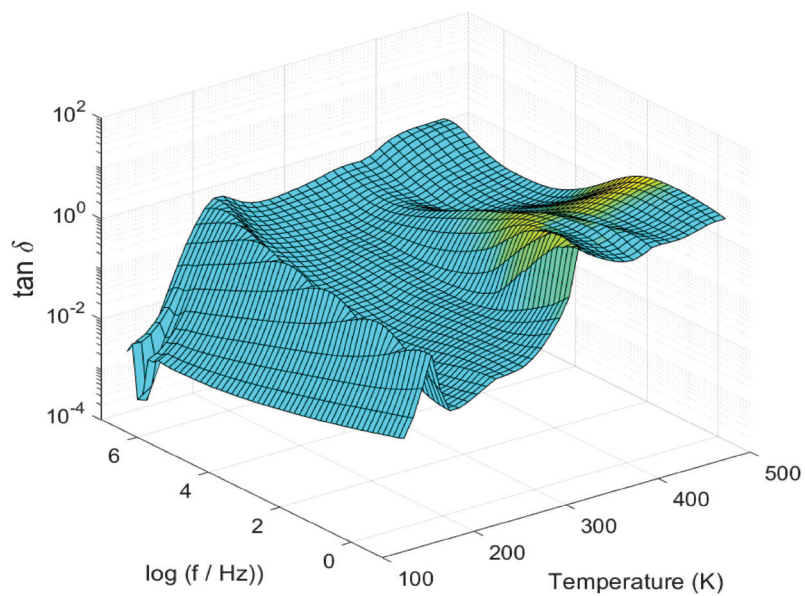


Figure 4.50: 3D plot of $\tan \delta$ and of the imaginary part (M'') of the complex electric modulus (M^*) of the sSEBS-Zr5 membrane.

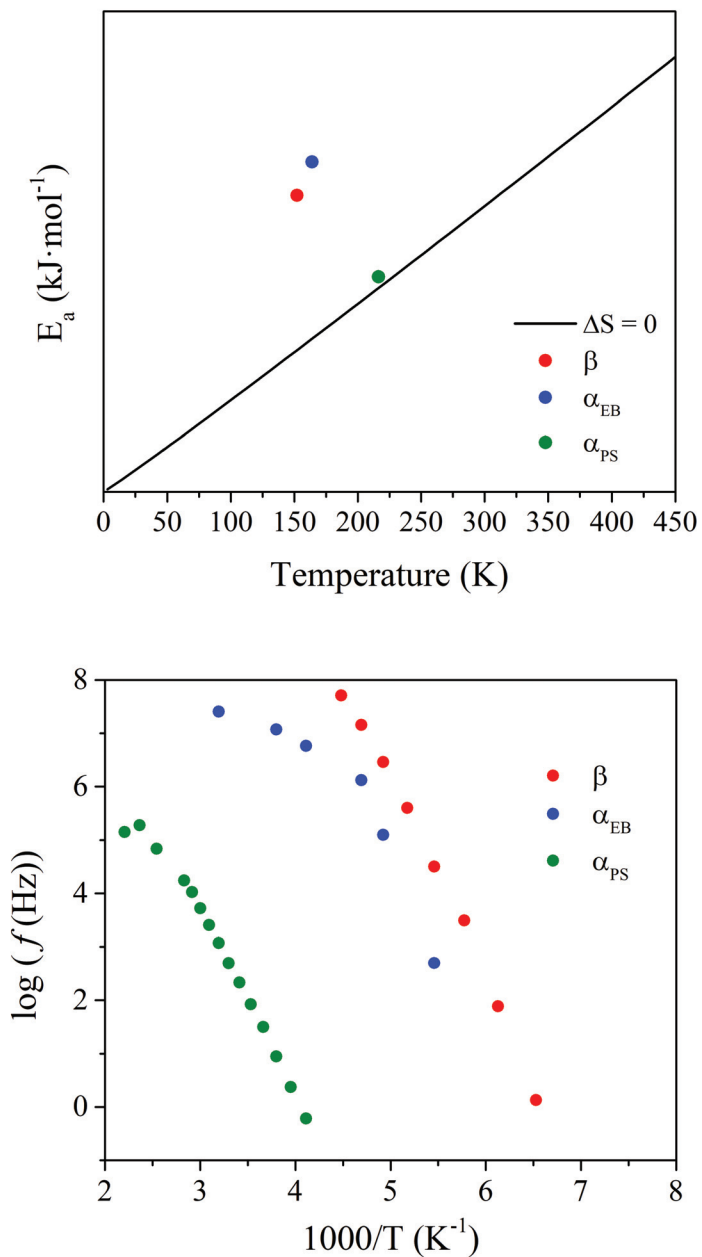


Figure 4.51: (Top) Eyring plot and (Bottom) Arrhenius plot of the sSEBS-Zr5 membrane.

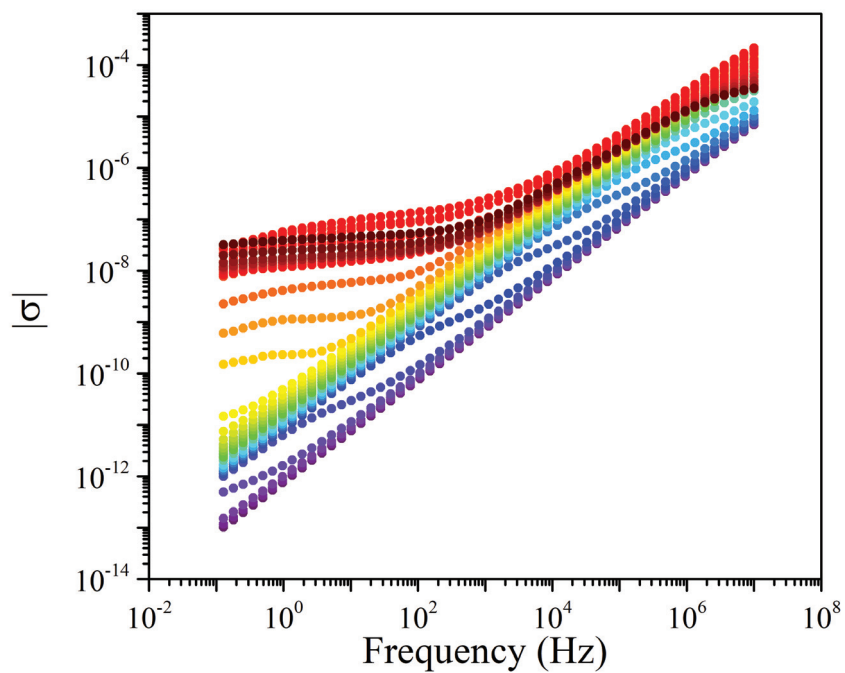


Figure 4.52: Isothermal curves of the module of the complex conductivity ($|\sigma|$) for the sSEBS-Zr5 membrane.

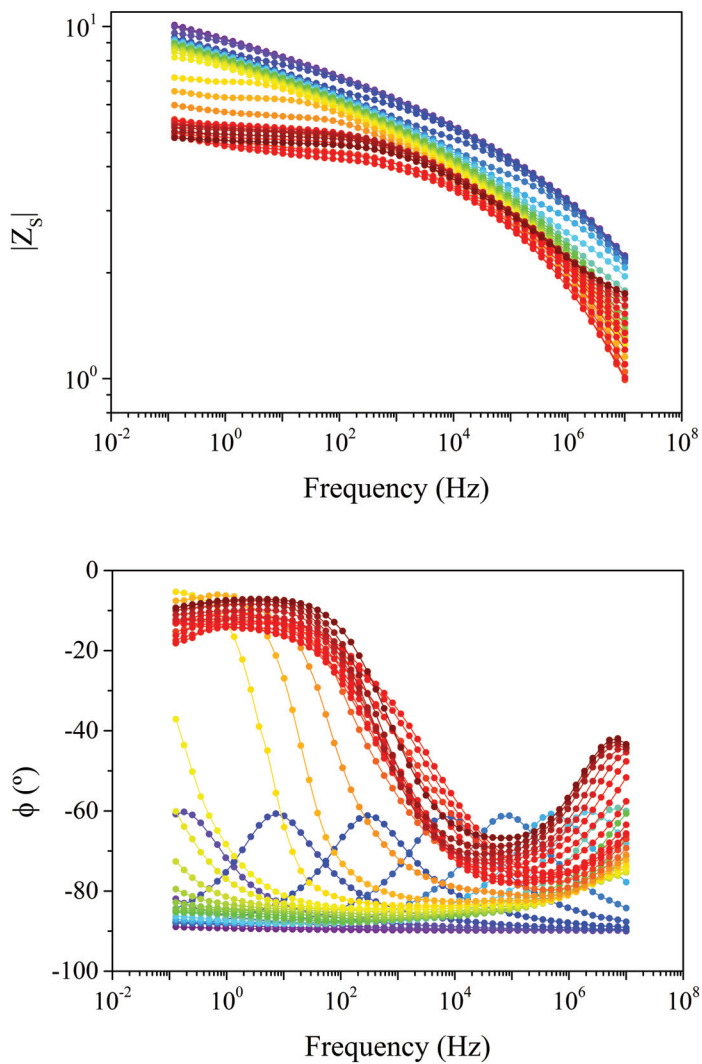


Figure 4.53: Phase angle (ϕ) and modulus of the serial impedance ($|Z_s|$) of the sSEBS-Zr5 membrane.

4.3.11 Analysis of the dielectric spectra of sSEBS-Zr10 membrane

The dielectric spectra was plotted in terms of the real (ϵ') and imaginary (ϵ'') parts of the complex dielectric permittivity (ϵ^*), $\tan \delta$, and the imaginary part of the electric modulus (M'') in Figures 4.54 - 4.55.

In Figure 4.56A the macromolecular origin of the dielectric relaxations is assessed through the Eyring model as derived by Starkweather. Like sSEBS and sSEBS-Zr5, the high values of E_a obtained for the β relaxation reflects a certain degree of cooperativity due to the narrow temperature range where the β and α_{EB} occur. Moreover, in the same manner than sSEBS-Zr5, the E_a obtained for the α_{PS} relaxation is lower than the one found for both, the β and α_{EB} relaxations. As confirmed by the Arrhenius plot, this result is induced by the plasticisation process that the α_{PS} relaxation undergoes.

In Figure 4.56B displays the Arrhenius plot, where the same relaxation zones (β , α_{EB} , and α_{PS}) exhibited in Figure 4.6..

In Figure 4.57 the isothermal curves of the module of the complex conductivity ($|\sigma|$) for the complete temperature range are displayed.

To determine the proton conductivity, the phase angle and the absolute value of the serial impedance (Z_s) are needed. Thus, both parameters are shown in Figure 4.58.

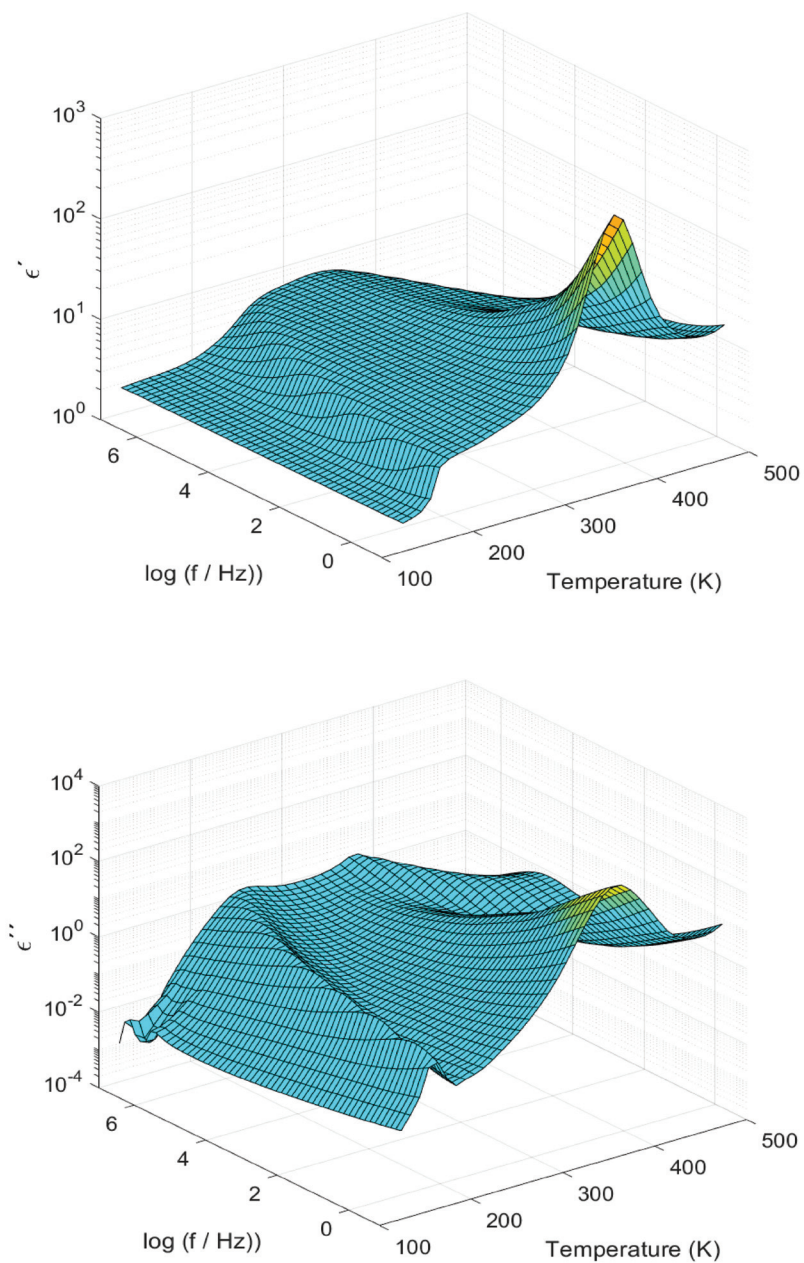


Figure 4.54: 3D plot of the real (ϵ') and imaginary part (ϵ'') parts of the complex permittivity (ϵ^*) of the sSEBS-Zr10 membrane.

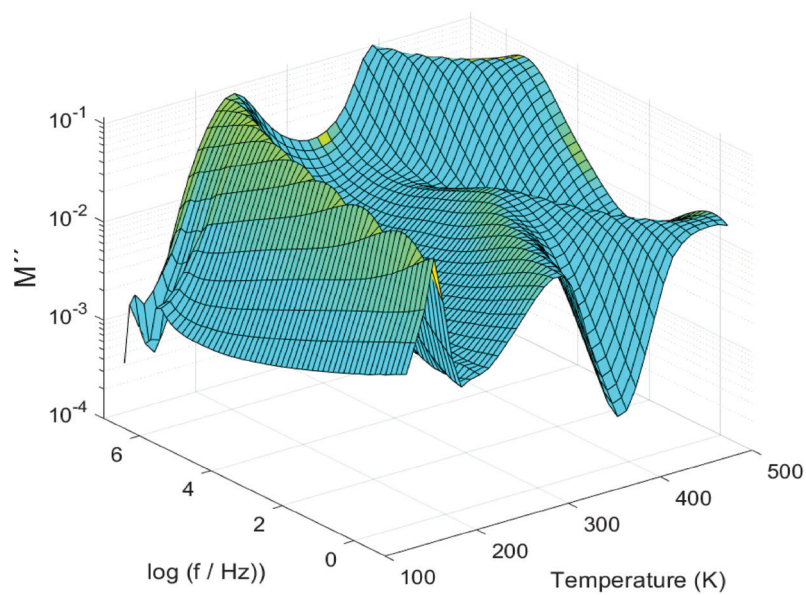
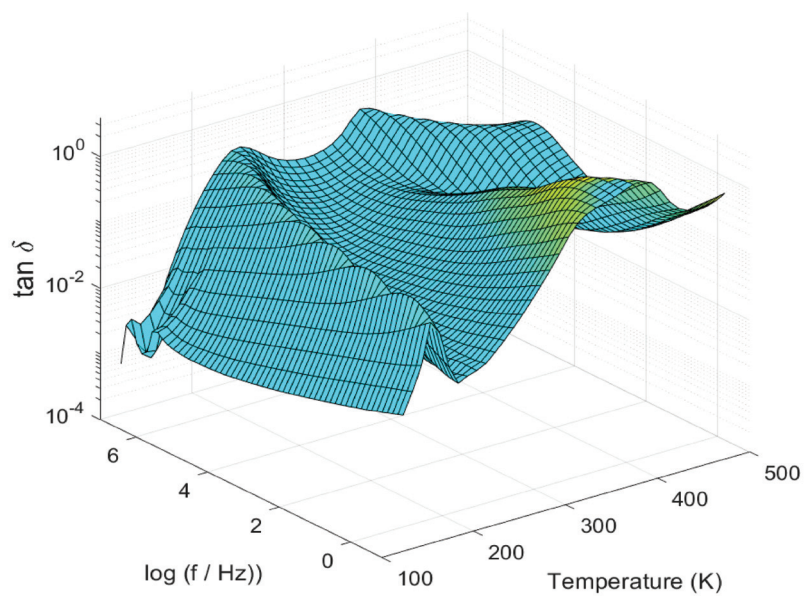


Figure 4.55: 3D plot of $\tan \delta$ and of the imaginary part (M'') of the complex electric modulus (M^*) of the sSEBS-Zr10 membrane.

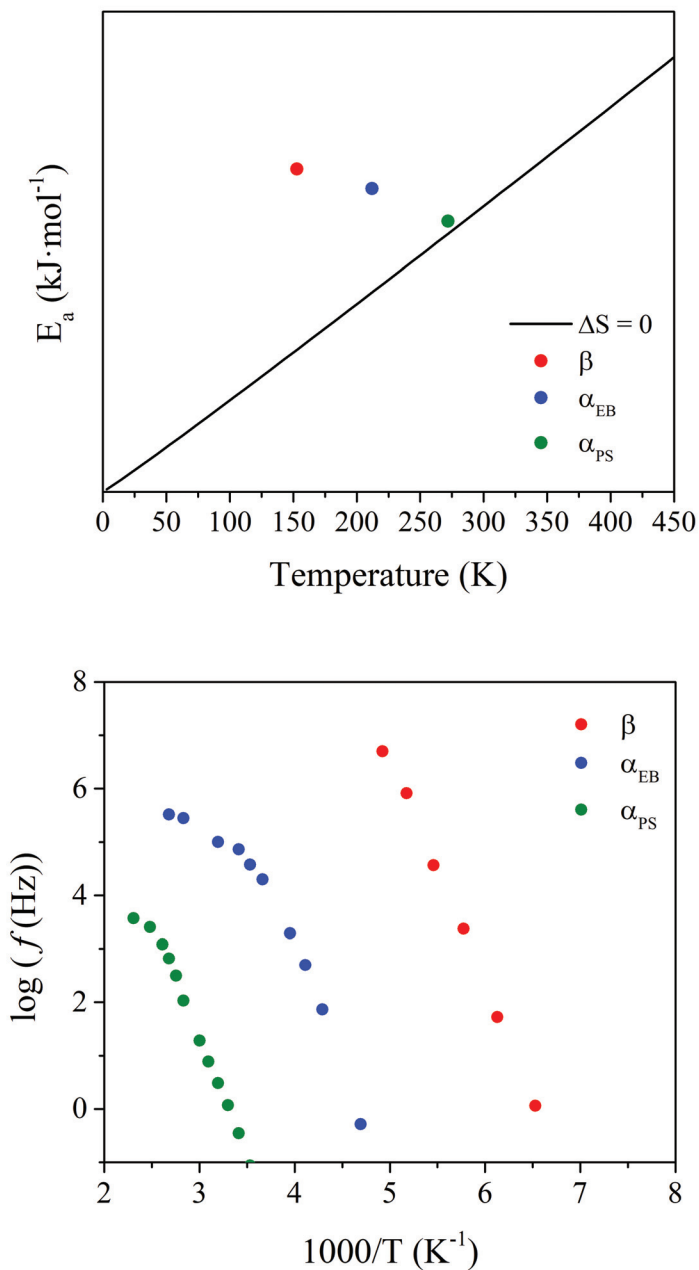


Figure 4.56: (Top) Eyring plot and (Bottom) Arrhenius plot of the sSEBS-Zr10 membrane.

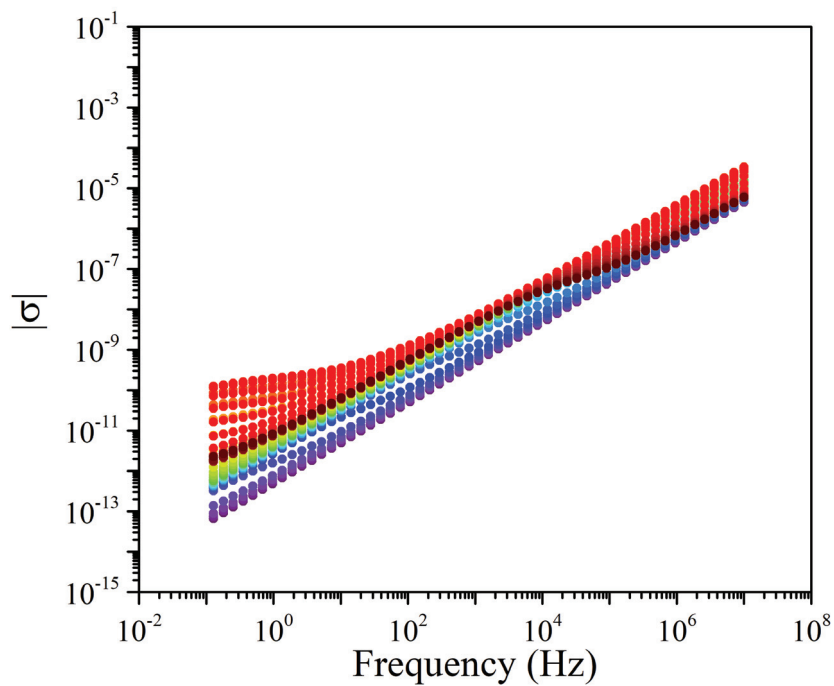


Figure 4.57: Isothermal curves of the module of the complex conductivity ($|\sigma|$) for the sSEBS-Zr10 membrane.

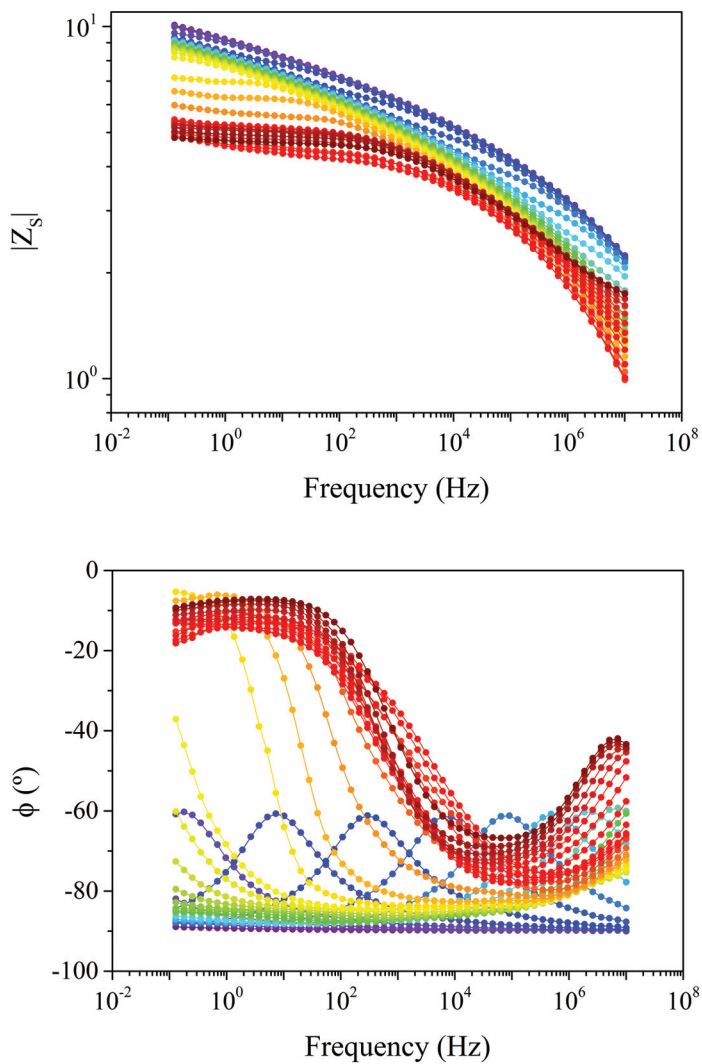


Figure 4.58: Phase angle (ϕ) and modulus of the serial impedance ($|Z_s|$) of the sSEBS-Zr10 membrane.

4.3.12 Analysis of the dielectric spectra of sSEBS-Zr20 membrane

The dielectric spectra was plotted in terms of the real (ϵ') and imaginary (ϵ'') parts of the complex dielectric permittivity (ϵ^*), $\tan \delta$, and the imaginary part of the electric modulus (M'') in Figures 4.59 - 4.60.

In Figure 4.61A the macromolecular origin of the dielectric relaxations is assessed through the Eyring model as derived by Starkweather. Like sSEBS, sSEBS-Zr5, and sSEBS-Zr10, the high values of E_a obtained for the β relaxation reflects a certain degree of cooperativity due to the narrow temperature range where the β and α_{EB} occur. In the same manner than sSEBS-Zr5 and sSEBS-Zr10, the E_a obtained for the α_{PS} relaxation is lower than the one found for both, the β and α_{EB} relaxations. As confirmed by the Arrhenius plot, this result is induced by the plasticisation process that the α_{PS} relaxation undergoes.

In Figure 4.61B displays the Arrhenius plot, where the same relaxation zones (β , α_{EB} , and α_{PS}) exhibited in Figure 4.6.

In Figure 4.62 the isothermal curves of the module of the complex conductivity ($|\sigma|$) for the complete temperature range are displayed.

To determine the proton conductivity, the phase angle and the absolute value of the serial impedance (Z_s) are needed. Thus, both parameters are shown in Figure 4.63.

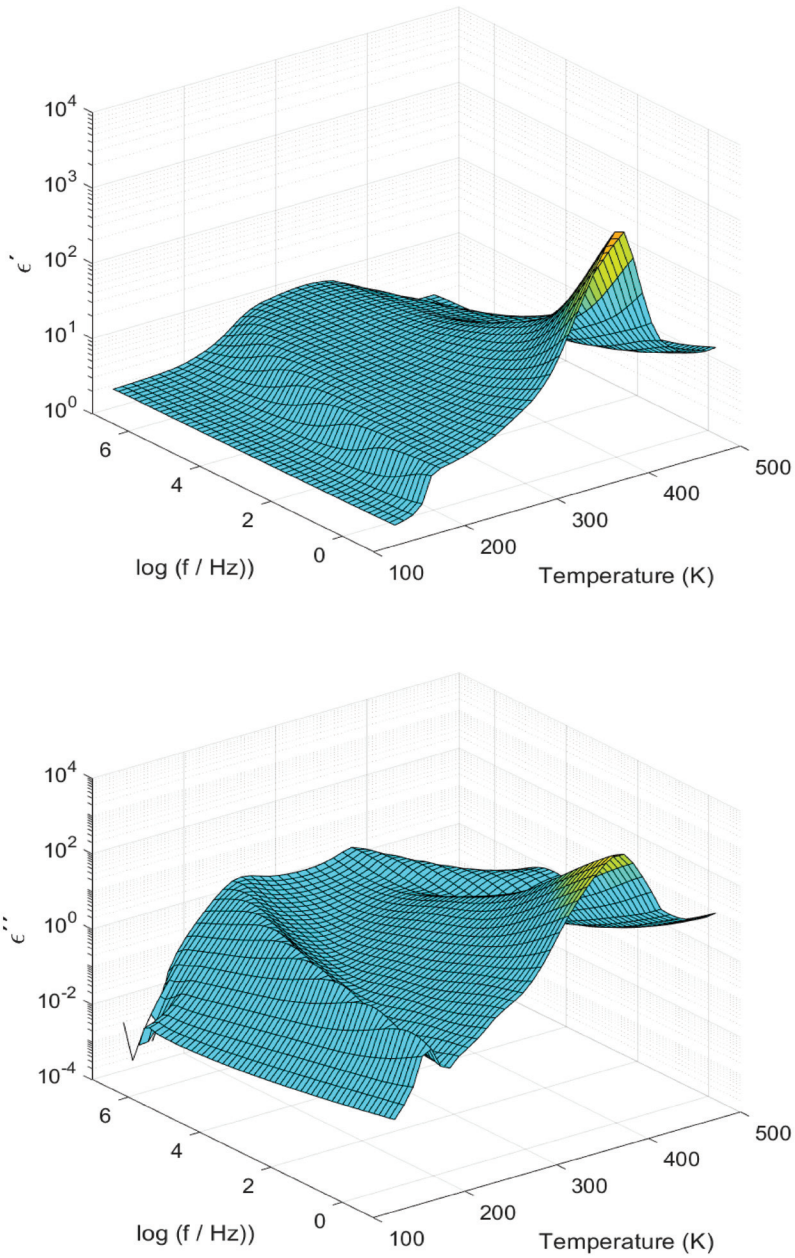


Figure 4.59: 3D plot of the real (ϵ') and imaginary part (ϵ'') parts of the complex permittivity (ϵ^*) of the sSEBS-Zr20 membrane.

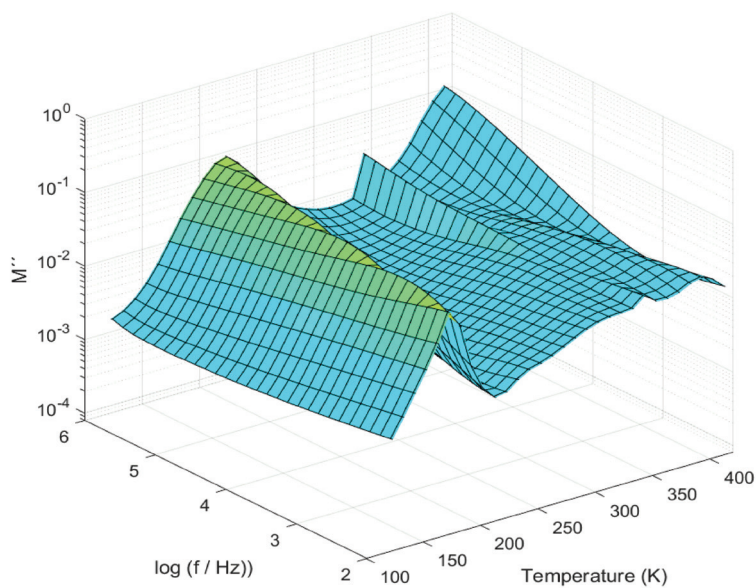
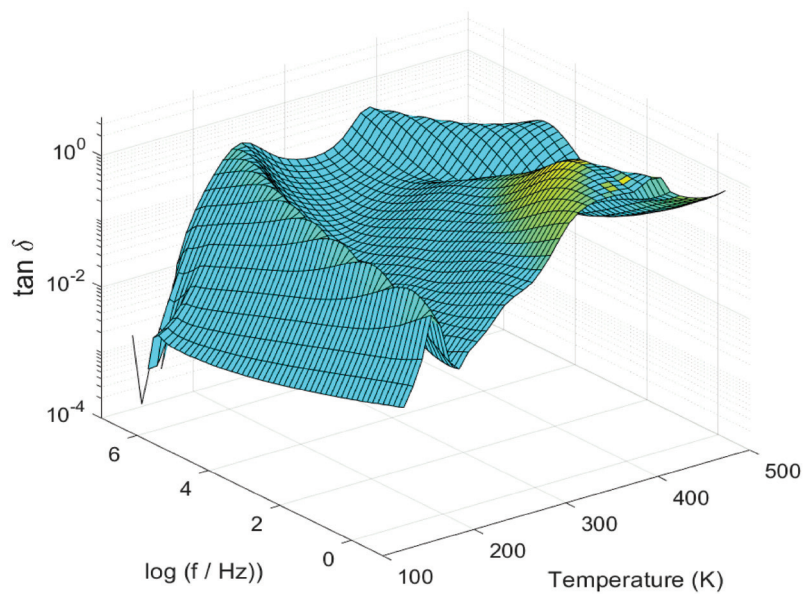


Figure 4.60: 3D plot of $\tan \delta$ and of the imaginary part (M'') of the complex electric modulus (M^*) of the sSEBS-Zr20 membrane.

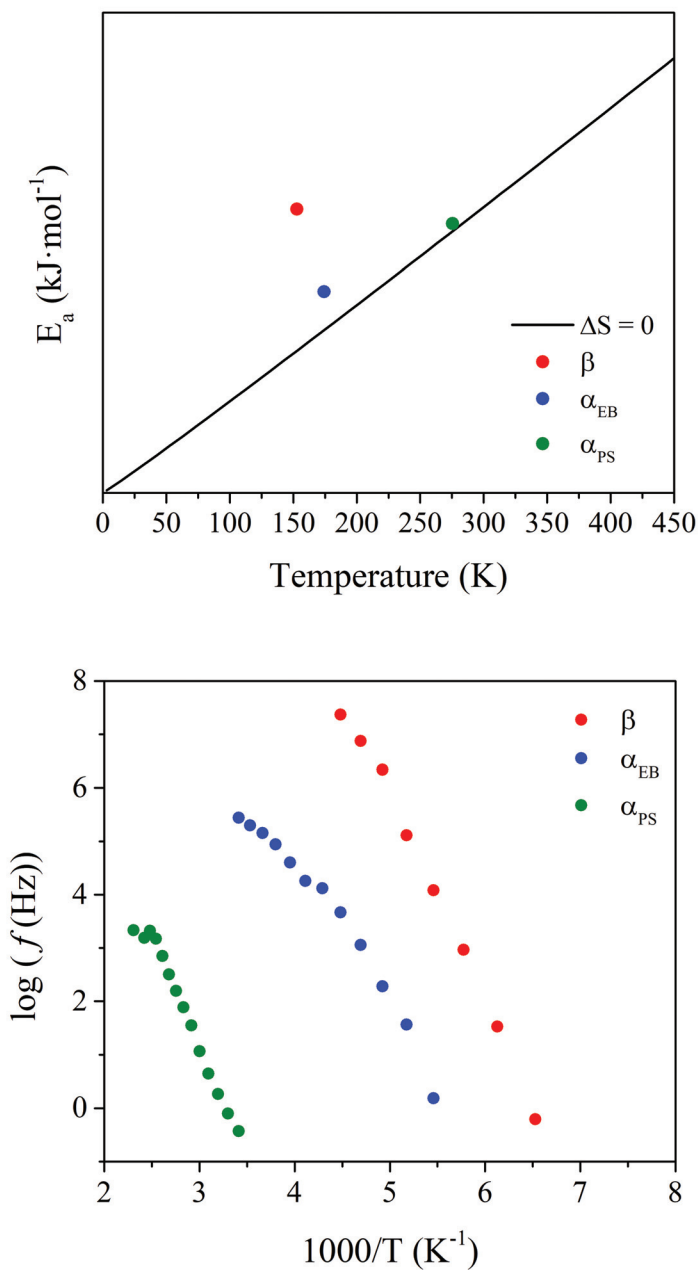


Figure 4.61: (Top) Eyring plot and (Bottom) Arrhenius plot of the sSEBS-Zr20 membrane.

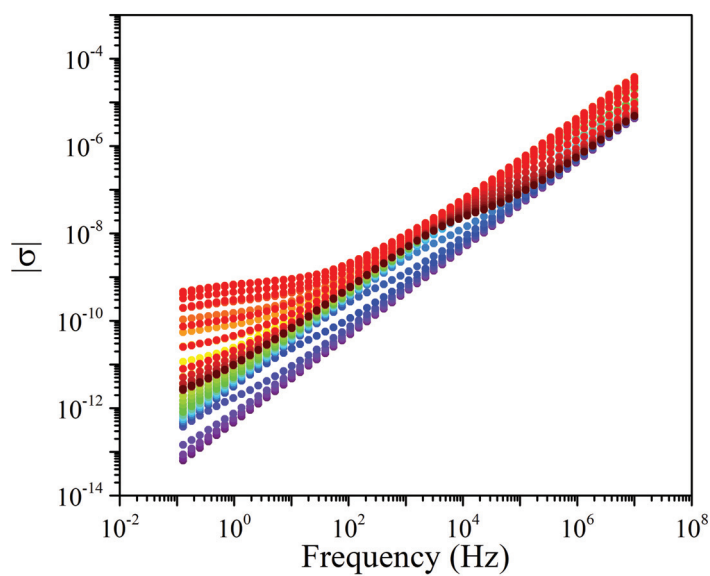


Figure 4.62: Isothermal curves of the module of the complex conductivity ($|\sigma|$) for the sSEBS-Zr20 membrane.

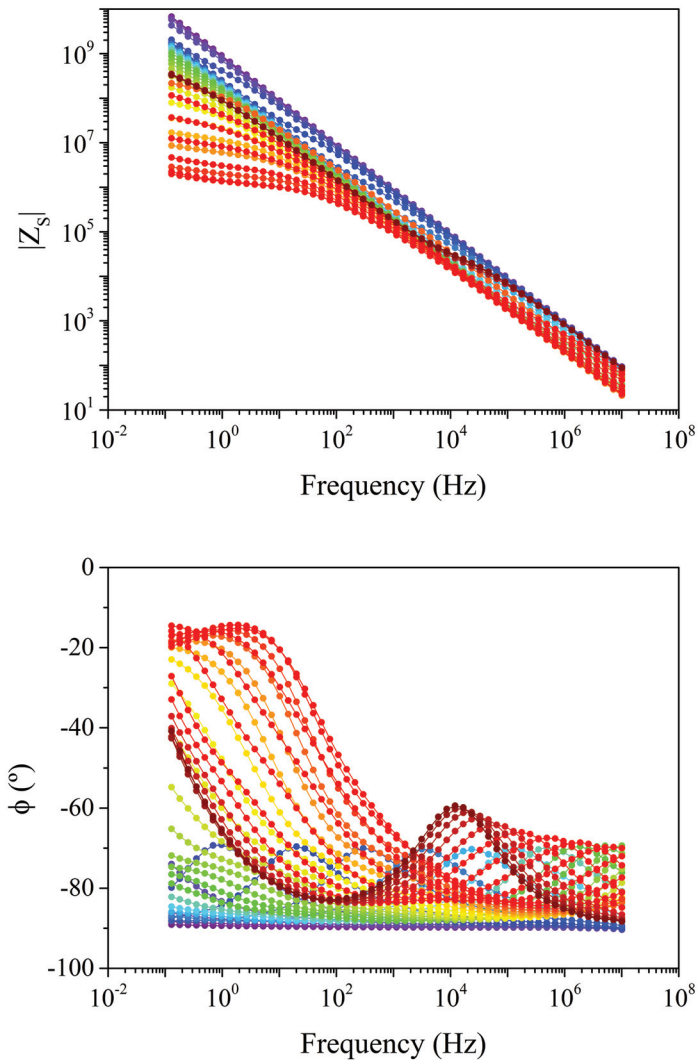


Figure 4.63: Phase angle (ϕ) and modulus of the serial impedance ($|Z_s|$) of the sSEBS-Zr20 membrane.

4.3.13 Analysis of the dielectric spectra of sSEBS-Zr40 membrane

The dielectric spectra was plotted in terms of the real (ϵ') and imaginary (ϵ'') parts of the complex dielectric permittivity (ϵ^*), $\tan \delta$, and the imaginary part of the electric modulus (M'') in Figures 4.64 - 4.65.

In Figure 4.66A the macromolecular origin of the dielectric relaxations is assessed through the Eyring model as derived by Starkweather. The same behaviour as in sSEBS-Zr20 is found. Briefly, like sSEBS, sSEBS-Zr5, sSEBS-Zr10, and sSEBS-Zr20, the high values of E_a obtained for the β relaxation reflects a certain degree of cooperativity due to the narrow temperature range where the β , and α_{EB} occur. In the same manner than sSEBS-Zr5, sSEBS-Zr10, and sSEBS-Zr20, the E_a obtained for the α_{PS} relaxation is lower than the one found for both, the β and α_{EB} relaxations. As confirmed by the Arrhenius plot, this result is induced by the plasticisation process that the α_{PS} relaxation undergoes.

In Figure 4.66B displays the Arrhenius plot, where the same relaxation zones (β , α_{EB} , and α_{PS}) exhibited in Figure 4.6.

In Figure 4.67 the isothermal curves of the module of the complex conductivity ($|\sigma|$) for the complete temperature range are displayed.

To determine the proton conductivity, the phase angle and the absolute value of the serial impedance (Z_s) are needed. Thus, both parameters are shown in Figure 4.68.

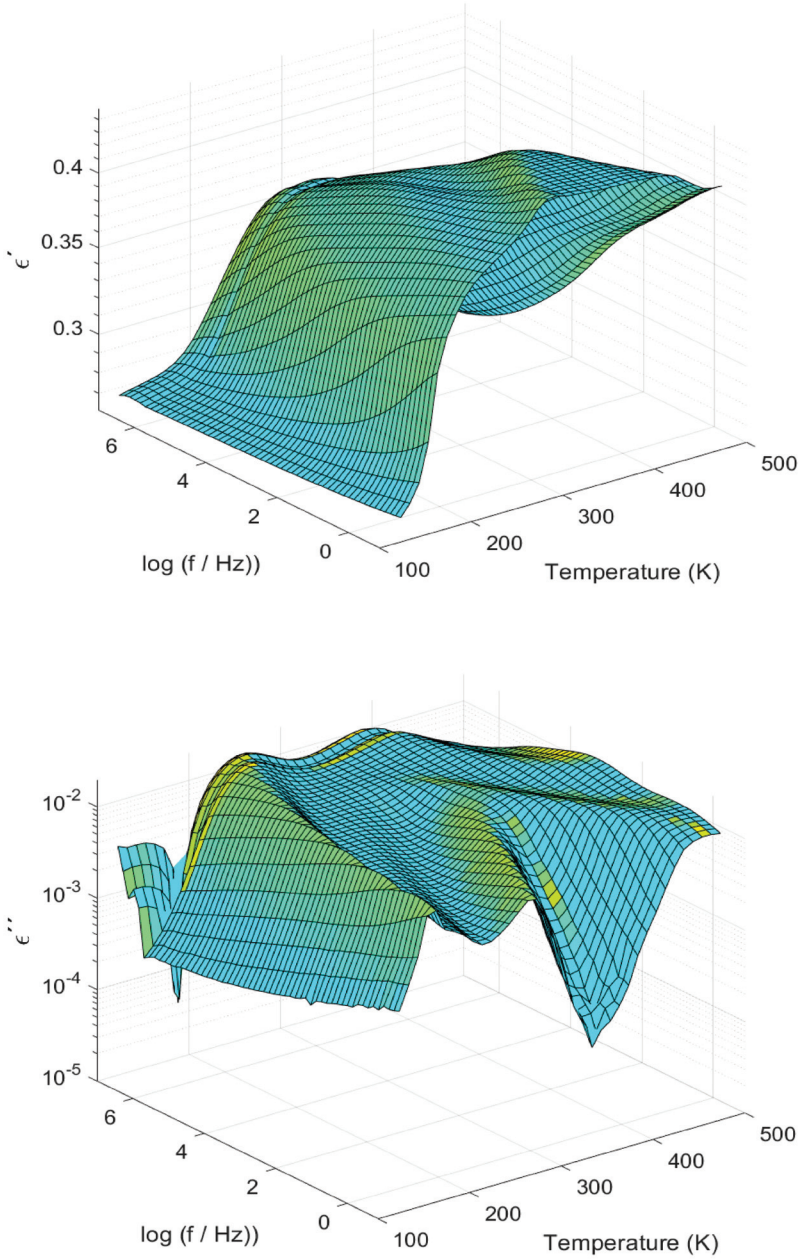


Figure 4.64: 3D plot of the real (ϵ') and imaginary part (ϵ'') parts of the complex permittivity (ϵ^*) of the sSEBS-ZrZr40 membrane.

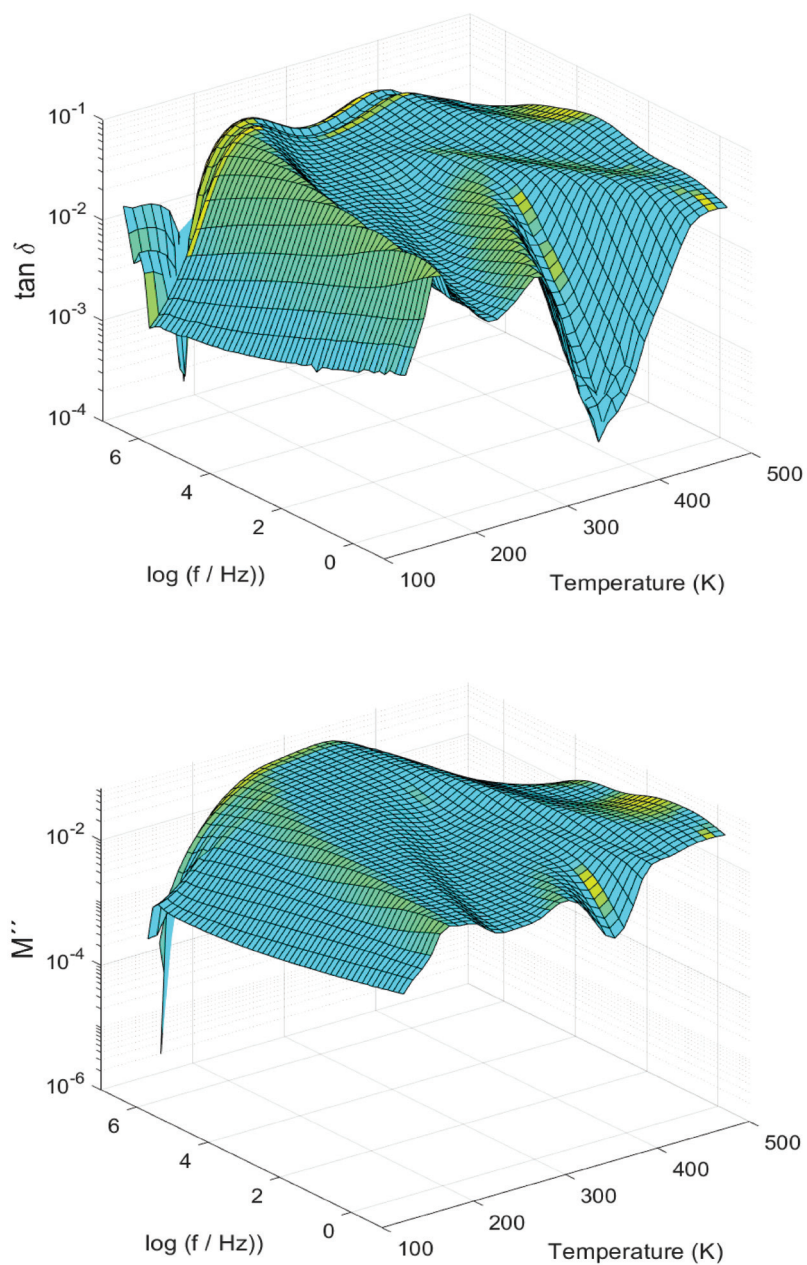


Figure 4.65: 3D plot of $\tan \delta$ and of the imaginary part (M'') of the complex electric modulus (M^*) of the sSEBS-Zr40 membrane.

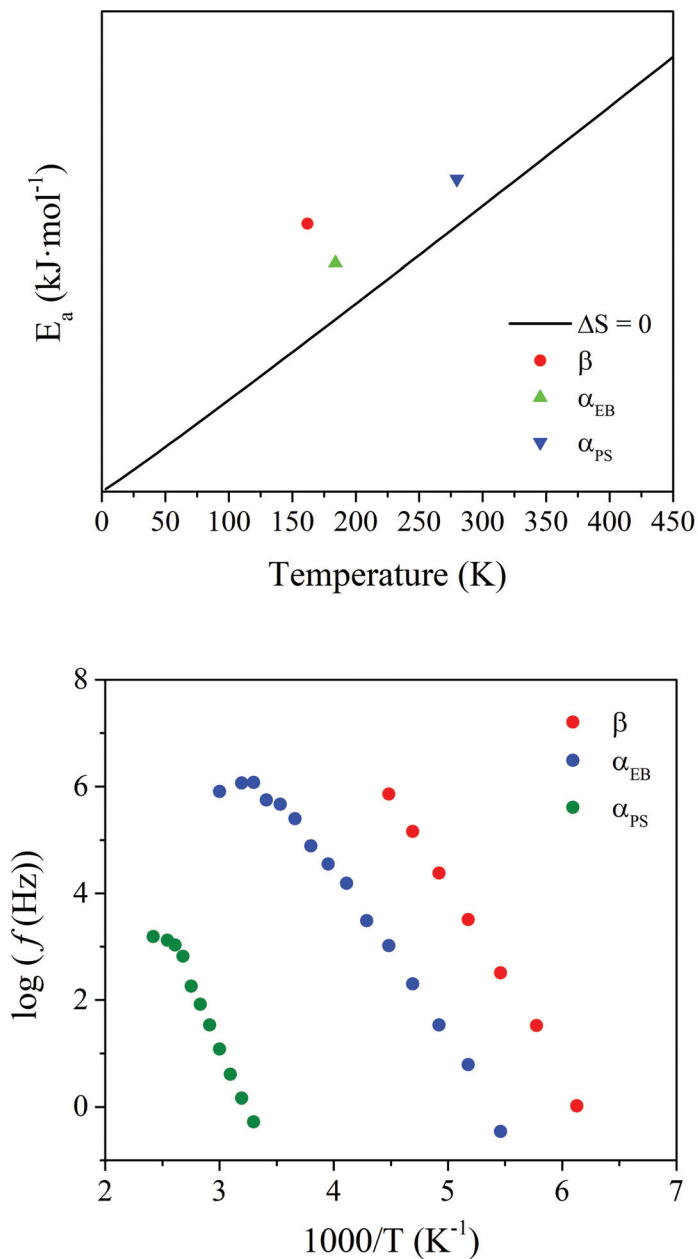


Figure 4.66: (Top) Eyring plot and (Bottom) Arrhenius plot of the sSEBS-Zr40 membrane.

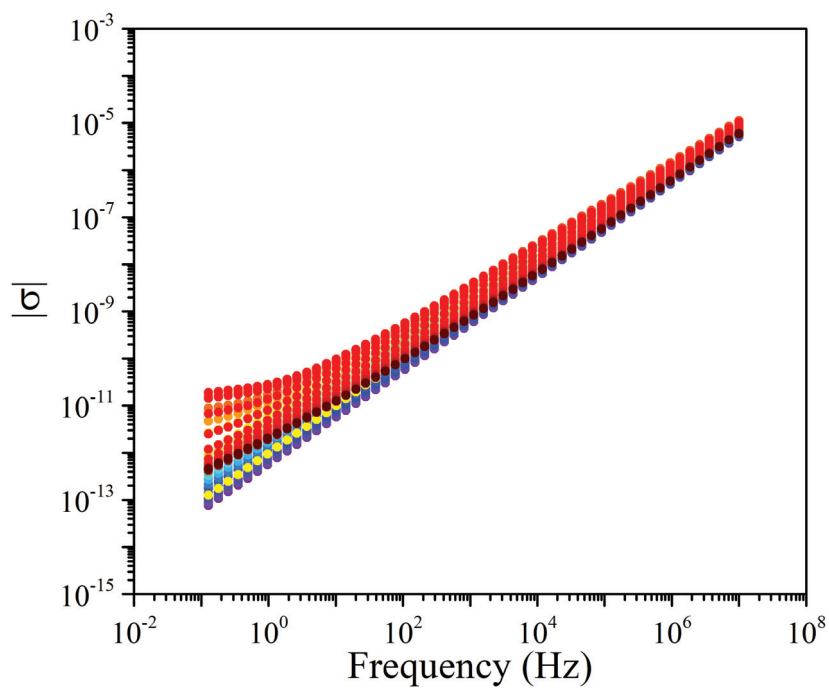


Figure 4.67: Isothermal curves of the module of the complex conductivity ($|\sigma|$) for the sSEBS-Zr40 membrane.

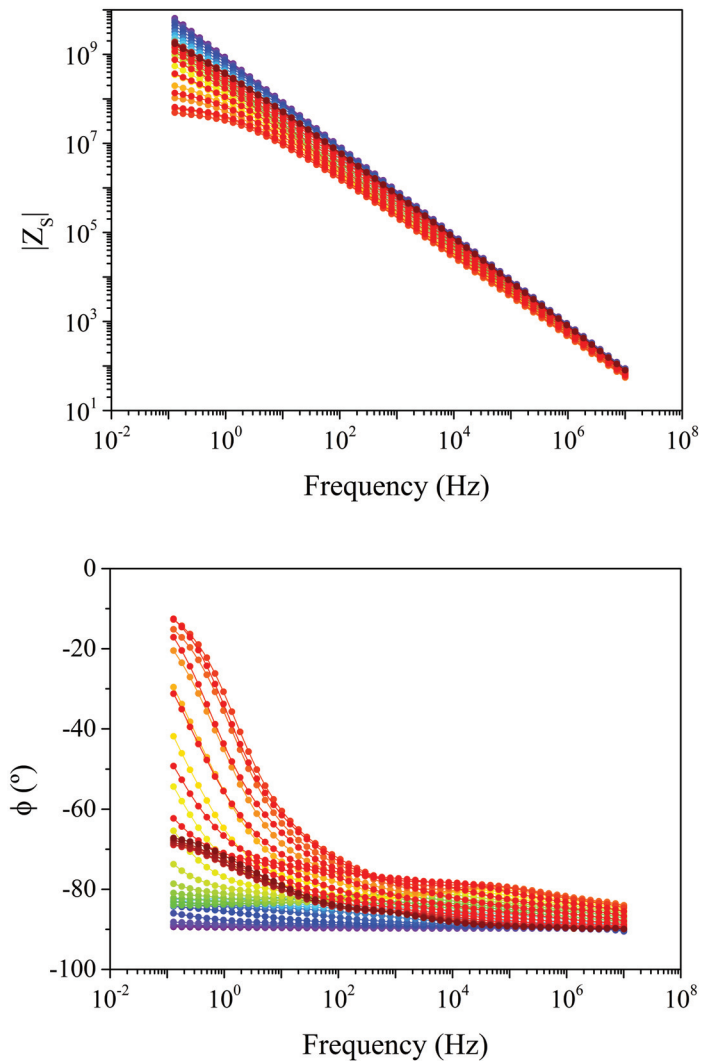


Figure 4.68: Phase angle (ϕ) and modulus of the serial impedance ($|Z_s|$) of the sSEBS-Zr40 membrane.

To conclude, part of the results presented in this section have been published in several scientific peer-reviewed articles (Contributions 2-4) listed in section 9.1, and it complements the discussion of the results included in section 4.4.

4.4 Discussion

4.4.1 Photocrosslinked and post-sulfonated SEBS-DVB membranes

The dielectric spectra of the membranes prepared with styrene-ethylene-butylene-styrene block copolymer (SEBS), mixed with divinylbenzene (DVB), photocrosslinked and subsequently sulfonated with different degrees of sulfonation consists of several relaxation processes that correspond to molecular motions of some atoms of the backbone, lateral chain or glass transition of each block. At higher temperatures and frequencies, external electrode polarization, Maxwell-Wagner-Sillars (MWS) polarization, and conductivity may be observed overlapped to the relaxation spectrum.

A weak relaxation zone at low temperature attributed to β relaxation as resulted from the movement in which participate a number of few atoms from the main or the lateral chain. That is, the reorientation of small angles in relation to the longitudinal axis of the polymer in corresponding poly(ethylene-butylene) (PEB) block.

At higher temperatures, two additional relaxations are observed, which may be related to both components of the block copolymer: ethylene-butylene and styrene. These relaxations are called: α_{EB} and α_{PS} respectively, in an increasing order of temperature.

In accordance, α_{EB} and α_{PS} can be attributed to the glass transition because the temperature peaks of each relaxation are in agreement with the DSC measurement to the poly(ethylene-butylene) (PEB) and poly(styrene) (PS) blocks, respectively.

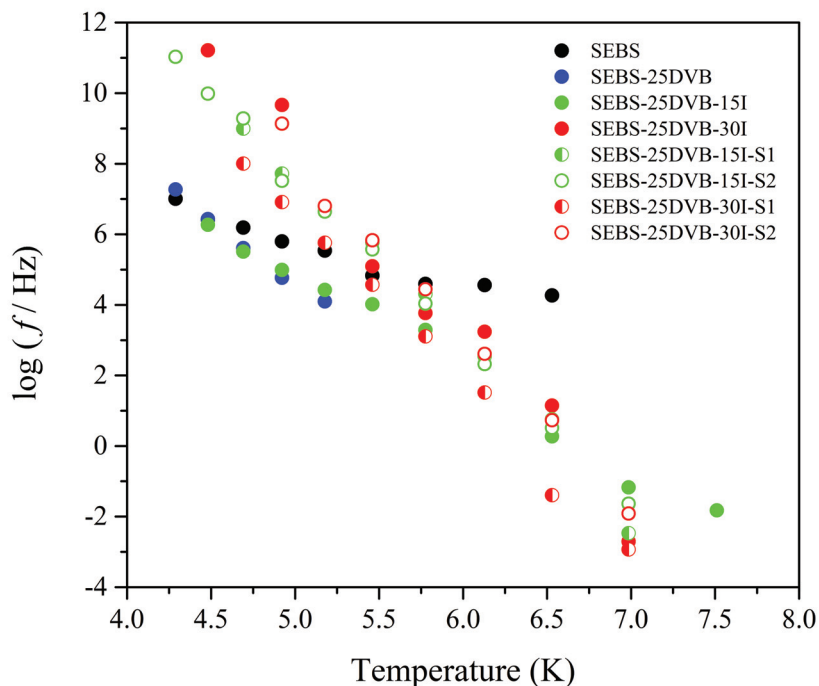


Figure 4.69: Arrhenius map containing the β relaxation for all the photocrosslinked membranes.

Figures 4.69, 4.70, and 4.71 shows the Arrhenius map for all the membranes, where the β , α_{EB} , and α_{PS} relaxation zones are included.

Thermal analysis of the relaxation times: The β relaxation zone.

The zone of β dielectric relaxation appears in the temperature range of 166 - 184 K at the frequency of 1 Hz. This relaxation is observed in the mechanical spectrum, but not all authors have been able to determine it [54].

Figure 4.72 exhibits how the loss dielectric permittivity varies due to the effect of photocrosslinking and subsequent sulfonation. As expected, the reticulation

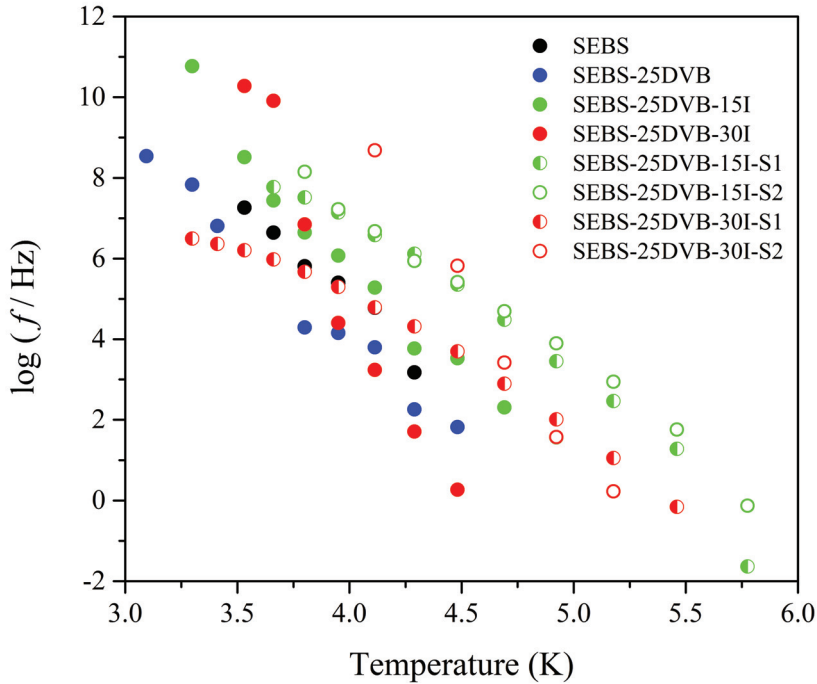


Figure 4.70: Arrhenius map containing the α_{EB} relaxation for all the photocrosslinked membranes.

hinders the molecular movement and the shape of the relaxation widens, due to the different environments of the carbons involved in the movement within the same molecule. However, what really affects the shape of relaxation is sulfonation. The sulfonated copolymers (SEBS-25DVB-15I-S1, SEBS-25DVB-15I-S2, SEBS-25DVB-30I-S1 and SEBS-25DVB-30I-S2) have the same shape and only the SEBS-25DVB-30I-S1 appears at slightly higher temperatures.

The values of the dielectric strength $\Delta\epsilon$ of the β relaxation were also calculated and are displayed in Table 4.2. The strength values increase with the addition of DVB, but decrease with the crosslinking. However, the biggest increment is

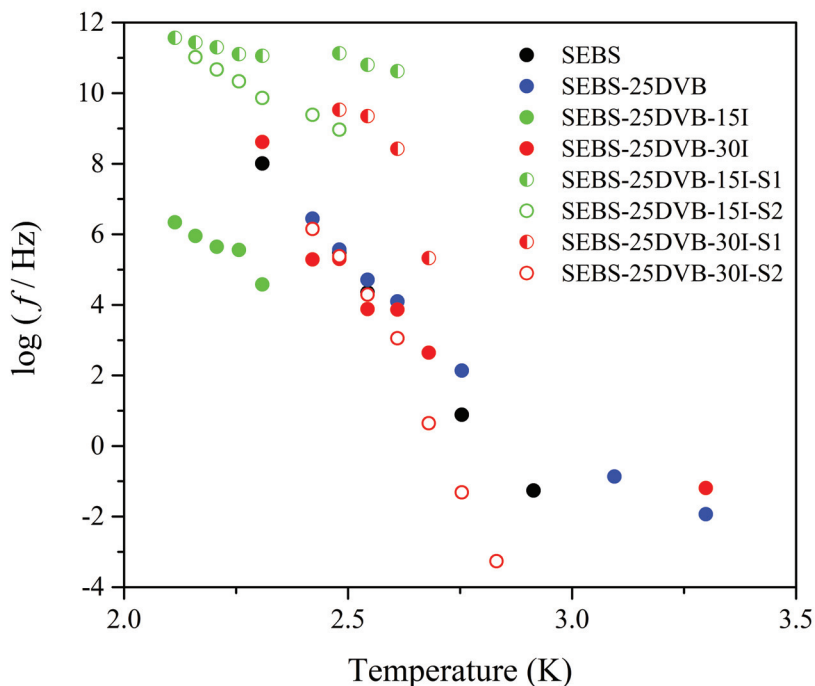


Figure 4.71: Arrhenius map containing the α_{PS} relaxation for all the photocrosslinked membranes.

produced by the sulfonation although these values do not increase linearly. The 25DVB-30I-S1 membrane has a higher value than membranes more sulfonated. This is a significant result that seems to indicate that a lineal increase of the sulfonation does not necessarily imply a linear increase in the number of atoms with the ability to move.

Table 4.3 displays the characteristic parameters of the Arrhenius model for all copolymers. The values of the apparent activation energy E_a obtained for the copolymer SEBS is $23 \text{ kJ} \cdot \text{mol}^{-1}$. When DVB is added to SEBS copolymer the apparent activation energy increases. The value for SEBS-25DVB is 69

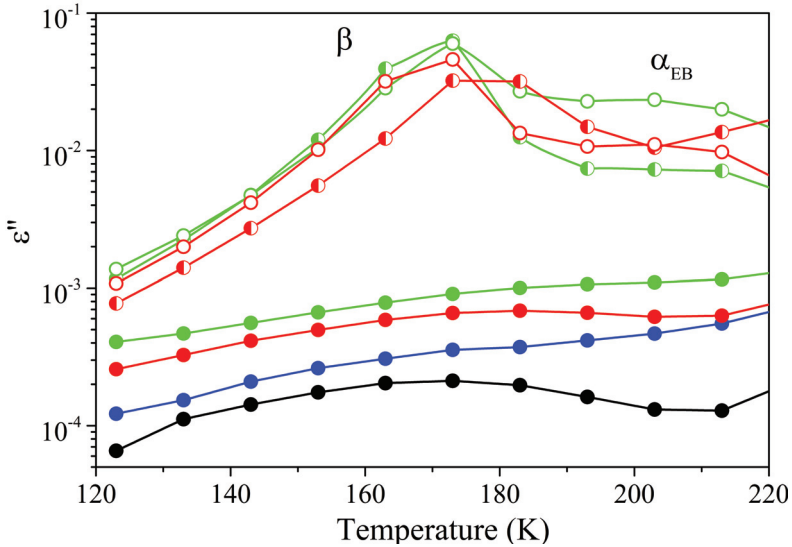


Figure 4.72: Isochronal curves of ε'' for the β relaxation of the photocrosslinked membranes.

$\text{kJ} \cdot \text{mol}^{-1}$. In both cases, these values would be characteristic of the reorientation movements of small angles of the carbons that take part of the chain movement in relation to the longitudinal axis of the polymer. Thus, the β dielectric relaxation would be associated with an intramolecular local mobility of small number of atoms of butylene backbone or lateral ethyl group, which are not affected by the presence of the styrene block phase [55].

All these results indicate that the molecular movement associated with relaxation is a localized movement within the same molecule with a very narrow relaxation time. The crosslinking produces a three-dimensional structure, which maintains the apparent activation energy around $90 \text{ kJ} \cdot \text{mol}^{-1}$ after the sulfonation. However, the sulfonation of the PS block modifies the intensity of the β -relaxation, although this movement occurs in the PEB block.

Table 4.2: Parameters of the dielectric strength of the β relaxation for all the photocrosslinked membranes.

Label	$\Delta\epsilon$		
	153 K	163 K	173 K
SEBS	0.001	0.001	0.002
SEBS-25DVB	0.004	0.006	0.006
SEBS-25DVB-15I	0.002	0.001	0.004
SEBS-25DVB-30I	0.015	0.001	0.009
SEBS-25DVB-15I-S1	0.212	0.183	0.171
SEBS-25DVB-15I-S2	0.140	0.113	0.097
SEBS-25DVB-30I-S1	0.473	0.135	0.147
SEBS-25DVB-30I-S2	0.208	0.161	0.184

Thermal analysis of the relaxation times: The α_{EB} relaxation zone.

The α -relaxation zone is associated with long-range chain segmental mobility of block copolymers, and is possible to distinguish two glass transitions corresponding to each one of the blocks. The dielectric relaxation is caused by the cooperative backbone movements in each of the two phases of segregated block copolymers, and have the peculiar characteristics of each block [54, 56-59]. As the photocrosslinking and the sulfonation have different effect on each relaxation, they were studied separately.

The α_{EB} relaxation peak appears between 225 and 250 K, as shown in Figure 4.73. In this case, significant modifications can be seen due to the photoirradiation or sulfonation of the membranes. The width and the temperature values of α_{EB} relaxation peak increase with the photocrosslinking although it depends on the exposure time. Once the copolymer was sulfonated the loss

Table 4.3: Parameters of the Arrhenius equation of the β relaxation for all the photocrosslinked membranes.

Sample	E_a (kJ · mol ⁻¹)	$T_{\max, 1 \text{ kHz}}$ (K)	R^2
SEBS	23	137	0.932
SEBS-25DVB	69	184	0.996
SEBS-25DVB-15I	54	176	0.993
SEBS-25DVB-30I	103	166	0.987
SEBS-25DVB-15I-S1	92	167	0.995
SEBS-25DVB-15I-S2	89	167	0.999
SEBS-25DVB-30I-S1	93	174	0.997
SEBS-25DVB-30I-S2	97	165	0.996

permittivity value increases significantly and the temperature value of α_{EB} relaxation peak decreases again, but a linear relationship is not established. This behaviour could be interpreted in terms of the heterogeneity of the ethylene-butylene block. Chains form aggregates where predominantly one or the other copolymer prevails and interphase zones must be produced, where the properties of the copolymer vary significantly. The molecular chains of sulfonated membranes start to move at lower temperatures but the SEBS-25DVB-30I-S1 membrane has a particular behaviour, which needs to be analysed.

Table 4.4 shows the $\Delta\varepsilon$ parameter, related to the width α_{EB} relaxation, which increases with the degree of photocrosslinking and with the sulfonation. The SEBS-25DVB-30I-S1 membrane has the lowest values among all the sulfonated membranes.

Table 4.5 displays the characteristic parameters obtained by adjusting the experimental data to the VFTH model. The photocrosslinking reduced the free

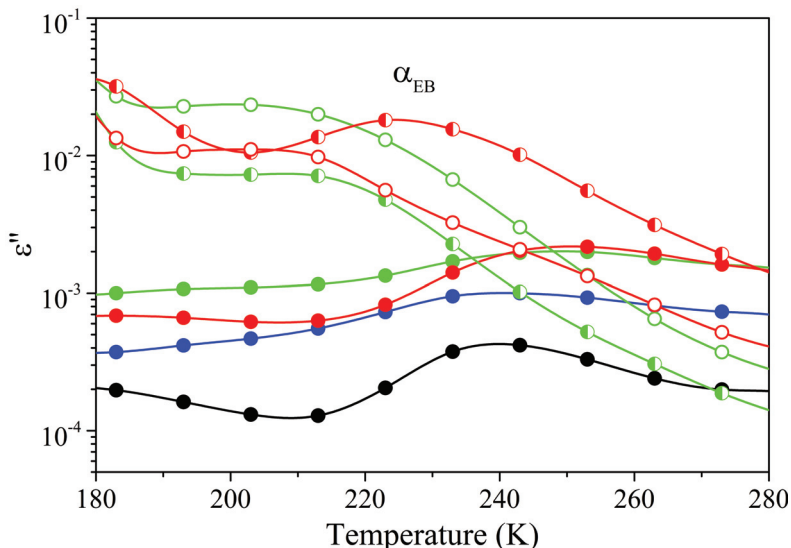


Figure 4.73: Isochronal curves of ε'' for the α_{EB} relaxation of the photocrosslinked membranes.

volume as it was expected. The SEBS-25DVB-30I-S1 membrane has more free volume coefficient than the other sulfonated membranes. These results could be explained due to the PEB domains are coupled by covalent interactions with the PS domains, so that, what happens in the PS domains should affect the PEB domains to some degree. The attachment of SO_3H groups on the PS blocks not only change cohesion in these crosslinked domains but also perturb chain conformations in the PEB region causing a decrease of their T_g . The more free volume, the less energy to overcome the α_{EB} relaxation.

Thermal analysis of the relaxation times: The α_{PS} relaxation zone.

Figure 4.74 shows the ε'' relaxation between 375 and 425 K. The photocrosslinking or sulfonation of the membranes slightly increases the temperature peak. Only the height of the α_{PS} dielectric relaxation progressively increases depending on the exposure time and the degree of sulfonation. The highest values corresponds to SEBS-25DVB-30I-S1 membrane, despite not being the most

Table 4.4: Parameters of the dielectric strength of the α_{EB} relaxation for all the photocrosslinked membranes.

Label	$\Delta\epsilon$		
	223 K	233 K	243 K
SEBS	0.035	0.032	0.003
SEBS-25DVB	0.001	0.001	0.001
SEBS-25DVB-15I	0.006	0.018	0.114
SEBS-25DVB-30I	0.013	0.020	0.023
SEBS-25DVB-15I-S1	0.104	0.117	0.110
SEBS-25DVB-15I-S2	0.177	0.174	0.114
SEBS-25DVB-30I-S1	0.072	0.067	0.068
SEBS-25DVB-30I-S2	0.180	0.055	0.322

sulfonated. This behaviour could be unexpected because SO_3H groups are linked to the phenyl ring of styrene block, and thus, it could be guessed that an increment will be found if the dipole moment per unit volume increases. However, it seems that the phenyl group could add restrictions on PS block if the number of these dipole is high. In addition, the shape of the α_{PS} dielectric relaxation indicates more homogeneity in the styrene block than that observed in the ethylene-butylene block.

Table 4.6 displays the $\Delta\epsilon$ parameters which increase with the degree of photocrosslinking and sulfonation. The SEBS-25DVB-15I-S1 and SEBS-25DVB-15I-S2 membranes have the highest values among all the sulfonated membranes. The reason for the prominent loss was contributed to the strong proton/charge conducting ability of the SO_3H groups on the sulfonated styrene blocks, leading to the dissipation of the charges within the sSEBS.

Table 4.5: Parameters of the VFTH equation of the α_{EB} relaxation for all the photocrosslinked membranes.

Sample	Log f_0 (Hz)	D	T_V (K)	Φ_g/B	$a_f \times 10^4$ (K ⁻¹)	R ²
SEBS	10.14 ± 1.03	4.79 ± 2.41	177.89	0.06	11.73	0.993
SEBS-25DVB	12.54 ± 0.44	7.89 ± 1.38	174.89	0.04	7.26	0.991
SEBS-25DVB-15I	30.39 ± 1.16	68.06 ± 3.88	120.00	0.01	1.22	0.990
SEBS-25DVB-30I	30.36 ± 1.43	61.13 ± 3.84	121.20	0.01	1.35	0.958
SEBS-25DVB-15I-S1	12.62 ± 0.66	14.08 ± 2.89	120.65	0.03	5.87	0.995
SEBS-25DVB-15I-S2	16.49 ± 1.90	52.94 ± 31.85	72.14	0.01	2.62	0.993
SEBS-25DVB-30I-S1	9.59 ± 0.42	13.10 ± 2.62	116.02	0.03	6.58	0.995
SEBS-25DVB-30I-S2	12.87 ± 0.39	17.19 ± 1.97	109.43	0.03	5.31	0.998

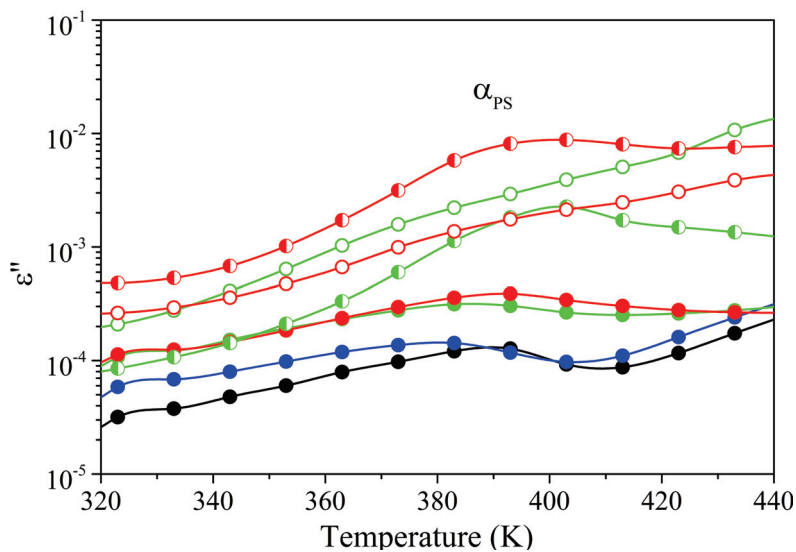
**Figure 4.74:** Isochronal curves of ε'' for the α_{PS} relaxation of the photocrosslinked membranes.

Table 4.6: Parameters of the dielectric strength of the α_{PS} relaxation for all the photocrosslinked membranes.

Label	$\Delta\epsilon$		
	383 K	393 K	403 K
SEBS	0.001	0.001	0.001
SEBS-25DVB	0.002	0.001	0.001
SEBS-25DVB-15I	0.012	0.012	0.010
SEBS-25DVB-30I	0.004	0.005	0.005
SEBS-25DVB-15I-S1	23.51	34.02	48.59
SEBS-25DVB-15I-S2	54.86	53.38	56.27
SEBS-25DVB-30I-S1	0.220	0.701	11.11
SEBS-25DVB-30I-S2	0.012	0.009	0.008

Table 4.7 shows the values of the adjustment parameters to the VFTH model for α_{PS} relaxation. The T_v calculated from the VFTH model for the polystyrene block increases significantly due to photocrosslinking, although it depends on the exposure time. Nevertheless, once the copolymer has been crosslinked, if it undergoes a sulfonation, the T_v value decreases again. Similarly, the coefficient of expansion values increase with crosslinking and decrease with sulfonation, but it is not possible to establish a linear relationship that points out both effects.

A tentative explanation could be related to the increasing restrictions on styrene block motions when rising the number of SO_3H groups which would lead to the formation of a sub-phase at higher sulfonation degrees. This would justify the largest vertical displacement observed between the curves for unsulfonated SEBS and the sulfonated series.

Table 4.7: Parameters of the VFTH equation of the α_{PS} relaxation for all the photocrosslinked membranes.

Sample	Log f_0 (Hz)	D	T_V (K)	Φ_g/B	$\alpha_f \times 10^4$ (K ⁻¹)	R ²
SEBS	19.30	15.81	269.33	0.01	2.35	0.990
SEBS-25DVB	18.44	27.35	210.03	0.01	1.74	0.991
SEBS-25DVB-15I	-	-	-	-	-	-
SEBS-25DVB-30I	10.14	3.95	303.19	0.04	8.34	0.828
SEBS-25DVB-15I-S1	-	-	-	-	-	-
SEBS-25DVB-15I-S2	14.90	3.59	330.84	0.04	8.43	0.996
SEBS-25DVB-30I-S1	16.13	7.60	288.13	0.02	4.57	0.932
SEBS-25DVB-30I-S2	21.81	21.09	259.21	0.01	1.83	0.990

All these results could indicate that the attachment of SO_3H groups to the PS blocks changes the cohesion of the crosslinked domains but also perturbs chain conformations in the PEB region, which have a significant influence on the molecular movement, and consequently, on the relaxation spectrum of each one of these SEBS based membranes.

Assessment of the sample's validity as PEM

In Figure 4.75 the values obtained for the proton conductivity (σ_{Prot}) are shown. The copolymers with a higher degree of photoirradiation present greater protonic conductivity but this does not increase with the degree of sulfonation, since in the copolymers with a higher degree of sulfonation the proton conductivity decreases, which means that an excessive amount of sulfonic groups is not adequate to facilitate proton mobility. In this case, the copolymer with the best proton conductivity is the SEBS-25DVB-30I-S1.

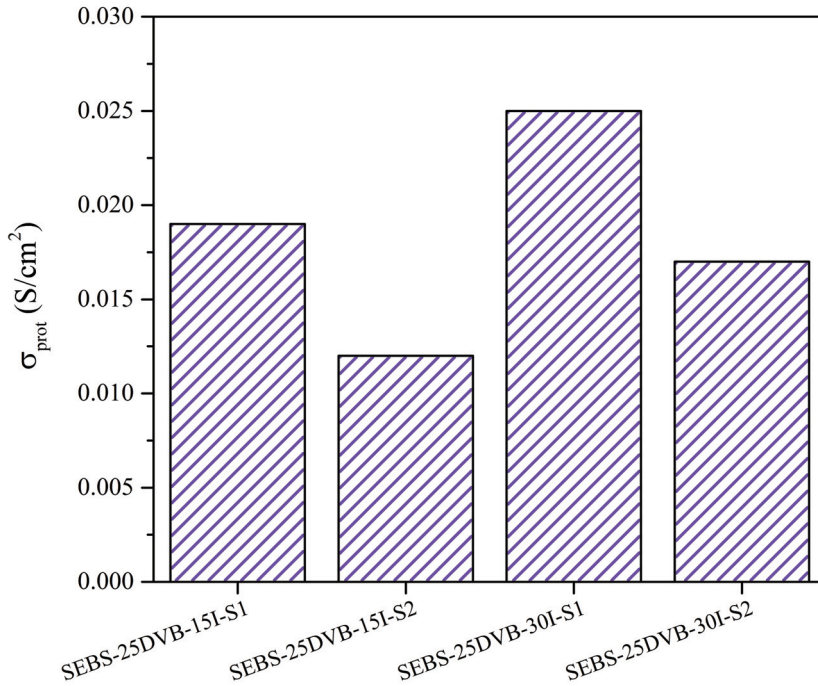


Figure 4.75: Numerically determined proton conductivity (dry) at 333 K for the photocrosslinked sSEBS membranes.

Through-plane proton conductivities of photocrosslinked and post-sulfonated membranes were measured at 333 K and 100% relative humidity in a fuel cell test station connected to a frequency response analyser. Contrary to what initially seemed foreseeable, the membranes subjected to a more intense sulfonation treatment (SEBS-25DVB-15I-S2 and SEBS-25DVB-30I-S2) showed lower conductivity as it is shown in Figure 4.76. These results are in total agreement with those obtained by the dielectric characterization since they had been already predicted a more severe restriction of mobility in the PS block when the number of phenyl groups functionalised with polar groups is considerably higher. This fact again probes that lineal increase of the sulfonation does not

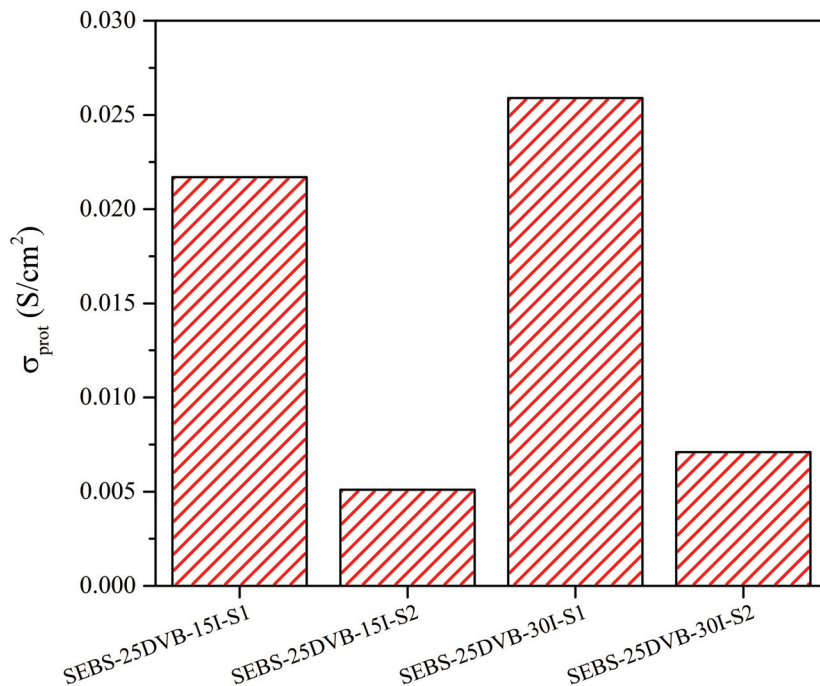


Figure 4.76: Experimentally determined protonic conductivity at 333 K and 100% relative humidity for the photocrosslinked membranes.

necessarily imply a linear increase in the number of atoms with the ability to move. Therefore, the results displayed in Figure 4.75 agree with the ones determined experimentally.

4.4.2 Hybrid sulfonated SEBS membranes

The FTIR spectra is displayed in Figures 4.77 and 4.78. The aim of the measurements is twofold; Firstly, to corroborate that the sulfonation process of SEBS has been successful, and secondly, to confirm that the addition of the inorganic sol-gel component into sSEBS has been properly done.

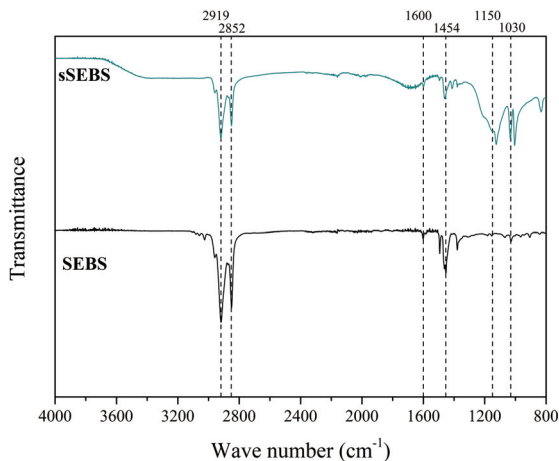


Figure 4.77: FTIR spectra of SEBS and sulfonated SEBS (sSEBS).

In Figure 4.77 the FTIR spectra of SEBS and sSEBS are displayed. In the region from 3150 to 2800 cm^{-1} there are several high intensity peaks attributed to the stretching of the C-H bond. Note that when the sulfonic groups are incorporated, the intensity of the peaks are slightly affected. However, it is in the 1800 - 800 cm^{-1} region where the sulfonation plays a major role. The characteristic bands of SEBS are located at 1600 and 1450 cm^{-1} [61], and are ascribed to the stretching of the phenyl group and the bending of the CH_2 group, respectively. In addition, the sulfonic groups are observed in the region 1150 - 1030 cm^{-1} where the different peaks represent the contribution of the SOH_3^- groups. The fact that the peak located at 1600 cm^{-1} , corresponding to the stretching of the phenyl group, decreases its intensity in the FTIR spectra of sSEBS in combination with the new peak appearing at 831 cm^{-1} , that corresponds to the stretching of the phenyl rings substituted with sulfonic groups [61], confirms that the sulfonation process has been successful.

The FTIR spectra of hybrid sSEBS with different infiltration times between 3600 - 800 cm^{-1} is displayed in Figure 4.78. In the 3150 - 2800 cm^{-1} region two high intensity peaks are observed, which are attributed to the stretching of

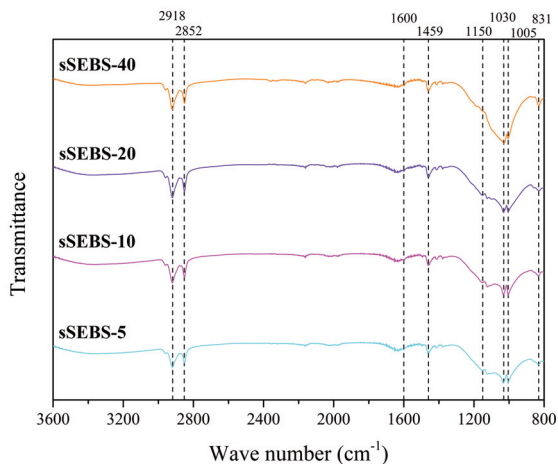


Figure 4.78: FTIR spectra the hybrid sulfonated SEBS.

the C-H bond. Augmenting the infiltration time does not produce a significant variation of the intensity. The peaks located at 1600, 1494 and 1459 cm^{-1} , related to the stretching of the C=C aromatic bonds of PS blocks, maintain its intensity as the infiltration time increments [63]. As previously mentioned, the effect of the sulfonation is observed in the several peaks appearing in the 1150-1030 cm^{-1} range, and more precisely, the two intense peaks located at 1150 cm^{-1} and 1030 cm^{-1} correspond to O=S=O symmetric and asymmetric stretching vibrations of sulfonated groups, respectively [64]. Moreover, the peaks located at the 1200 - 800 cm^{-1} region become broader and increment its intensity as the infiltration time increases due to the formation of M-O-M bonds, being M = Si, P or Zr. Additionally, the peak observed at 831 cm^{-1} is owed to the stretching vibrations of phenyl rings substituted with sulfonic groups at para-position [65]. Therefore, it can be concluded that the addition of the inorganic sol-gel component has been successful.

The obtained thermograms, displayed in Figure 4.79 - 4.81, show the DSC curves for 1st heating, 2nd heating, and the cooling of the neat SEBS, sulfonated

sSEBS, and hybrid sulfonated sSEBS-Zr membranes in the temperature range 273 to 450K.

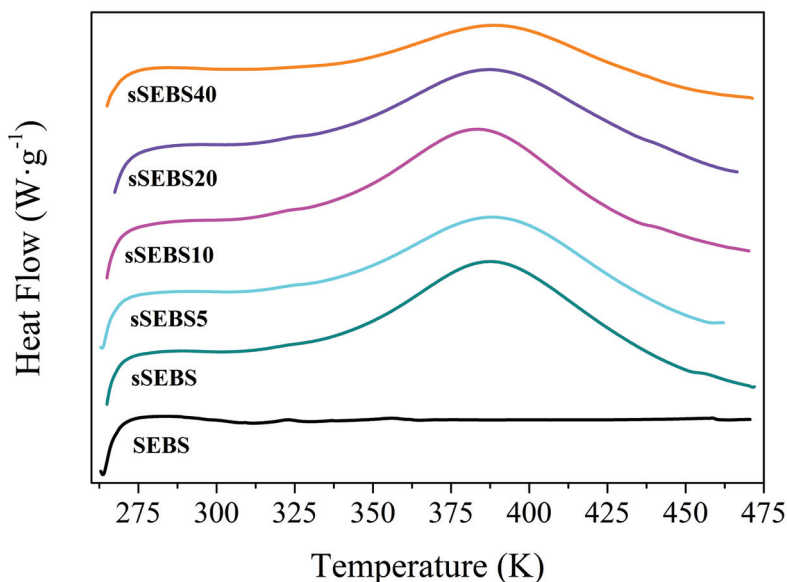


Figure 4.79: DSC thermogram of the 1st heating.

Concerning the hybrid sulfonated membranes, all the samples display the same two endothermic peaks regardless of the infiltration time. The endothermic peak associated with the glass transition of the PS block is mostly unaltered. Only the sSEBS-Zr10 displays a lower value (383K). According to some references, the addition of inorganic fillers related to the infiltration time, can be responsible for lowering the glass transition temperature [64,65].

The thermal stability of sSEBS and hybrid sSEBS-Zr membranes, displayed in Figure 4.82, was assessed through thermogravimetric analysis (TGA). These membranes present a multiple-stage degradation. In general, it is observed that the addition of the inorganic component has an increment in the thermal stability of these membranes. Accordingly, Mistry et al. [66], which analysed

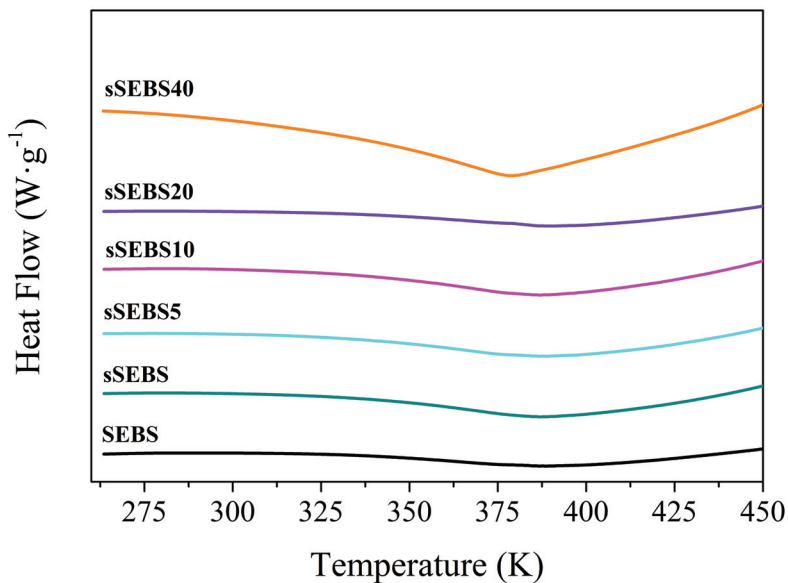


Figure 4.80: DSC thermogram of the cooling.

a series of hybrid membranes formed with sSEBS as matrix and silica as the inorganic filler, found that all hybrid membranes displayed enhanced thermal stability compared with sSEBS. Indeed, the onset of the thermal decomposition was found to increase between 313K to 363K. Accordingly, the results presented in Figure 4.82 show the same tendency. As the infiltration times increase, and therefore more extensive inorganic network is grown across the membrane, the thermal stability increases.

The dielectric spectra of the hybrid membranes display the same dielectric relaxations as in the case of the photocrosslinked and post-sulfonated ones. Consequently, a molecular motion labelled as β was observed at low temperatures. Additionally, due to SEBS microphase separated morphology, the membrane's spectra display several relaxations corresponding to the poly (ethylene-butylene) (PEB) and polystyrene (PS) blocks that were labelled as α_{EB} and

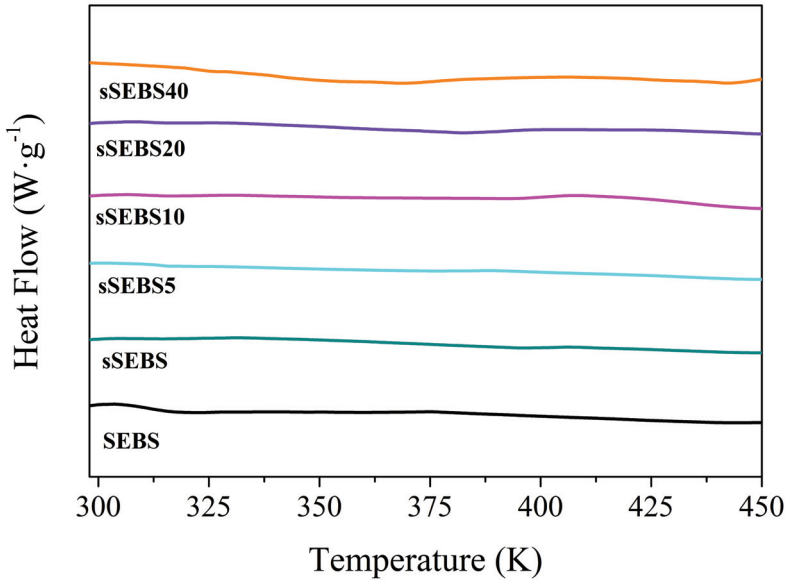
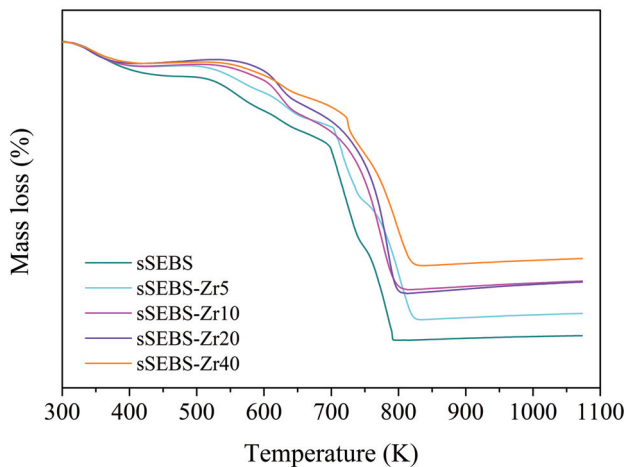


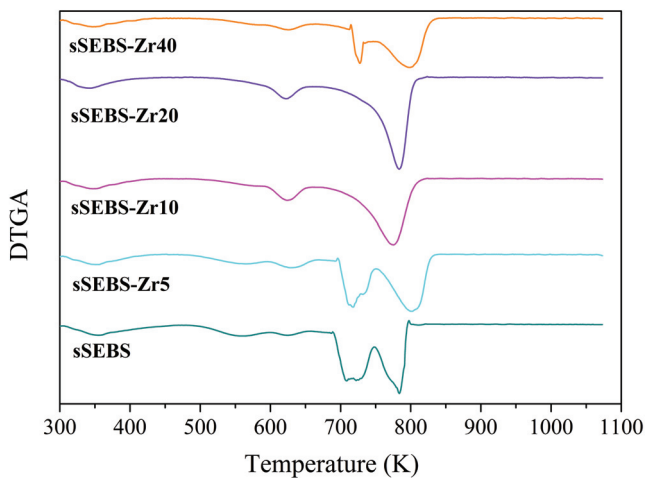
Figure 4.81: DSC thermogram of the 2nd heating.

α_{PS} , correspondingly. The two α relaxations are ascribed to the glass transition of both blocks.

Figures 4.83 - 4.85 displays the Arrhenius plot for all relaxation spectra of the sSEBS and hybrid sSEBS, which shows a more detailed view of the modifications induced by infiltration of $40SiO_2 - 40P_2O_5 - 20ZrO_2$ inorganic filler. The β relaxation gives a linear dependence for the relaxation time τ , thus confirming its non-cooperative nature. However, the α_{EB} and α_{PS} processes show a nonlinear relationship between temperature and relaxation times, characteristic of cooperative molecular motions. Therefore, the molecular motions will be analysed accordingly. The Arrhenius plot confirms the shift mentioned above toward lower frequencies of α_{PS} , which means a more significant plasticising effect caused by the formation of the inorganic network. However, prolonged infiltration does not necessarily observe the plasticising effect. For another



(a) Thermogravimetric curve displaying the weight loss.



(b) Differential thermogravimetric curve.

Figure 4.82: Thermogravimetric curves of sSEBS and all hybrid sSEBS (sSEBS-Zr5, sSEBS-Zr10, sSEBS-Zr20, and sSEBS-Zr40) membranes.

thing, the α_{EB} displays a shift towards higher temperatures characteristic of crosslinked microstructures, but the increment of the infiltration time does not

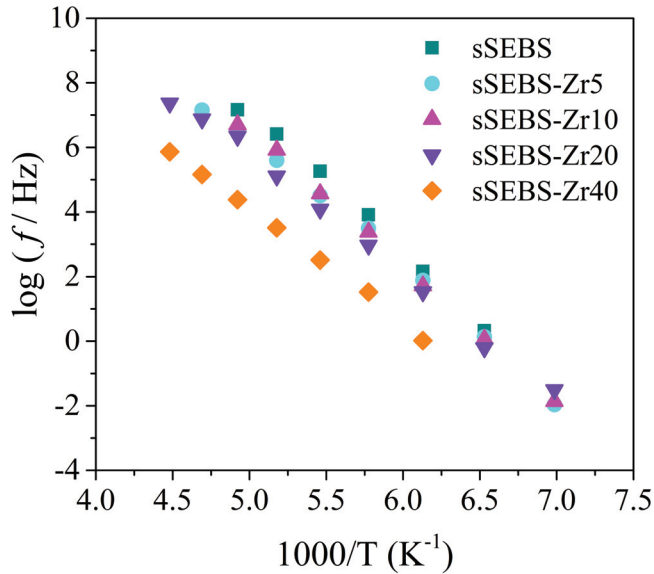


Figure 4.83: Arrhenius map for the sulfonated SEBS (sSEBS) and all hybrid sSEBS (sSEBS-Zr5, sSEBS-Zr10, sSEBS-Zr20 and sSEBS-Zr40) membranes.

have a clear tendency. For instance, the most significant shift is found for the sSEBS-Zr10 membrane. The membranes with 20 and 40 minutes of infiltration display a greater temperature than the sSEBS membrane, but the sSEBS-Zr10 is bigger. Therefore, such behaviour could be ascribed to the existence of an optimum infiltration time, $\tau_{inf} = 10\text{min}$. This time seems to display the right combination between the good values of electric permittivity and adequate cooperative motions of the PS block.

Thermal analysis of the relaxation times: The β relaxation zone.

The β relaxation is a non-cooperative molecular motion that appears at low temperatures, more precisely, in the range of 166 - 184 K at a frequency of 1 kHz. Its origin is still unclear among researchers, as it has always been spotted in the mechanical spectrum but not in the dielectric one. Figure 4.86 exhibits

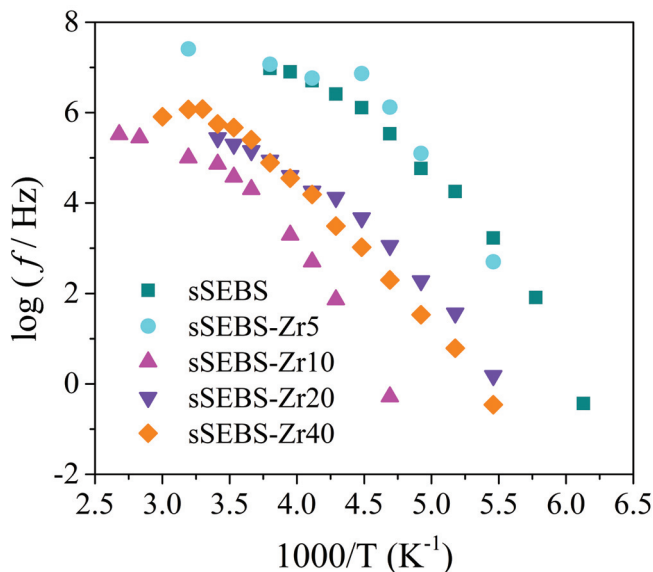


Figure 4.84: Arrhenius map for the sulfonated SEBS (sSEBS) and all hybrid sSEBS (sSEBS-Zr5, sSEBS-Zr10, sSEBS-Zr20 and sSEBS-Zr40) membranes.

the loss of dielectric permittivity at a frequency of 1 kHz of this β relaxation. It was observed that the maximum peak temperature of the sSEBS-Zr5, sSEBS-Zr10 and sSEBS-Zr20 β relaxations shift towards higher temperatures by the effect of the infiltration time. Still, this shift is more significant for the sSEBS-Zr40 relaxation peak.

As expected, as the amount $40SiO_2 - 40P_2O_5 - 20ZrO_2$ filler increases, Si, Zr and P molecules increase; consequently, the resultant oxide network extends along the surface and across the thickness of the membranes as the infiltration time increases. Thus, it takes more energy to excite the molecular motion, and subsequently, the entire relaxation process shifts towards higher temperatures.

Table 4.8 presents the apparent activation energy values E_a , which does not have a clear trend as a function of the infiltration time because they rise until 10 minutes and then decrease again. The strength decreases as the infiltration

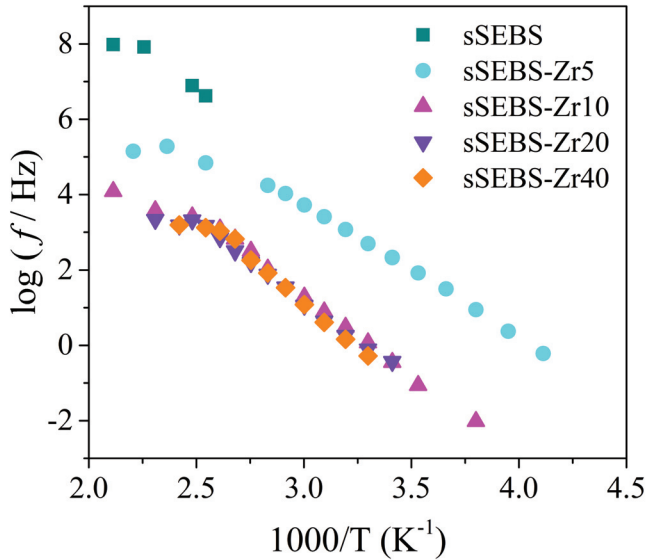


Figure 4.85: Arrhenius map containing the α_{PS} relaxation for the sulfonated SEBS (sSEBS) and all hybrid sSEBS (sSEBS-Zr5, sSEBS-Zr10, sSEBS-Zr20 and sSEBS-Zr40) membranes.

time increases, i.e., a more increasingly extended inorganic network over time. More precisely, sSEBS-Zr10 and sSEBS-Zr20 show similar values. The sSEBS-Zr40 shows the lowest values due to a more extensive deposition of P, Si and Zr oxides net that insulates the membrane, effectively decreasing the conduction of electrons. Consequently, these results imply a diminished number of molecules involved in the motion, which is an expected outcome considering that the electric conductivity diminishes with increasing infiltration time.

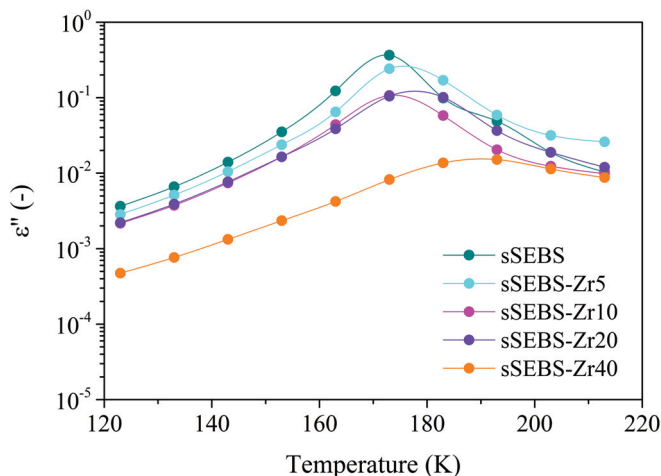


Figure 4.86: Isochronal curves of ε'' of the β relaxation relaxation for the sulfonated SEBS (sSEBS) and all hybrid SEBS (sSEBS-Zr5, sSEBS-Zr10, sSEBS-Zr20 and sSEBS-Zr40) at 1 kHz.

Table 4.8: Parameters of the Arrhenius equation of the β relaxation for the sSEBS and all hybrid sSEBS-Zr membranes.

Sample	Slope	Intercept	Ea (kJ · mol ⁻¹)	R ²
sSEBS	-4.15	27.68	72	0.991
sSEBS-Zr5	-3.87	25.45	74	0.992
sSEBS-Zr10	-4.21	27.59	81	0.999
sSEBS-Zr20	-3.71	24.26	71	0.996
sSEBS-Zr40	-3.50	21.57	67	0.998

Thermal analysis of the relaxation times: The α_{EB} relaxation zone.

Figure 4.87 displays the α_{EB} relaxation peak between 190 and 320 K at a frequency of 1 Hz. The presence of the $40SiO_2 - 40P_2O_5 - 20ZrO_2$ inorganic filler

increases by 30K after 5 minutes of infiltration time. However, after 10 minutes, the maximum temperature peak does not shift. The dynamic crosslinking created by the chemical bonds (M-OH, M-O-M with M = Si, P, Zr) hinders the mobility of the EB block, therefore, incrementing the temperature where the dielectric relaxation occurs.

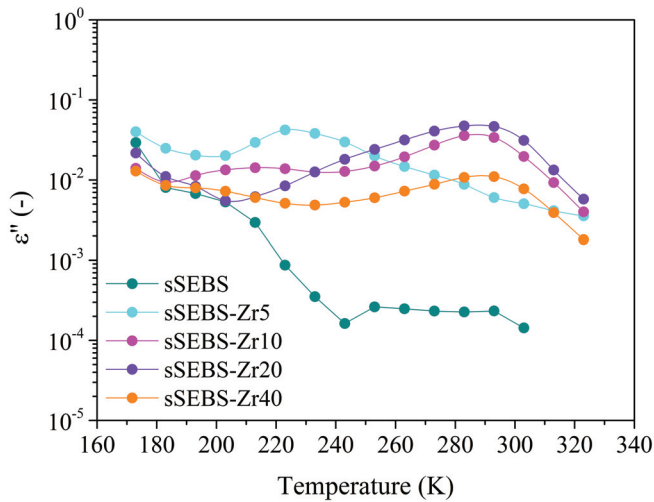


Figure 4.87: Isochronal curves of ε'' of the α_{EB} relaxation relaxation for the sulfonated SEBS (sSEBS) and all hybrid SEBS (sSEBS-Zr5, sSEBS-Zr10, sSEBS-Zr20 and sSEBS-Zr40) at 1 kHz.

Table 4.9 contains the values of the dielectric strength ($\Delta\varepsilon$) for a selected range of temperatures. The distribution of the inorganic filler on the surface and across the membrane generates a coating, which acts as an electric insulator. It is the case, for instance, of the sSEBS-Zr20 and sSEBS-Zr40, where fewer and fewer molecules can reorient with the applied electric field. Subsequently, the strength of the dielectric relaxation decreases significantly.

However, the hybrid membranes sSEBS-Zr show different tendencies when compared between them. The sSEBS-Zr5 has far larger values than the original sSEBS or the other hybrid membranes. This behaviour is explained because

Table 4.9: Parameters of the dielectric strength of the α_{EB} relaxation for the sSEBS and the hybrid sSEBS-Zr.

Label	$\Delta\epsilon$		
	213 K	223 K	243 K
SEBS	0.24	0.17	0.11
sSEBS-Zr5	0.36	0.41	0.44
sSEBS-Zr10	0.13	0.11	0.13
sSEBS-Zr20	0.01	0.05	0.03
sSEBS-Zr40	0.07	0.03	0.06

most of the inorganic network has located at the membrane's surface during a short infiltration time. Thus, these surface charges interact with the applied electric field, thus providing a stronger signal. Furthermore, the sSEBS-Zr10 is the most regular, and the values are not that far from the ones displayed by the sSEBS membrane

Table 4.10: Parameters of the VFTH equation of the α_{EB} relaxation for the sSEBS and the hybrid sSEBS-Zr membranes.

Sample	Log f_0 (Hz)	B (K)	T_{VFTH}	m	R^2
sSEBS	9.79	840.10	127.36	11	0.997
sSEBS-Zr5	8.48	358.98	156.25	7	0.998
sSEBS-Zr10	7.51	2559.87	123.72	5	0.996
sSEBS-Zr20	7.83	874.95	133.25	6	0.998
sSEBS-Zr40	10.01	1590.11	122.88	7	0.988

Table 4.10 contains the parameters for the VFTH model. Accordingly, the free volume coefficient reveals that sSEBS-Zr10 displays the lowest values of the fragility parameter and, accordingly, the strongest behaviour. This is in line with the low variability of the dielectric strength since polymers with lower fragility values can withstand sudden temperature changes, and their structure is not affected by them. This feature translates into a better membrane performance that might suffer temperature changes. On the other hand, the other hybrid membranes also display low values of the fragility parameter, thus, a strong behaviour. In any case, the increment of the infiltration time provides stronger behaviour thanks to the dynamic crosslinking.

Thermal analysis of the relaxation times: The α_{PS} relaxation zone.

The α_{PS} dielectric relaxation is a cooperative molecular motion that occurs at a temperature range from 375 K to 400 K at 1 kHz. Figure 4.88 displays the complex part of the dielectric permittivity. Immediately, it can be observed that the hybrid membranes sSEBS-Zr present higher losses than the sSEBS. The losses increment with the infiltration time is characteristic of the dynamic crosslinking. However, the hybrid membranes sSEBS-Zr40 display the lowest permittivity of the hybrid sSEBS. This result would indicate that the infiltration time cannot be increased continuously to improve the electrical properties of these hybrid membranes precisely due to the electrical insulating effect produced by the extensive deposition throughout the membrane.

Figure 4.88 shows a plasticisation effect. This plasticising effect causes a decrease in its temperature that gives rise to molecular motion related to the glass transition of the styrene phase. It occurs in the range of temperatures at which PEMFCs work. This result may indicate that at these temperatures, the mobility of the ions in the hybrid membranes sSEBS-Zr will be higher than in the only sulfonated membranes sSEBS.

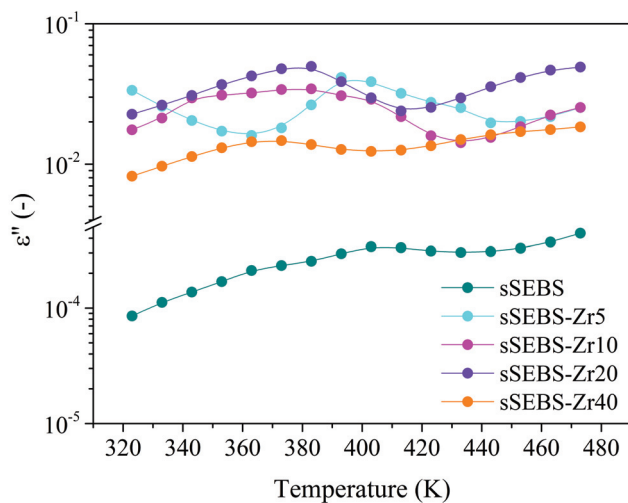


Figure 4.88: Isochronal curves of ε'' of the α_{PS} relaxation relaxation for the sulfonated SEBS (sSEBS) and all hybrid SEBS (sSEBS-Zr5, sSEBS-Zr10, sSEBS-Zr20 and sSEBS-Zr40) at 1 kHz.

Table 4.11: Parameters of the dielectric strength of the α_{PS} relaxation for the sSEBS and the hybrid sSEBS-Zr membranes.

Label	$\Delta\varepsilon$		
	333 K	343 K	353 K
SEBS	-	-	-
sSEBS-Zr5	0.11	0.12	0.12
sSEBS-Zr10	0.10	0.10	0.09
sSEBS-Zr20	0.07	0.07	0.06
sSEBS-Zr40	0.05	0.05	0.04

In Table 4.11 the plasticisation of the α_{PS} is evident because in the spectrum of sSEBS at this temperature range as no presence of this molecular motion. As

in the other cooperative motion, the sSEBS-Zr5 displays larger values thanks to the heterogeneous distribution of the filler. As the infiltration time increases, the values of the dielectric strength diminish. It is expected since it has been shown that a large filler's concentration acts as an electric insulator.

Table 4.12: Parameters of the VFTH equation of the α_{PS} relaxation for the sSEBS and the hybrid sSEBS-Zr.

Sample	Log f_0 (Hz)	B (K)	T_{VFTH}	m	R^2
sSEBS	14.89	1306.05	213.12	51	0.995
sSEBS-Zr5	8.31	4594.06	107.16	10	0.993
sSEBS-Zr10	7.33	2115.3	166.71	7	0.998
sSEBS-Zr20	8.01	818.01	107.78	16	0.988
sSEBS-Zr40	7.85	3074.41	140.19	15	0.991

The values gathered in Table 4.12 show higher fragility parameter values for sSEBS membranes. Nonetheless, the addition of the inorganic filler brings the lowest and strongest behaviour, as the drop registered by the hybrid membranes shows. It agrees with the data presented in the Arrhenius plot and reflects the same tendency observed for the α_{EB} dielectric relaxation.

However, there are no significant differences in the fragility value after infiltration times higher than 20 minutes. The main difference again is shown by the sSEBS-Zr10 membrane, which possesses the strongest behaviour of them all. According to the data presented here, it will withstand better any temperature variation than any of the other membranes. Considering only this parameter, the optimum infiltration time is around 10-20 minutes since it provides acceptable values of electric permittivity and induces dynamic crosslinking to bring closer the glass transitions of both blocks.

Assessment of the sample's validity as PEM

The proton conductivity at 333 K and dry conditions is plotted in 4.89. Regarding PEMFCs, a comprehensive analysis of the molecular mobility and the charge transfer mechanisms is shown to provide consistent data on the performance of a polymer as an electrolyte in a PEMFC.

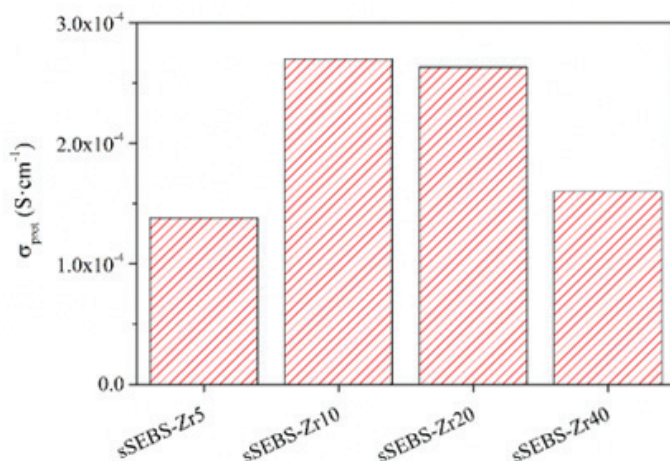


Figure 4.89: Through-plane protonic conductivity (dry) at 333 K for the hybrid sSEBS membranes. Source: [41].

In Figure 4.90 the Arrhenius plot for the σ_{DC} of all the copolymers is displayed. In the mid-temperature region, notable differences among the membranes are found. The reasons behind this change differ between membranes. In the case of the sSEBS-Zr5, ionic conduction always follows the path of least resistance, i.e., the lower energy barrier (E_a). These charges at the surface contribute to reducing the energy barrier and, therefore, explain the decoupling from the relaxation process, as already observed in other polymers [67,68]. Regarding the sSEBS-Zr40, the high concentration of inorganic component implies that the surface is completely coated [69], which acts as an electric insulator.

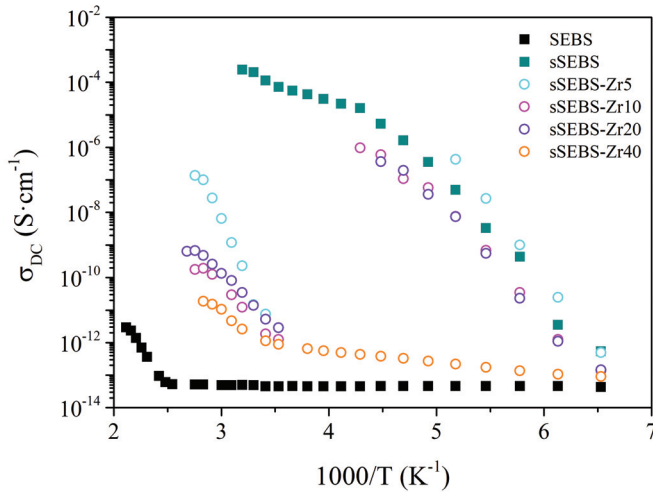


Figure 4.90: Arrhenius plot of the DC conductivity (σ_{DC}) for the neat (SEBS), sulfonated (sSEBS) and hybrid (sSEBS-Zr5, sSEBS-Zr10, sSEBS-Zr20, and sSEBS-Zr40) membranes.

Another significant difference is the shape of the curves. The hybrid membranes present a clear gap between molecular processes that seem to accentuate as the concentration increases. It spreads evenly across the entire depth of the membranes, and a stronger oxygen network delays the activation of the molecular processes.

In the high-temperature region, it is interesting to observe that all the membranes display the same charge carrier mechanism. At these temperatures, cooperative motions are easily activated, and therefore the relaxation process (α_{PS}) is coupled with the ion transferring.

Consequently, the membrane with better performance is the one where the ion diffusivity maintains their coupling with the molecular processes. Thus, it is clear that excessive addition of the inorganic component will induce an excessive amount of M-O-M' bonds, causing a blocking effect for proton transport. The coupling or decoupling from the molecular motions in the charge transfer

mechanisms plays an important role, which is decisive in the behaviour of these membranes when used as electrolytes in hydrogen PEMFC.

4.5 Summary

From the work performed in this chapter the following conclusions are reached:

- The sSEBS spectra shows that in the 1800-800 cm^{-1} region is where the sulfonation plays a major role, and therefore, it confirms that the sulfonation process has been successfully implemented.
- The photocrosslinking and subsequent sulfonation slightly modify the apparent activation energy of the β relaxation. However, the loss dielectric permittivity increases with the degree of sulfonation which is an indication of a light influence of PS block on the movement of PEB chains.
- Significant modifications are produced by the photocrosslinking and sulfonation processes on the α_{EB} relaxation, contrary to what was expected. The molecular chains of sulfonated membranes start to move at lower temperatures. The attachment of SO_3H groups on the PS blocks not only changes cohesion in these crosslinked domains but also perturbs chain conformations in the PEB region.
- The photocrosslinking or sulfonation of the membranes progressively increases the height of α_{PS} dielectric relaxation depending on the exposure time and the degree of sulfonation. It seems that the phenyl group could add restrictions on the PS block if the number of sulfonic groups is high.
- The membrane with more free volume and more molecular mobility (SEBS-25DVB-30I-S1) is the one with the highest proton conductivity. A linear increase of the sulfonation does not necessarily imply a linear increase in the number of atoms with the ability to move.
- Regarding the hybrid membranes, the broadening of the peaks and the increment in its intensity of the region located in the range 1200 - 800 cm^{-1} confirms that the addition of the inorganic sol-gel component has been successful.

- Increasing τ_{inf} induces the α_{EB} relaxation to be shifted towards higher temperatures because the dynamic crosslinking delays this molecular motion.
- Increasing τ_{inf} also affects the α_{PS} relaxation, facilitating the chain motion, and therefore, it is shifted towards lower frequencies and temperatures.
- The analysis of the relaxation times with respect to temperature shows that sSEBS-Zr10 possess the strongest behaviour, resulting in a more thermally stable structure. Therefore, considering the working temperature range of a DMFC, sSEBS-Zr10 will adapt better to any sudden temperature change without notably undermining its performance.
- The assessment of σ_{DC} reveals the presence of three zones where dissimilar behaviours are found. The first zone (Zone I) is located at very low temperatures where only local motions are active. A second zone (Zone II) is located at mid temperatures. sSEBS, sSEBS-Zr10 and sSEBS-Zr20 present a nonlinear relationship with respect to temperature; whereas SEBS, sSEBS-Zr5 and sSEBS-Zr40 have a linear relationship with respect to temperature. A third region (Zone III) is located at high temperatures, where no significant differences are found.
- The through-plane conductivity analysis was done at 60°C, and it shows that the sSEBS-Zr10 is the best performer among the hybrid sSEBS. Therefore, high values of τ_{inf} result in an excessive amount of M-O-M' bonds that generate a competition for the available proton sites.

4.6 References

- [1] L.H. Sperling, Introduction to physical polymer science, John Wiley & Sons, 2005.
- [2] T.P. Lodge, Block Copolymers: Past Successes and Future Challenges, *Macromol. Chem. Phys.* 204 (2003) 265-273.
- [3] H. Hu, M. Gopinadhan, C.O. Osuji, Directed self-Assembly of block copolymers: A tutorial review of strategies for enabling nanotechnology with soft matter, *Soft Matter* 10 (2014) 3867-3889.
- [4] L. Chen, S. Wang, Q. Yu, P.D. Topham, C. Chen, L. Wang, A comprehensive review of electrospinning block copolymers, *Soft Matter*. 15 (2019) 2490-2510.
- [5] H. Feng, X. Lu, W. Wang, N.G. Kang, J.W. Mays, Block copolymers: Synthesis, self-assembly, and applications, *Polymers (Basel)* 9 (2017).
- [6] R.A. Farrell, T.G. Fitzgerald, D. Borah, J.D. Holmes, M.A. Morris, Chemical interactions and their role in the microphase separation of block copolymer thin films, *International Journal of Molecular Sciences* 10 (2009) 3671-3712.
- [7] F.S. Bates, M. a. Hillmyer, T.P. Lodge, C.M. Bates, K.T. Delaney, G.H. Fredrickson, Multiblock Polymers: Panacea or Pandoras Box?, *Science* 336 (2012) 434-440.
- [8] K. Hagita, T. Aoyagi, Y. Abe, S. Genda, T. Honda, Deep learning-based estimation of FloryHuggins parameter of AB block copolymers from cross-sectional images of phase-separated structures, *Sci. Rep.* 11 (2021) 1-16.
- [9] S. Ma, Y. Hou, J. Hao, C. Lin, J. Zhao, X. Sui, Well-Defined Nanostructures by Block Copolymers and Mass Transport Applications in Energy Conversion, *Polymers (Basel)* 14 (2022).

- [10] M. Liu, Y. Qiang, W. Li, F. Qiu, A.C. Shi, Stabilizing the Frank-Kasper Phases via Binary Blends of AB Diblock Copolymers, *ACS Macro Lett.* 5 (2016) 1167-1171.
- [11] C.M. Bates, T. Seshimo, M.J. Maher, W.J. Durand, J.D. Cushen, L.M. Dean, G. Blachut, C.J. Ellison, C.G. Willson, Polarity-Switching Top Coats Enable Copolymer Domains, 338 (2012) 775-779.
- [12] T.W. Park, Y.L. Kang, M. Byun, S.W. Hong, Y.-S. Ahn, J. Lee, W.I. Park, Controlled self-assembly of block copolymers in printed sub-20 nm cross-bar structures, *Nanoscale Adv.* 3 (2021) 5083-5089.
- [13] J.J. Lessard, G.M. Scheutz, S.H. Sung, K.A. Lantz, T.H. Epps, B.S. Sumerlin, Block Copolymer Vitrimers, *J. Am. Chem. Soc.* 142 (2020) 283-289.
- [14] Y. Wang, D.F. Ruiz Diaz, K.S. Chen, Z. Wang, X.C. Adroher, Materials, technological status, and fundamentals of PEM fuel cells A review, *Mater. Today.* 32 (2020) 178-203.
- [15] Y.A. Elabd, M.A. Hickner, Block copolymers for fuel cells, *Macromolecules.* 44 (2011) 1-11.
- [16] A. Alaswad, A. Omran, J.R. Sodre, T. Wilberforce, G. Pignatelli, M. Dassisti, A. Baroutaji, A.G. Olabi, Technical and Commercial Challenges of Proton-Exchange Membrane (PEM) Fuel Cells, *Energies* 14 (2021).
- [17] R. Teruel-Juanes, B. Pascual-Jose, C. del Rio, O. García, A. Ribes-Greus, Dielectric analysis of photocrosslinked and post-sulfonated styrene-ethylene-butylene-styrene block copolymer based membranes, *React. Funct. Polym.* 155 (2020) 104715.
- [18] M.A. Abu-Saied, E.A. El-Desouky, E.A. Soliman, G.A. El-Naim, Novel sulphonated poly (vinyl chloride)/poly (2-acrylamido-2-methylpropane sul-

- phonic acid) blends-based polyelectrolyte membranes for direct methanol fuel cells, *Polym. Test.* 89 (2020) 106604.
- [19] H. Nagar, N. Sahu, V. V. Basava Rao, S. Sridhar, Surface modification of sulfonated polyethersulfone membrane with polyaniline nanoparticles for application in direct methanol fuel cell, *Renew. Energy* 146 (2020) 1262-1277.
- [20] C.A. Edmondson, J.J. Fontanella, S.H. Chung, S.G. Greenbaum, G.E. Wnek, Complex impedance studies of S-SEBS block polymer proton - conducting membranes, *Electrochim. Acta* 46 (2001) 1623-1628.
- [21] R. Teruel-Juanes, B. Pascual-Jose, C. del Río, O. García, A. Ribes-Greus, Dielectric analysis of photocrosslinked and post-sulfonated styrene-ethylene-butylene-styrene block copolymer based membranes, *React. Funct. Polym.* 155 (2020) 104715.
- [22] C. Del Rio, O. Garcia, E. Morales, P.G. Escribano, Single cell performance and electrochemical characterization of photocrosslinked and post-sulfonated SEBS-DVB membranes, *Electrochim. Acta* 176 (2015) 378-387.
- [23] H. Ahmad, S.K. Kamarudin, U.A. Hasran, W.R.W. Daud, A novel hybrid Nafion-PBI-ZP membrane for direct methanol fuel cells, *Int. J. Hydrogen Energy* 36 (2011) 14668-14677.
- [24] H. Ahmad, S.K. Kamarudin, U.A. Hasran, W.R.W. Daud, Overview of hybrid membranes for direct-methanol fuel-cell applications, *Int. J. Hydrogen Energy* 35 (2010) 2160-2175.
- [25] F. Bauer, M. Willert-Porada, Microstructural characterization of Zr - phosphate - Nafion® membranes for direct methanol fuel cell (DMFC) applications, *J. Memb. Sci.* 233 (2004) 141-149.

- [26] D. Dhanapal, M. Xiao, S. Wang, Y. Meng, A review on sulfonated polymer composite/organic-inorganic hybrid membranes to address methanol barrier issue for methanol fuel cells, *Nanomaterials* 9 (2019) 668.
- [27] Y. Huang, T. Cheng, X. Zhang, W. Zhang, X. Liu, Novel composite proton exchange membrane with long-range proton transfer channels constructed by synergistic effect between acid and base functionalized graphene oxide, *Polymer (Guildf)* 149 (2018) 305-315.
- [28] D.S. Kim, H.B. Park, J.W. Rhim, Y.M. Lee, Proton conductivity and methanol transport behavior of cross-linked PVA/PAA/silica hybrid membranes, *Solid State Ionics* 176 (2005) 117-126.
- [29] D.S. Kim, H.B. Park, J.W. Rhim, Y.M. Lee, Preparation and characterization of crosslinked PVA/SiO₂ hybrid membranes containing sulfonic acid groups for direct methanol fuel cell applications, *J. Memb. Sci.* 240 (2004) 37-48.
- [30] H.K. Kim, H. Chang, Organic/inorganic hybrid membranes for direct methanol fuel cells, *J. Memb. Sci.* 288 (2007) 188-194.
- [31] O. V. Lebedeva, E.I. Sipkina, Y.N. Pozhidaev, Hybrid membranes based on silica and 2-hydroxyethylmethacrylate-4-vinylpyridine copolymers, *Pet. Chem.* 56 (2016) 401-405.
- [32] S. Meenakshi, A.K. Sahu, S.D. Bhat, P. Sridhar, S. Pitchumani, A.K. Shukla, Mesoporous-structured-aluminosilicate-Nafion hybrid membranes for direct methanol fuel cells, *Electrochim. Acta* 89 (2013) 35-44.
- [33] A. Pagidi, M.M. Seepana, Synthesis of (Si-PWA)-PVA/PTFE high - temperature proton - conducting composite membrane for DMFC, *Int. J. Hydrogen Energy* 45 (2020) 25851-25861.
- [34] V. Parthiban, S. Akula, S.G. Peera, N. Islam, A.K. Sahu, Proton Conducting Nafion-Sulfonated Graphene Hybrid Membranes for Direct Methanol

- Fuel Cells with Reduced Methanol Crossover, *Energy and Fuels* 30 (2016) 725-734.
- [35] V. Parthiban, A.K. Sahu, Performance enhancement of direct methanol fuel cells using a methanol barrier boron nitride-Nafion hybrid membrane, *New J. Chem.* 44 (2020) 7338-7349.
- [36] C. Ru, Y. Gu, H. Na, H. Li, C. Zhao, Preparation of a Cross-Linked Sulfonated Poly(arylene ether ketone) Proton Exchange Membrane with Enhanced Proton Conductivity and Methanol Resistance by Introducing an Ionic Liquid-Impregnated Metal Organic Framework, *ACS Appl. Mater. Interfaces* 11 (2019) 31899-31908.
- [37] S. Shabanpanah, A. Omrani, M. Mansour Lakouraj, Fabrication and characterization of PVA/NNSA/GLA/nano-silica proton conducting composite membranes for DMFC applications, *Des. Monomers Polym.* 22 (2019) 130-139.
- [38] V. Vijayakumar, D. Khastgir, Hybrid composite membranes of chitosan/-sulfonated polyaniline/silica as polymer electrolyte membrane for fuel cells, *Carbohydr. Polym.* 179 (2018) 152-163.
- [39] Y. Wang, D. Wang, J. Wang, L. Wang, Preparation and characterization of a sol-gel derived silica/PVA-Py hybrid anion exchange membranes for alkaline fuel cell application, *J. Electroanal. Chem.* 873 (2020) 114342.
- [40] Y.P. Ying, S.K. Kamarudin, M.S. Masdar, Silica-related membranes in fuel cell applications: An overview, *Int. J. Hydrogen Energy* 43 (2018) 16068-16084.
- [41] B. Pascual-Jose, C. del Rio, J. Mosa, A. Ribes-Greus, Charge transfer mechanisms in 40SiO₂-40P₂O₅-20ZrO₂ /sulfonated styrene-ethylene-butylene-styrene hybrid membranes for low temperature fuel cells, *Polymer (Guildf)* (2022) 125436.

- [42] S. Havriliak, S. Negami, A complex plane representation of dielectric and mechanical relaxation processes in some polymers, *Polymer (Guildf)* 8 (1967) 161-210.
- [43] S. Havriliak, S. Negami, A complex plane analysis of dispersions in some polymer systems, *J. Polym. Sci. Part C Polym. Symp.* 14 (1966) 99-117.
- [44] J.M. Charlesworth, Deconvolution of overlapping relaxations in dynamic mechanical spectra, *J. Mater. Sci.* 28 (1993) 399-404.
- [45] H.W. Starkweather, Aspects of simple, non-cooperative relaxations, *Polymer (Guildf)* 32 (1991) 2443-2448.
- [46] B. Pascual-Jose, J.D. Badia, A. Múgica, F. Addiego, A.J. Müller, A. Ribes-Greus, Analysis of plasticization and reprocessing effects on the segmental cooperativity of polylactide by dielectric thermal spectroscopy, *Polymer (Guildf)* 223 (2021) 123701.
- [47] H. Vogel, Über die Dissociationswärme und den Einfluss der Temperatur auf den Dissociationsgrad der Elektrolyte, *Zeitschrift Für Phys. Chemie.* 4U (1889) 96.
- [48] H. Vogel, The law of the relation between the viscosity of liquids and the temperature, *Phys. Z.* 22 (1921) 645-646.
- [49] G. Tammann, W. Hesse, Die Abhängigkeit der Viscosität von der Temperatur bei unterkühlten Flüssigkeiten, *Zeitschrift Für Anorg. Und Allg. Chemie.* 156 (1926) 245-257.
- [50] G.S. Fulcher, Analysis of recent measurements of the viscosity of glasses, *J. Am. Ceram. Soc.* 8 (1925) 339-355.
- [51] Q. Qin, G.B. McKenna, Correlation between dynamic fragility and glass transition temperature for different classes of glass forming liquids, *J. Non. Cryst. Solids* 352 (2006) 2977-2985.

-
- [52] J.R. MacDonald, Comparison of the universal dynamic response power-law fitting model for conducting systems with superior alternative models, *Solid State Ionics* 133 (2000) 79-97.
- [53] X. Qian, N. Gu, Z. Cheng, X. Yang, E. Wang, and S. Dong, Methods to study the ionic conductivity of polymeric electrolytes using a.c. impedance spectroscopy, *J. Solid State Electrochem.* 6 (2001) 8-15.
- [54] H. Chen, M.K. Hassan, S.K. Peddini, K.A. Mauritz, Macromolecular dynamics of sulfonated poly (styrene-*b*-ethylene-*ran*-butylene-*b*-styrene) block copolymers by broadband dielectric spectroscopy, *Eur. Polym. J.* 47 (2011) 1936-1948.
- [55] S. Cervený, R. Bergman, G.A. Schwartz, P. Jacobsson, Dielectric α - and β -relaxations in uncured styrene butadiene rubber, *Macromolecules* 35 (2002) 4337-4342.
- [56] A. Kyritsis, P. Pissis, S.-M. Mai, C. Booth, Comparative Dielectric Studies of Segmental and Normal Mode Dynamics of Poly (oxybutylene) and Poly (oxyethylene) - Poly (oxybutylene) Diblock Copolymers, *Macromolecules* 33 (2000) 4581-4595.
- [57] I. Alig, G. Floudas, A. Avgeropoulos, N. Hadjichristidis, Junction Point Fluctuations in Microphase Separated Polystyrene - Polyisoprene - Polystyrene Triblock Copolymer Melts. A Dielectric and Rheological Investigation, *Macromolecules* 30 (1997) 5004-5011.
- [58] R. Lund, L. Willner, A. Alegría, J. Colmenero, D. Richter, Self-concentration and interfacial fluctuation effects on the local segmental dynamics of nanostructured diblock copolymer melts, *Macromolecules* 41 (2008) 511-514.
- [59] C. Lorthioir, A. Alegría, J. Colmenero, B. Deloche, Heterogeneity of the segmental dynamics of poly (dimethylsiloxane) in a diblock lamellar mesophase: dielectric relaxation investigations, *Macromolecules* 37 (2004) 7808-7817.

- [60] H.A. Bolados, M. Hernandez-Santana, L.J. Romasanta, M. Yazdani-Pedram, R. Quijada, M.A. López-Manchado, R. Verdejo, Electro-mechanical actuation performance of SEBS/PU blends, *Polymer (Guildf)* 171 (2019) 25-33.
- [61] F. Müller, C.A. Ferreira, L. Franco, J. Puiggalí, C. Alemán, E. Armelin, New sulfonated polystyrene and styreneethylene/butylene styrene block copolymers for applications in electro dialysis, *J. Phys. Chem. B.* 116 (2012) 1176711779.
- [62] Y.A. Elabd, E. Napadensky, Sulfonation and characterization of poly(styrene-isobutylene-styrene) triblock copolymers at high ion-exchange capacities, *Polymer (Guildf)* 45 (2004) 3037-3043.
- [63] Q. Wang, Y. Lu, N. Li, Preparation, characterization and performance of sulfonated poly(styrene-ethylene/butylene-styrene) block copolymer membranes for water desalination by pervaporation, *Desalination* 390 (2016) 33-46.
- [64] N.S. Karode, A. Poudel, L. Fitzhenry, S. Matthews, P.R. Walsh, A.B. Coffey, Evaluation of interfacial region of microphase-separated SEBS using modulated differential scanning calorimetry and dynamic mechanical thermal analysis, *Polym. Test.* 62 (2017) 268-277.
- [65] W.J. Lee, H.R. Jung, M.S. Lee, J.H. Kim, K.S. Yang, Preparation and ionic conductivity of sulfonated-SEBS/SiO₂/plasticizer composite polymer electrolyte for polymer battery, *Solid State Ionics* 164 (2003) 65-72.
- [66] M.K. Mistry, N.R. Choudhury, N.K. Dutta, R. Knott, Inorganic modification of block copolymer for medium temperature proton exchange membrane application, *J. Memb. Sci.* 351 (2010) 168-177.
- [67] C. Gainaru, E.W. Stacy, V. Bocharova, M. Gobet, A.P. Holt, T. Saito, S. Greenbaum, A.P. Sokolov, Mechanism of Conductivity Relaxation in Liquid and Polymeric Electrolytes: Direct Link between Conductivity and Diffusivity, *J. Phys. Chem. B.* 120 (2016) 11074-11083.

- [68] A. Kisliuk, V. Bocharova, I. Popov, C. Gainaru, A.P. Sokolov, Fundamental parameters governing ion conductivity in polymer electrolytes, *Electrochim. Acta* 299 (2019) 191-196.
- [69] P.G. Escribano, C. del Rio, E. Morales, M. Aparicio, J. Mosa, Infiltration of $40\text{SiO}_2\text{40P}_2\text{O}_5\text{20ZrO}_2$ sol-gel in sSEBS membranes for PEMFCs application, *J. Memb. Sci.* 551 (2018) 136-144.

Chapter 5

Membranes based on nanocomposite & crosslinked polymers

In this chapter the use of nanotechnology along with the consideration of a functionalization and stabilization approach to poly(vinyl alcohol) (PVA) is considered useful for the preparation of cost-effective polyelectrolyte membranes for DMFCs. The crosslinking and sulfonation by the use of SSA enhances the stability and increase the proton-conducting sites in the PVA structure. The presence of GO augments the stability, and remarkably decreases the methanol crossover. Therefore, in Chapter 5, the suitability of a series of nanocomposite and crosslinked PVA-based membranes for fuel cell applications is assessed.

5.1 Introduction

Poly(vinyl alcohol) (PVA) is a polymer that was originally prepared in 1924 by Herman and Haehnel through the hydrolysis of polyvinyl acetate in ethanol with potassium hydroxide.

Provided that the monomer, vinyl alcohol, does not exist in a stable form. Therefore, PVA is synthesized from the hydrolysis of acetate groups by ester interchange with methanol in the presence of anhydrous sodium methylate or aqueous sodium hydroxide [1,2].

Many different degrees of hydrolysis can be obtained as a result of the partial replacement of acetate groups by hydroxyl groups. Moreover, to alter the properties of PVA, abundant hydroxyl groups play an important role. The semicrystalline nature of PVA is due to hydrogen bonding between PVA chains [3].

Concerning commercial PVA production, where different grades are available, vinyl acetate is used as monomer, and PVA is obtained in different grades on the basis of viscosity and degree of hydrolysis [4]. PVA exists in different morphologies for variety of applications including pharmaceutical, biomedical and other [5,6].

The chemical structure of PVA is relatively simple with a pendant hydroxyl group. Figure 5.1 shows the chemical structure of the completely and partially hydrolyzed PVA, that exhibit different properties from each other [4,7].

The physical attributes of PVA, such as density, crystallinity, film formation, water solubility, molar volume, degree of polymerization, etc., depend upon the degree of hydrolysis, crystal precipitation, molecular mass and moisture. PVA is flexible, strong and hard, and possesses oxygen/aroma barrier properties. To prevent any PVA disruption in gas permeability, moisture must be avoided. Moreover, PVA is an excellent insulator, reaching conductivity values

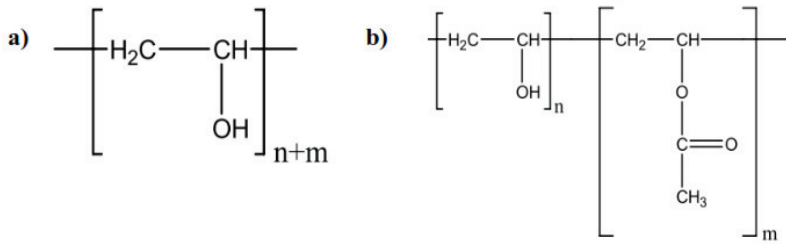


Figure 5.1: Chemical Structure of PVA: (a) completely hydrolyzed and (b) partially hydrolyzed. Source: [10].

of $10^{-10} \text{ S} \cdot \text{cm}^{-1}$. It is also a water-soluble polymer being considered biocompatible and biodegradable.

Physical modification of PVA is possible through several processes [4]. For instance, different physical, mechanical, chemical, and optical properties of PVA can be tuned using a variety of nanofillers. Indeed, Ahn et al. investigated PVA as reducing agent in graphene oxide (GO) dispersion. The patterns of reduced graphene oxide (RGO) nanosheets at different contents of PVA were verified through advanced analytical techniques. This decrease in reduction temperature could allow GO to be used in soft electronics [8]. Furthermore, crosslinking is needed to provide chemical stability to PVA in hydrophilic environments due to its high water solubility.

5.1.1 PVA-based membranes for fuel cells applications

Membranes based in poly(vinyl alcohol) (PVA) have been reported with high potential for proton exchange polyelectrolytes, as it is a cost-effective and widely available polymer, with great functionalization possibilities and known to be a good methanol barrier, hence being a good candidate to tackle the crossover phenomena that negatively affects DMFC performance [7,9]. Nevertheless, pure PVA has no proton conductivity, and thus, its structure is modified in order to enhance proton transport. Furthermore, improving its

mechanical strength and reduce its high water solubility are also desired characteristics that are sought after when fine-tuning the chemical structure of pure PVA. Accordingly, modifications can be done directly or via copolymerization.

Direct modification of PVA

Pure PVA can be directly modified with suitable sulfonating agents such as concentrated sulfuric acid, sulfoacetic acid, chlorosulfonic acid or propane sulfone in order to promote proton conductivity by attachment of sulfonic acid groups ($-SO_3H$) as side chain groups to the polymer backbone [10,11].

Modification of PVA by copolymerization

To obtain three dimensional networks in PVA membrane structure in order to improve its dimensional stability as well as its thermal and mechanical properties, the crosslinking method can be used [12]. However, this methodology must be used carefully, given that an excessive crosslinking degree increases the brittleness of the membrane reducing its mechanical properties. Hence, it is needed to reach a certain degree of compromise between both variables. Additionally, the introduction of proton-conducting groups, such as sulfonic acid groups, into PVA structure can be done through crosslinking reactions using sulfonated crosslinking agents. The different methods commonly used to crosslink PVA are:

- *Crosslinking by irradiation:* crosslinking reactions can be carried out through electron beams or γ -radiation. When PVA is irradiated, H- and OH- radicals arise from water molecules and react with PVA resulting in polymer radicals. These polymer radicals may interact between them by disproportion, and combination through inter- and/or intra- molecular crosslinking, giving a 3D polymer network.
- *Chemical crosslinking:* A variety of chemical crosslinking agents such as sulfosuccinic acid (SSA), poly(acrylic acid) (PAA) and glutaraldehyde

(GA) have been employed to form PVA network membranes. When an aldehyde (GA) is used as a crosslinking agent in acidic conditions, the hydroxyl groups of the PVA react with the aldehyde via acetal bond formation. While when carboxylic acid agents are used (SSA, PAA), an esterification reaction occurs between the alcohol groups of PVA and the carboxylic acid groups of the crosslinking agent.

Modification by blending

Polymer blend technology may represent a versatile approach to improve the properties of the PVA-based membranes. The miscibility of two polymers can be effectively improved by favouring specific interactions between their chains, such as hydrogen bonding, ion-dipole and ionic interactions, which can act as an efficient crosslinking agent of the blend, modifying its mechanical and swelling properties [13]. Acid and basic polymer blends, known as acid-base polymers, are commonly used as PEMs. The hydrogen bonding bridges and electrostatic interactions between acid and base polymers contribute notably to control the swelling of the membrane without a decrease in flexibility [13,14]. Therefore, membranes with high mechanical and thermal properties, low water uptake, reduced methanol crossover and high electrochemical performance can be obtained by polymer blending. PVA-based polymer blends have been prepared with a widely variety of sulfonated polymers like sPEEK, Nafion, poly(styrene sulfonic acid) (PSSA) and poly(2-acrylamido-2methylpropane sulfonic acid) (PAMPS) [13,15,16].

Composites with PVA

One of the most attractive alternatives to improve the performance of PVA membranes in fuel cell applications is the preparation of composite membranes. A polymer composite is defined as a multiphase system consisted of an organic polymer matrix reinforced with a filler [17,18]. The simplest method for the preparation of polymer composites is the blending method in which the filler

is directly mixed with the polymer matrix. The mixing can be done by melt blending or solution blending. The incorporation of filler into a polymer matrix strongly influences the original characteristics of the polymer, due to the strong interfacial interactions between the filler and the polymer matrix. The final properties of the polymer composites depend on the type (inorganic or organic), size and shape of filler that is incorporated, and the filler concentration and interactions with the polymer matrix [19]. The combination of inorganic fillers into organic polymer membranes improves the mechanical properties, the water uptake and the proton conductivity of the composite membrane whereas also suppresses methanol crossover by increasing the transport pathway tortuosity [12].

5.1.2 PVA-based composite membranes with graphene oxide (GO)

Graphene oxide (GO) is an amphiphilic material with a two-dimensional laminated structure which contains oxygen functional groups in its structure such as epoxy and hydroxyl groups on the basal plane, and carboxylic acid groups along the sheet edge according to the Lerf and Klinowski model [20,21], as shown in Figure 5.2.

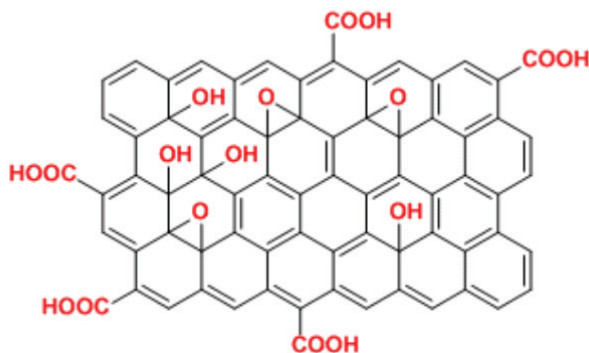


Figure 5.2: Chemical structure of graphene oxide (GO) proposed by Lerf and Klinowski. Source: [20,21].

GO is one of the most attractive inorganic nano-filler to prepare PVA-based composite membranes since is easy to disperse in polar polymers due to the oxygen functional groups contained in its structure. Moreover, its unique structure with high surface area, high mechanical strength, and electric insulating properties promote the formation of proton transport channels through the membrane, while simultaneously acting as a methanol barrier reducing the drawback of crossover [22,23].

In order to increase the proton conductivity of composite PEMs, the reactive oxygen functional groups of GO including epoxy, hydroxyl and carboxylic acid groups can be chemically modified [24]. Sulfonation is one of the most popular alternatives that are used for GO modification. The introduction of sulfonic acid groups ($-SO_3H$) in the structure improves the interfacial adhesion between the polymer and the filler and enhances the proton conductivity compared to those composite membranes prepared with GO. Direct sulfonation of GO by covalent attachment of sulfonic acid-containing aryl radicals has been extensively reported, resulting in a significantly improved proton conductivity at low levels of hydration [10, 25-30]. In Figure 5.3 the chemical structure of sulfonated graphene oxide (sGO) obtained by modification with aryl radicals is displayed. Therefore, the modification of GO by direct sulfonation seems an attractive strategy to enhance the mechanical and proton-conducting properties of composite membranes for fuel cell applications.

5.1.3 PVA/SSA/GO membranes

The combination of PVA and sulfosuccinic acid (SSA), may increase the mechanical properties, diminish swelling related problems and endorse dimensional stability to the polymer matrix [31]. Therefore, the work performed in Chapter 5 is the evaluation of the performance of a series of nanocomposite and crosslinked PVA-based membranes with a 30%wt. of SSA, as a function of GO concentration (0%, 0.50%, and 1% wt.).

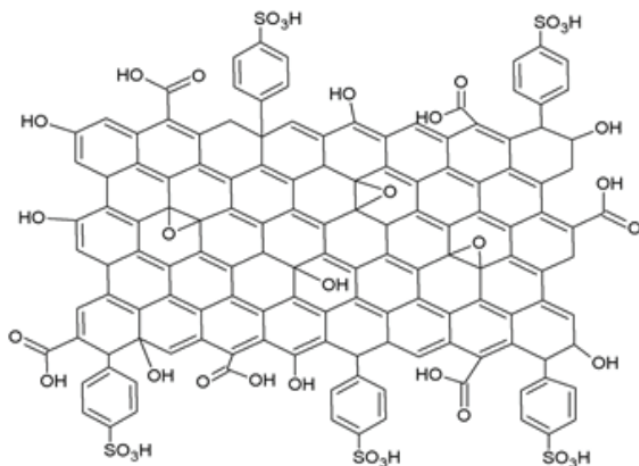


Figure 5.3: Chemical structure of the sulfonated graphene oxide (SGO) obtained by modification with aryl radicals. Source: [23].

In terms of chemical structure and reaction mechanism, the crosslinking of PVA and SSA will result in a tridimensional architecture with the generation of ester linkages between both carboxylic cues of SSA and pendant hydroxyl groups of PVA. In the literature, SSA concentration up to 50% has been considered. However, excessive crosslinking and sulfonation of the membranes result in higher rigidity and lower water swelling ability, that may promote cracking in the membranes and impair the proton conduction pathways, respectively [32,33].

The crosslinking process is usually carried at temperature above 373 K, so as thermally promoted esterification is allowed between hydroxyl groups of PVA and carboxylic species of SSA [34].

Moreover, given the absence of ionic species in the PVA structure necessary for the proton transport, the SSA possesses sulfonic functional groups, which are essential to promote proton transport across the membrane. Nevertheless, although reasonable behavior of the PVA/SSA membranes has been reported, it is still far from that of the Nafion® membranes [35-38].

In order to improve the performance of PVA/SSA membranes, graphene oxide (GO) may be a good alternative due to its nanometric scale, and good mechanical, chemical and electrical properties that may provide additional benefits to the membrane. Such is the case as the improvement of the proton conductivity, due to an increase in the surface area between the polymer matrix and the filler, as well as the reduction of the absorption of the fuel solution, which result in lower crossover phenomenon [39-44].

In terms of structure, the GO nanoparticles may be enclosed into the above described crosslinked structure, with the possibility of both chemically reaction with SSA molecules, and establishing intermolecular interactions with SSA and PVA by means of hydrogen bonding [10,45,46].

In terms of concentration of GO, percentages above 1%wt. have been reported to result in aggregation and agglomeration and difficulties for the GO dispersion in the PVA matrix [47], as well as the loss of proton conductivity [48,49].

5.2 Materials

Poly(vinyl alcohol) (PVA) with Mn 67 000 $g \cdot mol^{-1}$ (degree of hydrolysis min. 99%), glacial acetic acid (99.8% anhydrous), sulfosuccinic acid (SSA) (70%wt. solution in water) were all purchased from Sigma-Aldrich. Methanol from Pan-reac (99.9% purity) and Millipore water were used. All chemicals were used without further purification.

The graphene oxide (GO) was prepared from graphite powder using the Modified Hummers Method (MHM) [48,50,51]. Concisely, graphite powder (<20 μm) was mixed with H_2SO_4 and $NaNO_3$, below 293 K, after which $KMnO_4$ was progressively added under constant stirring. Then, the mixture was diluted in distilled water and the temperature increased to 371 K. To reduce the remaining $KMnO_4$, a H_2O_2 solution 30% was added and the solid phase was washed with HCl 37% and ethanol until neutral pH was reached. Finally, the

GO powder was filtered and dried in a vacuum oven at 333 K. All the reactive used for the GO preparation were purchased from Sigma-Aldrich.

Nanocomposite membranes based in PVA/SSA/GO were prepared by means of a solvent-casting procedure [52]. First, PVA (5 g) were dissolved in deionized water (100 mL) and magnetically stirred at 363 K for 8 h. Then, the aqueous solution of SSA was gradually added to the flask in order to achieve a 30% wt.PVA and it is further stirred for 24 h [53]. Afterwards, four identical aliquots of this solution were obtained, which were mixed with GO dispersions, refluxed at 363 K overnight and finally cooled down to room temperature. The GO dispersions containing the 0.50, and 1.00% wt.PVA were previously prepared in deionized water (10 mL) and sonicated for 1 h. Finally, the solutions were cast on a Teflon® mold dishes. Once dry, the membranes were cross-linked at 383 K during 2 h.

Therefore, the samples studied in Chapter 5 are labeled as M-0, M-0.50, and M-1, according to the GO percentage with respect to the PVA.

5.2.1 *Experimental methodology*

Fourier Transformed Infrared Spectroscopy (FTIR)

The chemical structure was assessed by means of Fourier transform infrared spectroscopy (FTIR). Analyses were carried out in a Thermo Nicolet 5700 infrared spectrometer with an attenuated total reflectance accessory (ATR). The spectra were collected from 4000 to 400 cm^{-1} at a resolution of 4 cm^{-1} along 64 scans. The spectra of three different locations of the sample were averaged. Backgrounds were collected and results were processed by means of the Omnic® Software.

Differential Scanning Calorimetry (DSC)

The thermal properties were assessed by means of differential scanning calorimetry (DSC) using a Mettler Toledo DSC 822 analyzer. Thermograms were obtained from 298 K to 493 K at $10\text{ K} \cdot \text{min}^{-1}$. All the experiments were run under nitrogen atmosphere ($50\text{ mL} \cdot \text{min}^{-1}$). Three consecutive scans of heating, cooling and heating were carried out. Samples were analyzed in triplicates and results were evaluated by means of the STARe® Software.

Thermogravimetric Analysis (TGA)

The thermo-oxidative stability of the membranes was assessed by means of thermogravimetric analysis (TGA) in a Mettler-Toledo TGA 851 analyzer. The samples, with a mass of about 4 mg were introduced in an alumina pans, with capacity of $70\ \mu\text{L}$, and were analyzed in triplicates from 298 to 1073 K with a heating rate of $10\text{ K} \cdot \text{min}^{-1}$, under an oxygen atmosphere ($50\text{ mL} \cdot \text{min}^{-1}$). Results were analyzed by means of the STARe® Software.

Dielectric Thermal Analysis (DETA)

The impedance measurements were conducted using a Novocontrol Broadband Dielectric Impedance Spectrometer (BDIS), connected to a Novocontrol Alfa-A Frequency Response Analyzer. The measurements were run in the frequency range of 10^{-2} to 10^{-7} Hz, at the temperature range 123K to 373K. The measurement were obtained under isothermal conditions by increasing in steps by 10K. The sample electrode assembly (SEA) consisted of two stainless steel electrodes filled with the sample. Consequently, the resulting SEA was directly placed in the cell. In the case that the conductivity is too high, and as result the dielectric relaxations are overlapped, a Teflon® film is inserted between the sample and one steel electrode.

5.3 Results

5.3.1 Analysis of the dielectric spectra of the M-0 membrane

The dielectric spectra was plotted in terms or the real (ϵ') and imaginary (ϵ'') parts of the complex dielectric permittivity (ϵ^*), $\tan \delta$, and the imaginary part of the electric modulus (M'') in Figures 5.4 - 5.5.

In Figure 5.6A the macromolecular origin of the dielectric relaxations is assessed through the Eyring model as derived by Starkweather. As observed, both dielectric processes are close to the zero-entropy line, and therefore, initially the macromolecular origin of both dielectric processes cannot be assigned to cooperative motions. Instead, non-cooperative molecular motions must be involved.

In Figure 5.6B the Arrhenius plot is displayed. It shows different relaxation zones. More precisely, two dielectric relaxations labelled β and $\alpha\beta$, respectively with increasing temperature. These movements are associated with motions of lateral groups, i.e. hydroxyl groups. Therefore, it validates the conclusions obtained from the macromolecular assessment.

In Figure 5.7 the isothermal curves of the module of the complex conductivity ($|\sigma|$) for the complete temperature range are displayed.

To determine the proton conductivity, the phase angle and the absolute value of the serial impedance (Z_s) are needed. Thus, both parameters are shown in Figure 5.8.

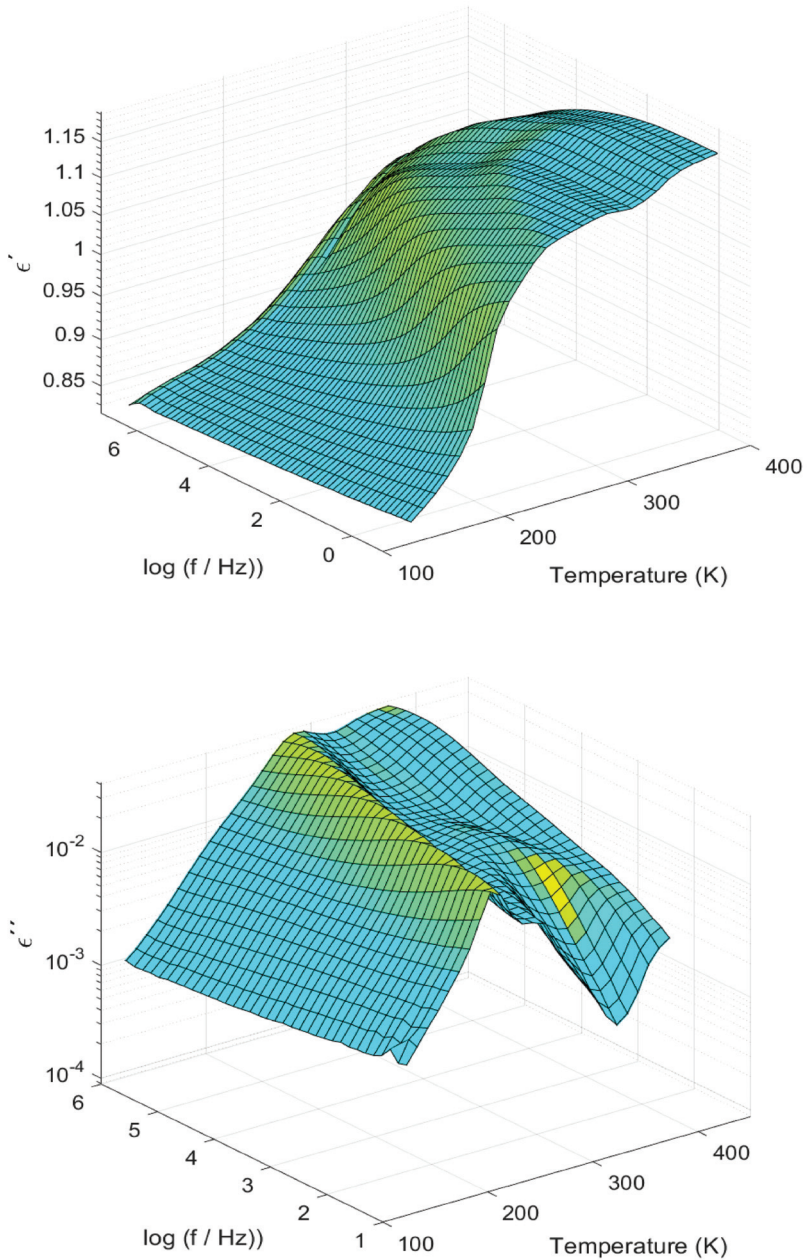


Figure 5.4: 3D plot of the real (ϵ') and imaginary part (ϵ'') parts of the complex permittivity (ϵ^*) of the M-0 membrane.

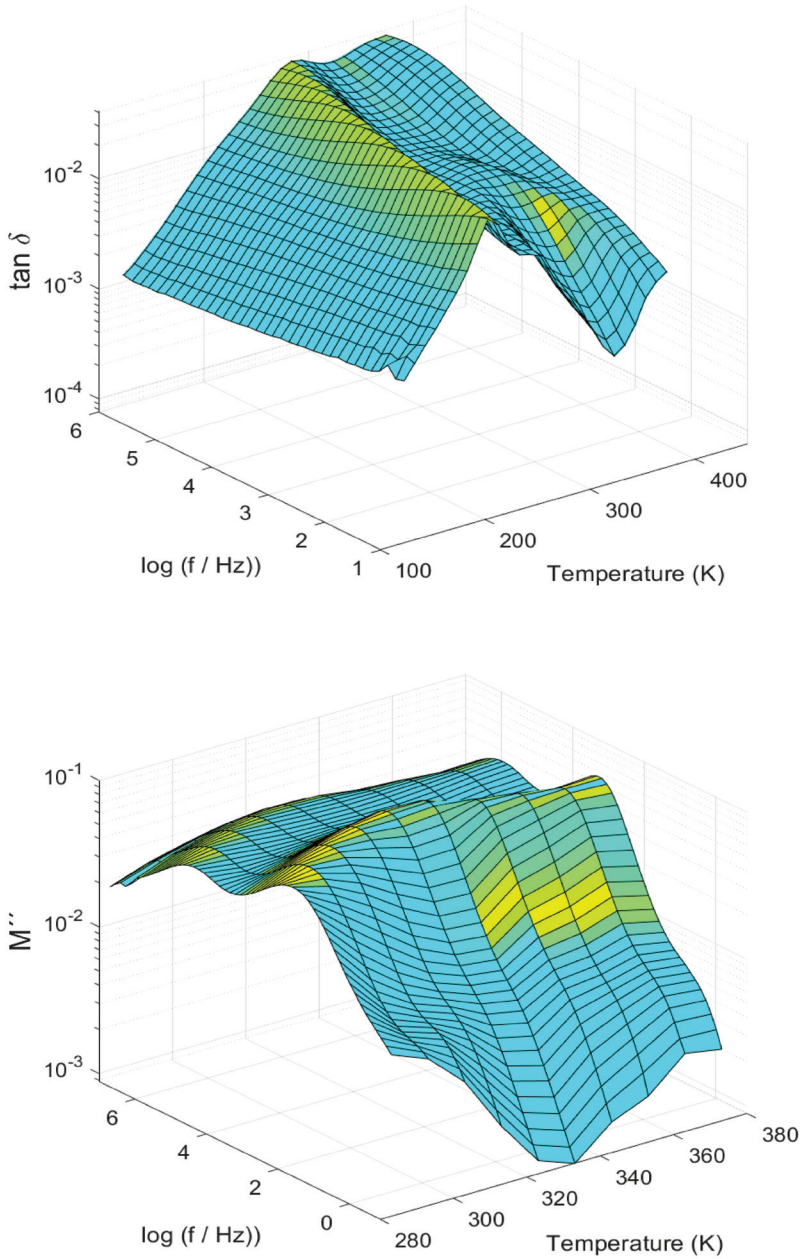


Figure 5.5: 3D plot of $\tan \delta$ and of the imaginary part (M'') of the complex electric modulus (M^*) of the M-0 membrane.

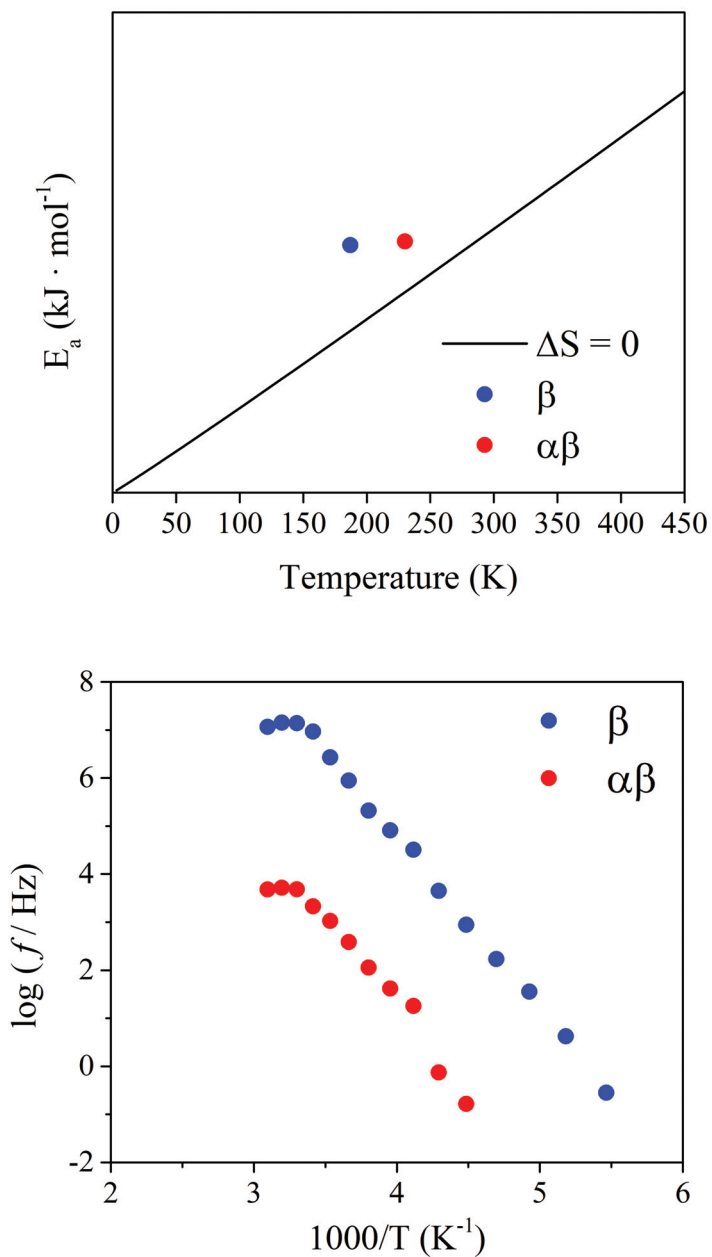


Figure 5.6: (Top) Eyring plot and (Bottom) Arrhenius plot of the M-0 membrane.

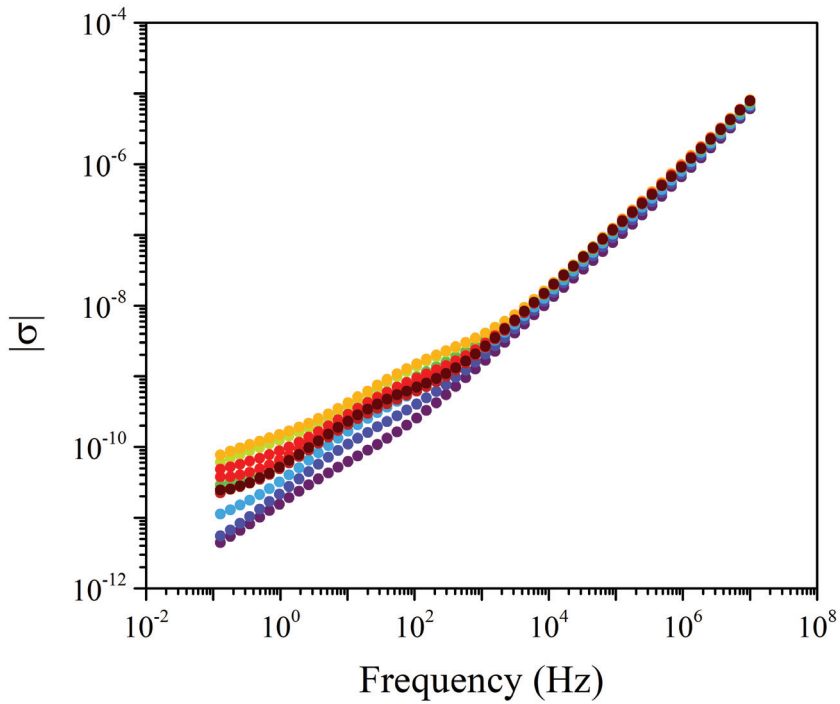


Figure 5.7: Isothermal curves of the module of the complex conductivity ($|\sigma|$) for the M-0 membrane.

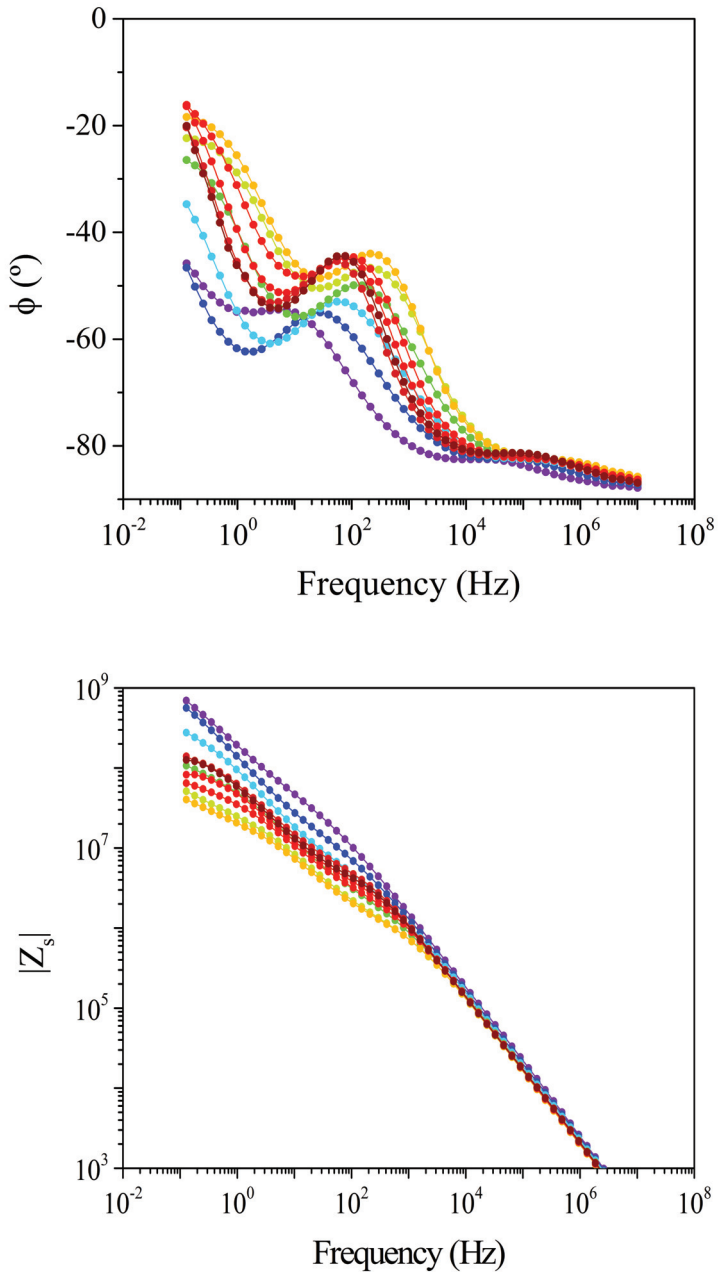


Figure 5.8: Phase angle (ϕ) and modulus of the serial impedance ($|Z_s|$) of the M-0 membrane.

5.3.2 Analysis of the dielectric spectra of the M-05 membrane

The dielectric spectra was plotted in terms of the real (ϵ') and imaginary (ϵ'') parts of the complex dielectric permittivity (ϵ^*), $\tan \delta$, and the imaginary part of the electric modulus (M'') in Figures 5.9 - 5.10.

In Figure 5.11A the macromolecular origin of the dielectric relaxations is assessed through the Eyring model as derived by Starkweather. As in the case of M-0, both dielectric relaxations are closed to the zero-entropy line, and therefore, the molecular motions associated must be of non-cooperative nature.

In Figure 5.11B the Arrhenius plot is displayed. It shows different relaxation zones. More precisely, two dielectric relaxations labelled β and $\alpha\beta$, respectively. The molecular origin is exactly the same as in the M-0 membrane. Thus, it validates the assessment of the macromolecular cooperativity.

In Figure 5.12 the isothermal curves of the module of the complex conductivity ($|\sigma|$) for the complete temperature range are displayed.

To determine the proton conductivity, the phase angle and the absolute value of the serial impedance (Z_s) is shown in Figure 5.13.

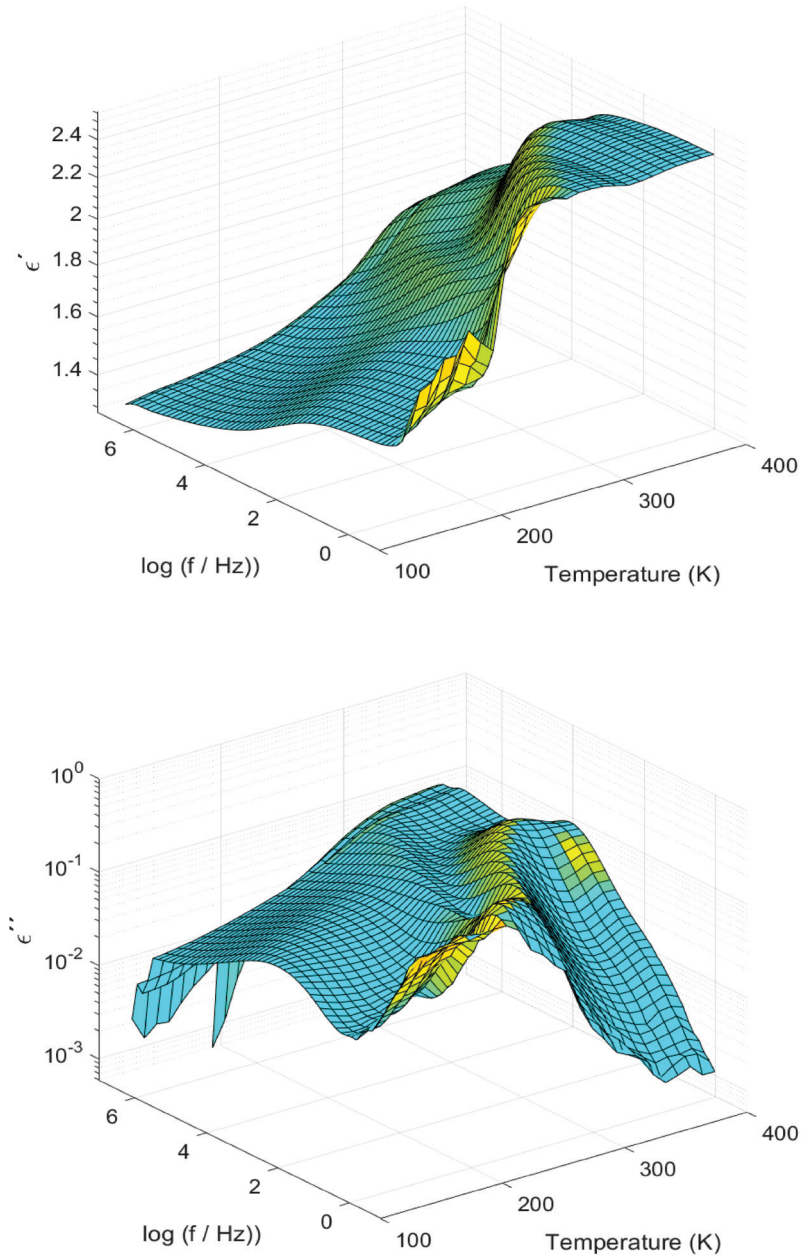


Figure 5.9: 3D plot of the real (ϵ') and imaginary part (ϵ'') parts of the complex permittivity (ϵ^*) of the M-05 membrane.

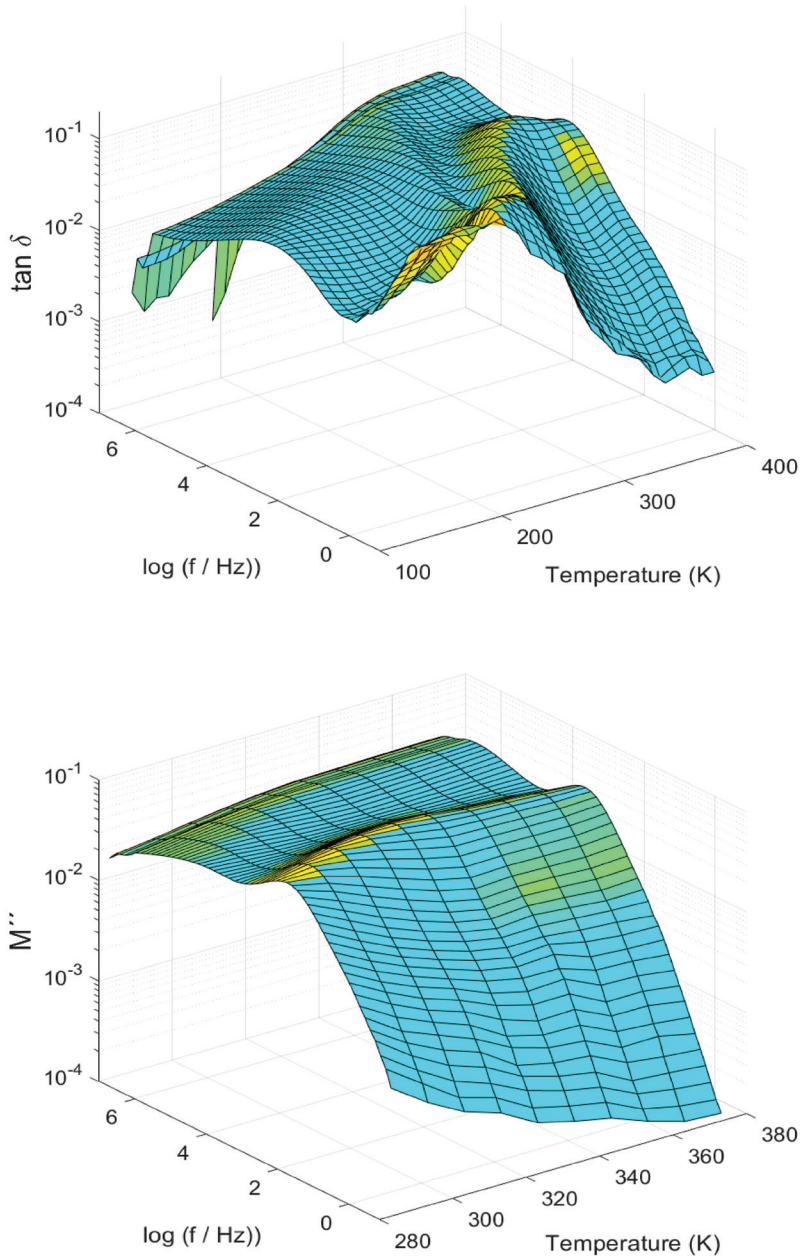


Figure 5.10: 3D plot of $\tan \delta$ and of the imaginary part (M'') of the complex electric modulus (M^*) of the M-05 membrane.

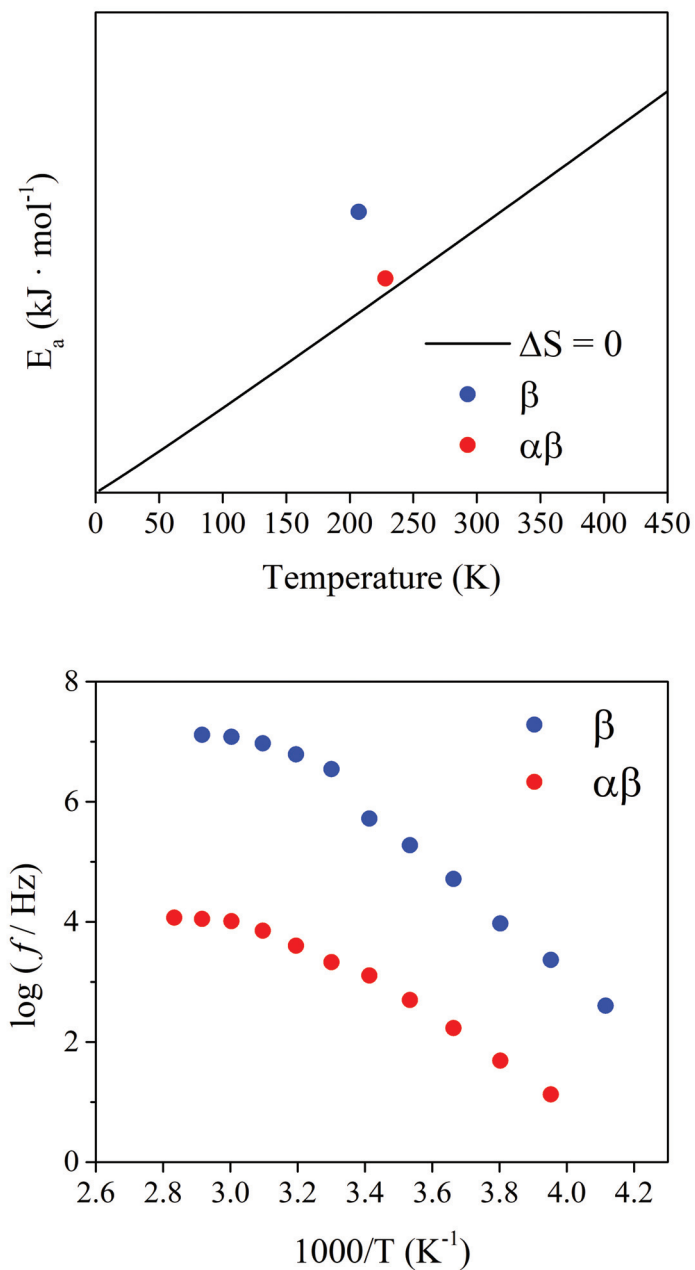


Figure 5.11: (Top) Eyring plot and (Bottom) Arrhenius plot of the M-05 membrane.

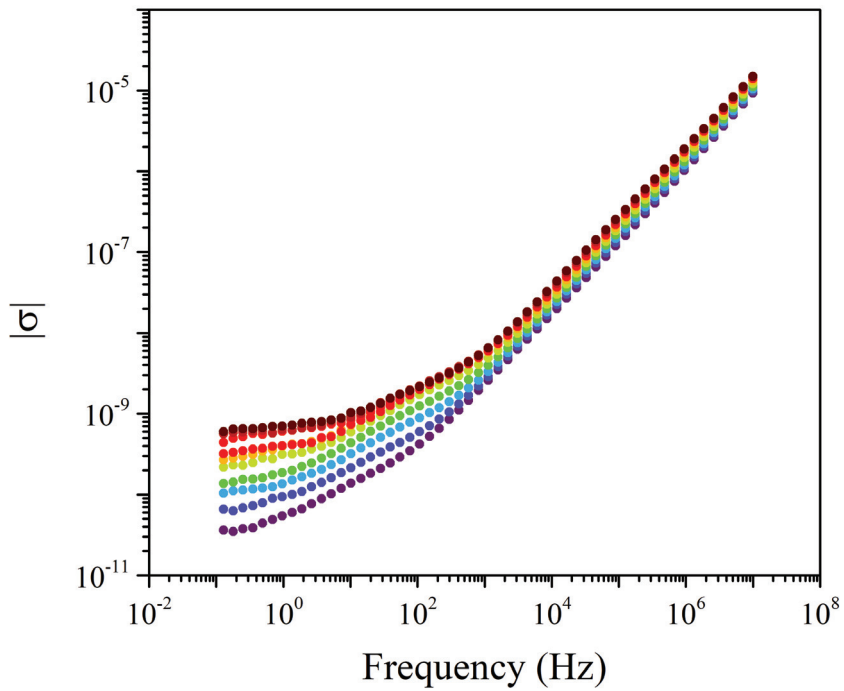


Figure 5.12: Isothermal curves of the module of the complex conductivity ($|\sigma|$) for the M-05 membrane.

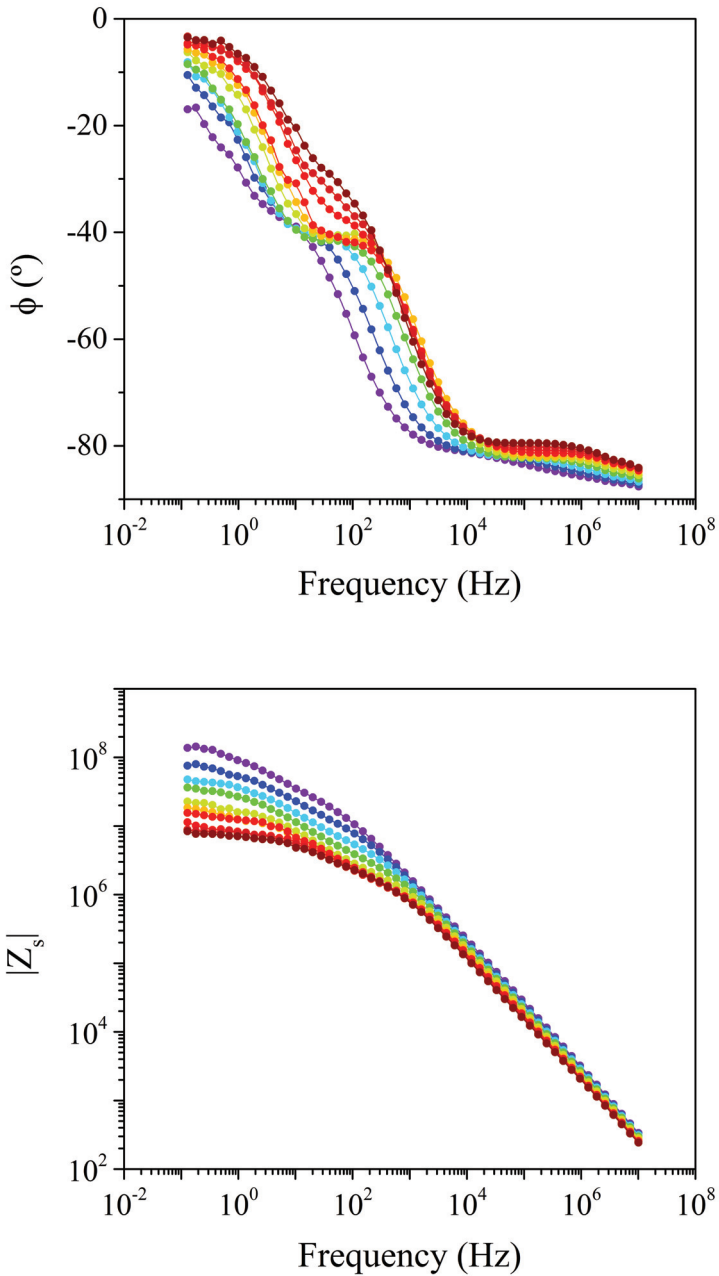


Figure 5.13: Phase angle (ϕ) and modulus of the serial impedance ($|Z_s|$) of the M-05 membrane.

5.3.3 Analysis of the dielectric spectra of the M-1 membrane

The dielectric spectra was plotted in terms of the real (ϵ') and imaginary (ϵ'') parts of the complex dielectric permittivity (ϵ^*), $\tan \delta$, and the imaginary part of the electric modulus (M'') in Figures 5.14 - 5.15.

In Figure 5.16A the macromolecular origin of the dielectric relaxations is assessed through the Eyring model as derived by Starkweather. As in the case of M-0 and M-05, both dielectric relaxations are closed to the zero-entropy line, and therefore, the molecular motions associated must be of non-cooperative nature.

In Figure 5.16B the Arrhenius plot is displayed. It shows different relaxation zones. More precisely, two dielectric relaxations labelled β and $\alpha\beta$, respectively. The molecular origin is exactly the same as in the M-0 and M-05 membrane. Thus, it validates the assessment of the macromolecular cooperativity.

In Figure 5.17 the isothermal curves of the module of the complex conductivity ($|\sigma|$) for the complete temperature range are displayed.

To determine the proton conductivity, the phase angle and the absolute value of the serial impedance (Z_s) is shown in Figure 5.18.

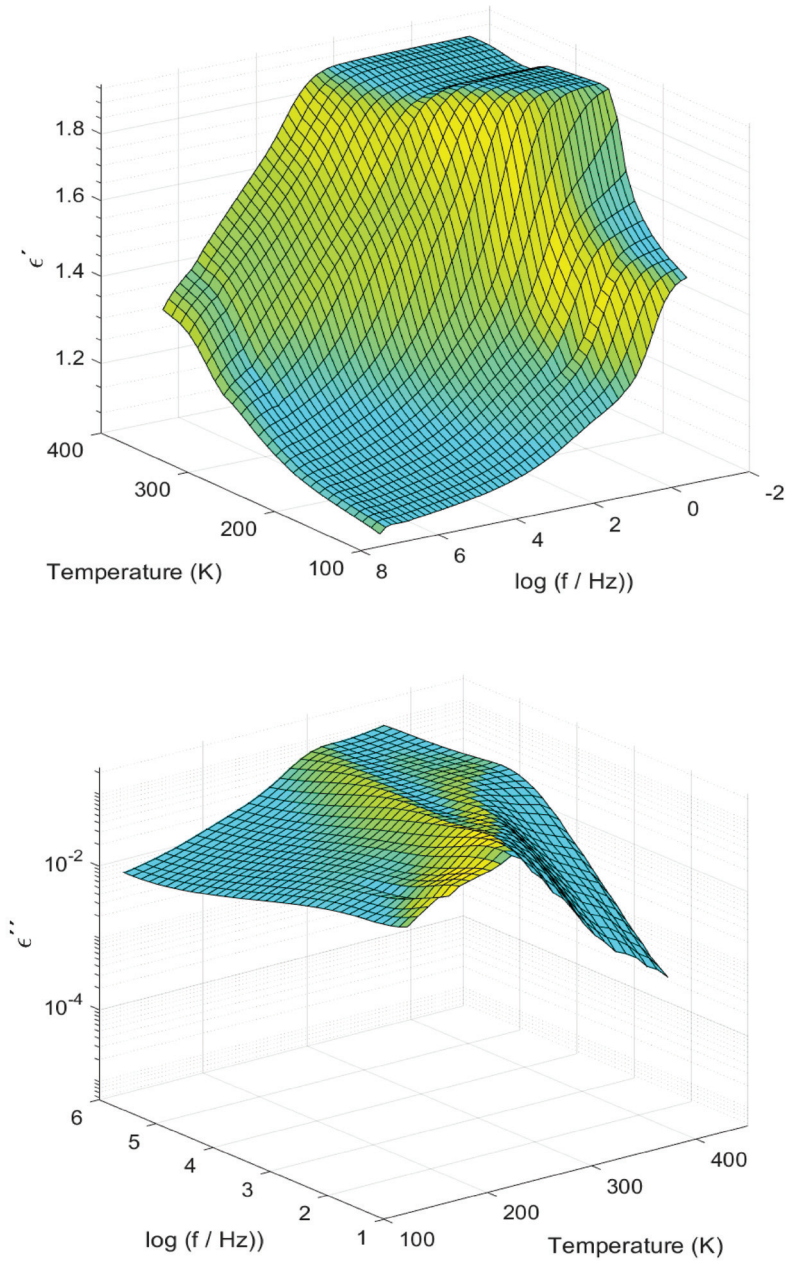


Figure 5.14: 3D plot of the real (ϵ') and imaginary part (ϵ'') parts of the complex permittivity (ϵ^*) of the M-1 membrane.

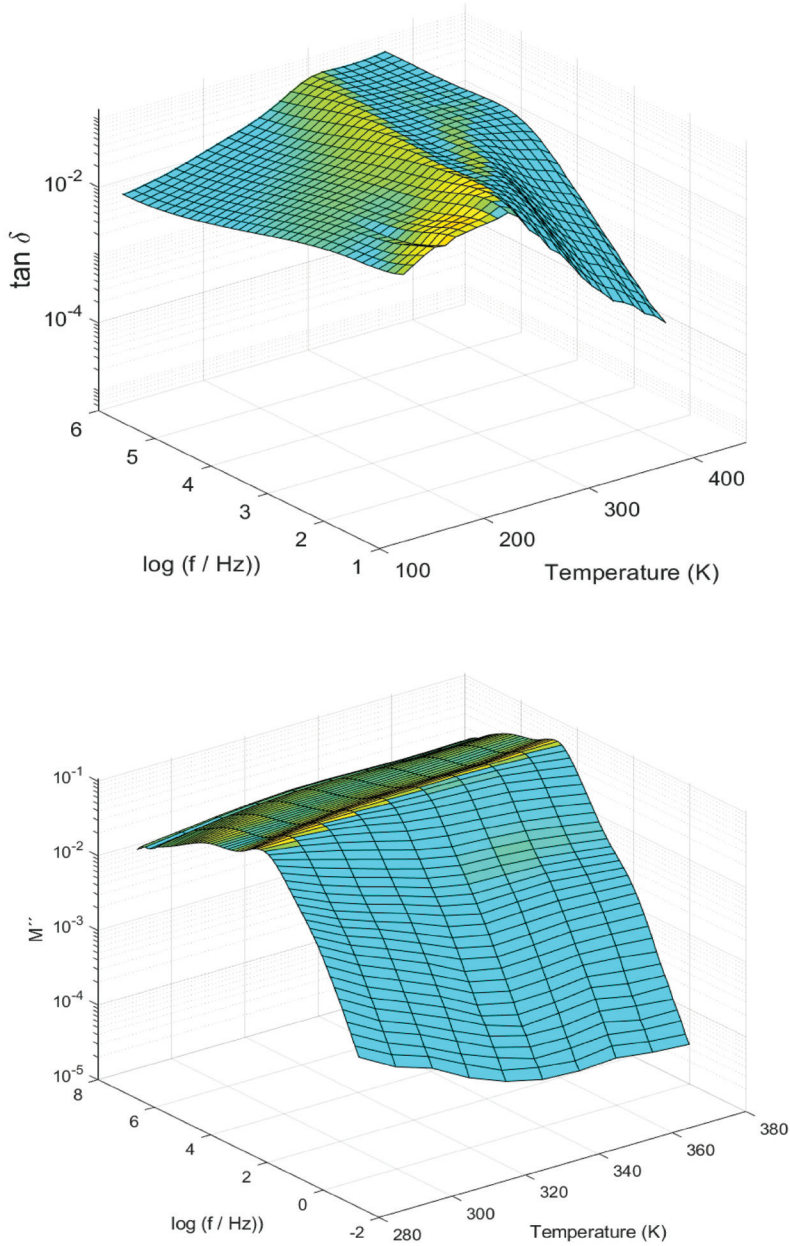


Figure 5.15: 3D plot of $\tan \delta$ and of the imaginary part (M'') of the complex electric modulus (M^*) of the M-1 membrane.

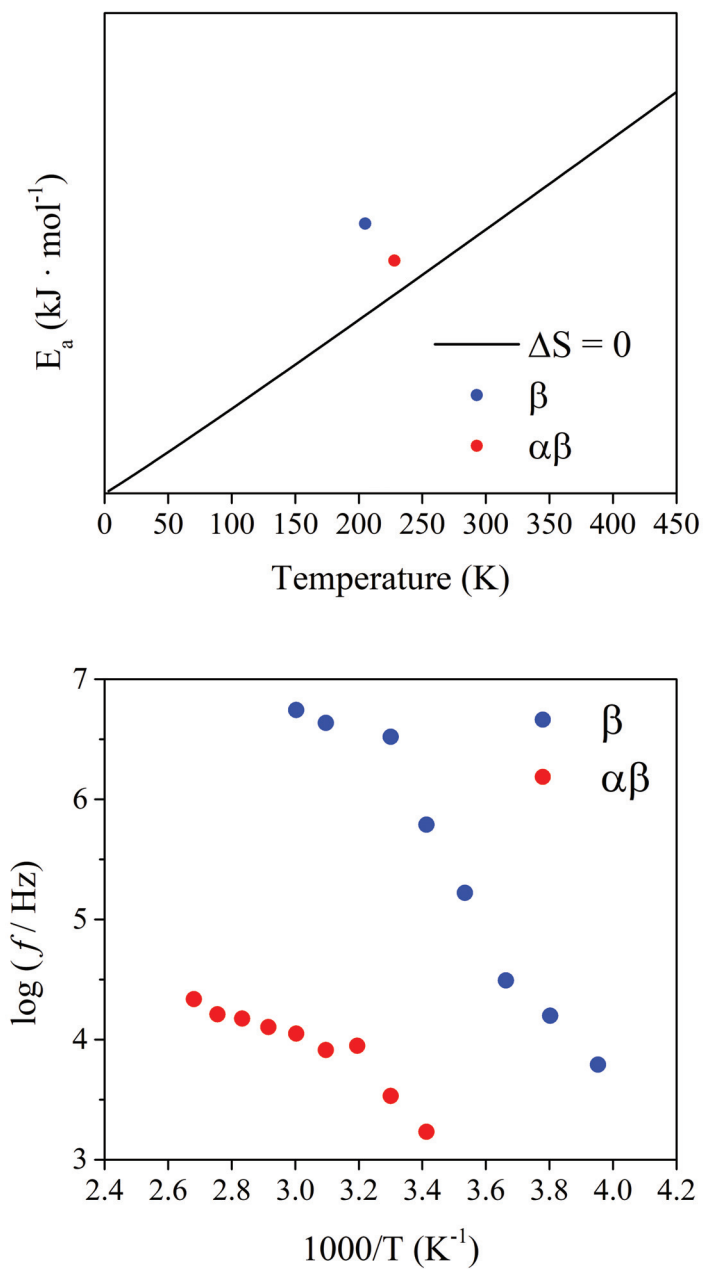


Figure 5.16: (Top) Eyring plot and (Bottom) Arrhenius plot of the M-05 membrane.

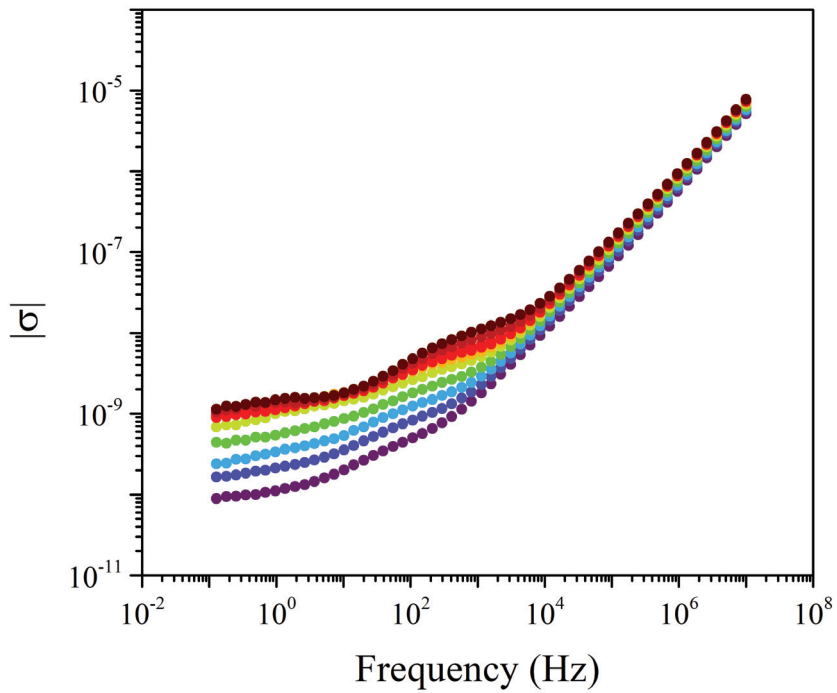


Figure 5.17: Isothermal curves of the module of the complex conductivity ($|\sigma|$) for the M-1 membrane.

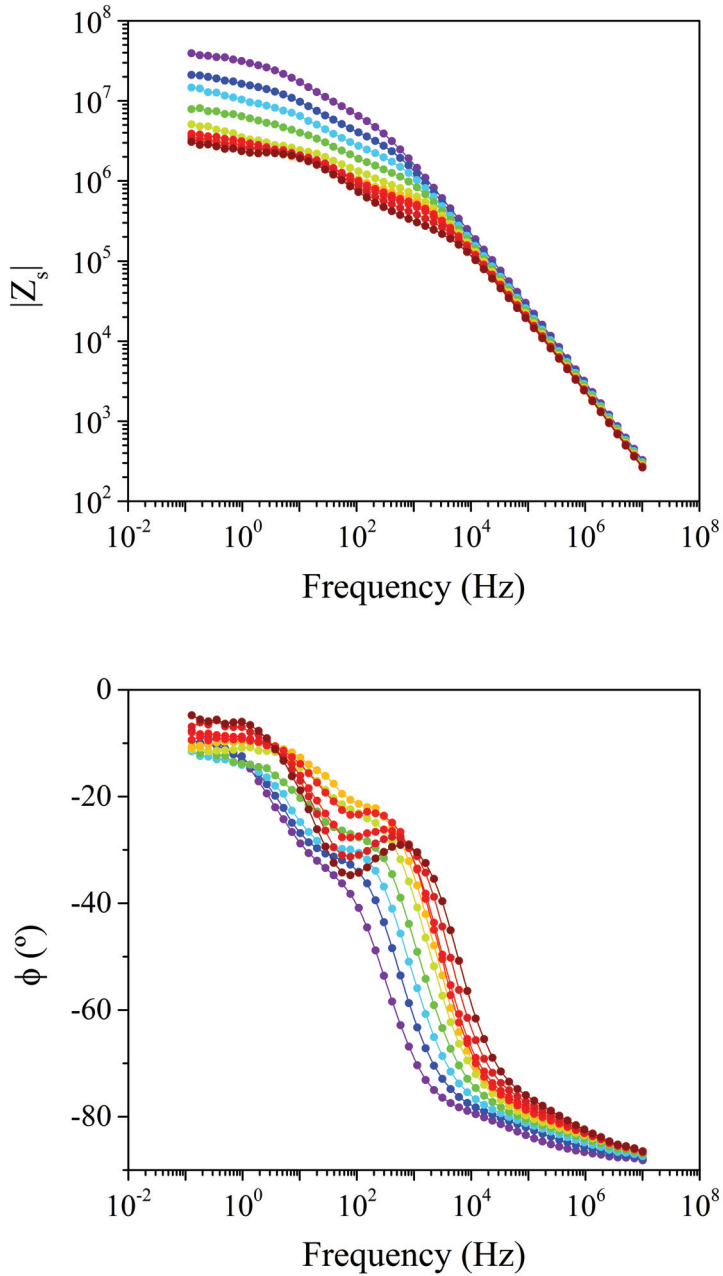


Figure 5.18: Phase angle (ϕ) and modulus of the serial impedance ($|Z_s|$) of the M-1 membrane.

To conclude, part of the results presented in this section have been published in a scientific peer-reviewed article (Contribution 5) listed in section 9.1, and it complements the discussion of the results included in section 5.4.

5.4 Discussion

The dielectric spectra, shown in Figure 5.19, reveals two dielectric processes labelled as β and $\alpha\beta$, respectively with increasing temperature order. The assessment of the macromolecular origin, displayed in Figure 5.20, of both relaxations revealed that non-cooperative local motions should be considered, and the motion of hydroxyl groups are identified as the most probable source [54-56].

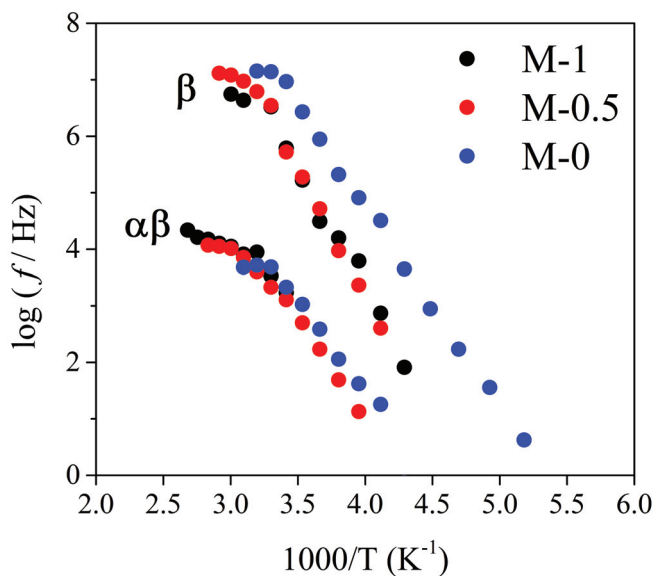


Figure 5.19: Arrhenius plot of all the membranes.

However, in Chapter 4 it has been shown the fact that the coupling or decoupling from the molecular motions in the charge transfer mechanism plays an important role, which is decisive in the behaviour of these membranes when

used as electrolytes in hydrogen PEMFC. Nevertheless, this does not occur when these membranes act as electrolytes in DMFC. When these membranes are used as electrolytes in DMFCs, the analysis needs to be completed with other data accounting for the crossover phenomena because this is the determining factor to obtain the maximum power density. Altogether, the crosslinking may bring stability to the membrane whereas the sulfonation approach, responsible for introducing proton-conducting sites in the polymer structure, may improve its proton conductivity. Therefore, since this set of membranes are intended for DMFCs, section 5.4 focuses on the evaluation of these properties.

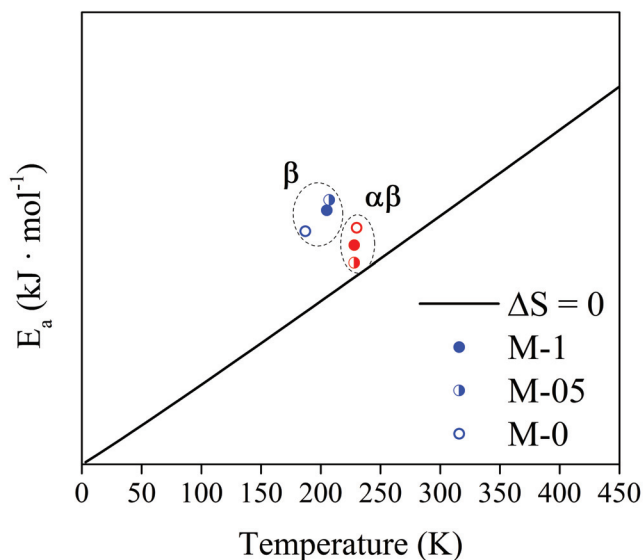


Figure 5.20: Eyring plot of all the membranes.

Consequently, FTIR spectra is analysed in order to investigate the existence of crosslinking and sulfonation. In Figure 5.21 the obtained spectra is plotted as a function of the GO content.

All the membranes showed the characteristic bands of the PVA, especially those corresponding to the OH stretching vibration from the intermolecular and in-

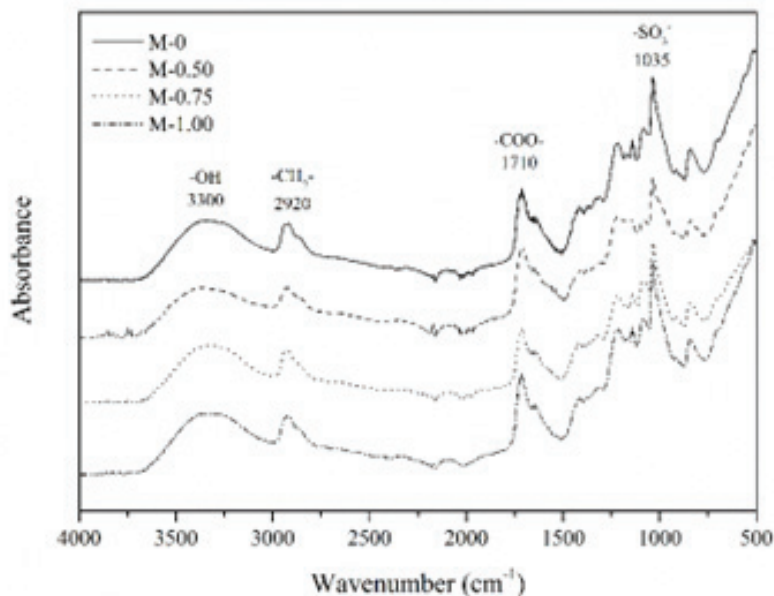


Figure 5.21: Fourier transform infrared spectra of the membranes.

tramolecular hydrogen bonds at 3300 cm^{-1} and CH_2 stretching at 2920 cm^{-1} [11]. Given the thermal crosslinking process with the SSA, the ester bond (COO) band was perceived in all cases [33]. The C=O stretching signal at 1710 cm^{-1} was also identified. The use of SSA as sulfonating agent resulted in an intense band around 1035 cm^{-1} , characteristic of the sulfonic groups (SO_3H), that may have overlapped the CO stretching band, expected at 1050 cm^{-1} [35, 53]. The main bands of the GO, expected at 1615 cm^{-1} for the C=C and at $1220\text{--}1250\text{ cm}^{-1}$ for the CO stretching were absent, possibly overlapped by the previously described signals of the PVA and SSA. The low GO content, between 0.50 and 1.00% wt., and the absence of the characteristic GO signals may also be correlated with a good particle dispersion [48].

The calorimetric thermograms, displayed in Figure 5.22, were characteristic for the PVA/SSA-based crosslinked membranes.

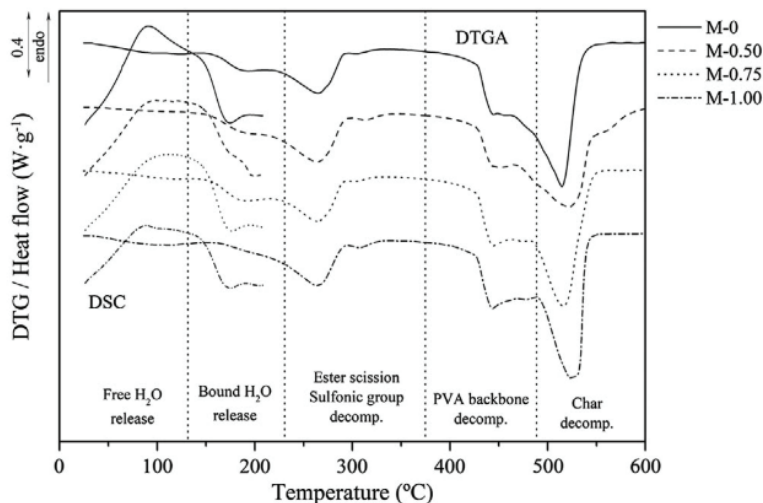


Figure 5.22: Superposed calorimetric (298 - 473 K) and derivative thermogravimetric (298 - 873 K) thermograms.

An amorphous morphology was suggested given the absence of the melting transitions, as reported before for the PVA-based membranes with a SSA content above 15 %wt [33,57]. The release of free (< 373 K) and bound water (> 373 K) were perceived as endothermic processes. The free water is expected to be occupying the free volume available in the membrane structure, while the bound water is assumed to be interacting by hydrogen bonding with the available sulfonic, hydroxyl and carboxyl groups [49]. Regarding the effect of the nanoparticles, the water release enthalpies decreased as the GO content increased, suggesting the lower ability of the membranes to host water molecules. Moreover, calorimetric thermograms were slightly displaced towards higher temperatures, which would imply stronger membrane-water interactions.

The acquired TGA thermograms, also displayed in Figure 5.22, revealed a multi-stage thermo-oxidative decomposition. The free and bound water release stages were corroborated along with the ester scission and sulfonic group decomposition, the PVA backbone decomposition and the char degradation [53]. More-

over, when bounded water is released, hydroxyl groups from the PVA molecules may be eliminated, giving as a result polyene structures [33]. The obtained results for these stages are gathered in Table 5.1 in terms of the mass loss contribution and peak temperature of the DTG curve.

Table 5.1: Characteristic peak temperatures and associated mass loss to the different thermo-oxidative decomposition stages as a function of the membrane composition.

Sample	Ester / -SO ₃ H		PVA backbone		Char		R ²
	T (°C)	Δm (%)	T (°C)	Δm (%)	T (°C)	Δm (%)	
M-0	264.84	16.80	443.31	30.59	514.43	31.00	2.23
M-05	263.99	18.71	444.52	26.95	521.52	34.27	3.00
M-1	264.16	19.04	443.69	28.48	523.96	34.32	3.67

As suggested by the calorimetric analysis, the peak temperatures of the water release were slightly displaced towards higher values and the mass contribution decreased as a function of the GO content. The peak temperature of the ester group scission and the sulfonic group decomposition remained almost constant around 537 K. However, the mass contribution for this stage slightly increased when GO was incorporated. The degradation of the ester bonds of the PVA-SSA and SSA-GO molecules may be the responsible for this higher mass contribution. Then, the PVA backbone decomposition occurred around 717 K. Finally, the char decomposition occurred from 787 K onwards, with a mass contribution of more than 30%. As expected, the residue varied between 2.23 and 3.67%, being higher as the GO content increased.

The water release enthalpy and consequent mass loss step decreased as a function of the GO proportion, which highlight the lower water content of the membranes when GO content increased. This observation may be correlated with a more compact structure due to the presence of GO particles, which resulted

into a less free volume architecture due to high interaction with PVA and SSA with subsequent less functional group availability for water incorporation.

Assessment of the sample's validity as PEM

In Figure 5.23 the logarithm of σ_{DC} is displayed, which increased as a function of temperature, due to the higher molecular mobility. The electric conductivity remained between 10^{-10} and $10^{-11} \text{ S} \cdot \text{cm}^{-1}$ for all studied membranes. Given the low electrical conductivity required for DMFC applications, these values can be considered as suitable [58].

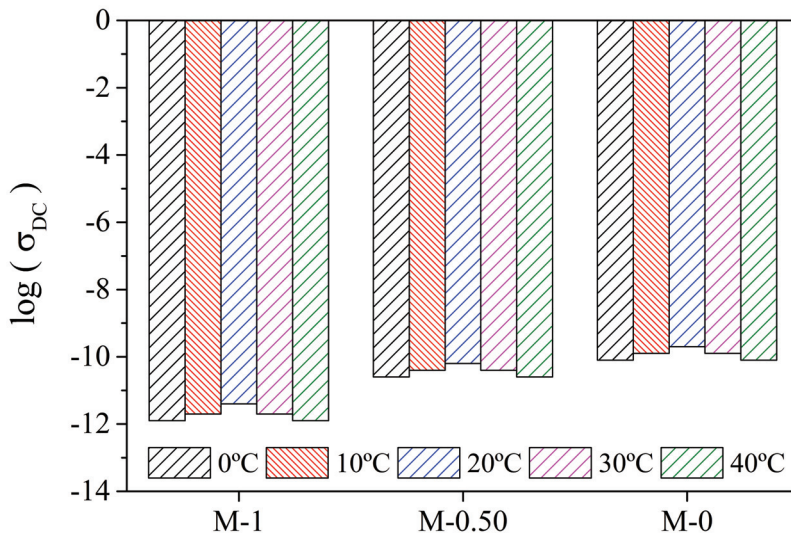


Figure 5.23: Logarithm of σ_{DC} as a function of the membrane composition and temperature, obtained from the membranes in their original (dry) state.

In Figure 5.24 the obtained values for the σ_{Prot} of the PVA/SSA/GO membranes in their original (dry) state as a function of temperature [59].

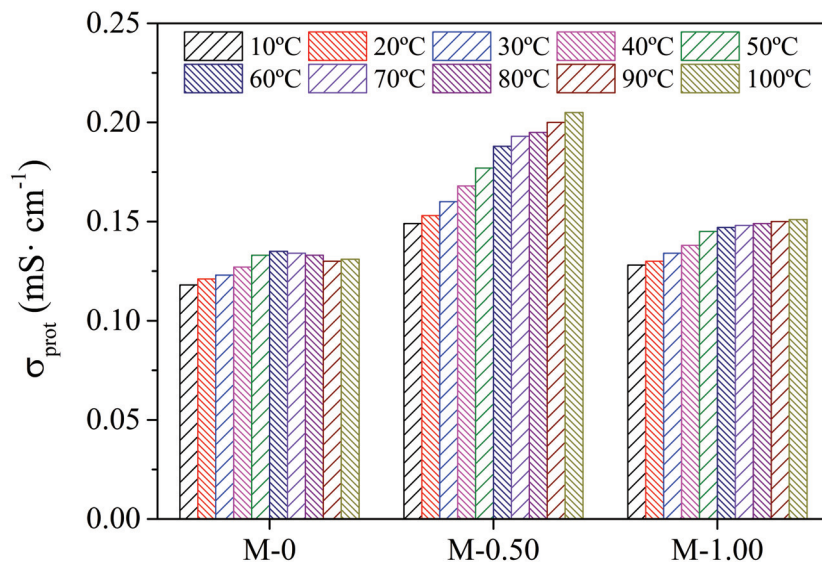


Figure 5.24: Numerical proton conductivity (σ_{Prot}) as a function of the membrane composition and temperature, obtained from the membranes in their original (dry) state.

Regarding proton conductivity (σ_{Prot}), it increased with the addition of GO and a maximum value was found for the M-0.50 membrane. Membranes were further analysed at the service temperature after being immersed in water during 24 h. Figure 5.25 compares the obtained σ_{prot} in the dry and wet states. Significant differences were perceived, including an increase of two orders of magnitude when the membranes were hydrated. This observation is strictly correlated to the contribution of the vehicular mechanism by means of the absorbed water molecules, both free and bound. Again, a maximum was obtained for the M-0.50 membrane. In particular, although this composition revealed a σ_{Prot} of $3.06 \text{ mS} \cdot \text{cm}^{-1}$ at 298 K, it was still lower than that of the Nafion®117 membrane with $37.4 \text{ mS} \cdot \text{cm}^{-1}$.

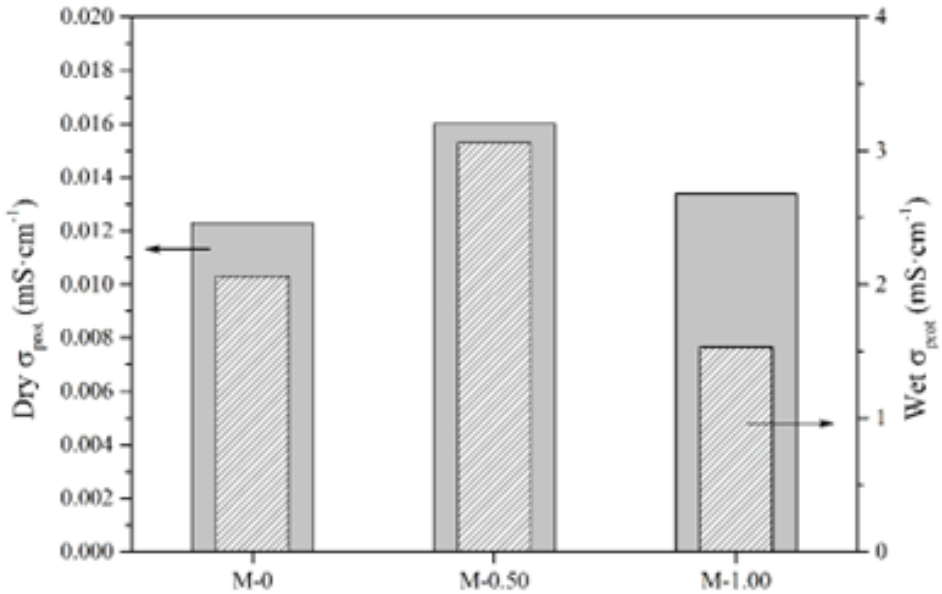


Figure 5.25: Comparison of the σ_{prot} in the dry and wet states as a function of the membrane composition.

As the proton transfer is understood as a combination of vehicular and Grotthuss mechanisms [60,61], the presence of GO in the membrane may have promoted a more compact structure, with lower free volume, in which the ionic sites for proton transport are closer. Thus, less molecules of water are required to proton transfer. However, when GO content increased reached 1%wt., the σ_{Prot} considerably decreased. The lower hydration ability of the membranes with high GO content may have reduced the crossover phenomenon found in previous sections but also the contribution of the water molecules to the vehicular proton transport mechanism. In addition, the ionic pathways may have been blocked by GO nanoparticles, which may have reduced the proton hopping mechanism and subsequently the overall proton conductivity [62].

According to the results found in this study, the Figure 5.26 schematizes the proposed contribution of the Grotthuss and vehicular proton transport mechanisms

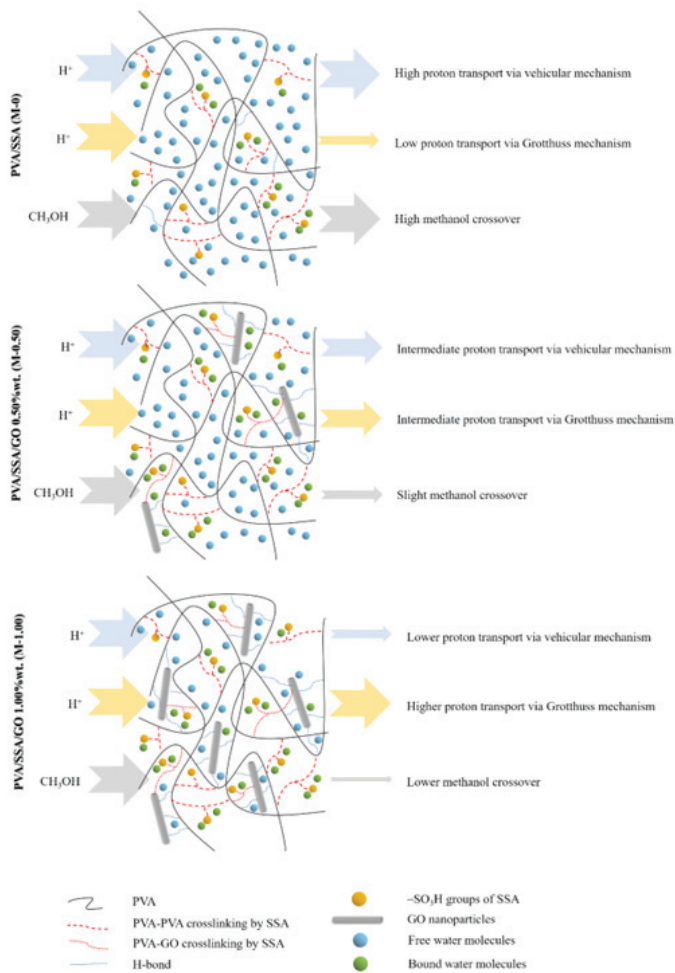


Figure 5.26: Scheme of the proposed contribution of the Grotthuss and vehicular proton transport.

and methanol crossover as a function of the GO content in the PVA/SSA/GO membranes.

5.5 Summary

From the work performed in this chapter the following conclusions are reached:

- Regardless of the amount of GO, they revealed a nonporous smooth and flat surface along with appropriate thermal stability, flexibility, and a low electric conductivity.
- The dielectric spectra reveal two dielectric processes labelled as β and $\alpha\beta$, respectively with increasing temperature order. The assessment of the macromolecular origin of both relaxations revealed that non-cooperative local motions should be consider. More precisely, with the motion of hydroxyl groups.
- In terms of performance in DMFC, it was demonstrated that the balance between both the proton conductivity and the ability of the membrane to slow down the crossover process is essential for a successful application.
- Proton conductivity increases with the inclusion of GO until a percentage of 0.50 wt%, the presence of GO in the membranes decreases the absorption of the methanol solution further as GO content increased.
- The membranes with GO proportion of 0.50 wt% combined good proton conductivity and high resistance to methanol permeability and exhibited appropriated behaviour with lower hydration levels for being used as poly-electrolytes in DMFC.

5.6 References

- [1] J. Maiti, N. Kakati, S.H. Lee, S.H. Jee, B. Viswanathan, Y.S. Yoon, Where do poly(vinyl alcohol) based membranes stand in relation to Nafion® for direct methanol fuel cell applications?, *J. Power Sources* 216 (2012) 48-66.
- [2] M.M. Victor, A.J.M. Valente, A. Papancea, S. Patachia, *Poly (vinyl alcohol)-based Polymer Membranes*, Nova Science Publishers, 2009.
- [3] N. Sammes, A. Smirnova, O. Vasylyev, *Fuel Cell Technologies: State And Perspectives: Proceedings of the NATO Advanced Research Workshop on Fuel Cell Technologies: State And Perspectives*, Kyiv, Ukraine from 6 to 10 June 2004, Springer Science & Business Media, 2005.
- [4] M. Aslam, M.A. Kalyar, Z.A. Raza, Polyvinyl alcohol: A review of research status and use of polyvinyl alcohol based nanocomposites, *Polym. Eng. Sci.* 58 (2018) 2119-2132.
- [5] M. Aslam, M.A. Kalyar, Z.A. Raza, Fabrication of reduced graphene oxide nanosheets doped PVA composite films for tailoring their opto-mechanical properties, *Appl. Phys. A Mater. Sci. Process* 123 (2017) 1-12.
- [6] E. Marin, J. Rojas, Y. Ciro, A review of polyvinilalcohol derivates: Promising materials for pharmaceutical and biomedical applications, *African J. Pharm. Pharmacol.* 8 (2014) 674-684.
- [7] C.Y. Wong, W.Y. Wong, K.S. Loh, W.R.W. Daud, K.L. Lim, M. Khalid, R. Walvekar, Development of Poly(Vinyl Alcohol)-Based Polymers as Proton Exchange Membranes and Challenges in Fuel Cell Application: A Review, *Polym. Rev.* 60 (2020) 171-202.
- [8] S. Il Ahn, K. Kim, J.R. Jung, K.Y. Kang, S.M. Lee, J.Y. Han, K.C. Choi, Reduction of graphene oxide film with poly (vinyl alcohol), *Chem. Phys. Lett.* 625 (2015) 36-40.

-
- [9] N.W. Deluca, Y.A. Elabd, Polymer electrolyte membranes for the direct methanol fuel cell: A review, *J. Polym. Sci. Part B Polym. Phys.* 44 (2006) 2201-2225.
- [10] H. Beydaghi, M. Javanbakht, E. Kowsari, Synthesis and characterization of poly(vinyl alcohol)/Sulfonated graphene oxide nanocomposite membranes for use in proton exchange membrane fuel cells (PEMFCs), *Ind. Eng. Chem. Res.* 53 (2014) 16621-16632.
- [11] S. Yun, H. Im, Y. Heo, J. Kim, Crosslinked sulfonated poly(vinyl alcohol)/sulfonated multi-walled carbon nanotubes nanocomposite membranes for direct methanol fuel cells, *J. Memb. Sci.* 380 (2011) 208-215.
- [12] S.J. Peighambaroust, S. Rowshanzamir, M. Amjadi, Review of the proton exchange membranes for fuel cell applications, Elsevier Ltd, 2010.
- [13] A.C. Dupuis, Proton exchange membranes for fuel cells operated at medium temperatures: Materials and experimental techniques, *Prog. Mater. Sci.* 56 (2011) 289-327.
- [14] H. Ahmad, S.K. Kamarudin, U.A. Hasran, W.R.W. Daud, Overview of hybrid membranes for direct-methanol fuel-cell applications, *Int. J. Hydrogen Energy.* 35 (2010) 2160-2175.
- [15] H.L. Lin, S.H. Wang, Nafion/poly(vinyl alcohol) nano-fiber composite and Nafion/poly(vinyl alcohol) blend membranes for direct methanol fuel cells, *J. Memb. Sci.* 452 (2014) 253-262.
- [16] M. Erkartal, A. Aslan, U. Erkilic, S. Dadi, O. Yazaydin, H. Usta, U. Sen, Anhydrous proton conducting poly(vinyl alcohol) (PVA)/ poly(2-acrylamido-2-methylpropane sulfonic acid) (PAMPS)/1,2,4-triazole composite membrane, *Int. J. Hydrogen Energy* 41 (2016) 11321-11330.

- [17] A.M. Herring, Inorganic-polymer composite membranes for proton exchange membrane fuel cells, *J. Macromol. Sci. Part C Polym. Rev.* 46 (2006) 245-296.
- [18] R.M. Wang, S.R. Zheng, Y.P. Zheng, Introduction to polymer matrix composites *Polym. Matrix Compos. Technol.* (2011).
- [19] S. Kango, S. Kalia, A. Celli, J. Njuguna, Y. Habibi, R. Kumar, Surface modification of inorganic nanoparticles for development of organic-inorganic nanocomposites - A review, *Prog. Polym. Sci.* 38 (2013) 1232-1261.
- [20] H. He, J. Klinowski, M. Forster, A. Lerf, A new structural model for graphite oxide, *Chem. Phys. Lett.* 287 (1998) 53-56.
- [21] A. Lerf, H. He, T. Riedl, M. Forster, J. Klinowski, ^{13}C and ^1H MAS NMR studies of graphite oxide and its chemically modified derivatives, *Solid State Ionics* 101103 (1997) 857-862.
- [22] K. Pourzare, Y. Mansourpanah, S. Farhadi, Advanced nanocomposite membranes for fuel cell applications: a comprehensive review, *Biofuel Res. J.* 3 (2016) 496-513.
- [23] Z.U. Khan, A. Kausar, H. Ullah, A review on composite papers of graphene oxide, carbon nanotube, polymer/GO, and polymer/CNT: Processing strategies, properties, and relevance, *Polym. Plast. Technol. Eng.* 55 (2016) 559-581.
- [24] S.H. Lee, D.R. Dreyer, J. An, A. Velamakanni, R.D. Piner, S. Park, Y. Zhu, S.O. Kim, C.W. Bielawski, R.S. Ruoff, Polymer brushes via controlled, surfaceinitiated atom transfer radical polymerization (ATRP) from graphene oxide, *Macromol. Rapid Commun.* 31 (2010) 281-288.
- [25] H. Beydaghi, M. Javanbakht, E. Kowsari, Preparation and physicochemical performance study of proton exchange membranes based on phenyl sul-

- fonated graphene oxide nanosheets decorated with iron titanate nanoparticles, *Polymer (Guildf)* 87 (2016) 26-37.
- [26] S. Neelakandan, K. Noel Jacob, P. Kanagaraj, R.M. Sabarathinam, A. Muthumeenal, A. Nagendran, Effect of sulfonated graphene oxide on the performance enhancement of acid-base composite membranes for direct methanol fuel cells, *RSC Adv.* 6 (2016) 51599-51608.
- [27] H.-C. Chien, L.-D. Tsai, C.-P. Huang, C. Kang, J.-N. Lin, F.-C. Chang, Sulfonated graphene oxide/Nafion composite membranes for high-performance direct methanol fuel cells, *Int. J. Hydrogen Energy* 38 (2013) 13792-13801.
- [28] A.K. Sahu, K. Ketpang, S. Shanmugam, O. Kwon, S. Lee, H. Kim, Sulfonated Graphene-Nafion Composite Membranes for Polymer Electrolyte Fuel Cells Operating under Reduced Relative Humidity, *J. Phys. Chem. C.* 120 (2016) 15855-15866.
- [29] R. Kumar, M. Mamlouk, K. Scott, Sulfonated polyether ether ketone-sulfonated graphene oxide composite membranes for polymer electrolyte fuel cells, *RSC Adv.* 4 (2014) 617-623.
- [30] R. Kumar, K. Scott, Freestanding sulfonated graphene oxide paper: A new polymer electrolyte for polymer electrolyte fuel cells, *Chem. Commun.* 48 (2012) 5584-5586.
- [31] D. Dhanapal, M. Xiao, S. Wang, Y. Meng, A review on sulfonated polymer composite/organic-inorganic hybrid membranes to address methanol barrier issue for methanol fuel cells, *Nanomaterials* 9 (2019).
- [32] E. Rynkowska, K. Fatyeyeva, S. Marais, J. Kujawa, W. Kujawski, Chemically and thermally crosslinked PVA-based membranes: effect on swelling and transport behavior, *Polymers (Basel)* 11 (2019) 1799.
- [33] J.M. Morancho, J.M. Salla, A. Cadenato, P. FernándezFrancos, X. Colomer, Y. Calventus, R. Ruíz, Thermal analysis of enhanced poly (vinyl alco-

- hol)based protonconducting membranes crosslinked with sulfonation agents for direct methanol fuel cells, *J. Appl. Polym. Sci.* 124 (2012) E57-E65.
- [34] M.M. Gomaa, C. Hugenschmidt, M. Dickmann, E.E. Abdel-Hady, H.F.M. Mohamed, M.O. Abdel-Hamed, Crosslinked PVA/SSA proton exchange membranes: correlation between physiochemical properties and free volume determined by positron annihilation spectroscopy, *Phys. Chem. Chem. Phys.* 20 (2018) 28287-28299.
- [35] D. Ebenezer, P. Haridoss, Effect of crosslinked poly (vinyl alcohol)/sulfosuccinic acid ionomer loading on PEMFC electrode performance, *Int. J. Hydrogen Energy.* 42 (2017) 4302-4310.
- [36] T. Remis, J. Kadlec, Influence of silicon oxide (SiO₂) and sulfosuccinic acid (SSA) loading on properties of poly (vinyl alcohol)(PVA) derived composite membranes, in: *J. Phys. Conf. Ser.*, IOP Publishing, (2018) 12035.
- [37] M.S. Tutgun, D. Sinirlioglu, S.U. Celik, A. Bozkurt, Investigation of nanocomposite membranes based on crosslinked poly (vinyl alcohol)sulfosuccinic acid ester and hexagonal boron nitride, *J. Polym. Res.* 22 (2015) 1-11.
- [38] N. Kakati, G. Das, Y.S. Yoon, Proton-conducting membrane based on epoxy resin-poly (vinyl alcohol)-sulfosuccinic acid blend and its nanocomposite with sulfonated multiwall carbon nanotubes for fuel-cell application, *J. Korean Phys. Soc.* 68 (2016) 311-316.
- [39] E. Özgirgin, Y. Devrim, A. Albostan, Modeling and simulation of a hybrid photovoltaic (PV) module-electrolyzer-PEM fuel cell system for micro-cogeneration applications, *Int. J. Hydrogen Energy* 40 (2015) 15336-15342.
- [40] D.C. Lee, H.N. Yang, S.H. Park, W.J. Kim, Nafion/graphene oxide composite membranes for low humidifying polymer electrolyte membrane fuel cell, *J. Memb. Sci.* 452 (2014) 20-28.

-
- [41] R.P. Pandey, G. Shukla, M. Manohar, V.K. Shahi, Graphene oxide based nanohybrid proton exchange membranes for fuel cell applications: An overview, *Adv. Colloid Interface Sci.* 240 (2017) 15-30.
- [42] Y. He, C. Tong, L. Geng, L. Liu, C. Lü, Enhanced performance of the sulfonated polyimide proton exchange membranes by graphene oxide: Size effect of graphene oxide, *J. Memb. Sci.* 458 (2014) 36-46.
- [43] T. Yuan, L. Pu, Q. Huang, H. Zhang, X. Li, H. Yang, An effective methanol-blocking membrane modified with graphene oxide nanosheets for passive direct methanol fuel cells, *Electrochim. Acta* 117 (2014) 393-397.
- [44] A. Ammar, A.M. Al-Enizi, M.A. AlMaadeed, A. Karim, Influence of graphene oxide on mechanical, morphological, barrier, and electrical properties of polymer membranes. *Arab J Chem.* 9 (2016) 274-286.
- [45] M. Yoo, M. Kim, Y. Hwang, J. Kim, Fabrication of highly selective PVA-g-GO/SPVA membranes via cross-linking method for direct methanol fuel cells, *Ionics (Kiel)* 20 (2014) 875-886.
- [46] X. Yang, L. Li, S. Shang, X. Tao, Synthesis and characterization of layer-aligned poly (vinyl alcohol)/graphene nanocomposites, *Polymer (Guildf)* 51 (2010) 3431-3435.
- [47] J. Liang, Y. Huang, L. Zhang, Y. Wang, Y. Ma, T. Guo, Y. Chen, Molecular-level dispersion of graphene into poly (vinyl alcohol) and effective reinforcement of their nanocomposites, *Adv. Funct. Mater.* 19 (2009) 2297-2302.
- [48] C. Gonzalez-Guisasola, A. Ribes-Greus, Dielectric relaxations and conductivity of cross-linked PVA/SSA/GO composite membranes for fuel cells, *Polym. Test.* 67 (2018) 55-67.

- [49] M.S. Kim, I. Jun, Y.M. Shin, W. Jang, S.I. Kim, H. Shin, The development of genipin-crosslinked poly (caprolactone)(PCL)/gelatin nanofibers for tissue engineering applications, *Macromol. Biosci.* 10 (2010) 91-100.
- [50] W. S. Hummers, R. E. Offeman, Preparation of Graphitic Oxide, *J. Am. Chem. Soc.* 80 (1958) 1339-1339.
- [51] L. Shahriary, A. Athawale, Graphene Oxide Synthesized by using Modified Hummers Approach, *Int. J. Renew. Energy Environ. Eng.* 2 (2014) 58-63.
- [52] C. Bao, Y. Guo, L. Song, Y. Hu, Poly(vinyl alcohol) nanocomposites based on graphene and graphite oxide: a comparative investigation of property and mechanism, *J. Mater. Chem.* 21 (2011) 13942.
- [53] A. Martinez-Felipe, C. Moliner-Estopiñan, C. T. Imrie, and A. Ribes-Greus, Characterization of crosslinked poly(vinyl alcohol)-based membranes with different hydrolysis degrees for their use as electrolytes in direct methanol fuel cells, *J. Appl. Polym. Sci.* 124 (2012) 1000-1011.
- [54] N.N. Rozik, A.A. Ward, A novel approach on poly(ionic liquid)-based poly(vinyl alcohol) as a hydrophilic/hydrophobic conductive polymer electrolytes, *Polym. Bull.* 75 (2018) 267-287.
- [55] A.S. Hickey, N.A. Peppas, Mesh size and diffusive characteristics of semicrystalline poly(vinyl alcohol) membranes prepared by freezing/thawing techniques, *J. Memb. Sci.* 107 (1995) 229-237.
- [56] J.B. Gonzalez-Campos, E. Prokhorov, I.C. Sanchez, J.G. Luna-Barcenas, A. Manzano-Ramirez, J. Gonzalez-Hernandez, Y. Lopez-Castro, R.E. Del Rio, Molecular dynamics analysis of PVA-AgNP composites by dielectric spectroscopy, *J. Nanomater.* (2012).
- [57] J. W. Rhim, H. B. Park, C. S. Lee, J. H. Jun, D. S. Kim, and Y. M. Lee, Crosslinked poly(vinyl alcohol) membranes containing sulfonic acid group:

- Proton and methanol transport through membranes, *J. Memb. Sci.* 238 (2004) 143-151.
- [58] A. Mahmoud, I. Dincer, A review on methanol crossover in direct methanol fuel cells: challenges and achievements, *Int. J. ENERGY Res.* 35 (2011) 1213-1228.
- [59] R. Riande, E., Diaz-Calleja, *Electrical Properties of Polymers.*, Boca Raton: CRC Press., 2004.
- [60] N. Agmon, The Grotthuss mechanism, *Chem. Phys. Lett.* 244, (1995) 456-462.
- [61] K.-D. Kreuer, A. Rabenau, and W. Weppner, Vehicle Mechanism, A New Model for the Interpretation of the Conductivity of Fast Proton Conductors, *Angew. Chemie Int. Ed.* 21 3 (1982) 208-209.
- [62] S. Al-Batty, C. Dawson, S. P. Shanmukham, E. P. L. Roberts, and S. M. Holmes, Improvement of direct methanol fuel cell performance using a novel mordenite barrier layer, *J. Mater. Chem. A* 4 (2016) 10850-10857.

Chapter 6

Membranes based on liquid crystals

In this chapter a series of liquid crystals are studied. This type of grafted poly(epichlorohydrin) is chosen for its ability to form channels that enhances proton conduction. Consequently, in Chapter 6, the suitability as PEM of a series of neat poly(epichlorohydrin-co-ethylene oxide)(PECH-co-EO) copolymer and two modified copolymers with a 20% or 40% of dendron 3,4,5-tris[4-(n-dodecan-1-yloxy)benzyloxy] benzoate units, together with a series of poly(epichlorohydrin) with the dendron 3,4,5-tris[4-(n-dodecan-1-yloxy)benzyloxy] benzoate is assessed.

6.1 Introduction

Poly(epichlorohydrin) (PECH) is a synthetic elastomer that is commonly used in a variety of industrial applications. It is a highly flexible polymer that has excellent resistance to water, oils, and chemicals, making it useful for applications such as seals, gaskets, and hoses. It also has good electrical insulation properties, making it suitable for electrical applications.

PECH can be synthesized through the polymerization of epichlorohydrin, a highly reactive organic compound. The polymerization can be carried out through a variety of methods, including cationic polymerization and anionic polymerization.

One of the primary advantages of PECH is its low toxicity and biocompatibility, which makes it useful in biomedical applications such as wound dressings and drug delivery systems. Additionally, PECH has been shown to have antimicrobial properties, making it useful in applications where microbial growth is a concern.

However, like many synthetic polymers, PECH is not biodegradable and can persist in the environment for a long time. It can also release toxic chemicals when incinerated, which can be harmful to human health and the environment.

Overall, PECH is a versatile synthetic elastomer with a range of useful properties. Its applications span from industrial uses to biomedical uses, but care should be taken to properly manage and dispose of it to minimize its impact on the environment.

PECH has been studied for its potential application as a proton exchange membrane (PEM) in proton exchange membrane fuel cells (PEMFCs). It has been investigated as an alternative to commonly used PEM materials such as perfluorinated sulfonic acid (PFSA) membranes due to its lower cost and better thermal stability. PECH membranes have shown good proton conductivity,

with values comparable to those of PFSA membranes, and they also exhibit good mechanical properties and chemical stability.

One study investigated the effect of crosslinking on the performance of PECH membranes in PEMFCs. The study found that crosslinking the PECH membranes with different crosslinking agents improved the thermal stability and mechanical properties of the membranes, while maintaining good proton conductivity.

Another study investigated the effect of blending PECH with sulfonated poly(ether ether ketone) (SPEEK) on the properties of the resulting composite membrane. The study found that the addition of PECH to SPEEK improved the water uptake and proton conductivity of the composite membrane, while maintaining good mechanical strength.

Overall, while more research is needed to fully evaluate the potential of PECH membranes in PEMFCs, the current studies suggest that PECH has promising properties as a PEM material and could be a viable alternative to PFSA membranes [1-4].

PECH grafted with dendritic side groups has been studied for fuel cell applications due to its availability to form channels, which facilitate the mobility of cations [5]. Some of the most relevant results are listed as follows [6-10]:

- Good proton conductivity: PECH has been shown to have good proton conductivity, with reported values ranging from 10^{-3} to $10^{-2} S \cdot cm^{-1}$ depending on the degree of ionization and membrane thickness. This is a critical factor for the performance of PEMFCs, as high proton conductivity is necessary for efficient proton transport across the membrane.
- Chemical stability: PECH-based membranes have been shown to have good chemical stability in acidic environments, which is important for their use in PEMFCs. Studies have reported that PECH membranes can

maintain their proton conductivity for extended periods of time in acidic solutions, indicating good chemical stability.

- Limited thermal stability: One challenge associated with the use of PECH in PEMFCs is its limited thermal stability. PECH has a relatively low glass transition temperature (T_g) of around 233 K, which can limit its use in high-temperature PEMFCs. However, there have been efforts to improve the thermal stability of PECH through various modifications.
- Mechanical strength: Another challenge associated with PECH-based membranes is their low mechanical strength. PECH membranes are relatively soft and can be easily deformed, which can lead to membrane damage and reduced performance. Researchers have investigated various methods to improve the mechanical strength of PECH membranes, including the addition of reinforcing materials and crosslinking.
- Performance in PEMFCs: Several studies have investigated the performance of PECH-based membranes in PEMFCs. Overall, the results have been promising, with reported power densities ranging from 100 mW/cm^2 to 500 mW/cm^2 depending on the membrane thickness, degree of ionization, and operating conditions. However, there is still room for improvement in terms of the mechanical and thermal properties of PECH-based membranes to further optimize their performance in PEMFCs.

Poly(epichlorohydrin-co-ethylene oxide) (P(ECH-co-EO)) is a copolymer consisting of both epichlorohydrin (ECH) and ethylene oxide (EO) monomers. The molecular structure of P(ECH-co-EO) can vary depending on the ratio of ECH and EO monomers used during polymerization. The copolymerization of ECH and EO is typically carried out in the presence of a base catalyst, which leads to the formation of ether linkages between the monomers. The resulting copolymer consists of a backbone of alternating ECH and EO units, with pendant groups consisting of hydroxyl and chloride functionalities. The presence of the EO units in the copolymer leads to an increase in the hydrophilicity of the

- Performance in PEMFCs: Several studies have investigated the performance of PEO-co-PECH membranes in PEMFCs. Overall, the results have been promising, with reported power densities ranging from 60 to 400 $mW \cdot cm^{-2}$ depending on the membrane thickness, degree of ionization, and operating conditions.
- Crosslinking: Crosslinking has been used to further improve the mechanical and chemical stability of PEO-co-PECH membranes. Crosslinked membranes have been found to exhibit improved mechanical properties, as well as better chemical stability in acidic environments.

Overall, PEO-co-PECH is a promising material for use as a polyelectrolyte in PEMFCs, with good proton conductivity, thermal stability, and improved mechanical and chemical properties compared to PECH. However, further research is needed to optimize the performance of PEO-co-PECH-based membranes in PEMFCs and to investigate their long-term stability.

Accordingly, in Chapter 6 two different membranes based on PECH are analysed. The first one, consists of dendronized copolymers of poly(epichlorohydrin) (PECH) partially grafted with the dendron 3,4,5-tris[4-(n-dodecan-1-yloxy) benzyloxy] benzoate. The final chemical structure is schematized in Figure 6.2. The backbones with their dendritic side groups form a self-assembled structure with arrangement into columnar channels, which complex behaviour is related to the interaction between both parts, and thus, it must be analysed as a whole [16-19]. These copolymers have the same dendritic side groups of the PAZE copolymers analysed in the previous work but differ in the presence of the basic oxygen atoms instead of nitrogen in their backbones.

Dendronized polymers and copolymers of poly(epichlorohydrin) (PECH) have already been studied. Percec et al. described the self-organized dendritic side groups and backbone. They demonstrated the final properties to selectively transport charges are dependent on the shape of the columnar self-assembly of the dendrimers, which design the supramolecular architecture [20-

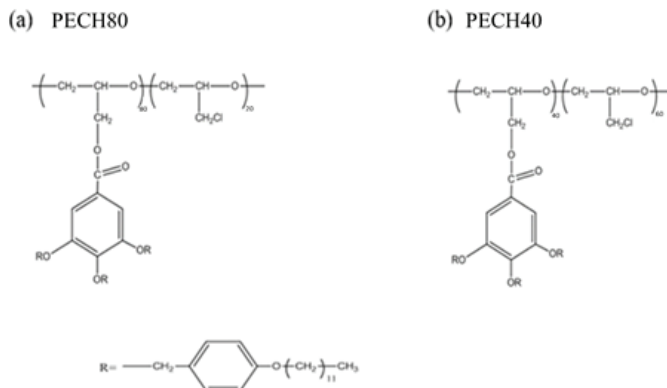


Figure 6.2: Molecular structure of the PECH40 and PECH80.

22]. Tylkowski et al. prepared a series of copolymers of PECH with large supramolecular systems, which have a columnar structure that allowed the formation of ion channels on the inner part [23].

Furthermore, dendronized polymers and copolymers of poly(epichlorohydrin) (PECH) and poly[2-(aziridin-1-yl) ethanol] (PAZE), with different proportions of dendritic 3,4,5-tris[4-(n-dodecan-1-yloxy) benzyloxy] benzoate side groups, has been widely investigated by our research group [24-32]. These membranes, in which the polymer columns were homeotropically oriented, have been submitted to thermal treatment during membrane preparation were analyzed elsewhere by the same authors [30,31]. These copolymers show an ability to change their shape, achieve orientation, and slightly crystallize. This behaviour was deeply analyzed by dielectric thermal analysis, supported by Differential Scanning Calorimetry (DSC), X-ray diffraction (XRD), and ^{13}C Cross Polarization Magic Angle Spinning (CP-MAS) NMR, which allowed to characterize these materials, as far as their structure and tendency to crystallize is concerned. These results indicate that modified PECHs were more flexible than PAZE copolymers and offered a higher free volume at a higher degree of modifica-

tions. Several factors, such as the number of dendritic side groups and their orientation, are responsible for cations mobility through channels.

The second membrane is a liquid crystalline poly (epichlorohydrin-co-ethylene oxide) (PECH-co-EO), grafted with 20% (CP20) and 40% (CP40) side chain dendron 3,4,5-tris[4-(n-dodecan-1-yloxy)benzyloxy] benzoate (Tap). The ethylene oxide unit in the polymeric backbone of P(ECH-co-EO) may act as a spacer, thus modifying the large supramolecular systems mobility because a large portion of free space is required to move self-organized dendritic side groups and backbone. In addition, it could favour interaction with cations and provide water-independent selective transport due to the electronegative oxygen atoms systems. Furthermore, the columns were submitted to an orientation process, which was of paramount importance to obtaining effective transport.

Consequently, Chapter 6 analyses the dielectric relaxation spectra, the electric and proton conductivity of the two families of copolymers, in order to understand the role of the backbone in self-assembled structures and the interaction between dendritic side groups.

6.2 Materials

6.2.1 *Liquid crystal membranes based on poly(epichlorohydrin)*

Commercial poly(epichlorohydrin) (PECH) was purchased from Aldrich. The copolymers were obtained by grafting the net poly(epichlorohydrin) with 3,4,5-tris[4-(n-dodecan-1-yloxy)benzyloxy] benzoate. Membranes were prepared out of these polymers using phase inversion precipitation onto a Teflon® substrate. Homeotropic orientation of the LC columns was obtained by following the thermal treatment reported elsewhere [25,26]. This orientation is perpendicular to the membrane surface and improves the formation of ionic channels, which allows efficient cation transport. The thermal treatment consists of heating the obtained membranes above the copolymer clearing temperature on Teflon®

support with a Linkam TP92 hot stage and keeping them at this temperature for ten minutes. Subsequently, they were slowly cooled ($0.5 \text{ K} \cdot \text{min}^{-1}$) to room temperature and then separated from the Teflon® support. Copolymers have been labelled PECH80 and PECH40, where 80 and 40 represent the degree of modification of the net polyethers, PECH. Oriented copolymers are labelled as PECH80-O and PECH40-O.

6.2.2 *Liquid crystal membranes based on poly(epichlorohydrin-co-ethylene oxide)*

Tetrahydrofuran (THF), P(ECH-co-EO) with PECH/PEO 1:1 and Tetrabutylammonium bromide (TBAB) $\geq 99\%$ were supplied by either Fluka or Sigma-Aldrich. Membranes were prepared by immersion precipitation method. The modified copolymer was dissolved in THF (30% w/w). After that, the homogeneous solution was cast by a casting machine (K-paint applicator, RK Paintcoat Instruments Ltd., United Kingdom) on an FEP (Fluorinated Ethylene Propylene) sheet support with a controlled thickness (gap size $300 \mu\text{m}$). Then, the support, including the wet film on top, was immersed in a bath of Milli-Q water in which the polymeric membrane was formed with an asymmetric structure. After 24 h, the formed membrane was dried overnight at room temperature. Moreover, the membranes were vacuum dried at room temperature 48 hours before weighing. In addition, the oriented samples of the CP20 and CP40 were prepared. The polymeric membrane (approx. 2 cm diameter) was placed on a hot stage (Linkam TP92, Linkam Scientific Instruments Ltd., Tadworth, UK) to achieve the homeotropically oriented structure of modified copolymer the baking process, described as follows. For annealing, membranes were heated up to 413 K. They were kept at the same temperature for 30 minutes. Then they were slowly cooled ($0.1 \text{ K} \cdot \text{min}^{-1}$) to 380 K, where they were held for 120 h. Afterwards, the membranes were allowed to cool to room temperature at $10 \text{ K} \cdot \text{min}^{-1}$. Finally, the uniform membranes were left at room temperature for 1 h and then detached from FEP support. These samples were labelled as CP20-O and CP40-O, respectively.

The labelling of the copolymers was performed according to the degree of modification. Thus, the labels CP0, CP20, and CP40 correspond to the P(ECH-co-EO) samples with a degree of modification of 0% (neat), 20%, and 40%, respectively.

6.2.3 *Experimental methodology*

Differential Scanning Calorimetry (DSC)

Aluminium capsules were filled with the samples, about 5 mg, and sealed. Then, they were subjected to a heating/cooling program with a rate of $10 \text{ K} \cdot \text{min}^{-1}$ over the 263K to 473K temperature range under an inert atmosphere with a flow rate of $100 \text{ mL} \cdot \text{min}^{-1}$ of nitrogen.

Dielectric Thermal Analysis (DETA)

The dielectric thermal analysis (DETA) was performed using a Dielectric Spectrometer from No-vocontrol Technologies GmbH & Co. KG, Hundsangen, Germany. The measurements were performed in the frequency range of 10^{-1} to 10^7 Hz between 123 K to 393 K, under isothermal conditions by increasing steps of 10 K. The dielectric experiments were performed in a cell constituted by two gold electrodes where the sample electrode assembly (SEA) was located.

6.3 Results

6.3.1 *Analysis of the dielectric spectra of the PECH40 membrane*

The dielectric spectra was plotted in terms of the real (ϵ') and imaginary (ϵ'') parts of the complex dielectric permittivity (ϵ^*), $\tan \delta$, and the imaginary part of the electric modulus (M'') in Figures 6.3 - 6.4.

In Figure 6.5A the macromolecular origin of the dielectric relaxations is assessed through the Eyring model as derived by Starkweather. The closeness of the γ relaxation to the zero-entropy line shows reveals its non-cooperative nature. Accordingly, the E_a values of the α_{Tg} and α_{Clear} lie far away from the zero-entropy line. Therefore, the macromolecular origin of both dielectric processes must be of cooperative origin.

In Figure 6.5B the Arrhenius plot is displayed. It shows different relaxation zones. More concretely, at low temperature relaxation labelled as γ that it has to be related with local motions of the copolymer. At high temperatures, two molecular motions are present, which are labelled as α_{Tg} and α_{Clear} , respectively. Given the results from the macromolecular assessment together with the temperature at which both processes are occurring, a cooperative origin must be assumed. Most probably, both relaxations are related to the glass transition and the clearing transition, respectively.

In Figure 6.6 the isothermal curves of the modulus of the complex conductivity ($|\sigma|$) for the complete temperature range are displayed.

To determine the proton conductivity, the phase angle and the absolute value of the serial impedance (Z_s) are needed. Thus, both parameters are shown in Figure 6.7.

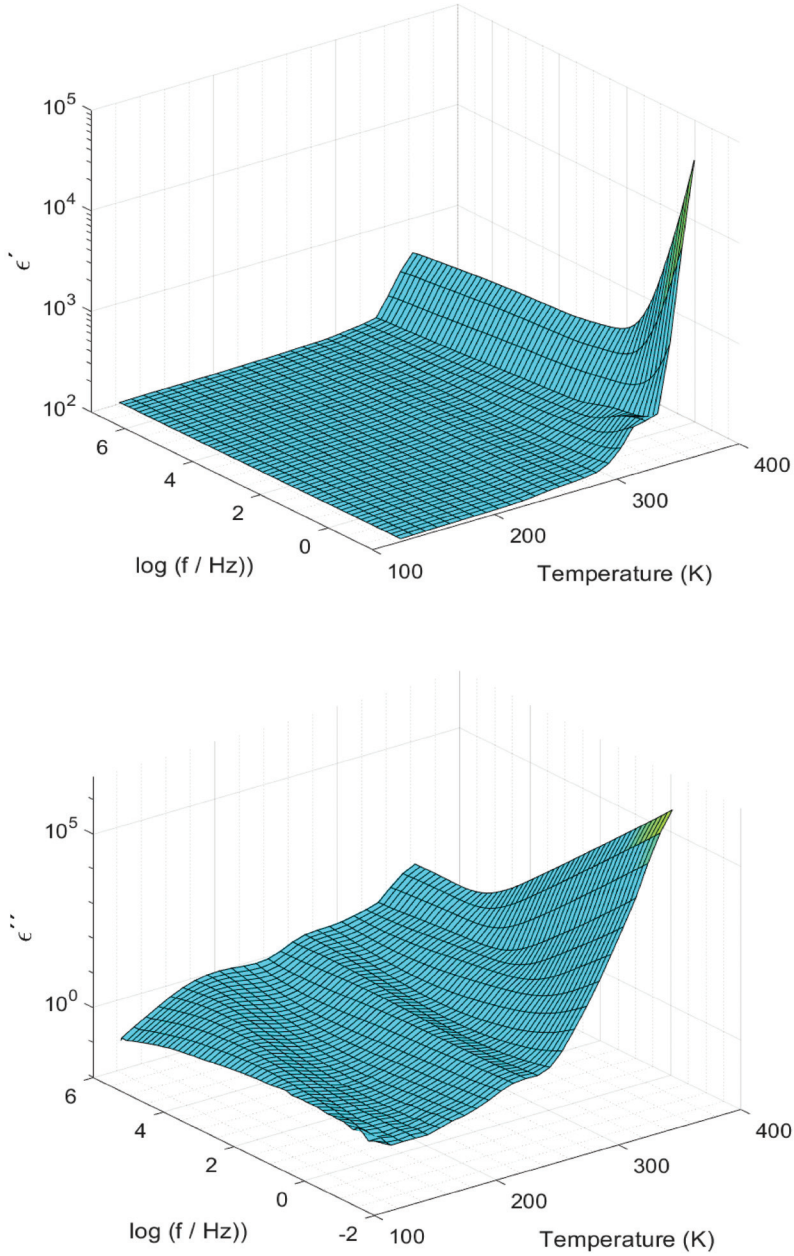


Figure 6.3: 3D plot of the real (ϵ') and imaginary part (ϵ'') parts of the complex permittivity (ϵ^*) of the PECH40 membrane.

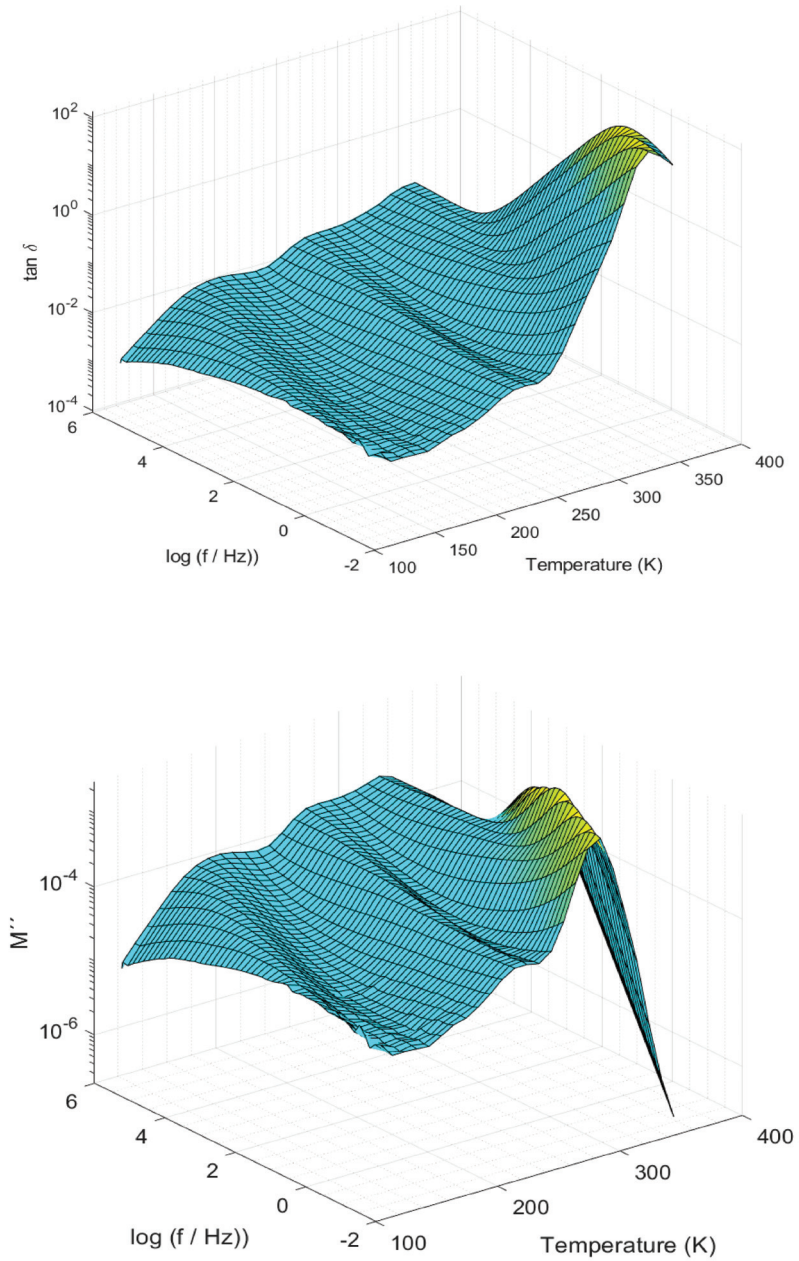


Figure 6.4: 3D plot of $\tan \delta$ and of the imaginary part (M'') of the complex electric modulus (M^*) of the PECH40 membrane.

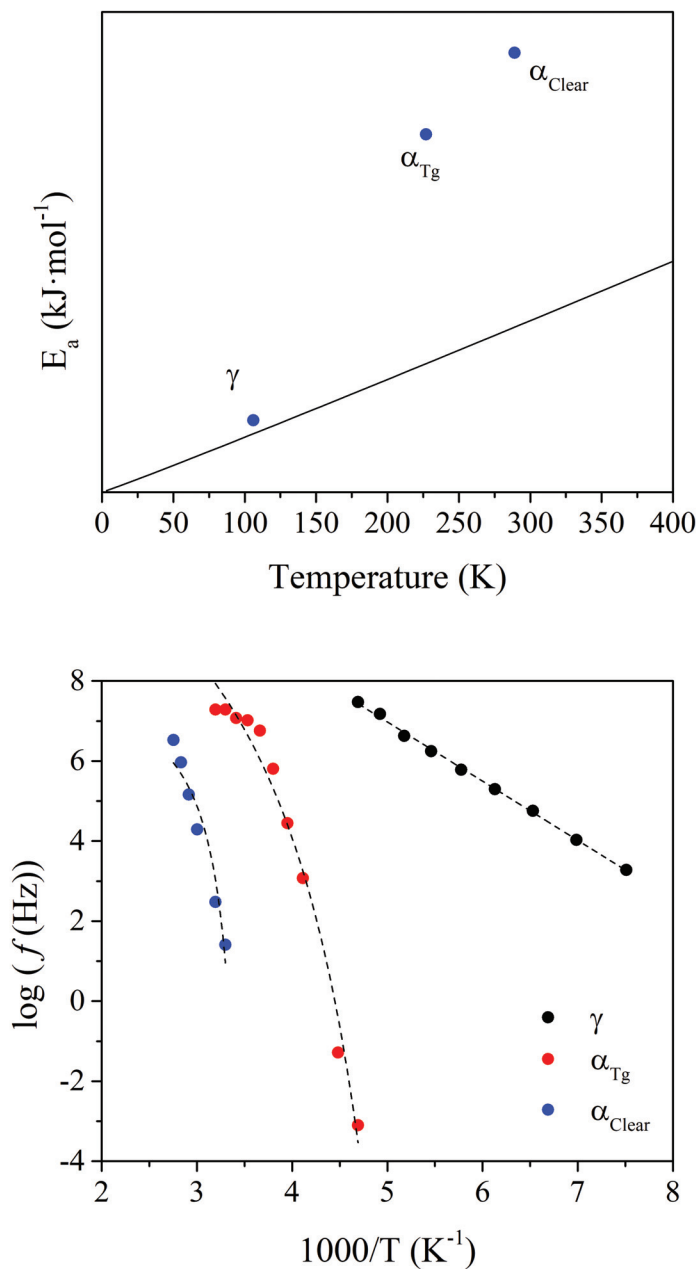


Figure 6.5: (Top) Eyring plot and (Bottom) Arrhenius plot of the PECH40 membrane.

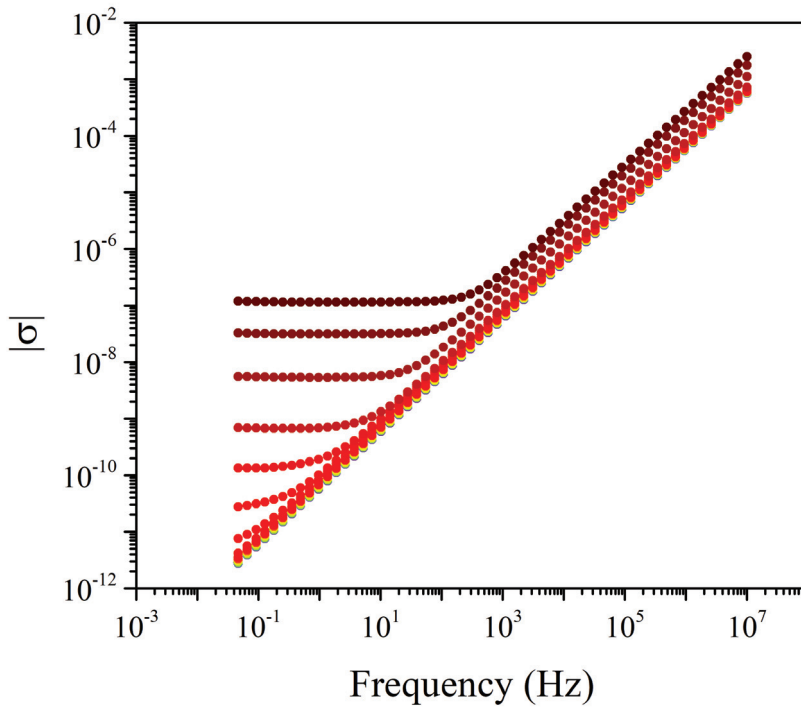


Figure 6.6: Isothermal curves of the modulus of the complex conductivity ($|\sigma|$) for the PECH40 membrane.

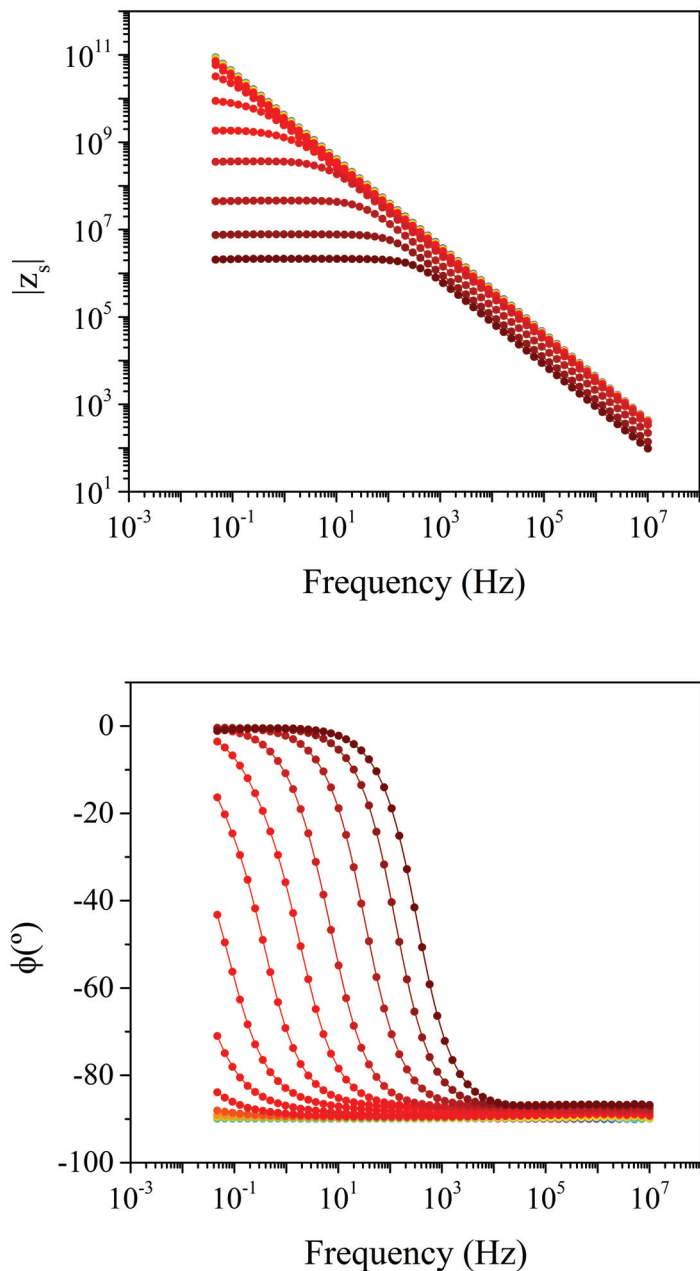


Figure 6.7: Phase angle (ϕ) and modulus of the serial impedance ($|Z_s|$) of the PECH40 membrane.

6.3.2 Analysis of the dielectric spectra of the PECH40-O membrane

The dielectric spectra was plotted in terms of the real (ϵ') and imaginary (ϵ'') parts of the complex dielectric permittivity (ϵ^*), $\tan \delta$, and the imaginary part of the electric modulus (M'') in Figures 6.8 - 6.9.

In Figure 6.10A the macromolecular origin of the dielectric relaxations is assessed through the Eyring model as derived by Starkweather. No significant differences with respect to the PECH40 membrane are found. Therefore, the same conclusions apply. Briefly, the E_a value displayed by the γ relaxation lie close to the zero-entropy line, and therefore, this is characteristic of non-cooperative motions. Contrarily, the E_a exhibited by the α_{Tg} and α_{Clear} relaxations lie far away from the zero-entropy line, and thus, this is a characteristic feature of a molecular motion of cooperative origin.

In Figure 6.10B the Arrhenius plot is displayed. It shows different relaxation zones. No significant differences with respect to the PECH40 membrane are found. Therefore, the same conclusions apply.

In Figure 6.11 the isothermal curves of the modulus of the complex conductivity ($|\sigma|$) for the complete temperature range are displayed.

To determine the proton conductivity, the phase angle and the absolute value of the serial impedance (Z_s) are needed. Thus, both parameters are shown in Figure 6.12.

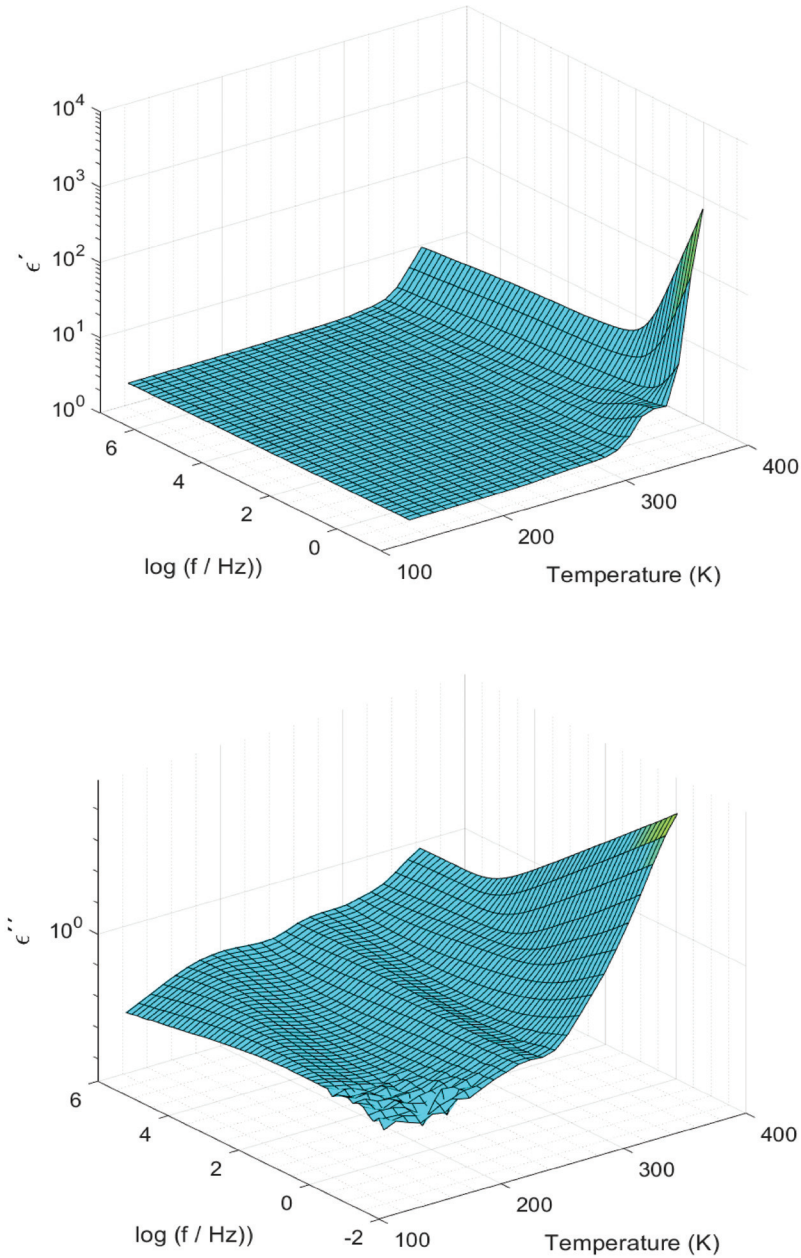


Figure 6.8: 3D plot of the real (ϵ') and imaginary part (ϵ'') parts of the complex permittivity (ϵ^*) of the PECH40-O membrane.

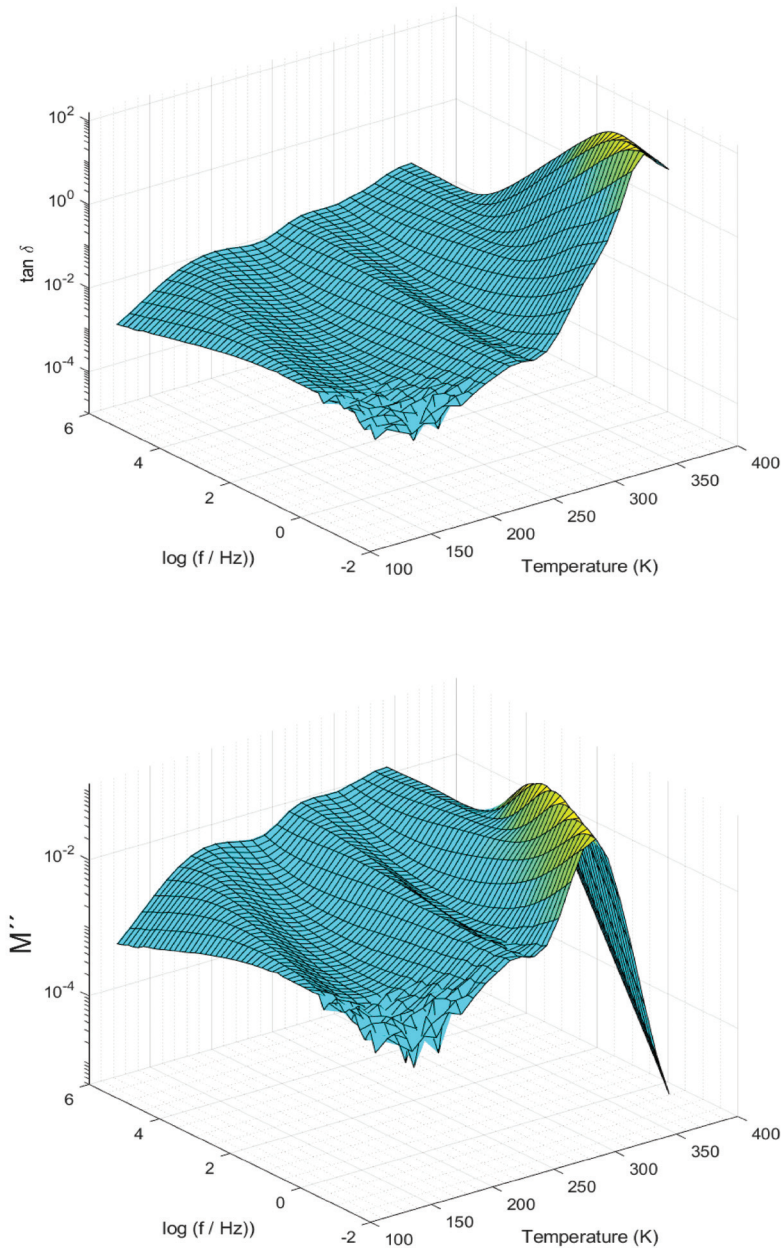


Figure 6.9: 3D plot of $\tan \delta$ and of the imaginary part (M'') of the complex electric modulus (M^*) of the PECH40-O membrane.

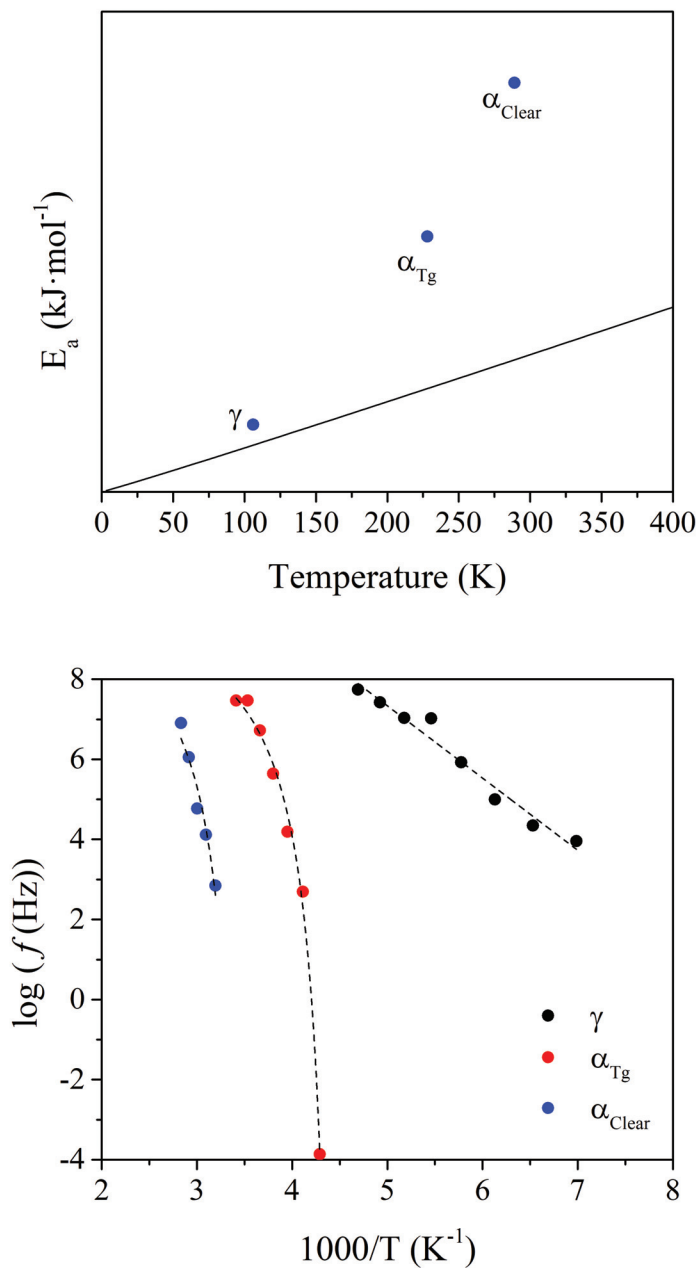


Figure 6.10: (Top) Eyring plot and (Bottom) Arrhenius plot of the PECH40-O membrane.

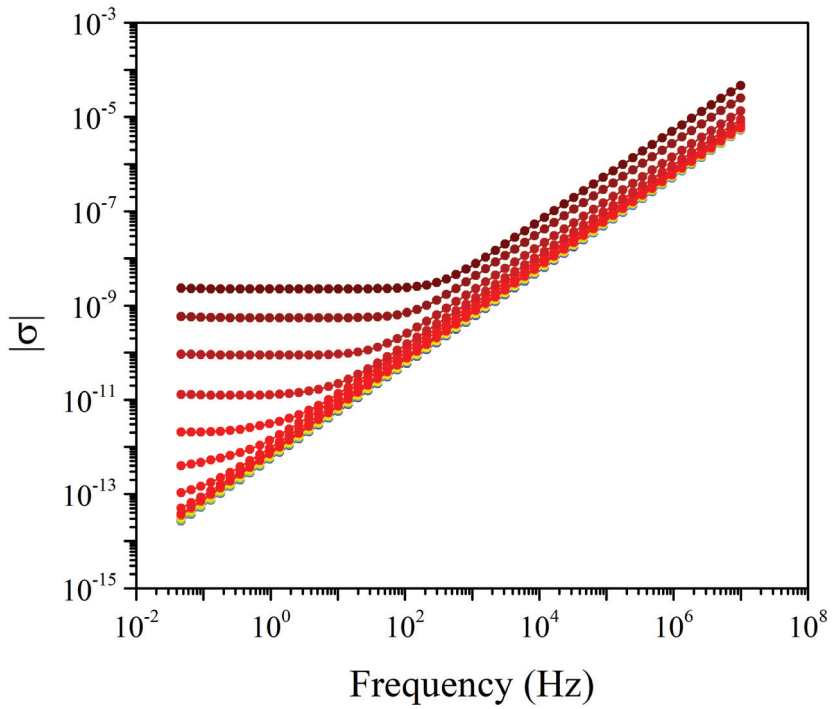


Figure 6.11: Isothermal curves of the modulus of the complex conductivity ($|\sigma|$) for the PECH40-O membrane.

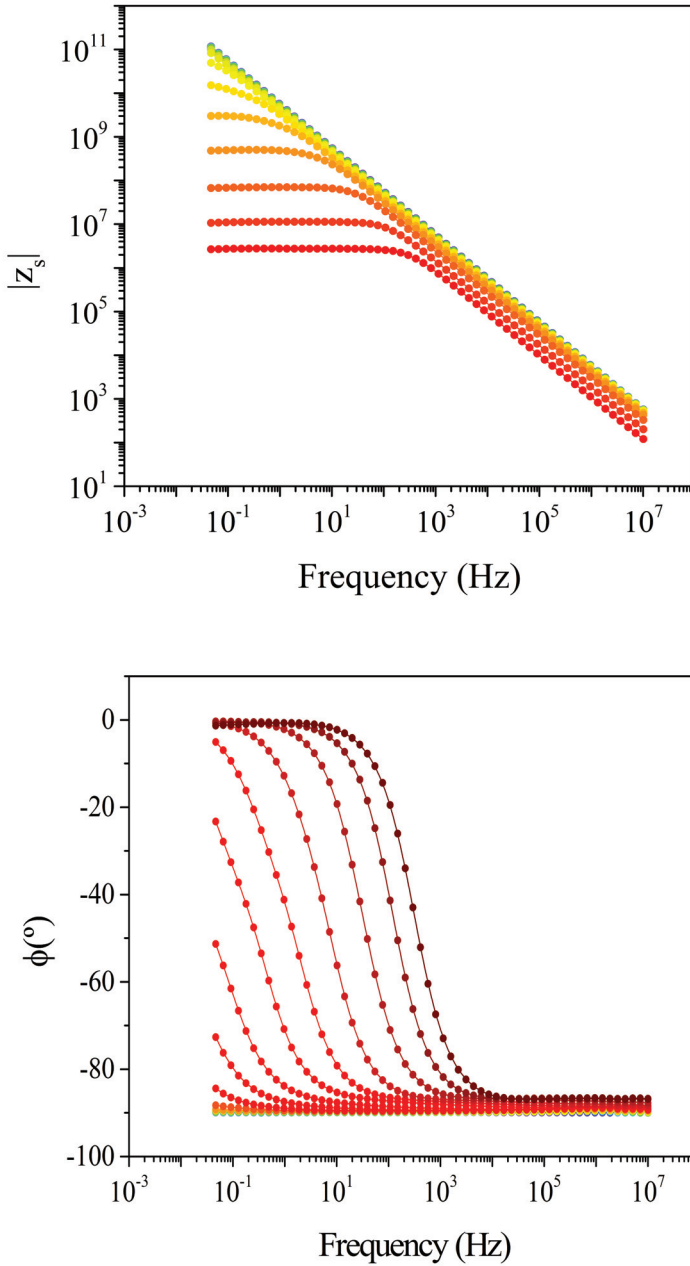


Figure 6.12: Phase angle (ϕ) and modulus of the serial impedance ($|Z_s|$) of the PECH40-O membrane.

6.3.3 Analysis of the dielectric spectra of the PECH80 membrane

The dielectric spectra was plotted in terms of the real (ϵ') and imaginary (ϵ'') parts of the complex dielectric permittivity (ϵ^*), $\tan \delta$, and the imaginary part of the electric modulus (M'') in Figures 6.13 - 6.14.

In Figure 6.15A the macromolecular origin of the dielectric relaxations is assessed through the Eyring model as derived by Starkweather. No significant differences with respect to the PECH40 and PECH40-O membrane regarding the γ and α_{Tg} are found. Briefly, the E_a value displayed by the γ relaxation lie close to the zero-entropy line, and therefore, this is characteristic of non-cooperative motions. Contrarily, the E_a exhibited by the α_{Tg} and α_{Clear} relaxations lie far away from the zero-entropy line, and thus, this is a characteristic feature of a molecular motion of cooperative origin. Note that the α_{Clear} relaxation, although its E_a value is lower than the one of α_{Tg} and those of PECH40 and PECH40-O, lies still far away from the zero-entropy line. Therefore, entropy cannot be disregarded, and thus, it has to be considered a cooperative motion.

In Figure 6.15B the Arrhenius plot is displayed. It shows different relaxation zones. The same dielectric relaxations as in the oriented and unoriented PECH40 membrane are found. Therefore, the same conclusions apply.

In Figure 6.16 the isothermal curves of the modulus of the complex conductivity ($|\sigma|$) for the complete temperature range are displayed.

To determine the proton conductivity, the phase angle and the absolute value of the serial impedance (Z_s) are needed. Thus, both parameters are shown in Figure 6.17.

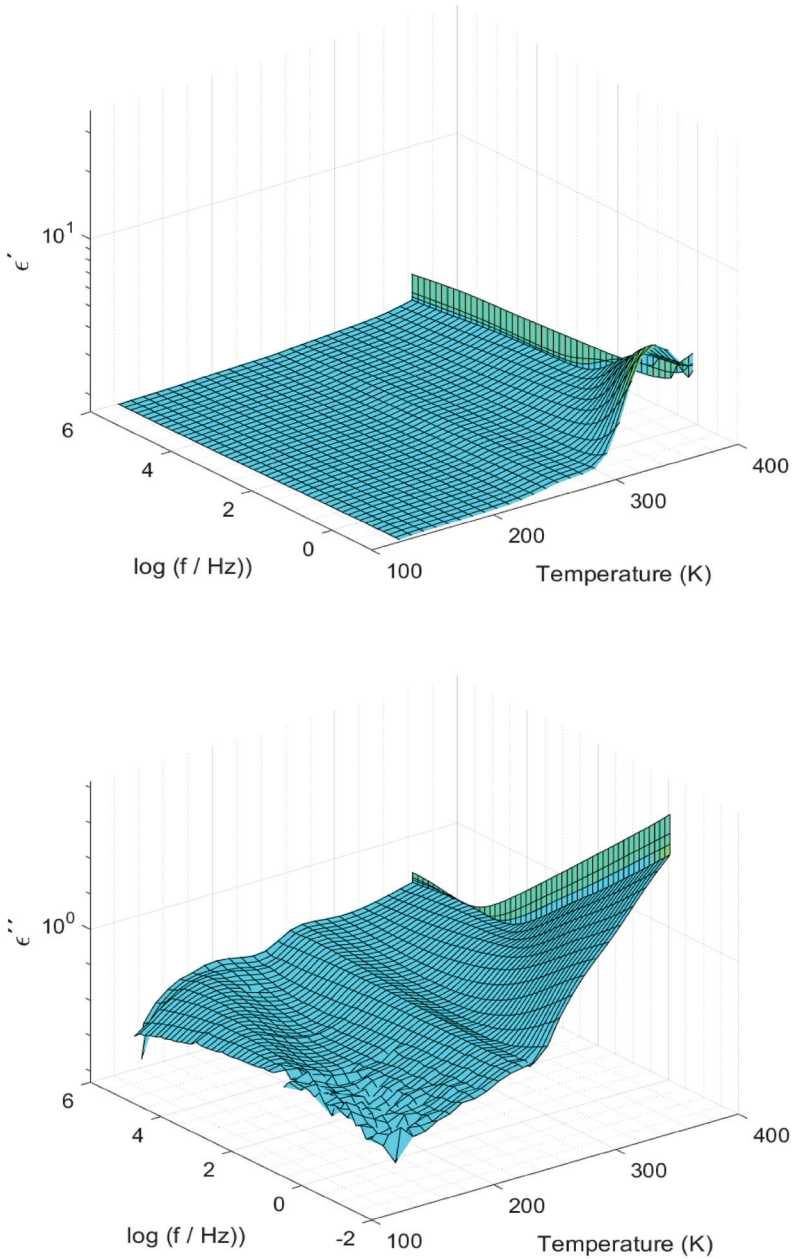


Figure 6.13: 3D plot of the real (ϵ') and imaginary part (ϵ'') parts of the complex permittivity (ϵ^*) of the PECH80 membrane.

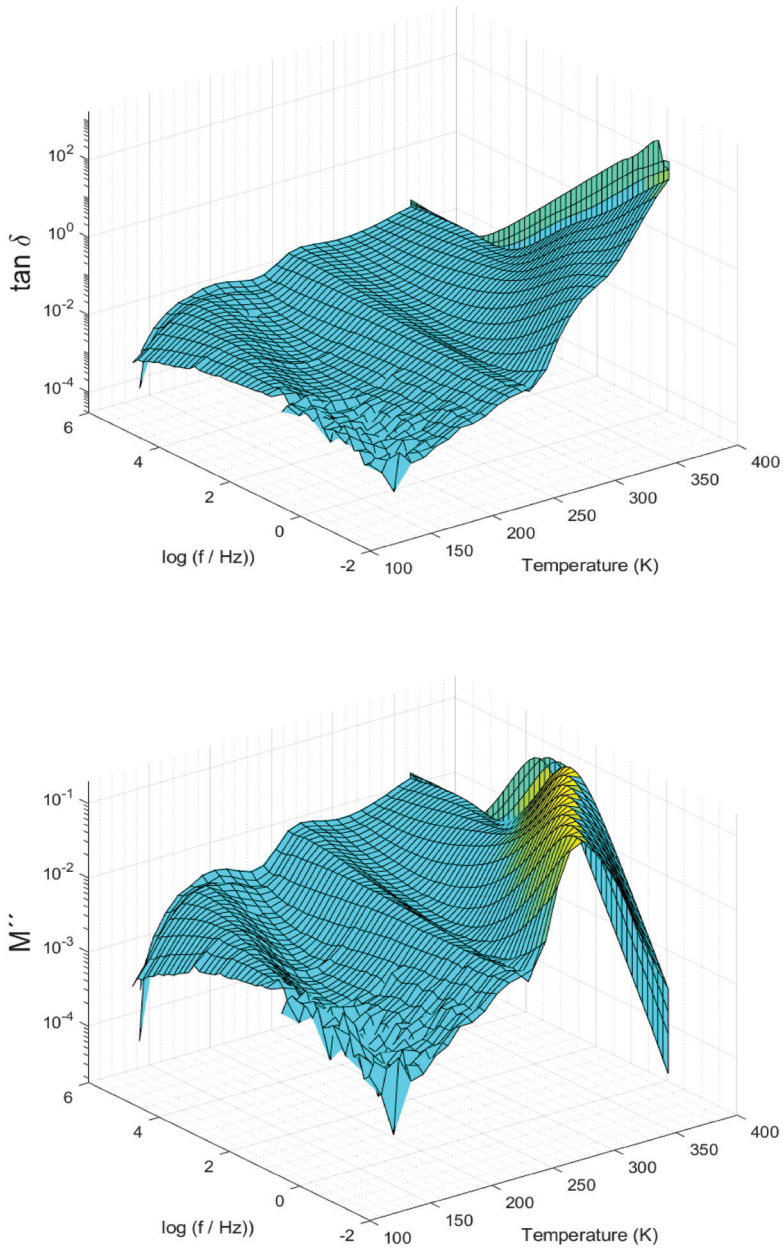


Figure 6.14: 3D plot of $\tan \delta$ and of the imaginary part (M'') of the complex electric modulus (M^*) of the PECH80 membrane.

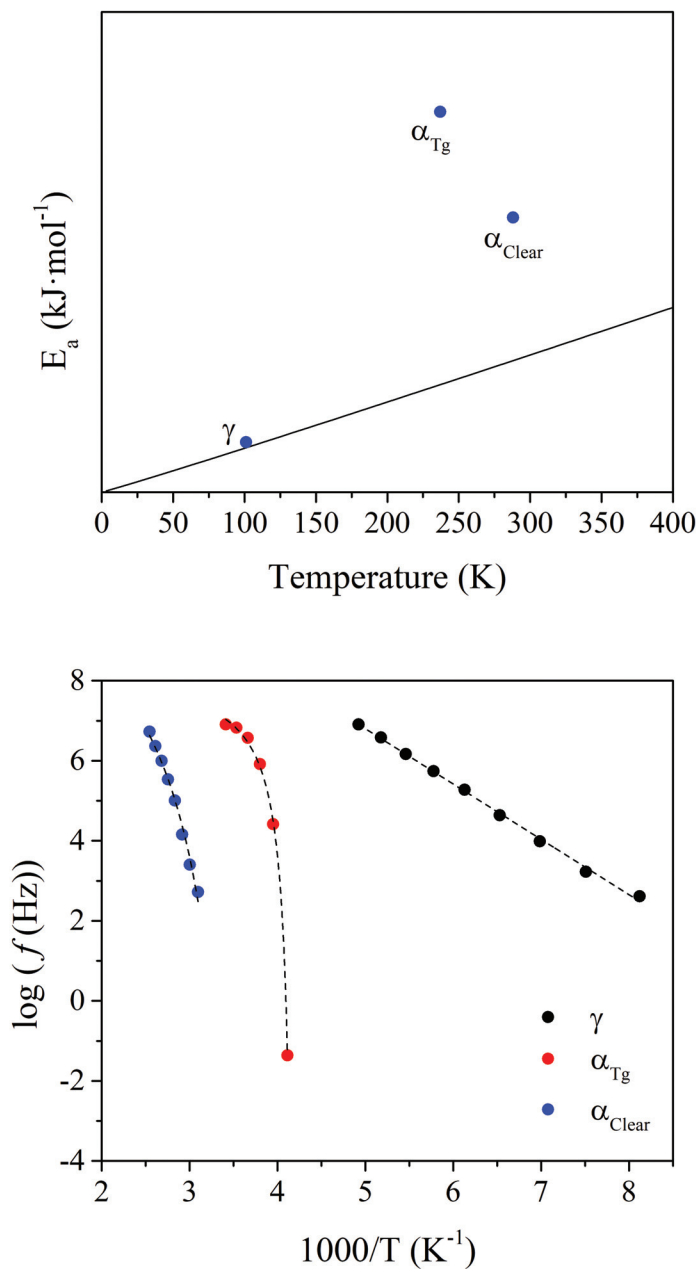


Figure 6.15: (Top) Eyring plot and (Bottom) Arrhenius plot of the PECH80 membrane.

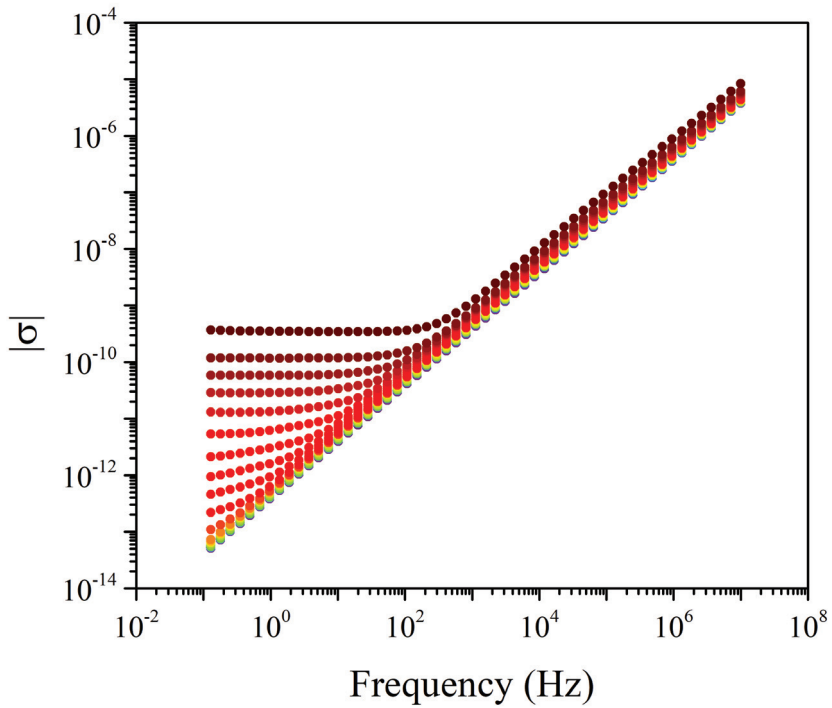


Figure 6.16: Isothermal curves of the modulus of the complex conductivity ($|\sigma|$) for the PECH80 membrane.

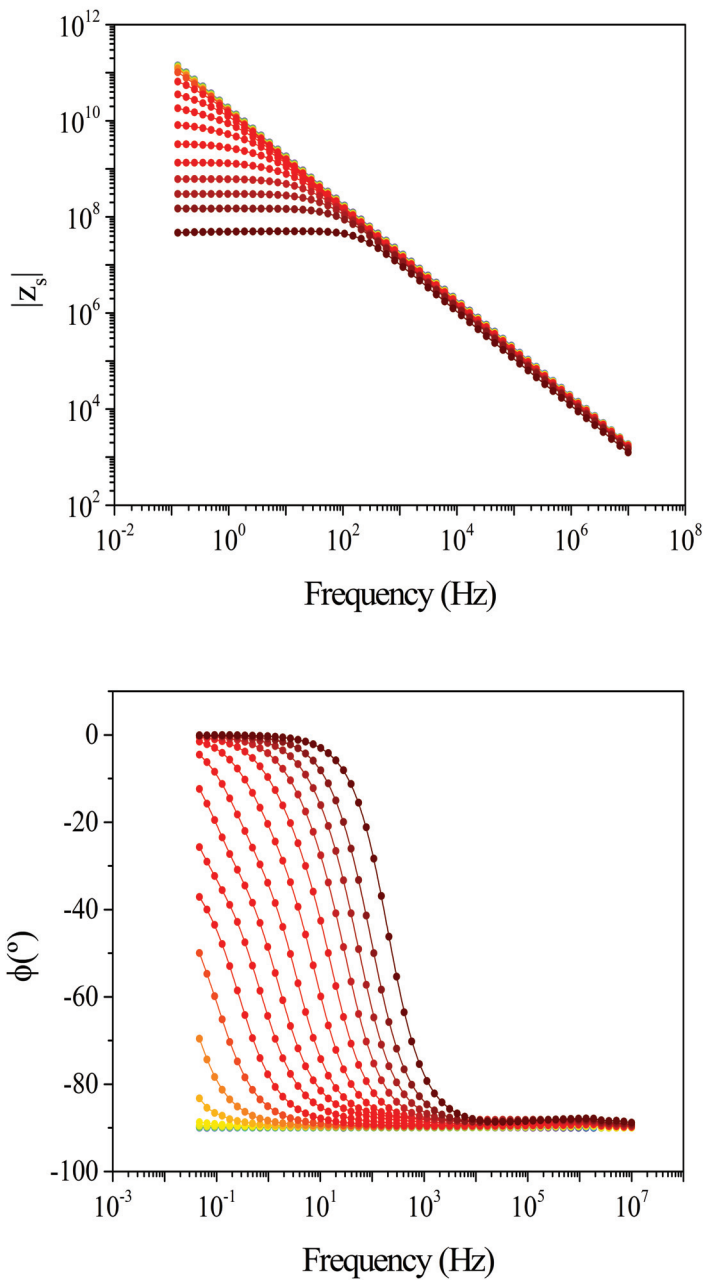


Figure 6.17: Phase angle (ϕ) and modulus of the serial impedance ($|Z_s|$) of the PECH80 membrane.

6.3.4 Analysis of the dielectric spectra of the PECH80-O membrane

The dielectric spectra was plotted in terms of the real (ϵ') and imaginary (ϵ'') parts of the complex dielectric permittivity (ϵ^*), $\tan \delta$, and the imaginary part of the electric modulus (M'') in Figures 6.18 - 6.19.

In Figure 6.20A the macromolecular origin of the dielectric relaxations is assessed through the Eyring model as derived by Starkweather. No significant differences with respect to the oriented and unoriented PECH40 membranes are found, and thus, the same conclusions apply. Briefly, the E_a value displayed by the γ relaxation lie close to the zero-entropy line, and therefore, this is characteristic of non-cooperative motions. Contrarily, the E_a exhibited by the α_{Tg} and α_{Clear} relaxations lie far away from the zero-entropy line, and thus, this is a characteristic feature of a molecular motion of cooperative origin.

In Figure 6.20B the Arrhenius plot is displayed. It shows different relaxation zones. No significant differences with respect to the oriented and unoriented PECH40 and PECH80 membranes are found, and subsequently, the three dielectric processes are assigned the same molecular motions.

In Figure 6.21 the isothermal curves of the modulus of the complex conductivity ($|\sigma|$) for the complete temperature range are displayed.

To determine the proton conductivity, the phase angle and the absolute value of the serial impedance (Z_s) are needed. Thus, both parameters are shown in Figure 6.22.

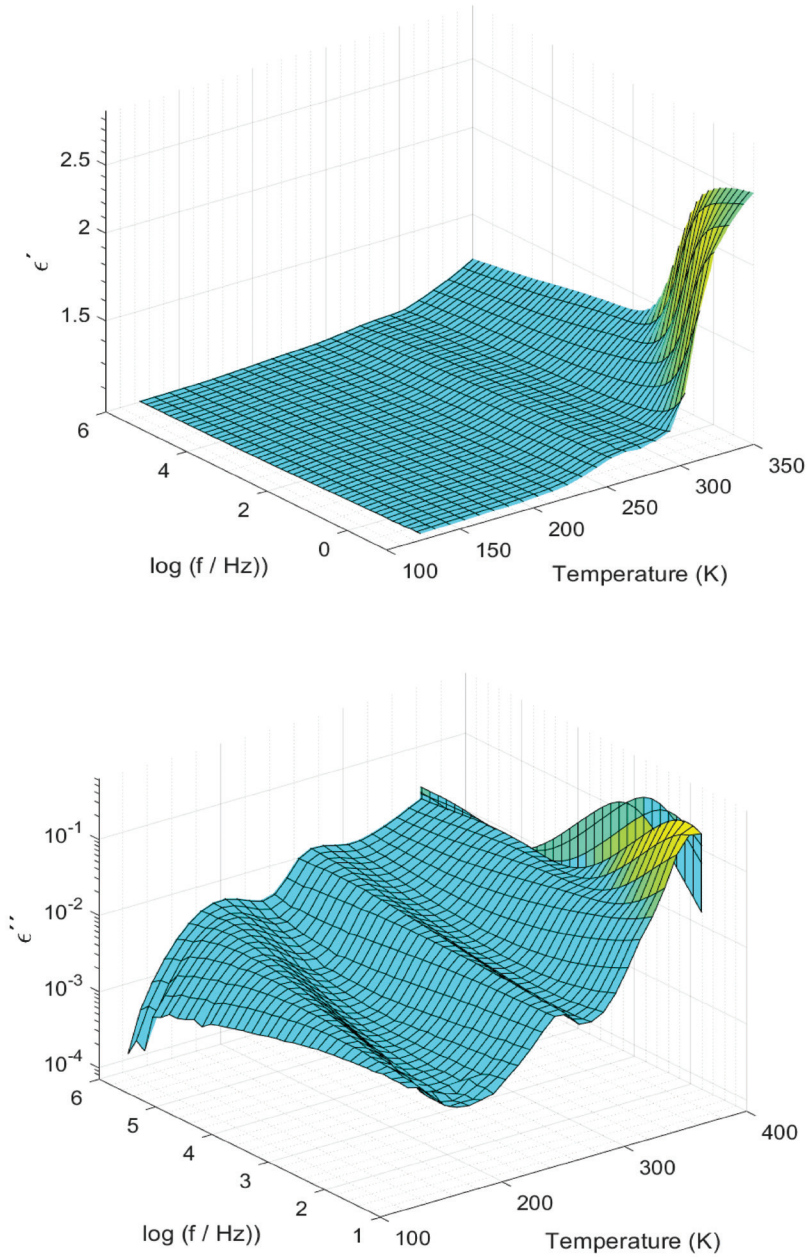


Figure 6.18: 3D plot of the real (ϵ') and imaginary part (ϵ'') parts of the complex permittivity (ϵ^*) of the PECH80-O membrane.

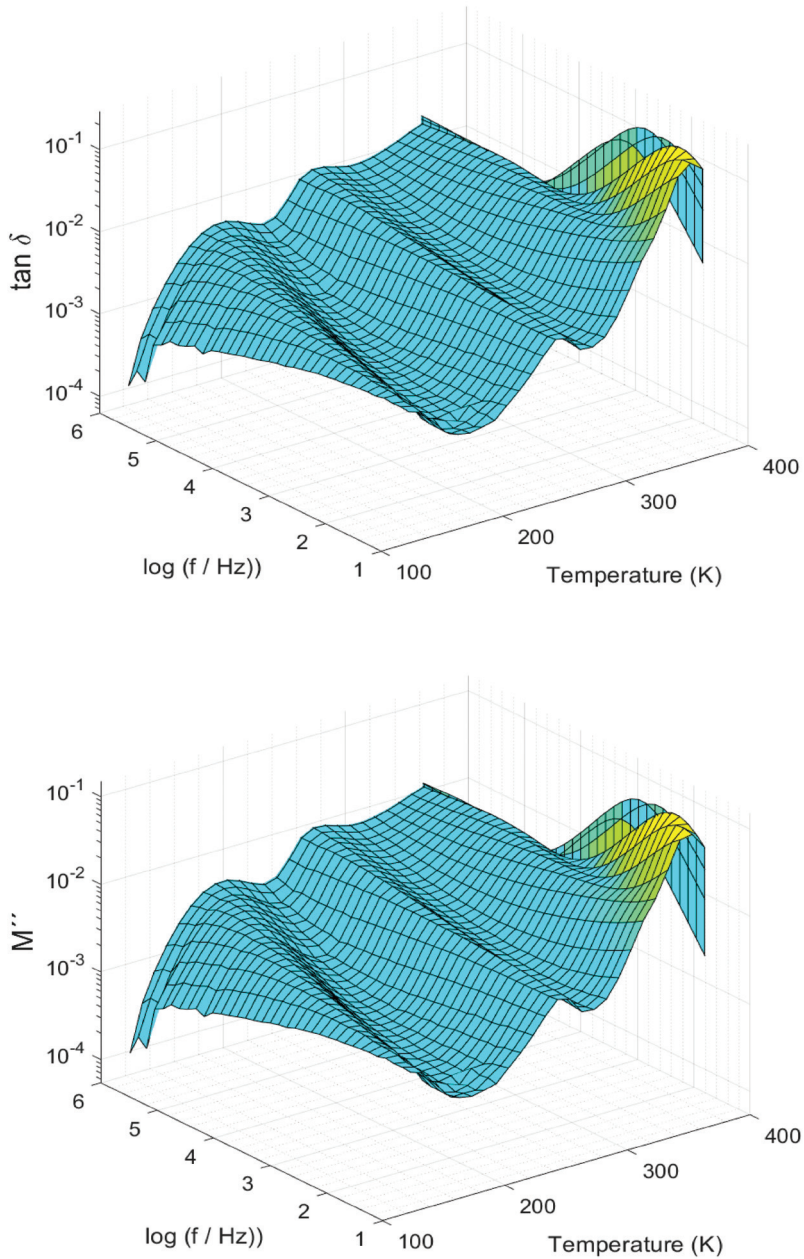


Figure 6.19: 3D plot of $\tan \delta$ and of the imaginary part (M'') of the complex electric modulus (M^*) of the PECH80-O membrane.

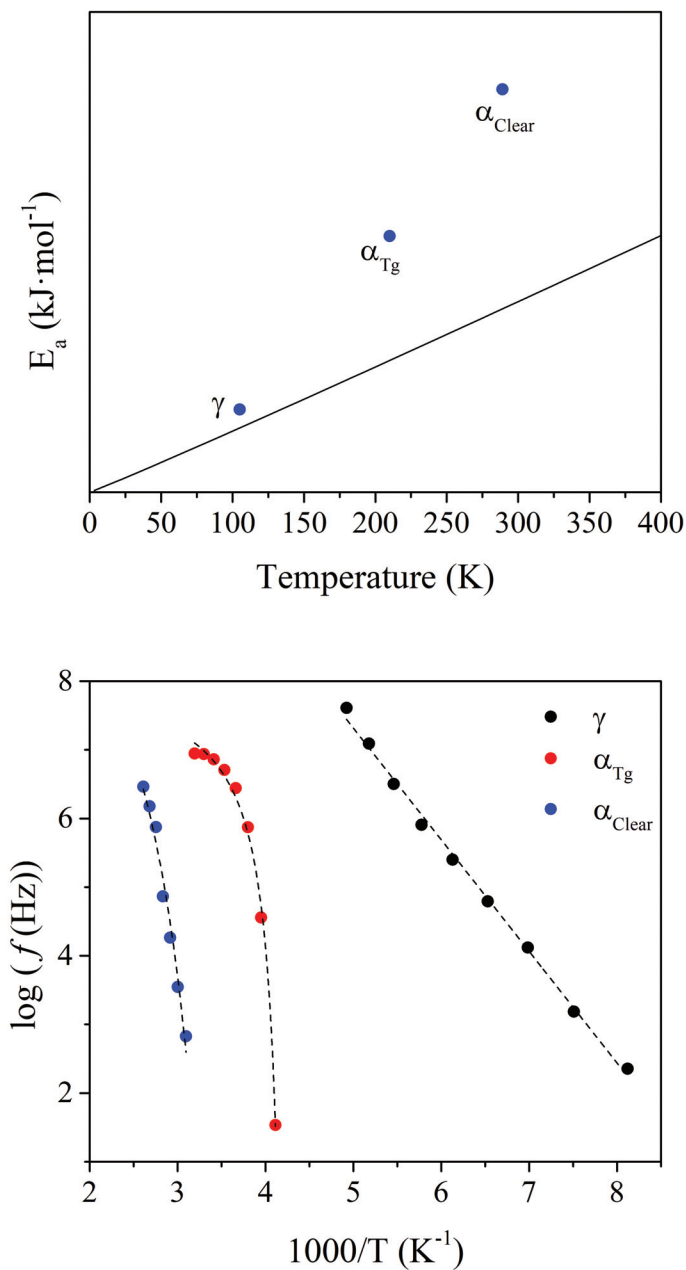


Figure 6.20: (Top) Eyring plot and (Bottom) Arrhenius plot of the PECH80-O membrane.

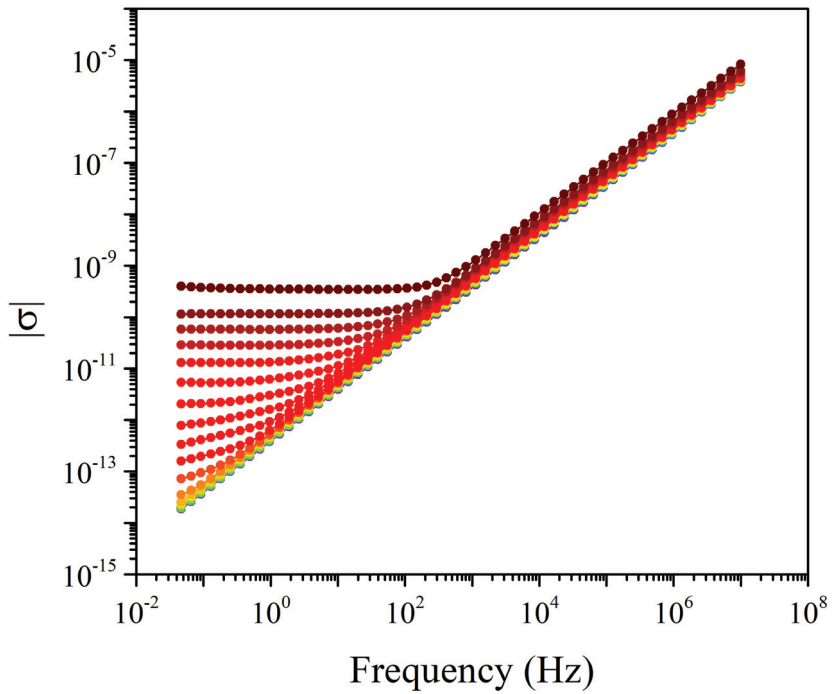


Figure 6.21: Isothermal curves of the modulus of the complex conductivity ($|\sigma|$) for the PECH80-O membrane.

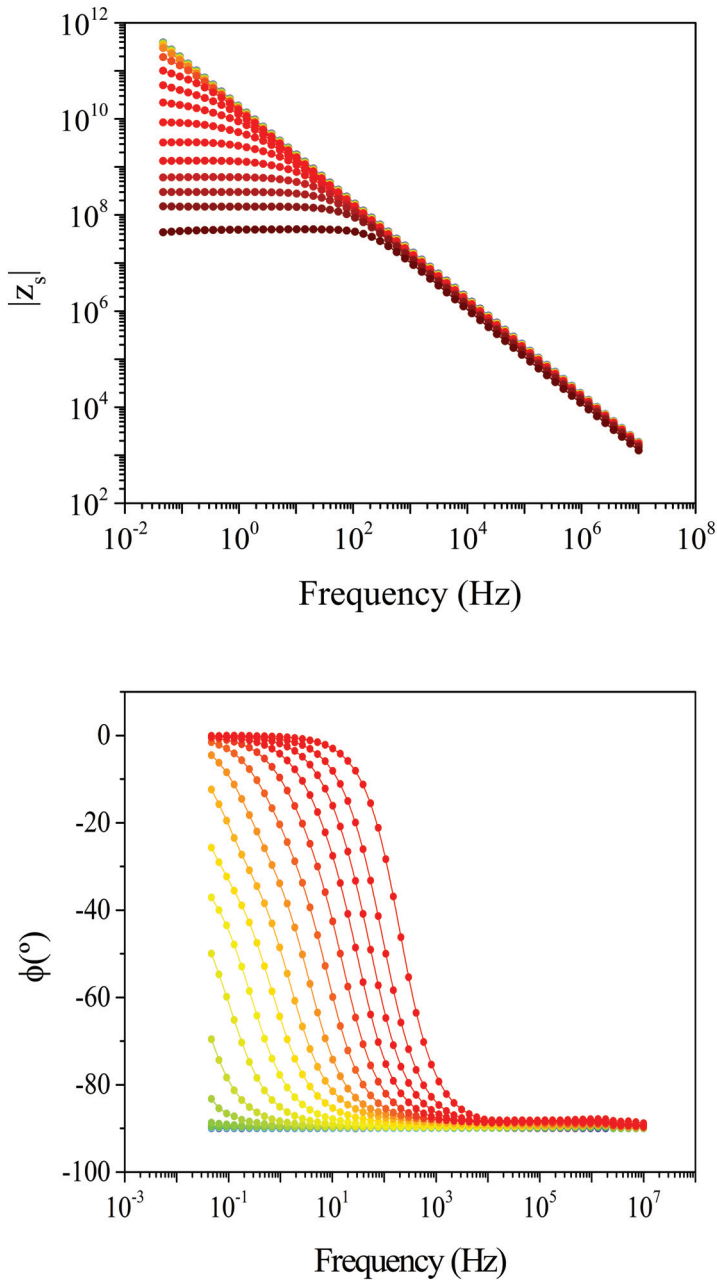


Figure 6.22: Phase angle (ϕ) and modulus of the serial impedance ($|Z_s|$) of the PECH80-O membrane.

6.3.5 Analysis of the dielectric spectra of the CPO membrane

The dielectric spectra was plotted in terms of the real (ϵ') and imaginary (ϵ'') parts of the complex dielectric permittivity (ϵ^*), $\tan \delta$, and the imaginary part of the electric modulus (M'') in Figures 6.23 - 6.24.

In Figure 6.25A the macromolecular origin of the dielectric relaxations is assessed through the Eyring model as derived by Starkweather. At low temperatures, there are two dielectric processes which E_a values lie very close to the zero-entropy line. Therefore, both dielectric processes can be regarded as non-cooperative. At higher temperatures, both processes display E_a values that lie far away from the zero-entropy line. Therefore, the entropy cannot be disregarded which means that both dielectric processes are of cooperative nature.

In Figure 6.25B the Arrhenius plot is displayed. It shows different relaxation zones. There are two dielectric processes at low temperatures, labelled as γ and β , respectively. These dielectric processes must be associated to local motions of the copolymer. Furthermore, at high temperatures, there are two dielectric processes that has been labelled as α_{Tg} and $\alpha_{melting}$. Consequently, the molecular motions ascribed to these dielectric processes are the glass transition and the motions originated from the melting process.

In Figure 6.26 the isothermal curves of the modulus of the complex conductivity ($|\sigma|$) for the complete temperature range are displayed.

To determine the proton conductivity, the phase angle and the absolute value of the serial impedance (Z_s) are needed. Thus, both parameters are shown in Figure 6.27.

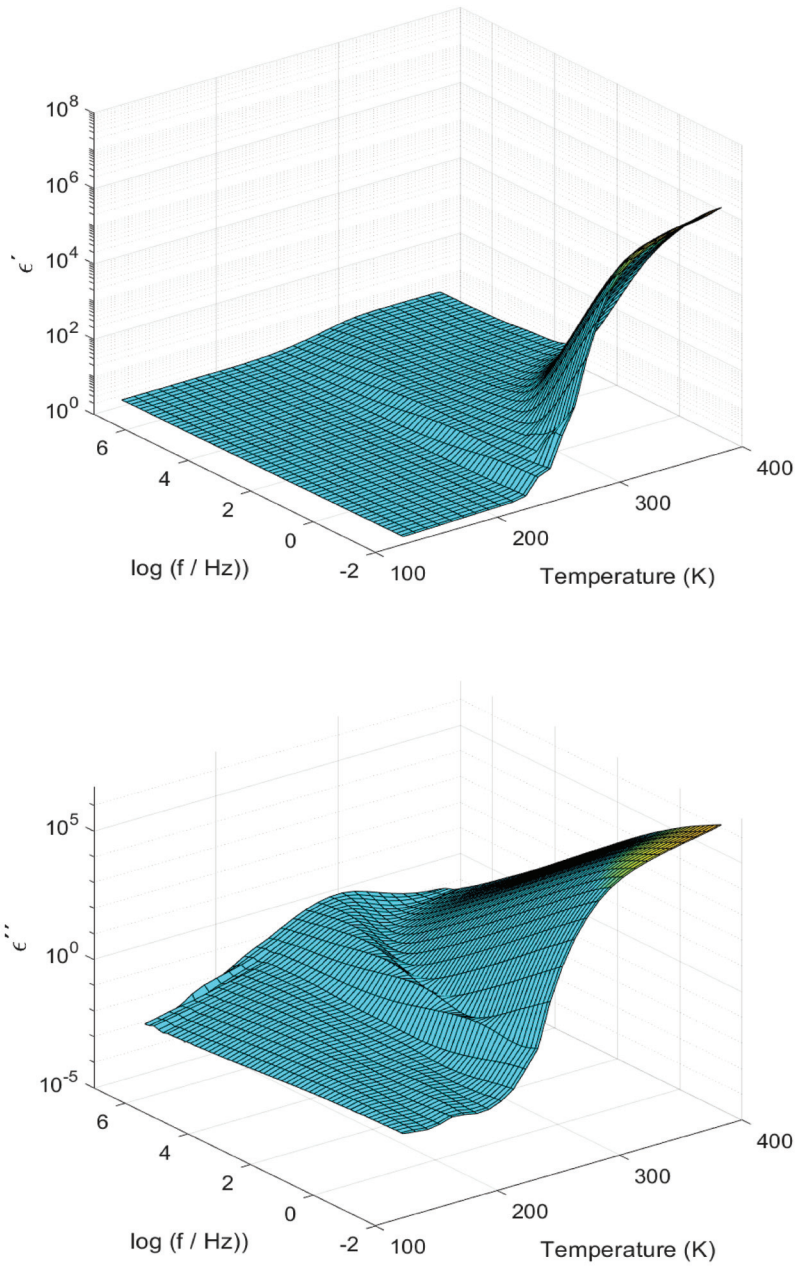


Figure 6.23: 3D plot of the real (ϵ') and imaginary part (ϵ'') parts of the complex permittivity (ϵ^*) of the CP0 membrane.

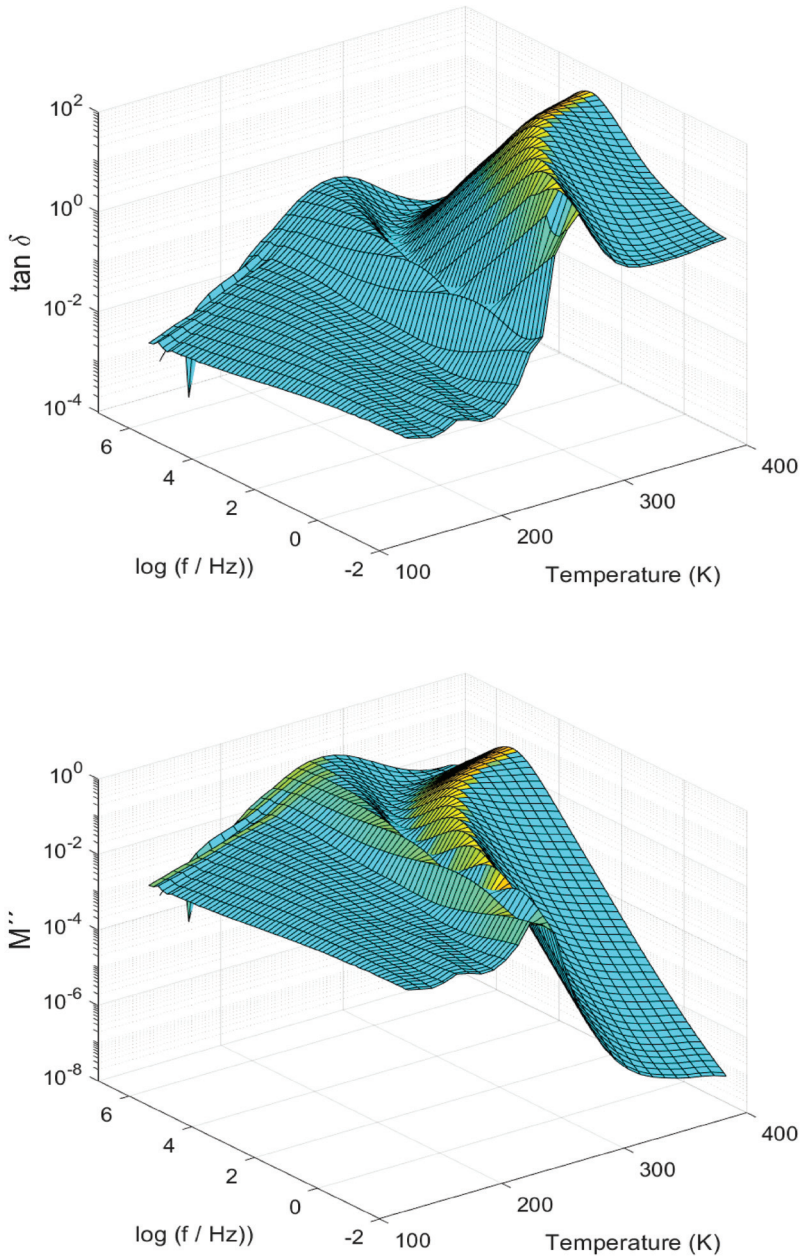


Figure 6.24: 3D plot of $\tan \delta$ and of the imaginary part (M'') of the complex electric modulus (M^*) of the CP0 membrane.

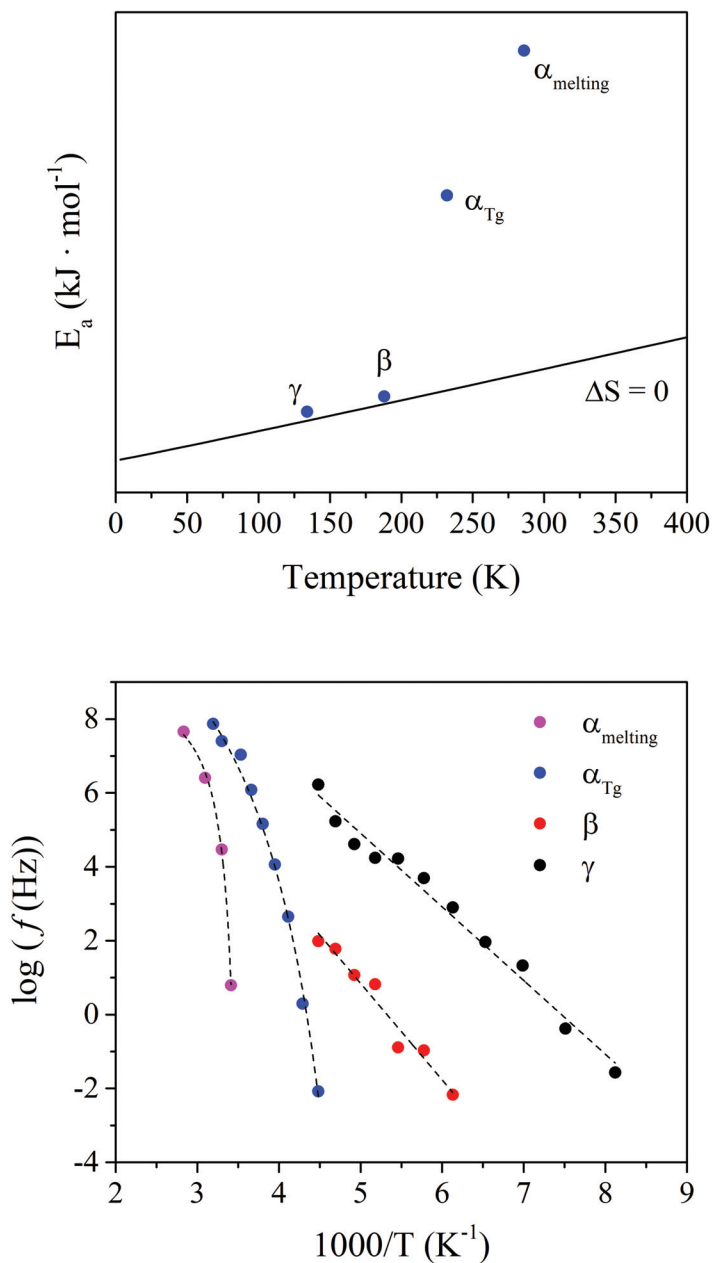


Figure 6.25: (Top) Eyring plot and (Bottom) Arrhenius plot of the CP0 membrane.

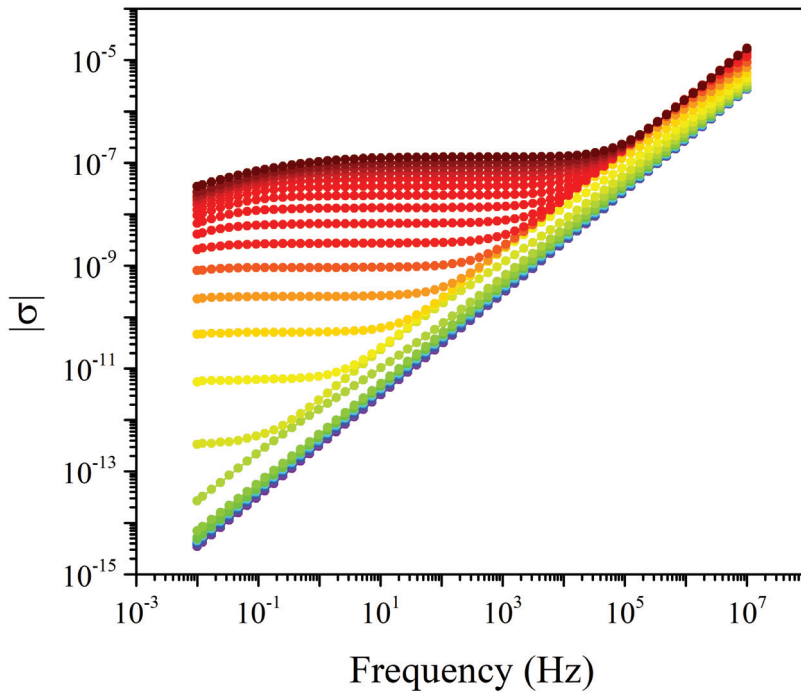


Figure 6.26: Isothermal curves of the modulus of the complex conductivity ($|\sigma|$) for the CP0 membrane.

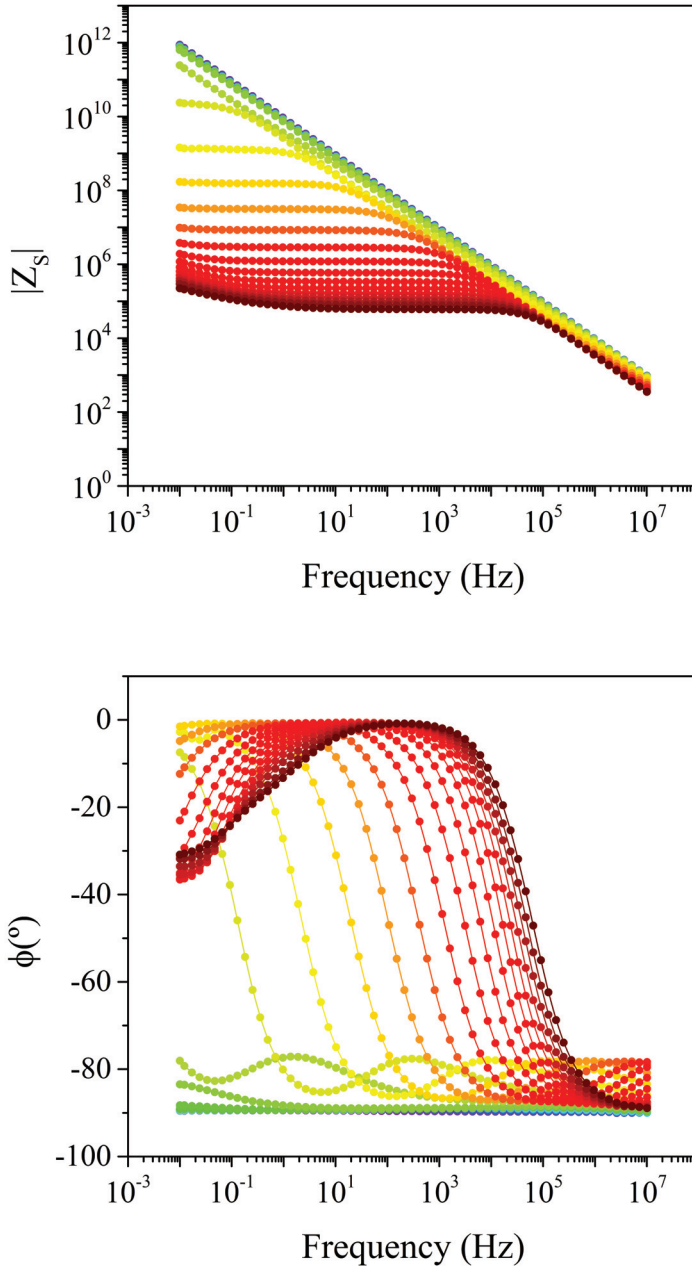


Figure 6.27: Phase angle (ϕ) and modulus of the serial impedance ($|Z_s|$) of the CP0 membrane.

6.3.6 Analysis of the dielectric spectra of the CP20 membrane

The dielectric spectra was plotted in terms of the real (ϵ') and imaginary (ϵ'') parts of the complex dielectric permittivity (ϵ^*), $\tan \delta$, and the imaginary part of the electric modulus (M'') in Figures 6.28 - 6.29.

In Figure 6.30A the macromolecular origin of the dielectric relaxations is assessed through the Eyring model as derived by Starkweather. Concerning the macromolecular assessment of the five dielectric processes. Therefore, the δ , γ and β relaxations display E_a values that lie close to the zero-entropy line, and therefore, both dielectric processes can be considered as non-cooperative. On the other hand, the E_a values of the α_{Tg} and $\alpha_{melting}$ relaxations is characteristic of cooperative molecular motions.

In Figure 6.30B the Arrhenius plot is displayed. It shows different relaxation zones. The CP20 displays five dielectric processes. Three of them are found at low temperatures, and are labelled as δ , γ and β , respectively. Moreover, in the high-temperature region two dielectric processes of cooperative origin are found, and labelled as α_{Tg} and $\alpha_{melting}$. Regarding the high-temperature region, the same molecular origin as in the CP0 membrane could be ascribed.

In Figure 6.31 the isothermal curves of the modulus of the complex conductivity ($|\sigma|$) for the complete temperature range are displayed.

To determine the proton conductivity, the phase angle and the absolute value of the serial impedance (Z_s) are needed. Thus, both parameters are shown in Figure 6.32.

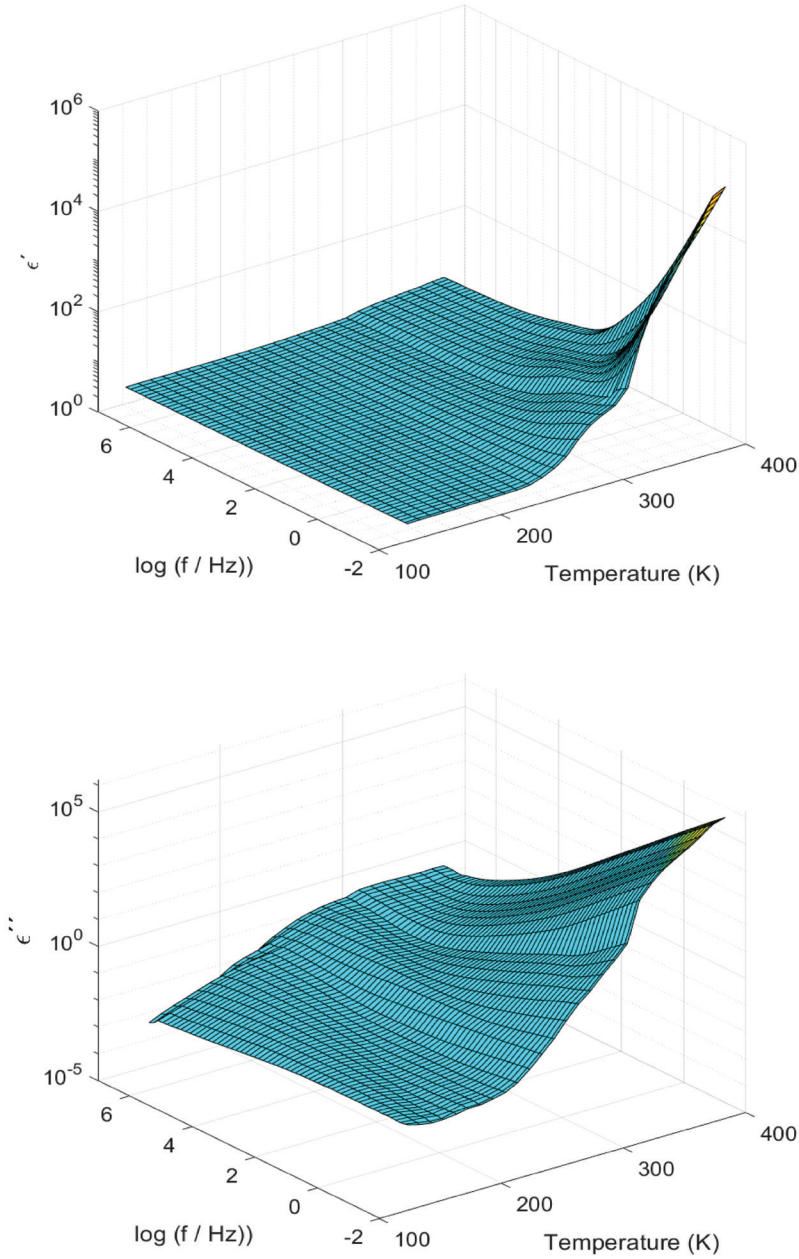


Figure 6.28: 3D plot of the real (ϵ') and imaginary part (ϵ'') parts of the complex permittivity (ϵ^*) of the CP20 membrane.

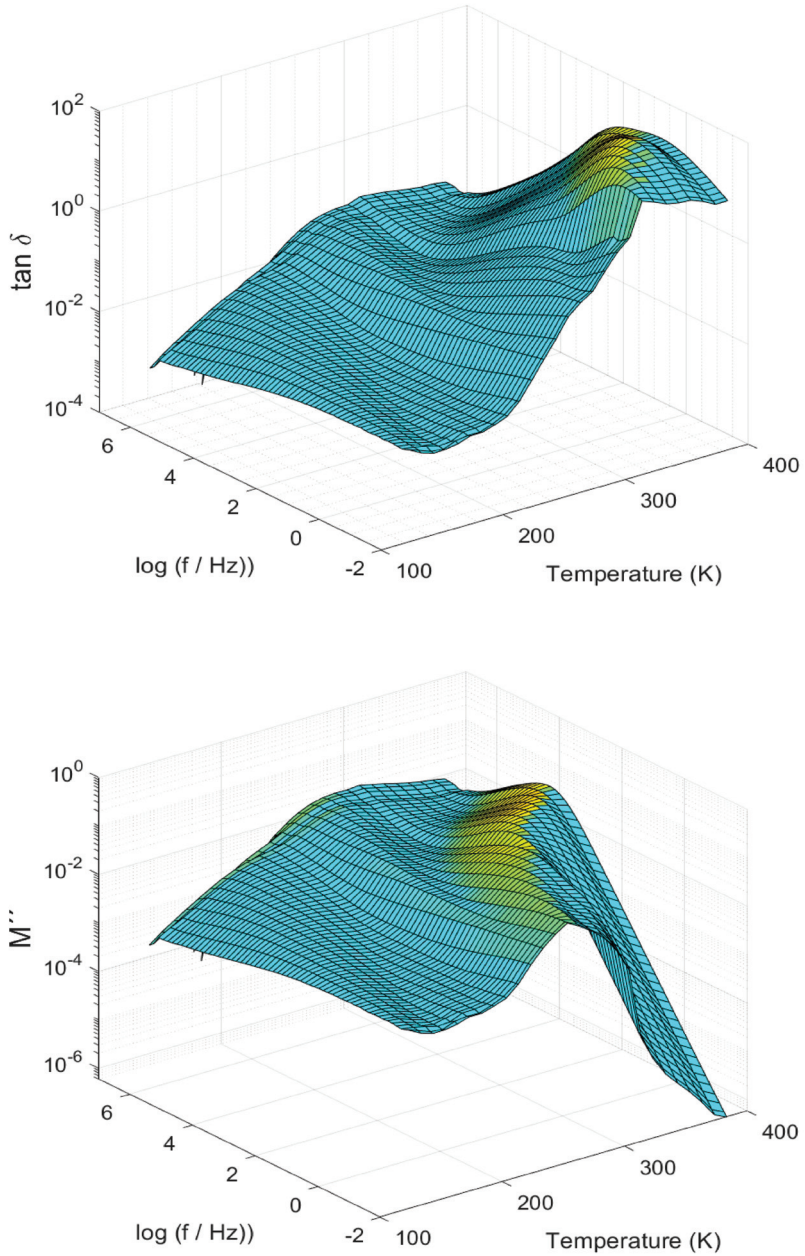


Figure 6.29: 3D plot of $\tan \delta$ and of the imaginary part (M'') of the complex electric modulus (M^*) of the CP20 membrane.

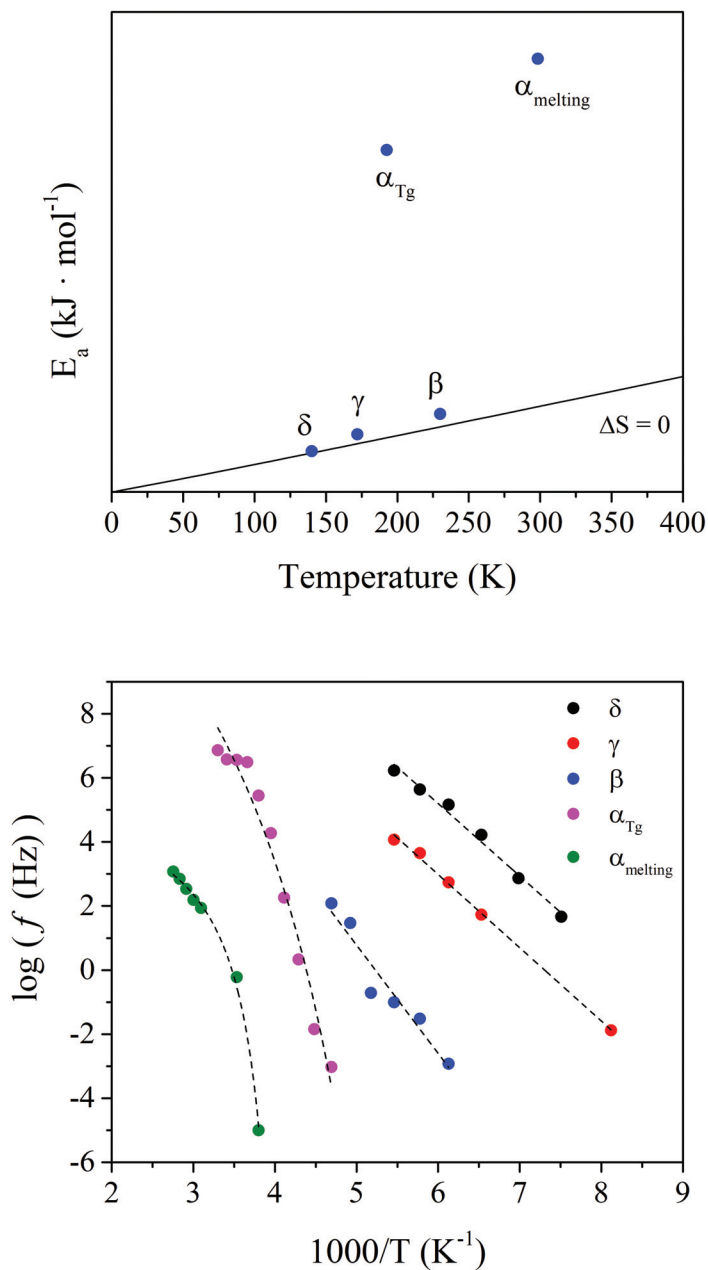


Figure 6.30: (Top) Eyring plot and (Bottom) Arrhenius plot of the CP20 membrane.

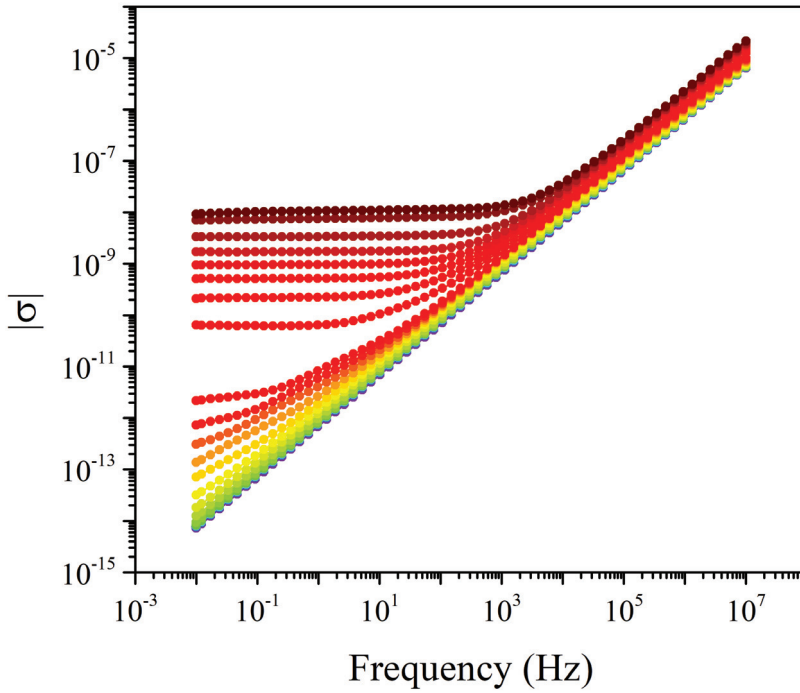


Figure 6.31: Isothermal curves of the modulus of the complex conductivity ($|\sigma|$) for the CP20 membrane.

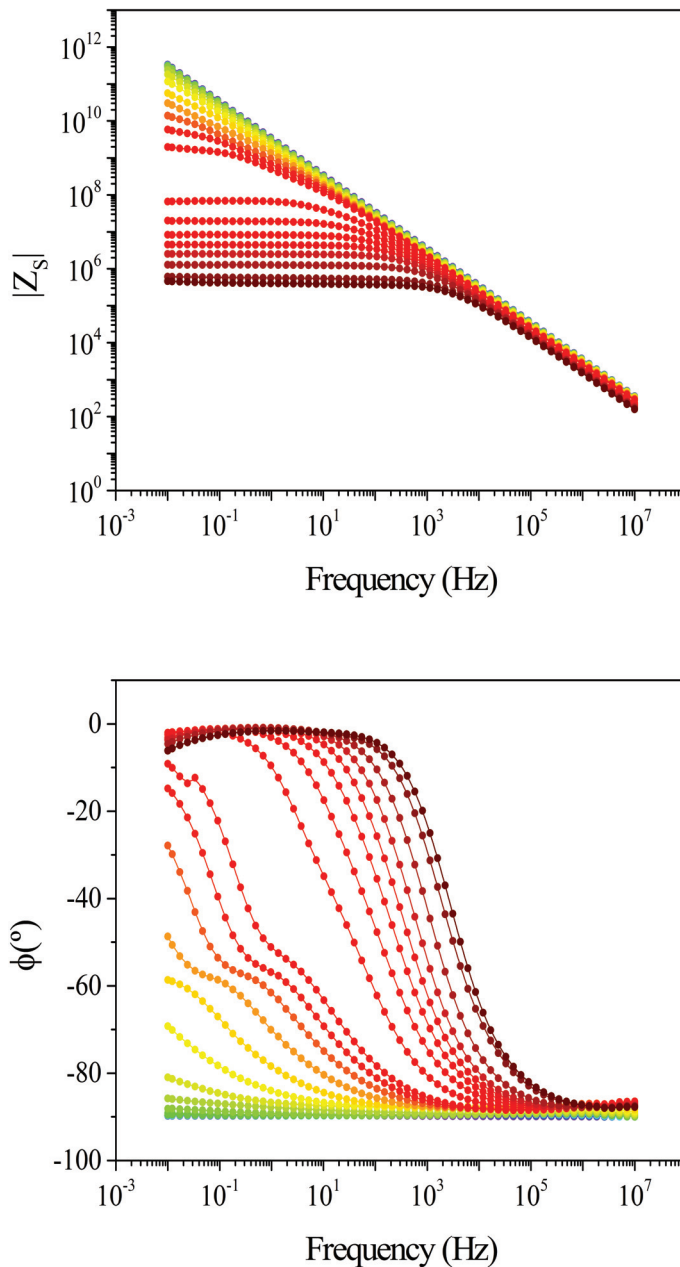


Figure 6.32: Phase angle (ϕ) and modulus of the serial impedance ($|Z_s|$) of the CP20 membrane.

6.3.7 Analysis of the dielectric spectra of the CP20-O membrane

The dielectric spectra was plotted in terms of the real (ϵ') and imaginary (ϵ'') parts of the complex dielectric permittivity (ϵ^*), $\tan \delta$, and the imaginary part of the electric modulus (M'') in Figures 6.33 - 6.34.

In Figure 6.35A the macromolecular origin of the dielectric relaxations is assessed through the Eyring model as derived by Starkweather. No differences with respect to the equivalent unoriented (CP20) membrane are found. Therefore, the same conclusions apply. Briefly, the δ , γ and β relaxations display E_a values that lie close to the zero-entropy line, and therefore, both dielectric processes can be considered as non-cooperative. On the other hand, the E_a values of the α_{Tg} and $\alpha_{melting}$ relaxations is characteristic of cooperative molecular motions.

In Figure 6.35B the Arrhenius plot is displayed. It shows different relaxation zones. The same five dielectric processes as in the unoriented membrane (CP20) are found. Accordingly, three dielectric relaxations are located at low temperatures (δ , γ and β) and the others occur at higher temperatures (α_{Tg} and $\alpha_{melting}$). The molecular origin is the same as the unoriented (CP20) membrane.

In Figure 6.36 the isothermal curves of the modulus of the complex conductivity ($|\sigma|$) for the complete temperature range are displayed.

To determine the proton conductivity, the phase angle and the absolute value of the serial impedance (Z_s) are needed. Thus, both parameters are shown in Figure 6.37.

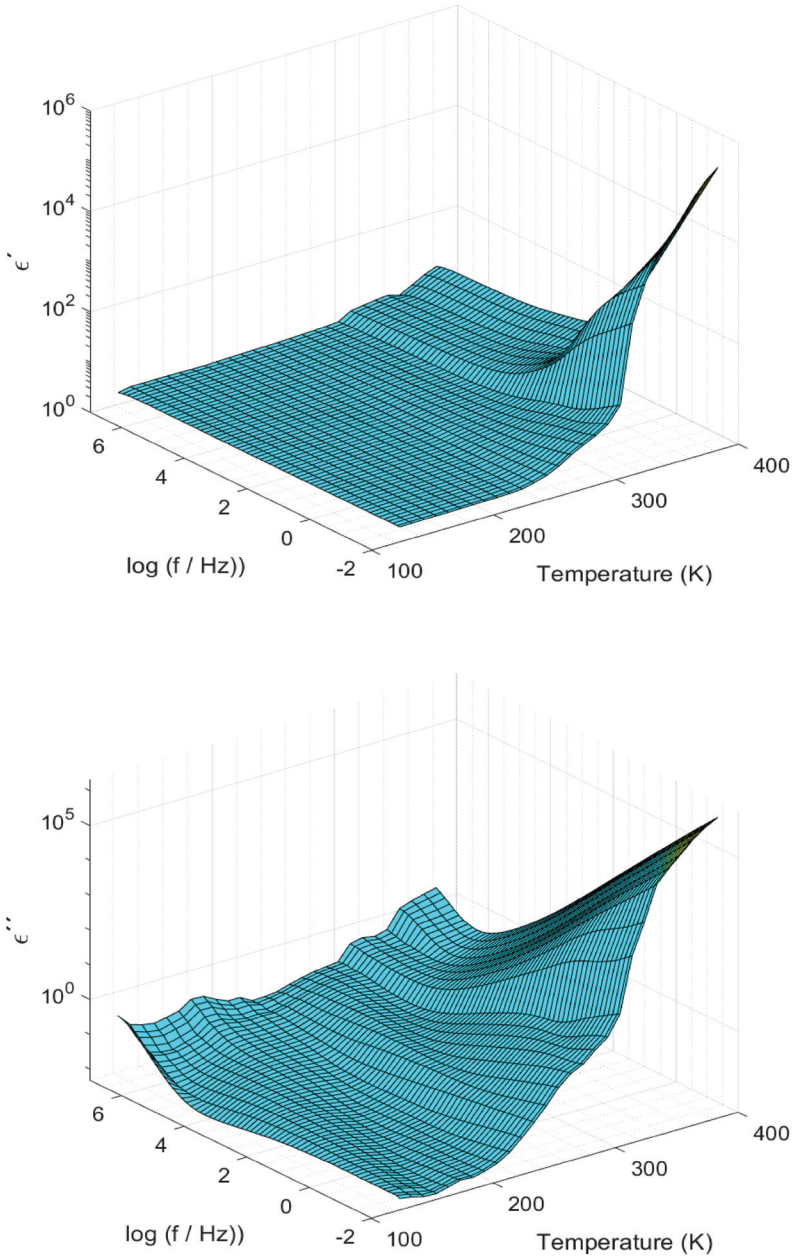


Figure 6.33: 3D plot of the real (ϵ') and imaginary part (ϵ'') parts of the complex permittivity (ϵ^*) of the CP20-O membrane.

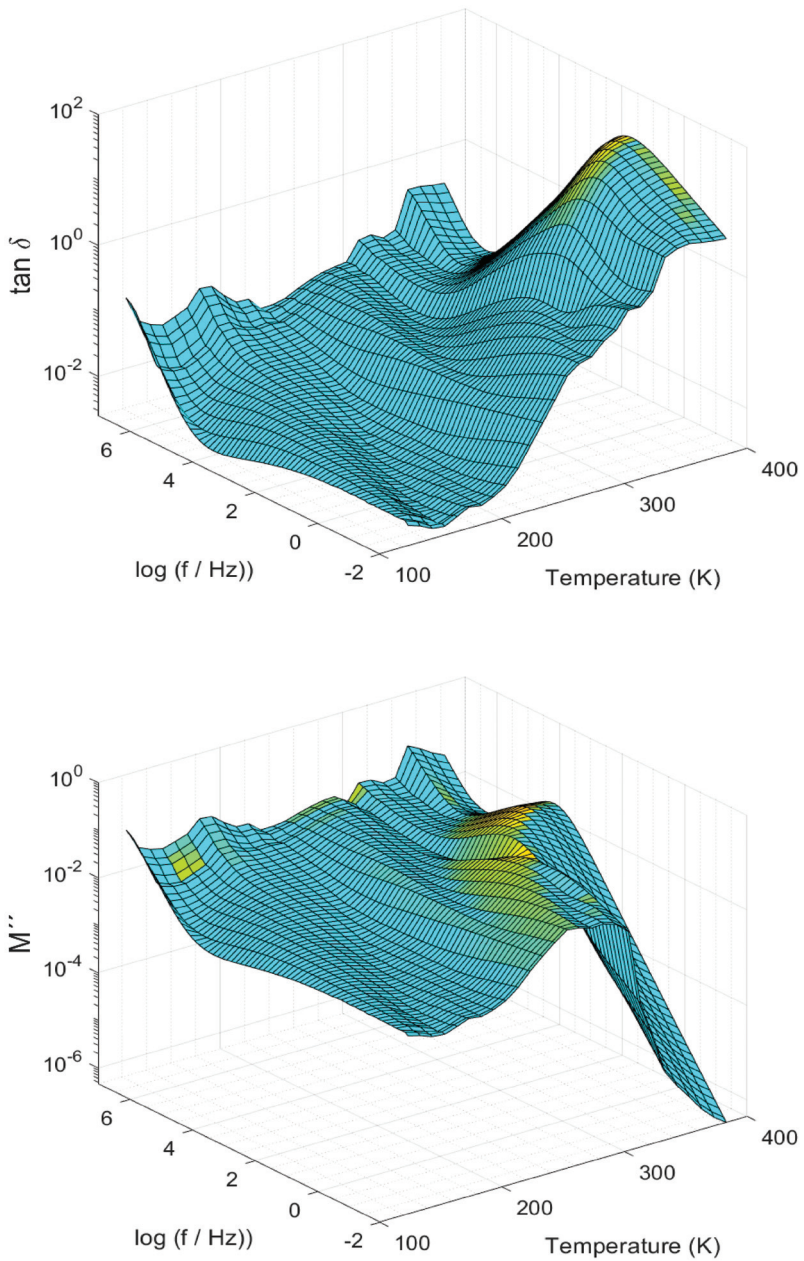


Figure 6.34: 3D plot of $\tan \delta$ and of the imaginary part (M'') of the complex electric modulus (M^*) of the CP20-O membrane.

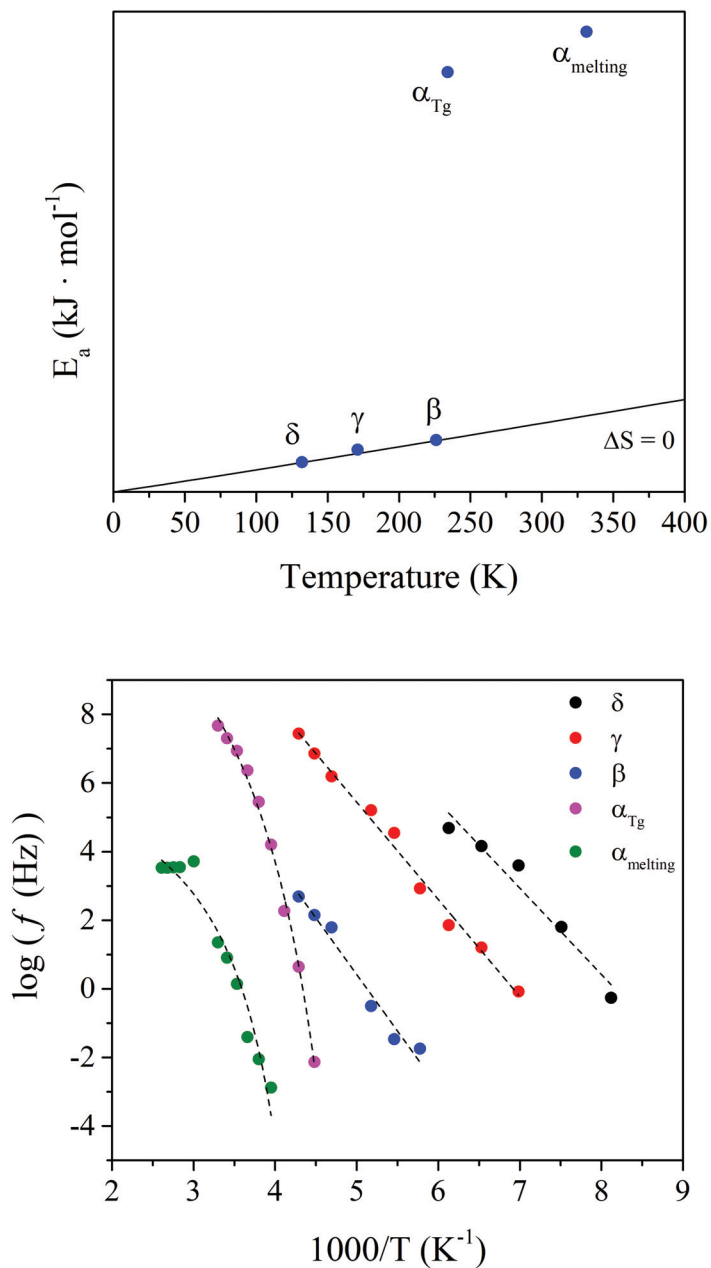


Figure 6.35: (Top) Eyring plot and (Bottom) Arrhenius plot of the CP20-O membrane.

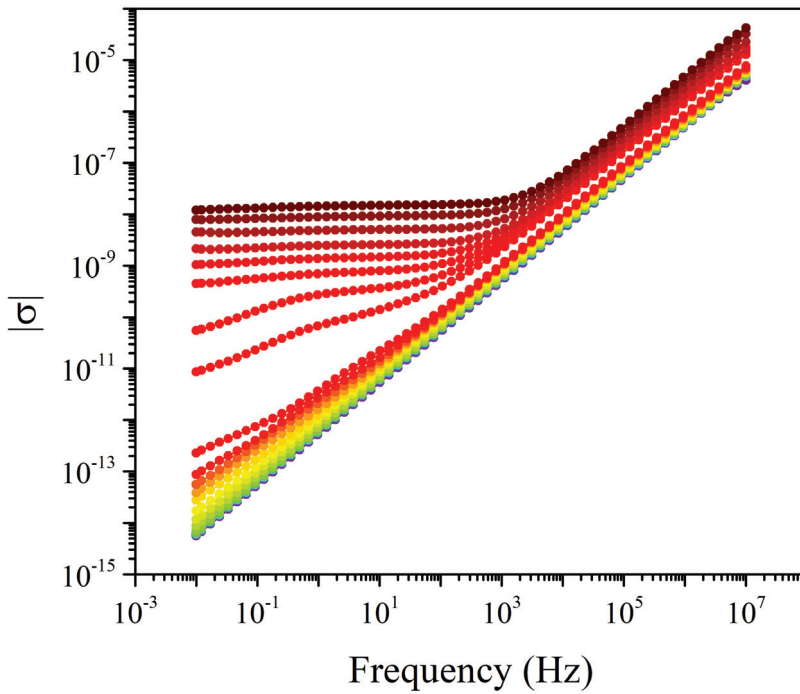


Figure 6.36: Isothermal curves of the modulus of the complex conductivity ($|\sigma|$) for the CP20-O membrane.

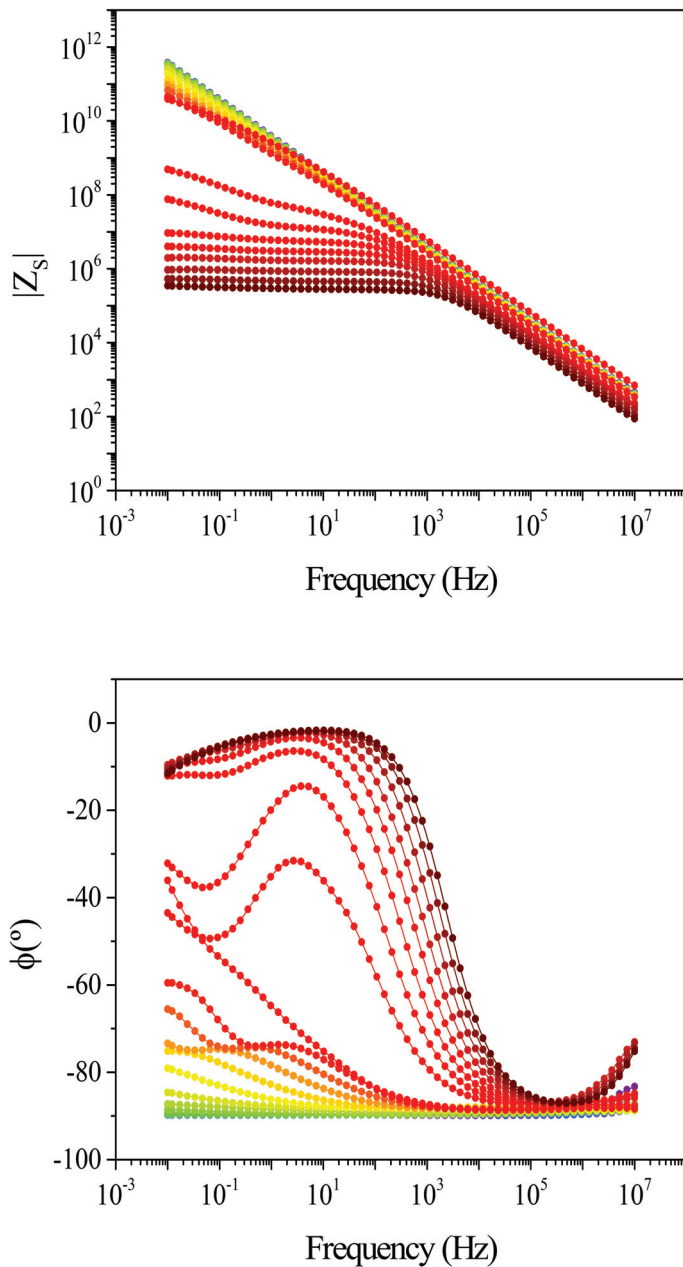


Figure 6.37: Phase angle (ϕ) and modulus of the serial impedance ($|Z_s|$) of the CP20-O membrane.

6.3.8 Analysis of the dielectric spectra of the CP40 membrane

The dielectric spectra was plotted in terms of the real (ϵ') and imaginary (ϵ'') parts of the complex dielectric permittivity (ϵ^*), $\tan \delta$, and the imaginary part of the electric modulus (M'') in Figures 6.38 - 6.39.

In Figure 6.40A the macromolecular origin of the dielectric relaxations is assessed through the Eyring model as derived by Starkweather. No differences with respect to the other modified unoriented (CP20) or oriented (CP20-O) membranes are found. Therefore, the same conclusions apply. Briefly, the δ , γ and β relaxations display E_a values that lie close to the zero-entropy line, and therefore, both dielectric processes can be considered as non-cooperative. On the other hand, the E_a values of the α_{Tg} and $\alpha_{melting}$ relaxations is characteristic of cooperative molecular motions.

In Figure 6.40B the Arrhenius plot is displayed. The same relaxation processes found in CP20 and CP20-O membranes are found. Consequently, three dielectric processes (δ , γ and β) located at low temperatures. Moreover, at the high-temperature region, the α_{Tg} and $\alpha_{melting}$ dielectric relaxations are found. The same molecular origin as in the CP20 and CP20-O membranes can be considered.

In Figure 6.41 the isothermal curves of the modulus of the complex conductivity ($|\sigma|$) for the complete temperature range are displayed.

To determine the proton conductivity, the phase angle and the absolute value of the serial impedance (Z_s) are needed. Thus, both parameters are shown in Figure 6.42.

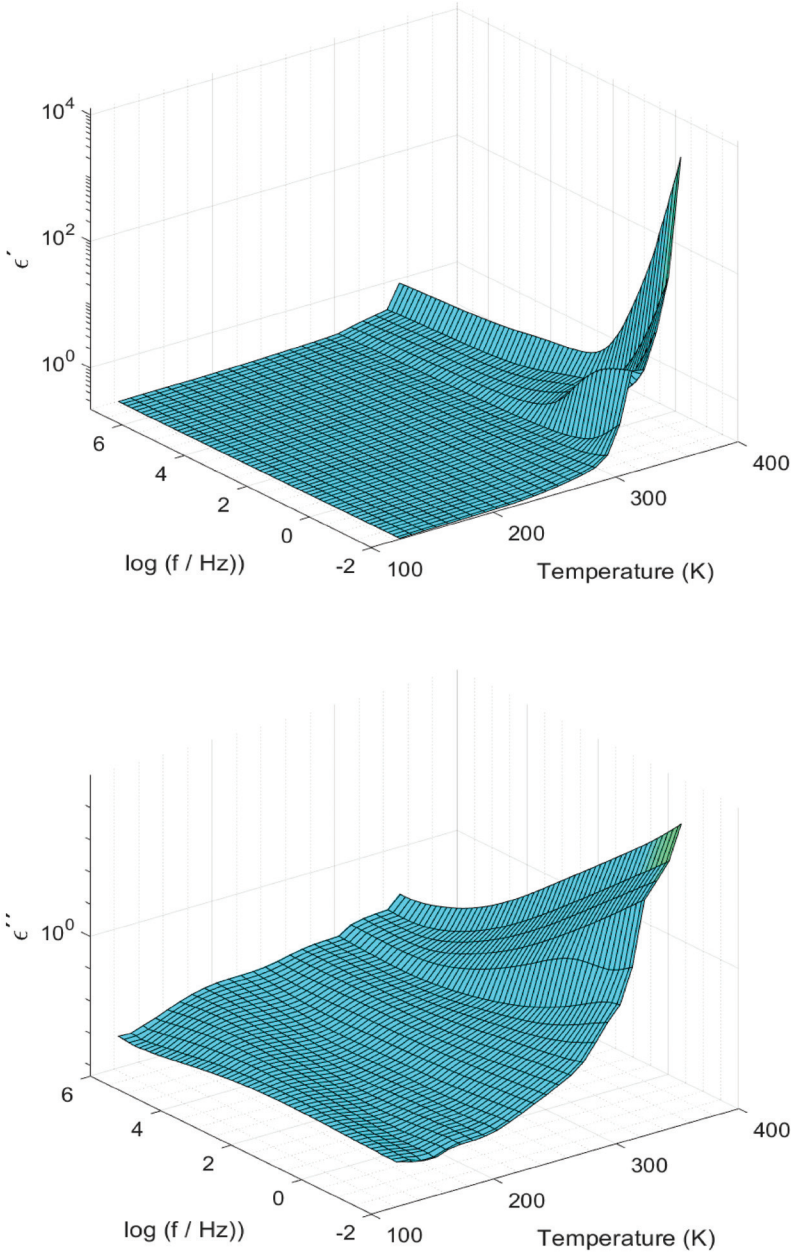


Figure 6.38: 3D plot of the real (ϵ') and imaginary part (ϵ'') parts of the complex permittivity (ϵ^*) of the CP40 membrane.

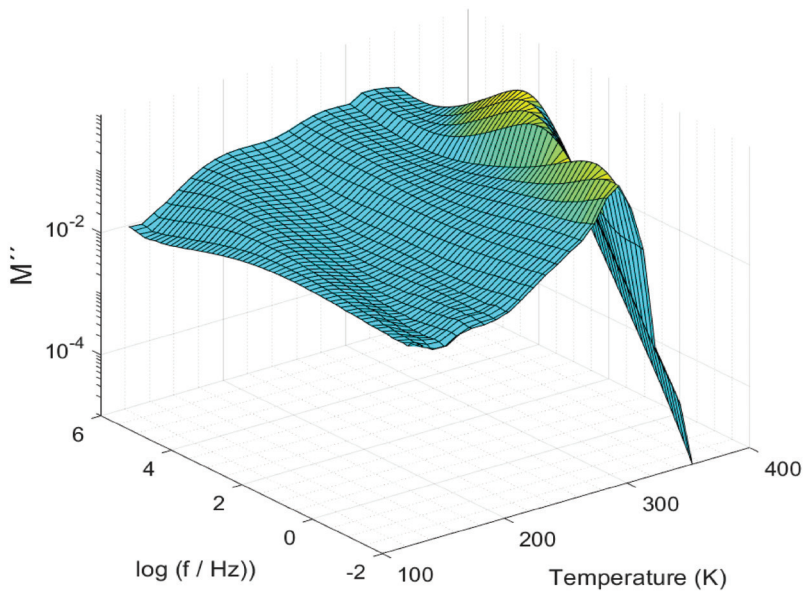
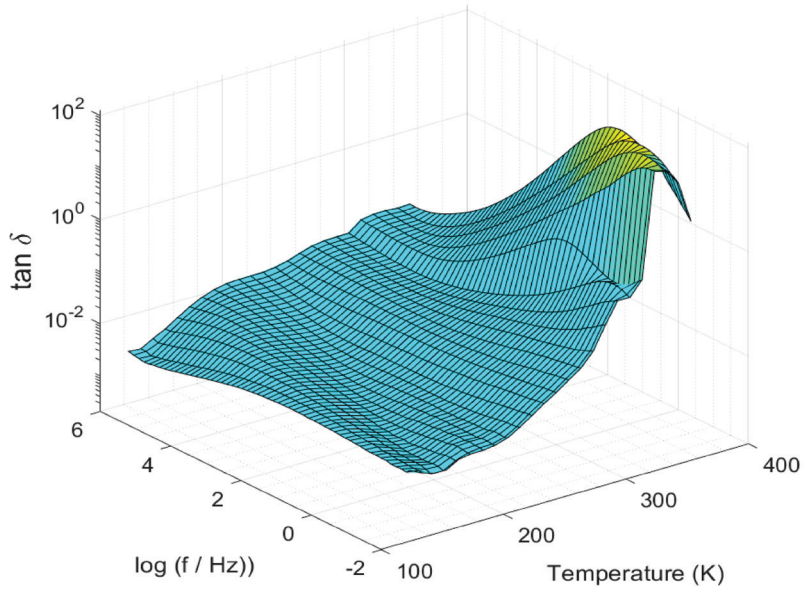


Figure 6.39: 3D plot of $\tan \delta$ and of the imaginary part (M'') of the complex electric modulus (M^*) of the CP40 membrane.

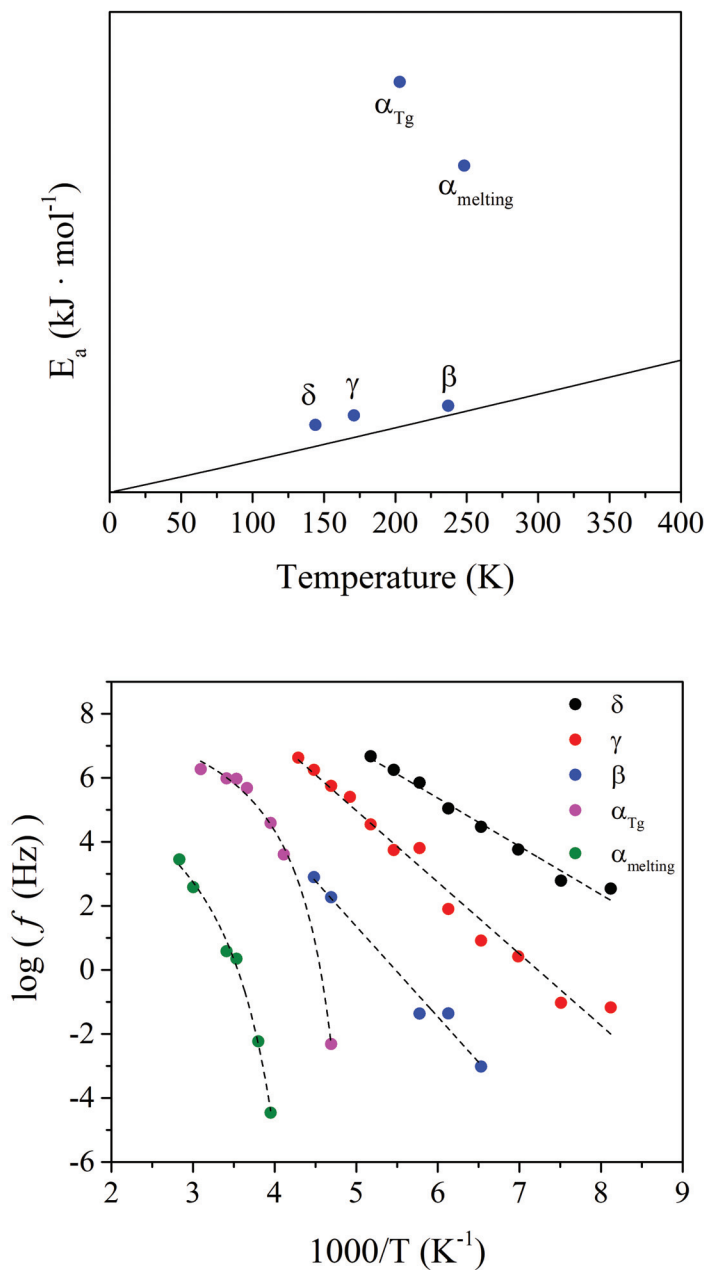


Figure 6.40: (Top) Eyring plot and (Bottom) Arrhenius plot of the CP40 membrane.

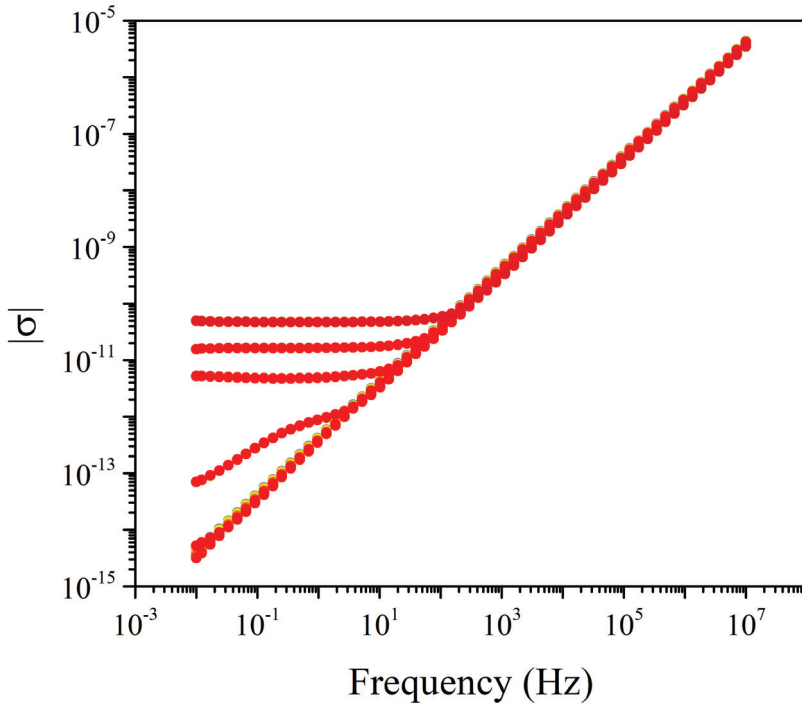


Figure 6.41: Isothermal curves of the modulus of the complex conductivity ($|\sigma|$) for the CP40 membrane.

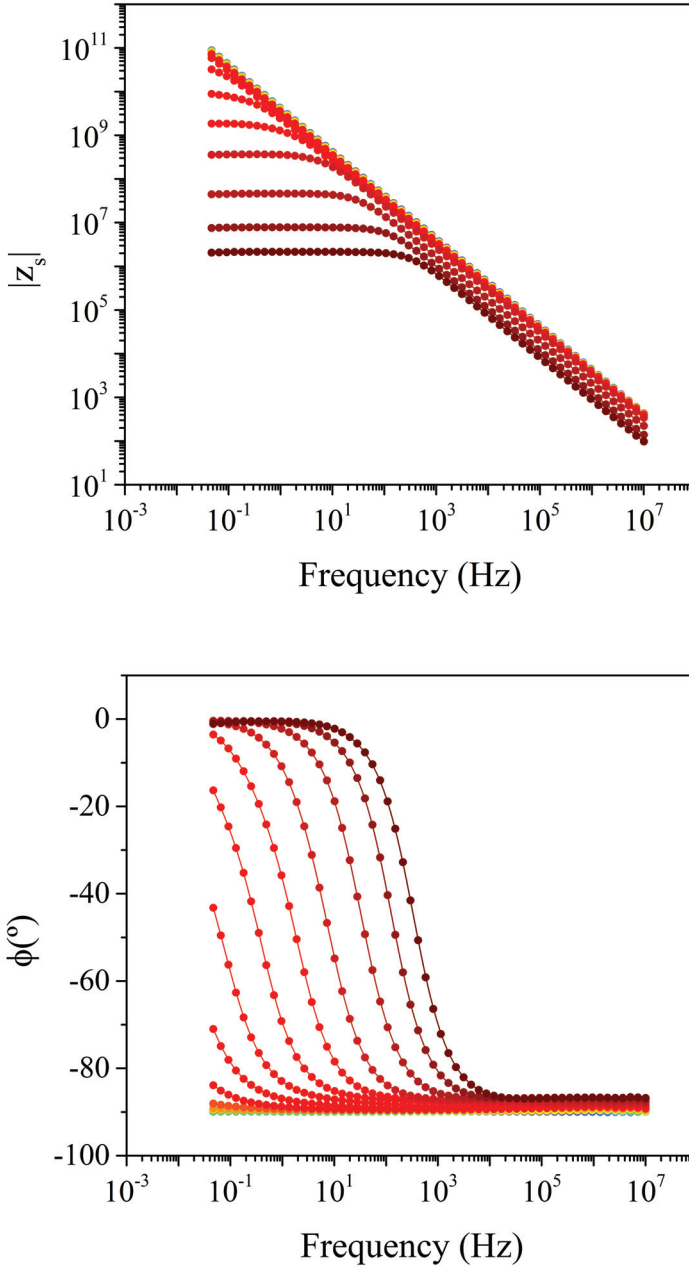


Figure 6.42: Phase angle (ϕ) and modulus of the serial impedance ($|Z_s|$) of the CP40 membrane.

6.3.9 Analysis of the dielectric spectra of the CP40-O membrane

The dielectric spectra was plotted in terms of the real (ϵ') and imaginary (ϵ'') parts of the complex dielectric permittivity (ϵ^*), $\tan \delta$, and the imaginary part of the electric modulus (M'') in Figures 6.43 - 6.44.

In Figure 6.45A the macromolecular origin of the dielectric relaxations is assessed through the Eyring model as derived by Starkweather. No differences with respect to the unoriented (CP40) membrane are found. Therefore, the same conclusions apply. Briefly, the δ , γ and β relaxations display E_a values that lie close to the zero-entropy line, and therefore, both dielectric processes can be considered as non-cooperative. On the other hand, the E_a values of the α_{Tg} and $\alpha_{melting}$ relaxations is characteristic of cooperative molecular motions.

In Figure 6.45B the Arrhenius plot is displayed. It shows different relaxation zones. The same relaxation processes found in CP20, CP20-O, and CP40 membranes are found. Consequently, three dielectric processes (δ , γ and β) located at low temperatures. Moreover, at the high-temperature region, the α_{Tg} and $\alpha_{melting}$ dielectric relaxations are found. The same molecular origin as in the CP20, CP20-O, and CP40 membranes can be considered.

In Figure 6.46 the isothermal curves of the modulus of the complex conductivity ($|\sigma|$) for the complete temperature range are displayed.

To determine the proton conductivity, the phase angle and the absolute value of the serial impedance (Z_s) are needed. Thus, both parameters are shown in Figure 6.47.

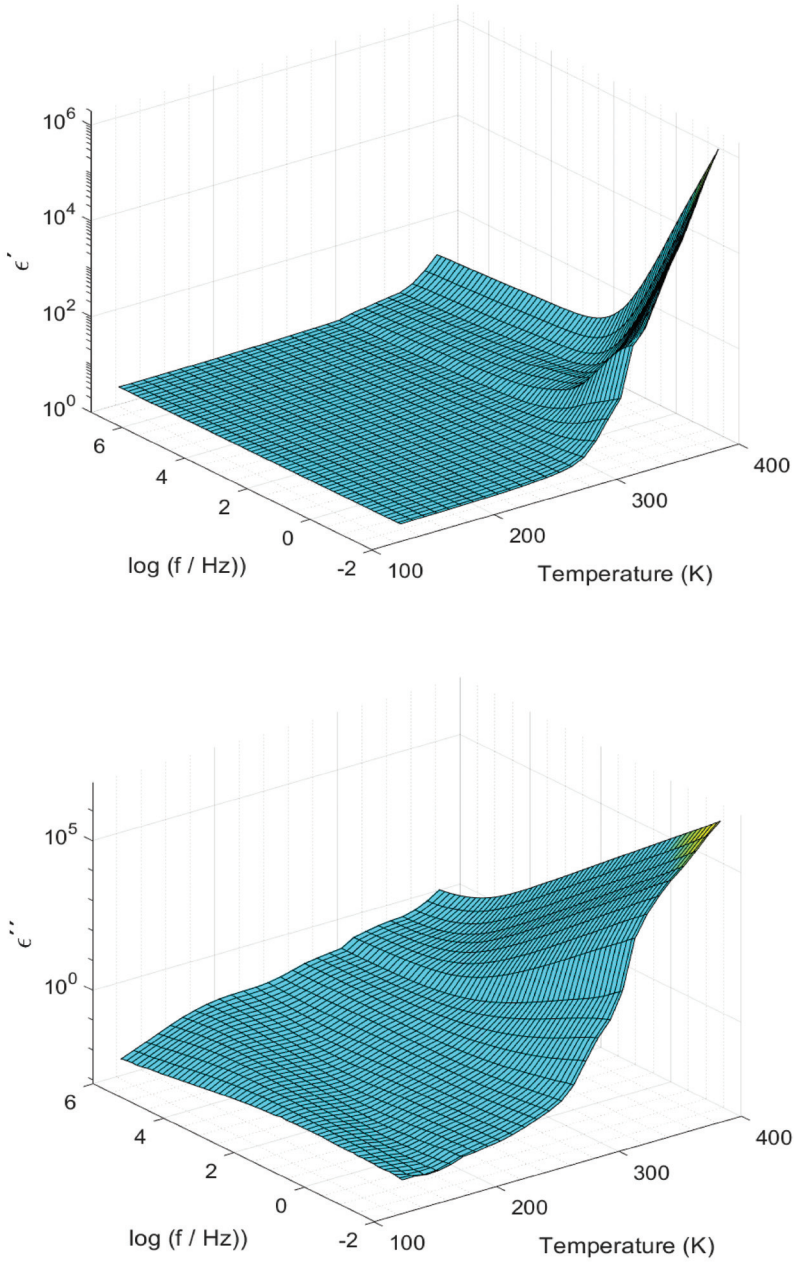


Figure 6.43: 3D plot of the real (ϵ') and imaginary part (ϵ'') parts of the complex permittivity (ϵ^*) of the CP40-0 membrane.

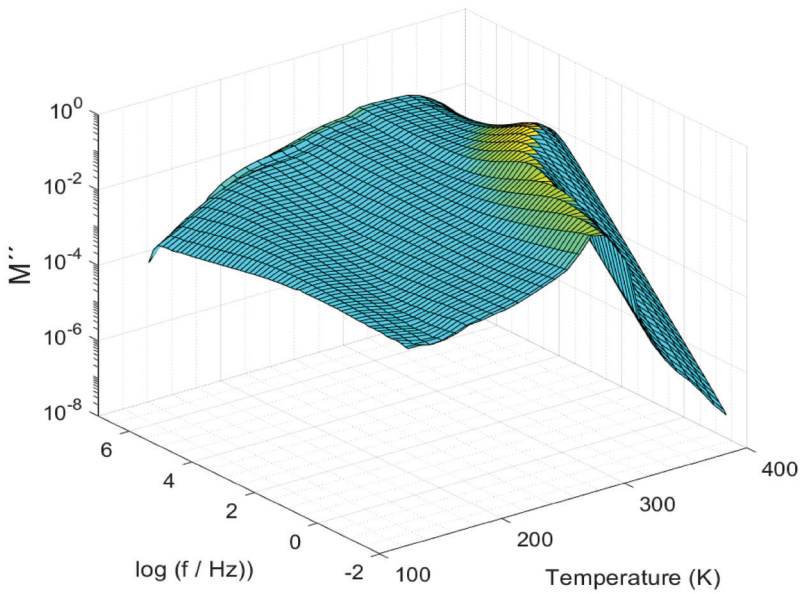
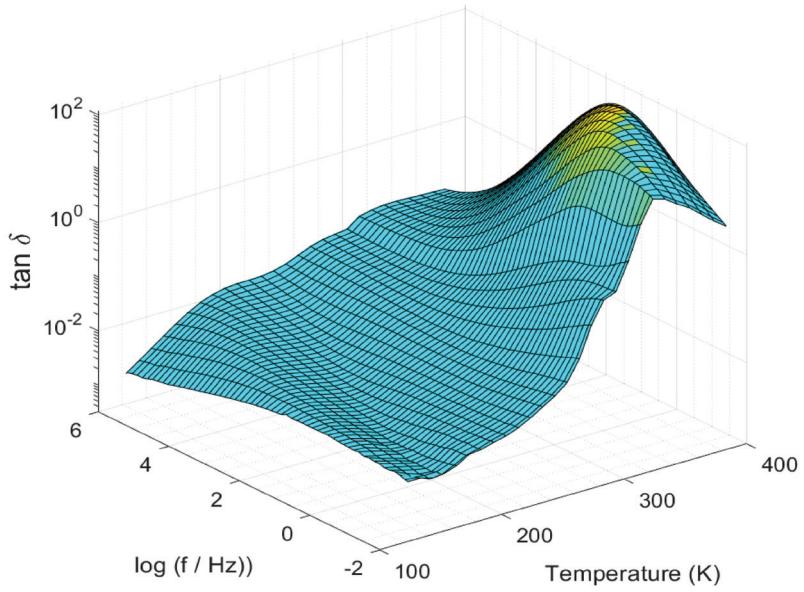


Figure 6.44: 3D plot of $\tan \delta$ and of the imaginary part (M'') of the complex electric modulus (M^*) of the CP40-0 membrane.

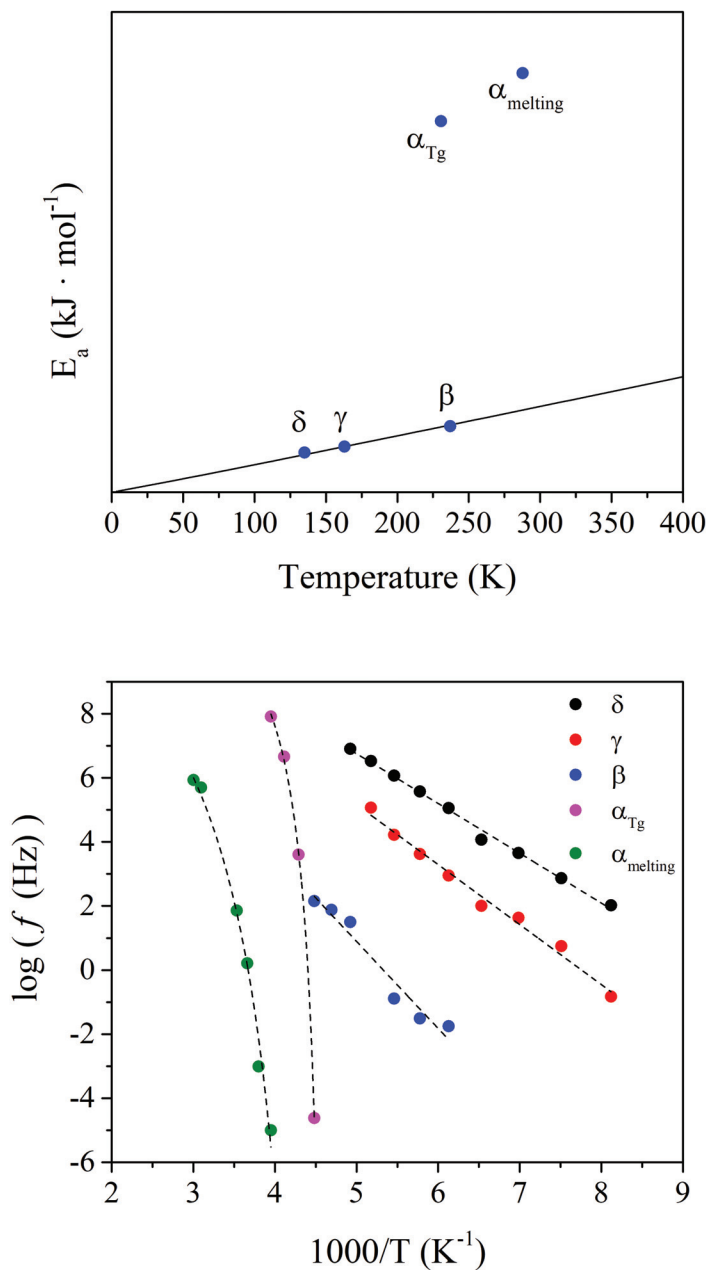


Figure 6.45: (Top) Eyring plot and (Bottom) Arrhenius plot of the CP40-0 membrane.

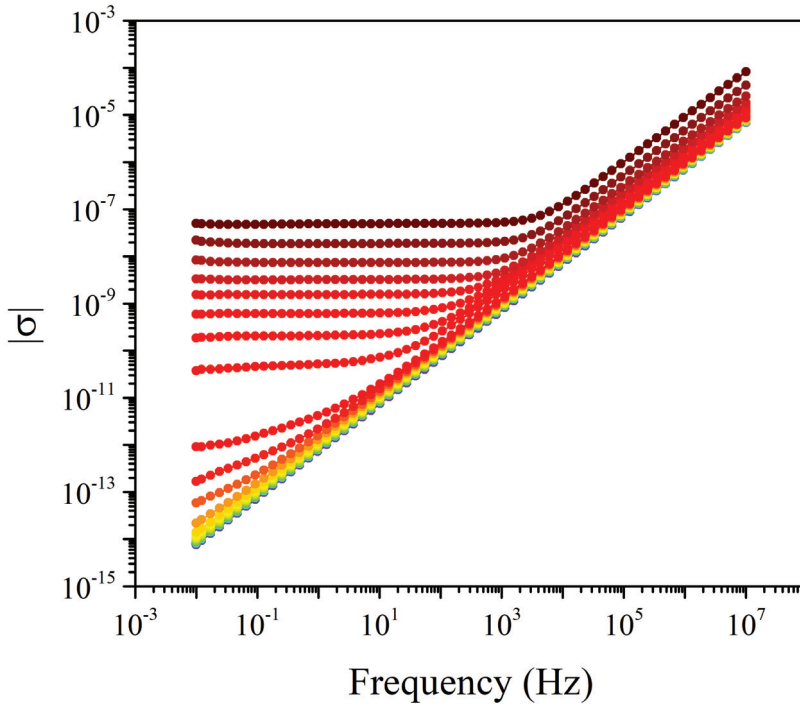


Figure 6.46: Isothermal curves of the modulus of the complex conductivity ($|\sigma|$) for the CP40-0 membrane.

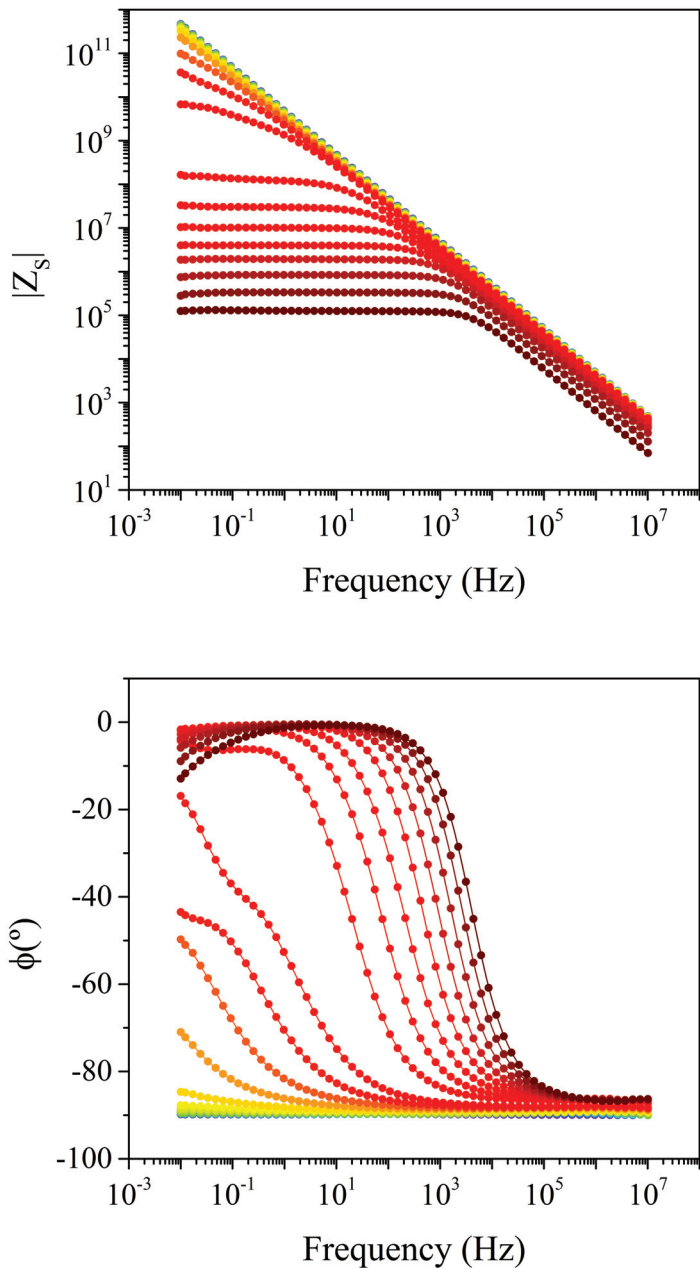


Figure 6.47: Phase angle (ϕ) and modulus of the serial impedance ($|Z_s|$) of the CP40-0 membrane.

To conclude, part of the results presented in this section have been published in several scientific peer-reviewed articles (Contributions 6 - 8) listed in section 9.1, and it complements the discussion of the results included in section 6.4.

6.4 Discussion

6.4.1 *Liquid crystal membranes based on poly(epichlorohydrin)*

The dielectric spectra of the PECH copolymers consists of at least two broad and complex dielectric relaxations, which may be the result of overlapped molecular mobilities, as observed in Figure 6.48.

Accordingly, the Arrhenius plot describing all the PECH copolymers is shown in Figure 6.49. Three different dielectric processes are observed, and it has been labelled as γ , α_{Tg} , and α_{Clear} with increasing temperature. The macromolecular assessment of these relaxations is done through the Eyring-Starkweather model, and the results for the relaxations of all the PECH copolymers are shown in Figure 6.50.

Subsequently, considering the analysis already performed in section 6.3, these dielectric relaxations may be related to the molecular motions of the benzyloxy group of the side dendrons, the glass transition, and the clearing of the mesophase, respectively. Note that the clearing is a typical transition of thermotropic liquid crystals, based on the predominance of thermal motions over the weak interactions between the dipole-type molecules or dispersion forces that determine the arrangement into a liquid crystalline phase. These interactions are strong enough to maintain associations between molecules in a preferred orientation; however, molecules keep their freedom to move, since they are not covalently bound. In the case of the systems under investigation, the grafted tapered moieties form layers with their neighbours that are arranged at different angles, giving a liquid crystal with a helical arrangement. Thus, these moieties are placed parallel, but at the same time, they can move one each other along

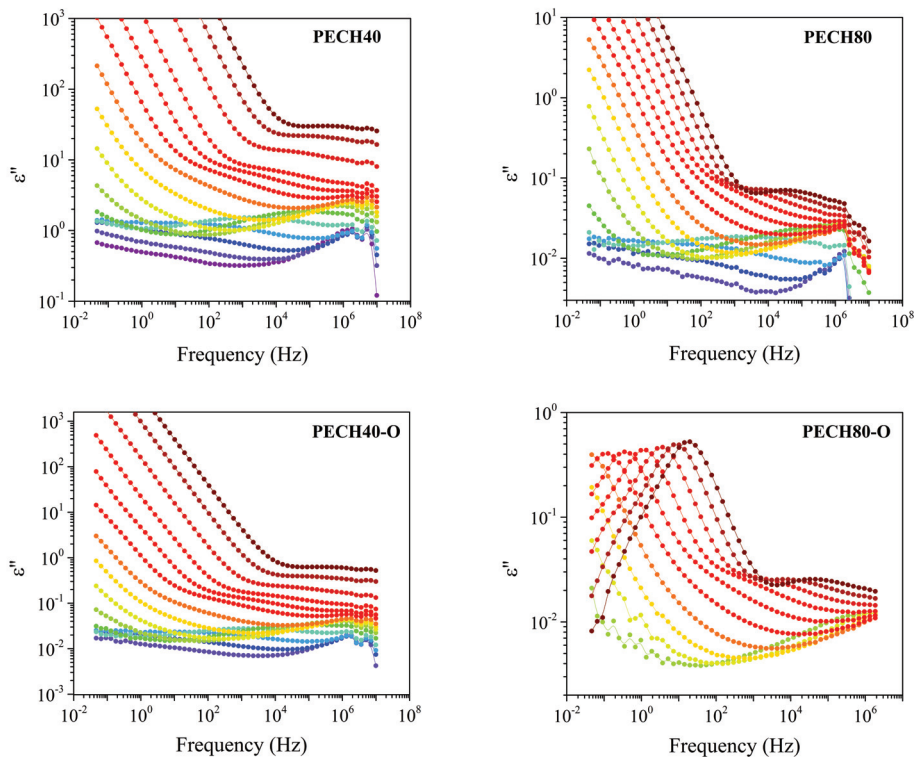


Figure 6.48: Isothermal plots curves of the imaginary (ϵ'') part of the complex (ϵ^*) permittivity for the unoriented and oriented PECH membranes from 213 to 363 K.

their axes. When the temperature is raised above the clearing point, thermal motions prevail over dispersion forces, and the polymeric material undergoes a first-order transition and turns isotropic.

To compare and analyse the dielectric spectrum of these systems different factors such as chain flexibility, structure regularity, and modification extent must be taken into account. The former can be responsible for an easier, but not necessarily stable, arrangement of the polymers into compact, ordered, or pseudo-ordered domains. Moreover, the presence of side dendrons gives rise to an exo-recognition process, which favours polymer self-organization. Structure reg-

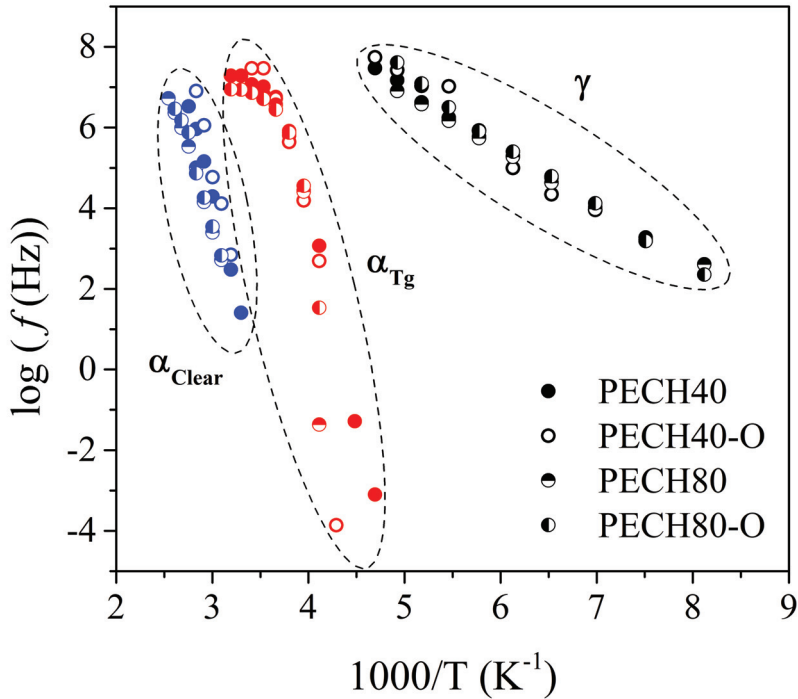


Figure 6.49: Arrhenius map for the oriented and unoriented copolymers.

ularity is crucial for the formation of a stable crystalline phase. Nevertheless, the dielectric relaxation spectrum does not show large differences between the oriented and unoriented samples. The thermal orientation affected similarly PECH copolymers.

The γ relaxation was located at low temperatures between 132 K and 128 K at a frequency of 1 kHz. The apparent activation energies E_a lie between 25 and 35 $\text{kJ} \cdot \text{mol}^{-1}$. These low values are characteristic of orientational changes of small angles concerning the longitudinal backbone of the copolymer. These motions were ascribed to the local mobility of the local secondary phenyl-aliphatic chain of the dendritic liquid crystal. The increase in the grafting degree

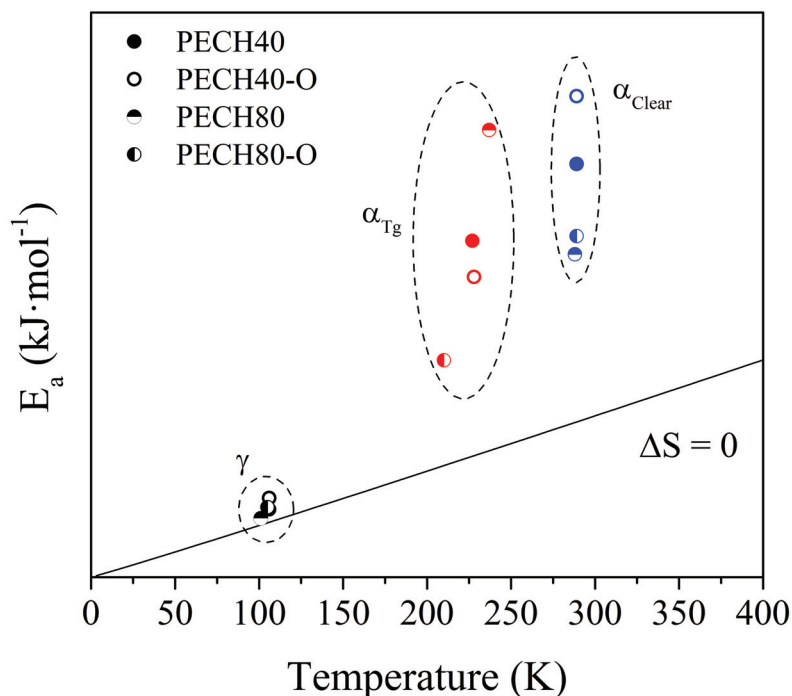


Figure 6.50: Eyring map for the oriented and unoriented copolymers.

has a slight increase in apparent activation energies. The orientation during the preparation of the membrane also shifted the position of the maxima to higher temperatures. Polymer orientation determines a more ordered arrangement of polymer structure. Therefore, more energy is needed to activate the dielectric relaxations in PECH copolymers. These results agree with those obtained from similar copolymers, and confirm that orientation decreases the molecular motion of the lateral chains, and subsequently the permittivity of the membranes [33].

Concerning the α_{Tg} , the chain segment relaxes when the available free volume is higher than a critical volume which is defined by the cooperative length of the segments. The results from the temperature dependence of the relaxation

times are gathered in Table 6.1. Accordingly, the values of the dynamic fragility parameter D are low enough to correspond, as Angell classification, as fragile systems. The dynamic fragility parameter D is lower in the oriented and un-oriented PECH80 copolymers than in the PECH40 ones. This is in line with the high values of the free-volume coefficients Φ/B and the thermal expansion coefficients α_f . However, T_{VFTH} (K) is higher in PECH80 copolymers, which indicates higher stability of these copolymers above the glass transition. Thus, PECH80 copolymers maintain a self-organized columnar structure more stably than PECH40 ones at temperatures below the glass transition [35-38].

Table 6.1: VFTH parameters of α_{T_g} relaxation for unoriented and oriented PECH80 and PECH40 copolymers.

Sample	Log f_0 (Hz)	D	T_{VFTH} (K)	Φ_g/B	$\alpha_f \times 10^4$ (K ⁻¹)	R ²
PECH40	9.7	1.6	220	0.145	28.9	0.95
PECH40-O	9.7	1.8	221	0.129	25.7	0.99
PECH80	8.1	0.6	237	0.377	75.4	0.99
PECH80-O	7.9	0.6	233	0.344	68.9	0.99

Nevertheless, when the systems approach the glass transition, the lower values of the parameter D in the PECH80 copolymers indicate the growth of macromolecular rearrangements, which provoke the crank-shaft motion and promote a quick loosening of the rigid glassy structure. This heterogeneous behaviour near the glass transition and below the clearing transition, indicate that some side chains are already quite mobile, whereas others are still very rigid. This equilibrium between mobility and stabilization of the dendritic chains allows turning these polymers into efficient membranes for ionic transport applications.

In Table 6.2 the VFTH parameters for the α_{Clear} relaxation are gathered. The parameter D exhibits higher values for both oriented and unoriented PECH80 copolymers than for PECH40 ones. Besides, PECH40 has a T_{VFTH} temperature related to the clearing relaxation higher than PECH80 copolymers. These

Table 6.2: VFTH parameters of the α_{Clear} relaxation for unoriented and oriented PECH80 and PECH40 copolymers.

Sample	Log f_0 (Hz)	D	T_{VFTH} (K)	Φ_g/B	$\alpha_f \times 10^4$ (K ⁻¹)	R ²
PECH40	8.50	0.89	-	-	-	0.92
PECH40-O	9.80	1.90	280	-	-	0.93
PECH80	10.40	4.40	260	0.04	8.7	0.98
PECH80-O	10.50	4.4	260	0.04	8.7	0.97

results indicate that dispersion forces prevail when the number of the grafted dendritic group increases. Thus, the polymeric material undergoes a first-order transition and turns isotropic faster.

Assessment of the sample's validity as PEM

In Figure 6.51 the numerical proton conductivity is displayed. The tendency is to increment the proton conductivity with increasing temperature. Subsequently, the highest value is always obtained for the highest temperature. Regarding the thermal orientation process, it does not seem to play a big role in the case of the PECH-40 membranes. However, it is remarkable the difference between the oriented and unoriented membranes when the PECH-80 membranes are considered. In this case, the orientation plays a significant role.

The values of σ_{prot} obtained are very low. To that respect, note that in Figures 6.7, 6.12, 6.17, and 6.22 it is observed that the phase angle (ϕ) tends to 0° at high temperatures, whereas in the operative temperature range of a low-temperature PEMFC ϕ tends to values around -90°. Accordingly, although σ_{prot} can still be estimated, the error increases as the value of ϕ deviates from 0.

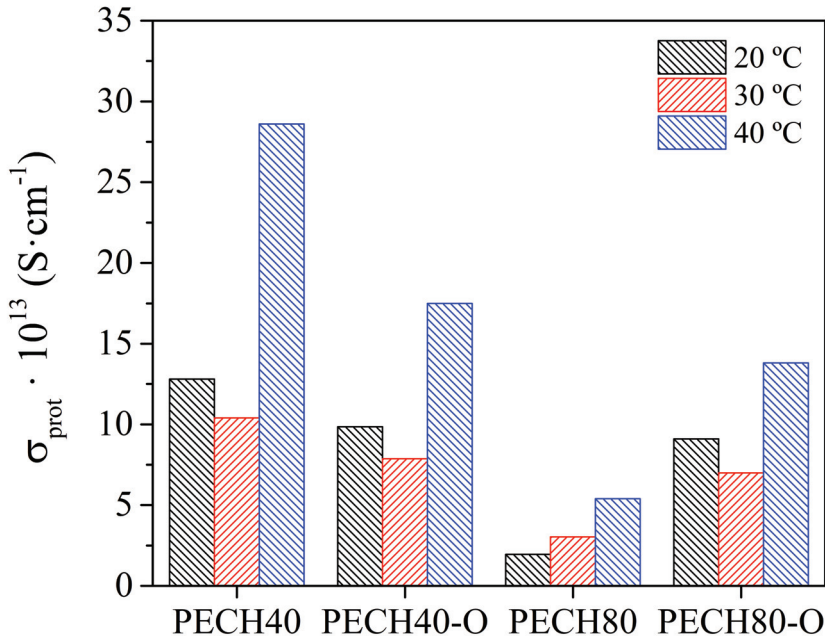


Figure 6.51: Numerical σ_{prot} for the oriented and unoriented copolymers.

6.4.2 *Liquid crystal membranes based on poly(epichlorohydrin-co-ethylene oxide) copolymers*

Analysis of the neat copolymer (CP0)

The dielectric spectra of the CP0 membrane is shown in Figures 6.23 - 6.24, and it is formed by two or three dielectric relaxations. The Arrhenius plot for the CP0 is shown in Figure 6.25B. Accordingly, at low temperature two dielectric processes appear that may be caused by different molecular motions related to the dendritic side groups. The main segmental relaxation related to the glass

transition appears at high temperatures. Subsequently, all relaxation processes are related to the chain motions in the amorphous or interface domain.

The γ relaxation occurs at low temperatures, between 123 K and 153 K, at the frequency of 10^{-1} Hz. Some discrepancies have been raised about the origin of this molecular motion. This relaxation could be generated by local twisting in amorphous segments in the fold structure on crystal surfaces. Nonetheless, this dielectric relaxation could also be attributed to local motions in the amorphous phase as it occurs in other crystalline polymers [39]. As shown in Table 6.3, an apparent activation energy (E_a) value of $38 \text{ kJ} \cdot \text{mol}^{-1}$ is found.

The β relaxation occurs between 163K to 203 K at a frequency of 10^{-1} Hz. This molecular relaxation zone may be attributed to the sum of two dielectric relaxations of the neat PEO, the β and the γ' relaxations, respectively. For this copolymer, both molecular relaxations at high frequencies have shown a tendency to merge. Indeed, a remarkable feature of the dielectric spectrum of PEO is the tendency to merge several processes, and it is common to refer to them as $\beta + \gamma'$ or $\beta + \gamma' + \gamma$ [39]. The γ' relaxation is attributed to the motion of PEO segments in interface regions [39]. The β relaxation is attributed to cooperative motions in the amorphous part of PEO [39,40]. An E_a value of $50 \text{ kJ} \cdot \text{mol}^{-1}$ is found. Compared with other published values there are differences that may be due to the difficulty in separating each relaxation.

Table 6.3: Parameters for the Arrhenius model. Apparent activation energy (E_a) and temperature peak for CP0.

Relaxation	Slope	Intercept	E_a ($\text{kJ} \cdot \text{mol}^{-1}$)	$T_{\text{max},1}$ kHz (K)	R^2
γ	-1.99	14.87	38	183	0.981
β	-2.61	13.92	50	239	0.953

The α_{Tg} is attributed to the glass transition of the PECH segments is found between 213 K and 313 K at a frequency of 10^{-1} Hz. This peak may be

associated with the glass transition of PECH, since it tends to be the relaxation dominating the entire spectrum at this temperature range [40]. An E_a value of $245 \text{ kJ} \cdot \text{mol}^{-1}$ is found, as shown in Table 6.4.

Table 6.4: Parameters for the VFTH model and derived parameters for studying the dynamic fragility of the CP0 membrane.

Sample	Log f_0 (Hz)	D	T_{VFTH} (K)	Φ/B	$\alpha_f \times 10^4$ (K ⁻¹)	E_{aTg} (kJ·mol ⁻¹)	R ²
α_{Tg}	13.77	13.32	174	0.03	0.56	244.70	0.995
α_{Clear}	8.15	0.58	283	0.17	3.56	327.40	0.997

The α_{melting} occurs in the temperature range from 323 K to 383 K at a frequency of 10^{-1} Hz, and it is attributed to the molecular motion that promotes the melting. An E_a value of $327 \text{ kJ} \cdot \text{mol}^{-1}$ is found. The high value of the free-volume (Φ_{Tg}) coefficient together with the high dilatation coefficient (α) validates the assignation done.

Analysis of the modified oriented and unoriented copolymers (CP20, CP20-O, CP40, CP40-O)

The dielectric spectra, shown in Figure 6.52, of CP20, CP20-O, CP40-O, and CP40-O copolymers also exhibit a complex spectrum with broad dielectric relaxation zones, which consists of five molecular motions, three at low temperatures (δ , γ , and β) and two at high temperatures (α_{Tg} and α_{melting}). The Arrhenius plot for all the modified oriented and unoriented copolymers is displayed in Figure 6.53.

The macromolecular assessment of these relaxations is done through the Eyring-Starkweather model, and the results for all the copolymers are shown in Figure 6.54. Accordingly, the δ , γ and β processes can be estimated to be non-cooperative due to the E_a values obtained lie close to the zero-entropy line. Contrarily, the E_a values concerning the α_{Tg} , and the α_{melting} dielectric pro-

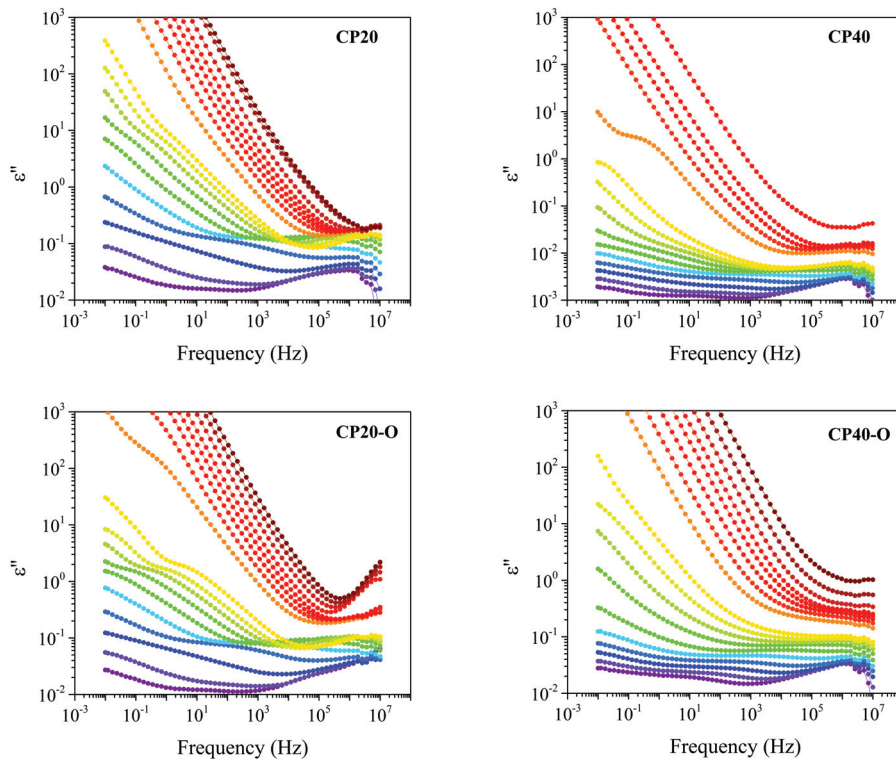


Figure 6.52: Isothermal plots curves of the imaginary (ϵ'') part of the complex (ϵ^*) permittivity for the unoriented and oriented copolymer membranes from 213 to 383 K.

cesses lie far away from the zero-entropy line, and thus, it can be considered to be cooperative.

Changing the degree of modification from 20% to 40% does not impact the number of dielectric relaxations occurring in the spectra. However, the temperature range, where some of these processes occur, is shifted. However, it is interesting to note that the orientation process seems to equal the spectra of the CP20-O and CP40-O to the point that the degree of modification does not matter. This could mean that the same number of molecules are in motion

in both cases (CP40 and CP40-O), but the difference would be in the level of restrictions found.

Concerning the δ relaxation, the orientation process does not seem to produce notable differences. The apparent activation energy (E_a) values varying between 28 - 49 $\text{kJ} \cdot \text{mol}^{-1}$, according to the values found in previous work for similar PECH and PAZE copolymers [33,41]. As in these copolymers, the thermal orientation increases (E_a) in both copolymers. Therefore, this dielectric relaxation is attributed to an intramolecular movement related to the benzyloxy group of the dendrimers.

The γ relaxation coincides with the molecular arrangements observed in the neat copolymer. Therefore, this dielectric relaxation is attributed to the same movement that originates the γ relaxation in the CP0. The E_a values obtained vary between 36 - 56 $\text{kJ} \cdot \text{mol}^{-1}$, and is in accordance with the value of 37 $\text{kJ} \cdot \text{mol}^{-1}$ found for CP0. Since the origin of this relaxation is due to the PEO segments, the concentration of dendrimers should not play a significant role in its dynamics.

The β relaxation is observed from 173 K to 213 K at 10^{-1} Hz. It has the exact macromolecular origin that in CP0, i.e., the motion of the amorphous regions of the PEO segments. The Arrhenius map shows a tendency of all the modified copolymers to shift towards lower frequencies, although the temperature range is maintained. Consequently, there is a lowering of the E_a values found to vary between 52 - 65 $\text{kJ} \cdot \text{mol}^{-1}$ compared to the value of 80 $\text{kJ} \cdot \text{mol}^{-1}$ displayed by the CP0. In this case, it is interesting to note that the process of thermal orientation cannot be considered the root cause since the variation found in the value of E_a between the unoriented and its equivalent oriented membrane is negligible. Similar E_a values were found for CP40-O and the CP40. However, the significant differences between the degree of crystallization would also indicate that the degree of crystallinity should not be considered responsible for this behaviour [42]. Another option affecting E_a values could be the different concentrations of dendrimers; nevertheless, they are attached to the PECH seg-

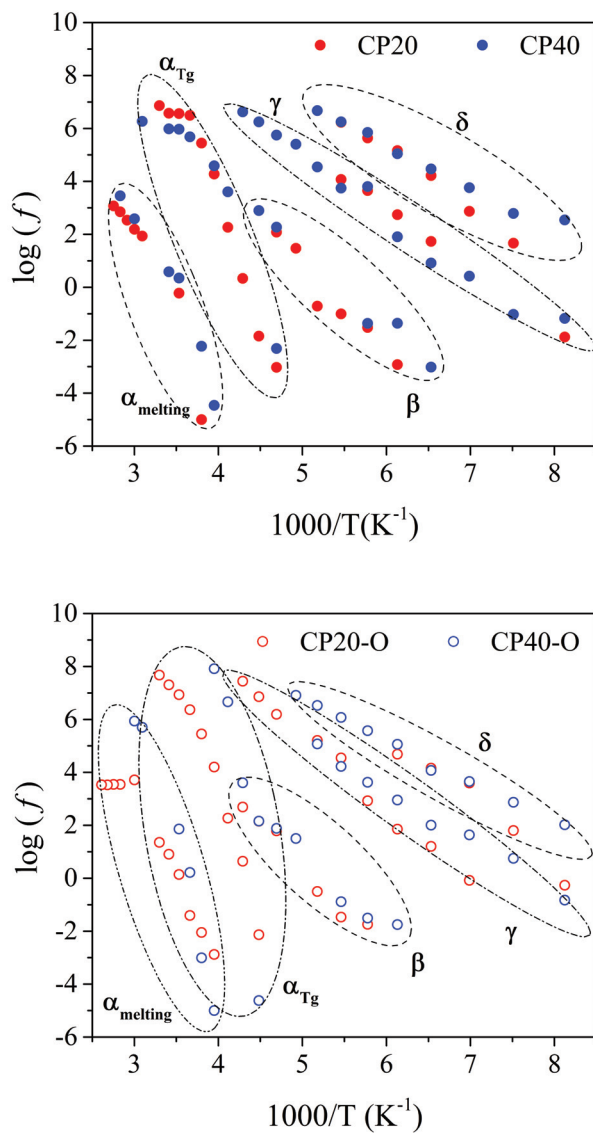


Figure 6.53: Arrhenius map for the unoriented (full symbols) and oriented (hollow symbols) modified copolymers.

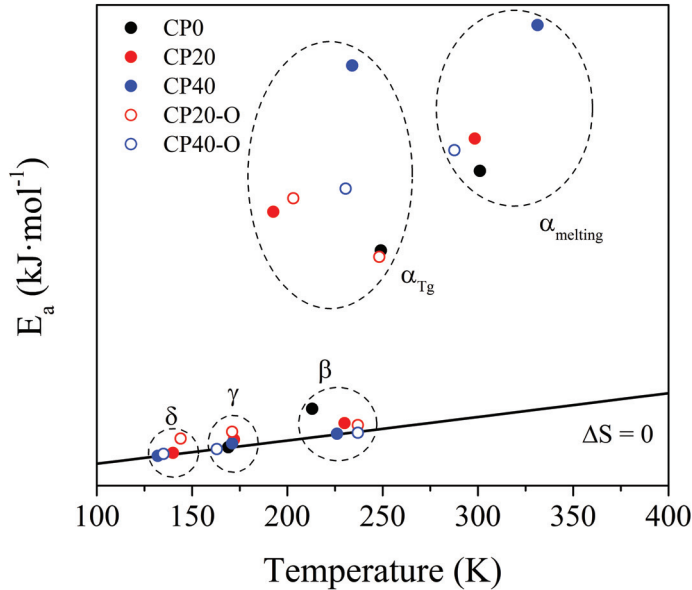


Figure 6.54: Eyring plot for the pure, unoriented (full symbols) and oriented (hollow symbols) modified copolymers.

ments, thus meaning that the percentage of PEO remains the same for all the samples [42]. Therefore, the reason for the shift in frequencies and the consequent lowering in apparent activation energy must be related to confinement effects [39,40].

Either the glass transition of the PECH, the motions giving rise to the melting and clearing processes are cooperative motions. Therefore, a Vogel-Fulcher-Tamman-Hesse model is needed to determine the thermal dependence of the relaxation times. The parameters for the best fit are gathered in Table 6.5 and Table 6.6 for the α_{Tg} and $\alpha_{melting}$, respectively.

As the fragility index (m) of the CP0 is 55, adding the dendrimers tends to reduce the fragile behaviour in both copolymers CP20 and CP40, and the higher the concentration, the stronger it becomes. However, the oriented copolymers,

Table 6.5: Parameters for the VFTH model and derived parameters for studying the α_{Tg} relaxation of the modified oriented and unoriented copolymers.

Sample	Log f_0 (Hz)	T_{VFTH} (K)	m	Φ_{Tg}	$\alpha_f \times 10^4$ (K ⁻¹)	E_{aTg} (kJ·mol ⁻¹)	R^2
CP20	2.39	238.07	113	0.04	1.76	361	0.995
CP20-O	13.53	178.59	59	0.03	0.62	238	0.995
CP40	5.54	218.57	48	0.05	1.24	479	0.995
CP40-O	12.59	206.21	79	0.03	0.53	349	0.998

Table 6.6: Parameters for the VFTH model and derived parameters for studying the $\alpha_{melting}$ relaxation of the modified oriented and unoriented copolymers.

Sample	Log f_0 (Hz)	T_{VFTH} (K)	m	Φ_{Tg}	$\alpha_f \times 10^4$ (K ⁻¹)	E_{aTg} (kJ·mol ⁻¹)	R^2
CP20	15.41	150.14	25	0.03	0.36	285	0.963
CP20-O	9.19	184.04	59	0.03	0.61	299	0.998
CP40	8.25	191.53	12	0.01	0.19	437	0.994
CP40-O	15.23	186.05	22	0.01	0.24	309	0.998

although the values tend to increase the fragility index towards the CP0, especially in the case of the CP20 when the concentration of dendrimers is still low.

Concerning the free volume (Φ), the CP0 presented a value of 0.03, and the addition of a low concentration of dendrimers (CP20) does not produce changes in the free volume in both oriented and unoriented copolymers. These values agree with the values displayed for most of the polymeric systems, which lie in the 0.025 ± 0.005 range [43]. On the contrary, when the concentration of dendrimers increases (CP40), the free volume diminishes significantly. It is important to remark that the orientation process does not produce any variation in the available free volume. These results confirm that molecular motions are hindered in the case of the CP40, as is to be expected.

The E_{aTg} of CP0 copolymer is $244.70 \text{ kJ} \cdot \text{mol}^{-1}$. The addition of dendrimers increases the apparent activation energy, which is higher in increasing the concentration of the dendrimers. The restrictions imposed by the higher concentration of dendrimers, resulting in less free space, are reflected by higher apparent activation energy and agree with the increment in the glass transition temperature found in the previous work [44]. Nevertheless, the orientation slightly increases the activation energy of CP20 and significantly decreases the value of the CP40. This result could mean that in CP40, the orientation of the dendrons favours the stabilization of the overall structure of the copolymer.

Regarding the $\alpha_{melting}$, the fragile behaviour prevails, and these copolymers are not thermally stable at this range of temperatures. The values displayed by the free volume parameter (Φ) in combination with the high values of the dilatation coefficient confirm the proposed origin of this molecular motion.

Assessment of the sample's validity as PEM

Figures 6.26, 6.31, 6.36, 6.41, and 6.46 display the isochronal curves of the modulus of the electric conductivity ($|\sigma|$) for all the copolymers. The conductivity reaches a stable plateau at relatively low temperatures compared to the modified copolymers. Globally, the addition of the dendrimers slightly changed the conductivity, and both copolymers exhibit similar values. Nevertheless, it can be noted that at low concentrations, the CP20 and CP20-O behaviour is very similar and not far from the values of CP0. This result indicates that the charge transfer mechanisms have not been heavily modified yet. On the other hand, at higher dendrimer concentration, the hindering of the mobility by the restrictions imposed by the dendrimers disturb the charge transfer mechanisms and ($|\sigma|$) values decrease. It is noteworthy that the orientation process improves this situation and reduces the restrictions imposed by the dendrimers, obtaining better $|\sigma|$ values than the unoriented copolymer comparable, if not better in some temperatures, to those of the CP0.

Jonscher's model is used to determine both components of the electric conductivity, i.e., the DC (σ_{DC}) and the AC (σ_{AC}), respectively. In Figure 6.55, the best fits for the modified and unmodified copolymers of σ_{DC} are plotted. Regarding σ_{DC} , as expected, the CP0 displays the highest values, whereas the CP20 and CP40 perform worse. However, these results confirm that the orientation of the main chain diminishes the restrictions imposed by the dendrimers and the values of conductivity, especially in CP40 copolymer obtained values of conductivity closer to the CP0. Furthermore, the obtained values of the n -parameter vary between 0.92 and 0.99. In addition, these results confirm that the thermal orientation process does not have a significant impact because it is not altering the values of the exponential parameter; there is only a smoothing of the values for all temperatures.

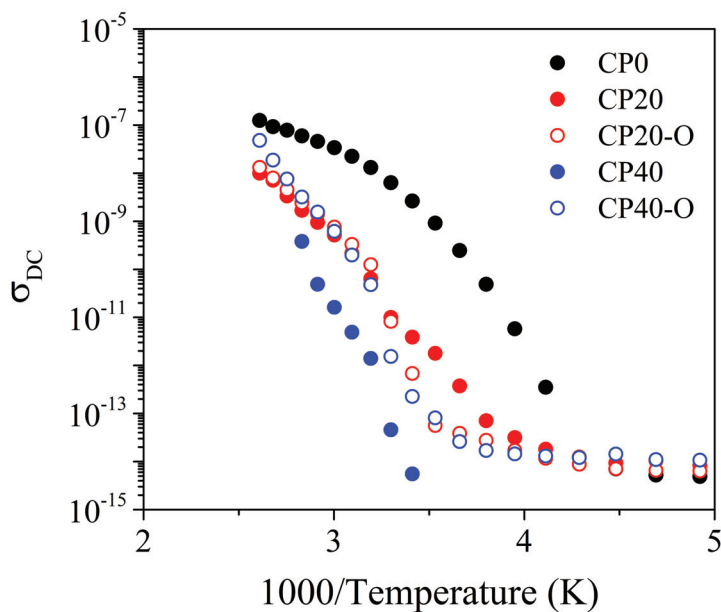


Figure 6.55: DC conductivity for the neat (CP0), modified unoriented (CP20, CP40), and oriented (CP20-O, CP40-O) copolymers.

Figure 6.56 shows the values for the through-plane proton conductivity at three temperatures (293 K, 303 K, and 313 K) for all the copolymers. At all these temperatures, the proton conductivity decreases as the concentrations of dendrimers increase. The one direction conductivity of cations depends on the effective cavity of the channel. The transport of cations in the narrow channels is responsible for limiting cations conductivity, and the polyether backbone also involves cation transport. However, in the case of protons, conduction also occurs through an additional coordination site which lies on the lateral ester group that actively interacts with protons during their transport. It was observed that only protons could be transported via both the main chain and the lateral ester groups.

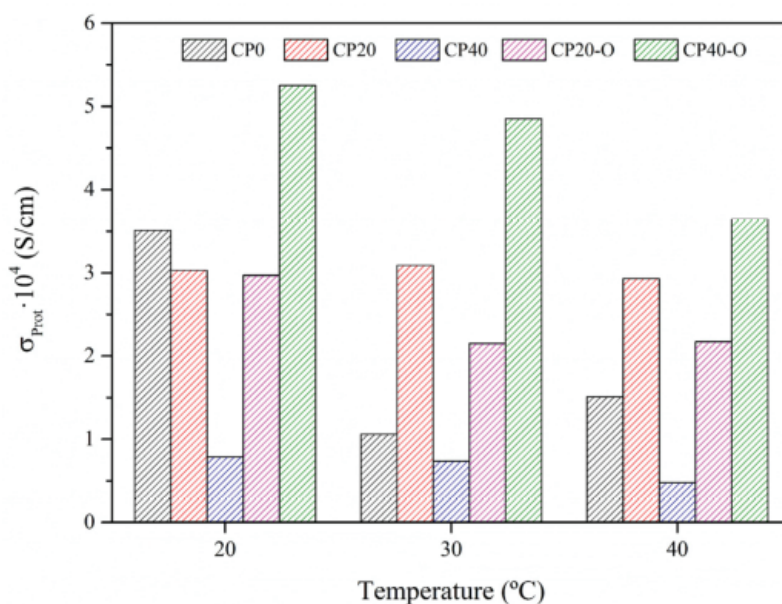


Figure 6.56: Proton conductivity for the neat (CP0) and modified oriented (CP20, CP40) and oriented (CP20-O, CP40-O) membranes at three different temperatures.

However, Figure 6.56 shows that the thermal orientation slightly decreases the proton conductivity at low dendrimer concentrations while increasing significantly at high dendrimers concentrations. The values obtained for CP40-O are

higher than even CP0. These results confirm the significant impact of the dendron concentration and thermal orientation of the main chain in the design of these copolymers. Both factors alter the molecular motion, as confirmed by the dielectric spectrum and the charge transfer mechanism.

6.5 Summary

From the work performed in this chapter the following conclusions are reached:

- The dendronized copolymers, obtained by the chemical modification of poly(epichlorohydrin) (PECH) with the dendron 3,4,5-tris[4-(n-dodecan-1-yloxy)benzyloxy]benzoate, partially organize into a crystalline structure and a liquid crystal mesophase.
- The thermal treatment applied for membrane orientation enhances nano-crystalline structures.
- The dielectric spectra of PECH80 and PECH40 consists of three dielectric relaxations labelled as γ , α_{Tg} , and α_{Clear} , in order of increasing temperature.
- The γ relaxation is associated with the reorientation of the benzyloxy substituent of the mesogenic side group. The addition of mesogenic side groups to the structure of PECHs does not affect the dynamic of the benzyloxy substituents. However the crystalline organization, promoted by thermal treatment, increases the E_a of both copolymers.
- The α_{Tg} is related to the glass transition. The modification degree is the most relevant factor for α_{Tg} relaxations of both PECH copolymers.
- The dendritic side chains induces a crystalline order, which somewhat constrains the α_{Tg} relaxation process of the amorphous portions.
- The dynamic fragility displays lower values for PECH80 copolymers than the PECH40 ones, and the self-organized columnar structure is more stable at temperatures below the glass transition. At temperatures near the glass transition, the crank-shaft movement promotes a quicker loosening of the ordered glass structure in PECH80 than in PECH40.

- The α_{Clear} relaxation occurs near α_{Tg} relaxation and is related to a precursor motion of the disassembling of the polymeric columns. A higher number of grafted dendritic group enhances the dispersion forces and the polymeric material turns isotropic faster.
- The dielectric spectra of the neat copolymer (CP0) consists of four dielectric relaxations: γ , $\beta + \gamma'$, α_{Tg} , and $\alpha_{melting}$, in increasing order of temperature.
- PECH and PEO display a similar glass transition temperature. However, PECH prevails, generating a complex zone where the segmental and local motions of the amorphous fraction of PEO co-exist.
- The dielectric spectra of the modified unoriented and oriented copolymers with 20% and 40% of dendrimers groups involves five dielectric relaxations: δ , γ , β , α_{Tg} and $\alpha_{melting}$, in increasing order of temperature.
- The δ relaxation was attributed to the local motions of the benzyloxy group of the dendrimers. The orientation does not play a significant role in this relaxation process.
- The γ relaxation in the modified unoriented and oriented copolymers has the same molecular origin as in the neat copolymer. This dielectric relaxation is favoured by a high degree of crystallinity in conjunction with the thermal orientation process.
- The β relaxation display the same complex dynamics between the cooperative and local motions of the PEO and the segmental motions of the PECH are found.
- The α_{Tg} is also ascribed to the cooperative motions of PECH. The thermal orientation process did not produce significant variations at low concentrations of dendrimers. On the contrary, significant variations were found at high concentrations.

- The $\alpha_{melting}$ displayed high values of both the free volume parameter and the dilatation coefficient, confirming its proposed macromolecular origin.
- CP0 displayed the highest values of σ_{DC} . In contrast, CP40 was the worst performer. The reason were the high levels of restrictions imposed by the high concentration of dendrimers.
- The values of the n-parameters showed that the ideal long-range pathways were not being altered by the thermal orientation or the addition of dendrimers.
- The analysis of σ_{prot} confirms that the thermal orientation process combined with a high concentration of dendrimers can enhance σ_{prot} while maintaining low enough electric conductivity values.

6.6 References

- [1] Jia, L., Zhang, H., Yang, J., Hu, X., Fang, S., Cross-linked poly (epichlorohydrin) membranes with different cross-linking agents for proton exchange membrane fuel cells, *Journal of Power Sources* 224 (2013) 17-24.
- [2] Wang, Q., Luo, Y., Zhao, C., Wei, Z., Poly(epichlorohydrin) based composite membranes for proton exchange membrane fuel cells, *Journal of Power Sources* 228 (2013) 1-9.
- [3] Li, H., Li, J., Zhang, J., Wang, H., Zhang, H., Preparation and characterization of sulfonated poly(ether ether ketone) and poly(epichlorohydrin) blend membranes for proton exchange membrane fuel cells, *International Journal of Hydrogen Energy*, 40 (2015) 1892-1901.
- [4] Bae, J., Kim, Y., Lee, S., Preparation and characterization of sulfonated poly(epichlorohydrin) membranes for proton exchange membrane fuel cells, *Journal of Industrial and Engineering Chemistry* 33 (2016) 40-45.

- [5] Percec, V.; Heck, J., Liquid Crystalline Polymers Containing Mesogenic Units Based on Half-Disc and Rod-like Moieties. 1. Synthesis and Characterization of 4-(11-Undecan-1-yloxy)-4-[3,4,5-Tri(p-n-Dodecan-1- yloxy-benzyloxy) benzoate] Biphenyl Side Groups, *J. Polym. Sci. Part A* 29 (1991) 591597.
- [6] Bae, J., Lee, J., Kim, Y. S., Choi, Y., Poly(epichlorohydrin) membranes with carboxylic acid groups for direct methanol fuel cell applications, *Journal of Power Sources*, 195 (2010) 7779-7784.
- [7] Huang, X., Li, X., Zhao, Q., A review of polyelectrolytes for proton exchange membrane fuel cells, *Journal of Materials Chemistry A* 6 (2018) 2918-2933.
- [8] Lin, X., Li, J., Liu, F., Quaternization of poly (epichlorohydrin) for proton exchange membrane fuel cell, *International Journal of Hydrogen Energy* 41 (2016) 14370-14377.
- [9] Li, X., Cheng, J., Zhao, Q., Quaternized poly(epichlorohydrin) as proton exchange membrane for fuel cell applications, *Journal of Power Sources* 274 (2015) 211-219.
- [10] Wang, C., Wang, C., Zhang, H., Poly(epichlorohydrin)-based anion exchange membranes for direct methanol fuel cell application, *International Journal of Hydrogen Energy* 39 (2014) 12448-12456.
- [11] Chen, H., Dong, H., Li, Y., Li, X., Poly(epichlorohydrin-co-ethylene oxide) membranes for high-temperature proton exchange membrane fuel cells, *Journal of Power Sources* 307 (2016) 197-204.
- [12] Liu, H., Wang, Y., Liu, S., Fang, S., Yan, F., Crosslinked poly (epichlorohydrin-co-ethylene oxide) anion exchange membranes for alkaline fuel cells, *Journal of Power Sources* 308 (2016) 169-178.

-
- [13] Liu, Y., Wang, X., Cheng, J., Zhang, S., Zhao, Q., Sulfonated poly (epichlorohydrin-co-ethylene oxide) as proton exchange membrane for fuel cell application, *Journal of Power Sources* 243 (2013) 382-389.
- [14] Qi, Z., Li, Y., Dong, H., Li, X., Crosslinked poly(epichlorohydrin-co-ethylene oxide) membranes for proton exchange membrane fuel cells, *Journal of Membrane Science* 573 (2019) 493-502.
- [15] Sun, J., Li, Y., Dong, H., Li, X., Investigation of crosslinked poly (epichlorohydrin-co-ethylene oxide) membranes for high temperature proton exchange membrane fuel cells, *International Journal of Hydrogen Energy*, 42 (2017) 15223-15230.
- [16] Sakalyte, A.; Reina, J.A., Giamberini, M. Liquid crystalline polyamines containing side dendrons: Toward the building of ion channels based on polyamines, *Polymer* 54 (2013) 5133-5140.
- [17] Ronda, J.C.; Reina, J.A.; Giamberini, M. Self-organized liquid-crystalline polyethers obtained by grafting tapered mesogenic groups onto poly (epichlorohydrin): Toward biomimetic ion channels 2, *J. Polym. Sci. Part A Polym. Chem.* 42 (2004) 326-340.
- [18] Bogdanowicz, K.A.; Bhosale, S.V.; Li, Y.; Vankelecom, I.F.J.; Garcia-Valls, R.; Reina, J.A.; Giamberini, M. Mimicking nature: Biomimetic ionic channels. *J. Memb. Sci.* 509 (2016) 10-18.
- [19] Rosen, B.M.; Wilson, C.J.; Wilson, D.A.; Peterca, M.; Imam, M.R.; Percec, V., Dendron-Mediated self-assembly, disassembly, and self-organization of complex systems. *Chem. Rev.* 109 (2009) 6275-6540.
- [20] Percec, V.; Ahn, C.-H.; Ungar, G.; Yeardley, D.J.P.; Möller, M.; Sheiko, S.S. Controlling polymer shape through the self-assembly of dendritic side-groups. *Nature* 391 (1998) 161-164.

- [21] Percec, V.; Schlueter, D.; Ungar, G.; Cheng, S.Z.D.; Zhang, A. Hierarchical control of internal superstructure, diameter, and stability of supramolecular and macromolecular columns generated from tapered monodendritic building blocks. *Macromolecules* 31 (1998) 1745-1762.
- [22] Percec, V.; Glodde, M.; Bera, T.K.; Miura, Y.; Shiyanovskaya, I.; Singer, K.D.; Balagurusamy, V.S.K.; Heiney, P.A.; Schnell, I.; Rapp, A., Self-organization of supramolecular helical dendrimers into complex electronic materials, *Nature* 419 (2002) 384.
- [23] Tylkowski, B.; Castelao, N.; Giamberini, M.; Garcia-Valls, R.; Reina, J.A.; Gumí, T., The importance of orientation in proton transport of a polymer film based on an oriented self-organized columnar liquid-crystalline polyether, *Mater. Sci. Eng. C* 32 (2012) 105-111.
- [24] Bhosale, S.V.; Rasool, M.A.; Reina, J.A.; Giamberini, M., New Liquid Crystalline Columnar Poly(epichlorohydrin-co-ethylene oxide) Derivatives Leading to Biomimetic Ion Chanel, *Polym. Eng. Sci.* 53 (2013) 159-167.
- [25] Bogdanowicz, K.A.; Bhosale, S. V.; Li, Y.; Vankelecom, I.F.J.; Garcia-Valls, R.; Reina, J.A.; Giamberini, M., Mimicking nature: Biomimetic ionic channels, *J. Memb. Sci.* 509 (2016) 10-18.
- [26] Bogdanowicz, K.A.; Rapsilber, G.A.; Reina, J.A.; Giamberini, M., Liquid crystalline polymeric wires for selective proton transport, part 1: Wires preparation, *Polymer (Guildf)* 92 (2016) 50-57.
- [27] Bogdanowicz, K.A.; Sistas, P.; Reina, J.A.; Giamberini, M., Liquid crystalline polymeric wires for selective proton transport, part 2: Ion transport in solid-state, *Polymer (Guildf)*, 92 (2016) 58-65.
- [28] Teruel-Juanes, R.; Pascual-Jose, B.; Graf, R.; Reina, J.A.; Giamberini, M.; Ribes-Greus, A., Effect of Dendritic Side Groups on the Mobility of Modified Poly(epichlorohydrin) Copolymers, *Polymers (Basel)* 13 (2021) 1961.

-
- [29] Montané, X.; Bhosale, S.V.; Reina, J.A.; Giamberini, M., Columnar liquid crystalline polyglycidol derivatives: A novel alternative for proton-conducting membranes, *Polymer (Guildf)* 66 (2015) 100-109.
- [30] Montané, X.; Bogdanowicz, K.A.; Colace, G.; Reina, J.A.; Cerruti, P.; Lederer, A.; Giamberini, M., Advances in the design of self-supported ion-conducting membranes-new family of columnar liquid crystalline polyamines. Part 1: Copolymer synthesis and membrane preparation. *Polymer (Guildf)* 105 (2016) 298-309.
- [31] Montané, X.; Bogdanowicz, K.A.; Prats-Reig, J.; Colace, G.; Reina, J.A.; Giamberini, M., Advances in the design of self-supported ion-conducting membranes New family of columnar liquid crystalline polyamines. Part 2: Ion transport characterisation and comparison to hybrid membranes, *Polymer (Guildf)* 105 (2016) 234-242.
- [32] Sakalyte, A.; Reina, J.A.; Giamberini, M., Liquid crystalline polyamines containing side dendrons: Toward the building of ion channels based on polyamines, *Polymer (Guildf)* 54 (2013) 5133-5140.
- [33] Teruel-Juanes, R.; Bogdanowicz, K.A.; Badia, J.D.; Sáenz de Juano-Arbona, V.S. de; Graf, R.; Reina, J.A.; Giamberini, M.; Ribes-Greus, A., Molecular Mobility in Oriented and Unoriented Membranes Based on Poly[2-(Aziridin-1-yl)ethanol], *Polymers (Basel)* 13 (2021) 1060.
- [34] Zare, A.; Pascual-Jose, B.; De la Flor, S.; Ribes-Greus, A.; Montané, X.; Reina, J.A.; Giamberini, M. Membranes for cation transport based on dendronized poly(Epichlorohydrin-co-ethylene oxide). part 1: The effect of dendron amount and column orientation on copolymer mobility. *Polymers (Basel)* 13 (2021) 3532.
- [35] Angell, C.A., Perspective on the glass transition. *J. Phys. Chem. Solids* 49 (1988) 863-871.

- [36] Angell, C.A. Relaxation in liquids, polymers and plastic crystals Strong/fragile patterns and problems, *J. Non-Cryst. Solids* (1991) 131133.
- [37] Adam, G.; Gibbs, J.H., On the temperature dependence of cooperative relaxation properties in glass-forming liquids, *J. Chem. Phys.* 43 (1965) 139-146.
- [38] Turnbull, D.; Cohen, M.H., Free-volume model of the amorphous phase: Glass transition, *J. Chem. Phys.* 34 (1961) 120-125.
- [39] Reyes-Rodriguez, J.L.; Solorza-Feria, O.; García-Bernabé, A.; Giménez, E.; Sahuquillo, O.; Compañ, V., Conductivity of composite membrane-based poly (ether-ether-ketone) sulfonated (SPEEK) nanofiber mats of varying thickness, *RSC Adv.* 6 (2016) 56986-56999.
- [40] Jin, X.; Zhang, S.; Runt, J., Observation of a fast dielectric relaxation in semi-crystalline poly(ethylene oxide). *Polymer (Guildf)*, 43 (2002) 6247-6254.
- [41] Jonscher, A.K., Dielectric relaxation in solids, *J. Phys. D. Appl. Phys.* 32 (1999) R57.
- [42] Tammann, G.; Hesse, W., Die Abhängigkeit der Viscosität von der Temperatur bei unterkühlten Flüssigkeiten, *Zeitschrift für Anorg. und Allg. Chemie* 156 (1926) 245-257.
- [43] Silva, M.A.; De Paoli, M.-A.; Felisberti, M.I., Flory-Huggins interaction parameter of poly (ethylene oxide)/poly (epichlorohydrin) and poly (ethylene oxide)/poly (epichlorohydrin-co-ethylene oxide) blends, *Polymer (Guildf)* 39 (1998) 2551-2556.
- [44] Zare, A.; Montan, X.; Reina, A.; Giamberini, M., Membranes for Cation Transport Based on Dendronized Characterization and Transport Properties, 13 (2021) 3915.

Chapter 7

Membranes based on covalent adaptable networks

In this chapter a covalent adaptable network is studied. This type of thermoset networked polymers close the gap with thermoplastics thanks to the presence of reversible bonds in the structure. The main advantage in the usage of this type of chemistries is to obtain the best of both worlds; i.e. good mechanical properties at working temperatures, like thermosets, while displaying physical properties such as self-healing, weldability, and recyclability that are characteristic of thermoplastics. Indeed, these features justify the study of its applicability in polymer electrolytes. Therefore, in Chapter 7, the suitability of a poly(thiourethane) network for fuel cell applications is assessed.

7.1 Introduction

Thermosets are a class of polymers that display good dimensional stability, chemical inertia and rigidity that is achieved once the structure is cured. However, after the curing process is completed it is very difficult to re-shape or reprocess it. Accordingly, a manner to achieve polymer networks with a certain degree of plasticity is by introducing exchangeable chemical bonds in the structure, thus, leading to a dynamic crosslinking. This type of chemistry allows for macroscopic flow without any risk of losing the networks' performance [1].

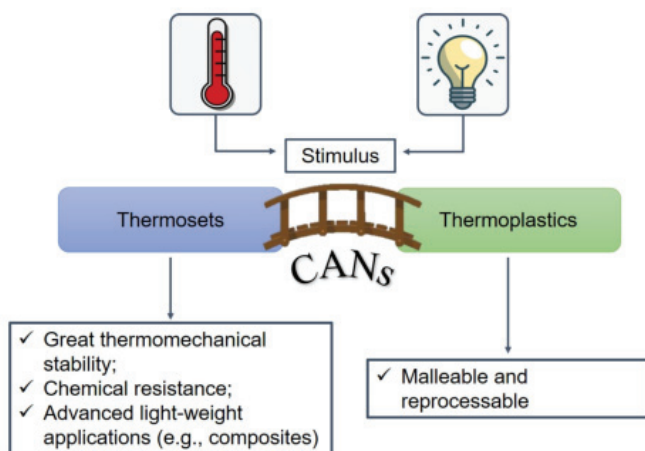


Figure 7.1: Covalent Adaptable Networks (CANs) understood the intermediate stage where the best of both worlds, thermosets and thermoplastics, is achieved. Source: [2].

Furthermore, these polymer networks would display good mechanical properties at work temperatures, as thermosets do. At the same time, these networks would exhibit also good self-healing, weldability, and recyclability capacities, attributes that thermosets do not possess since these features are characteristic of thermoplastics. Consequently, polymer networks that contain these dynamic bonds are known as covalent adaptable networks (CANs) [2,3].

Consequently, CANs are a class of polymer networks that are designed to possess the ability to undergo reversible covalent bond exchange reactions under

external stimuli, such as heat, light, or mechanical stress. This unique property allows CANs to exhibit self-healing, shape-memory, and recyclability, among other functionalities [4].

CANs are formed by covalent bonds between monomers, which can be either small molecules or macromolecules, and are crosslinked by reversible covalent bonds, such as disulfide, boronic ester, imine, or dynamic covalent bond. The reversible nature of these bonds enables the network to undergo reconfiguration and repair, leading to its ability to self-heal [5,6].

CANs have potential applications in various fields, including coatings, adhesives, electronic devices, and biomaterials. In the biomedical field, CANs can be used to create implantable devices and drug delivery systems that respond to biological stimuli. They can also be used in tissue engineering and wound healing [7].

However, despite their advantages, CANs still face challenges in terms of their mechanical properties and stability. The dynamic nature of the covalent bonds can also limit their application in some environments where high temperatures or harsh chemicals are present. Nonetheless, researchers continue to explore ways to optimize and improve the performance of CANs [4-8].

Viscoelastic properties of CANs

The viscoelastic behaviour of CANs is determined by two characteristic temperatures related to physical transitions in the structure. Firstly, the glass transition temperature (T_g) corresponding to the long range segmental motions. Secondly, the freezing topology temperature (T_v) that is related to the bond exchange reaction that originates the dynamic crosslinking. Furthermore, the dynamic crosslinking depends on the timescale of the bond exchange reactions. When it becomes shorter than the time scale of the material deformation, the process is activated and the CAN is able to rearrange its topology resulting in a viscoelastic liquid [3].

Generally, it is accepted that below T_v it is very difficult for bond exchange reactions to take place. However, recently the consensus has broken down since more experimental techniques are used in the study of CANs, and subsequently, new insights arise [2,3].

For example, Hubbard et al. discuss that the bond exchange reaction can occur at every low temperature. However, the T_v acts as the onset temperature where the time scales of the process become significant. Additionally, Schoustra et al. reported that actual T_v values can be much lower than the initially estimated value [1].

This proves that the molecular dynamics associated with the bond exchange reaction can occur at temperatures lower than those previously estimated. Therefore, being able to determine the onset of T_v and its position with respect to T_g is crucial to determine, as well as to fine-tune, the overall profile of the polymeric network [1-3].

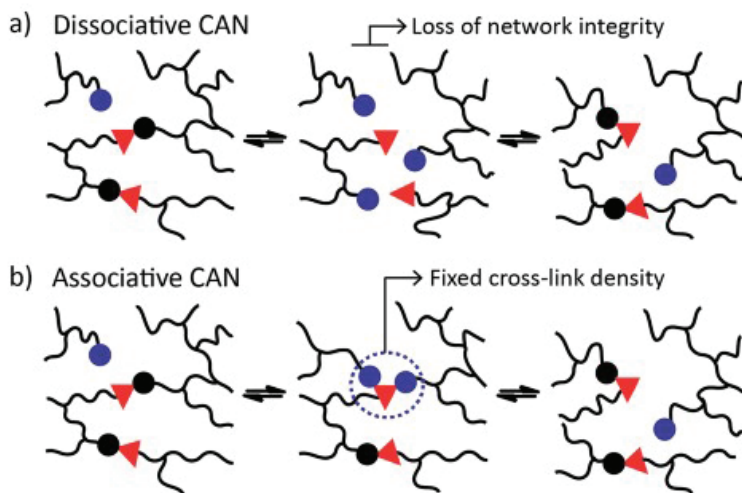


Figure 7.2: (a) Dissociative CANs where bond breakage precedes bond formation; (b) Associative CANs, also known as vitrimers, where bond formation precedes bond breakage. Source: [3]

In addition CANs can be classified regarding the bond exchange mechanism exhibited, as displayed in Figure 7.2. Consequently, two types exist: associatives or dissociatives. The former group includes the CANs where the dynamic bonds are first broken and formed again, while the latter the opposite occurs, and thus, bond breakage prevails over bond formation.

Suitability of CANs as proton-exchange membranes

CANs have been explored as potential materials for proton exchange membranes (PEMs) in fuel cells. PEMs play a critical role in the performance and durability of fuel cells by allowing the transfer of protons while blocking the transport of electrons. CANs have been investigated as an alternative to conventional PEMs, such as perfluorinated sulfonic acid membranes, due to their tunable properties and potential for self-healing [9,10].

Several studies have reported the synthesis and characterization of CAN-based PEMs, which exhibit good proton conductivity and thermal stability. For example, a study by Liu et al. (2019) reported the preparation of imine-based CAN PEMs that showed high proton conductivity and thermal stability up to 453 K. Similarly, another study by Li et al. (2020) demonstrated the synthesis of boronic acid-based CAN PEMs with excellent mechanical properties and good proton conductivity [11].

However, despite these promising results, the suitability of CANs as PEMs still faces some challenges. One of the main issues is the relatively low water uptake of CANs, which can limit their proton conductivity under low-humidity conditions. The dynamic nature of the covalent bonds in CANs may also limit their long-term stability and durability in fuel cell applications, as well as the need for specific conditions to allow for bond exchange [12,13].

Overall, while CANs show potential as PEMs in fuel cells, further research is needed to optimize their properties and address the challenges associated with their use in practical applications [9-13].

General properties of poly(thiourethane)

Poly(thiourethane) is a polymer made by reacting an isocyanate with a dithiol or diamine. It is a type of polyurethane that contains sulfur atoms in its backbone. When compared to polyurethanes (PUs), exhibit certain advantages. For instance, it displays properties such as biocompatibility, flexibility, excellent optical transparency. Moreover, the homogeneous structure reduces the gap between the relaxation processes, and thus, occurring in a narrow range of temperatures. PTU is a relatively new class of polymer, and it has been the subject of increasing interest due to its potential applications in a range of fields, including biomedical engineering, coatings, adhesives, and materials science. Some of the most relevant information on PTU includes the following [14-18]:

- *Synthesis:* PTU can be synthesized by the reaction of isocyanates with thiourea compounds under appropriate reaction conditions. The resulting polymer has a crosslinked network structure, and its properties can be tuned by varying the types and ratios of the reactants, as well as the reaction conditions.
- *Properties:* PTU exhibits a range of properties that make it attractive for various applications. For example, it has good mechanical properties, including high elasticity and toughness, as well as good chemical and thermal stability. PTU is also biocompatible and can be used in biomedical applications such as tissue engineering and drug delivery.
- *Applications:* PTU has been investigated for a range of applications, including biomedical devices such as implantable sensors and drug delivery systems, as well as coatings and adhesives for industrial and consumer applications. PTU has also been explored as a potential material for energy storage applications such as supercapacitors.
- *Advantages and challenges:* PTU offers several advantages over other types of polymers, including its biocompatibility, mechanical properties,

and ease of synthesis. However, challenges associated with PTU include its relatively low solubility and difficulty in processing, as well as the need for toxic isocyanates in its synthesis.

Several types of reversible exchange reactions have been explored for the preparation of covalent adaptable networks, such as transesterification, transamination, disulfide exchange, transalkylation, siloxane equilibrium, dioxaborolane metathesis, amine-urea exchange and transcarbamoylation [19]. Since in Chapter 7 the CAN chosen is a polythiourethane network, it has already been demonstrated that from the previously listed reactions the transcarbamoylation is responsible for the bond exchange reaction [20,21].

In polyurethanes the transcarbamoylation of carbamate groups might vary depending on the chemical units present in the structure. Therefore, the ascription of the associative and dissociative routes might be cumbersome. According to Alabiso et al. the associative route could occur similarly to transesterification, where the carbamate units are associated via catalysed interaction or by nucleophilic addition of -OH groups. Contrarily, the dissociative route is linked with detrimental side-reactions at high temperatures. The dissociative bond exchange by transcarbamoylation is significantly slower than the transesterification of transamination [2].

In summary, PTU is a promising polymer with a range of attractive properties for various applications. Further research is needed to optimize its properties and overcome the challenges associated with its use in practical applications.

PTU is a versatile polymer with excellent physical properties that make it suitable for a wide range of applications, including coatings, adhesives, and sealants. Some of the most relevant physical properties of poly(thiourethane) are the following [22-26]:

- *Hardness:* Poly(thiourethane) is known for its hardness and can range from a soft rubber-like material to a hard plastic-like material.

- *Tensile strength:* Poly(thiourethane) has a high tensile strength, meaning it can withstand a significant amount of stress before breaking or deforming.
- *Elasticity:* Poly(thiourethane) has good elasticity and can be stretched and returned to its original shape without damage.
- *Chemical resistance:* Poly(thiourethane) is resistant to many chemicals, including acids, bases, and solvents.
- *UV stability:* Poly(thiourethane) is UV stable and does not degrade when exposed to sunlight or other UV sources.
- *Water resistance:* Poly(thiourethane) is water-resistant and can be used in applications where exposure to water or moisture is expected.

Furthermore, PTU is a thermosetting polymer that exhibits interesting thermal properties, which are complex and depend on several factors. The thermal properties of PTU make it a promising material for various applications, including adhesives, coatings, and composites. The most remarkable ones are mentioned as follows [22-26]:

- *Glass transition temperature (T_g):* The T_g of PTU is influenced by its chemical composition, molecular weight, crosslinking density, and processing conditions. Typically, the T_g of PTU is in the range of 213 to 343 K.
- *Decomposition temperature:* The decomposition temperature of PTU depends on its chemical composition, molecular weight, crosslinking density, and processing conditions. The decomposition temperature of PTU can be influenced by the presence of additives or fillers.
- *Thermal stability:* PTU exhibits good thermal stability, which makes it suitable for high-temperature applications. The thermal stability of PTU

can be enhanced by increasing the crosslinking density or incorporating additives.

- *Heat capacity:* The heat capacity of PTU is influenced by its chemical composition, molecular weight, crosslinking density, and processing conditions. Typically, the heat capacity of PTU is in the range of 1.2-1.6 J/gK.
- *Thermal conductivity:* The thermal conductivity of PTU is relatively low compared to other materials, such as metals or ceramics. The thermal conductivity of PTU can be influenced by its chemical composition, molecular weight, crosslinking density, and processing conditions.

Concerning its glass transition temperature (T_g), as a result of its amorphous nature, its value vary depending on its chemical structure and composition. Generally, the T_g of PTU can range from 233 to 343 K. The T_g can be influenced by factors such as the degree of crosslinking, the types and ratios of the reactants used in the synthesis, and the molecular weight of the polymer chains [27,28].

Moreover, PTU can exhibit good thermal stability and a relatively high T_g compared to other polymers, which makes it attractive for use in high-temperature applications. However, it is important to note that the T_g of PTU can also influence its mechanical properties, including stiffness and elasticity. Higher T_g values generally lead to a stiffer and more brittle material, while lower T_g values lead to a more flexible and elastomeric material [29,30].

Overall, the T_g of PTU can be tailored to suit specific application requirements by adjusting its chemical composition and processing conditions. Further research is needed to optimize the T_g of PTU and explore its potential applications [27-31].

Regarding its dielectric properties, PTU exhibits interesting properties. The dielectric spectra of poly(thiourethane) are complex and depend on several factors, like its chemical composition, molecular weight, crosslinking density, and

processing conditions. The dielectric properties of poly(thiourethane) make it a promising material for various applications, including capacitors, sensors, and electronic devices [32-36]:

- *Dielectric constant:* PTU has a dielectric constant that is generally in the range of 2-5, depending on the frequency and temperature. The dielectric constant of PTU increases with increasing frequency and decreases with increasing temperature.
- *Dielectric loss:* PTU exhibits dielectric losses, which are characterized by the imaginary part of the complex permittivity. The dielectric loss of PTU is influenced by its chemical composition, molecular weight, crosslinking density, and processing conditions.
- *Relaxation processes:* PTU exhibits multiple relaxation processes in its dielectric spectra, which are associated with different molecular motions. The relaxation processes in PTU are influenced by its chemical composition, molecular weight, crosslinking density, and processing conditions.
- *Frequency dependence:* The dielectric spectra of PTU exhibit a strong frequency dependence, which is due to the presence of multiple relaxation processes. The frequency dependence of the dielectric spectra of PTU can provide insights into its molecular structure and dynamics.

Given the advantages that the self-welding and stress dissipation properties could provide to a proton-exchange membrane, the dielectric properties of a PTU network with different catalyst percentages are assessed in Chapter 7 to characterize the proton conductivity, but also the molecular motions, including the one originating the trans-thiocarbamylation reaction. Subsequently being able to assess the impact that they have on the charge transfer mechanism that will promote both, electron and proton conduction.

7.2 Materials

Hexamethylene diisocyanate (HDI), trimethylolpropane tris(3-mercaptopropionate) (S3), and dibutyltin dilaurate (DBTDL) from Merck were used as received. Briefly, the sample (HDI-S3) was prepared, as shown in Figure 7.3, by mixing stoichiometric amounts of HDI and S3 and adding a 1%, and 4% w/w DBTDL as the catalyst, homogenized, and then cured in the oven at 333, 353, 373, and 423 K for two hours at each temperature [19]. The sample was dried for three hours at 373 K before the measurement. Therefore the samples studied in Chapter 7 are labelled as HDI-S3-1%, and HDI-S3-4%.

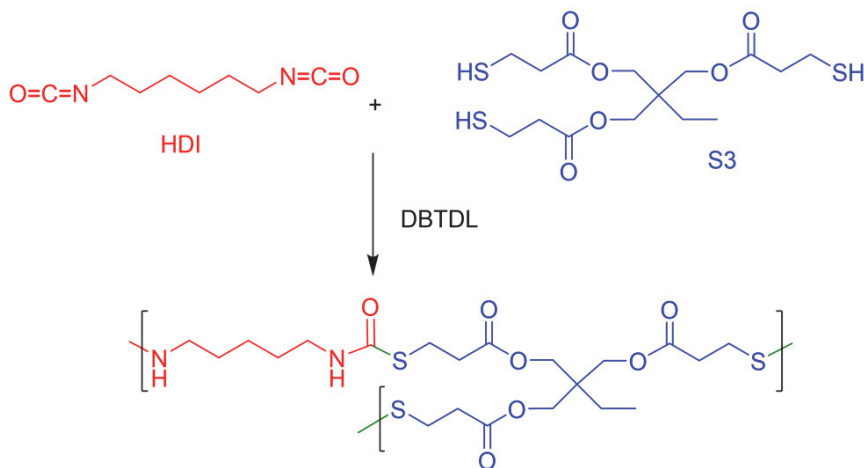


Figure 7.3: Synthesis route of the HDI-S3 network.

7.2.1 Experimental methodology

Fourier Transformed Infrared Spectroscopy (FTIR)

The chemical structure was assessed through Fourier Transform Infrared Spectroscopy (FTIR). Analyses were carried out in a Thermo Nicolet 5700 infrared

spectrometer with an attenuated total reflectance accessory (ATR). The spectra were collected from 4000 to 400 cm^{-1} at a resolution of 4 cm^{-1} along 64 scans. The spectra of three different locations of the sample were averaged. Backgrounds were collected, and results were processed through the Omnic® Software.

Differential Scanning Calorimetry (DSC)

The differential scanning calorimetry (DSC) analyses were evaluated using Mettler Toledo DSC822e equipment. Aluminium capsules were filled with the samples, between 2 and 4 mg, and sealed. Then, they were subjected to a heating/cooling program with a rate of 5 $K \cdot min^{-1}$ over the 263 K to 403 K temperature range under an inert atmosphere with a flow rate of 50 $mL \cdot min^{-1}$ of nitrogen.

Thermogravimetric Analysis (TGA)

The thermogravimetric analysis (TGA) was carried out with a Mettler Toledo TGA/STDA 851e setup. Samples with a mass between 2 and 5 mg were placed into 70 μL alumina capsules. An empty capsule was used as a blank to take the reference baseline. The analyses were performed with a heating rate of 30 $K \cdot min^{-1}$ over the 303 K to 1073 K temperature range using an oxidative atmosphere with a flux of 50 $mL \cdot min^{-1}$ of oxygen.

Dielectric Thermal Analysis (DETA)

The impedance measurements were conducted using a Novocontrol Broadband Dielectric Impedance Spectrometer (BDIS), connected to a Novocontrol Alfa-A Frequency Response Analyzer. The measurements were run in the frequency range of 10^{-1} to 10^{-7} Hz, at the temperature range 123 K to 523 K. All the measurements were performed under isothermal conditions by increasing in steps of 10K in the temperature range from 123 K to 200 K and in steps of 2.5 K in the temperature range from 213 K to 523 K. This change in the temperature

step was made considering the narrow temperature range in which relaxation processes start in the HDI-S3 CAN. Thus, a better resolution of every dielectric process can be obtained. The sample electrode assembly (SEA) consisted of two stainless steel electrodes filled with the sample. Consequently, the resulting SEA was directly placed in the cell.

7.3 Results

7.3.1 Analysis of the dielectric spectra of the HDI-S3-1% membrane

The dielectric spectra was plotted in terms of the real (ϵ') and imaginary (ϵ'') parts of the complex dielectric permittivity (ϵ^*), $\tan \delta$, and the imaginary part of the electric modulus (M'') in Figures 7.4 - 7.5.

In Figure 7.6A the macromolecular origin of the dielectric relaxations is assessed through the Eyring model as derived by Starkweather. The closeness of the γ_1 , γ_2 and β to the zero-entropy line reveal its non-cooperative nature. Concerning the β dielectric process, its E_a value is higher due to its closeness with the α_{Tg} , and therefore, it is influenced by its cooperativity. On the other hand, the E_a values of the α_{Tg} and α^* lie far away from the zero-entropy line. Therefore, the macromolecular origin of both dielectric processes must be of cooperative origin.

In Figure 7.6B the Arrhenius plot is displayed. It shows different relaxation zones. At low temperatures, the γ_1 , γ_2 , and β dielectric processes are found. Thus, its molecular origin has to be related with local motions of the copolymer. On the other hand, in the high-temperature region, the α_{Tg} , and the α^* are present. Given the results from the macromolecular assessment together with the temperature at which both processes are occurring, a cooperative origin must be assumed. Most probably, both relaxations are related to the glass transition and the clearing transition, respectively.

In Figure 7.7 the isothermal curves of the modulus of the complex conductivity ($|\sigma|$) for the complete temperature range are displayed.

To determine the proton conductivity, the phase angle and the absolute value of the serial impedance (Z_s) are needed. Thus, both parameters are shown in Figure 7.8.

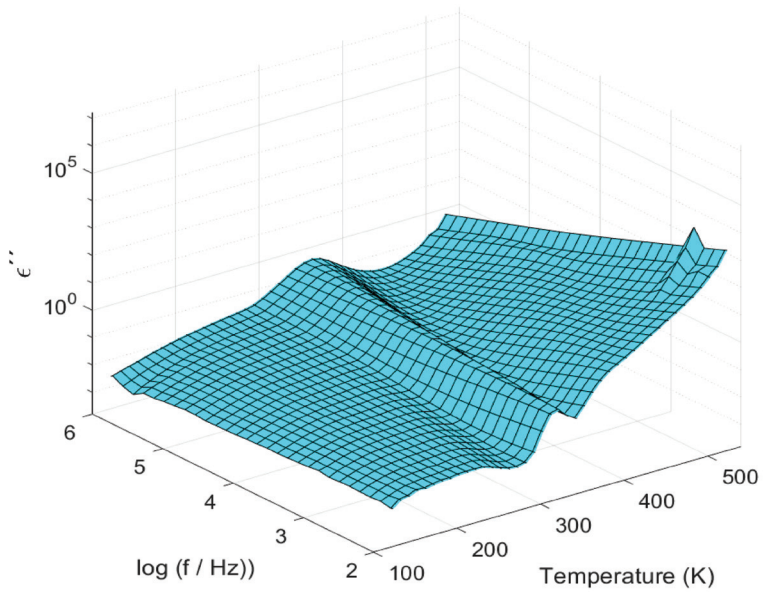
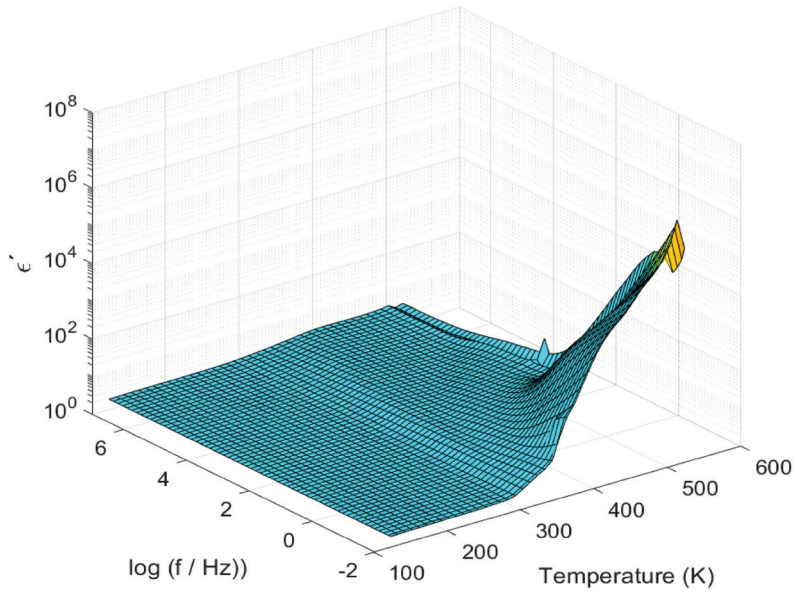


Figure 7.4: 3D plot of the real (ϵ') and imaginary part (ϵ'') parts of the complex permittivity (ϵ^*) of the HDI-S3-1% membrane.

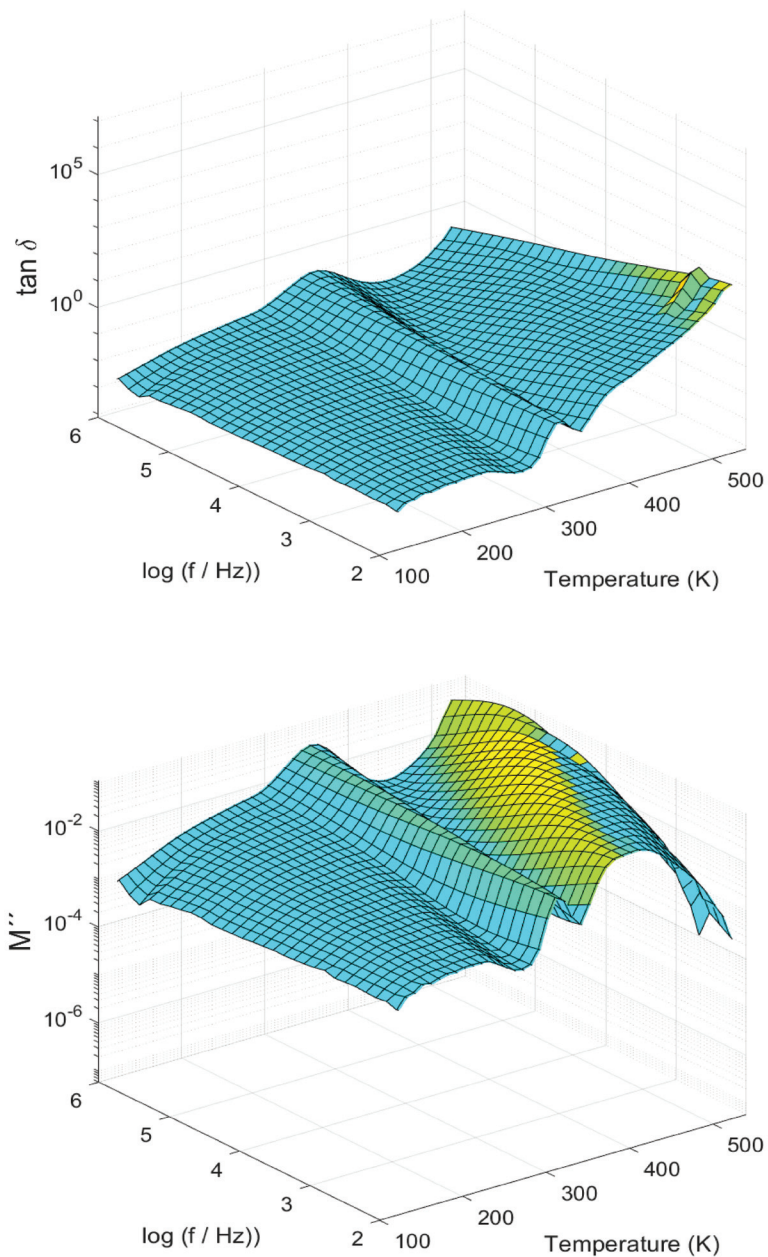


Figure 7.5: 3D plot of $\tan \delta$ and of the imaginary part (M'') of the complex electric modulus (M^*) of the HDI-S3-1% membrane.

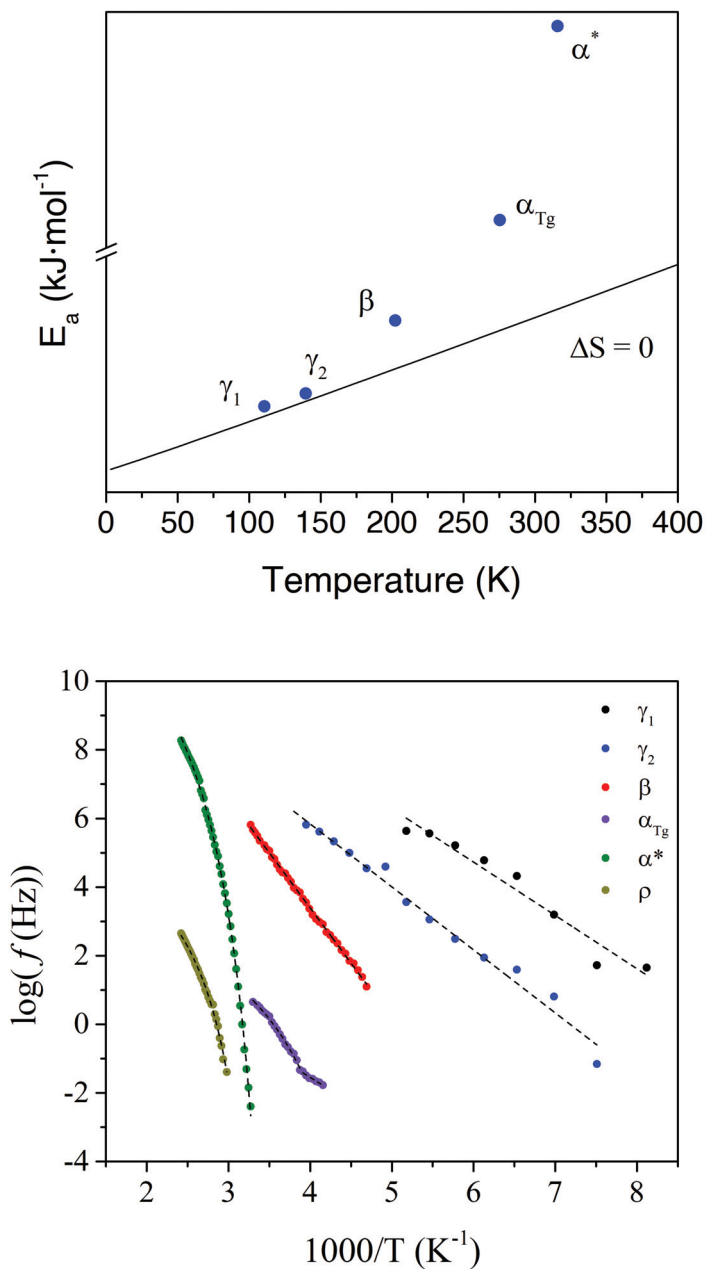


Figure 7.6: (Top) Eyring plot and (Bottom) Arrhenius plot of the HDI-S3-1% membrane.

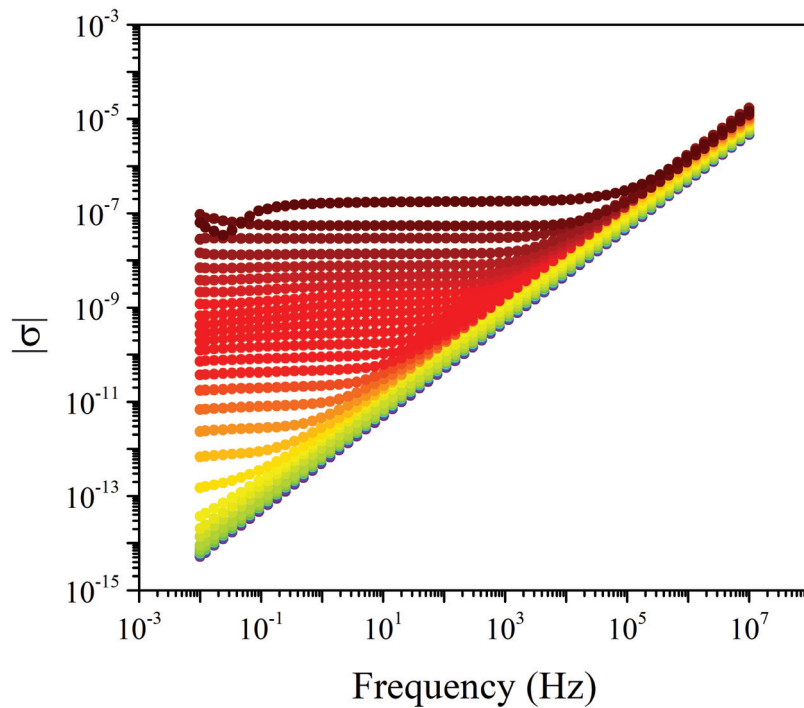


Figure 7.7: Isothermal curves of the modulus of the complex conductivity ($|\sigma|$) for the HDI-S3-1% membrane.

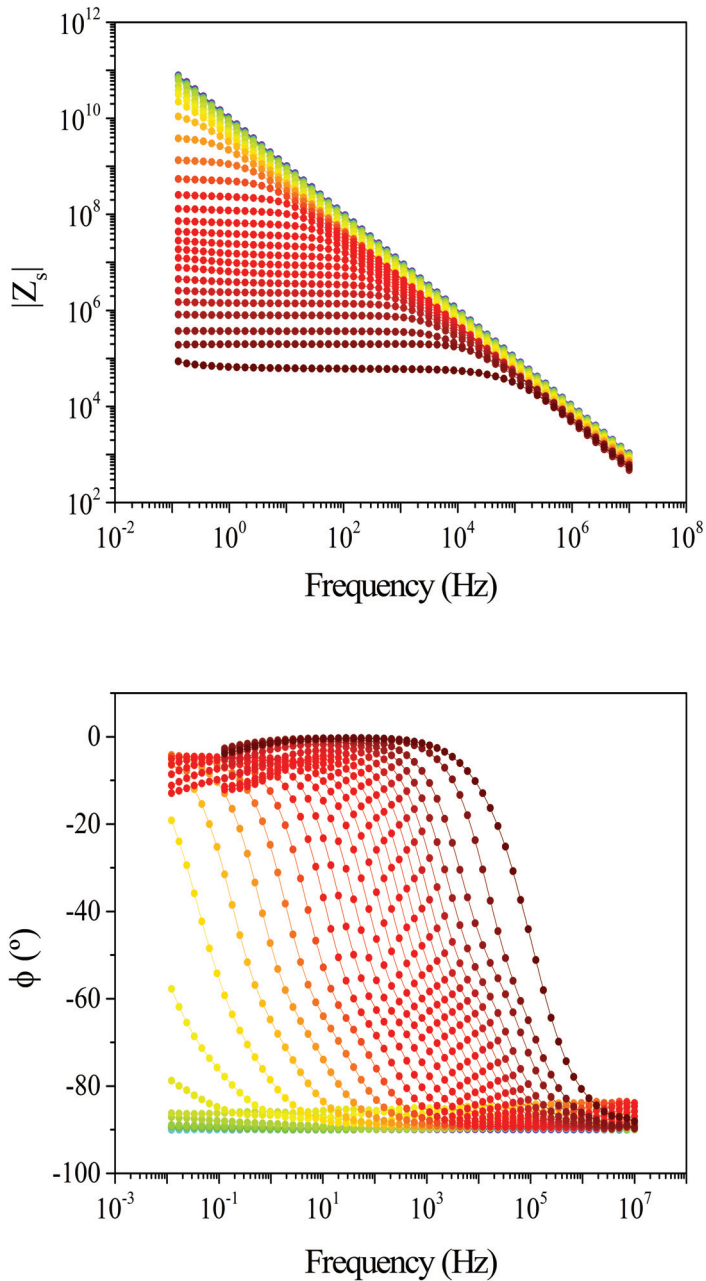


Figure 7.8: Phase angle (ϕ) and modulus of the serial impedance ($|Z_s|$) of the HDI-S3-1% membrane.

7.3.2 Analysis of the dielectric spectra of the HDI-S3-4% membrane

The dielectric spectra was plotted in terms of the real (ϵ') and imaginary (ϵ'') parts of the complex dielectric permittivity (ϵ^*), $\tan \delta$, and the imaginary part of the electric modulus (M'') in Figures 7.9 - 7.10.

In Figure 7.11A the macromolecular origin of the dielectric relaxations is assessed through the Eyring model as derived by Starkweather. The closeness of the γ_1 , γ_2 and β to the zero-entropy line reveal its non-cooperative nature. Concerning the β dielectric process, its E_a value is higher due to its closeness with the α_{Tg} , and therefore, it is influenced by its cooperativity. On the other hand, the E_a values of the α_{Tg} and α^* lie far away from the zero-entropy line. Therefore, the macromolecular origin of both dielectric processes must be of cooperative origin.

In Figure 7.11B the Arrhenius plot is displayed. It shows different relaxation zones. At low temperatures, the γ_1 , γ_2 , and β dielectric processes are found. Thus, its molecular origin has to be related with local motions of the copolymer. On the other hand, in the high-temperature region, the α_{Tg} , and the α^* are present. Given the results from the macromolecular assessment together with the temperature at which both processes are occurring, a cooperative origin must be assumed. Most probably, both relaxations are related to the glass transition and the clearing transition, respectively.

In Figure 7.12 the isothermal curves of the modulus of the complex conductivity ($|\sigma|$) for the complete temperature range are displayed.

To determine the proton conductivity, the phase angle and the absolute value of the serial impedance (Z_s) are needed. Thus, both parameters are shown in Figure 7.13.

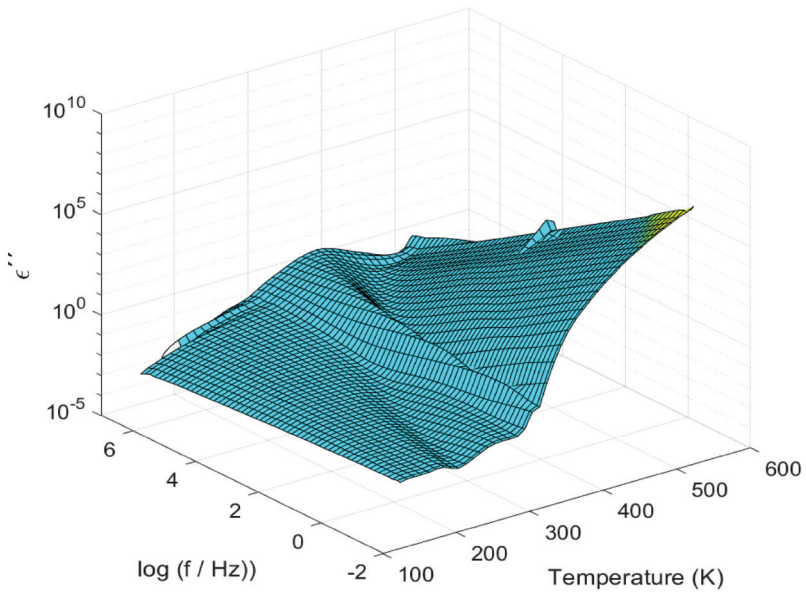
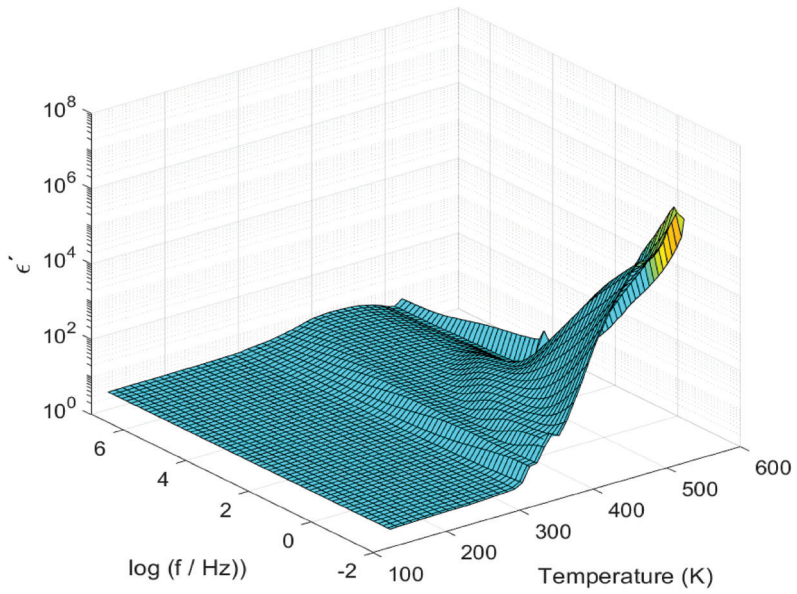


Figure 7.9: 3D plot of the real (ϵ') and imaginary part (ϵ'') parts of the complex permittivity (ϵ^*) of the HDI-S3-4% membrane.

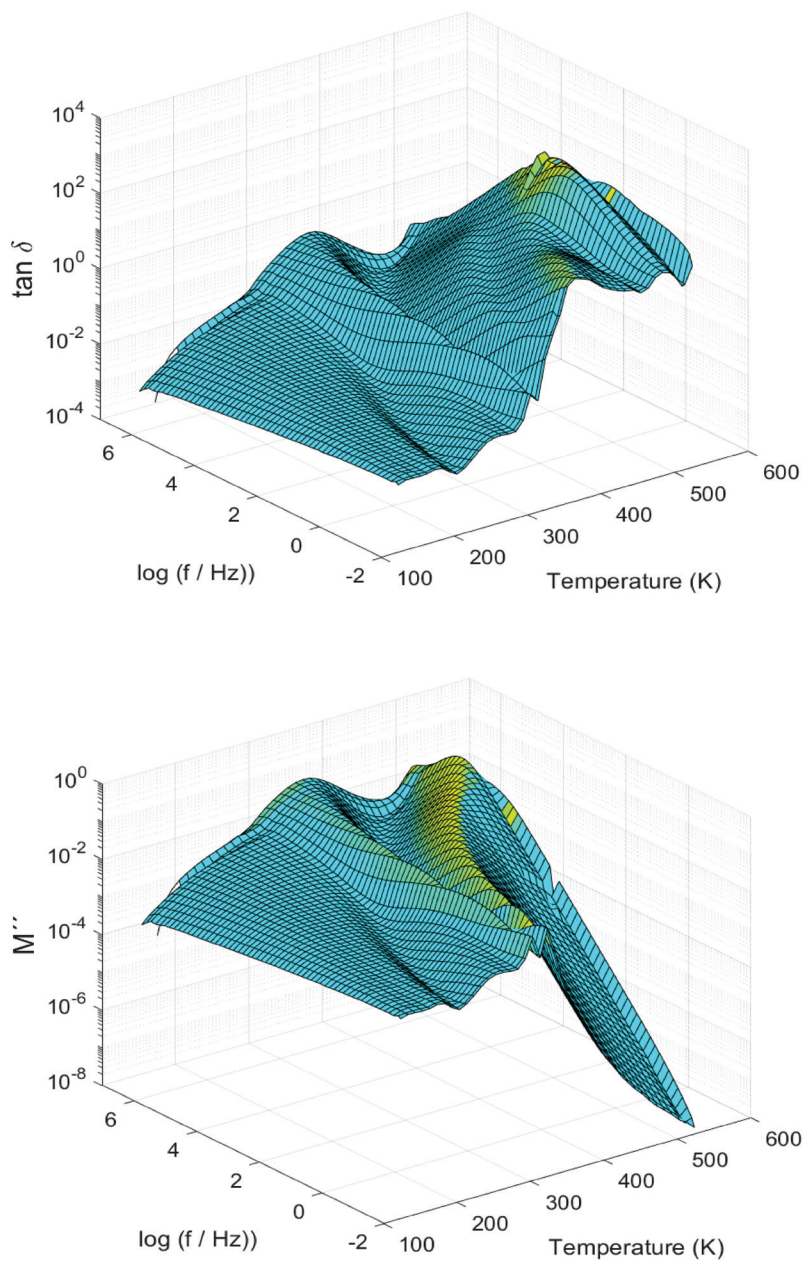


Figure 7.10: 3D plot of $\tan \delta$ and of the imaginary part (M'') of the complex electric modulus (M^*) of the HDI-S3-4% membrane.

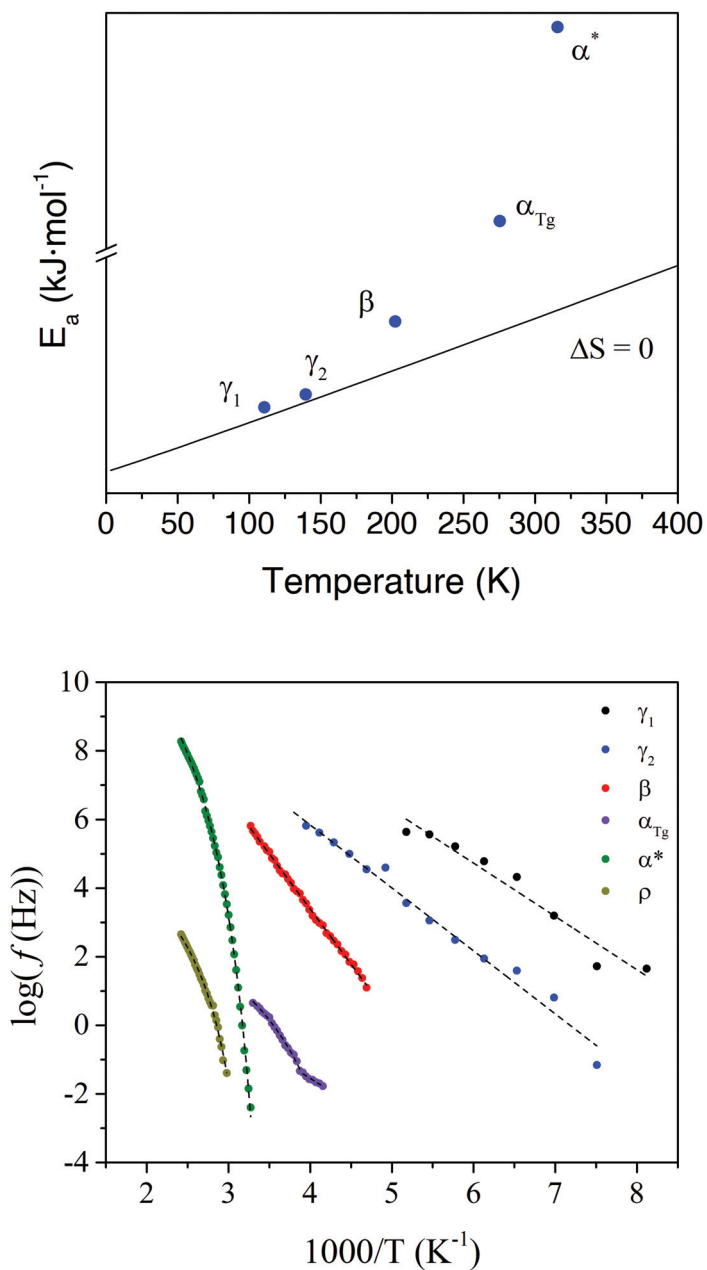


Figure 7.11: (Top) Eyring plot and (Bottom) Arrhenius plot of the HDI-S3-4% membrane.

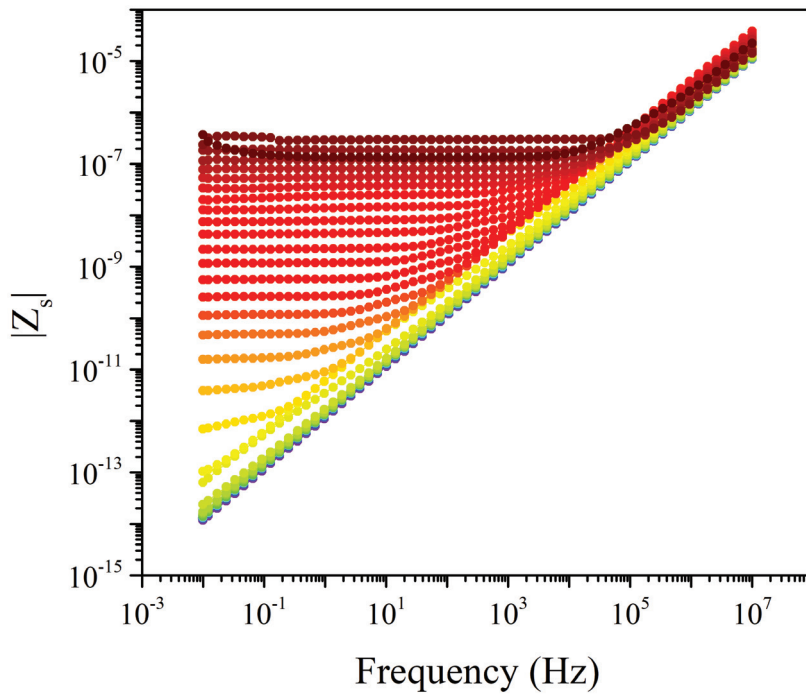


Figure 7.12: Isothermal curves of the modulus of the complex conductivity ($|\sigma|$) for the HDI-S3-4% membrane.

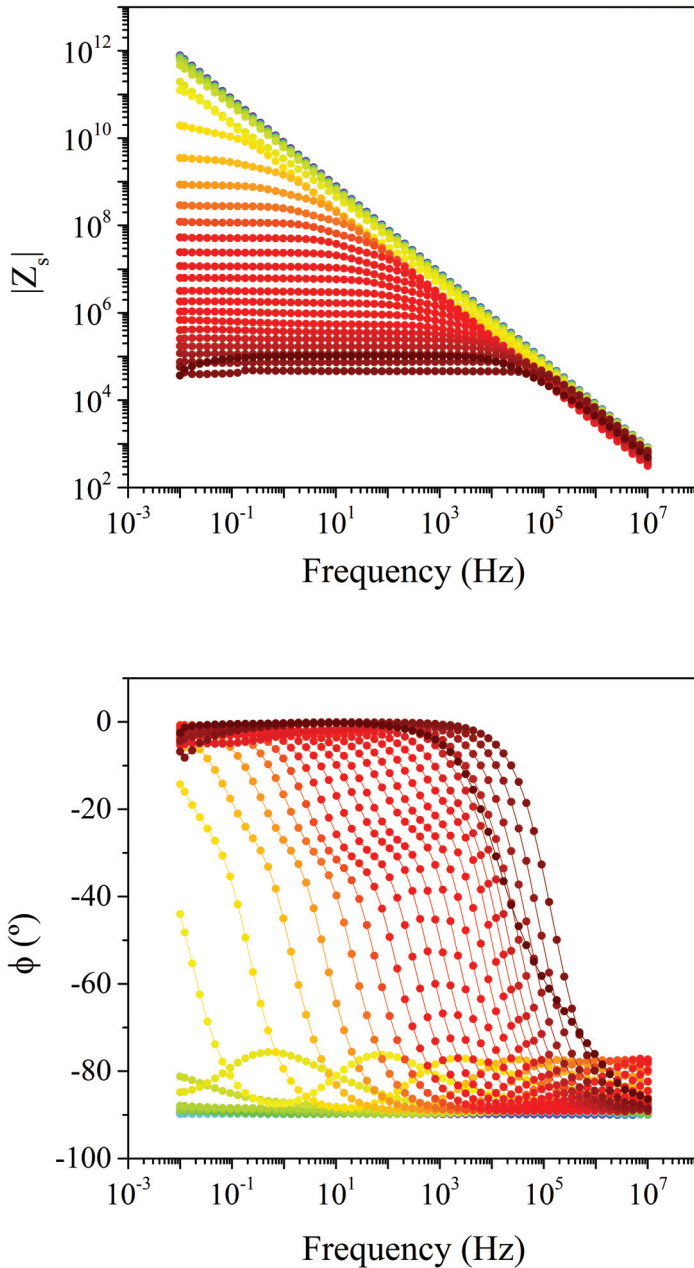


Figure 7.13: Phase angle (ϕ) and modulus of the serial impedance ($|Z_s|$) of the HDI-S3-4% membrane.

To conclude, part of the results presented in this section have been published in a scientific peer-reviewed article (Contribution 9) listed in section 9.1, and it complements the discussion of the results included in section 7.4.

7.4 Discussion

The FTIR spectra is shown in Figure 7.14, to confirm that the PTU network's formation is completed.

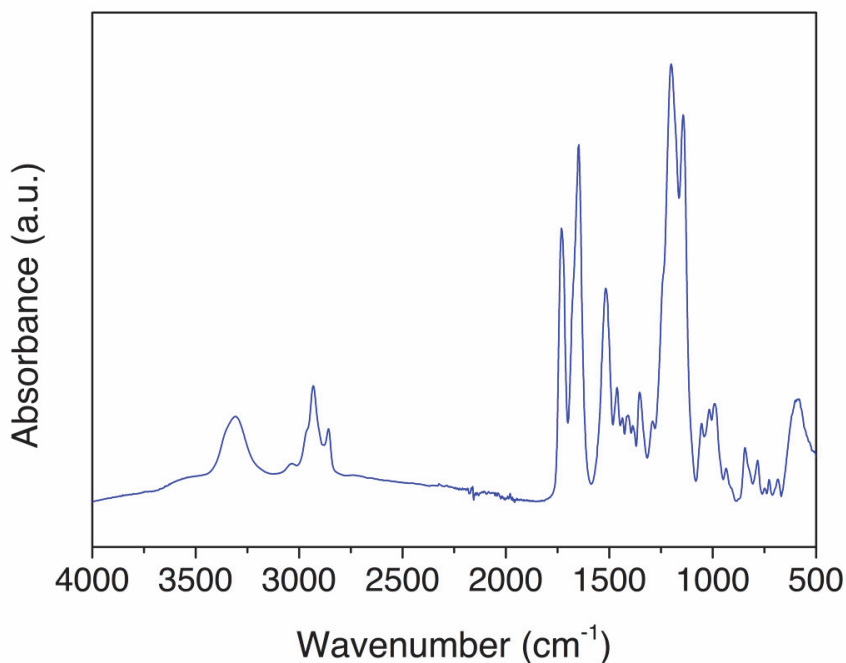


Figure 7.14: FTIR spectrum of the HDI-S3 sample.

The C-H stretching band and the asymmetric and symmetric C-H stretching of CH_2 were found at 3034 cm^{-1} and 2932 cm^{-1} , respectively. In addition, the C=O stretching corresponding to the ester linkage, present in the S3, was found at 1731 cm^{-1} . Hydrogen bonded and non-hydrogen bonded C=O stretching bands of the thiourethane group were located at 1649 cm^{-1} and 1680 cm^{-1} ,

respectively. Moreover, N-H bending and N-H stretching bands, located at 1514 cm^{-1} and 3303 cm^{-1} , confirmed the thiourethane linkage. Besides, the wide bands between 3500 cm^{-1} and 3000 cm^{-1} due to O-H stretching and the asymmetric peak around 1600 cm^{-1} , corresponding to the bending band of water, acknowledged interactions with water molecules [21].

The thermal stability of the sample was assessed through thermogravimetric analysis (TGA). The weight loss as a function of time was studied through thermogravimetric thermograms and differential curves, as shown in Figure 7.15, where several mass-loss stages are found. The first small-scale mass-loss stage may be due to the evaporation of remnant-bound humidity, but it is a few percentage. The subsequent more prominent mass-loss stage is found above 523K and is associated with the elimination of carbonyl sulphide during the decomposition process of the thiourethane [37,38]. Furthermore, the next stage related to the peak around 613K is attributed to the β -elimination processes of the esters of the thiol structural units [19-21]. At last, the mass-loss between 673 and 773 K agrees with the degradation of the backbone. Therefore, membranes can be considered thermally stable in the operative range of low temperature fuel cells.

The isochronal plots of imaginary (ϵ'') part of the complex permittivity are displayed in Figure 7.16 for the HDI-S3-1% and HDI-S3-4%, respectively. As observed, it is a complex spectra. Accordingly, the dielectric spectrum initially displays six relaxations. The first region is located at low temperatures, and labelled in order of increasing temperature as γ_1 , γ_2 and β , respectively. The other relaxations are located at mid to high temperatures, and the three dielectric relaxations have been labelled as α_{Tg} , α^* , and ρ , which may be related to the glass transition, bond exchange, and interfacial polarization, respectively.

Regarding the catalyst, its effect is seen in Figure 7.17. Accordingly, the dielectric process α^* initiates earlier in the HDI-S3-4% membrane. Hence, the catalyst is acting effectively since it facilitates the α^* dielectric relaxation.

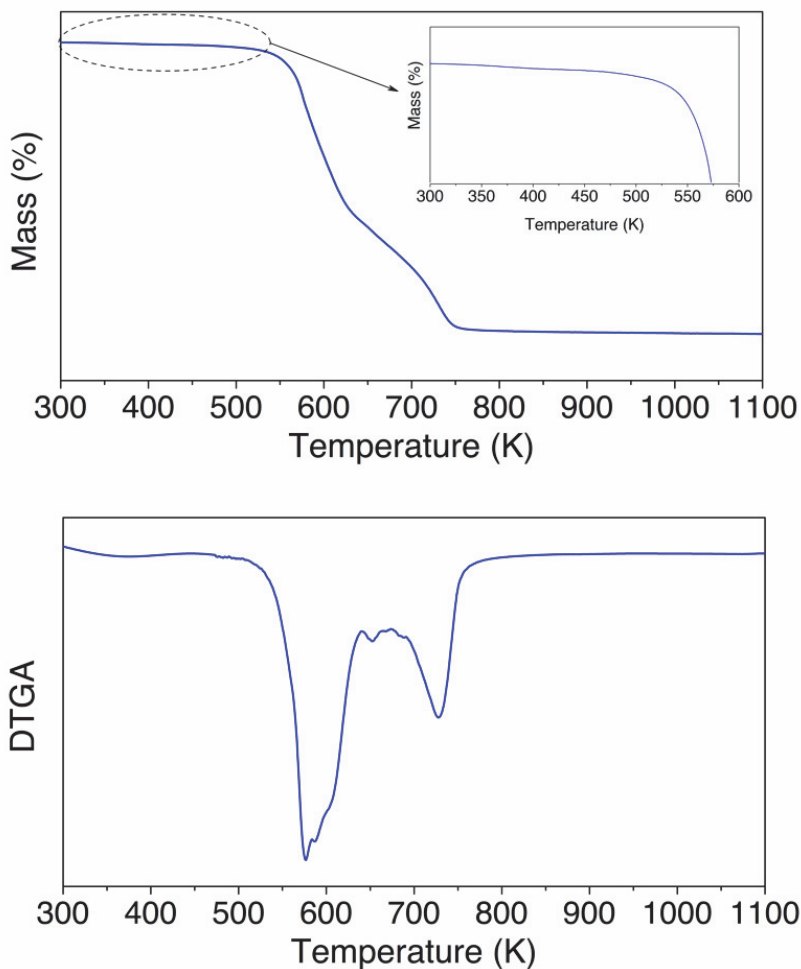


Figure 7.15: Thermogravimetric curves for the HDI-S3-DBTDL-4% sample.

Concerning the low-temperature region, the Arrhenius plot displayed in Figure 7.18 show that the γ_1 and γ_2 processes are mostly indistinguishable since they overlap each other. Subsequently, they must arise from a very similar molecular motion, and a very similar apparent activation energy should be expected. The β -process arises at higher temperatures. This dielectric process displays a lower

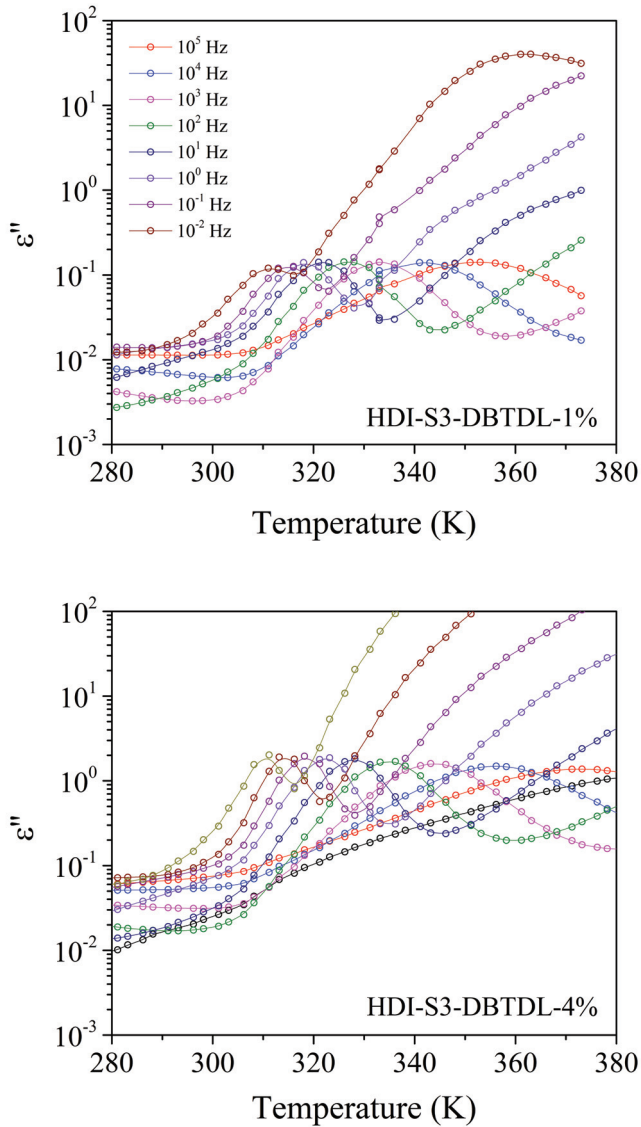


Figure 7.16: Isochronal curves of the imaginary (ϵ'') part of the complex permittivity (ϵ^*) for the HDI-S3-1% and HDI-S3-4%.

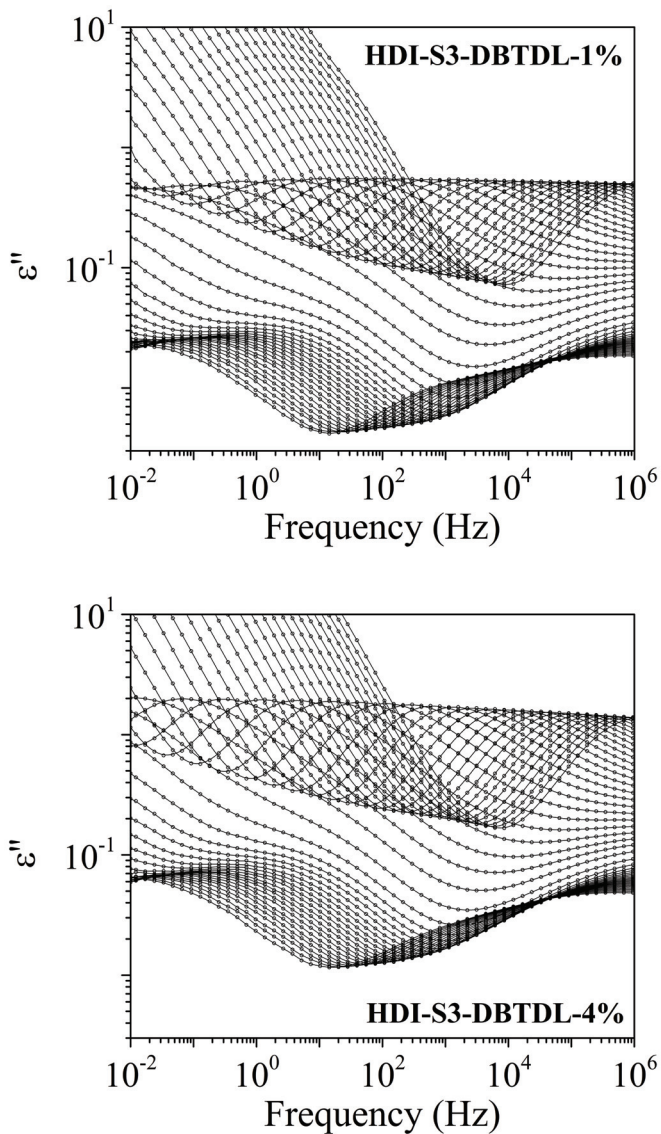


Figure 7.17: Isothermal curves for the HDI-S3-DBTDL 1% and HDI-S3-DBTDL 4% samples between 255.65K and 373K.

intensity and is visible in a narrow temperature range because it is quickly overlapped by another dielectric process appearing at lower frequencies.

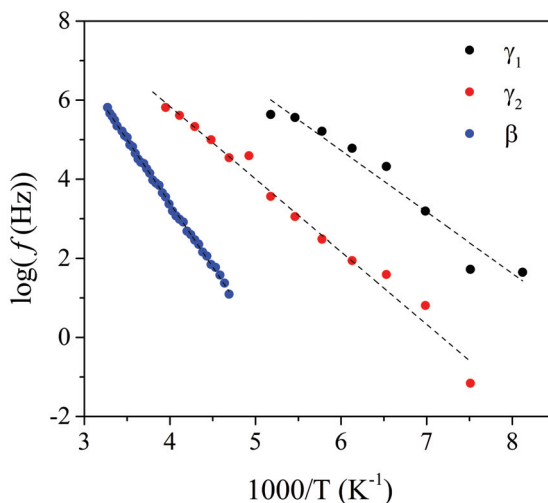


Figure 7.18: Arrhenius plot for the low-temperature zone. Solid lines represent fitted lines.

According to the temperature dependence observed in Figure 7.18, all of them can be assigned a non-cooperative behaviour, and thus, the thermal dependence has been adequately assessed using an Arrhenius function. Consequently, as shown in Table 7.1, the obtained values for the γ_1 , γ_2 and β dielectric processes are 30, 36, and 62 $\text{kJ} \cdot \text{mol}^{-1}$, respectively. Thus, the γ_1 and γ_2 may be related to the motion of $(\text{CH}_2)_n$, which could be found at the catalyst DBTDL pivoting thanks to the carbonyl group and at the end groups of the crosslinked structure, respectively. Concerning the β relaxation there are also some discordances regarding its molecular origin. Nonetheless, the notion that this dielectric process is severely affected by humidity is of general consensus [39-42]. Consequently, the only zones that can be hydrophilic are the carbonyl groups located in the thiourethane and ester moieties.

The Arrhenius plot for the high-temperature relaxation zone is displayed in Figure 7.19. Accordingly, the temperature dependence of all the dielectric re-

laxations is nonlinear. The corresponding parameters are gathered in Table 7.2.

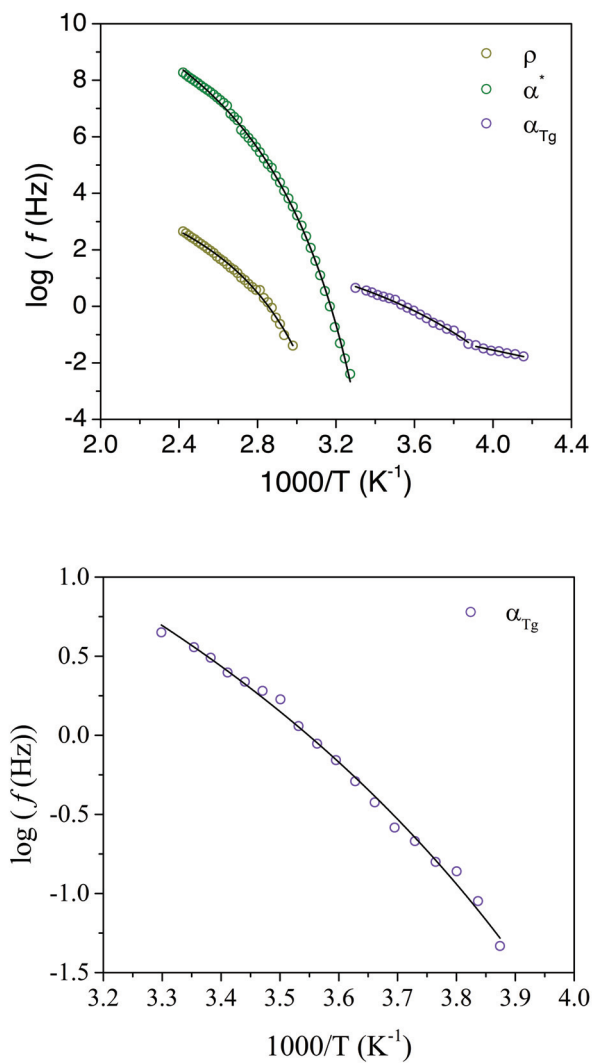


Figure 7.19: Arrhenius plot for the high-temperature zone. Solid lines represent fitted lines.

Figure 7.1: Best fit of the HN parameters for the HDI-S3-DBTDL-4%.

Temperature (K)	α_{HN}	β_{HN}	$\Delta\epsilon$
265.65	0.43	0.98	0.38
270.65	0.43	1	0.39
285.65	0.46	1	0.39
295.65	0.44	1	0.51
298.65	0.44	1	0.55

Figure 7.2: VFTH Parameters and derived parameters for the α_{Tg} , α^* , and ρ dielectric relaxations.

Process	Log f_0 (Hz)	T_{VFTH} (K)	D	Φ_{Tg}	E_{aTg} (kJ·mol ⁻¹)	R ²
α_{Tg}	2.38	257.66	0.54	0.04	268	0.997
α^*	11.81	269.33	4.70	0.03	540	0.999
ρ	5.65	275.92	3.51	0.06	273	0.995

The ρ -process that could be ascribed to the interfacial polarization (Maxwell-Wagner-Sillars (MWS)) due to its heterogeneous microstructure [39-47]. The α_{Tg} -process is overlapped by the dielectric process associated with the bond exchange reaction, as indicated by the red line in Figure 7.20. As shown in Figure 7.21 the catalyst is not inducing significant variations in the α_{Tg} -process, as it would be expected.

This result was already expected because the HDI-S3 is completely cured, which means the crosslinking process is completed. Subsequently, large segmental motions are not expected, while the bond exchange reaction supposes a much greater motion of dipoles. Moreover, this process is found in the same temperature range in DSC, as shown in Figures 7.22. The more prominent α^* , which

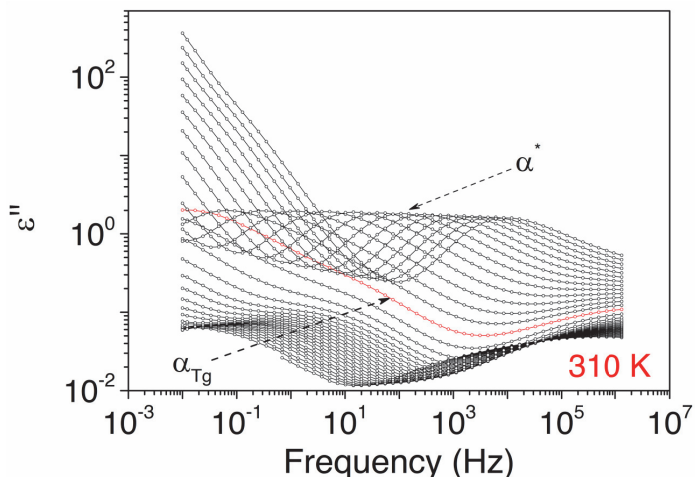


Figure 7.20: Isothermal curves for the HDI-S3-DBTDL-4% sample in the temperature range between 255 and 343 K. The red line signals the onset temperature for the bond exchange reaction.

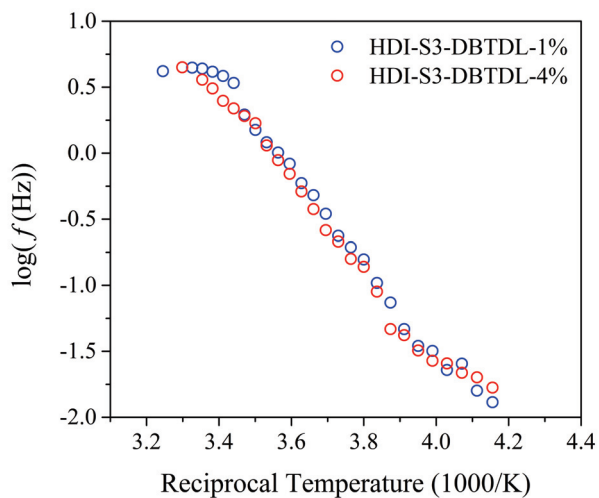


Figure 7.21: Arrhenius plot comparing the α_{Tg} dielectric relaxation for the HDI-S3-DBTDL-1% and HDI-S3-DBTDL-4%.

may be attributed to the molecular dynamics of the bond exchange reaction occurring in this temperature range [48,49].

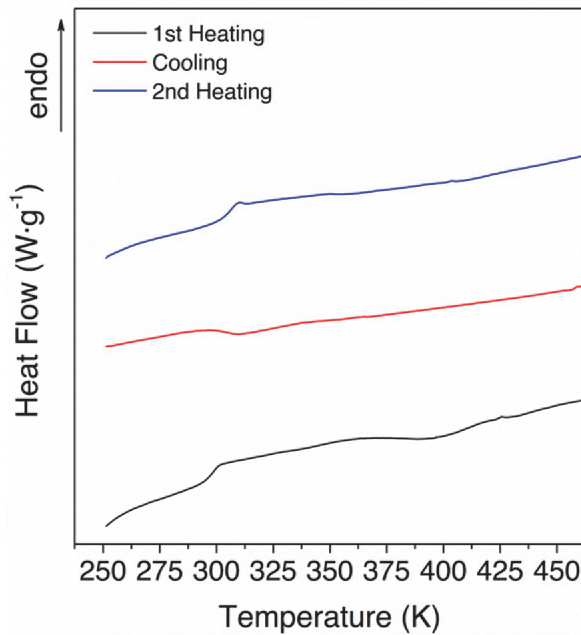


Figure 7.22: DSC thermograms of the 1st heating, cooling, and 2nd heating for the HDI-S3-DBTDL-4% sample.

The Havriliak-Negami shape and strength parameters (α_{HN} , β_{HN} and $\Delta\varepsilon$) corresponding to the α_{Tg} are gathered in Table 7.2. A general review of these parameters indicates that the values of the strength parameter increased with increasing temperature. At low temperatures, this increment is slow, whereas at high temperatures, it increases significantly. This is expected due to the interaction with the α^* -process. In addition, the shape parameters indicated that the relaxation distribution of the α_{Tg} process was similar to the Cole-Cole function. This type of behaviour has already been observed in other thermoset polymers, for instance, the work by Nuñez-Regueira et al. in a cured epoxy DGEBA [50].

The value obtained for the fragility parameter (D) denotes a fragile behaviour. This is expected provided the nature of the dielectric process. The value for the free-volume coefficient of the α^* -process presents an expected normal value, considering that for most systems, this value lies in the interval 0.025 ± 0.005 [51]. On the contrary, the ρ -process displays a higher value (0.06) which can be considered that is overlapped with the bond exchange mechanism, which is already active. Regarding the apparent activation energy (E_a), the α_{T_g} displays a value of $268 \text{ kJ} \cdot \text{mol}^{-1}$. Furthermore, the value for the α^* -process is $513 \text{ kJ} \cdot \text{mol}^{-1}$. This value accounts for the energy associated with the complete molecular dynamics originated in the network once T_v is reached, and can be obtained thanks to the ability of the DETA technique to provide raw data in several orders of magnitude.

The isothermal curves for the modulus of the complex conductivity (σ^*) are plotted in Figures 7.7 and 7.12. The Jonscher's model is used to determine the DC conductivity (σ_{DC}). The values corresponding to the best fit for a selected range of temperatures are gathered in Table 7.3.

Figure 7.3: VFTH Parameters and derived parameters for the α_{T_g} , α^* , and ρ dielectric relaxations.

Temperature (K)	σ_{DC}	$A \cdot 10^{15}$	n	R^2
361	2.20×10^{-11}	8.84×10^1	1	0.904
366	3.67×10^{-11}	5.61×10^3	1	0.998
378	1.12×10^{-10}	8.31×10^2	1	0.997
403	6.96×10^{-10}	8.65×10^1	1	0.977
413	1.42×10^{-09}	6.51×10^1	1	0.959

The n -parameter displays a value of 1, which means that the long-range pathways necessary for ion transfer are not altered. The values of σ_{DC} augment

with increasing temperature, which signifies a thermally activated process. The σ_{DC} values are influenced by the cooperative dielectric relaxations that may be coupled with the ion transferring. Therefore, it shows the influence on the electrical conductivity of the α^* and ρ relaxations. Furthermore, an estimation of the apparent activation energy is done and a value of $129 \text{ kJ} \cdot \text{mol}^{-1}$ is obtained. In a previous article an assessment of the apparent activation energy of the process was performed through stress relaxation. However, in the literature, the apparent activation energy obtained through DETA for stoichiometric thiol systems was found to be $110\text{-}120 \text{ kJ} \cdot \text{mol}^{-1}$ [52,53].

Assessment of the sample's validity as PEM

The values obtained for the proton conductivity (σ_{prot}) are displayed in Figure 7.15. Results show that the conductivity is very low, although it increments with temperature. This is somewhat expected given the characteristic features of the HDI-S3-DBTDL-4%, and this is independent of the catalyst percentage. Indeed, before 310K the values are around 10^{-13} , which is extremely low. The analysis of the σ_{DC} revealed that the conductivity below this temperature could be disregarded. Moreover, the microstructure of the HDI-S3-DBTDL-4% does not contain ionic channels or ionic groups that promotes neither proton hopping or vehicular transport.

On the other hand, an increment in the values of σ_{prot} is observed at temperatures higher than 310 K. This increment is caused by the coupling of the segmental and bond exchange motions with the conductivity. The values of the free-volume coefficient in Table 7.3 for the α^* (0.03) and ρ (0.06) processes reflect this. Subsequently, it is expected that an increment in both electric and proton conductivity occurs, even if the latter is of very low intensity. Nonetheless, at 390 K a value around 10^{-9} is reached, which is still very low for fuel cell applications. Therefore, further structural modifications are needed.

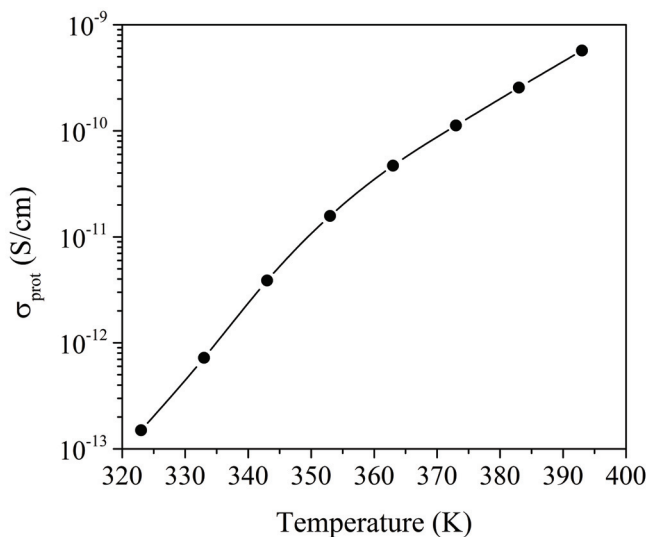


Figure 7.23: Proton conductivity (σ_{prot}) of the HDI-S3-DBTDL-4%.

7.5 Summary

From the work performed in this chapter the following conclusions are reached:

- The absence of an absorption peak characteristic for unreacted isocyanate, together with the appearance of those typical of thiourethane, confirm that the formation of the PTU network was completely successfully.
- DSC data showed that the glass transition temperature is found to be around 310 K, which is in accordance with similar network structures.
- TGA data proved that the HDI-S3-DBTDL does not show significant degradation in the operating temperature of a PEMFC.
- DMA data located the α_{Tg} occurring between 308 K and 322 K. Moreover, an E_a value of $216 \text{ kJ} \cdot \text{mol}^{-1}$ was estimated.

- The dielectric spectra of HDI-S3-DBTDL consists of six dielectric processes: three of them at low temperatures (γ_1 , γ_2 , and β), and the rest are located at higher temperatures (α_{Tg} , α^* , ρ).
- The molecular origin of the γ_1 and γ_2 may be related to the motion of the $(CH_2)_n$, which could be found at the catalyst DBTDL pivoting thanks to the carbonyl group and at the end groups of the crosslinked structure, respectively.
- The molecular origin of the β relaxation is ascribed to the carbonyl groups located in the thiourethane and ester moieties, provided that this relaxation process is severely affected by humidity.
- The dielectric processes α_{Tg} , α^* , and ρ are ascribed to the glass transition, bond exchange, and interfacial polarization, respectively.
- The analysis of the dielectric spectra reveals a temperature range for the bond exchange reaction, from 303 K to 435 K, but the onset temperature where the time scale of the bond exchange becomes more relevant is located at 310 K.
- Incrementing the percentage of catalysts results in a facilitation of the α^* relaxation.
- The analysis of the temperature dependence of σ_{DC} would suggest that the HDI-S3-DBTDL CAN has a dissociative molecular exchange mechanism.
- Results show that σ_{prot} values are very low, although it increments with temperature. The catalyst percentage does not play a role in the proton transport, as expected. The analysis of σ_{prot} shows that it could be disregarded below 310 K. However, an increment is observed at temperatures higher than 310 K. Nonetheless, at 390 K a value around 10^{-9} is reached, which is still very low for fuel cell applications. Future work to fine-tuning these set of membranes to increment σ_{prot} is needed.

7.6 References

- [1] N.J. Van Zee, R. Nicolaÿ, Vitrimers: Permanently crosslinked polymers with dynamic network topology, *Prog. Polym. Sci.* 104 (2020) 101233.
- [2] W. Alabiso, S. Schlögl, The impact of vitrimers on the industry of the future: Chemistry, properties and sustainable forward-looking applications, *Polymers (Basel)* 12 (2020) 1660.
- [3] W. Denissen, J.M. Winne, F.E. Du Prez, Vitrimers: Permanent organic networks with glass-like fluidity, *Chem. Sci.* 7 (2016) 30-38.
- [4] Harada, A., Takashima, Y., From molecular to macroscopic level science of self-healing materials, *Chemical Society Reviews*, 45 (2016) 4792-4828.
- [5] Yang, J., Ye, Y., Pan, X., Covalent adaptable networks: A versatile platform for designing self-healing materials, *Chemical Engineering Journal* 381 (2020) 122635.
- [6] Chen, Q., Liang, S., Thouas, G. A., Elastomer, R., Covalent adaptable networks: smart, reconfigurable and responsive network systems, *Polymer Chemistry* 10 (2019) 5831-5844.
- [7] Ghosh, S., Saha, S., Covalent Adaptable Networks: Progress in Synthesis and Applications, *ACS Applied Polymer Materials*, 2 (2020) 2446-2467.
- [8] Huang, L., Li, J. Covalent adaptable networks for advanced applications, *Journal of Materials Chemistry A*, 8 (2020) 14954-14970.
- [9] Liu, H., Liu, H., Wang, Y., Lin, H., Wang, Z., Imine-based covalent adaptable networks as proton exchange membranes with high conductivity and stability, *ACS Applied Materials & Interfaces*, 11 (2019) 21817-21825.
- [10] Li, X., Wang, R., Zhou, S., Shen, J., Xu, G., Synthesis and characterization of boronic acid-based covalent adaptable networks as proton exchange

- membranes for fuel cell applications, *Journal of Power Sources* 473 (2020) 228632.
- [11] Mecheri, B., Peng, X., Hui, X., Ji, X., Li, Y., Li, W., Ma, X., Covalent adaptable network membranes for proton exchange membranes fuel cells, *Journal of Membrane Science* 599 (2020) 117812.
- [12] Li, Y., Peng, X., Ji, X., Wu, M., Ma, X., Covalent adaptable network membranes with improved stability and proton conductivity for high temperature proton exchange membrane fuel cells, *Journal of Membrane Science* 563 (2018) 510-518.
- [13] Peng, X., Li, Y., Ji, X., Ma, X., Design and application of covalent adaptable network membranes in proton exchange membrane fuel cells, *Energy & Environmental Science*, 12 (2019) 2386-2407.
- [14] Chen, W., Fan, J., Guo, Y., Wang, Y., Synthesis and characterization of poly(thiourea-urethane) networks with tunable mechanical properties, *Polymer Chemistry* 10 (2019) 2467-2475.
- [15] Abd El-Hady, B., Osman, M. A., Abdelrazek, E. M., Darwish, S. M., Biocompatible poly(thiourea-urethane) elastomers as promising materials for tissue engineering applications: Synthesis, characterization and in vitro cytotoxicity evaluation, *Materials Science and Engineering: C* 118 (2021) 111419.
- [16] Zare, Y., Mansoori, Y., Ghasemi, I., Poly(thiourethane) as a new material for supercapacitor application: Electrochemical properties and energy storage performance, *Journal of Applied Polymer Science* 138 (2021) 50057.
- [17] Lendlein, A., Kelch, S., Shape-memory polymers, *Angewandte Chemie International Edition*, 41 (2002) 2034-2057.

- [18] Duan, J., Yan, Y., Zhang, X., Zhou, J., Synthesis and characterization of novel poly(thiourea-urethane) elastomers based on N-methylated urethane diisocyanate, *Journal of Polymer Research* 28 (2021) 1-10.
- [19] F. Gamardella, S. De la Flor, X. Ramis, A. Serra, Recyclable poly(thiourethane) vitrimers with high T_g . Influence of the isocyanate structure, *React. Funct. Polym.* 151 (2020) 104574.
- [20] F. Gamardella, F. Guerrero, S. De la Flor, X. Ramis, A. Serra, A new class of vitrimers based on aliphatic poly(thiourethane) networks with shape memory and permanent shape reconfiguration, *Eur. Polym. J.* 122 (2020) 109361.
- [21] F. Gamardella, S. Muñoz, S. De la Flor, X. Ramis, A. Serra, Recyclable organocatalyzed poly(Thiourethane) covalent adaptable networks, *Polymers (Basel)* 12 (2020) 1-18.
- [22] T. Saito, Y. Gotoh, and T. Ota, "Thermal Properties and Morphology of Crosslinked Polyurethane-Polythiourethane Blends," *Polymer Journal*, vol. 33, no. 7, pp. 566-572, 2001.
- [23] C. M. J. Huynh, R. S. Porter, and S. S. Gubbins, Molecular Modeling of Polyurethane and Polythiourethane Networks: Effect of Thiourea Linkages on Thermomechanical Properties, *Macromolecules* 34 (2001) 5632-5641.
- [24] X. Jia, H. Lu, and J. Shen, Thermal Properties and Crosslinking Behavior of Polyurethane-Polythiourethane Hybrid Coatings, *Progress in Organic Coatings* 85 (2015) 22-29.
- [25] Y. Li, H. Xu, Q. Lu, Y. Yang, and W. Yu, Thermal Properties and Crosslinking Structure of Polyurethane/Polythiourethane Networks, *Journal of Applied Polymer Science* 135 (2018) 46167-46174.

-
- [26] K. Radhakrishnan, C. Prasanthi, R. Viswanathan, and S. Sivaramakrishnan, Synthesis, Characterization and Thermal Properties of Polyurethane-Polythiourethane Blends, *Journal of Applied Polymer Science* 90 (2003) 2382-2387.
- [27] Cheng, H., Liu, Y., Poly(thiourethane): Synthesis and properties. *Journal of Applied Polymer Science* 134 (2017) 44781.
- [28] Li, Y., Li, L., Li, H., Wu, Y., Liu, Q., Li, X., Thermally stable poly(thiourethane-urethane)s with controllable glass transition temperature, *Journal of Polymer Science Part A: Polymer Chemistry*, 54 (2016) 1731-1738.
- [29] Zhu, M., Cao, S., Zhang, H., Wang, Y., Cao, X. Synthesis and properties of poly(thiourethane) networks containing both urea and thiourea moieties, *Polymer Chemistry* 10 (2019) 1013-1023.
- [30] Lee, H., Lee, K. Y., Shin, J. H., Lee, J. H., Kim, B. S., Biocompatible and biodegradable poly(thiourethane-urea)s: Synthesis, characterization, and cytotoxicity, *Polymer Bulletin* 74 (2017) 1925-1940.
- [31] Bai, Y., Zeng, Y., Wu, L., Wang, J., Zhang, L., Chen, S. Synthesis, characterization and thermal properties of novel poly(thiourethane-urethane) thermosets, *Polymer* 224 (2021) 123852.
- [32] A. Arshadi and S. A. Mousavi, "Dielectric Spectroscopy of Polyurethane and Polythiourethane Films," *Polymer Engineering and Science*, vol. 53, no. 4, pp. 785-793, 2013.
- [33] R. F. Nunes and L. C. Costa, "Dielectric Relaxation Spectroscopy of Polyurethane and Polyurethane-Polyaniline Blends," *Journal of Applied Polymer Science*, vol. 117, no. 4, pp. 2004-2012, 2010.

- [34] R. T. Krishnan and S. Thomas, "Dielectric Relaxation Spectroscopy of Polyurethane-Polysiloxane Copolymer Blends," *Journal of Applied Polymer Science*, vol. 116, no. 2, pp. 714-722, 2010.
- [35] A. S. Ameen and A. Arshadi, "Influence of Molecular Weight on Dielectric Properties of Polythiourethane Films," *Polymer Engineering and Science*, vol. 58, no. 7, pp. 1206-1213, 2018.
- [36] J. P. Sanetra and R. P. Singh, "Dielectric Relaxation and Conductivity in Polyurethane and Polyurea Nanocomposites," *Journal of Applied Polymer Science*, vol. 112, no. 6, pp. 3619-3629, 2009.
- [37] F. Gamardella, A. Serra, X. Ramis, S. De la Flor, Actuator behaviour of tailored poly(Thiourethane) shape memory thermosets, *Polymers (Basel)* 13 (2021).
- [38] M. Rogulska, A. Kultys, E. Olszewska, New thermoplastic poly(thiourethane-urethane) elastomers based on hexane-1,6-diyl diisocyanate (HDI), *J. Therm. Anal. Calorim.* 114 (2013) 903-916.
- [39] W. Yu, M. Du, D. Zhang, Y. Lin, Q. Zheng, Influence of dangling chains on molecular dynamics of polyurethanes, *Macromolecules* 46 (2013) 7341-7351.
- [40] A.M. Castagna, D. Fragiadakis, H. Lee, T. Choi, J. Runt, The role of hard segment content on the molecular dynamics of poly(tetramethylene oxide)-based polyurethane copolymers, *Macromolecules* 44 (2011) 7831-7836.
- [41] A. Kanapitsas, P. Pissis, Dielectric relaxation spectroscopy in crosslinked polyurethanes based on polymer polyols, *Eur. Polym. J.* 36 (2000) 1241-1250.
- [42] G. Georgoussis, A. Kyritsis, P. Pissis, Y. V. Savelyev, E.R. Akhranovich, E.G. Privalko, V.P. Privalko, Dielectric studies of molecular mobility and

- microphase separation in segmented polyurethanes, *Eur. Polym. J.* 35 (1999) 2007-2017.
- [43] D. Fragiadakis, J. Runt, Molecular dynamics of segmented polyurethane copolymers: Influence of soft segment composition, *Macromolecules* 46 (2013) 4184-4190.
- [44] A. Kanapitsas, P. Pissis, J.L. GomezRibelles, M. Monleon Pradas, E.G. Privalko, V.P. Privalko, Molecular Mobility and Hydration Properties of Segmented Polyurethanes with Varying Structure of Soft- and Hard-Chain Segments, *J. Appl. Polym. Sci.* 71 (1997) 1209-1221.
- [45] K.N. Raftopoulos, B. Janowski, L. Apekis, K. Pielichowski, P. Pissis, Molecular mobility and crystallinity in polytetramethylene ether glycol in the bulk and as soft component in polyurethanes, *Eur. Polym. J.* 47 (2011) 2120-2133.
- [46] C. Tsonos, L. Apekis, K. Viras, L. Stepanenko, L. Karabanova, L. Sergeeva, Electrical and dielectric behavior in blends of polyurethane-based ionomers, *Solid State Ionics* 143 (2001) 229-249.
- [47] P. Pissis, A. Kanapitsas, Y. V. Savelyev, E.R. Akhranovich, E.G. Privalko, V.P. Privalko, Influence of chain extenders and chain end groups on properties of segmented polyurethanes. II. Dielectric study, *Polymer (Guildf)* 39 (1998) 3431-3435.
- [48] C. Bowman, F. Du Prez, J. Kalow, Introduction to chemistry for covalent adaptable networks, *Polym. Chem.* 11 (2020) 5295-5296.
- [49] S.K. Schoustra, T. Groeneveld, M.M.J. Smulders, The effect of polarity on the molecular exchange dynamics in imine-based covalent adaptable networks, *Polym. Chem.* 12 (2021) 1635-1642.
- [50] L. Nuñez-Regueira, C.A. Gracia-Fernandez, S. Gomez-Barreiro, Characterization of a thermoset by thermal analysis techniques: Criterion to

assign the value of the α -transition temperature by dielectric analysis, *J. Appl. Polym. Sci.* 96 (2005) 2027-2037.

- [51] E. Riande, R. Diaz-Calleja, M. Prolongo, R. Masegosa, C. Salom, *Polymer viscoelasticity: stress and strain in practice*, 1st ed., CRC Press, 2000.
- [52] M. Podgorski, N. Spurgin, S. Mavila, C.N. Bowman, Mixed mechanisms of bond exchange in covalent adaptable networks: monitoring the contribution of reversible exchange and reversible addition in thiolsuccinic anhydride dynamic networks, *Polym. Chem.* 11 (2020) 5365-5376.
- [53] N.J. Bongiardina, K.F. Long, M. Podgorski, C.N. Bowman, Substituted Thiols in Dynamic ThiolThioester Reactions, *Macromolecules.* 54 (2021) 8341-8351.

Part III

Conclusions & Future work

Chapter 8

Conclusions and future work

8.1 Conclusions

The main goal of this thesis was to develop a robust and reliable procedure, that allows designing proton exchange membranes, by means of characterizing and analysing polymeric materials to predict, through dielectric thermal analysis (DETA), their behaviour in operating conditions.

Consequently, the main conclusions of this thesis are organized according to the different types of polymeric microstructures analysed. Accordingly, in Chapter 8 a summary of the main findings discussed in Chapters 4, 5, 6, and 7 is presented.

8.1.1 Membranes based on block copolymers

The analysis of the dielectric spectra of membranes prepared with styrene-ethylene-butylene-styrene block copolymer (SEBS), mixed with divinylbenzene (DVB), photocrosslinked, and subsequently sulfonated with different degrees of sulfonation revealed that the membrane with more free volume and more molecular mobility was the one with the highest proton conductivity. Thus, the highest values were found for the SEBS-25DVB-30I-S1 membrane, despite not being the most sulfonated. Therefore, a linear increase of the sulfonation does not necessarily imply a linear increase in the number of atoms with the ability to move.

Regarding the hybrid membranes, the analysis of the dielectric spectra revealed that increasing the infiltration time (τ_{inf}) induces the α_{EB} relaxation to be shifted towards higher temperatures because the dynamic crosslinking delays this molecular motion. Moreover, increasing τ_{inf} also affects the α_{PS} relaxation, facilitating the chain motion, and therefore, it is shifted towards lower frequencies and temperatures. This is important since it has an effect on σ_{DC} that displays a different behaviours depending on the coupling/uncoupling with the segmental motions, which undoubtedly affects the proton conductivity. To that respect, the sSEBS-10 ($\tau_{inf} = 10min$) was found to be the best performer, and subsequently, it was found that high values of τ_{inf} resulted in an excessive

amount of M-O-M' bonds that generate a competition for the available proton sites. In general, the numerical results are in agreement with the experimental ones.

8.1.2 Membranes based on nanocomposite and crosslinked membranes

Provided that these set of membranes were developed to be used primarily in DMFCs, it was demonstrated that the balance between both the proton conductivity and the ability of the membrane to slow down the crossover process is essential for a successful application. Furthermore proton conductivity increases with the inclusion of GO until a percentage of 0.50 wt%, the presence of GO in the membranes decreases the absorption of the methanol solution further as GO content increased. Therefore, the membranes with GO proportion of 0.75 wt% combined good proton conductivity and high resistance to methanol permeability and exhibited appropriated behaviour with lower hydration levels for being used as polyelectrolytes in DMFC. In general, the numerical results are in agreement with the experimental ones.

8.1.3 Membranes based on liquid crystals

The analysis of the dielectric spectra of membranes prepared with PECH40 and PECH80 revealed that the dendritic side chains induces a crystalline order, which somewhat constrains the α_{Tg} relaxation process of the amorphous portions. Furthermore, the dynamic fragility displays lower values for PECH80 copolymers than the PECH40 ones, and the self-organized columnar structure is more stable at temperatures below the glass transition. Near the glass transition, the crank-shaft movement promotes a quicker loosening of the ordered glass structure in PECH80 than in PECH40.

The analysis of the copolymer membranes showed that CP0 displayed the highest values of σ_{DC} . In contrast, CP40 was the worst performer. The reason were

the high levels of restrictions imposed by the high concentration of dendrimers. The analysis of σ_{prot} confirms that the thermal orientation process combined with a high concentration of dendrimers can enhance σ_{prot} while maintaining low enough electric conductivity values.

8.1.4 Membranes based on covalent adaptable networks

The analysis of the dielectric spectra reveals a temperature range for the bond exchange reaction, from 303 K to 435 K, but the onset temperature where the time scale of the bond exchange becomes more relevant is located at 310 K. The analysis of the temperature dependence of σ_{DC} would suggest that the HDI-S3 CAN has a dissociative molecular exchange mechanism. Results show that σ_{prot} values are very low, although it increments with temperature. The analysis of σ_{prot} shows that it could be disregarded below 310 K. However, an increment is observed at temperatures higher than 310 K. Nonetheless, at 390 K a value around 10^{-9} is reached, which is still very low for fuel cell applications.

8.2 Future work

The main objective of this doctoral thesis has been to develop a methodology that allows the analysis of various polymeric membranes with different microstructures through Dielectric Thermal Analysis (DETA), with the purpose to determine structure-property relationships that will provide insights into the molecular dynamics, which efficiently favours the charge transfer mechanisms, with special focus on proton transport. Indeed, given that this methodology provides reliable results, i.e., it allows to understand how the molecular motions can promote or prevent proton conduction in simulated operating conditions, future work is related to the improvement of the characteristics of some of the polymers studied which displayed promising features.

Furthermore, a future work would be the development of new cost-effective non-fluorinated polymer membranes. Accordingly, membranes from agri-waste

residues like cellulose nanofibers, chitosan/lignin, or PVA/SSA together with a cellulose hydrogel will be developed. Hopefully, this new set of membranes would solve the technological drawbacks found on the current samples, together with a subsequent reduction of costs which would result in a mass usage of fuel cell technology.

Additionally, another very important aspect to assess is the post-mortem analysis of the membranes. Currently, numerical methods used to assess the service life of the membranes. In the proposed research line, the obtained results would be validated through DETA analysis in combination with experimental data obtained from test rigs (monocell or stack) where real operating conditions can be applied. Moreover, new test rigs would be fabricated focusing on test that characterize only the proton conduction through the membrane. Subsequently, this research would provide more realistic data that definitely provides the causes of the membrane failure in real operating conditions. Therefore, the obtained results contribute to enhance the operation of proton exchange membranes, as a means to improve the efficiency of PEMFCs, and to promote their implementation on a mass usage.

All this future work is already endorsed by several research projects that have already been granted, and are already in the execution phase.

- **POLYELMETH:** Desarrollo, Validacion y Comportamiento en Servicio de Polielectrolitos para Pilas de Combustible y Electrolizadores Reversibles de Metanol, and is supported by the Spanish Ministry of Science and Innovation (PID2020-116322RB-C31).
- **INNOMAT-H2:** Diseño y validación de materiales innovadores para su desarrollo como electrolitos de pilas de combustible de intercambio protonico en vehículos project that forms part of the Advanced Materials programme, and is supported by the Spanish Ministry of Science and Innovation with funding from the European Union NextGenerationEU (PRTR-C17.11) and by Generalitat Valenciana.

- **DEFIANCE:** Definition of fuel cell powertrain architectures for the decarbonization of road freight transport supporting the hydrogen economy deployment, and is supported by Generalitat Valenciana (CIPROM / 2021 / 039).
- **DIVERGENT:** Diseño de Estrategias de Control Avanzadas para la Nueva Generacion de Camiones de Pila de Combustible Promoviendo la Descarbonizacion del Sector Transporte, and is supported by the Spanish Ministry of Science and Innovation with funding from the European Union NextGenerationEU (TED2021-131463B-I00).

Part IV

Annexes

Chapter 9

Dissemination of research results

In Chapter 9 a list of the scientific articles that have been published in indexed JCR journals, together with the list of scientific congresses attended have been included. Accordingly, Contribution 1 is related to the content developed in Chapter 3. Contributions 2-4 refer to the results discussed in Chapter 4. Contribution 5 refers to the results discussed in Chapter 5. Contributions 6-8 refer to the results discussed in Chapter 6. Finally, Contribution 9 refers to the results discussed in Chapter 7.

9.1 Scientific publications indexed in JCR journals

- **Contribution 1:** Analysis of plasticization and reprocessing effects on the segmental cooperativity of polylactide by dielectric thermal spectroscopy. DOI: <https://doi.org/10.1016/j.polymer.2021.123701>.
- **Contribution 2:** Dielectric analysis of photocrosslinked and post-sulfonated styrene-ethylene-butylene-styrene block copolymer based membranes. DOI: <https://doi.org/10.1016/j.reactfunctpolym.2020.104715>.
- **Contribution 3:** Dielectric properties OF 40SiO₂40P₂O₅20ZrO₂ /sulfonated styrene-ethylene-butylene-styrene hybrid membranes for proton exchange membrane fuel cells. DOI: <https://doi.org/10.1016/j.polymer.2023.125814>.
- **Contribution 4:** Charge transfer mechanisms in 40SiO₂40P₂O₅20ZrO₂ /sulfonated styrene-ethylene-butylene-styrene hybrid membranes for low temperature fuel cells. DOI: <https://doi.org/10.1016/j.polymer.2022.125436>.
- **Contribution 5:** Performance of Sulfonated Poly(Vinyl Alcohol)/Graphene Oxide Polyelectrolytes for Direct Methanol Fuel Cells. <https://doi.org/10.1002/ente.202000124>.
- **Contribution 6:** Effect of Dendritic Side Groups on the Mobility of Modified Poly (epichlorohydrin) Copolymers. <https://doi.org/10.3390/polym13121961>.
- **Contribution 7:** Membranes for Cation Transport Based on Dendronized Poly (epichlorohydrin-co-ethylene oxide). Part 1: The Effect of Dendron Amount and Column Orientation on Copolymer Mobility. <https://doi.org/10.3390/polym13203532>.

- **Contribution 8:** Dielectric Properties in Oriented and Unoriented Membranes Based on Poly (Epichlorohydrin-co-Ethylene Oxide) Copolymers : Part III. <https://doi.org/10.3390/polym14071369>.
- **Contribution 9:** Analysis of Poly(thiourethane) Covalent Adaptable Network through Broadband Dielectric Spectroscopy. <https://doi.org/10.1021/acsapm.2c01543>.

9.2 Scientific Congresses

Here is the list of all the scientific congresses attended during the time of execution of the present PhD thesis.

1. XI Congreso Nacional y II Internacional de Ingeniería Termodinámica (11-CNIT, 2019).
2. 7th International Conference on Biobased and Biodegradable Polymers (BIOPOL, 2019).
3. XII National and y III International Conference on Engineering Thermodynamics (12-CNIT, 2022).
4. XVI Meeting of the Group Specialized in Polymers of the Spanish Royal Society of Chemistry and Spanish Royal Society of Physics (GEP-SLAP, 2022).
5. 11th Conference on Dielectric Spectroscopy and its applications (BDS, 2022).

